Method development for biomolecular solid-state NMR spectroscopy

Accessing structure and dynamics of biomolecules in the solid-state

D I S S E R T A T I O N

zur Erlangung des akademischen Grades

doctor rerum naturalium
(Dr. rer. nat.)
im Fach Biophysik

eingereicht an der
Mathematisch-Naturwissenschaftlichen Fakultät I
der Humboldt-Universität zu Berlin

von
Dipl.-Biochem. Sam Asami

Präsident der Humboldt-Universität zu Berlin:
Prof. Dr. Jan-Hendrik Olbertz

Dekan der Mathematisch-Naturwissenschaftlichen Fakultät I:
Prof. Stefan Hecht, Ph.D.

Gutachter:
1. Prof. Dr. Bernd Reif
2. Prof. Dr. Andreas Möglich
3. Prof. Dr. Hartmut Oschkinat

Tag der mündlichen Prüfung: 14.01.2014

Meinen Eltern, meinem Bruder, meinen Freunden

Abstract

The investigation of the structure and dynamics of biomolecules is fundamental for the understanding of their functional activity. Solid-state Nuclear Magnetic Resonance (NMR) spectroscopy provides a methodology to access both at an atomic level. Traditionally, solid-state NMR employs the detection of heteronuclei with low gyromagnetic ratios, which compromise the spectral sensitivity. Protons have the largest gyromagnetic ratio and their direct detection is, in principle, most beneficial in terms of sensitivity. As opposed to molecules in solution, for which ^{1}H,^{1}H dipolar couplings are averaged to zero by molecular tumbling, these interactions are retained in the solid-state and cause severe line broadening. Deuteration chemically dilutes the ^{1}H,^{1}H dipolar coupling network and was recently shown to enable proton detection of amide and methyl resonances in perdeuterated and selectively Ile/Leu/Val methyl-labeled protein samples, respectively. Resonances, other than methyls, however, could not be observed in deuterated samples, so far. In particular, ^{1}Hα,^{13}Cα sites are important probes for structure and dynamics.

In this thesis, a novel labeling scheme for solid-state NMR spectroscopy, the Reduced Adjoining Protonation (RAP) scheme, is introduced, which allows proton detection of all aliphatic sites, as shown for the microcrystalline SH3 domain of α-spectrin. The protein was expressed in *E. coli*, using a minimal medium, containing uniformly deuterated ^{13}C-glucose and 5-25% H_2O (95-75% D_2O), respectively. These samples yield high-resolution, ^{1}H-detected ^{1}H,^{13}C correlation spectra. The proton line widths are on the order of 0.04-0.1 ppm (25-60 Hz at a ^{1}H Larmor frequency of 600 MHz), employing scalar coupling based magnetization transfers at a Magic Angle Spinning (MAS) frequency of 20 kHz, while high-power decoupling of protons was not required. In addition, the benefit of high MAS frequencies was investigated. We find, that the sensitivity can be increased by a factor of 4-4.5, raising the MAS frequency from 20 kHz to 60 kHz.

^{1}H- and ^{13}C-detected 3D assignment experiments are implemented, which allowed us to assign 90% of the ^{1}Hα,^{13}Cα backbone and side chain resonances of α-spectrin SH3. As the chemical shift is dependent on the structural motif, it can be employed to derive secondary structure information. Furthermore, a ^{1}H-detected H(H)CH 3D experiment is introduced, to obtain long-range ^{1}H,^{1}H contacts, which can be used for the determination of the tertiary structure.

To obtain artifact-free relaxation data, the RAP labeling scheme was modified. Use of deuterated glycerol with alternating $^{12}C/^{13}C$ labeling yields sparsely proton labeled, ^{13}C dilute samples, in which spin diffusion is suppressed. To probe sub-microsecond dynamics, we report experiments to determine ^{13}C T_1 relaxation times and $^{1}H,^{13}C$ dipolar coupling tensors for backbone and side chain resonances, respectively. The latter give direct access to model-free order parameters. The combination of RAP-glycerol labeling and fast spinning is shown to sufficiently suppress coherent contributions, which currently distort the quantification of dynamics in the solid-state, and enable the determination of motional amplitudes and correlation times.

Furthermore, we show, that the RAP labeling scheme can be applied to non-crystalline systems, such as amyloid fibrils of the Alzheimer's disease peptide $A\beta_{1\text{-}40}$. Using ^{1}H-detection, we obtained high-resolution $^{1}H,^{13}C$ correlation spectra, which are essential for investigating the structure and dynamics of the fibrils.

Finally, we applied the perdeuteration approach to the L7Ae-box C/D protein-RNA complex from *P. furiosus*, which is involved in site-specific ribose methylation. We obtained high-resolution, ^{1}H-detected $^{1}H,^{15}N$, as well as $^{13}C,^{13}C$ correlation spectra of the protein-RNA complex. In addition, we established a methodology to determine accurate distance and angular restraints for the protein-RNA interface and propose approaches for the chemical shift assignment of RNA resonances.

Zusammenfassung

Die Erforschung der Struktur und Dynamik von Biomolekülen ist wesentlich für das Verständnis über ihre Funktion. Festkörper-Kernresonanz-Spektroskopie (NMR) ermöglicht eine Untersuchung beider Aspekte auf atomarer Ebene. Üblicherweise nutzt die Festkörper-NMR die Detektion von Heterokernen mit kleinem gyromagnetischen Verhältnis, wodurch die spektrale Sensitivität beeinträchtigt wird. Protonen besitzen das größte gyromagnetische Verhältnis und daher ist ihre direkte Detektion, in Bezug auf die Sensitivität, vorteilhaft. Im Gegensatz zu Molekülen im Lösungsmittel, für welche ^{1}H,^{1}H dipolare Kopplungen durch molekulares Taumeln zu Null gemittelt sind, bleiben diese Interaktionen im Festkörper bestehen und verursachen starke Linienverbreiterungen. Das ^{1}H,^{1}H dipolare Kopplungsnetzwerk wird durch Deuterierung chemisch verdünnt und ermöglicht, wie kürzlich gezeigt, die Protonendetektion von Amid- und Methyl-Resonanzen in perdeuterierten bzw. selektiv Ile/Leu/Val Methyl-markierten Proteinproben. Ausgenommen von Methylen, konnten bisher jedoch keine weiteren Resonanzen in deuterierten Proben beobachtet werden. Insbesondere sind ^{1}Hα,^{13}Cα Reste wichtige Messsonden für Struktur und Dynamik.

Im Rahmen der vorliegenden Arbeit, wird ein neuartiges Markierungsschema für die Festkörper-NMR-Spektroskopie vorgestellt, das sogenannte *Reduced Adjoining Protonation* (RAP) Schema, welches die Protonendetektion sämtlicher Aliphaten erlaubt, so wie hier gezeigt für die mikrokristalline SH3 Domäne von α-Spektrin. Das Protein wurde in *E. coli* im Minimalmedium exprimiert, welches uniform deuterierte ^{13}C-Glucose, sowie 5-25% H_2O (95-75% D_2O) enthielt. Hochaufgelöste, ^{1}H-detektierte ^{1}H,^{13}C Korrelationsspektren wurden erhalten. Die Protonenlinienbreiten sind in der Größenordnung von 0.04-0.1 ppm (25-60 Hz bei einer ^{1}H Larmorfrequenz von 600 MHz), unter Verwendung von Magnetisierungstransfers, basierend auf der skalaren Kopplung, bei einer Rotationsfrequenz im magischen Winkel (MAS) von 20 kHz, während eine Hochleistungsentkopplung von Protonen nicht erforderlich war. Des Weiteren wurde der Vorteil von hohen MAS-Frequenzen untersucht. Dabei stellten wir fest, dass die Sensitivität um einen Faktor 4-4.5 gesteigert werden kann, wenn die MAS Frequenz von 20 kHz auf 60 kHz gesteigert wird.

^{1}H- und ^{13}C-detektierte 3D Zuordnungsexperimente wurden implementiert, welche uns die Zuordnung von 90% der ^{1}Hα,^{13}Cα Rückgrat- und Seitenketten-Resonanzen von α-Spektrin SH3 erlaubten. Da die chemische Verschiebung abhängt vom Strukturmotiv, kann sie verwendet werden, um Sekundärstruktur-Informationen abzuleiten. Darüber hinaus

wurde ein ^{1}H-detektiertes H(H)CH 3D Experiment entwickelt, um weitreichende ^{1}H,^{1}H Kontakte zu ermitteln, welche für die Bestimmung der Tertiärstruktur genutzt werden können.

Um artefaktfreie Relaxationsdaten zu erhalten, wurde das RAP-Markierungsschema modifiziert. Bei der Verwendung von deuteriertem Glycerol mit alternierender ^{12}C/^{13}C Markierung werden ^{1}H- und ^{13}C-verdünnte Proben erhalten, in denen Spindiffusion unterdrückt ist. Für die Untersuchung von Sub-Mikrosekunden-Dynamik werden Experimente vorgestellt zur Bestimmung von ^{13}C T_1 Relaxationszeiten und ^{1}H,^{13}C dipolaren Kopplungstensoren für Rückgrat- und Seitenketten-Resonanzen. Letztere gewähren den direkten Zugang zu Modell-unabhängigen Orderparametern. Es wird gezeigt, dass die Kombination aus RAP-Glycerol-Markierung und schneller Rotation kohärente Beiträge, welche derzeitig die Quantifizierung von Dynamik im Festkörper verfälschen, hinreichend unterdrückt und dabei die Ermittlung von Amplituden und Korrelationszeiten von Bewegungen ermöglicht.

Des weiteren zeigen wir, dass das RAP-Markierungsschema auf nicht-kristalline Systeme, wie Amyloidfibrillen des $A\beta_{1\text{-}40}$ Peptids der Alzheimer-Krankheit, angewendet werden kann. Unter Verwendung von ^{1}H-Detektion, erhielten wir hochaufgelöste ^{1}H,^{13}C Korrelationsspektren, welche essenziell für die Untersuchung von Struktur und Dynamik der Fibrillen sind.

Schließlich wurde der Perdeuterierungsansatz auf den L7Ae-box C/D Protein-RNA Komplex aus *P. furiosus* angewendet, welcher an spezifischer Ribose-Methylierung beteiligt ist. Wir erhielten hochaufgelöste, ^{1}H-detektierte ^{1}H,^{15}N, sowie ^{13}C,^{13}C Korrelationsspektren des Protein-RNA Komplexes. Weiterhin haben wir eine Methode zur Bestimmung genauer Abstands- und Winkelinformationen für die Protein-RNA Schnittstelle etabliert und schlagen Ansätze vor, für die Zuordnung der chemischen Verschiebungen von RNA-Resonanzen.

Contents

Abbreviations

AEC Anion-Exchange Chromatography

AF *Archaeoglobus fulgidus*

APP β-amyloid precursor protein

BPTI Bovine Pancreatic Trypsin Inhibitor

CP cross polarization

CPPI cross polarization phase-inverted

CSA Chemical Shift Anisotropy

CSD Chemical Shift Anisotropy Enabled Spin Diffusion

CV column volume

DD Dipole-Dipole

FID Free Induction Decay

HETCOR Heteronuclear Correlation

HMQC Heteronuclear Multiple Quantum Correlation

HSQC Heteronuclear Single Quantum Coherence

INEPT Insensitive Nuclei Enhanced by Polarization Transfer

LB Luria–Bertani

MALDI Matrix-Assisted Laser Desorption/Ionization

MAS Magic Angle Spinning

MD Molecular Dynamics

MFF Model-Free Formalism

NMR Nuclear Magnetic Resonance

NOE Nuclear Overhauser Effect

ODC over day culture

ONC over night culture

PAR Proton Assisted Recoupling

PDSD Proton-Driven Spin Diffusion

PF *Pyrococcus furiosus*

PRE Paramagnetic Relaxation Enhancement

RAP Reduced Adjoining Protonation

RDC Residual Dipolar Coupling

REDOR Rotational-Echo Double-Resonance

RFDR Radio-Frequency-Driven Dipolar Recoupling

RMSD Root-Mean-Square Deviation

SEC Size-Exclusion Chromatography

SH3 Src homology 3

TEM Transmission Electron Microscopy

TOBSY Total Through-Bond Correlation Spectroscopy

TROSY Transverse Relaxation Optimized Spectroscopy

1 Introduction

1.1 NMR spectroscopy in structural biology

The knowledge of atomic-resolution structures of biomolecules is crucial for the understanding of their functional dynamics. To date, the most established techniques for determination of high-resolution structures are X-ray crystallography and solution-state Nuclear Magnetic Resonance (NMR) spectroscopy, while both techniques yield highly similar structures [Wagner et al., 1992]. Within the domain of eukaryotes, up to now, 81% and 13% of the structures were solved by X-ray diffraction (resolution $\leq$3 Å) and solution-state NMR spectroscopy, respectively, according to the RCSB Protein Data Bank. It should be noted, that the first X-ray structures were determined in the late 1950s [Kendrew et al., 1958, Muirhead and Perutz, 1963, Blake et al., 1965], whereas first NMR structures were reported in the early 1980s [Braun et al., 1983, Arseniev et al., 1984, Clore et al., 1985, Kaptein et al., 1985, Williamson et al., 1985, Wagner et al., 1987]. Therefore, X-ray crystallography has, in principle, a time lead over NMR spectroscopy of about 20 years. However, in 2012, still 3962 (85%) and 334 (7%) out of 4662 structures were solved by X-ray and solution-state NMR spectroscopy, hinting a faster access to three-dimensional structures by crystallography.

Crystallization often represents the bottleneck in course of structure determination by X-ray crystallography. Thereby, the most time-consuming step comprises the probing of conditions to yield diffracting and adequately sized single crystals [Durbin and Feher, 1996, Chayen and Saridakis, 2008]. This step, is avoided by application of solution-state NMR, as it only requires solubility at sufficient concentrations for data collection. Though, the major limitation of solution-state NMR spectroscopy is the rotational correlation time of the solvated biomolecule, which is, to first approximation, proportional to the molecular weight. Up to molecular weights

of 30-40 kDa, traditional NMR approaches for structure determination can be employed [Tugarinov et al., 2005]. Structural information can be extracted by NMR from two main sources [Clore and Gronenborn, 1987, 1998a, Kanelis et al., 2001, Wuthrich, 2003], torsional angle and through-space distance restraints, respectively.

The measurement of three-bond scalar coupling constants, as $^3J_{\mathrm{HN}\alpha}$, $^3J_{\mathrm{C'C'}}$ and $^3J_{\mathrm{C}\gamma\mathrm{C'}}$, directly gives rise to torsional angle restraints ϕ (backbone) and χ_1 (side chain) [Karplus, 1963, Bax et al., 1994, Hu and Bax, 1996, Clore et al., 1998]. ψ backbone torsion angles can be obtained by measuring cross-correlated relaxation between the ^{15}N,^{1}H(i) and ^{13}Cα,^{1}Hα($i-1$) dipoles [Reif et al., 1997], or between the ^{13}Cα,^{1}Hα(i) dipole and the ^{13}C' Chemical Shift Anisotropy (CSA) [Yang et al., 1997c]. However, it was shown, that the chemical shift difference to the respective random coil value is highly dependent on the secondary structure motif [Spera and Bax, 1991, Wishart et al., 1991]. Therefore, more frequently, dihedral angles are derived from chemical shift values, performing a database search over sequence and chemical shift homology [Cornilescu et al., 1999, Shen et al., 2009]. A structure determination approach, based solely on protein chemical shifts, has also been reported for small proteins up to $\approx$16 kDa [Shen et al., 2008].

The second and particularly essential source of structural information, the distance restraint, is derived from through-space experiments. In solution-state NMR, these experiments rely on measuring the inter-proton Nuclear Overhauser Effect (NOE) [Overhauser, 1953a,b, Anderson and Freeman, 1962]. The dipolar cross-relaxation rate constant, and therefore the NOE, is proportional to r^{-6}, with r being the inter-proton distance [Solomon, 1955, Jeener et al., 1979, Meier and Ernst, 1979, Kumar et al., 1980, Cavanagh et al., 1996]. That way, the NOE correlates cross-peak intensities in multi-dimensional experiments to distance information, which can be used to determine the tertiary structure fold [Oschkinat et al., 1988, Clore and Gronenborn, 1991].

Since the upper distance limit, which can be probed by the ^{1}H,^{1}H NOE, is about 5 Å, the NOE only provides local information. Therefore, domain orientations are difficult to obtain [Kanelis et al., 2001]. Long-range orientational information can be determined by Residual Dipolar Coupling (RDC) experiments [Bastiaan et al., 1987, Tolman et al., 1995, Tjandra and

Bax, 1997c, Bax et al., 2001]. The dipolar Hamiltonian for dissolved molecules is given by [Abragam, 1961]

$$H_D = -\delta_{\mathrm{D},ij} \left\langle \frac{3\cos^2\theta - 1}{2} \right\rangle I_{zi} I_{zj}, \tag{1.1}$$

where $\delta_{\mathrm{D},ij}$ is the dipolar coupling anisotropy, θ is the angle between the vector connecting nuclei i and j and the applied magnetic field, and I_{zi} and I_{zj} are the spin operators for the two nuclei, respectively. The angular bracket denotes a time average over a single molecule [Meiler et al., 2001], which is equal to zero in an isotropic environment, as internal and molecular tumbling motions occur on time scales shorter than the ^{1}H,^{13}C or ^{1}H,^{15}N dipolar interaction in Hz (< 1 µs). However, placing any molecule, paramagnetic or diamagnetic, in a magnetic field, induces a magnetic dipole moment, that is proportional to its magnetic susceptibility tensor χ and to the square of the external magnetic field [Lohman and Maclean, 1978, 1979]. The interaction energy, resulting from these induced magnetic dipole moments, will align the molecule in the magnetic field. However, the Brownian motion disturbs the ordering. A molecular alignment is only achieved as long as the interaction energies are larger than the thermal energy kT [Prestegard and Kishore, 2001]. Due to the negligibly small induced magnetic dipole moments, diamagnetic molecules undergo nearly isotropic tumbling and the dipolar Hamiltonian in equation 1.1 averages to zero.

To enhance the alignment and to yield measurable dipole splittings, anisotropic alignment media, as bicelles [Clore and Gronenborn, 1998b, Prestegard et al., 2000], are employed. The dissolved proteins adopt some of the order of the bicelles and, therefore, the molecules still tumble rapidly, as required for high-resolution spectroscopy, but they tumble anisotropically. This induces dipole splittings, which can be tuned by adjusting the concentration of the bicelles [Prestegard, 1998]. The combination of different alignment media and dipolar coupled probes, such as ^{1}H,^{15}N, ^{1}H,^{13}C, ^{13}C,^{13}C, then allows to determine, for example, domain orientations, which usually display an unsufficient number of inter-domain NOEs for traditional structure determination [Ramirez and Bax, 1998, Clore et al., 1999, Al-Hashimi et al., 2000, Skrynnikov et al., 2000]. The resolution loss due to the slow tumbling regime for large proteins can partially be compensated by deuteration and the application of Transverse Relaxation Optimized Spectroscopy (TROSY) [Pervushin et al., 1997]. The introduction of TROSY was

a turning point in solution-state NMR as it allows to investigate structure and dynamics of dissolved biomolecules with molecular weights of several hundreds of kDa [Salzmann et al., 1998, Pervushin, 2000, Fiaux et al., 2002, Tugarinov et al., 2002, Fernandez and Wider, 2003]. In terms of interference of two relaxation mechanisms (DD/CSA for backbone and DD/DD for methyls, where DD means Dipole-Dipole), TROSY selects exclusively the slowly relaxing component to reduce transverse relaxation and extends the molecular size-limitation to about 1 MDa [Fernandez and Wider, 2003, Tugarinov et al., 2003, Sprangers and Kay, 2007, Kay, 2011]. Very recently, a most promising approach was presented, which, in principle, allows to offset the spectroscopic size-limitation for large, dissolved molecular complexes by use of MAS solid-state NMR spectroscopy [Mainz et al., 2009]. The method is based on transient protein sedimentation [Bertini et al., 2011b].

However, large complexes of several MDa, membrane proteins in their native lipid environment, and, especially, insoluble protein aggregates, as the biomedically important amyloid fibrils, are difficult or impossible to study by high-resolution solution-state NMR spectroscopy. This is due to exceedingly long rotational correlation times for these systems and the $J(0)$ dependency of T_2 relaxation. On the other hand, solid-state NMR is not subject to any size-limitation, because solid-state samples do not undergo molecular reorientations. Here, the averaging of anisotropic interactions is achieved actively by Magic Angle Spinning (MAS) [Andrew et al., 1958, Lowe, 1959]. Both the CSA and the dipolar coupling Hamiltonian depend on the second Legendre polynomial $P_2(\cos\theta) = \frac{1}{2}\left(3\cos^2\theta - 1\right)$. Here, θ is the angle between the magnetic field $\vec{B}_0$ and the z-axis in the principal axis frame of the shielding tensor (for CSA) or the internuclear dipole vector (for the dipolar coupling), respectively. Therefore, for averaging of anisotropic interactions, the sample is rotated at the magic angle $\theta_{\mathrm{MA}} = \arccos 1/\sqrt{3} = 54.7°$ at which $P_2(\cos\theta_{\mathrm{MA}}) = 0$. The CSA Hamiltonian reduces to its isotropic part and the dipolar coupling to zero, as the dipolar coupling tensor is traceless [Duer, 2002].

This is illustrated in Figure 1.1, assuming only a CSA or dipolar coupling Hamiltonian, respectively. The static spectra of the solid powder display broad resonances with a typical line shape (black curves), which results from sampling the contributions of all crystallite orientations. In contrast, the simulated solution-state spectrum shows in both cases (CSA and DD)

narrow resonances (orange), indicating the intrinsic high resolution yielded by solution-state NMR.

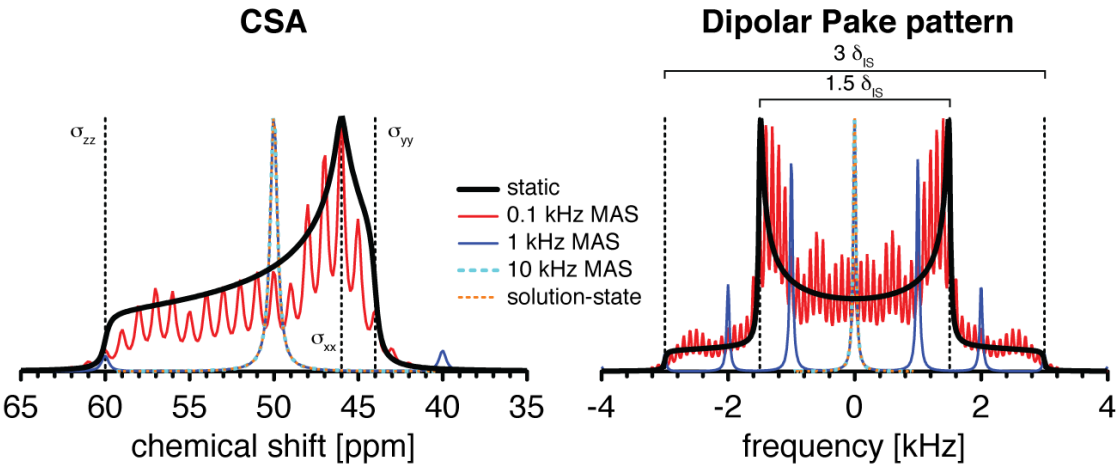

Figure 1.1: NMR spectra under the influence of CSA (left) and the dipolar coupling Hamiltonian (right) were simulated for a static (black) and rotating powder at the magic angle (red, blue, cyan), as well as for a dissolved molecule (orange). Numerical simulations were carried out using the SIMPSON software package [Bak et al., 2000]. All spectra were apodized by applying 50 Hz line broadening prior to Fourier transformation. The principal components of the CSA shielding tensor for a single ^{1}H spin were $\sigma_{xx} = \sigma_{22} = 44$ ppm, $\sigma_{yy} = \sigma_{33} = 46$ ppm, $\sigma_{zz} = \sigma_{11} = 60$ ppm, which yields an asymmetry of $\eta = 0.2$. The virtual, external magnetic field was set to 2.3 T (100 MHz). For simulating a typical dipolar Pake pattern [Pake, 1948, Levitt, 2008], a ^{1}H,^{1}H spin pair with a dipolar coupling anisotropy, δ_{IS}, of 2 kHz was assumed. At fast spinning ($\omega_r \gg \omega$) the central frequency obtained for the solid powder sample coincides with the isotropic value for the dissolved molecule, undergoing ideal isotropic tumbling.

Spinning a solid-state powder sample around the magic angle with respect to the applied magnetic field, collapses the broad powder pattern into spinning sidebands, occuring at multiples of the spinning frequency $\pm\omega_r$ [Herzfeld and Berger, 1980]. The sidebands accumulate to a narrow central transition at sufficiently fast spinning frequencies ($\omega_r \gg \omega$). Therefore, anisotropic contributions are eliminated, which, in principle, yields the same resolution as in solution-state NMR (Figure 1.1, cyan).

Nowadays, MAS probes are available, which enable spinning frequencies up to 60-70 kHz. However, higher rotation frequencies of up to 100-150 kHz are required to average the strong ^{1}H,^{1}H dipolar coupling network, which predominantly limits the resolution in the solid-state [Samoson et al., 2001, Marchetti et al., 2012]. Particularly, ^{1}H spectroscopy is severely impeded as ^{1}H,^{1}H spin pairs display the largest dipolar couplings owing to the large ^{1}H gyromagnetic ratio. On the other hand, homonuclear ^{13}C,^{13}C and heteronuclear ^{1}H,^{13}C and ^{1}H,^{15}N dipolar

couplings are reduced by almost an order of magnitude (2-25 kHz for typical bond lengths) as compared to homonuclear ^{1}H,^{1}H couplings (≈100 kHz assuming the same distances). Therefore, protein solid-state NMR spectroscopy of uniformly protonated samples is essentially based on ^{13}C- and ^{15}N-detection, respectively, since heteronuclear dipolar couplings are sufficiently averaged at currently available rotation frequencies.

Structure determination in the solid-state adopts many aspects from the ^{1}H-detected solution-state NMR approach [Luca et al., 2003]. Similarly, ϕ, ψ and χ_1 dihedral angles can be accurately determined as for dissolved proteins [Feng et al., 1997, Hong et al., 1997, Fujiwara et al., 1998, Reif et al., 2000], which yielded e.g. the three-dimensional structure of a small tripeptide [Rienstra et al., 2002b]. However, most commonly, dihedral angles are derived from chemical shifts [Cornilescu et al., 1999] (*vide supra*).

As opposed to solution-state NMR, accurate distances can be obtained in the solid-state by recoupling of specific dipolar coupled nuclei [Kovacs et al., 2007]. Various sequences were proposed [Roberts et al., 1987, Hohwy et al., 2000, Zhao et al., 2001a,b, Dvinskikh et al., 2005, 2003], as Rotational-Echo Double-Resonance (REDOR) [Gullion and Schaefer, 1989, Gullion, 1998, Pan et al., 1990, Jaroniec et al., 2000] for heteronuclear and rotational-resonance [Raleigh et al., 1988] for homonuclear distance measurements, respectively. Accurate distances enabled the structure determination of peptides and small peptide fragments [Jaroniec et al., 2002, Rienstra et al., 2002b]. In larger systems, as for example proteins, the resolution is limited due to spectral crowding and accurate distance determination becomes challenging as the number of recoupled spins is increased due to a higher spin density, which complicates the data analysis. Therefore, in analogy to the solution-state ^{1}H,^{1}H NOE approach, rather a multitude of roughly estimated through-space distance restraints are incorporated for structure determination, using unambiguous and, as shown recently, ambiguous distance restraints [Linge et al., 2001, Castellani et al., 2002, Zech et al., 2005, Ferguson et al., 2006, Franks et al., 2008, Loquet et al., 2008, Manolikas et al., 2008, Wasmer et al., 2008, Jehle et al., 2010b, 2011, Loquet et al., 2012, Park et al., 2012, Shahid et al., 2012].

In solid-state NMR, traditionally, NCOCX and NCACX experiments are employed for sequential assignments [Baldus et al., 1998, Pauli et al., 2001], which are supplemented with

a ^{13}C,^{13}C homonuclear mixing scheme as Proton-Driven Spin Diffusion (PDSD) [Szeverenyi et al., 1982], RAD/DARR [Takegoshi et al., 2001, 2003, Morcombe et al., 2004], Radio-Frequency-Driven Dipolar Recoupling (RFDR) [Bennett et al., 1992, 1998], or Proton Assisted Recoupling (PAR) [De Paepe et al., 2008], respectively. These experiments are following the principles of solution-state NMR experiments, as HNCO, HNCA, HNCACB and HC(C)(CO)NH-TOCSY [Ikura et al., 1990a, Kay et al., 1990, Montelione et al., 1992, Grzesiek et al., 1993, Lyons et al., 1993, Grzesiek and Bax, 1992, Farmer and Venters, 1995]. Especially PDSD, and the more recently proposed PAR sequence, yield short- as well as long-range contacts, which are essential to determine the tertiary protein fold, since these mixing sequences are less prone to dipolar truncation [Grommek et al., 2006, De Paepe et al., 2008]. Furthermore, dipolar truncation can be reduced by labeling of non-consecutive carbon nuclei [LeMaster and Kushlan, 1996, Hong and Jakes, 1999, Castellani et al., 2002, Lundstrom et al., 2007, Loquet et al., 2010, 2011].

1.2 High resolution and high sensitivity: the deuteration approach

The first application of protein deuteration was demonstrated in solution-state NMR spectroscopy in the late 1960s, while the approach has been highly extended over the past decades [Crespi et al., 1968, Markley et al., 1968, Crespi and Katz, 1969, Kalbitzer et al., 1985, Lemaster and Richards, 1988, Lemaster, 1994, Yamazaki et al., 1994a, Grzesiek et al., 1995, Shan et al., 1996, Garrett et al., 1997, Gardner and Kay, 1998]. Nowadays, deuteration, as well as TROSY techniques, are routinely applied to improve spectral sensitivity and resolution, as ^{1}H,^{1}H dipole mediated line broadening is chemically suppressed [Pervushin et al., 1997, Fiaux et al., 2002, Tugarinov et al., 2002, Fernandez and Wider, 2003].

In the solid-state, peptide and protein deuteration was introduced about thirty years later by Zilm, Reif and co-workers [Reif et al., 2001, Reif and Griffin, 2003, Reif et al., 2003, Morcombe et al., 2005, Chevelkov et al., 2006, Hologne et al., 2006, Linser et al., 2011b, Reif, 2012]. As molecular tumbling is absent in the solid-state, anisotropic interactions are not averaged (cf. Figure 1.1, page 5). Therefore, the strong ^{1}H,^{1}H dipolar coupling network induces severe line broadening, particularly to ^{1}H resonances, as ^{1}H possesses the largest gyromagnetic ratio. In

this manner, ^{1}H-detection is strongly impeded in the solid-state.

Employing ^{1}H,^{1}H homonuclear decoupling sequences, proton line widths of about 100-500 Hz can be achieved [Bielecki et al., 1989, Levitt et al., 1993, Vinogradov et al., 1999, Sakellariou et al., 2000, Bosman et al., 2004], which are still two orders of magnitude larger than solution-state line widths. However, it was shown, that in the solid-state, the proton line width of exchangeable protons can amount to 20-40 Hz, in case heavily deuterated samples are employed [Chevelkov et al., 2006, Schanda et al., 2009, Akbey et al., 2010, Knight et al., 2011, Lewandowski et al., 2011a], since the ^{1}H,^{1}H dipolar network is diluted. To enable ^{1}H-detected ^{1}H,^{15}N correlation experiments in the solid-state, the protein sample is expressed, using uniformly deuterated glucose, as well as ^{15}N-labeled ammonium chloride [Chevelkov et al., 2006]. To further dilute the ^{1}H,^{1}H dipolar coupled spin bath, the purified protein is back-exchanged in a buffer containing 10-20% H_2O and 90-80% D_2O, respectively.

Methyl protons are accessible by making use of specific precursors for amino acid biosynthesis [Agarwal et al., 2006, Agarwal and Reif, 2008, Huber et al., 2011, Schanda et al., 2011a, Huber et al., 2012], or by exploiting the fact that commercially available precursors are typically not 100% enriched in ^{2}H [Agarwal and Reif, 2008]. The deuteration scheme is not only applicable to microcrystalline proteins, but is also successfully implemented in amyloid fibrils, membrane proteins [Linser et al., 2011b] and, as shown in the present thesis, protein-RNA complexes (section 3.7, page 137).

Deuteration not only improves the resolution by increasing the effective T_2 times, it also enables ^{1}H-detection in the solid-state [Reif and Griffin, 2003, Chevelkov et al., 2006]. Proton detection can, in principle, provide a gain in sensitivity by a factor of 8 and 31, compared to the ^{13}C- or ^{15}N-detected version of the experiment, respectively, according to $(\gamma_H/\gamma_X)^{3/2}$ (X = ^{13}C, ^{15}N) [Cavanagh et al., 1996]. Therefore, proton is preferred over heteronuclear detection. However, in practice, to determine a sensitivity enhancement factor also the quality factor and the geometry of the rf coil has to be considered [Ishii et al., 2001], yielding a slightly smaller enhancement [Reif and Griffin, 2003].

In biomolecular solid-state NMR spectroscopy, routinely cross polarization (CP) is employed, in order to improve the experimental sensitivity of low-abundant spins (Figure 1.2A), such as

^{13}C and ^{15}N, which are coupled to a proton spin bath [Hartmann and Hahn, 1962, Pines et al., 1973, Schaefer and Stejskal, 1976, Stejskal et al., 1977]. *S* spin (^{13}C, ^{15}N) detection is common in the solid-state, as direct *I* spin (^{1}H) detection is hampered by large ^{1}H,^{1}H dipolar couplings. However, *S* spins usually possess low gyromagnetic ratios, compromising the achievable sensitivity per unit time. To obtain $I \quad S$ CP in rotating solids and increase the *S* polarization, the Hartmann-Hahn matching condition has to be fulfilled (zero-quantum condition) [Hartmann and Hahn, 1962, Marks and Vega, 1996, Rovnyak, 2008]

$$\omega_{1I} \quad \omega_{1S} = k\omega_r, \tag{1.2}$$

in which ω_{1I} and ω_{1S} are the spin-lock fields applied to the *I* and *S* channels, ω_r is the MAS rotation frequency and $k = \pm 1, \pm 2$ [Marks and Vega, 1996], respectively. Matching the sideband at $k = \pm 1$ yields optimal sensitivity for short spin-lock contact times. At very long contact times the $k = \pm 2$ sidebands are about equally populated [Meier, 1992]. To broaden the CP matching profile, an amplitude ramp is employed [Metz et al., 1994]. An intensity maximum is obtained by centering the ramp on a sideband, matching the Hartmann-Hahn condition, and by adjusting the ramp size to cover the full-width of the sideband. The ramp can be implemented by linearly changing the rf field strength on the *I* or *S* channel, respectively.

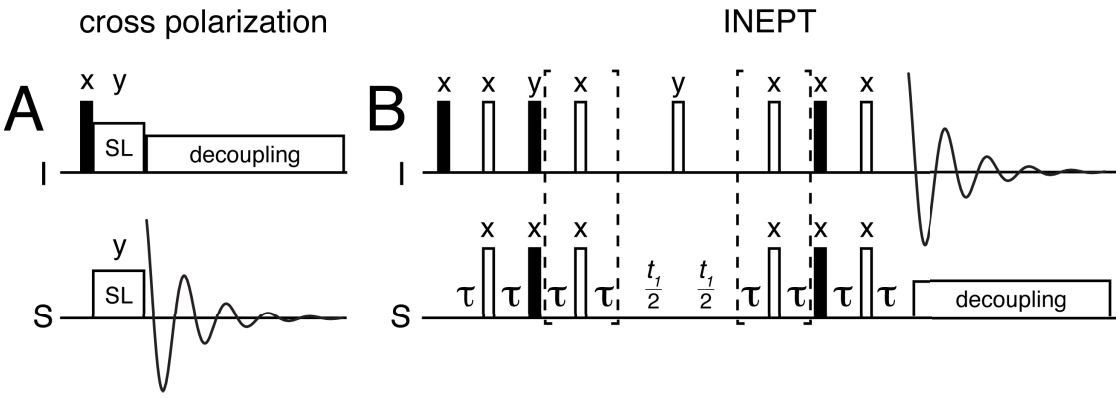

Figure 1.2: Sensitivity enhancement of *S* spins with a typically low gyromagnetic ratio and abundance by employing (A) a cross polarization (CP) ("SL" means spin-lock) or (B) an Insensitive Nuclei Enhanced by Polarization Transfer (INEPT) sequence, respectively. Including the bracketed part, yields a refocussed INEPT sequence. The *I* spin is an abundant, high-γ nucleus, usually ^{1}H.

In solution-state NMR spectroscopy, the most established heteronuclear polarization transfer

technique, Insensitive Nuclei Enhanced by Polarization Transfer (INEPT), is used for improving the sensitivity of low-γ nuclei [Becker et al., 1969, Bodenhausen and Freeman, 1977, Morris and Freeman, 1979]. As opposed to CP, INEPT solely relies on through-bond scalar transfers. The typical INEPT building block is depicted in Figure 1.2B. Immediately before the first bracket, the magnetization has evolved to an anti-phase operator [Sorensen et al., 1983, Cavanagh et al., 1996], $2I_zS_x$, while setting the τ delay to $1/4J_{IS}$. Here, J_{IS} is the heteronuclear scalar coupling constant between spin I and S, respectively. Applying a decoupling field to the I spins at this point of the pulse sequence would eliminate the S spin magnetization due to destructive interference, as the positive and negative component of the anti-phase doublet would cancel each other. Extending the sequence by another so-called spin echo element (sequence in brackets), yields the in-phase operator, S_x. The experiment including the spin echo is known as refocussed INEPT [Burum and Ernst, 1980, Morris, 1980].

In principle, the enhancement factor for both CP and INEPT is given by the ratio γ_I/γ_S. However, a further sensitivity gain per unit time is achieved by excitation of I spins as compared to S spins. Most commonly, the I spin is ^{1}H and the S spin ^{13}C or ^{15}N, respectively. As the ^{1}H T_1 relaxation times are about an order of magnitude shorter than ^{13}C and ^{15}N T_1 times, I excited experiments require a significantly shorter recycle delay for recovery of Boltzmann magnetization.

1.3 Protein dynamics

Globular proteins are typically tightly packed, however, can undergo substantial motion on the pico- to millisecond time scale. Often, this motion is linked to function [Levy et al., 1981a, Karplus and Petsko, 1990, Henzler-Wildman et al., 2007, Henzler-Wildman and Kern, 2007, Markwick et al., 2008]. The NMR-relaxation relevant time scales of protein motions can be divided into a fast (ps-ns) and slow motional (µs-ms) regime, respectively (Figure 1.3). On the fast time scale methyl rotations and rotameric jumps occur, next to molecular tumbling of dissolved molecules. Folding, as well as loop and domain motions usually occur on slower time scales. X-ray diffraction samples, in principle, a larger range of motions, as compared to NMR

spectroscopy, since it is also sensitive to very fast motions in the femtosecond regime. However, X-ray diffraction usually yields a motional average, whereas any particular motional time scale can be probed by a variety of NMR experiments [Mittermaier and Kay, 2006, Henzler-Wildman and Kern, 2007, Kleckner and Foster, 2011].

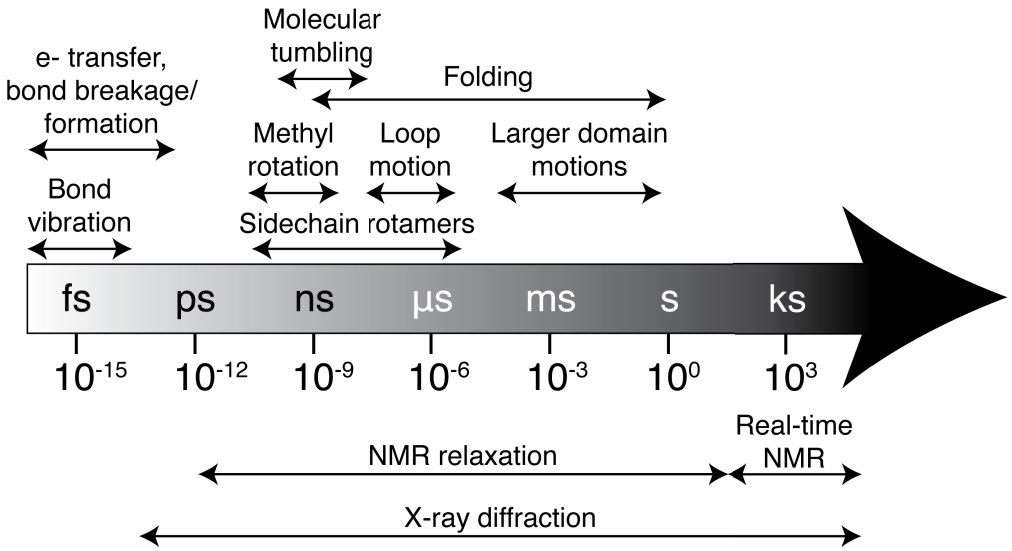

Figure 1.3: Functional relevant time scales of protein dynamics. The different processes (top) and biophysical methods (bottom) are related to a time scale of femto- to kiloseconds. The figure was modified from [Henzler-Wildman and Kern, 2007, Kleckner and Foster, 2011].

For a thermodynamical and kinetical understanding of motions occuring for folded proteins, an energy-landscape concept was introduced [Frauenfelder et al., 1979, Ansari et al., 1985, Frauenfelder et al., 1991, Henzler-Wildman and Kern, 2007], which is illustrated in Figure 1.4. A protein in an equilibrium conformation can assume a very large number of conformational substates, which form the scaffold for protein motions [Austin et al., 1975, Cooper, 1976]. In Figure 1.4 two tiers of substates are depicted, indicating the hierarchical nature of protein motions. Tier-0 dynamics comprises fluctuations in the slow motion regime (µs-ms), in which the free energy of the distinct states are separated by several kT [Henzler-Wildman and Kern, 2007]. Many biological processes, as enzyme catalysis, signal transduction and protein-protein interactions occur on this time scale.

However, the protein is not statically confined within a tier-0 state. It rather fluctuates on a faster time scale (ps-ns) around the average structure. These small-amplitude fluctuations,

described by tier-1 dynamics (Figure 1.4), sample a large ensemble of structurally similar states, separated by energy barriers of less than kT.

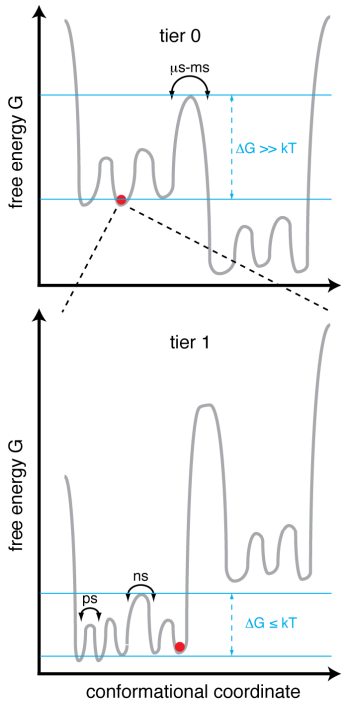

Figure 1.4: Schematic energy landscape of protein motions, illustrating the hierarchical arrangement of conformational substates. The figure was modified from [Ansari et al., 1985, Henzler-Wildman and Kern, 2007].

NMR spectroscopy is sensitive to both fast and slow motions and enables the determination of the time scale of transitions as well as structural parameters in atomic resolution. µs-ms motions can be probed by relaxation dispersion experiments [Loria et al., 1999, Palmer, 2004, Tollinger et al., 2012]. The present thesis addresses rather fast time scale motions, which can be investigated by T_1 relaxation experiments, as well as by dipolar order parameters. An introduction to both dynamics probes, order parameter and T_1, will be given in the respective sections 3.4 (page 74) and 3.5 (page 97).

1.4 Objectives of the thesis

Biological magic angle spinning (MAS) solid-state Nuclear Magnetic Resonance (NMR) spectroscopy has developed rapidly over the past two decades, facilitating structural studies of crys-

talline [Castellani et al., 2002, Zech et al., 2005, Franks et al., 2008, Jehle et al., 2010b] and non-crystalline systems [Jaroniec et al., 2002, Ferguson et al., 2006, Petkova et al., 2006, Wasmer et al., 2008, Loquet et al., 2012, Park et al., 2012, Shahid et al., 2012]. For the structure determination of a protein by solid-state NMR, routinely ^{13}C,^{13}C distance [Castellani et al., 2002], as well as dihedral restraints [Reif et al., 2000, Rienstra et al., 2002a] are employed. Thereby, aliphatic resonances are essential to access tertiary structure information of a protein, since long-range restraints between side chains are fundamental for defining the protein fold [Liu et al., 1992, Gardner et al., 1997, Zwahlen et al., 1998, Huber et al., 2011].

In the solid-state, sparsely ^{13}C labeled proteins are employed to determine long-range ^{13}C,^{13}C restraints [LeMaster and Kushlan, 1996, Hong and Jakes, 1999, Castellani et al., 2002, Lundstrom et al., 2007, Loquet et al., 2010, 2011, 2012], while reducing dipolar truncation, which attenuates long-range interactions. Rather than ^{13}C, protons are ideally suited to deliver non-trivial distance restraints due to their peripheral localization within the side chain and their large gyromagnetic ratio.

However, the so far established ^{13}C-detected experiments for the determination of structural restraints suffer from a low signal-to-noise level due to the detection of low-γ nuclei. Furthermore, high-resolution ^{1}H spectra of non-exchangeable, aliphatic protons are difficult to achieve in the solid-state, even when homonuclear decoupling schemes are employed [Bielecki et al., 1989, Vinogradov et al., 1999, Lesage et al., 2003], which is due to the large, intrinsic ^{1}H,^{1}H dipolar couplings.

This was the starting point of the present thesis. As part of it, we introduced the Reduced Adjoining Protonation (RAP) labeling scheme, which enables ^{1}H-detection of aliphatic resonances with high resolution and sensitivity, while bypassing homo- and heteronuclear high-power ^{1}H decoupling, which protects the biological samples against heat denaturation. In order to reduce the proton density of non-exchangeable aliphatic protons in a protein, we prepared highly deuterated, uniformly ^{13}C,^{15}N isotopically enriched samples of the Src homology 3 (SH3) domain of chicken α-spectrin, using u-[^{2}H,^{13}C] glucose and 5-25% H_2O (95-75% D_2O) in the M9 bacterial growth medium, based on approaches known from solution-state NMR [Kushlan and Lemaster, 1993, Nietlispach et al., 1996, Hochuli et al., 2000, Shekhtman et al., 2002].

Employing α-spectrin SH3 as a model system, we show, that using the RAP labeling scheme, proton detected high resolution ^{1}H,^{13}C correlation spectra are obtained, which enable full ^{1}H,^{13}C backbone and side chain resonance assignment, as well as the determination of long-range ^{1}H,^{1}H distance restraints. The RAP labeling was also combined with sparse ^{13}C-labeling, yielding an additional, significant resolution improvement in the ^{13}C dimension.

It will be demonstrated, that fast Magic Angle Spinning (MAS) frequencies $\geq$40 kHz further enhance the sensitivity and resolution of ^{1}H and ^{13}C resonances and, especially, enable the determination of motional information, derived from backbone and side chain T_1 times and order parameters, respectively. We show, that, besides fast spinning, sufficient suppression of coherent contributions simultaneously requires ^{1}H and ^{13}C spin dilution.

The RAP labeling scheme was applied to A$\beta_{1\text{-}40}$ amyloid fibrils, introduced in section 1.5.2 (page 16). In non-crystalline systems, spectral resolution and sensitivity are usually compromised, due to a lower degree of sample homogeneity as compared to crystals. Furthermore, these systems do not provide high expression yields, which further impairs the sensitivity. This made the application of the RAP labeling scheme particularly beneficial, as it enables proton detection and adds the proton chemical shift dimension to the traditional ^{13}C and ^{15}N dimensions, respectively. Well dispersed ^{1}H,^{13}C correlation spectra of A$\beta_{1\text{-}40}$ were yielded, which is a prerequisite to obtain assignments and distance restraints for a structural characterization of the fibrils.

Probing the accessibility of a protein-RNA complex (introduced in section 1.5.3, page 17) by solid-state NMR was a further objective of the thesis. So far, biomolecular solid-state NMR spectroscopy mostly centers on protein investigations, while RNA or DNA have been studied in very few cases [Riedel et al., 2006, Jehle et al., 2010a, Huang et al., 2011b], which, however, is not reflective of a minor biological importance, as fundamental biochemical processes involve RNA and DNA. We show, that perdeuteration yields high-resolution spectra for protein and RNA. Spectral differences, encountered for protonated and deuterated RNA, provide accurate distance and angular restraints for the protein-RNA interface, which can be used for structure calculation of large protein-RNA complexes, as solid-state NMR is not subject to a size or solubility limitation.

1.5 Investigated biological systems

In the present thesis, three different biological systems were employed, the SH3 domain of chicken α-spectrin, $A\beta_{1\text{-}40}$ amyloid fibrils, as well as the L7Ae-box C/D protein-RNA complex, respectively. These systems will be introduced in the following.

1.5.1 SH3 domain of α-spectrin

The Src homology 3 (SH3) domain is a small, globular protein domain, which contains about 60-85 residues and forms a β-barrel structure, as illustrated in Figure 1.5 [Musacchio et al., 1992, 1994]. The SH3 domain binds to proline-rich ligands [Cicchetti et al., 1992, Ren et al., 1993] and is shared among signaling proteins, such as tyrosine kinases of the Src family, v-/c-Crk, PI-3 kinase and PLCγ, as well as cytoskeletal proteins, such as α-/β-spectrin and Abp1 [Geli et al., 2000, Mayer, 2001, Kay, 2012], respectively. The SH3 domain was found in yeast and amoeba, as well as in invertebrates and vertebrates, the evolutionary conservation indicates a vital cellular function.

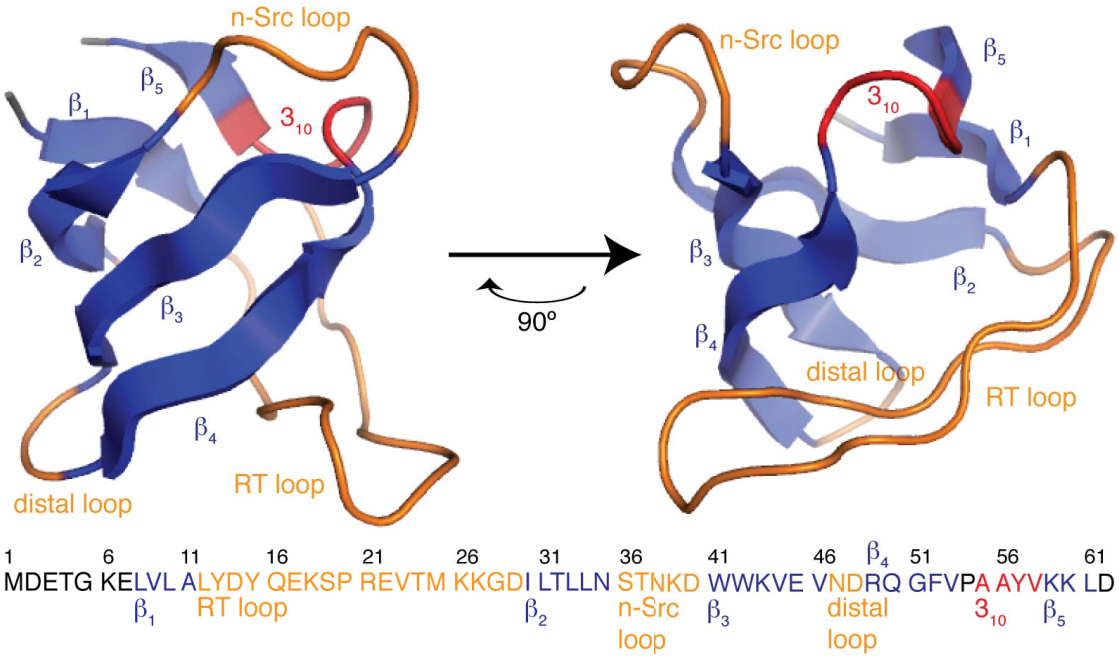

Figure 1.5: Crystal structure of the Src homology 3 (SH3) domain of chicken α-spectrin (PDB: 2NUZ) [Chevelkov et al., 2007b]. The amino acid sequence is given at the bottom of the figure. The protein structure and sequence are color-coded, according to the secondary structure elements.

The SH3 domain of chicken α-spectrin is represented in Figure 1.5 [Musacchio et al., 1992, Viguera et al., 1996, Chevelkov et al., 2007b]. The fold is essentially formed by five anti-parallel β-strands and three loops, namely, the RT, the n-Src and the distal loop, respectively [Camara-Artigas et al., 2010]. Although various SH3 domains adopt a highly similar β-barrel fold, different conformations for the RT and n-Src loops were obtained [Feng et al., 1995, Morken et al., 1998, Kay et al., 2000]. As the flank sequence of a ligand binds to a groove between the two loops, the interaction of the ligand and both loops is fundamental for sequence specificity. Furthermore, it was shown, that the amyloidogenic property of PI3-SH3 can be "transferred" to α-spectrin SH3, which does not form amyloid fibrils, by transplanting a stretch of six residues from PI3-SH3 to the RT loop of α-spectrin SH3 [Ventura et al., 2004].

The SH3 domain of chicken α-spectrin was used in the present thesis as a model system for establishing a new labeling scheme for solid-state NMR spectroscopy. Besides substantiated prior knowledge about the crystal structure and dynamics [Musacchio et al., 1992, Castellani et al., 2002, Chevelkov et al., 2007a,b,c, Agarwal et al., 2008, Chevelkov et al., 2008, Chevelkov and Reif, 2008, Chevelkov et al., 2009a,b, 2010], which simplify validating experimental and simulated data, a high protein amount was yielded for α-spectrin SH3 in *E. coli* cells.

1.5.2 A$\beta_{1\text{-}40}$ amyloid fibrils

Amyloid fibrils are typically straight, filamentous aggregates of peptides or proteins, typically with a diameter of 10 nm and lengths of 100 nm to several μm [Sipe, 1992, Tycko, 2006]. They can be visualized by Transmission Electron Microscopy (TEM) with negative staining, as shown in Figure 1.6A. Fibrils are associated with several diseases, such as Alzheimer's disease, type 2 diabetes and Parkinson's disease [Sacchettini and Kelly, 2002]. Due to the insolubility of the fibrils, solid-state NMR spectroscopy became an invaluable tool for structural investigations, as solubility is a prerequisite for alternative high-resolution methods, such as X-ray crystallography and solution-state NMR spectroscopy. In this manner, the first high-resolution structures of fibrils could be determined in the solid-state (cf. Figure 1.6B) [Jaroniec et al., 2002, Heise et al., 2005, Ferguson et al., 2006, Petkova et al., 2006, Shewmaker et al., 2006, Wasmer et al., 2008].

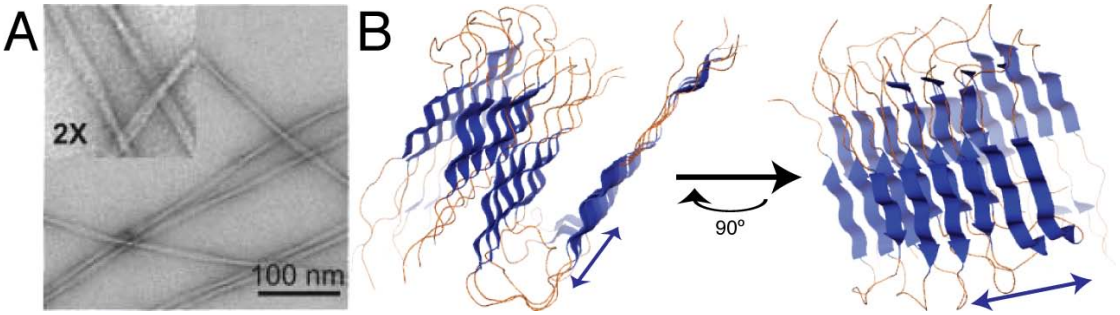

Figure 1.6: (A) Transmission Electron Microscopy (TEM) image of amyloid fibrils formed by the human $A\beta_{1\text{-}40}$ peptide. The image was taken from Petkova et al. [2005]. (B) Quaternary structural model of $A\beta_{1\text{-}40}$ fibrils (PDB: 2LMN) [Petkova et al., 2006]. The blue double arrow indicates the long, fibrillar axis.

$A\beta_{1\text{-}40}$ is produced by the proteolysis of β-amyloid precursor protein (APP), an ubiquitous, single-transmembrane, receptor-like protein [Selkoe, 2001, Haass and Selkoe, 2007]. The cleavage is mediated by γ-secretase. The γ-cut occurs variably after Aβ amino acids 38, 40 or 42. The different fragments possess different self-aggregating potentials, however, only $A\beta_{1\text{-}42}$ shows a strong oligomerization propensity *in vivo*.

As shown in a number of studies, homogeneous $A\beta_{1\text{-}40}$ fibril samples can be obtained, which enables high-resolution solid-state NMR spectroscopy [Petkova et al., 2005, 2006, Bertini et al., 2011a, Dasari et al., 2011, Lopez Del Amo et al., 2012, Lopez del Amo et al., 2012]. Following these protocols, $A\beta_{1\text{-}40}$ fibrils were prepared, while employing the herein introduced Reduced Adjoining Protonation (RAP) labeling scheme, which facilitates ^{1}H-detection of aliphatic resonances in the solid-state and adds the ^{1}H dimension to the traditional ^{13}C and ^{15}N dimensions, respectively.

1.5.3 L7Ae-box C/D protein-RNA complex

In the past decades, primarily protein samples have been studied in the solid state, while only few investigations of RNA or DNA have been reported [Riedel et al., 2006, Cherepanov et al., 2010, Huang et al., 2010, Jehle et al., 2010a, Huang et al., 2011b, Sergeyev et al., 2011]. However, many fundamental biochemical processes are carried out by protein-RNA complexes, the most prominent of which is the translation machinery. Prior to assembly of the eukaryotic ribosome, which catalyzes translation of messenger RNA, the RNA of the ribosomal subunits

becomes extensively modified [Maden, 1990]. The modifications consist of conversion of uridine to pseudouridine, base and 2'-O-ribose methylation, which cluster predominantly within functionally crucial regions [Decatur and Fournier, 2002]. It is suggested, that the modifications play an important role in RNA folding [Helm, 2006].

In eukaryotes, the site-specific methylation of 2'-O-ribose units is guided by small nucleolar RNAs (snoRNAs) [Kiss-Laszlo et al., 1998, Kiss, 2001]. These snoRNAs are defined by two conserved sequence elements, the C box (RUGAUG, where R is purine) and D box (CUGA) [Tyc and Steitz, 1989, Ye et al., 2009] (Figure 1.7). The snoRNAs are complexed with specific proteins and assemble to form ribonucleoprotein particles (snoRNPs). In archaea, the small ribonucleoprotein particle (sRNP) is composed of a box C/D snoRNA-like RNA (sRNA) and three proteins, L7Ae, Nop56/58, and fibrillarin, of which fibrillarin is the methyltransferase [Omer et al., 2002, Moore et al., 2004, Oruganti et al., 2007]. The assembly of archaeal sRNP is initiated by the binding of L7Ae to box C/D RNA. Upon binding, the sRNA folds into a K-turn motif [Moore et al., 2004, Falb et al., 2010].

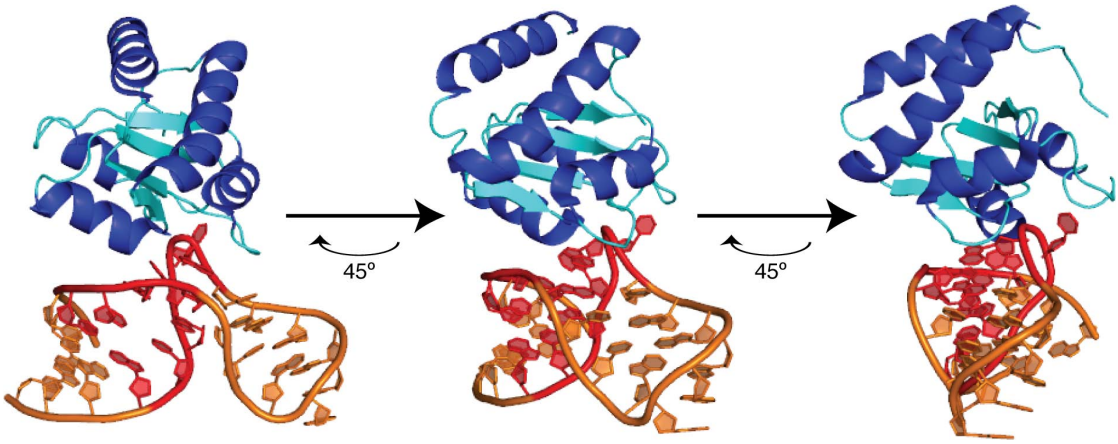

Figure 1.7: Illustration of the crystal structure of the L7Ae-box C/D RNA complex from *Archaeoglobus fulgidus* (AF) (PDB: 1RLG) [Moore et al., 2004]. The box C/D elements are highlighted in red, the remaining nucleobases in gold. β-sheets and loops of L7Ae are in cyan, helices in marine blue.

Here, we studied the protein-RNA interaction of the archaeal L7Ae protein from *Pyrococcus furiosus* (PF) with a 26-mer box C/D RNA. So far, high-resolution structures are only available from *Archaeoglobus fulgidus* (AF) [Moore et al., 2004], represented in Figure 1.7. However, by making use of a deuteration approach, the protein-RNA interface of the complex from PF was determined by solid-state NMR spectroscopy, as discussed in section 3.7 (page 137).

2 Materials and Methods

2.1 SH3 domain of chicken α-spectrin

2.1.1 Transformation of *E. coli* cells

The SH3 domain of chicken α-spectrin was cloned into a pET3d vector with an ampicillin resistance gene (the vector was kindly provided by Dr. Anne Diehl, FMP Berlin). For transformation, 20 µL of chemically competent *E. coli* BL21 DE3 cells (Novagen) were incubated for 5 min at +4 °C with 1 µL plasmid (≈570 ng/L). Afterwards, the cells were incubated for 45 s at +42 °C and again stored for 5 min at +4 °C. Finally, 250 µL of Luria–Bertani (LB) medium was added, followed by incubation for 1 h at +37 °C.

The transformed cells were dispersed on LB agar plates, containing 100 µg/mL carbenicillin. Carbenicillin was employed, instead of ampicillin, due to its enhanced stability in presence of β-lactamases. The plates were stored at +37 °C over night. The following day, up to five single-colony clones were picked and their expression profiles checked, as described in the next section.

2.1.2 Test expression of α-spectrin SH3

To check the expression level of different clones, 3 mL of LB medium was prepared for each clone, containing 100 µg/mL carbenicillin. Each medium was inoculated with one single-colony and incubated at +37 °C, under 180 rpm shaking (Infors HT Multitron). The OD(600 nm) was followed, until an absorption of 0.6 was attained.

The expression was induced by adding 1 mM IPTG and 100 µg/mL carbenicillin (end concentrations). Prior to induction, 25 µL of each culture was again dispersed on LB agar plates, which

were incubated over night at +37 °C. After 3-6 h the cells were harvested by centrifugation at 2,300 *g*. The expression level of the different clones was determined qualitatively by SDS-PAGE [Schagger and von Jagow, 1987]. The expression of isotopically enriched α-spectrin SH3 was continued with the best clone.

2.1.3 Expression of isotopically enriched α-spectrin SH3

In the present thesis, differently isotopically enriched samples of α-spectrin SH3 were prepared (Table 2.1), mainly utilizing the Reduced Adjoining Protonation (RAP) labeling scheme, which is described in this section. To achieve a high level of isotope incorporation, *E. coli* was grown on M9 minimal medium. The expression, purification and crystallization protocol for α-spectrin SH3 were initially developed by Musacchio et al. [1992] and further optimized for solid-state NMR spectroscopy by Pauli et al. [2000].

The isotopical composition of the M9 medium is crucial for the desired labeling pattern. Isotopically labeled M9 medium was prepared as described in the caption of Table 2.1. For the preparation of RAP samples, an uniformly deuterated carbon source was employed, either using u-[^{2}H,^{13}C]-glucose or [u-^{2}H, 2-^{13}C]-glycerol. The respective samples are hereafter referred to as "RAP" and "RAP-glycerol". For all preparations, isotopically enriched ammonium, $^{15}NH_4Cl$, was used.

To investigate the influence of the ^{1}H/^{2}H-ratio in the M9 expression medium on the ^{1}H-density at non-exchangeable aliphatic protein sites, different RAP samples were prepared by varying the D_2O-content in the M9 medium from 75% to 95% (Table 2.1). For the "RAP-glycerol" sample, a M9 medium, containing 90% D_2O, was used, which was supplemented with $Na^{1}H^{13}CO_3$ [LeMaster and Kushlan, 1996, Castellani et al., 2002].

Furthermore, an only valine/leucine methyl-labeled sample was prepared. For incorporation of selective isotope labels into methyl groups of valine and leucine residues, u-[^{2}H,^{12}C]-glucose and α-ketoisovalerate was employed and a M9 medium, containing 100% D_2O (referred to as the "$^{13}CD_2H$" sample) [Tugarinov et al., 2006].

For an 1 L culture, 2x3 mL LB medium, containing 100 µg/mL carbenicillin, was inoculated with the best clone from before (section 2.1.2, page 19) and incubated at +37 °C and 180 rpm

Table 2.1: Employed M9 media for the expression of α-spectrin SH3. For all isotopically labeled preparations, deuterated M9 salt (5x stock, composition for 1 L medium: 80 g $Na_2HPO_4x2H_2O$, 20 g KH_2PO_4, 5 g NaCl, pH 7.2–7.3) and deuterated trace elements (100x stock, for 500 mL: 2.5 g EDTA, 250 mg $FeSO_4$, 25 mg $ZnCl_2$, 5 mg $CuSO_4$, pH 7.5-7.7) were employed. The carbenicillin end concentration was 100 µg/mL. For the sample referred to as "$^{13}CD_2H$", two times in D_2O lyophilized u-[^{2}H,^{12}C] glucose and α-ketoisovalerate were employed. In the precursor molecule ($^{13}CD_2H-CD(CD_3)-CO-COO^-$) all protons were replaced by deuterons, except for a single proton, which was attached to only one of the two methyl groups. This methyl group was isotopically ^{13}C enriched, while all the remaining carbons were ^{12}C. When a fully deuterated M9 medium was necessary, as for the $^{13}CD_2H$ sample, Thiamin (1 mg/mL), Biotin (0.1 mg/mL), $MgSO_4$ (1 M), $CaCl_2$ (1 M) and carbenicillin (60 mg/mL) stocks were prepared in D_2O as well.

sample	nitrogen source (end concentration)	carbon source (end concentration)	D_2O-content in M9 medium [%]	precursor (end concentration)
RAP	$^{15}NH_4Cl$ (0.5 g/L)	u-[^{2}H,^{13}C]-glucose (2 g/L)	95, 85, 75	none
RAP-glycerol	$^{15}NH_4Cl$ (0.5 g/L)	[u-^{2}H, 2-^{13}C]-glycerol (2 g/L)	90	$Na^1H^{13}CO_3$ (2 g/L)
$^{13}CD_2H$	$^{15}NH_4Cl$ (0.5 g/L)	2-[^{2}H,^{12}C]-glucose (2 g/L)	100	3-Met-^{13}C 3-Met-D2,3,4,4,4-D4 (100 mg/L)

shaking (over day culture (ODC)). The ODC was grown until an OD(600 nm) of about 1.0 was achieved. 4 mL of the ODC was centrifuged for 15 min at 2,300 *g* and +30 °C.

200 mL unlabeled M9 medium was prepared, as described in the caption of Table 2.1. The pellet of the ODC was resuspended in 10 mL unlabeled M9 medium and added to the remaining 190 mL. The culture was incubated over night at +37 °C at 180 rpm shaking (over night culture (ONC)).

The following day, 1.01 L labeled M9 medium was prepared (preparation details in Table 2.1) and cells from the 200 mL ONC were harvested by centrifugation in sterile 500 mL buckets for 20 min at 2,300 *g* and +30 °C. The pellet was washed once with 10 mL of labeled M9 medium and resuspended again in 40 mL medium.

2x480 mL labeled M9 medium was placed into two baffled 2 L flasks ("Schikanekolben"). Each flask was inoculated with 20 mL cell suspension to achieve a start OD(600 nm) of ≈0.2. After incubation for ≈4-5 h at +37 °C and 140 rpm shaking, the OD(600 nm) increased to ≈0.5. The temperature of the shaking chamber was cooled down to +22 °C and after 30 min 1 mM IPTG as well as 100 µg/mL carbenicillin (end concentrations) were added to each flask.

For the $^{13}CD_2H$ sample, the precursor was added and incubated for 1 h, before inducing with 1 mM IPTG. In all cases, the suspension was incubated for 24 h and harvested by centrifugation

at 6,700 *g* and +4 °C. The pellet was washed once with 20 mM Tris-HCl (pH 8.0), resuspended in ≈40 mL washing buffer and shock frozen for final storage at -80 °C.

2.1.4 Purification of α-spectrin SH3

Anion-Exchange Chromatography (AEC) was used as the first purification step. As approximated by ExPASy [Gasteiger et al., 2003], the isoelectric point of α-spectrin SH3 is 5.3, hence it is negatively charged at alkaline pH and binds the column. The employed filling material for the AEC column was Q Sepharose Fast Flow (GE Healthcare). Two different column sizes were used, 96 mL and 216 mL, according to the total expression volume, 1-2 L or 3-4 L, respectively.

Prior to purification, the cell pellet was thawed at +4 °C. 10 µg/mL DNAse I and 1 x Complete Protease Inhibitor Cocktail (Roche) tablet were added and incubated for 1 h at +4 °C. The cells were disrupted by French press and centrifuged at 75,000 *g* and +10 °C for 30 min to remove membrane fragment parts. The supernatant was diluted with buffer A (composition given in Table 2.2) to approximately 80% of the column volume (CV) of the employed anion-exchange column.

After injection of the cell supernatant (3 mL/min flow rate), unbound organic molecules were removed by washing with 2 CV buffer A. Bound molecules were eluted by a linear gradient of 0-9% of buffer B (8 CV). α-spectrin SH3 fractions were pooled (monitored by SDS-PAGE) and the pH shifted to 3.5 by titration, using a 3 M citric acid solution. The pool was concentrated by ultrafiltration (Millipore system with Millipore Ultrafiltration Membranes, 1000 Da cutoff) at 3 bar to achieve a protein concentration of about 10-12 mg/mL. To prevent precipitation, the protein concentration should not exceed 14 mg/mL.

The concentrate was steril filtrated (0.2 µm) and further purified by Size-Exclusion Chromatography (SEC). A column with 494 mL volume was used, packed with Superdex 75 prep grade (GE Healthcare). After injection (1 mL/min flow rate), 0.5 CV were eluted before fractionation of 1 CV. Again, α-spectrin SH3 fractions were pooled and, finally, dialyzed against 5 L water at pH 3.5 (Table 2.2). The dilution factor was about 0.01.

Besides SDS PAGE, the quality of purified protein was also checked by MALDI mass spectrometry (kindly carried out by Heike Stephanowitz, FMP Berlin).

Table 2.2: α-spectrin SH3 purification buffers for anion-exchange and size-exclusion chromatography, and dialysis.

buffer	composition
AEC buffer A	20 mM Tris, pH 8.5 (adjusted with 30% HCl)
AEC buffer B	20 mM Tris, 1 M NaCl, pH 8.5 (adjusted with 30% HCl)
SEC buffer	20 mM citric acid, 150 mM NaCl, pH 3.5 (adjusted with 4 M NaOH)
Dialysis buffer	water, pH 3.5 (adjusted with 30% HCl)

2.1.5 Microcrystallization of α-spectrin SH3

α-spectrin SH3 was microcrystallized as described earlier [Pauli et al., 2000]. However, to achieve high deuteration at exchangeable sites, the original protocol was partly modified, as will be described in the following.

For filling a 3.2 mm rotor, 15-20 mg of protein were lyophilized and dissolved two times in D_2O (pH 3.5). The dry powder was dissolved to a protein end concentration of 5 mg/mL. 100 mM $(NH_4)_2SO_4$ (from 1 mM stock solution, dissolved in D_2O, pH 3.5) was added. If paramagnetic doping was required, 75–100 mM Cu(II)EDTA was supplemented (350 mM stock solution, dissolved in D_2O, pH 3.5).

Prior to initialization of the crystallization, the solution was steril filtrated (0.2 µm). The crystallization was initialized by a pH shift to pH 8.0 by addition of ≈50-100 µL NaOD (3% stock solution). Portions of 10-20 µL were added and the pH checked by pH indicator sticks (pH 4.5-10, Roth). As soon as a pH of ≈8 was achieved, the solution was stored in the fridge at +4 °C. The first crystals became visible after about 20 min, the total crystallization period took about 24 h. However, all samples were stored for at least 48 h before packing into rotors.

2.1.6 Preparation of solid-state samples of α-spectrin SH3

Depending on the total volume of the employed 3.2 mm rotor, 10-20 mg of α-spectrin SH3 crystals were filled by centrifugation. To obtain maximum filling, the rotors were spun in a 3.2 mm probe at a MAS frequency of 20 kHz for 30-60 min. Since the packed material was spun against the rotor wall, a hole opened in the middle of the rotor, which could be filled with more protein material. Usually this procedure was repeated once or twice. In case, the available

protein material was not enough for refilling, the solvent excess in the hole was removed by a tissue to improve solvent suppression.

1.3 mm rotors were packed by ultracentrifugation for ≈20 min at a relative centrifugal force of ≈135,000 *g*, employing an ultracentrifuge device [Bockmann et al., 2009].

To investigate the tightness of seal of 1.3 mm rotors at high MAS frequencies, two different glues were utilized, which are referred to as glue "A" and "B". Glue "A" is a fast gluing ("UHU plus schnellfest 2-K-Epoxidharzkleber", UHU®) and glue "B" a slowly gluing epoxy ("slow-setting epoxy adhesive", Araldite®), the latter requires at least 12 hours to set, unlike glue "A", which requires a few minutes. Three different 1.3 mm rotors were filled with water. Two rotors were glued either with glue "A" or "B". One rotor was kept untreated as a control. Rotor "B" was measured for >12 hours after gluing. For the protein samples, only glue "B" was employed. For comparison, glue "A" was used once for a protein sample, as shown in Figure 3.22B (page 63).

2.1.7 Preparation of solution-state samples of α-spectrin SH3

Samples, suited for solution-state NMR spectroscopy, were prepared to determine the proton concentration at non-exchangeable sites and to check the sample quality. About 2-4 mg α-spectrin SH3 were dissolved in ≈500 µL H_2O/D_2O (95% / 5%) and filled in a 5 mm solution-state NMR tube.

2.2 A$\beta_{1\text{-}40}$ amyloid fibril peptide

As shown in the preceding section, the RAP labeling scheme was applied to microcrystalline α-spectrin SH3. Additionally, the applicability of this scheme to a fibrillar system was investigated. Subject was the A$\beta_{1\text{-}40}$ peptide, which is found in high concentrations in plaques in the brain of Alzheimer's disease patients [Iwatsubo et al., 1994]. In the following, the protocols for expression and purification of A$\beta_{1\text{-}40}$ is presented, as well as preparation of fibrils for solid-state NMR experiments.

2.2.1 Transformation and expression of isotopically enriched Aβ1-40

Aβ1-40 was cloned into a pET3d vector with a kanamycin resistance gene (the vector was kindly provided by Dr. Muralidhar Dasari). The transformation and test expressions were conducted as described before (sections 2.1.1 and 2.1.2, page 19). In the present thesis, two Aβ1-40 samples were prepared, employing 5% and 15% RAP labeling, respectively. The media were prepared as described in Table 2.1 (page 21). For each sample, 4 L cultures were employed.

In contrast to α-spectrin SH3, isotopically enriched Aβ1-40 was not expressed over night. After induction with 1 mM IPTG at an OD(600 nm) of 0.6, the cell suspension was incubated for 6 h (180 rpm, +37 °C) and harvested by centrifugation. The cells were washed with 20 mM Tris-HCl (pH 8.0). The final resuspended pellet was shock frozen and stored at -80 °C.

2.2.2 Purification of Aβ1-40 from inclusion bodies

Following the expression protocol described above, the major fraction of Aβ1-40 was expressed into inclusion bodies [Dasari et al., 2011]. The purification of Aβ1-40 from inclusion bodies is described in the following [Carrio et al., 2000, Wang et al., 2008, Dasari et al., 2011, Dasari, 2011, Linser et al., 2011b]. The previously frozen cell pellet was thawed at +4 °C. 10 µg/mL DNAse I and 1 x Complete Protease Inhibitor Cocktail (Roche) tablet were added and incubated for 1 h at +4 °C. The suspension was sonicated 2 × 2 min (30% amplitude) on ice in the cold room and centrifuged at 23,700 *g* for 15 min at +4 °C.

The pellet was resuspended in about 4 × 40 mL Tris/Triton buffer (composition given in Table 2.3). 40 mL were filled into four open-top centrifugation tubes. The suspension was sonicated 2 × 30 s with an amplitude of 10% on ice in the cold room and again centrifuged at 23,700 *g* for 15 min at +4 °C.

At this step, the pellet was resuspended in Tris buffer to remove the Triton and sonicated and centrifuged as before. The last washing step was repeated one more time. Finally, the pellet was shock frozen and stored at -80 °C.

To achieve a high purity, Aβ1-40 was further purified by chromatography, kindly carried out by Uwe Fink (FMP, Berlin). Therefore, the frozen pellet was thawed on ice and resuspended in a freshly prepared GdHCl buffer (Table 2.3) and finally purified by reversed-phase chromatog-

Table 2.3: $A\beta_{1\text{-}40}$ purification buffers.

buffer	composition
Tris buffer	20 mM Tris, pH 8.5 (adjusted with 30% HCl)
Tris/Triton buffer	20 mM Tris, 0.4% Triton-X (v/v), pH 8.5 (adjusted with 30% HCl)
GdHCl buffer	20 mM Tris, 8000 mM guanidine hydrochloride

raphy [Dasari, 2011].

The $A\beta_{1\text{-}40}$ fractions were pooled (monitored by SDS-PAGE) and the pool lyophilized for $\approx$3 d and stored at -80 °C. From an initial expression volume of 4 L, 40-50 mg of lyophilized $A\beta_{1\text{-}40}$ peptide were obtained.

2.2.3 Preparation of $A\beta_{1\text{-}40}$ amyloid fibrils

Amyloid fibrils for solid-state NMR investigations were prepared as described by del Amo et al. [2012]. To yield homogeneous samples, fibrils were grown in the presence of fibrillar seeds [Paravastu et al., 2009]. 12 generations of seeds were prepared. For generation 1-10 unlabeled, synthetic peptide was employed (kindly provided by Dr. Michael Beyermann, FMP Berlin). For generation 11-12 the 5% RAP labeled $A\beta_{1\text{-}40}$ peptide was used.

For preparation of a monomeric $A\beta_{1\text{-}40}$ solution, lyophilized, unlabeled, synthetic peptide (generation 1-10, prepared by Dr. Muralidhar Dasari, FMP Berlin) was dissolved in 20 mM NaOH to obtain an end concentration of 100 µM of peptide. The solution was centrifuged at 18,000 rpm for 10 min, using a tabletop centrifuge, in order to remove oligomeric aggregates. PBS buffer was added to yield an end concentration of 50 mM NaCl and 20 mM Na_2HPO_4 at pH 7.0-7.2, as well as 0.01% NaN_3. The solution was then sonificated for 10 min. Sonification was applied to all seeds prior to their usage. Fibrils were grown under continuous agitation (120 min^{-1}) at 23 °C for 4 days (generation 1).

The seeds from generation 1 were sonificated for 10 min and 10% (v/v) was added to a fresh, monomeric solution of 100 µm $A\beta_{1\text{-}40}$, prepared as before (*vide supra*). This 2^{nd} generation was grown for 2 days under the same agitation conditions. The procedure was repeated for generation 3-10, except, that seeds of generation 3-6 were grown for only 2 h and 7-10 for 4 h,

respectively.

For generations 11 and 12 isotopically labeled material was employed, using deuterated stock solutions (NaOD, PBS, NaN_3). The here employed 5% RAP labeled $A\beta_{1\text{-}40}$ peptide was two times dissolved and lyophilized in deuterated ammonium hydroxide (pH 1.5) to replace labile protons by deuterons. 100 µM monomeric, labeled $A\beta_{1\text{-}40}$ solution was prepared, as described above for the unlabeled peptide, and used to obtain generation 11-12, while employing 5% (v/v) seeding.

For the final fibrillization, the 5% RAP labeled $A\beta_{1\text{-}40}$ peptide was dissolved in 14 mM NaOD. Thereby, two different fibril samples were prepared. For the first sample, hereafter referred to as S1, ≈12 mg of monomeric $A\beta_{1\text{-}40}$ was employed and fibrils were grown under agitation for 14 d. These fibrils were directly packed into a 3.2 mm rotor by centrifugation. The fibrillization was monitored by Transmission Electron Microscopy (TEM) (Figure 2.1).

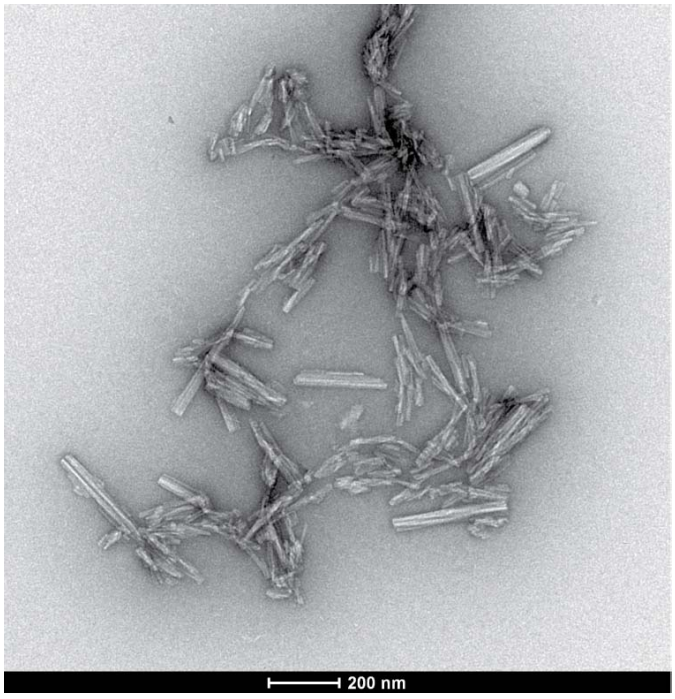

Figure 2.1: TEM image of 5% RAP labeled $A\beta_{1\text{-}40}$ fibrils (kindly recorded by Dr. Dorothea Lorenz, FMP Berlin). The fibrils were sonificated for 3 min prior to TEM.

For the second sample, referred to as S2, ≈10 mg monomeric 5% RAP labeled $A\beta_{1\text{-}40}$ was used, and the fibrils were also grown under agitation for 14 d, however, in the presence of 75 mM

Cu(II)EDTA (end concentration). Additionally, the S2 fibrils were washed two times with a PBS buffer containing 40% (v/v) uniformly deuterated glycerol. Both samples were packed into 3.2 mm rotors.

2.2.4 Preparation of A$\beta_{1\text{-}40}$ solution-state NMR samples

A solution-state NMR sample of monomeric A$\beta_{1\text{-}40}$ was prepared, using a 15% RAP sample. Therefore, lyophilized peptide was dissolved in a sodium hydroxide solution (75% H_2O / 25% D_2O) to yield an end concentration of 90 µM. The solution was steril filtrated (0.2 µm).

2.3 L7Ae-box C/D RNA complex from *Pyrococcus furiosus*

Here, the preparation of solid-state NMR samples of a L7Ae-box C/D protein-RNA complex from *Pyrococcus furiosus* (PF) is described. The preparation and purification of protein and RNA, as well as the complex formation, were carried out by Magdalena Rakwalska-Bange (EMBL Heidelberg).

The L7Ae protein from PF was expressed and purified as described elsewhere; the 26mer RNA was transcribed and purified according to established procedures [Jehle et al., 2010a]. For the ^{1}H- and ^{2}H-RNA samples u-[^{1}H,^{13}C,^{15}N] and u-[^{2}H,^{13}C,^{15}N] nucleotides were employed, respectively. Both assembled complexes (1:1 molar ratio) were back-exchanged in a buffer with a H_2O / D_2O ratio of 10% / 90% for 2-4 weeks to allow for sufficient ^{1}H/^{2}H exchange.

Prior to precipitation, the protein concentration was 7 mg/mL, dissolved in a 10% H_2O / 90% D_2O buffer with 40 mM HEPES, 14% PEG 400, and 50 mM magnesium acetate. The precipitation of the complex was induced by vapor diffusion using a SpeedVac at 60 mbar and +30 °C. As expected from the crystallization conditions [Moore et al., 2004], the complex precipitated at half volume. The final precipitates of the ^{1}H- (≈10 mg) and ^{2}H-RNA (≈2 mg) complexes were filled into 3.2 mm rotors by centrifugation.

The solid-state NMR experiments were carried out using Bruker Biospin Avance spectrometers operating at ^{1}H Larmor frequencies of 600 MHz and 700 MHz, respectively, employing commercial 3.2 mm triple-resonance probes. Details about temperature and MAS settings are

given in the figure captions in section 3.7 (page 137). The ^{1}H,^{15}N magnetization transfer was achieved by a ramped cross polarization step, matching the $n = 1$ Hartmann-Hahn condition. The ^{15}N evolution was ^{1}H- and ^{13}C-decoupled, whereas the ^{1}H evolution was ^{15}N-decoupled, respectively. For all nuclei, low-power WALTZ-16 [Shaka et al., 1983] decoupling with a rf field strength of 2-3 kHz was applied.

3 Results

3.1 Reduced Adjoining Protonation (RAP): Characterization and optimal RAP sample

To improve resolution and sensitivity in solid-state Nuclear Magnetic Resonance (NMR) spectroscopy of biomolecules, deuteration, accompanied by exchange of amide protons, was suggested to reduce the proton dipolar network and facilitate proton detection [Chevelkov et al., 2006]. Here, the Reduced Adjoining Protonation (RAP) labeling scheme is introduced, which enables proton detection of non-exchangeable aliphatic sites.

3.1.1 Expression and purification of α-spectrin SH3

The SH3 domain of chicken α-spectrin SH3 was chosen as a model system for establishing a new labeling scheme for solid-state NMR spectroscopy, since, next to advantageous spectroscopic properties, high protein expression levels can be yielded. As shown in Figure 3.1, the tag-free full-length protein can be obtained in high purity, after Anion-Exchange Chromatography (AEC) and Size-Exclusion Chromatography (SEC). Employing the RAP labeling scheme, the protein yield of α-spectrin SH3 was about 30-40 mg per liter expression medium.

3.1.2 ^{1}H/^{2}H concentration in RAP samples of α-spectrin SH3

The RAP labeling was designed to enable proton detection of aliphatic sites in the solid-state. Therefore, partial deuteration was employed to reduce the ^{1}H,^{1}H dipolar network and enhance coherence lifetimes. However, backbone, methine, methylene and methyl sites possess one to three non-exchangeable proton nuclei, respectively. Since the effective ^{1}H/^{2}H concentration

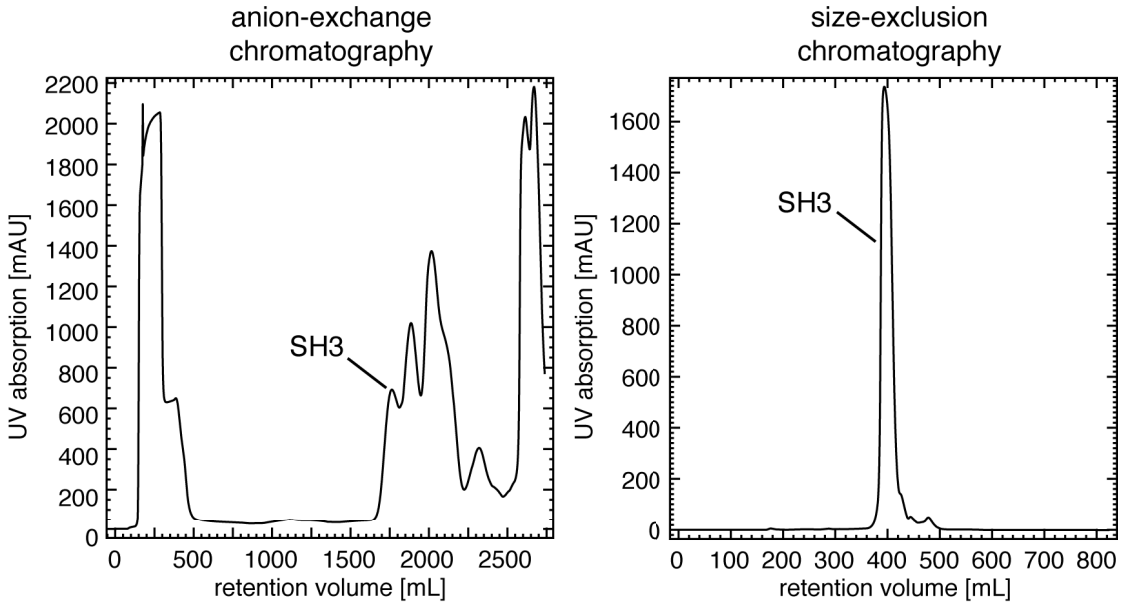

Figure 3.1: AEC and SEC chromatograms of a α-spectrin SH3 15% RAP sample, indicating the high efficiency of the purification procedure.

at the protein aliphatic sites is dependent on the $^{1}H/^{2}H$ concentration of the cell expression medium and the bacterial metabolism, we aimed to experimentally determine the absolute proton concentration at each aliphatic site.

Statistically, the isotope distribution for the methyl isotopomers $^{13}CH_3$, $^{13}CDH_2$, $^{13}CD_2H$ and $^{13}CD_3$ is $p^3/3p^2q/3pq^2/q^3 = 0.0001 : 0.007 : 0.14 : 0.86$ (using $p = 0.05$, $q = 1 \quad p$ for a 5% RAP sample, which refers to a sample, expressed in M9 medium containing 5% H_2O and 95% D_2O). Here, the remaining 3% protonation, originating from the utilized 97% deuterated ^{13}C-glucose [Agarwal and Reif, 2008], was neglected. For methylene isotopomers $^{13}CH_2$, ^{13}CDH, and $^{13}CD_2$, the statistical distribution is $p^2/2pq/q^2 = 0.002 : 0.1 : 0.9$.

Since the proton incorporation is stochastically applying the RAP labeling, it was required to experimentally determine the absolute proton concentration in RAP samples. As a first step, the experimental protein molecular weights for different RAP samples were determined by Matrix-Assisted Laser Desorption/Ionization (MALDI) mass spectrometry (carried out by Heike Stephanowitz, FMP, Germany) (Figure 3.2A). As expected, the molecular weight of the protein decreases as the ^{1}H concentration increases (5%, 15%, 25% H_2O) due to the respec-

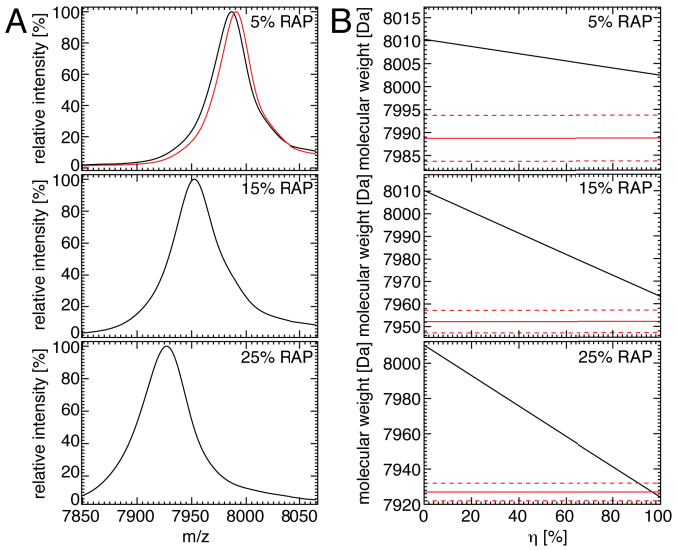

Figure 3.2: Determination of the ^{1}H-concentration in α-spectrin SH3 RAP samples by MALDI mass spectrometry. (A) MALDI spectra for a 5%, 15% and 25% RAP sample. The maxima correspond to 7986.9 Da (7990.6 Da), 7952.2 Da and 7927.0 Da, respectively. For the 5% RAP sample spectra from two different protein preparations were plotted, indicating the high reproducibility of the labeling scheme. (B) The theoretical molecular weight for the 5%, 15% and 25% RAP samples was plotted as a function of the solvent fraction, according to equation 3.1. The experimental value is indicated by a red horizontal line (solid). The uncertainty of the measurement is about ±5 Da (dashed red line).

tive reduction of the concentration of the heavier ^{2}H isotope (95%, 85%, 75% D_2O). The major obstacle for the determination of the proton concentration in RAP samples is the uncertainty about the portion of protons originating from the solvent and from the carbon source, respectively, since the protonation/deuteration is fractional. The following equation was employed, for estimating the theoretical molecular weight, M_{th}, of α-spectrin SH3 RAP samples:

$$\begin{aligned} M_{\mathrm{th}} = n(C)\left[p(^{13}C)\times M(^{13}C)+(1 \quad p(^{13}C))\times M(^{12}C)\right]+ \\ n(N)\left[p(^{15}N)\times M(^{15}N)+(1 \quad p(^{15}N))\times M(^{14}N)\right]+ \\ n(O)\times M(^{16}O)+n(S)\times M(^{32}S)+ \\ n_\eta(H)\times M(^{1}H)+(n_{\mathrm{total}}(H) \quad n_\eta(H))\times M(^{2}H) \end{aligned} \tag{3.1}$$

Here, M is the atomic mass of the respective isotope, p the isotope fraction, n the number of nuclei and $n_{\mathrm{total}}(H)$ the total number of proton sites, which amounts to 517 at pH 3.5. The isotope fraction for ^{13}C and ^{15}N was $p(^{13}C) = p(^{15}N) = 0.99$, respectively, according to the

purity of the employed precursors. $n_\eta(H)$ is a function of an empirical ratio η, which takes the ratio of both potential proton sources (solvent and glucose) into account. In this manner, $\eta = 0$ means, that 0% of the protons/deuterons stem from the solvent, while 100% originate from the glucose. $n_\eta(H)$ is defined as:

$$n_\eta(H) = n_{\mathrm{NH}}(H) + n_{\eta,\mathrm{gluc}}(H) + n_{\eta,\mathrm{solv}}(H),$$

with

$$\begin{aligned} n_{\eta,\mathrm{gluc}}(H) = &\quad \eta \times p_{\mathrm{gluc},^1\mathrm{H}} \times n_{\mathrm{stable}}(H) \\ n_{\eta,\mathrm{solv}}(H) = &\quad \eta \times p_{\mathrm{solv},^1\mathrm{H}} \times n_{\mathrm{stable}}(H), \end{aligned}$$

$n_{\mathrm{stable}}(H)$ is the number of non-exchangeable protonation sites and amounts to 389, whereas $n_{\mathrm{NH}}(H)$ is the number of labile, exchangeable $^1\mathrm{H}^\mathrm{N}$ protons, which amounts to 128 at the employed pH of 3.5. Here, $p_{\mathrm{gluc},^1\mathrm{H}}$ is equal to 0.03, which is the estimated purity of the employed u-[^{2}H,^{13}C]-glucose. $p_{\mathrm{solv},^1\mathrm{H}}$ takes the H_2O/D_2O ratio into account, which was used in the M9 expression medium of the respective RAP sample. For a specific α-spectrin SH3 RAP sample, the theoretical molecular weight M_{th} (equation 3.1) is only a function of η.

In Figure 3.2B M_{th} is plotted in dependency of η. Obviously, the experimentally determined molecular weights (solid red lines) cannot be fitted to this model, the weights are generally overestimated. However, to determine site-specific proton concentrations in RAP samples, solution-state NMR experiments were carried out, as described in the following.

To determine the site-specific ^{1}H concentrations, 2D TROSY-HN(CO)CA [Salzmann et al., 1999] experiments using solution-state NMR spectroscopy were recorded. During the $^{13}C\alpha$ evolution period, only deuterium and nitrogen has been decoupled, while the $^1H\alpha$,$^{13}C\alpha$ scalar coupling was allowed to evolve. Therefore, $^{13}C\alpha$,$^2H\alpha$ moieties appeared as singlets, whereas amino acids containing protonated $^{13}C\alpha$,$^1H\alpha$ were split into doublets. The absolute proton concentration was determined by calculating the ratio

$$\eta = \frac{2V_a}{V_a + V_b}, \tag{3.2}$$

where V_a and V_b are the peak volumes of the peaks denoted as a and b in the inset of Figure 3.3. Here, instead of peak volumes, we employed the peak areas of the 1D slices along the peak maxima in the ω_1-^{13}C dimension to determine the absolute proton concentration

$$\eta = \frac{2}{1+p}, \tag{3.3}$$

with $p = I_a/I_b$, where I_a and I_b are the peak areas of the aforementioned peaks a and b in the inset of Figure 3.3. The degree of protonation for 13 non-overlapping peaks are summarized in Table 3.1. For ^{1}Hα backbone resonances the experimental average value amounted to $(7.0 \pm 1.9)\%$. Following the same approach, the proton concentration of a RAP sample, grown on a M9 medium containing 15% H_2O and 85% D_2O, was determined as well. Here, the average value for ^{1}Hα amounted to $(16.7 \pm 2.1)\%$.

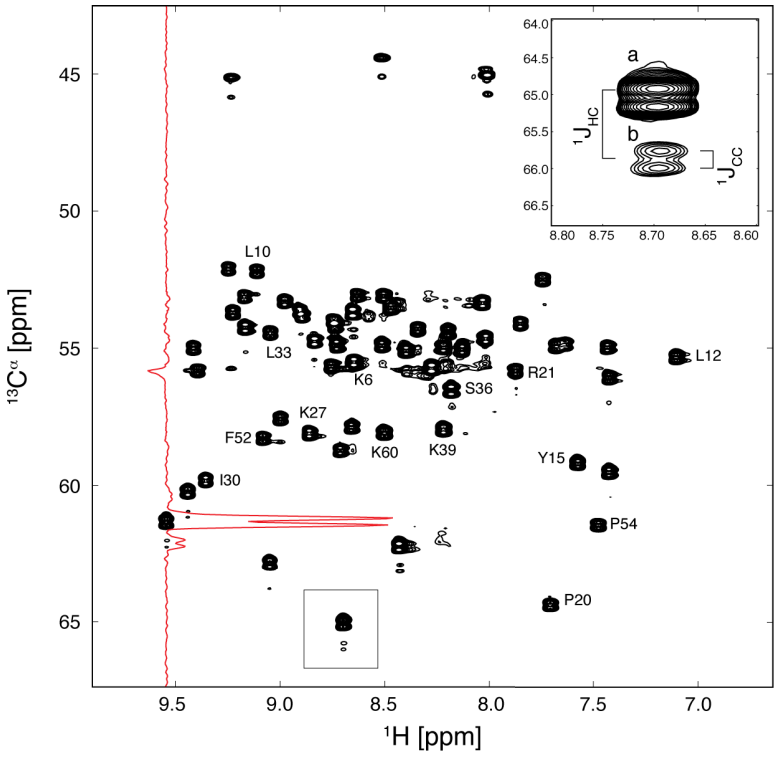

Figure 3.3: 2D TROSY HN(CO)CA spectrum of ≈460 µM α-spectrin SH3, obtained by growing *E. coli* on a M9 medium containing u-[^{2}H,^{13}C]-glucose and 5% H_2O. The sample pH was adjusted to 3.5. The spectrum was recorded at 300 K and an external magnetic field strength of 14.09 T (600 MHz). *Reproduced with permission from Asami, S., et al., J. Am. Chem. Soc., 2010, 132 (43), pp 15133–15135. Copyright 2010 American Chemical Society. DOI: 10.1021/ja106170h.*

Table 3.1: Concentration of protons at the $^{13}C\alpha$ position for a 5% α-spectrin SH3 RAP sample, according to the peak intensities determined from the HN(CO)CA experiment in Figure 3.3. The peak intensities were obtained using TOPSPIN v2.1 (Bruker, BioSpin). The average proton concentration amounts to $(7.0 \pm 1.9)\%$. *Reproduced with permission from Asami, S., et al., J. Am. Chem. Soc., 2010, 132 (43), pp 15133–15135. Copyright 2010 American Chemical Society. DOI: 10.1021/ja106170h.*

residue	K6	L10	L12	Y15	P20	R21	I30	L33	S36	K39	F52	P54	K60
^{1}H level [%]	4.3	8.4	5.3	7.4	4.9	8.9	8.3	7.5	7.9	7.6	9.4	3.6	7.3

The degree of protonation at side chain carbons of a 5% α-spectrin SH3 RAP sample was determined in solution using a constant-time HSQC experiment [Vuister and Bax, 1992], employing ^{2}H and ^{15}N decoupling during the ^{13}C constant-time evolution period. The spectra (Figure 3.4) yield the different isotopomers ($^{13}CH_3$, $^{13}CDH_2$, $^{13}CD_2H$, $^{13}CH_2$, ^{13}CDH, ^{13}CH) of the individual side chain methyl, methylene and methine groups, respectively. The amount of protonation, p_i, of the isotopomers was calculated as the fraction of the intensity of a cross peak in the deuterated sample relative to the corresponding peak volume in a reference spectrum. The reference spectrum was recorded with the same pulse sequence (constant-time HSQC), using an uniformly protonated, u-[^{1}H,^{13}C,^{15}N] α-spectrin SH3 sample. The results for several residues are summarized in Table 3.2. The overall proton concentration for methyl groups was on the order of 1% to 2%. For methylene groups, we found a proton concentration on the order of 3-5%. The amount of protonation f was calculated according to

$$f = \frac{1}{a} \sum_{i=0}^{a-1} p_i \, (a - i) \, . \tag{3.4}$$

p_i is the aforementioned volume fraction, specified in Table 3.2. For methylene groups $a = 2$ and $i = 0, 1$, referring to $^{13}CH_2$ and ^{13}CDH isotopomers, respectively. For methyl groups, $a = 3$ and $i = 0, 1, 2$, referring to $^{13}CH_3$, $^{13}CDH_2$ and $^{13}CD_2H$ moieties. Hence, using equation 3.4, the overall concentration of protons for methylene and methyl groups is described by

$$f_{\text{methylene}} = \frac{1}{2} \left(2 p_{\text{CH}_2} + p_{\text{CDH}} \right) \tag{3.5}$$

and

$$f_{\text{methyl}} = \frac{1}{3}\left(3p_{\text{CH}_3} + 2p_{\text{CDH}_2} + p_{\text{CD}_2\text{H}}\right), \tag{3.6}$$

respectively. Similarly for a α-spectrin SH3 sample grown on 15% H_2O, the methyl and methylene proton concentration was determined to be on the order of 11-13% and 10-16%, respectively.

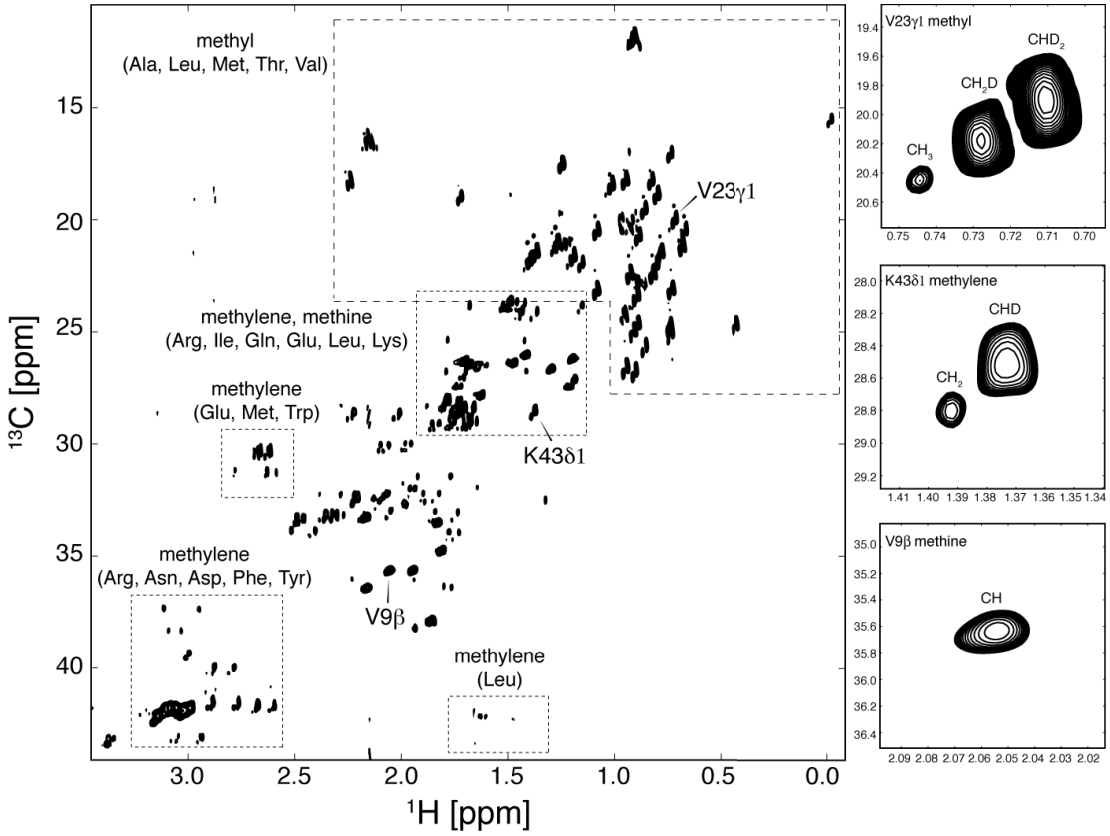

Figure 3.4: Constant-time HSQC spectrum of an u-[^{13}C,^{15}N] α-spectrin SH3 sample, which was expressed in a medium containing 5% H_2O and u-[^{2}H,^{13}C]-glucose. The refocused INEPT magnetization transfer time from ^{1}H to ^{13}C was 3.9 ms, corresponding to $1/2J_{HC}$. The constant-time period was set to 27 ms, corresponding to $1/J_{CC}$. A RF field strength of 1 kHz and 2 kHz was applied for GARP decoupling on the ^{15}N and ^{2}H channel, respectively. The spectral regions for methyls, methylenes and methines are highlighted by dashed boxes. The remaining peaks originate from Arg, Asp, Glu, Gln, Ile, Met, Lys, Pro methylene groups, as well as from Ile-β and Val-β methine groups, respectively. *Reproduced with permission from Asami, S., et al., J. Am. Chem. Soc., 2010, 132 (43), pp 15133–15135. Copyright 2010 American Chemical Society. DOI: 10.1021/ja106170h.*

In conclusion, it was shown by solution-state NMR, that all aliphatic sites of α-spectrin SH3 RAP samples (expressed in M9 medium with a H_2O level ≥5%) are protonated, while maintain-

Table 3.2: Concentration of side chain protons, as determined from the peak volumes extracted from the constant-time HSQC experiment in Figure 3.4. The sample was produced in a medium containing 5% H_2O and u-[^{2}H,^{13}C]-glucose. The proton concentration was calculated relative to a reference peak volume of an uniformly protonated u-[^{13}C,^{15}N] α-spectrin SH3 sample, yielding the fraction $p_i = V_i/V_{i,ref}$. The overall proton concentration is described by f (equation 3.4). The peak volumes were calculated with CcpNmr v2.1.2 [Vranken et al., 2005]. Only non-overlapping peaks were selected for quantification. *Reproduced with permission from Asami, S., et al., J. Am. Chem. Soc., 2010, 132 (43), pp 15133–15135. Copyright 2010 American Chemical Society. DOI: 10.1021/ja106170h.*

	^{1}H,^{13}C [ppm, ppm]			$p_i = V_i/V_{i,ref}$ [%]			f [%]
Residue	1*	2*	3*	1*	2*	3*	
E3β1	2.25, 28.91	2.22, 28.58	–	1.1	3.1	–	2.65
E3β2	2.04, 28.87	2.01, 28.60	–	1.1	2.8	–	2.57
V9γ2	1.11, 23.62	1.10, 23.36	1.08, 23.06	0.1	0.4	2.0	1.01
V23γ1	0.75, 20.46	0.73, 20.19	0.71, 19.91	0.1	0.3	0.9	0.56
I30δ	0.94, 12.24	0.92, 12.00	0.90, 11.77	0.2	1.1	3.1	1.99
T32γ	1.22, 22.11	1.21, 21.83	1.19, 21.56	0.1	0.9	2.5	1.57
K39α	4.33, 58.33	–	–	8.1	–	–	8.10
K43δ1	1.39, 28.82	1.37, 28.53	–	2.0	5.0	–	4.47
V46γ1	1.04, 18.91	1.03, 18.65	1.01, 18.37	0.1	0.4	1.5	0.85
V46γ2	1.11, 20.96	1.10, 20.69	1.08, 20.42	0.04	0.4	1.3	0.73

* Numbering refers to the isotopomers $^{13}CH_3$, $^{13}CDH_2$ and $^{13}CD_2H$ (1, 2, 3) for methyls, $^{13}CH_2$ and ^{13}CDH (1, 2) for methylenes, ^{13}CH (1) for methines and to $^{13}C\alpha$,$^1H\alpha$ (1).

ing a high deuteration level, which is beneficial in terms of spectral sensitivity and resolution, as discussed in section 3.1.4.1 (page 40). However, significant protonation of aliphatic sites was also validated by solid-state NMR for α-spectrin SH3 microcrystals by comparing ^{13}C,^{13}C RFDR correlation spectra, employing either ^{1}H- or ^{13}C-excitation (section 3.1.4.6, page 56).

3.1.3 ^{1}H-detected ^{1}H,^{13}C HMQC spectra of α-spectrin SH3 in the solid-state

Employing a microcrystalline α-spectrin SH3 5% RAP sample, we recorded ^{1}H-detected ^{1}H,^{13}C Heteronuclear Multiple Quantum Correlation (HMQC) spectra in the solid-state, using the pulse sequence depicted in Figure 3.5. To improve the resolution for the side chain region, 2-3 kHz low-power WALTZ-16 ^{2}H decoupling was used during the ^{13}C evolution period [Shaka et al., 1983]. The ^{2}H offset was set to the middle of the aliphatic region. Furthermore, during the direct acquisition period, the ^{1}H,^{13}C scalar coupling was decoupled, employing 2-3 kHz low-power WALTZ-16 decoupling on the ^{13}C channel.

Already at a moderate Magic Angle Spinning (MAS) frequency of 20 kHz and an external magnetic field strength of 14.1 T (^{1}H Larmor frequency of 600 MHz), high resolution was ob-

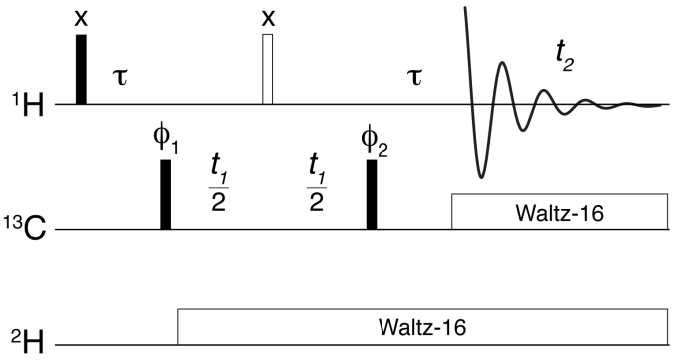

Figure 3.5: ^{1}H,^{13}C Heteronuclear Multiple Quantum Correlation (HMQC) pulse sequence for detection of aliphatic resonances. Solid and open bars represent $\pi/2$ and π pulses, respectively. The MAS frequency was adjusted to 20 kHz. A rf field strength of 73 kHz and 83 kHz was used on the ^{1}H and ^{13}C channel, respectively. The duration of τ was set to 3.9 ms corresponding to $1/2J_{HC}$. A rf field strength of 2.5 kHz was applied for WALTZ-16 decoupling [Shaka et al., 1983] on the ^{13}C and ^{2}H channel, respectively. The phase cycle ϕ_1 = x, -x, ϕ_2 = x, x, -x, -x and ϕ_{rec} = x, -x, -x, x was employed. The ^{1}H and ^{2}H carrier frequency was positioned on the HDO and D_2O resonance, respectively. Quadrature detection in ω_1 was achieved using TPPI [Marion and Wuthrich, 1983]. No special care was taken for solvent suppression. *Reproduced with permission from Asami, S., et al., J. Am. Chem. Soc., 2010, 132 (43), pp 15133–15135. Copyright 2010 American Chemical Society. DOI: 10.1021/ja106170h.*

tained for the entire aliphatic region (Figure 3.6A). We obtained high-resolution spectra for all aliphatic proton-carbon pairs, in particular for the ^{1}Hα,^{13}Cα backbone, side chain and methyl region, respectively (Figure 3.6B-D). Especially the methyls yielded high resolution and sensitivity, since they experience a reduced dipolar coupling anisotropy due to fast rotation around their three-fold axis (typically in the picosecond range, cf. section 3.4.4, page 85).

The experimental proton line widths in Figure 3.6 varied between 25 Hz for Thr37γ2, and 60 Hz for Thr37α, respectively. The carbon line width is determined by ^{13}C,^{13}C scalar couplings and was on the order of 110 Hz (Thr37α). The ^{13}C,^{13}C scalar couplings were resolved, particularly visible in the methyl region (Figure 3.6D).

Additionally, the presented RAP labeling scheme allowed to avoid high-power decoupling schemes due to the dilution of the proton network. 2-3 kHz WALTZ-16 decoupling was sufficient to achieve ^{13}C decoupling during ^{1}H detection. For comparison, the proton line width for an uniformly protonated α-spectrin SH3 sample was about 170 Hz [Chevelkov et al., 2003]. Sensitivity and resolution of resonances in the methyl region of the spectrum were not compromised, even though the amount of protons had been increased dramatically in comparison to previously presented approaches, where ^{1}H,^{13}C correlations have been recorded, using only the

residual protonation, originating from the proton impurities of the utilized deuterated glucose (97% deuterated) and D_2O medium (99% deuterated) [Agarwal and Reif, 2008].

3.1.4 Optimal degree of protonation of α-spectrin SH3 RAP samples

3.1.4.1 Sensitivity and resolution as a function of protonation and MAS frequency

The ^{1}H dipolar network, which is the major obstacle for applying proton detection in the solid-state, can be reduced by deuteration, when employing the RAP labeling scheme, which yields random protonation at non-exchangeable sites. We carried out a systematic study on the optimal degree of random backbone and side chain protonation in RAP samples as a function of the MAS frequency. In particular, we compared ^{1}H sensitivity and line width of microcrystalline α-spectrin SH3 in the MAS frequency range of 20-60 kHz for samples prepared with 5-25% H_2O in the *E. coli* M9 minimal growth medium.

NMR experiments were carried out using Bruker Biospin Avance spectrometers operating at ^{1}H Larmor frequencies of 500 MHz and 850 MHz, respectively, using a commercial 1.3 mm triple-resonance probe. The 1.3 mm probe of the 850 MHz spectrometer was equipped with an additional external ^{2}H coil [Huber et al., 2012]. At all MAS frequencies, the effective sample temperature was adjusted to ≈20 °C, using the chemical shift difference between the solvent resonance and Leu8δ2, respectively. ^{1}H,^{13}C HMQC experiments were performed as described in the prior section (section 3.1.3, page 38). The employed rf fields on the ^{1}H and ^{13}C channels for hard pulses were ≈80-90 kHz and ≈80-100 kHz, respectively. Low-power ^{1}H, ^{2}H and ^{13}C decoupling of 1-3 kHz was applied, using the WALTZ-16 decoupling scheme [Shaka et al., 1983].

For normalization of the absolute signal intensities of the different samples, ^{13}C 1D spectra were recorded for the 5%, 15% and 25% RAP sample, without ^{1}H and ^{2}H decoupling. For these experiments, a recycle delay of 30 s was employed, setting the MAS frequency to 40 kHz.

The spectra were processed with NMRPipe [Delaglio et al., 1995] and analyzed by CcpNmr v2.1.5 [Vranken et al., 2005] and in-house Python scripts, using the I/O routines of nmrglue v0.2 [Helmus and Jaroniec, 2013]. To compensate for the magnet drift, we corrected the relative frequency shift for each increment of the 2D ^{1}H,^{13}C HMQC spectrum by adding a frequency

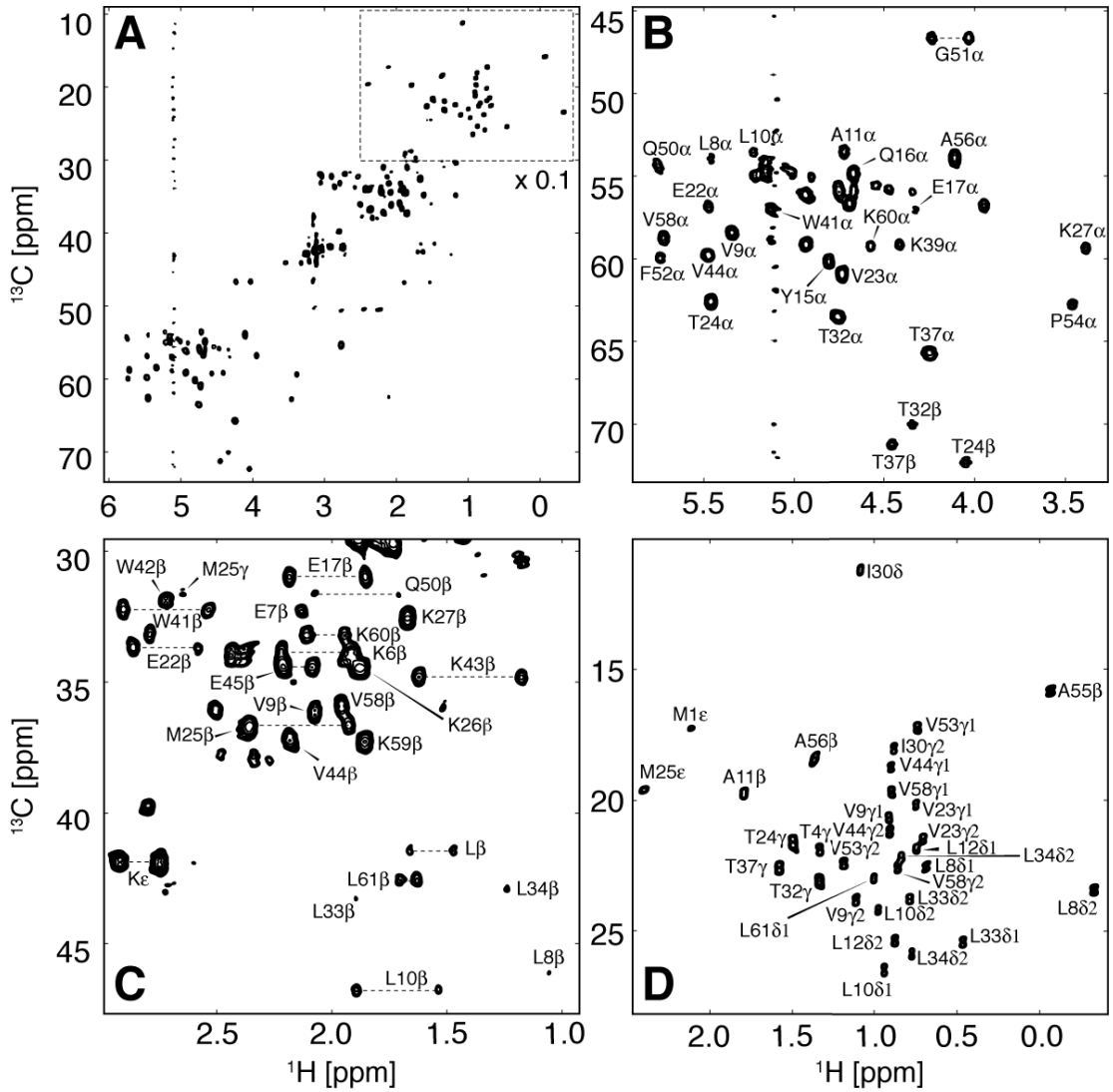

Figure 3.6: MAS solid-state ^{1}H-detected ^{1}H,^{13}C HMQC spectrum of a 5% α-spectrin SH3 RAP sample. The spectrum was recorded at 600 MHz (14.1 T), setting the MAS frequency to 20 kHz. The effective temperature was adjusted to 17 °C. The acquisition times in the direct and indirect dimension were set to 52 ms and 21 ms, respectively. The full spectrum (A) is represented enlarged in (B), (C) and (D), displaying the ^{1}Hα,^{13}Cα region, ^{1}Hβ,^{13}Cβ region, and the methyl region, respectively. The methyl region in (A) has been scaled by a factor of 0.1. Details on experimental parameters are given in Figure 3.5. *Reproduced with permission from Asami, S., et al., J. Am. Chem. Soc., 2010, 132 (43), pp 15133–15135. Copyright 2010 American Chemical Society. DOI: 10.1021/ja106170h.*

offset, that was calculated using a fifth order polynomial function. The parameters for the offset correction were determined using the resolved Leu8δ2 methyl resonance.

To investigate the achievable sensitivity and resolution of randomly protonated RAP samples (5%, 15%, 25%), 1D ^{1}H,^{13}C HMQC spectra were recorded at MAS rotation frequencies ranging from 20 kHz to 64 kHz, respectively. Figure 3.7A shows the bulk sensitivity for backbone and methyl resonances under these conditions. The spectra reveal, that higher MAS frequencies were beneficial for the sensitivity. For the 5% and 25% RAP sample, the signal increases up to a plateau at a MAS frequency of ≈40 kHz and ≈50 kHz, respectively. The sensitivity gain is ≈3.5 (≈4.5) and ≈2.0 (≈4.0) fold for backbone and methyl resonances for the 5% (25%) RAP sample. This progression was expected, since the ^{1}H,^{1}H dipolar network in the 5% RAP sample was extensively diluted. Therefore, rotational averaging of the dipolar Hamiltonian has a smaller impact on dipole mediated line broadening and hence the signal-to-noise ratio, as compared to less diluted samples, such as the 25% RAP sample.

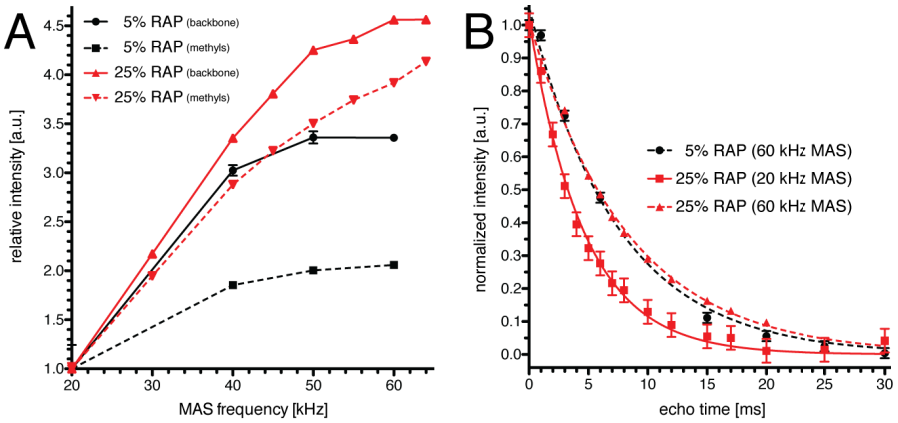

Figure 3.7: Bulk sensitivity and ^{1}H T_2 times as a function of the MAS frequency for α-spectrin SH3 RAP samples grown on M9 medium containing either 5% or 25% H_2O, respectively. (A) Integral intensity for backbone and methyl resonances for the first FID from a ^{1}H,^{13}C HMQC experiment as a function of the MAS frequency. The signal intensity reaches a plateau at a MAS frequency of ≈40 (≈50) kHz for the 5% (25%) RAP sample. The sensitivity gain amounts to a factor of ≈3.5 (≈4.5) and ≈2.0 (≈4.0) for backbone and methyl resonances. (B) ^{1}H signal dephasing in a T_2 echo experiment at 20 kHz and 60 kHz. The T_2 time for the 25% RAP sample increases from 4.6 ms to 8.2 ms at higher spinning frequencies and becomes comparable to the bulk T_2 of the 5% RAP sample (7.5 ms). *Reproduced with kind permission from Asami, S., et al., J. Biol. NMR, 2012, 54 (2), pp 155-168. Copyright 2012 Springer Science and Business Media. DOI: 10.1007/s10858-012-9659-9.*

The effective ^{1}H T_2 time for the 5% and the 25% RAP samples at 20 kHz and 60 kHz rotation frequency was determined using a spin echo experiment (Figure 3.7B). For this purpose, the HMQC scheme (cf. Figure 3.5, page 39) was modified by insertion of an echo, prior to the

first $1/2J_{HC}$ delay. The T_2 time for the 25% RAP sample increases from 4.6 ms to 8.2 ms at 60 kHz and becomes comparable to the bulk T_2 of the 5% RAP sample (7.5 ms at 60 kHz). This indicates, that homogeneous line broadening was already averaged at a MAS frequency of 60 kHz.

As dipolar relaxation through protons is the major source for relaxation for aliphatic sites, ^{1}H T_1 times were expected to increase with higher MAS frequencies, which potentially compromises the sensitivity per unit time in ^{1}H excited experiments. However, for the 25% RAP sample, the bulk ^{1}H T_1 time increases experimentally only insignificantly from ≈0.8 s to ≈0.9 s.

Figure 3.8A shows 2D ^{1}H,^{13}C HMQC spectra, recorded for a 25% RAP sample, when increasing the MAS frequency from 20 kHz to 40 kHz. The top row represents the 1D projections of the respective 2D spectra. The first contour level is depicted in the projections by a dashed line (in red), which was kept at an equal absolute signal intensity for all plots. Obviously, the signal-to-noise ratio improved with higher MAS frequencies, in particular for the ^{1}Hα,^{13}Cα backbone region, alongside with a significant improvement of the spectral resolution, as can be seen in Figure 3.8B. Here, the backbone region of a 2D ^{1}H,^{13}C HMQC spectrum of a 5% α-spectrin SH3 RAP sample at 20 kHz MAS and a ^{1}H Larmor frequency of 600 MHz (left) is compared to a spectrum of a 25% RAP sample at 40 kHz and 850 MHz (right), respectively. The backbone resolution was significantly improved at 40 kHz, even though a less diluted sample was employed. This was due to an increased effective ^{13}Cα T_2 time and the higher external magnetic field strength.

In Figure 3.9A, the MAS dependent signal intensity is represented for individual residues. In the left column, the relative peak intensities were plotted. As expected, the highest relative sensitivity for the backbone as well as for methyl resonances was achieved for the 25% RAP sample. A less pronounced gain was observed for the 15% and 5% RAP sample, respectively. On average (Figure 3.9B), the relative gain in sensitivity was on the order of 2-4 fold (Table 3.3). Since methyl groups undergo fast rotations around their threefold axis (cf. section 3.4.4, page 85), methyl protons experience a reduced dipolar coupling anisotropy $d_{\text{met}} = \left| d_{CH} \times \frac{1}{2}\left(3\cos^2\theta - 1\right)\right| \approx \frac{1}{3} d_{CH}$ ($\theta = 109.5°$). Therefore, effectively a larger gain was observed for backbone resonances in comparison to methyls.

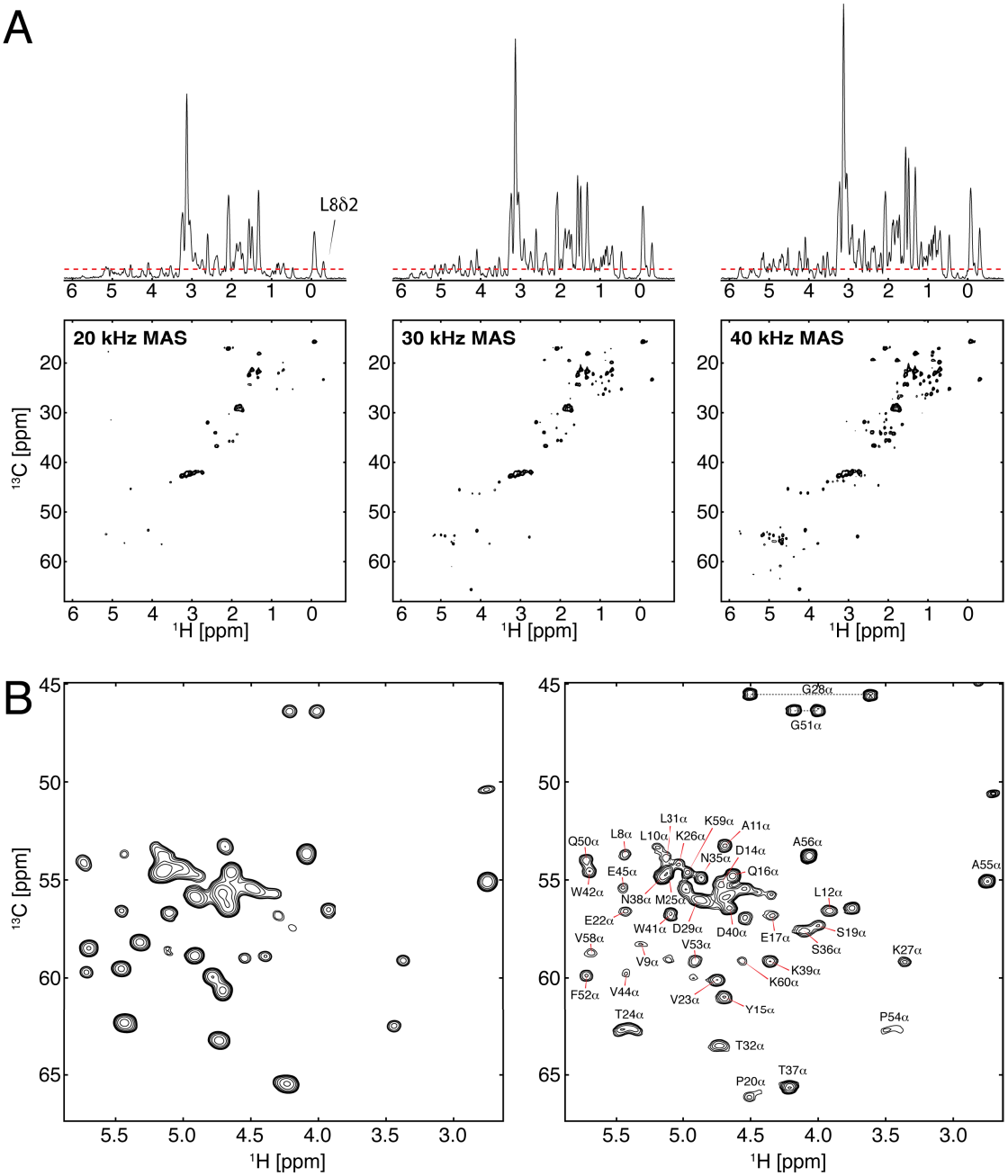

Figure 3.8: Sensitivity and resolution for α-spectrin SH3 RAP samples as a function of the MAS frequency and for different external magnetic field strengths. (A) 2D ^{1}H,^{13}C HMQC spectra for a 25% RAP sample at different MAS rotation frequencies. The top row shows the projection onto the ω_2 dimension for the respective 2D spectrum. The dashed red line depicts the first contour level, which was set to be equal for all spectra. We observed a significant increase in sensitivity for both backbone and side chain resonances. (B) ^{1}Hα,^{13}Cα backbone region of a 5% RAP sample at 20 kHz MAS and a ^{1}H Larmor frequency of 600 MHz (left), compared to a spectrum of a 25% RAP sample at 40 kHz and 850 MHz (right), respectively. We observed an improved resolution at higher spinning frequencies and magnetic fields, even though a less diluted sample was employed. The assignments were obtained from a 3D HCC experiment (section 3.2, page 64). *Reproduced with kind permission from Asami, S., et al., J. Biol. NMR, 2012, 54 (2), pp 155-168. Copyright 2012 Springer Science and Business Media. DOI: 10.1007/s10858-012-9659-9.*

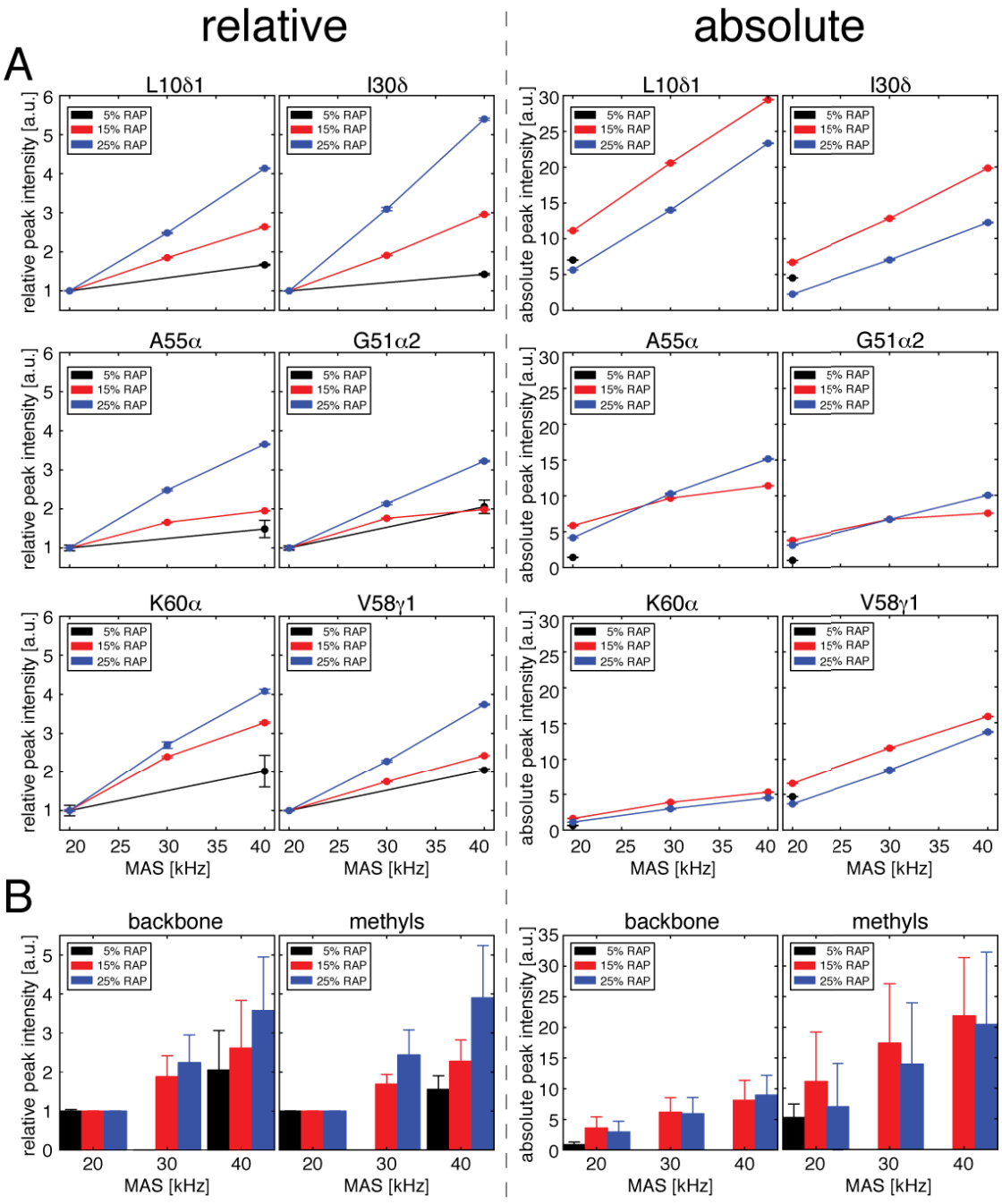

Figure 3.9: (A) MAS dependent signal intensities for individual peaks in 5%, 15% and 25% α-spectrin SH3 RAP samples, respectively, extracted from a 2D ^{1}H,^{13}C HMQC experiment. In the left column, the signal intensities were normalized with respect to their intensities at 20 kHz MAS. The right column shows absolute signal intensities in arbitrary units. (B) Average peak intensities for backbone and methyl groups for different RAP samples at a relative (left) and an absolute scale (right), according to the values in Table 3.3. Absolute intensities were normalized by the sample amount, using direct excitation ^{13}C 1D experiments. *Reproduced with kind permission from Asami, S., et al., J. Biol. NMR, 2012, 54 (2), pp 155-168. Copyright 2012 Springer Science and Business Media. DOI: 10.1007/s10858-012-9659-9.*

Table 3.3: Average gain in sensitivity for a 5%, 15% and 25% α-spectrin SH3 RAP sample, respectively, at increasing MAS frequencies. The absolute average X was determined as $\frac{1}{N}\sum_{i=1}^{N} x_{i,j}$, the relative as $\frac{1}{N}\sum_{i=1}^{N} x_{i,j}/x_{i,1}$, where N refers to the number of resonances, $x_{i,j}$ to the absolute signal intensity for residue i. $j = 1,2,3$ refers to the MAS frequencies 20 kHz, 30 kHz and 40 kHz,respectively. The error in the determination of the signal intensities was estimated as $\frac{1}{\sqrt{N}}\Delta n + \frac{1}{N}\sqrt{\sum_{i=1}^{N}(x_i - X)^2}$, where Δn refers to the noise level, x_i to the individual peak intensity and X to the average intensity. The absolute intensities were scaled according to intensities in directly excited ^{13}C 1D spectra. A graphic representation of these values is given in Figure 3.9B. *Reproduced with kind permission from Asami, S., et al., J. Biol. NMR, 2012, 54 (2), pp 155-168. Copyright 2012 Springer Science and Business Media. DOI: 10.1007/s10858-012-9659-9.*

		Relative			Absolute		
		20 kHz	30 kHz	40 kHz	20 kHz [a.u.]	30 kHz [a.u.]	40 kHz [a.u.]
backbone	5% RAP	1.0 ± 0.0	–	2.1 ± 1.0	0.9 ± 0.4	–	–
	15% RAP	1.0 ± 0.0	1.9 ± 0.5	2.6 ± 1.2	3.6 ± 1.8	6.2 ± 2.4	8.1 ± 3.2
	25% RAP	1.0 ± 0.0	2.2 ± 0.7	3.6 ± 1.4	3.0 ± 1.8	5.9 ± 2.7	9.0 ± 3.2
methyls	5% RAP	1.0 ± 0.0	–	1.6 ± 0.3	5.2 ± 2.2	–	–
	15% RAP	1.0 ± 0.0	1.7 ± 0.2	2.3 ± 0.5	11.1 ± 8.1	17.4 ± 9.7	21.9 ± 9.5
	25% RAP	1.0 ± 0.0	2.4 ± 0.6	3.9 ± 1.3	7.0 ± 7.1	14.0 ± 10.0	20.5 ± 11.8

In order to find the optimum degree of protonation in terms of absolute signal intensities, we plotted the distribution of the absolute signal intensities for the 15% and 25% RAP sample in Figure 3.10. Here, the intensities have been scaled according to the amount of protein in the rotor. For normalization of the absolute signal intensities of the different samples, ^{13}C 1D spectra were recorded for the 5%, 15% and 25% RAP sample, without ^{1}H and ^{2}H decoupling. For these experiments, a recycle delay of 30 s was employed, setting the MAS frequency to 40 kHz. Scaling factors for normalization were determined on the basis of the peak intensities of the bulk ^{13}C' signals.

Clearly, a shift to higher intensities is observed for higher MAS frequencies for both samples (Figure 3.10). Evidently, at 20 kHz MAS the number of high intensity peaks for backbone and methyls is larger for the 15% in comparison to the 25% RAP sample. At a MAS frequency of 40 kHz, the average sensitivity of backbone resonances reaches its maximum value for the 25% RAP sample, and the methyl sensitivity has its optimum for a 15% RAP sample.

3.1.4.2 Experimental and simulated ^{1}H line width at fast spinning

Dipole mediated line broadening contributes significantly to the detected ^{1}H line width, whereas the line width approximately scales linearly with the rotor period [Ernst et al., 2001, Reif and

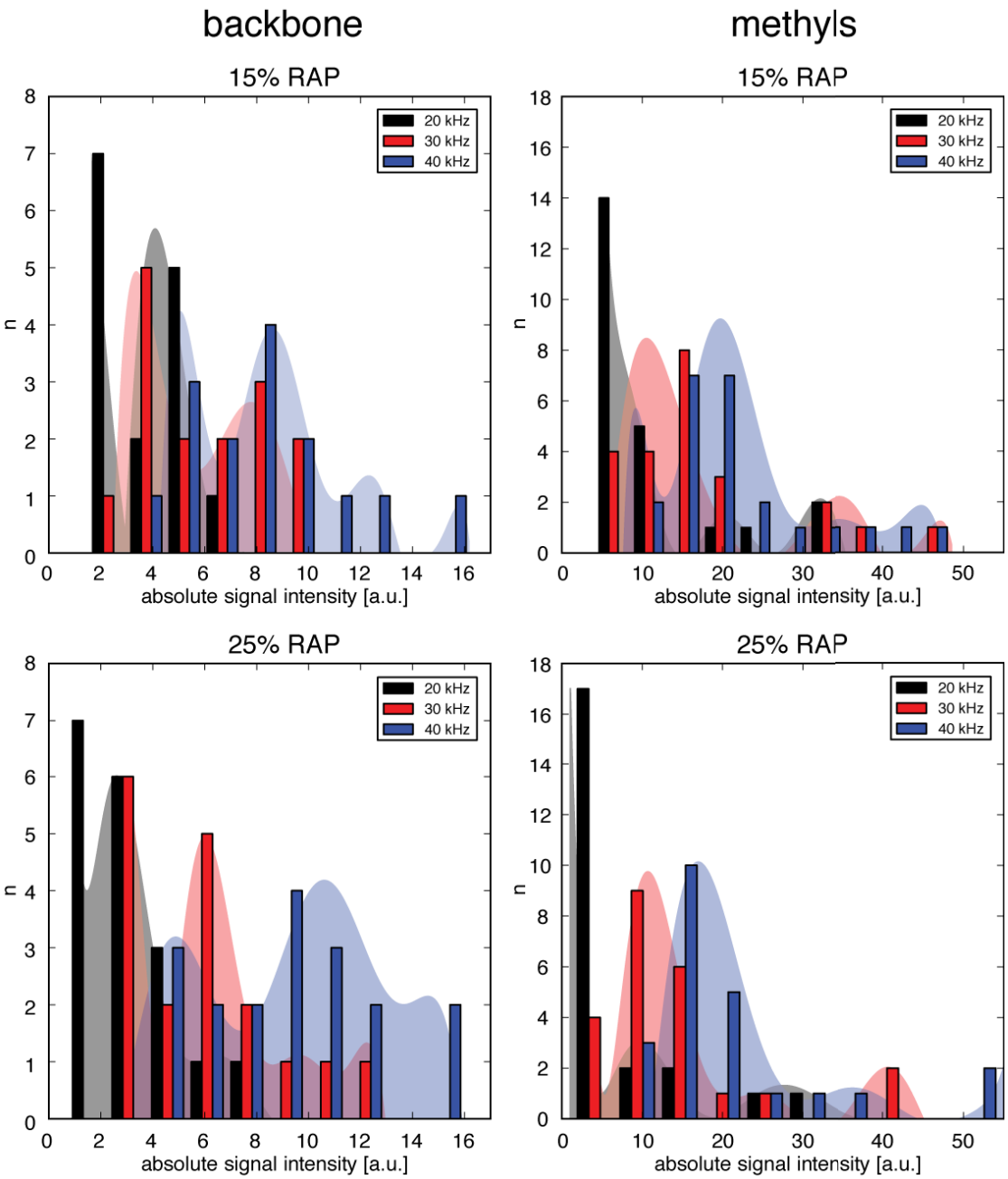

Figure 3.10: Distribution of absolute signal intensities in 15% and 25% α-spectrin SH3 RAP samples at different MAS frequencies, with backbone and methyl resonances separated in the left and right column, respectively. The number of bins was set to ten for all plots. *Reproduced with kind permission from Asami, S., et al., J. Biol. NMR, 2012, 54 (2), pp 155-168. Copyright 2012 Springer Science and Business Media. DOI: 10.1007/s10858-012-9659-9.*

Griffin, 2003]. Along these lines, the ^{1}H line width of a 25% RAP sample was determined as a function of the MAS frequency. As can be seen for backbone as well as for methyl resonances, the line width reduces significantly for higher spinning frequencies (Figure 3.11). The resolution seemed to approach an asymptotic limit above 40 kHz. At 40 kHz, the line width of the 25% RAP sample approaches the average line width determined for the 5% RAP sample (Figure 3.12A). The achievable ^{1}H line width at 40 kHz MAS for a 25% RAP sample was on the order of (49 $\pm$ 11) Hz for the backbone, and (44 $\pm$ 9) Hz for methyl protons, respectively (Figure 3.12B). Thus, high MAS frequencies almost compensated line broadening effects of the less dilute sample.

Numerical simulations showed similar results for the ^{1}H line width at increasing MAS rotation frequencies. The ^{1}H line width was determined for a proton within a four-spin system, as a function of MAS and ^{1}H Larmor frequency. The spin system was created with SIMMOL [Bak et al., 2002], using proton coordinates of a lysine molecule, and simulated by SIMPSON [Bak et al., 2000]. For the simulations in Figure 3.13A the spin system was composed of four proton spins, as depicted by the structural model, whereas for Figure 3.13B the ^{1}Hβ2 proton was substituted by a deuteron. For the spin system, only the ^{1}Hα, ^{1}Hβ1, ^{1}Hβ2 and ^{1}Hγ1 nuclei of lysine were retained, setting their isotropic chemical shift values to 5 ppm, 3.5 ppm, 3.4 ppm and 2.5 ppm, respectively. Only the dipolar couplings for ^{1}Hα,^{1}Hβ1, ^{1}Hα,^{1}Hβ2, ^{1}Hα,^{1}Hγ1, ^{1}Hβ1,^{1}Hγ1, ^{1}Hβ2,^{1}Hγ1 were considered and set according to the distance of the respective pair of nuclei. The ^{1}Hα line width was simulated as a function of the MAS (20-70 kHz) and ^{1}H Larmor frequency (400-1000 MHz). Furthermore, the simulation was performed with an altered spin system, in which ^{1}Hβ2 was substituted by a deuteron. The ^{1}H,^{2}H dipolar couplings were adjusted accordingly and a quadrupolar coupling constant of 150 kHz was assumed.

As expected, high spinning frequencies, as well as high magnetic fields, are favorable in terms of resolution, as the dipole mediated line broadening was almost suppressed for both spin systems. However, replacing a single proton by a deuteron led to a significant reduction of the ^{1}H line width, especially at low spinning frequencies and external magnetic fields.

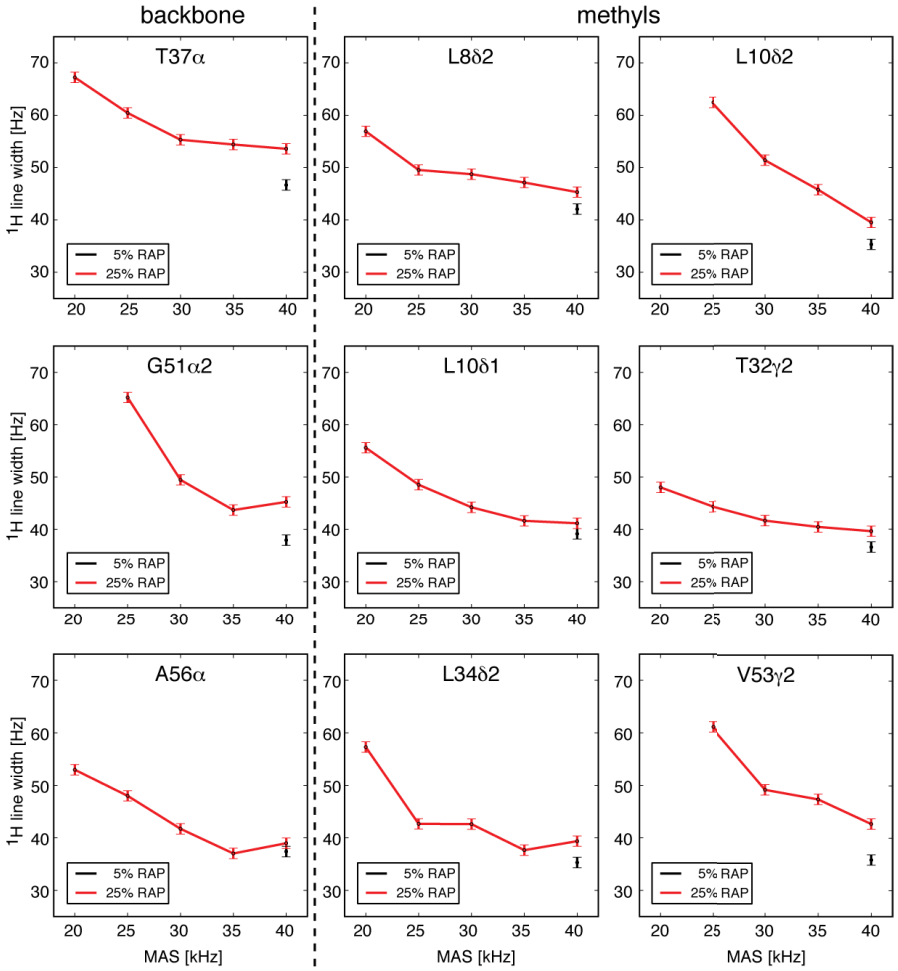

Figure 3.11: ^{1}H line width of backbone (left column) and methyl resonances (right column) as a function of the MAS frequency for a 5% and 25% RAP sample of α-spectrin SH3. *Reproduced with kind permission from Asami, S., et al., J. Biol. NMR, 2012, 54 (2), pp 155-168. Copyright 2012 Springer Science and Business Media. DOI: 10.1007/s10858-012-9659-9.*

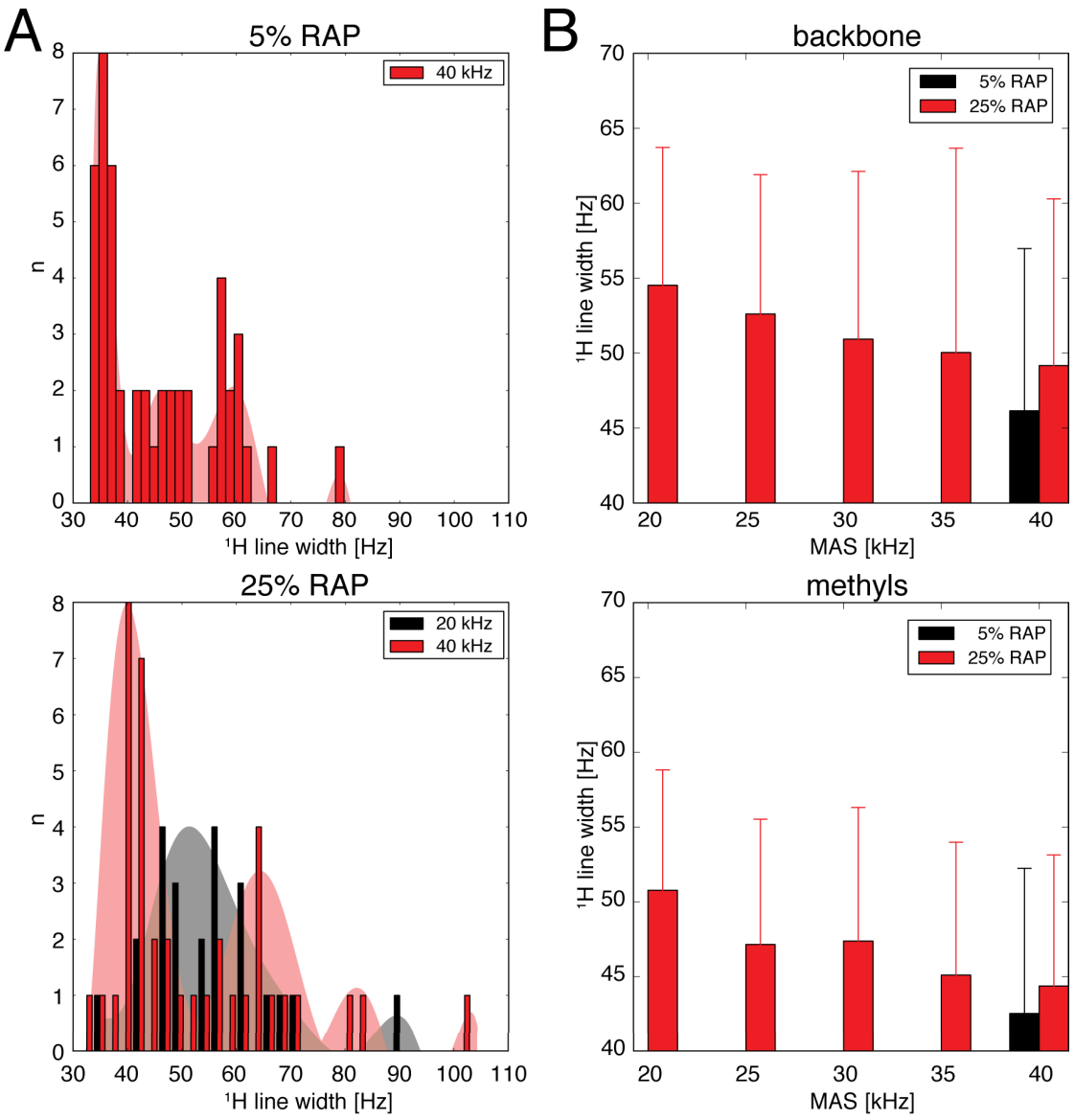

Figure 3.12: (A) Distribution of the ^{1}H line width for a 5% and 25% RAP sample of α-spectrin SH3 at a MAS frequency of 20 kHz and 40 kHz, respectively. (B) Average ^{1}H line width in the MAS frequency range of 20-40 kHz. Backbone and methyl resonances were plotted separately. *Reproduced with kind permission from Asami, S., et al., J. Biol. NMR, 2012, 54 (2), pp 155-168. Copyright 2012 Springer Science and Business Media. DOI: 10.1007/s10858-012-9659-9.*

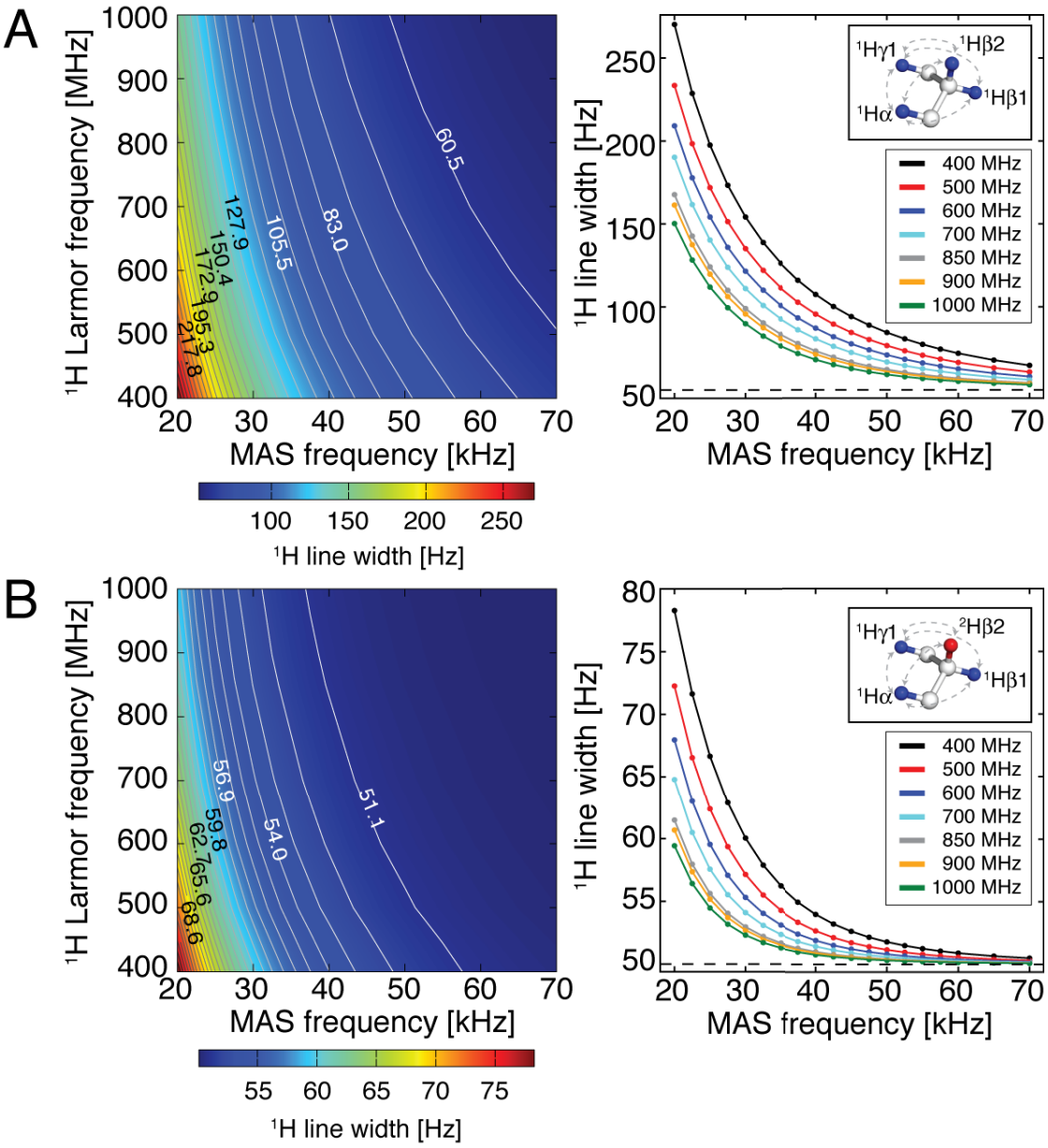

Figure 3.13: ^{1}H line width as a function of the MAS and the ^{1}H Larmor frequency, simulated for the indicated four spin system. (A) Simulation carried out using four ^{1}H spins. (B) Simulation performed with three ^{1}H spins and one ^{2}H spin. For this simulation, ^{1}Hβ2 was substituted by a deuteron. Dashed lines in the structure indicate the dipolar couplings employed in the simulation. For apodization a line broadening of 50 Hz was applied (dashed line in the simulation). In all cases, the ^{1}H line width was determined for the ^{1}Hα resonance. *Reproduced with kind permission from Asami, S., et al., J. Biol. NMR, 2012, 54 (2), pp 155-168. Copyright 2012 Springer Science and Business Media. DOI: 10.1007/s10858-012-9659-9.*

3.1.4.3 Sensitivity vs. ^{1}H line width

Sensitivity and resolution were correlated upon change of the MAS rotation frequency (Figure 3.14). For accuracy, peaks with high signal-to-noise ratios were selected. The approximate clustering of the population into loop and β-sheet indicated, that fast spinning had a greater influence on resonances of residues, which are located in β-sheets, than for residues in loops. This is presumably due to a higher rigidity of the β-sheets. For example, Leu33δ2 and Leu10δ1, which reside in a β-sheet, were strongly MAS-dependent, unlike Leu12δ2, which was found in a loop region.

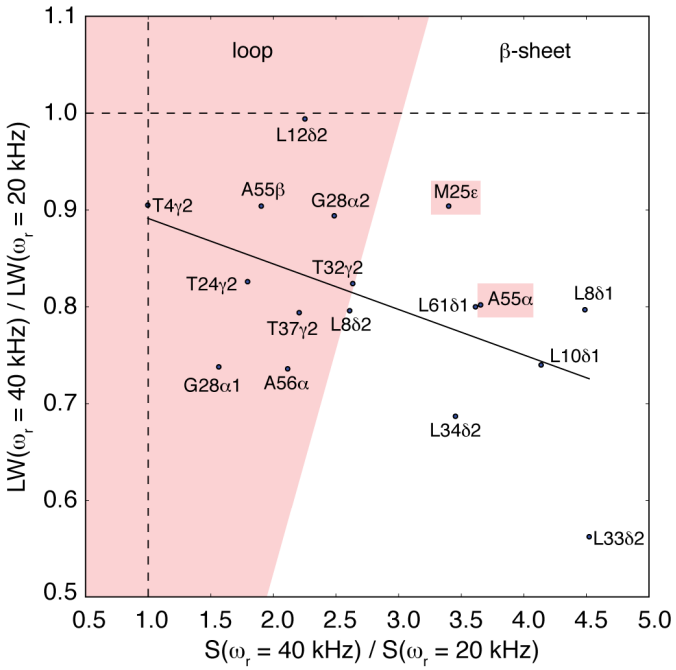

Figure 3.14: Relation between the ratio of ^{1}H line width and the gain in sensitivity for a 25% RAP sample, measured at a MAS frequency of 20 kHz and 40 kHz. Overall, the gain in sensitivity and the reduction in line width were correlated. The shaded area in the diagram highlights residues, which are located in loop regions. *Reproduced with kind permission from Asami, S., et al., J. Biol. NMR, 2012, 54 (2), pp 155-168. Copyright 2012 Springer Science and Business Media. DOI: 10.1007/s10858-012-9659-9.*

3.1.4.4 Improvement of ^{13}C resolution by fast spinning and homonuclear ^{13}C,^{13}C decoupling

In extensively deuterated microcrystalline protein samples, the carbon line width is essentially determined by homonuclear scalar couplings to adjacent carbon nuclei, since at high MAS frequencies and magnetic fields the ^{13}C,^{13}C dipolar couplings do not contribute significantly to the ^{13}C line width. Selectively labeled precursors, such as [2]-^{13}C or [1,3]-^{13}C glycerol [LeMaster and Kushlan, 1996, Hong and Jakes, 1999, Castellani et al., 2002], could be employed to isotopically label primarily non-consecutive carbon nuclei in the protein and to remove ^{13}C,^{13}C scalar couplings.

For consecutively carbon labeled samples various homonuclear *J*-decoupling techniques have been suggested for solid-state samples [Straus et al., 1996, Chevelkov et al., 2005b, Igumenova and McDermott, 2005, Shi et al., 2008, Laage et al., 2009, Kehlet et al., 2011]. For backbone ^{13}Cα carbons, evolution of the ^{13}C' and ^{13}Cβ coupling can be suppressed by application of bandselective pulses. Figure 3.16 shows 2D ^{1}Hα,^{13}Cα correlations obtained for a 15% RAP sample of α-spectrin SH3. To yield optimal water suppression, the ^{13}C evolution period was designed in a constant-time fashion [Paulson et al., 2003]. In the absence of homonuclear decoupling, the ^{1}Hα,^{13}Cα region of the spectrum was rather poorly resolved (Figure 3.16A), yielding ^{13}Cα line widths on the order of 105 Hz. ^{13}C',^{13}Cα and ^{13}Cβ,^{13}Cα scalar couplings, which are on the order of 55 Hz and 35 Hz, respectively, contribute significantly to the broadening of the ^{13}Cα resonances.

To improve the resolution in the ^{1}Hα,^{13}Cα spectral region, we employed adiabatic HS2 inversion pulses during the ^{13}Cα evolution period (Figure 3.15). The enhancement of the resolution can be clearly appreciated from Figure 3.16B. The ^{13}Cα line widths were reduced to $\approx$35-60 Hz and a gain in resolution of about a factor of two was obtained.

Alternatively, a constant-time experiment [Vuister and Bax, 1992] can be carried out to yield a similar improvement in resolution. In the absence of high-power proton decoupling and at moderate rotation frequencies, however, backbone coherence lifetimes are short and constant-time experiments become too insensitive.

Side chain carbons are more difficult to decouple by bandselective pulses due to the chemical

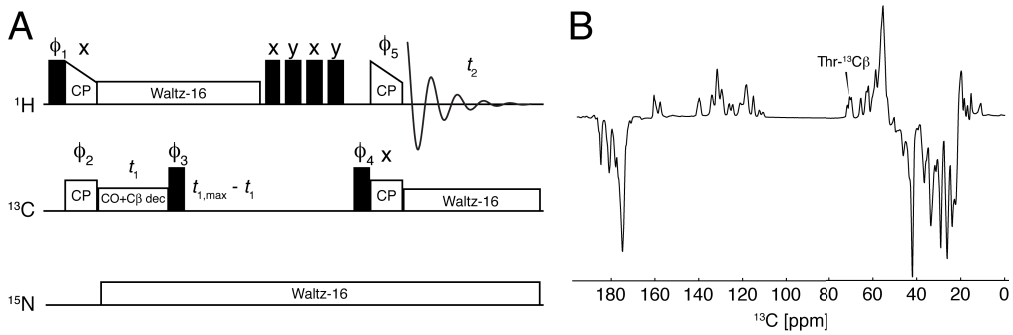

Figure 3.15: (A) ^{1}H-detected 2D (H)CH experiment with ^{13}C'+^{13}Cβ-decoupling. Water suppression was achieved with a constant-time MISSISSIPPI sequence [Paulson et al., 2003, Zhou and Rienstra, 2008]. ϕ_1 = (y, -y), ϕ_2 = (x, x, -x, -x), ϕ_3 = (y), ϕ_4 = (y), ϕ_5 = (x, x, x, x, -x, -x, -x, -x), ϕ_{rec} = (y, -y, -y, y), (-y, y, y, -y). (B) Inversion profile of the utilized adiabatic HS2 pulse. *Reproduced with kind permission from Asami, S., et al., J. Biol. NMR, 2012, 52 (1), pp 31-39. Copyright 2012 Springer Science and Business Media. DOI: 10.1007/s10858-011-9591-4.*

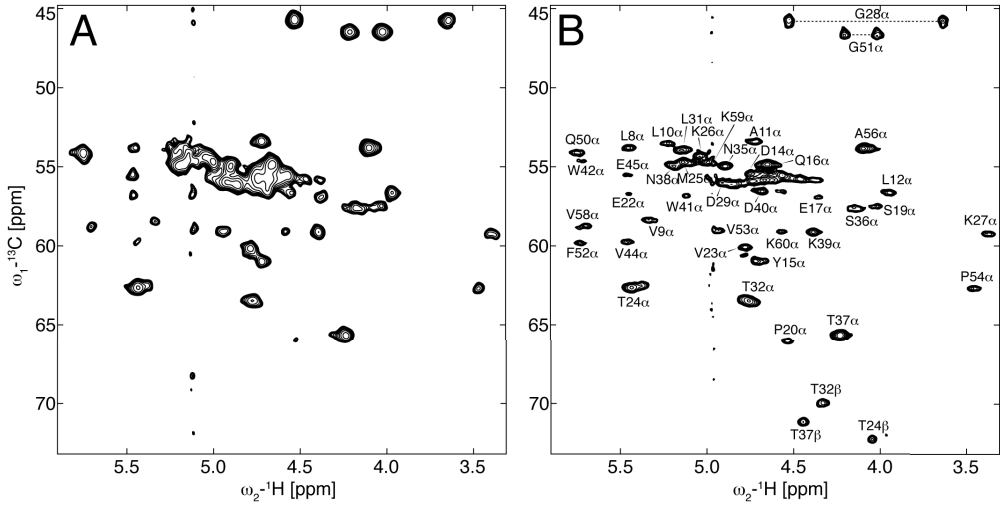

Figure 3.16: ^{1}Hα,^{13}Cα correlation spectra of a 15% RAP sample of α-spectrin SH3. (A) Without and (B) with ^{13}C'+^{13}Cβ homonuclear scalar decoupling during ω_1, employing the pulse sequence shown in Figure 3.15A. The spectra were recorded at 600 MHz, setting the MAS rotation frequency to 24 kHz. *Reproduced with kind permission from Asami, S., et al., J. Biol. NMR, 2012, 52 (1), pp 31-39. Copyright 2012 Springer Science and Business Media. DOI: 10.1007/s10858-011-9591-4.*

shift overlap of the *J*-coupled atoms. In this case, constant-time experiments (Figure 3.17A) have to be employed, but typically require long ^{13}C coherence lifetimes and, therefore, high-power decoupling on the order of 100-150 kHz during the constant-time periods [Tian et al., 2009], even for deuterated proteins [Tang et al., 2010].

Here, we estimated the side chain resolution and the ^{13}C coherence lifetimes via 1D constant-time HSQC experiments [Vuister and Bax, 1992] for a 5% and 25% α-spectrin SH3 RAP sample at 20 kHz and 60 kHz MAS (Figure 3.17B), respectively. The constant-time delay was set to 28.6 ms, according to $1/J_{C^{\alpha},C^{\beta}}$. At 20 kHz MAS, the resolved signal of Leu8δ2 was barely detectable in both samples. Overall, all side chain resonances, especially the methyl resonances in the 25% RAP sample, displayed very low peak intensities. Setting the MAS frequency to 60 kHz yielded a significant increase of the effective T_2 time for side chain carbons. The peak intensity of the resolved Leu8δ2 signal increased up to a factor of ≈2 and ≈8 for the 5% and 25% RAP sample, respectively. 2D constant-time HSQC spectra are shown in Figure 3.37 (page 93).

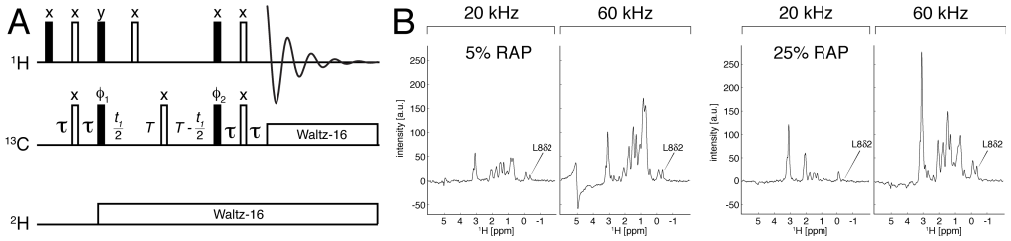

Figure 3.17: (A) ^{1}H,^{13}C constant-time HSQC pulse sequence, omitting ^{13}C' selective refocussing pulses [Vuister and Bax, 1992]. 2.5 kHz WALTZ-16 decoupling [Shaka et al., 1983] was applied on the ^{13}C and ^{2}H channel, respectively. The phase cycle, ϕ_1 = x, -x, ϕ_2 = x, x, -x, -x and ϕ_{rec} = x, -x, -x, x, was employed. (B) First increment of a constant-time ^{1}H,^{13}C HSQC experiment of a 5% and 25% RAP sample of a microcrystalline sample of the α-spectrin SH3 domain at 20 kHz and 60 kHz MAS frequency, respectively. The constant-time period $T = 1/J_{C^{\alpha},C^{\beta}}$ was set to 28.6 ms. The gain in sensitivity for Leu8δ2 was on the order of ≈2 and ≈8 fold for the 5% and 25% RAP sample, respectively. *Reproduced with kind permission from Asami, S., et al., J. Biol. NMR, 2012, 54 (2), pp 155-168. Copyright 2012 Springer Science and Business Media. DOI: 10.1007/s10858-012-9659-9.*

3.1.4.5 Optimization of homonuclear ^{13}C,^{13}C mixing

Active recoupling of the ^{13}C,^{13}C dipolar interactions is essential in deuterated samples, as the transfer amplitudes in Proton-Driven Spin Diffusion (PDSD) experiments is typically not sufficient to yield efficient mixing. In Figure 3.18, the performance of the dipolar mixing se-

quences PDSD [Szeverenyi et al., 1982], adiabatic RFDR [Leppert et al., 2003] and RAD/DARR [Takegoshi et al., 2001, 2003, Morcombe et al., 2004] are compared, employing an uniformly protonated, as well as a 5% RAP sample of α-spectrin SH3, respectively. We found a similar mixing performance for a 5% RAP labeled sample (B: adiabatic RFDR spectrum, using a mixing time of 15 ms), in comparison to the uniformly protonated SH3 sample (A: PDSD spectrum, using a mixing time of 20 ms).

Application of PDSD mixing to a severely proton diluted 5% RAP sample yielded a very limited number of cross peaks (C), even though the mixing time was increased to 50 ms. Under these conditions, RAD/DARR spectra (D-F) displayed a significantly improved mixing profile [Huang et al., 2011a]. In the experiment, a rf field is applied either on the ^{1}H channel (D), on the ^{2}H channel (E), or, as recently proposed [Akbey et al., 2009], simultaneously on the ^{1}H and the ^{2}H channels (F). Simultaneous irradiation only yielded marginal improvements over single-channel irradiation. For the cross peak Thr32 ^{13}Cβ,^{13}Cα, we find a relative cross peak intensity of 47% for RFDR, and 15% for ^{1}H+^{2}H RAD/DARR, respectively (the percentage indicates the ratio of the cross peak volume to the sum of the cross and diagonal peak volumes). In total, the adiabatic RFDR sequence (subjacent spectrum in black in plots (C-F)) displayed by far the best mixing profile amongst PDSD and RAD/DARR and was, therefore, employed in 3D HCC and CCH assignment experiments, described in section 3.2 (page 64).

3.1.4.6 Proton versus carbon excitation

In terms of sensitivity, proton excitation is in principle more favorable due to the higher gyromagnetic ratio of protons and their short T_1 relaxation times. However, ^{1}H-excited experiments are not easily feasible as protons are randomly distributed in RAP samples. In a 15% RAP sample, approximately 17% of all ^{13}Cα carbons, and 10-16% of the side chain carbons are protonated (section 3.1.2, page 31). To probe whether proton or carbon excitation was more favorable, we compared in the following the sensitivity of ^{1}H- and ^{13}C-excited 2D ^{13}C,^{13}C RFDR experiments (Figure 3.19A).

In RAP samples (in contrast to uniformly deuterated samples), uniform excitation of all side chain carbons is not an issue due to a more or less isotropic incorporation of protons in all po-

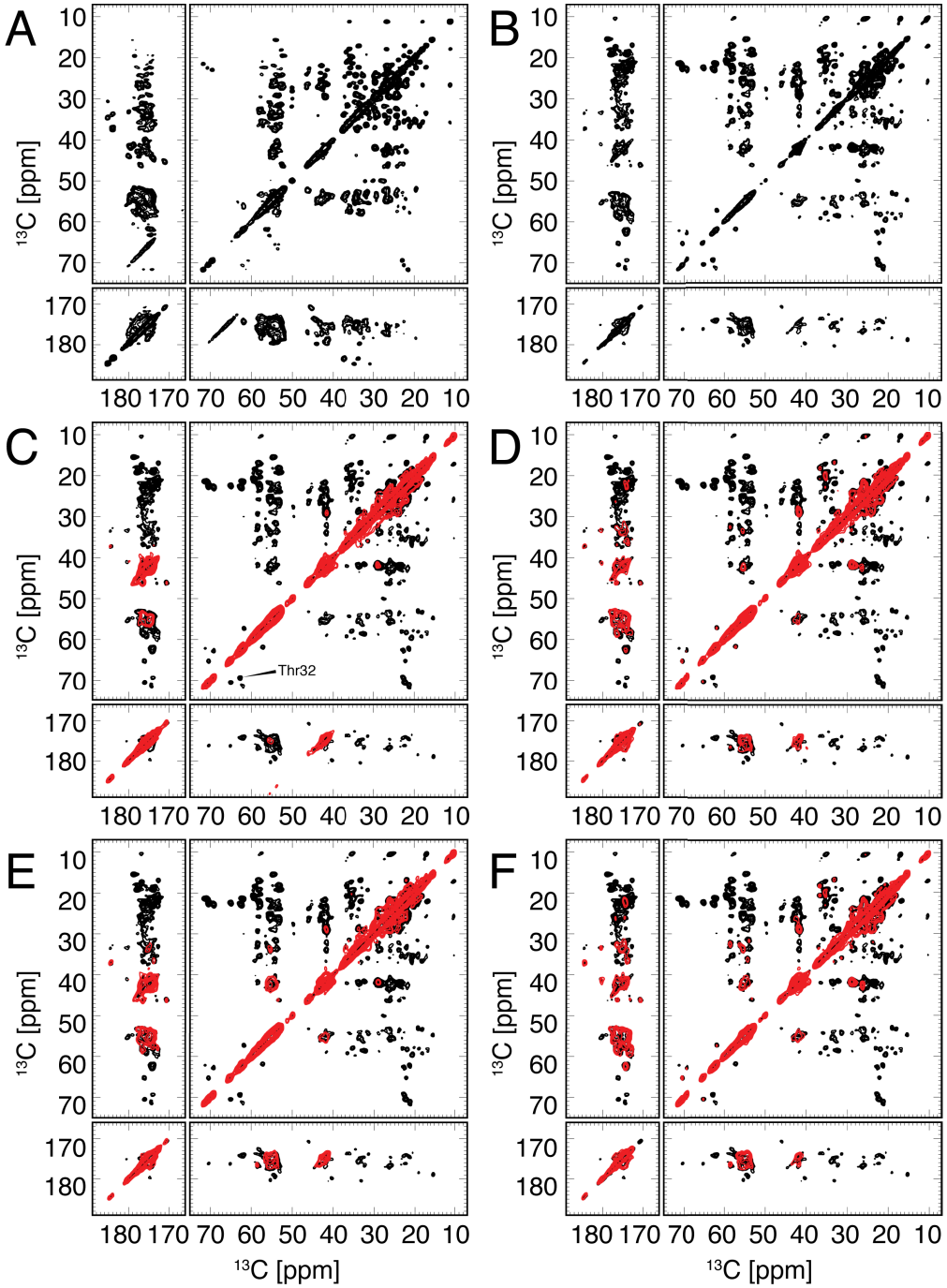

Figure 3.18: (A) PDSD spectrum of an uniformly [^{1}H,^{13}C,^{15}N] labeled α-spectrin SH3 sample, recorded at 400 MHz and 11 kHz MAS. The mixing time was set to 20 ms. (B) Adiabatic RFDR spectrum acquired for a 5% RAP sample at 600 MHz and 20 kHz MAS. The mixing period was adjusted to 15 ms. This spectrum was used as a reference for figures (C-F). The superimposed red spectra in (C-F) are PDSD and RAD/DARR spectra with rf irradiation on the ^{1}H, ^{2}H and ^{1}H+^{2}H channel, respectively. All spectra (C-F) were recorded using a total mixing time of 50 ms, and a 5% SH3 RAP sample. The rf field strength was set to the $n = 1$ rotational resonance condition. *Reproduced with permission from Asami, S., et al., Acc. Chem. Res., 2013, 46 (9), pp 2089–2097. Copyright 2013 American Chemical Society. DOI: 10.1021/ar400063y.*

sitions (cf. Table 3.2, page 38). Therefore, approximately the same number of correlations was observable in the ^{1}H-, as compared to the ^{13}C-excited experiment (Figure 3.19B), respectively. Missing peaks originate from residues located at the flexible N-terminus or in loop regions (e.g. Val46). These residues are mobile and magnetization is not transferred by cross polarization.

Both RFDR experiments, ^{1}H- and ^{13}C-excited, were recorded with a recycle delay of 3 s and the same number of scans, employing adiabatic RFDR for ^{13}C,^{13}C mixing [Leppert et al., 2003]. The mixing time was set to 9.9 ms with $t_1(\max) = 4.3$ ms. The first increment of the two experiments yielded rather similar intensities (Figure 3.19C). It should be noted, that the recycle delay for the ^{1}H-excited RFDR experiment could have been reduced to $\approx$0.5 s, since the apparent T_1 time for protons was much shorter than for carbons. Thus, the ^{1}H-excited experiment yielded an approximately $\approx 2.5\times$ larger sensitivity (per unit time) in comparison to the ^{13}C-excited experiment.

To further increase the achievable sensitivity, the ^{1}H,^{13}C cross polarization transfer step (2CP, Figure 3.20A, left) was supplemented with a 90° ^{13}C pulse for direct carbon excitation and an additional ^{2}H,^{13}C transfer step (3CP, Figure 3.20A, right). Cross polarization employing rf fields on two or three channels (^{1}H,^{13}C and ^{1}H+^{2}H,^{13}C), are referred to as 2CP and 3CP, respectively. The CP contact time for 2CP and 3CP was 1 ms, with a ^{13}C rf field of 24 kHz and a ^{1}H rf field strength ramped linearly around the $n = 1$ Hartmann-Hahn matching condition. The MAS frequency was set to 18 kHz. The ^{2}H rf field for ^{2}H,^{13}C CP was ramped between 38 kHz and 59 kHz (n = 2-3). Experimentally, it was found, that ^{2}H,^{13}C CP sensitivity benefits from high power levels, especially for the backbone resonances, even though spinning sidebands with $n > 1$ are matched. However, with the available rf power on the ^{2}H channel the whole ^{2}H spectrum could not be excited and using maximum power to achieve the $n = 1$ condition might damage the probe. The 2CP and 3CP experiments were carried out using a 600 MHz spectrometer.

Employing 3CP yields a gain in the signal-to-noise ratio for the ^{13}Cα region of approximately a factor of 1.6 (Figure 3.20B). A similar observation was reported recently for uniformly deuterated and ^{1}H back-exchanged samples [Akbey et al., 2011]. In this context, a four channel probe with high-power capabilities for ^{1}H, ^{2}H, ^{13}C and low-power capabilities for ^{15}N would be desirable. Simultaneous cross polarization among ^{1}H, ^{13}C and ^{2}H, in combination with scalar decou-

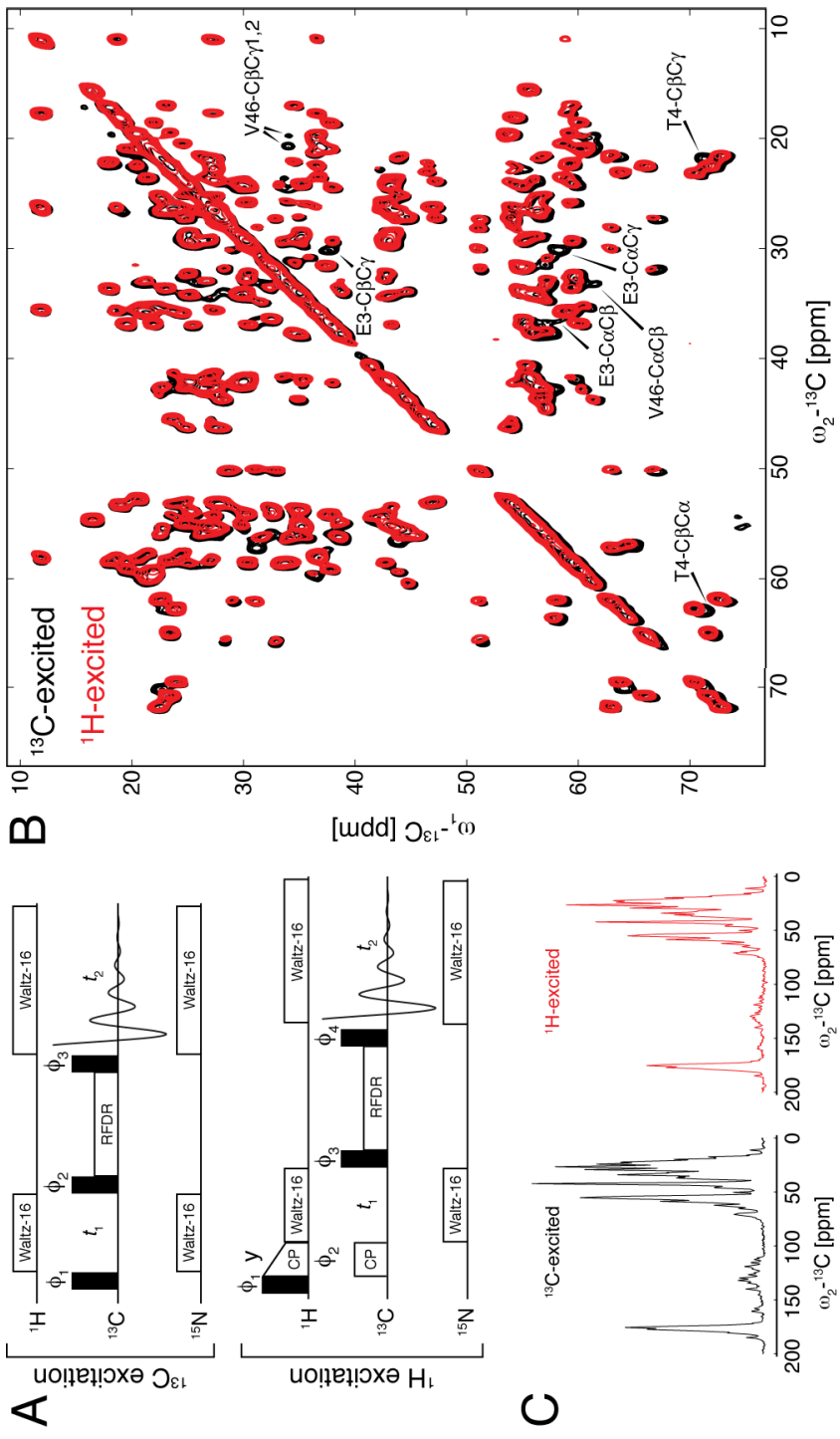

Figure 3.19: ^{13}C- versus ^{1}H-excitation in a 15% RAP sample of α-spectrin SH3. (A) ^{13}C-excited experiment: ϕ_1 = (-x, x), ϕ_2 = (x), ϕ_3 = (-x, -x, x, x), ϕ_{rec} = (-x, x, x, -x). ^{1}H-excited experiment: ϕ_1 = (-x, x), ϕ_2 = (y, y, y, y, -y, -y, -y, -y), ϕ_3 = 8(x), ϕ_4 = 8(-x), ϕ_{rec} = (-x, x, x, -x), 2(x, -x, -x, x), (-x, x, x, -x). (B) Superposition of a ^{13}C- (black) and ^{1}H- (red) excited ^{13}C,^{13}C RFDR spectrum. The ^{13}C- and ^{1}H-excited ^{13}C,^{13}C correlation experiments were recorded, employing adiabatic RFDR for ^{13}C,^{13}C mixing [Leppert et al., 2003], using a mixing time of 9.9 ms with t_1^{max} = 4.3 ms and a recycle delay of 3 s. Missing peaks in the ^{1}H-excited spectrum were labeled with their respective assignment. (C) First increments of the ^{13}C- and ^{1}H-excited experiment, respectively. Both spectra were recorded with the same number of scans and recycle delay. *Reproduced with kind permission from Asami, S., et al., J. Biol. NMR, 2012, 52 (1), pp 31-39. Copyright 2012 Springer Science and Business Media. DOI: 10.1007/s10858-011-9591-4.*

pling in the direct and indirect evolution periods (Figure 3.20C) would yield another increase in performance. The use of Optimum Control (OC) in pulse sequence design might further allow to improve sensitivity by reducing the required rf fields on the ^{2}H channel [Wei et al., 2011].

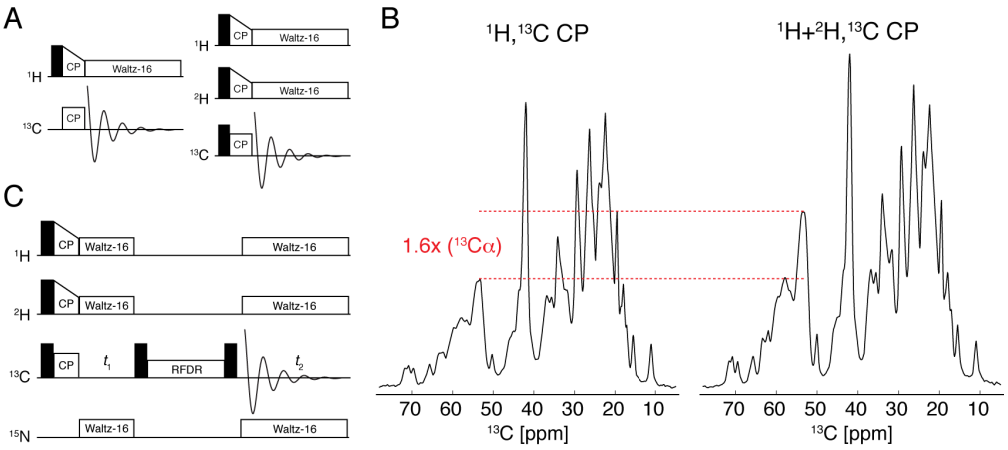

Figure 3.20: Simultaneous ^{1}H+^{2}H,^{13}C cross polarization (3CP) yields a significant improvement in sensitivity. (A) Pulse scheme for the ^{1}H,^{13}C 2CP (left) and ^{1}H+^{2}H,^{13}C 3CP (right) experiment. (B) Comparison of the sensitivity of 2CP and 3CP experiments. (C) 3CP ^{13}C,^{13}C RFDR pulse sequence for a 4-channel probe. *Reproduced with kind permission from Asami, S., et al., J. Biol. NMR, 2012, 52 (1), pp 31-39. Copyright 2012 Springer Science and Business Media. DOI: 10.1007/s10858-011-9591-4.*

3.1.4.7 Isotopomeric purity in RAP samples

In addition to line width and sensitivity, the isotopomeric purity, and thus, the spectral quality, has to be taken into account to identify the ideal amount of H_2O in the bacterial growth medium for Reduced Adjoining Protonation (RAP) labeling. For this labeling scheme, a distribution of the methyl isotopomers, $^{13}CH_3$, $^{13}CDH_2$, $^{13}CD_2H$ and $^{13}CD_3$, is obtained. However, in the employed experiments, only isotopomers, that contain protons, were detected. The proton concentration in RAP samples can be adjusted by the $[H_2O]/[D_2O]$ ratio in the M9 medium (as shown before in section 3.1.2, page 31). Neglecting the residual 3% protonation originating from the 97% deuterated [^{13}C]-glucose [Agarwal and Reif, 2008], the isotopomeric ratio of $^{13}CD_2H$ to $^{13}CDH_2$ can be determined, to first order approximation, by calculating

$$\frac{3(1 \quad p)^2 p}{3(1 \quad p)p^2} \equiv \frac{1 \quad p}{p}, \tag{3.7}$$

where p corresponds to the ratio $[H_2O]/[D_2O]$. As can be seen in Figure 3.21A, $^{13}CD_2H$ is the highest populated isotopomer for the employed 5-25% RAP samples. This also was found experimentally (Table 3.2, page 38).

For a 25% RAP sample, the averaged peak volume ratio $[^{13}CD_2H]/[^{13}CDH_2]$ was on the order of three and, therefore, the $^{13}CDH_2$ isotopomer was sufficiently populated for detection. In a 2D ^1H,^{13}C HMQC spectrum recorded at a spinning frequency of 40 kHz this lower populated isotopomer could be observed (Figure 3.21B). To determine the ratio of isotopomers, the experimentally determined peak ratio was multiplied by a factor of two to account for the number of bound protons.

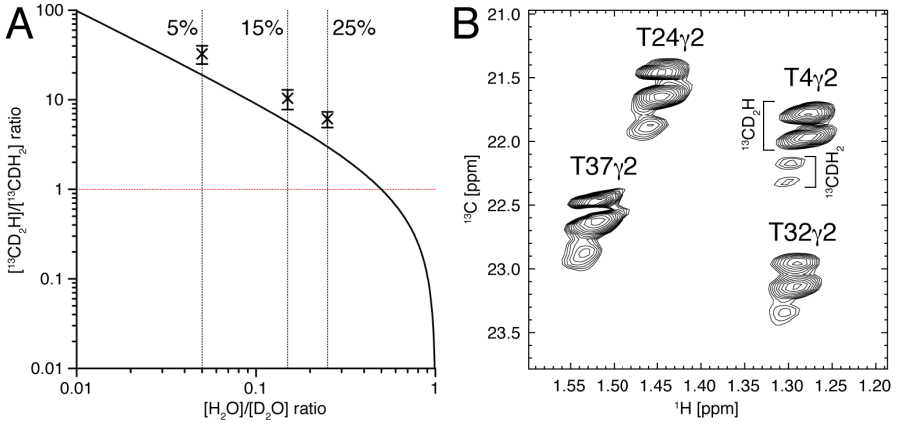

Figure 3.21: Isotopomeric mixtures in RAP samples. (A) The ratio of the isotopomers $[^{13}CD_2H]/[^{13}CDH_2]$ is plotted as a function of $[H_2O]/[D_2O]$ in the bacterial growth medium. For a statistical incorporation of protons, this ratio, $[^{13}CD_2H]/[^{13}CDH_2]$, corresponds to $(1 \quad p)/p$ (equation 3.7), where p corresponds to $[H_2O]/[D_2O]$. The 5%, 15% and 25% RAP samples are indicated by dashed vertical lines. Error bars indicate averaged ratios from solution-state and solid-state NMR data, as obtained earlier (Table 3.2, page 38). Here, the experimentally determined ratio $[^{13}CD_2H]/[^{13}CDH_2]$ was scaled to account for the number of bound protons (see main text). (B) 2D ^1H,^{13}C HMQC spectrum of a 25% α-spectrin SH3 RAP sample at 850 MHz ^1H Larmor frequency and 40 kHz MAS. The most populated isotopomers, $^{13}CD_2H$ and $^{13}CDH_2$, could be detected. The isotopomers showed the typical isotope induced chemical shift differences of 0.02 ppm and 0.3 ppm [Gardner et al., 1997] in the ^1H and ^{13}C dimension, respectively. *Reproduced with kind permission from Asami, S., et al., J. Biol. NMR, 2012, 54 (2), pp 155-168. Copyright 2012 Springer Science and Business Media. DOI: 10.1007/s10858-012-9659-9.*

3.1.4.8 Tightness of seal of 1.3 mm rotors

High MAS frequencies imply strong centrifugal forces on the rotor and the contained sample. The g-force, that a sample in a 1.3 mm rotor at 60 kHz experiences, is about four times larger than the force for a sample in a 3.2 mm rotor at 20 kHz (calculated for the inner radii). It can there-

fore be assumed, that the tightness of seal deteriorates with faster spinning. Since the solvent matrix is essential for protein stability, solvent leakage can be problematic for protein samples. Therefore the influence of two different epoxy glues on impermeability was investigated (Figure 3.22A).

Three 1.3 mm rotors were filled with water and either glued with glue "A" (UHU epoxy), glue "B" (Araldite) or kept untreated (see also section 2.1.6, page 23). The left y-axis in Figure 3.22A depicts the normalized water integral and the right y-axis the MAS frequency, respectively. The untreated rotor showed already after ≈5 min a >99.9% water loss. By contrast, glue "A" provided a significant improvement for the tightness of seal at 20 kHz. However, after ≈1 h spinning the remaining water content decreased to about 10%. Increase of the MAS frequency to 30 kHz induced an almost total loss of the water signal. Glue "B" showed the best performance concerning the tightness of seal. After ≈1 h at 60 kHz MAS, the water content remained at ≈90%. After an additional period of ≈15 h, the water signal decreased steadily to ≈20%.

Rotation induces a lateral force on the solvent, which promotes leakage. This is in particular a problem for samples of pure water without protein. By contrast, the protein will rather be compacted at the wall of the rotor. Subsequently, two 1.3 mm rotors were filled with a 25% RAP α-spectrin SH3 sample. The rotors were either sealed with glue "A" or "B", respectively. The first increment of a ^{1}H,^{13}C HMQC experiment reveals, that the protein in rotor "B" remains stable after several hours spinning at 60 kHz MAS, whereas the protein in rotor "A" becomes denatured after ≈1 h (Figure 3.22B).

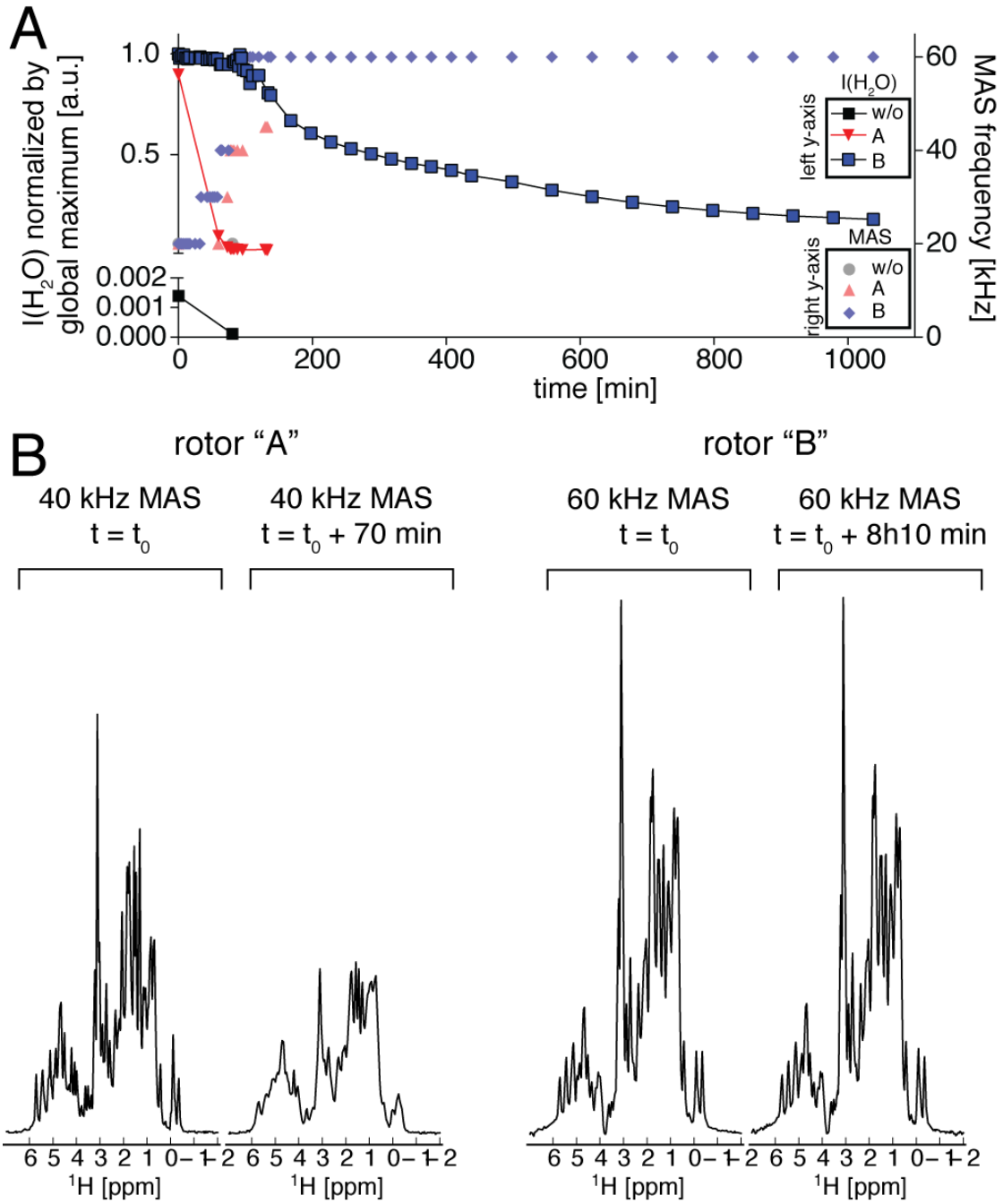

Figure 3.22: Tightness of seal of a 1.3 mm rotor at 20-60 kHz MAS employing different procedures for sealing. In the experiments, the top and bottom caps were either sealed with glue "A" (UHU epoxy), glue "B" (Araldite), or kept unsealed. (A) Water integral of fully water-filled 1.3 mm rotors as a function of time and MAS frequency. Glue "B" induced a significantly higher H_2O tightness. (B) 1D $^{1}H,^{13}C$ HMQC spectra of two 25% RAP α-spectrin SH3 samples sealed with glue "A" (left) and "B" (right), respectively. Clearly, the sample in rotor "B" remained stable, even after hours at 60 kHz MAS, while the sample in rotor "A" became denaturated after minutes and only 40 kHz MAS. *Reproduced with kind permission from Asami, S., et al., J. Biol. NMR, 2012, 54 (2), pp 155-168. Copyright 2012 Springer Science and Business Media. DOI: 10.1007/s10858-012-9659-9.*

3.2 ^{1}H- and ^{13}C-detected aliphatic backbone and side chain assignment experiments

Assignments are essential to proceed with investigations of structure and dynamics. For methyl groups, a ^{1}H-detected out-and-back (H)CCH Total Through-Bond Correlation Spectroscopy (TOBSY) experiment has been proposed [Agarwal and Reif, 2008], which employs refocused INEPT transfers in combination with ^{13}C homonuclear mixing. Due to the intrinsically short $^{13}C\alpha$ T_2 coherence lifetimes at moderate rotation frequencies, (H)CCH TOBSY type experiments are not suitable for the assignment of $^{1}H\alpha$,$^{13}C\alpha$ cross peaks. Furthermore, $^{1}H\alpha$,$^{13}C\alpha$ backbone assignments are complicated due to artifacts, which arise from the residual solvent signal. Here, we present 3D HCC and CCH type correlation experiments, which allowed us to assign ≈90% of the $^{1}H\alpha$,$^{13}C\alpha$ backbone, and side chain resonances of a 15% RAP sample of α-spectrin SH3. In both experiments, ^{13}C,^{13}C homonuclear mixing is achieved, using an adiabatic RFDR sequence [Leppert et al., 2003], as it yielded an optimal mixing profile (cf. section 3.1.4.6, page 56).

In the 3D CCH experiment, acquisition times of 36.4 ms, 8.1 ms and 4.6 ms were employed in the direct ^{1}H dimension (ω_3) and the indirect ^{13}C dimensions, ω_2 and ω_1, respectively. ^{13}C excitation was facilitated by paramagnetic doping to reduce the recycle delay. This way, the T_1 relaxation time of the bulk $^{13}C\alpha$ magnetization was reduced to ≈3.5 s. Use of a recycle delay of 1 s allowed to select for methylene and methyl resonances.

The 3D HCC experiment was acquired using acquisition times of 11.5 ms, 4.9 ms and 5.1 ms in the direct ^{13}C dimension (ω_3) and the indirect ^{1}H and ^{13}C dimension (ω_1, ω_2). The recycle delay was set to 0.6 s.

To record the ^{13}C-detected 3D HCC assignment experiment, an α-spectrin SH3 sample was employed, which was prepared, using 10% H_2O and 90% D_2O in the crystallization buffer. For the ^{1}H-detected 3D CCH experiment, a sample crystallized from 100% D_2O was employed. In all experiments, 2-3 kHz low-power WALTZ-16 [Shaka et al., 1983] decoupling was used. Quadrature detection was achieved using TPPI [Marion and Wuthrich, 1983].

To assign the $^{1}H\alpha$,$^{13}C\alpha$ backbone region, we performed a ^{1}H-detected 3D CCH correlation

experiment, which is represented in Figure 3.23A. In this experiment, the ^{1}Hα chemical shift is correlated with the chemical shift of the directly bound ^{13}Cα carbon, and after a homonuclear mixing step, with the chemical shift of ^{13}C'/^{13}Cβ. The experiment allows to assign backbone as well as side chain resonances. All expected ^{13}C resonances throughout the whole side chain could be detected (Figure 3.24A). Figure 3.24B relates schematically the different stages of the pulse scheme in Figure 3.23A to the molecular frame, employing the amino acid lysine as an example. In the proton detected experiment, observation of the ^{1}Hα,^{13}Cα correlations is complicated due to solvent suppression artifacts. These difficulties might be overcome as soon as pulsed field gradients become routinely available for MAS solid-state NMR applications [Chevelkov et al., 2003].

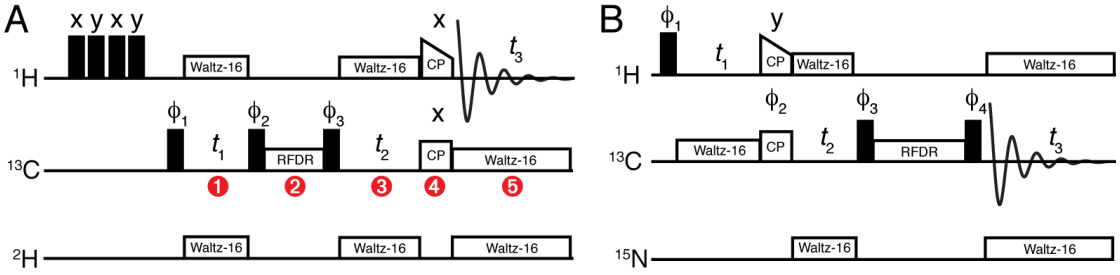

Figure 3.23: (A) 3D CCH and (B) HCC experiments for assignment of aliphatic resonances in RAP labeled protein samples. (A) ^{1}H-detected, ϕ_1 = (y, -y), ϕ_2 = (y), ϕ_3 = (y, y, -y, -y), ϕ_{rec} = (y, -y, -y, y). (B) ^{13}C-detected, ϕ_1 = (-x, x), ϕ_2 = 4(y), 4(-y), ϕ_3 = 8(x), 8(-x), ϕ_{rec} = (-x, x, x, -x), 2(x, -x, -x, x), (-x, x, x, -x). *Reproduced with kind permission from Asami, S., et al., J. Biol. NMR, 2012, 52 (1), pp 31-39. Copyright 2012 Springer Science and Business Media. DOI: 10.1007/s10858-011-9591-4.*

To entirely circumvent water interference, a ^{13}C-detected HCC experiment can be recorded, employing the pulse scheme shown in Figure 3.23B. The sequence started out with an indirect proton evolution period ω_1(^{1}H). Magnetization was transferred then via cross polarization (CP) to carbons, followed by a first ^{13}C evolution period ω_2(^{13}C). After ^{13}C,^{13}C homonuclear mixing, the carbon signal was detected in a second ^{13}C dimension, ω_3(^{13}C), facilitating unambiguous resonance assignments. Heteronuclear scalar decoupling was achieved by application of low-power WALTZ-16 decoupling [Shaka et al., 1983], employing a rf field strength on the order of 2-3 kHz.

In total, ≈90% of backbone and side chain resonances were unambiguously assigned. Representative strips from this experiment are depicted in Figure 3.25. Assignments obtained this

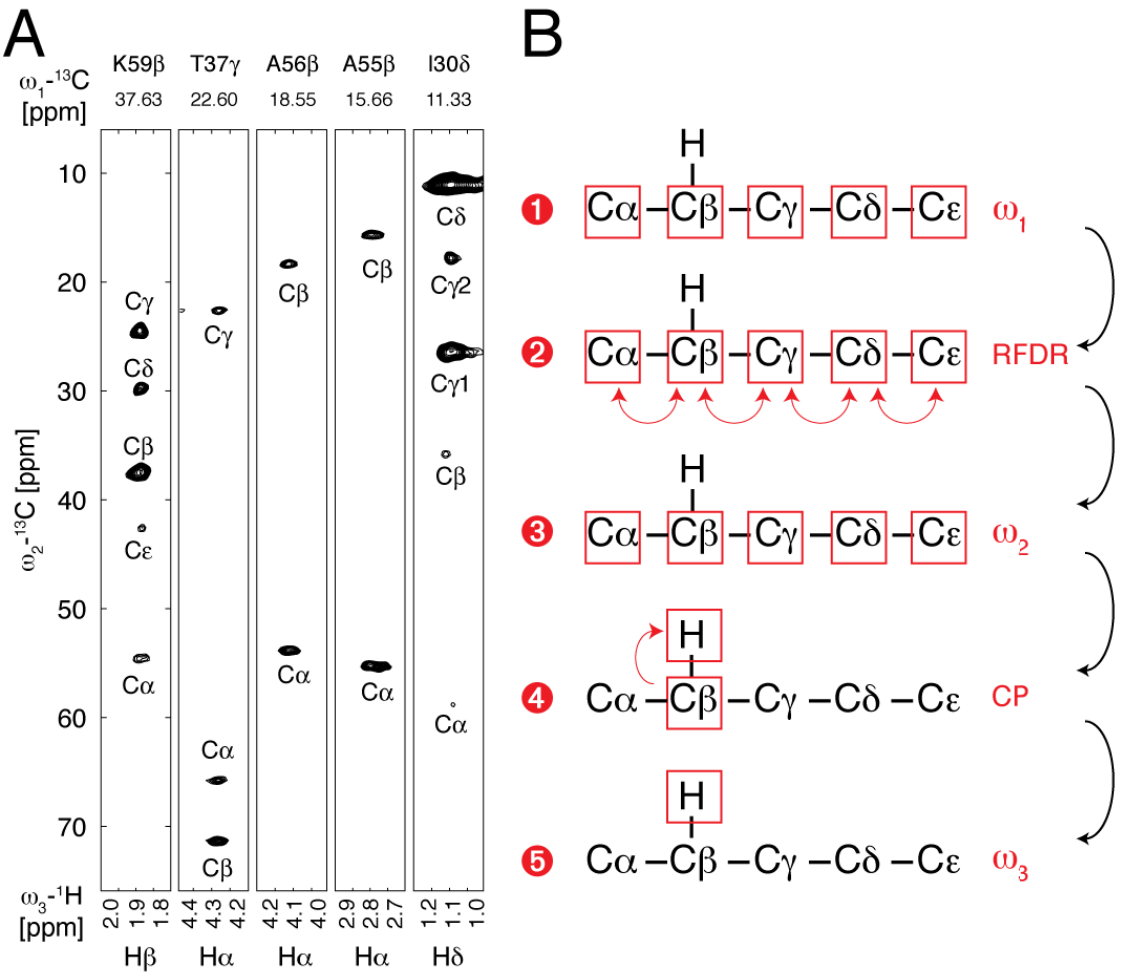

Figure 3.24: (A) 2D strips extracted from the ^{1}H-detected, ^{13}C-excited 3D CCH correlation experiment, using the 15% α-spectrin SH3 RAP sample. The external magnetic field was 16.4 T (700 MHz) and the MAS frequency was adjusted to 18 kHz. The assignments on the top and at the bottom of the strips indicate the carbon and proton nuclei, which evolved during t_1 and t_3, respectively. All expected intraresidual correlations were observed. (B) Schematic representation of lysine, highlighting the distribution of magnetization at the different stages of the pulse scheme from Figure 3.23A. *Reproduced with kind permission from Asami, S., et al., J. Biol. NMR, 2012, 52 (1), pp 31-39. Copyright 2012 Springer Science and Business Media. DOI: 10.1007/s10858-011-9591-4.*

way were employed to annotate Figure 3.26 and 3.27, which show 2D ^{1}H,^{13}C correlation spectra of a 25% RAP-glucose and a 10% RAP-glycerol sample of α-spectrin SH3, respectively. The RAP-glycerol labeling scheme will be presented in section 3.5.1 (page 103). A table with the experimental ^{1}H and ^{13}C chemical shifts is given in the appendix (Table 2, page 215 and Table 3, page 217).

Since the 15% RAP sample, employed for recording the 3D HCC experiment, contained approximately 10% protons at exchangeable sites, most of the $^{1}H^{N}$ chemical shifts could be assigned as well (Figure 3.25). Correlations between $^{1}H^{N}$ and $^{13}C\alpha/^{13}C'$ were due to long-range through-space connectivities [Agarwal et al., 2010].

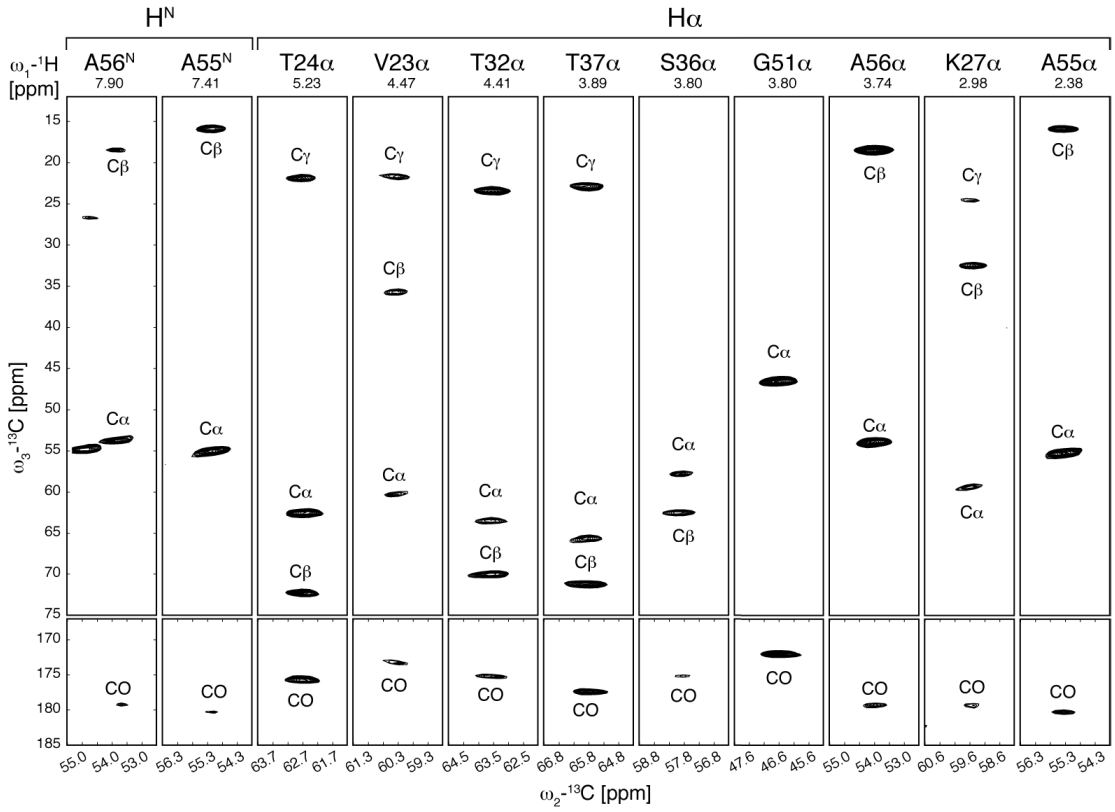

Figure 3.25: 2D strips extracted from the ^{13}C-detected 3D HCC correlation experiment recorded for the 15% α-spectrin SH3 RAP sample (with 10% back-exchanged protons), employing the sequence, illustrated in Figure 3.23B. $^{1}H^{N}$ as well as $^{1}H\alpha$ chemical shifts were unambiguously assigned by correlating $^{13}C\alpha$ to $^{13}C\beta/^{13}C'$ chemical shifts. Note, that the direct dimension $\omega_3(^{13}C)$ is represented as the vertical dimension. The MAS frequency was set to 18 kHz, at an external magnetic field of 16.4 T (700 MHz). *Reproduced with kind permission from Asami, S., et al., J. Biol. NMR, 2012, 52 (1), pp 31-39. Copyright 2012 Springer Science and Business Media. DOI: 10.1007/s10858-011-9591-4.*

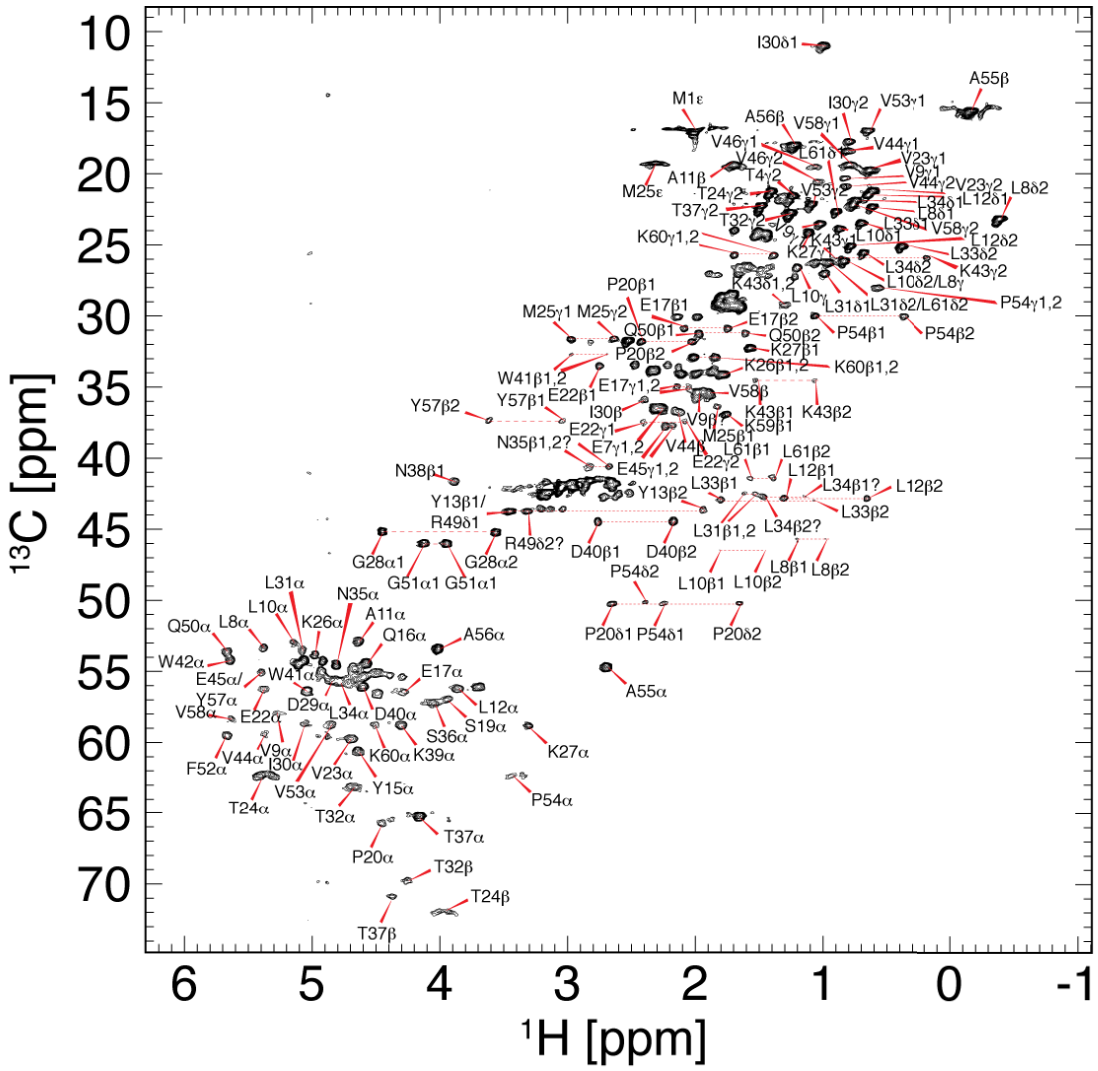

Figure 3.26: ^{1}H,^{13}C HMQC correlation spectrum of a 25% α-spectrin SH3 RAP sample at a MAS frequency of 40 kHz. The effective temperature was adjusted to ≈15-20 °C and the external magnetic field was 20 T (850 MHz). *Reproduced with permission from Asami, S., et al., Acc. Chem. Res., 2013, 46 (9), pp 2089–2097. Copyright 2013 American Chemical Society. DOI: 10.1021/ar400063y.*

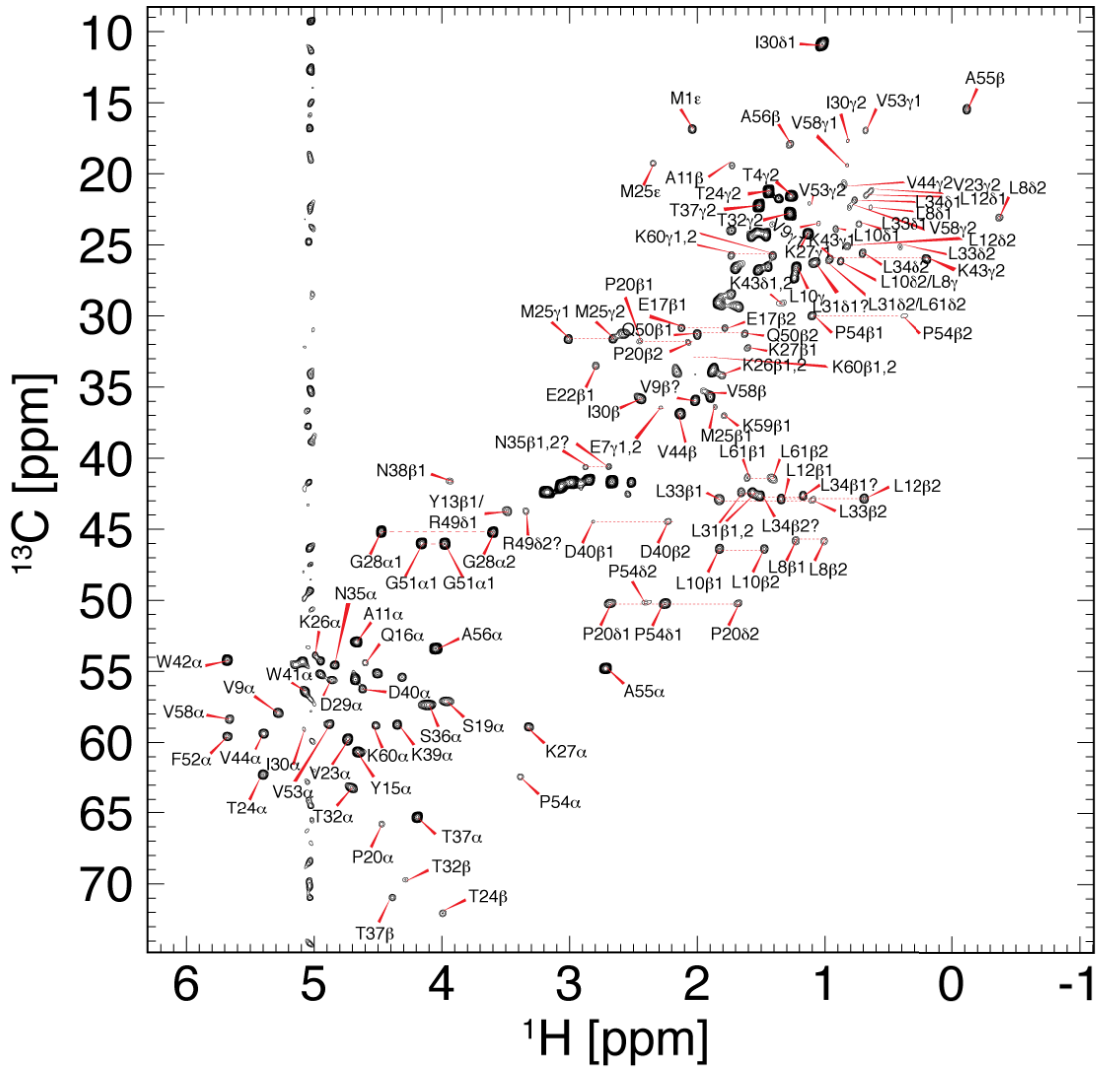

Figure 3.27: Refocussed ^{1}H,^{13}C HSQC spectrum of a 10% RAP sample, expressed in a M9 minimal medium with [u-^{2}H, 2-^{13}C]-glycerol (see Table 2.1, page 21 for preparation details). The pulse sequence is given in Figure 3.41B (page 104), but omitting the inversion recovery delay. The rotation frequency was set to 50 kHz, further parameters are given in the caption of Figure 3.26.

In the ^{13}C-detected HCC experiment, the Hartmann-Hahn matching condition during the CP transfer step (Figure 3.23B) was optimized to yield maximum sensitivity for aliphatic resonances and minimum intensity for ^{13}C' (Figure 3.28) [Baldus et al., 1998, Laage et al., 2008]. This way, the spectral width in the $\omega_2(^{13}C)$ dimension could be reduced to 70 ppm, suppressing at the same time folding artifacts from ^{13}C' resonances. In case the experiment would be recorded in such a way, that magnetization transfer to ^{13}C' is maximized, sequential assignments via $^{1}H^{N}(i)$–$^{13}C\alpha(i)$ and $^{1}H^{N}(i)$–$^{13}C'(i \quad 1)$ correlations would be obtained. This experiment is superior in terms of sensitivity in comparison to the HNCACX experiments as it lacks the magnetization transfer step to $^{15}N(i)$. Alternatively, amide protons in RAP samples can be assigned using HNCA or HNCACB experiments [Linser et al., 2008], a combination of 3D HNCO and HN-CACO experiments [Linser et al., 2010] or using long-range H/C dipolar transfers in perdeuterated samples, as recently proposed [Linser, 2012].

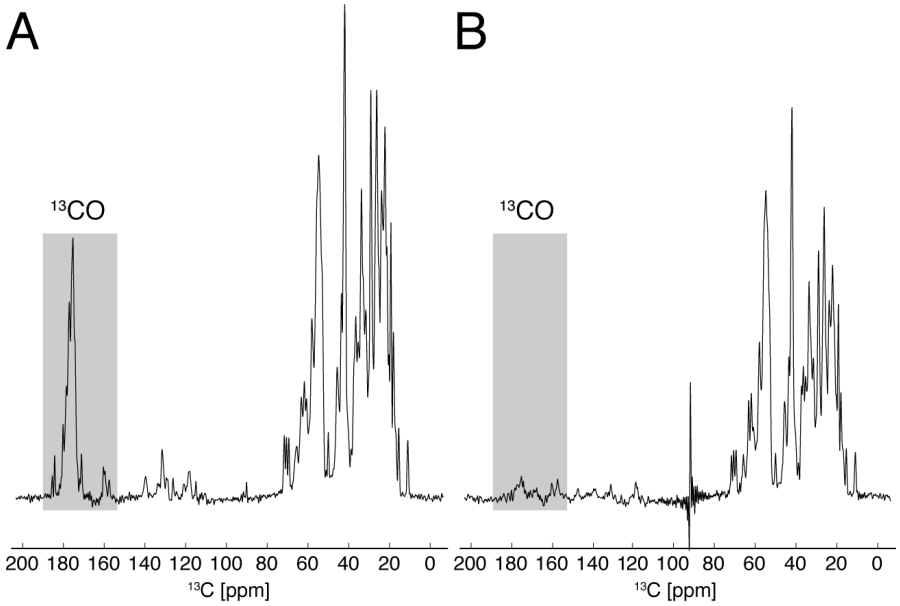

Figure 3.28: Optimization of selective excitation during the ^{1}H,^{13}C CP magnetization transfer for a 25% RAP sample. $^{1}H^{N}$ amide protons were back-exchanged in a 30%/70% H_2O/D_2O buffer. The ^{13}C offset was set to the middle of the aliphatic region and the CP contact time to 1000 µs. The spectra were recorded at a MAS frequency of 20 kHz and an external magnetic field of 16.4 T (700 MHz). Either a (A) linear ramp from 100-75% or (B) no ramp was employed. Omitting the ramp during CP and optimizing for maximum sensitivity for aliphatic resonances reduced the $^{13}C'$ signals (gray shaded area) by almost a factor of 10. *Reproduced with permission from Asami, S., et al., Acc. Chem. Res., 2013, 46 (9), pp 2089–2097. Copyright 2013 American Chemical Society. DOI: 10.1021/ar400063y.*

In Figure 3.29 the α-spectrin SH3 backbone chemical shifts obtained in the solid-state were compared with the shifts found in solution at pH 7.3 [van Rossum et al., 2001]. Both, ^{1}Hα and ^{13}Cα chemical shifts, were well correlated, yielding a Spearman's correlation coefficient of 0.909 and 0.991 for ^{1}Hα and ^{13}Cα, respectively. This indicated, that the α-spectrin SH3 protein structure in the crystal and in solution are highly similar. Small chemical shift differences arose from residues, which were involved in crystal contacts. In particular, we found deviations from an ideal correlation for the ^{1}Hα shift of Ser19 and the ^{13}Cα shift of Pro20, respectively. These residues were within 6 Å to the aromatic rings of Tyr13 and Tyr57 of a molecule in a symmetry related unit cell.

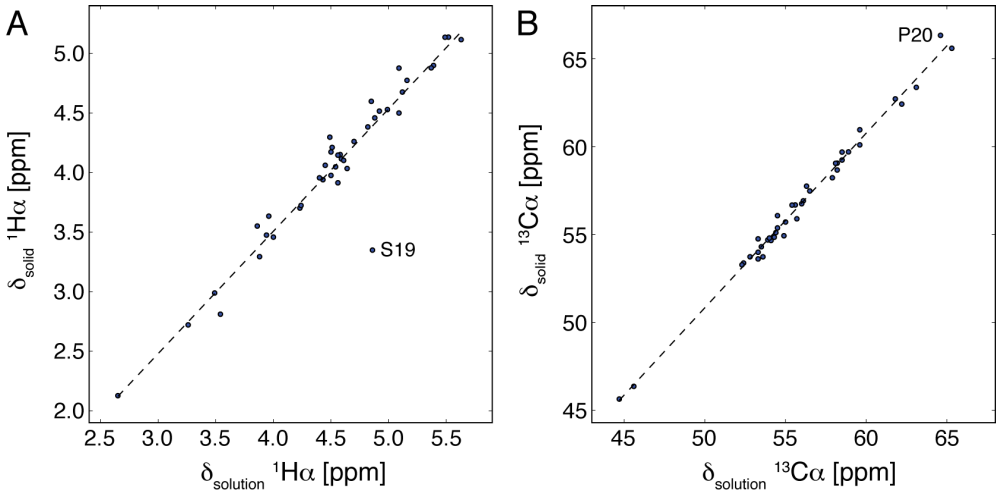

Figure 3.29: Correlation diagram of solution-state versus solid-state NMR chemical shifts for (A) ^{1}Hα and (B) ^{13}Cα in α-spectrin SH3. *Reproduced with kind permission from Asami, S., et al., J. Biol. NMR, 2012, 52 (1), pp 31-39. Copyright 2012 Springer Science and Business Media. DOI: 10.1007/s10858-011-9591-4.*

3.3 Determination of structural distance restraints with RAP samples

In addition to correlation spectroscopy, as discussed in the previous section (3.2, page 64), the presented labeling scheme enables access to ^{1}H,^{1}H distance restraints among side chains in a 3D H(H)CH experiment, as shown in Figure 3.30A. In the experiment, a first proton evolution period is followed by a ^{1}H,^{1}H magnetization mixing step, utilizing a rotor synchronized adiabatic RFDR mixing scheme [Leppert et al., 2003]. After mixing, magnetization was transferred to ^{13}C for chemical shift evolution and finally to ^{1}H for detection, using a scalar HMQC type sequence. Due to the fact, that the proton spin system was sufficiently dilute, long range interactions could be obtained, without truncation of the dipolar coupling.

Figure 3.30B shows the experimental results, focussing on correlations involving Ala11 and Met25 in the hydrophobic core of the α-spectrin SH3. The ^{13}C resolved ^{1}H(ω_1),^{1}H(ω_3) planes showed all expected correlations between Met25ϵ, Ala11β, Val53γ2 and L10δ2. The structure of the protein is represented in Figure 3.30C. The shortest methyl-methyl proton distances were between 4.5 Å and 5.6 Å.

In contrast to previous approaches, in which the exchangeable protons had to be partially replaced with deuterons [Knight et al., 2011, Linser et al., 2011a], the presented RAP labeling scheme does not require an ^{1}H/^{2}H exchange step. This will be of particular importance for the investigation of membrane proteins, which have very stable amide protons, that might not exchange within months.

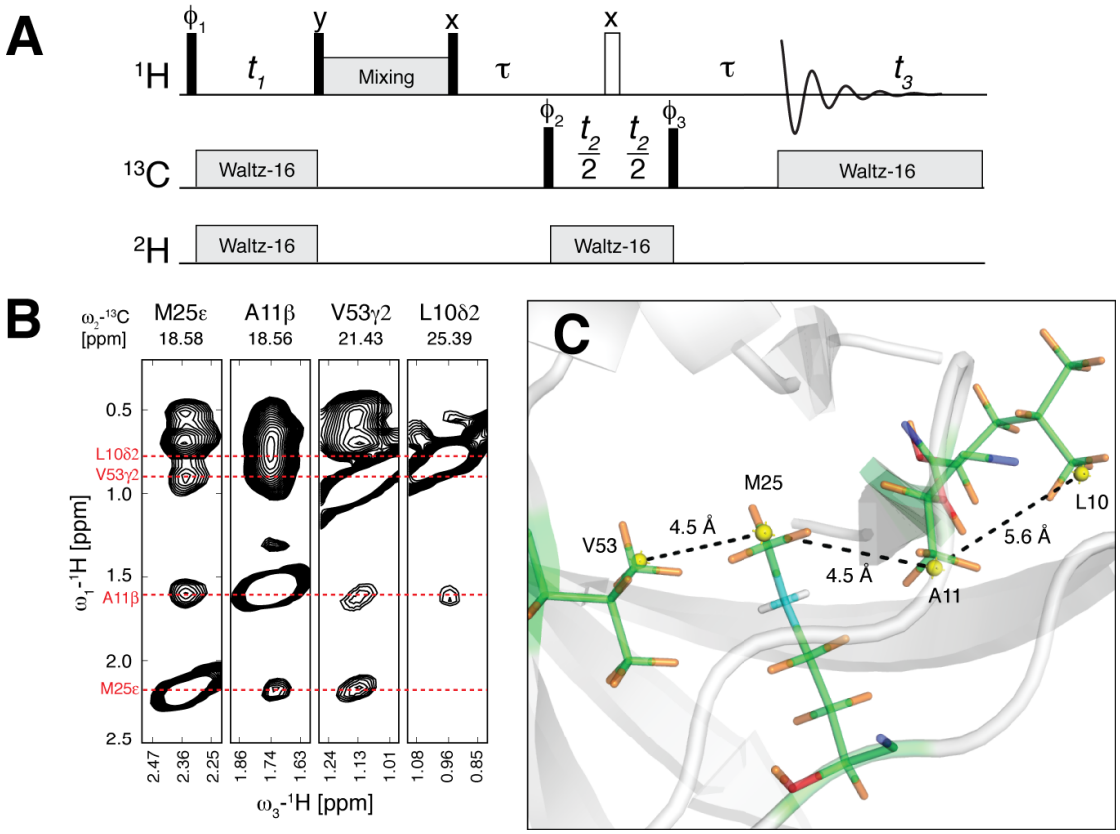

Figure 3.30: 3D H(H)CH correlation experiment for the determination of long-range ^{1}H,^{1}H distances in the solid-state. For ^{1}H,^{1}H mixing, a rotor synchronized adiabatic RFDR mixing scheme was used with a mixing time of 8 ms and a rf field of 55 kHz [Leppert et al., 2003]. τ was set to 3.4 ms corresponding to $1/2J_{HC}$. The MAS frequency was adjusted to 20 kHz on a 600 MHz spectrometer. The effective temperature was ≈17 °C. The acquisition times were 57 ms, 10 ms and 8 ms in the direct ^{1}H- and the indirect ^{13}C- and ^{1}H-dimension, respectively. 16 scans were accumulated for every increment, while employing the phase cycle: ϕ_1 = y,-y, ϕ_2 = 2(x),2(-x), ϕ_3 = 4(x),4(-x) and ϕ_{rec} = y,-y,-y,y,-y,y,y,-y. The total acquisition time amounted to 3 d. The ^{1}H carrier frequency was positioned on the HDO resonance. Quadrature detection in ω_1 and ω_2 was achieved using TPPI [Marion and Wuthrich, 1983]. (B) 2D stripes along the ω_2-^{13}C dimension of Met25ε, Ala11β, V53γ2 and L10δ2. (C) The local proximity of those residues is illustrated using the crystal structure (PDB: 1U06) [Chevelkov et al., 2005d]. *Reproduced with permission from Asami, S., et al., J. Am. Chem. Soc., 2010, 132 (43), pp 15133–15135. Copyright 2010 American Chemical Society. DOI: 10.1021/ja106170h.*

3.4 Probing sub-μs motions via ^{1}H,^{13}C dipole tensor anisotropy and asymmetry

The following section describes the experimental determination of the ^{1}H,^{13}C dipolar coupling tensor, which is a direct probe for the motional symmetry and amplitude of sub-μs dynamics. The parameters were compared to a Molecular Dynamics (MD) simulation and X-ray crystallography data. The experiments were carried out using Reduced Adjoining Protonation (RAP) and selectively methyl-labeled Val/Leu α-spectrin SH3 samples.

The dipolar coupling is a powerful probe for fast dynamical processes on the ps-ns timescale. In the absence of motion, the dipolar coupling between two nuclei i and j can be expressed in Cartesian coordinates in the principal axis frame by a traceless second rank tensor:

$$\widehat{D}_{ij} = \delta_{D,\text{rigid}} \widehat{d}_{ij}. \tag{3.8}$$

The rigid-limit dipolar coupling anisotropy (in the absence of sub-μs motions), $\delta_{D,\text{rigid}}$, is defined as [Haeberlen, 1976, Smith, 1999, Bak et al., 2000, Duer, 2002, Levitt, 2008, Schanda et al., 2011a]

$$\delta_{D,\text{rigid}} = \frac{-\gamma_i \gamma_j \mu_0 \hbar}{r_{ij}^3 4\pi}, \tag{3.9}$$

where μ_0 is the magnetic constant, γ_i and γ_j are the gyromagnetic ratios of nuclei i and j, respectively, $\hbar$ is the reduced Planck constant and r_{ij} the internuclear distance. The $\widehat{d}_{ij}$ tensor is described by

$$\begin{aligned}
\widehat{d}_{ij} &= \mathbb{1} - 3\widehat{e}_{ij} \otimes \widehat{e}_{ij} \\
&= \begin{bmatrix} 1 & 0 & 0 \\ 0 & 1 & 0 \\ 0 & 0 & 1 \end{bmatrix} - 3 \begin{bmatrix} 0 \\ 0 \\ 1 \end{bmatrix} \otimes \begin{bmatrix} 0 & 0 & 1 \end{bmatrix} \\
&= \begin{bmatrix} 1 & 0 & 0 \\ 0 & 1 & 0 \\ 0 & 0 & 1 \end{bmatrix} - 3 \begin{bmatrix} 0 & 0 & 0 \\ 0 & 0 & 0 \\ 0 & 0 & 1 \end{bmatrix} = \begin{bmatrix} 1 & 0 & 0 \\ 0 & 1 & 0 \\ 0 & 0 & -2 \end{bmatrix},
\end{aligned} \tag{3.10}$$

where the dyadic product

$$\widehat{a}\otimes\widehat{b} = \begin{bmatrix} a_1 \\ a_2 \\ a_3 \end{bmatrix} \otimes \begin{bmatrix} b_1 & b_2 & b_3 \end{bmatrix} = \begin{bmatrix} a_1b_1 & a_1b_2 & a_1b_3 \\ a_2b_1 & a_2b_2 & a_2b_3 \\ a_3b_1 & a_3b_2 & a_3b_3 \end{bmatrix} \tag{3.11}$$

was employed. As stated above, the tensor $\widehat{d}_{ij}$ is traceles ($\mathrm{Tr}(\widehat{d}_{ij}) = 0$).

In the presence of motions, which occur with correlation times shorter than $1/\delta_{D,\mathrm{rigid}}$ (approximately 10-100 μs), the dipolar coupling anisotropy becomes partially averaged, which yields a reduced, effective anisotropy δ_D. To quantify the motional amplitude, an order parameter S can be introduced as a prefactor in equation 3.9, which varies between zero (high mobility) and one (rigid), respectively.

The description of the motion of two dipolar coupled nuclei by only one order parameter is only sufficient, if the motion is isotropic. In this case, the motional averaged dipole tensor remains axially symmetric. For anisotropic motions, the dipole tensor becomes asymmetric. An asymmetry parameter η can be introduced to allow for a general case of motion, as described earlier [Meier et al., 1982, Tritt-Goc et al., 1986, Tritt-Goc, 1995, Schanda et al., 2011a]. In this manner, the dipole tensor can be redefined as

$$\widehat{D}_{ij} = \delta_D \begin{bmatrix} 1+\eta & 0 & 0 \\ 0 & 1-\eta & 0 \\ 0 & 0 & -2 \end{bmatrix} \tag{3.12}$$

with

$$\delta_D = S\frac{-\gamma_i\gamma_j\mu_0\hbar}{r_{ij}^3 4\pi} \tag{3.13}$$

[Gross et al., 1997]. The formalism includes the asymmetry parameter η and the order parameter S, respectively. The tensor $\widehat{D}_{ij}$ remains traceless.

As can be seen from the r_{ij}^{-3} dependency in equation 3.9, the dipolar coupling acts through space. However, motional parameters are usually determined for directly bonded nuclei, like

^{1}Hα,^{13}Cα, ^{1}H^{N},^{15}N, ^{13}C',^{15}N, since accurate bond lengths are known from neutron diffraction studies [Alkaraghouli and Koetzle, 1975]. Using the bond lengths, the rigid-limit dipolar coupling anisotropy, $\delta_{D,\text{rigid}}$, can be calculated using equation 3.9. Therefore, the experimentally observed anisotropy, δ_D (equation 3.13), can only be equal to or less than $\delta_{D,\text{rigid}}$. In this manner, the ratio of the experimentally determined dipolar coupling anisotropy to the rigid-limit value gives directly access to the order parameter S and, hence, to the motional amplitude:

$$S = \frac{\delta_D}{\delta_{D,\text{rigid}}}. \tag{3.14}$$

The dipolar coupling anisotropy, as well as the asymmetry, can be determined by fitting the experimental data to a grid of simulated data, as will be described in section 3.4.2 (page 80).

3.4.1 ^{1}H-detected REDOR experiment: theoretical and experimental approach for the determination of ^{1}H,^{13}C dipolar coupling tensors

Several approaches have been introduced to obtain one-bond dipolar coupling constants for rotating solids. All approaches rely on the application of a dipolar recoupling sequence to in-phase S_x magnetization. The most prominent dipolar recoupling sequences are T-MREV [Hohwy et al., 2000, Franks et al., 2005, Helmus et al., 2010], symmetry-based pulse sequences ($R18_1^7$, $R18_2^5$) [Yang et al., 2009, Zhao et al., 2001a,b], cross polarization phase-inverted (CPPI) [Dvinskikh et al., 2003, 2005, Chevelkov et al., 2009a] and Rotational-Echo Double-Resonance (REDOR) sequences [Gullion and Schaefer, 1989, Pan et al., 1990, Jaroniec et al., 2000], respectively. Recently, Schanda et al. [2011b] carried out a comparative study about recoupling sequences to identify the optimal sequence for deuterated proteins. In contrast to the listed sequences, which were designed for uniformly protonated proteins, ^{1}H,^{1}H dipolar couplings are largely reduced in perdeuterated or Reduced Adjoining Protonation (RAP) samples and at the nowadays available high spinning speeds (60-67 kHz). However, the REDOR sequence proved to be the best sequence in terms of insensitivity to rf miscalibration and inhomogeneity and independency with regard to I- and S-spin Chemical Shift Anisotropy (CSA), respectively. The only significant error source applying REDOR sequences were remote protons. However, this error source is al-

most circumvented by employing deuterated samples, which yield isolated dipolar coupled spin pairs (^{1}H,^{13}C or ^{1}H,^{15}N).

For the determination of ^{1}H,^{13}C dipolar coupling tensors, a ^{1}H-detected REDOR sequence was employed, as illustrated in Figure 3.31A. For evolution of in-phase S_x magnetization, a refocused INEPT sequence was utilized. Here, S referred to a ^{13}C and I to a ^{1}H nucleus, respectively. Dipolar recoupling was accomplished by two REDOR blocks, following a xy-16 phase cycling scheme to eliminate resonance offset effects [Gullion and Schaefer, 1991]. For a better understanding of the REDOR sequence, in the following, the dipolar frequency ω_D under MAS will be described.

The time-dependent interaction Hamiltonian for a dipolar coupled $I-S$ spin pair under MAS at a frequency ω_r is described as [Haeberlen and Waugh, 1968, Pan et al., 1990]

$$\mathscr{H}_{IS}(t) = \omega_D(\alpha,\beta,t) I_z S_z. \tag{3.15}$$

Here, the dipolar frequency ω_D is

$$\omega_D(\alpha,\beta,t) = \pm\frac{1}{2}\delta_D\left\{\sin^2\beta\cos[2(\alpha+\omega_r t)] - \sqrt{2}\sin(2\beta)\cos(\alpha+\omega_r t)\right\}, \tag{3.16}$$

where α and β are polar angles defining the orientation of the internuclear dipolar $I-S$ vector in a coordinate system with z parallel to the magic angle rotation axis. The time evolution of the Hamiltonian can be calculated by the average Hamiltonian $\overline{\mathscr{H}}$ [Haeberlen and Waugh, 1968]

$$\overline{\mathscr{H}} = \frac{1}{\tau_r}\int_0^{\tau_r} \mathscr{H}_{IS}(t')dt', \tag{3.17}$$

The average dipolar transition frequency, $\overline{\omega_D}$, is obtained by integration of equation 3.17 and leads to

$$\overline{\omega_D}(\alpha,\beta,t')\Big|_{t'=0}^{t'=\tau_r} = \pm\frac{1}{2}\frac{\delta_D}{\tau_r}\left\{\frac{\sin^2\beta\sin[2(\alpha+\omega_r t')]}{2\omega_r} - \frac{\sqrt{2}\sin(2\beta)\sin(\alpha+\omega_r t')}{\omega_r}\right\}\Bigg|_{t'=0}^{t'=\tau_r}. \tag{3.18}$$

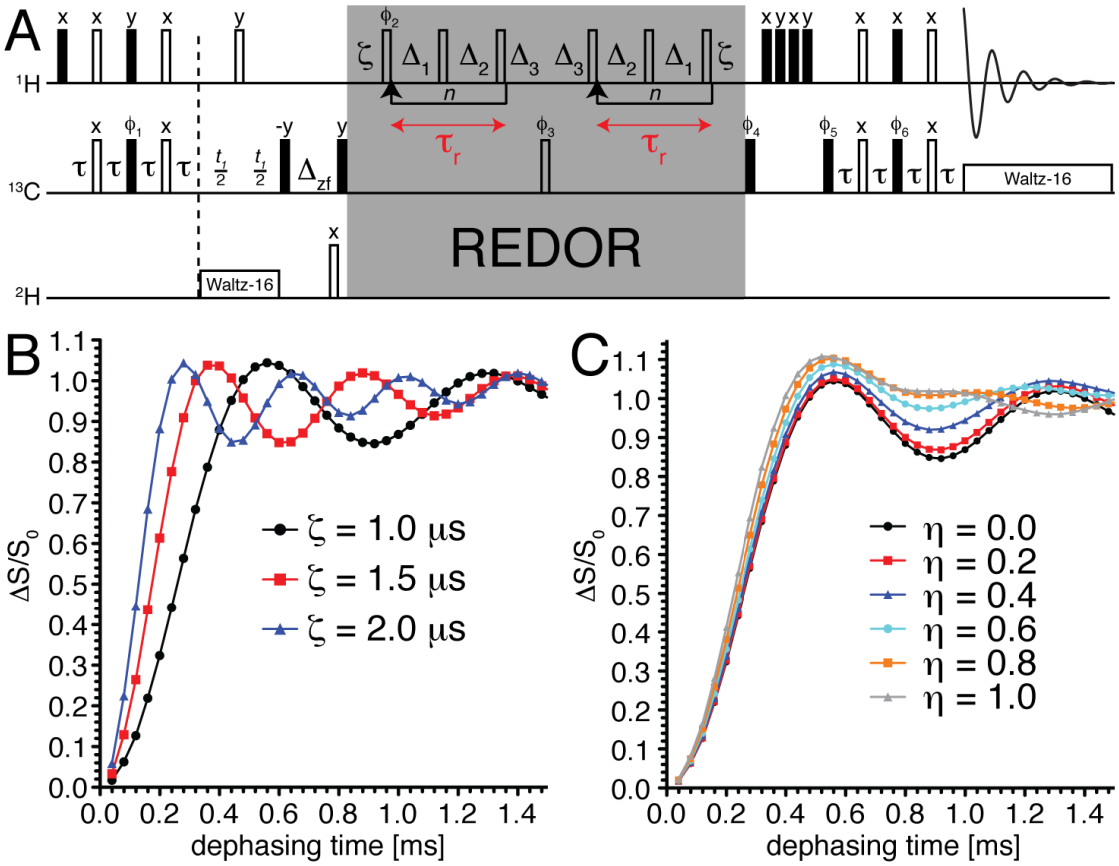

Figure 3.31: (A) ^{1}H-detected ^{1}H,^{13}C REDOR pulse sequence adapted from Schanda et al. [2011a]. The phase cycle was as follows: ϕ_1 = (x, x, -x, -x), ϕ_2 = (x, y, x, y), (y, x, y, x), (-x, -y, -x, -y), (-y, -x, -y, -x), ϕ_3 = (x, -x), ϕ_4 = 2×(-y, -y, -y, -y), 2×(y, y, y, y), ϕ_5 = (y, -y), ϕ_6 = (x, x, x, x), (-x, -x, -x, -x), ϕ_{rec} = (x, -x, -x, x), (-x, x, x, -x), (-x, x, x, -x), (x, -x, -x, x). ϕ_2 followed the xy-16 scheme and was reset to its first phase for every increment. During the first (second) REDOR recoupling block, ϕ_2 was incremented (decremented). τ was set to $1/4J_{HC} \approx 1.92$ ms and the z-filter delay Δ_{zf} to 2-5 ms. The oscillation of the REDOR curve was altered by the delay ζ. The total REDOR period was a multiple of the rotor period τ_r and equal to $2\tau_r(1+n)$, in which n was the number of cycles, as depicted in the pulse scheme. Quadrature detection in ω_1 was achieved usind TPPI [Marion and Wuthrich, 1983]. In (B) numerical spin simulations were performed using SIMPSON [Bak et al., 2000] to determine the optimal experimental parameters in terms of the ζ-delay and the recoupling rf field strengths. Here, the influence of the ζ-delay is illustrated by plotting REDOR dephasing curves with ζ equal to 1.0 µs, 1.5 µs and 2.0 µs, respectively. The ^{1}H,^{13}C dipole anisotropy was set to -20 kHz and the MAS frequency to 50 kHz. (C) Numerical simulations were performed using the same parameters as in (B), while varying the asymmetry η of the ^{1}H,^{13}C dipole tensor from 0.0 to 1.0 in steps of 0.2 and keeping the ζ-delay constant at 1.0 µs.

Since $\omega_r = \frac{2\pi}{\tau_r}$, both time-dependent terms, $\sin[2(\alpha + \omega_r t')]$ and $\sin(\alpha + \omega_r t')$, simplify to $\sin(2\alpha)$ and $\sin(\alpha)$ setting $t' = 0$ or $t' = \tau_r$. In total, $\overline{\omega_D} = 0$ and, hence, the dipolar coupling Hamiltonian is equal to zero over one rotor period. This is the analytical result in the absence of a recoupling sequence.

To determine an expression in the presence of REDOR recoupling, it should be noted, that during the REDOR block (Figure 3.31A) equally spaced π pulses are applied on the I spin (^{1}H), usually at the middle of every rotor period. As will be discussed at the end of this section, the variation of the timing between these pulses modulates the oscillation of the dephasing curves. However, for a simplified case, we assume, that the π pulse is applied at the time point τ_1. In this manner, the sign of the average dipolar transition frequency is reversed by the π pulse (to minus) after the time point τ_1, which yields

$$\overline{\omega_D} = \frac{1}{\tau_r}\left\{\int_0^{\tau_1} \omega_D(\alpha,\beta,t)dt' - \int_{\tau_1}^{\tau_r} \omega_D(\alpha,\beta,t)dt'\right\}. \tag{3.19}$$

Hence, application of the REDOR sequence yields $\overline{\omega_D} \neq 0$ and the dipolar coupling is recoupled. Since the dipolar transition frequency is a function of the dipolar coupling anisotropy, δ_D (equation 3.16), the anisotropy can be extracted by fitting the oscillation of $\overline{\omega_D}$.

To normalize the REDOR dephasing signal (referred to as S) and correct for ^{13}C T_2 magnetization decay during the recoupling period, an additional set of experiments has to be acquired with the same settings, but omitting the π pulses on the I spin. The signal in the reference experiments is referred to as S_0. Finally, the normalized REDOR difference signal, $\mathscr{S}$, is described by [Mueller, 1995]

$$\mathscr{S} = \frac{\Delta S}{S_0} = \frac{S_0 - S}{S_0} = 1 - \frac{1}{4\pi}\int_0^{2\pi} d\alpha \int_0^{\pi} \sin\beta d\beta \cos(\Delta\Phi_n), \tag{3.20}$$

with

$$\Delta\Phi_n = \sqrt{32}\delta_D n \tau_r \sin\beta\cos\beta\sin\alpha, \tag{3.21}$$

in which n is the number of dephasing cycles during the REDOR block (Figure 3.31A).

Here, a symmetric dipole tensor was assumed. However, to take account of an asymmetric dipole tensor, as well as finite pulse effects and I and S spin CSA, respectively, numerical simulations using SIMPSON [Bak et al., 2000] were carried out.

As shown in Figure 3.31B, the oscillation of the REDOR dephasing curve can be modulated by adjusting the ζ-delay [Schanda et al., 2010, 2011b]. Since the sampling frequency is limited to integer multiples of the rotor period, optimizing the ζ-delay improves the sampling of the data points.

To determine the influence of the dipole tensor asymmetry η on the shape of the REDOR curve, simulated dephasing signals were plotted as a function of the asymmetry (Figure 3.31C). The oscillation becomes damped with increasing asymmetry, which is an advantageous property, since it can be used as a direct probe for anisotropic motions, as will be shown in section 3.4.4 (page 85).

3.4.2 Details about experimental setup and data analysis

The details about the determination of ^{1}H,^{13}C dipole tensor anisotropy and asymmetry are described in this section. To enable an accurate determination of these parameters, spectra with high resolution and sensitivity are required. In this manner, microcrystals of a 15% α-spectrin SH3 RAP sample were employed, which have been cocrystallized with 100 mM Cu(II)EDTA to reduce the ^{1}H T_1 times and hence the recycle delay. The recycle delay was set to 0.8 s (optimized for ^{1}Hα backbone protons). The REDOR sequence shown in Figure 3.31A was employed, which utilizes refocused INEPT transfer steps for generation of in-phase ^{13}C S_x magnetization during the recoupling period. The resolution and sensitivity were further improved by a high spinning frequency of 40 kHz (see Figure 3.7, page 42) and by application of proton detection. In total, well-resolved ^{1}H,^{13}C 2D spectra with high sensitivity were acquired in $\approx$2 h (signal-to-noise for Leu8δ2 was $\approx 20:1$).

Two REDOR series were recorded with a ζ-delay of 1.1 µs and 1.5 µs, respectively. For every series, reference experiments were acquired at every fifth dephasing point by setting the rf power for the ^{1}H π pulses during the REDOR period to 0 kHz. The magnetization decay of the reference experiments can be described by a linear function, as illustrated in Figure 3.32.

To normalize the REDOR dephasing curves according to equation 3.20 (page 79), the reference intensity for every data point was interpolated from the linear fit (Figure 3.32). The peak

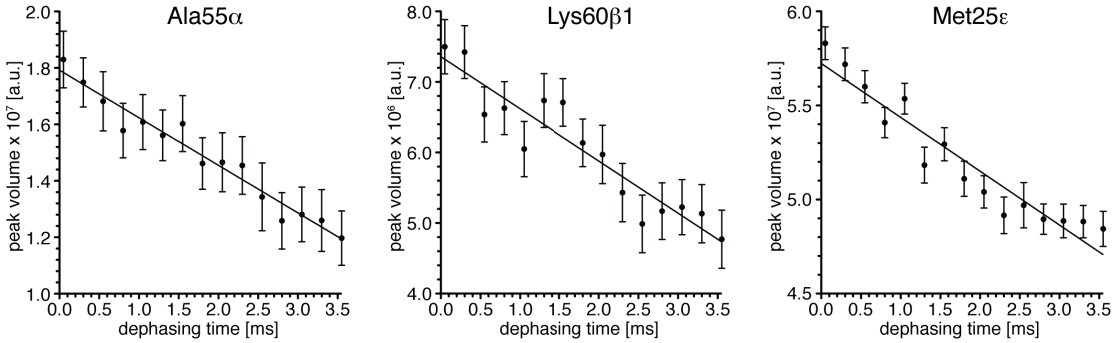

Figure 3.32: ^{13}C S_x signal decay in REDOR reference experiments of a 15% α-spectrin SH3 RAP sample, fitted by a linear function. The correlation coefficient R^2 is between 0.87 and 0.96. Here, the experimental series with a ζ-delay of 1.1 μs was employed.

volumes for the dephasing and the reference experiment, referred to as S and S_0, respectively, were determined by integration of the spectrum. The measuring uncertainty of the peak volumes, δS and δS_0, were set to two times the standard deviation of the noise ($2\sigma_{\text{noise}}$). The noise was determined by averaging over 1,000 randomly placed boxes in the noise region, while the integration box of the noise and the box of the respective protein resonance had the same size. The error for the normalized intensities, $\delta\mathscr{S}$ (equation 3.20, page 79), was determined by 10,000 Monte Carlo simulations (details for the Monte Carlo simulations are given below).

As discussed in the introduction of this section (page 74), the experimentally obtained ^{1}H,^{13}C dipolar coupling anisotropy is, in general, reduced by the order parameter (see equation 3.13, page 75). Therefore, for a quantitative description of the amplitude and the symmetry of the motion, the dipolar coupling anisotropy and the asymmetry parameter, δ_D and η, have to be determined by the experiment.

To extract both parameters from the experimental data, a grid of simulated dephasing curves was created, using SIMPSON [Bak et al., 2000]. The dipolar coupling anisotropy was varied from -20 Hz to -23,500 Hz in -20 Hz steps, while the asymmetry was varied from 0.0 to 1.0 in 0.05 steps. To improve the fitting, a simultaneous fit of both REDOR series (with ζ-delays of

1.1 µs and 1.5 µs) was performed, while minimizing the RMSD

$$\mathrm{RMSD} = \left\{ \frac{1}{n} \sum_{i=1}^{n} \left[\mathscr{S}_i^{\mathrm{sim}}(\delta_{D,k}, \eta_l) - \mathscr{S}_i^{\mathrm{exp}} \right]^2 \right\}^{0.5}_{(\zeta=1.1\ \mu\mathrm{s})} + \left\{ \frac{1}{n} \sum_{i=1}^{n} \left[\mathscr{S}_i^{\mathrm{sim}}(\delta_{D,k}, \eta_l) - \mathscr{S}_i^{\mathrm{exp}} \right]^2 \right\}^{0.5}_{(\zeta=1.5\ \mu\mathrm{s})}, \tag{3.22}$$

where $\mathscr{S} = \frac{\Delta S}{S_0}$ is the normalized REDOR dephasing signal, n is the number of acquired dephasing points, k and l are indices for δ_D and η values on the generated grid, respectively. RMSD values were calculated over the entire grid and the k, l pair at the global RMSD minimum was chosen as the best fit value for δ_D and η, respectively.

To estimate the error of the dipole anisotropy and asymmetry, Monte Carlo simulations were performed. For each resonance, the best fitting, simulated dephasing curve can be described by the vectors

$$\vec{f}_{x,\mathrm{best}} = (x_1, x_2, x_3, \ldots . x_n)^T, \tag{3.23}$$

$$\vec{f}_{y,\mathrm{best}} = (y_1, y_2, y_3, \ldots, y_n)^T, \tag{3.24}$$

in which x_i and y_i are the dephasing time and normalized dephasing signal, respectively.

The squared measuring uncertainty of the normalized dephasing curves, $\delta\mathscr{S}$ (*vide supra*), was used as the variance, σ^2. For every resonance, N vectors (indexed by m)

$$\Delta\vec{f}_{y,\mathrm{best},m} = (\Delta y_1, \Delta y_2, \Delta y_3, \ldots, \Delta y_n)^T. \tag{3.25}$$

were generated, according to the Box-Muller sampling of a normal distribution [Box and Muller, 1958], using the variance σ^2. The effective vector was calculated as

$$\vec{f}^{\mathrm{MC}}_{y,\mathrm{best},m} = \vec{f}_{y,\mathrm{best}} + \Delta\vec{f}_{y,\mathrm{best},m}. \tag{3.26}$$

For every $\vec{f}^{\mathrm{MC}}_{y,\mathrm{best},m}$ vector, a RMSD minimization was performed to determine the best fitting parameters, $\delta^{\mathrm{MC}}_{D,m}$ and η^{MC}_m, respectively. Finally, for every analyzed resonance, the average and

the standard deviation over the N values of $\delta_{D,m}^{\mathrm{MC}}$ and η_m^{MC} were determined and listed as $\delta_D \pm \Delta\delta_D$ and $\eta \pm \Delta\eta$ in the appendix (page 215).

Using the ^{1}H,^{13}C rigid-limit dipolar coupling values, the squared order parameter, S^2, was calculated according to equation 3.14 (page 76). S^2 and η are given in Figure 3.33. To visualize the convergence of the fit, RMSD contour plots are shown as insets to the dephasing curves.

3.4.3 Backbone, side chain and methyl dipole tensors of α-spectrin SH3

Representative experimental REDOR dephasing curves for backbone, side chain and methyl resonances are plotted in Figure 3.33. Large variations in the oscillation of the dephasing curves were determined for the different moieties. Theoretically, the dipolar coupling anisotropy for methyl groups is reduced by a factor of three (for the tetrahedral angle $\theta_{HCC} = 109.5°$), due to fast rotation around the methyl three-fold axis:

$$\delta_{D,met} = \left|\delta_D \cdot \tfrac{1}{2}\left(3\cos^2\theta_{HCC} - 1\right)\right| \approx \tfrac{1}{3}\delta_D. \tag{3.27}$$

In this manner, the oscillation of a methyl dephasing curve is significantly reduced, as compared to a backbone dephasing curve, as apparent for Ala56α and Ala56β in Figure 3.33, respectively. But large differences in the dipole coupling anisotropy were also detected for non-methyl residues, as can be seen, for example, for the ^{1}Hβ1,^{13}Cβ1 dipole tensor of Lys60.

The quantification of the dynamical parameters reveals, that, for example, Lys60β1 has an over two times smaller squared order parameter ($S^2 = 0.19 \pm 0.01$), as compared to Lys59β1 ($S^2 = 0.43 \pm 0.02$, not shown, cf. Table 5, page 221), indicating a higher motional amplitude for Lys60β1. However, the asymmetry parameters are very similar ($\eta = 0.31 \pm 0.22$ for Lys59β1 and $\eta = 0.25 \pm 0.23$ for Lys60β1), hinting at a similar underlying motional mode.

In addition, we also determined REDOR dephasing curves using a sparsely ^{13}C labeled 10% RAP-glycerol sample of α-spectrin SH3, which was expressed using [u-^{2}H, 2-^{13}C]-glycerol as the carbon source. In this sample, the carbon nuclei were non-consecutively isotopically enriched (the RAP-glycerol labeling scheme is presented in section 3.5.1, page 103). However, due to limited measuring time (all REDOR experiments were carried out externally at Bruker

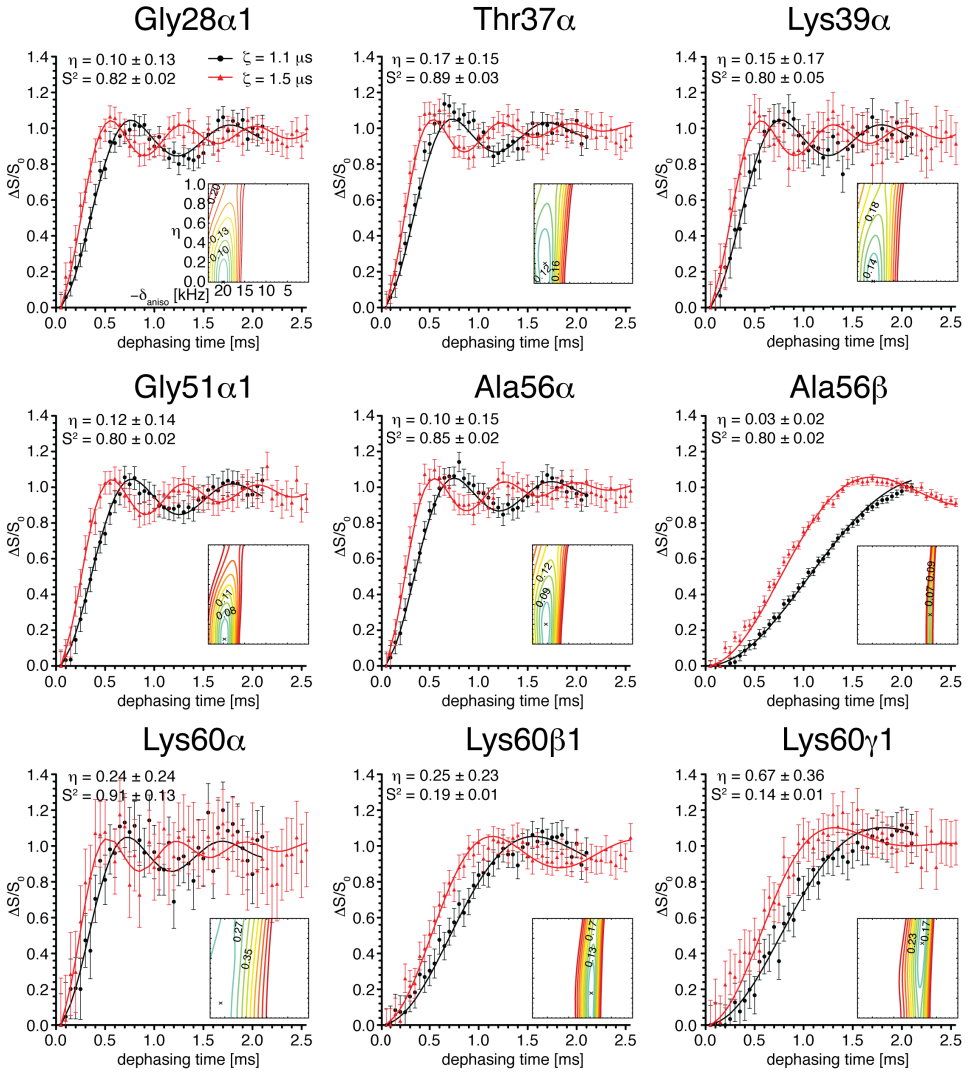

Figure 3.33: (A) Experimental REDOR dephasing curves for dipolar coupled ^{1}H,^{13}C backbone, side chain and methyl resonances, respectively, using a 15% α-spectrin SH3 RAP sample, cocrystallized with 100 mM Cu(II)EDTA. The external magnetic field was 11.7 T (500 MHz). The sample was packed into a 1.9 mm rotor and spun at a MAS frequency of 40 kHz (±5 Hz). Here, the rotor caps were glued as described in Materials and Methods (section 2.1.6, page 23). The effective sample temperature was adjusted to 15-20 °C. The pulse sequence, illustrated in Figure 3.31A, was employed, but omitting the ^{2}H-decoupling due to the limitation of the probe, which only contained two channels. To improve the fitting, two datasets with different ζ-delays (1.1 µs, black, and 1.5 µs, red) were fitted simultaneously. Two times the standard deviation of the noise was employed as the measuring uncertainty of the peak volumes. The errors of the order and asymmetry parameter were determined by 1,000 Monte Carlo simulations. Duplicate experiments at 0.05 ms dephasing were acquired in the beginning, middle and the end of the experimental series. They displayed equal intensities, within the estimated measuring uncertainty. The fitting of the dephasing curves was performed over a grid search, as described in the main text. The inset contour plots show the RMSD between the fitted and the experimental curves, as a function of the dipole coupling anisotropy and asymmetry (equation 3.22, page 82). All contour plots are equally scaled, therefore, the tick marks were labeled only for the contour plot in the upper left. The best fit value was marked with a cross. Order parameters were determined using equation 3.14 (page 76). We assumed a ^{1}Hα,^{13}Cα bond length of 1.11 Å [Alkaraghouli and Koetzle, 1975, Yao et al., 2001] and a ^{1}H,^{13}C methyl bond length of 1.15 Å [Henry and Szabo, 1985, Ishima et al., 2001], which yielded a rigid-limit dipolar coupling anisotropy of -22090.2 Hz and -21794.4 Hz, respectively. For methyl groups, the rigid-limit dipole coupling anisotropy was divided by three, according to equation 3.27 (page 83), yielding $S^2_{\mathrm{met}} = 9\ \left(\delta_D/\delta_{D,\mathrm{rigid}}\right)^2$.

BioSpin in Karlsruhe, Germany, with the kind technical support of Dr. Sebastian Wegner), the REDOR dephasing signal was only obtained up to a dephasing time of ≈1 ms, as shown in Figure 3.34A. After all, dipolar coupling anisotropies were extracted, which showed a good correlation to the values obtained using the 15% RAP sample (Figure 3.34B). Outliers were attributed to the lower sensitivity, employing the RAP-glycerol sample (only 10% protons), as well as to insufficient data sampling. In the present thesis, primarily dipolar parameters of the 15% RAP sample were used, unless mentioned otherwise.

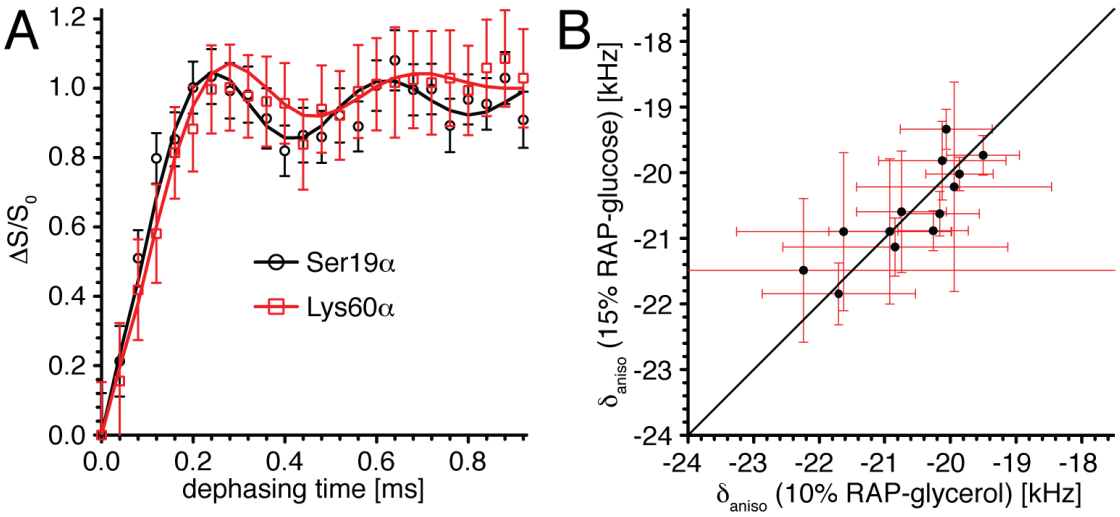

Figure 3.34: Comparison of dipolar coupling anisotropies using a 10% RAP-glycerol and a 15% RAP-glucose sample of α-spectrin SH3. (A) REDOR dephasing curves for the backbone $^{13}C\alpha$ resonances of Ser19 (black) and Lys60 (red), respectively, using the 10% RAP-glycerol sample, were plotted. (B) Linear correlation of dipolar coupling anisotropies obtained for both samples. The linear correlation coefficient was ≈0.6, while setting the y-intercept to zero and the slope to one.

3.4.4 Methyl dynamics: REDOR MAS NMR, X-ray crystallography and MD simulation

^{1}H,^{13}C dipolar coupling anisotropies are motional probes for ps-ns dynamics and, therefore, ideally suited for the investigation of methyl dynamics. At room temperature, methyl groups steadily undergo fast rotations around their local threefold axis with correlation times on the ps timescale. The amplitude of this fast, axially symmetric rotation is characterized by an order parameter, S_f^2 [Woessner, 1962a, Lipari and Szabo, 1982b, Nicholson et al., 1992, Ishima et al.,

2001],

$$S_f^2 = (P_2(\cos\theta_{HCC}))^2 = \left(\frac{3\cos^2\theta_{HCC} - 1}{2}\right)^2, \tag{3.28}$$

yielding $S_f^2 \approx 0.111$ for an ideal tetrahedral geometry ($\theta_{HCC} = 109.5°$). Due to the ps timescale, which is much smaller than $1/\delta_{D,\text{rigid}}$, the dipole coupling anisotropy is averaged by this rotational motion.

Further averaging is induced by rotameric jumps along the symmetry threefold axis (e.g. $^{13}C\alpha$,$^{13}C\beta$ axis for Val), which occur on a slower timescale and are typically in the low ns regime (0.2-2 ns) [Nicholson et al., 1992, Skrynnikov et al., 2002]. The order parameter, related to rotameric jumps (or generally to motions of the symmetry axis), is referred to as S_{axis}. Thus, a generalized order parameter, S^2_{met}, for the threefold methyl axis can be defined as [Lipari and Szabo, 1982b]

$$S^2_{\text{met}} = S_f^2 \times S^2_{\text{axis}} = 0.111 \times S^2_{\text{axis}}. \tag{3.29}$$

Using a selectively Val/Leu methyl-labeled α-spectrin SH3 sample, we recorded ^{1}H-detected REDOR spectra, using the pulse sequence depicted in Figure 3.31A. As can be seen in Figure 3.35A, a significant motional amplitude for the threefold methyl symmetry axis of Val23, Leu31 and Val46 was detected (S_{axis} was in the range of 0.11-0.26), while Val58 displayed a ≈2-6 times smaller squared order parameter ($S_{\text{axis}} = 0.62$). Similarly, the tensor asymmetry parameter η was determined to be in the range of 0.6-0.84 for Val23, Leu31 and Val46, respectively, and equal to 0.2 for Val58. The small uncertainties (0.00-0.13) reveal the high quantitative significance of the experimental η values. Hologne et al. [2005] determined the asymmetry of the methyl ^{2}H tensor by fitting ^{2}H pake patterns of u-[^{2}H,^{13}C,^{15}N] α-spectrin SH3, which yielded an η of 0.59 ± 0.01 for Val23γ. The value matched the ^{1}H,^{13}C dipole tensor asymmetry determined here for the selectively Val/Leu methyl-labeled α-spectrin SH3 sample (0.60 ± 0.03).

By definition (equation 3.12, page 75), $\eta > 0$ indicates an anisotropic averaging of the dipole tensor. In terms of methyl dynamics in the solid state, anisotropic averaging is mainly caused by unequally populated rotameric jumps, which yield $\eta > 0$ [Schanda et al., 2011a]. Based on

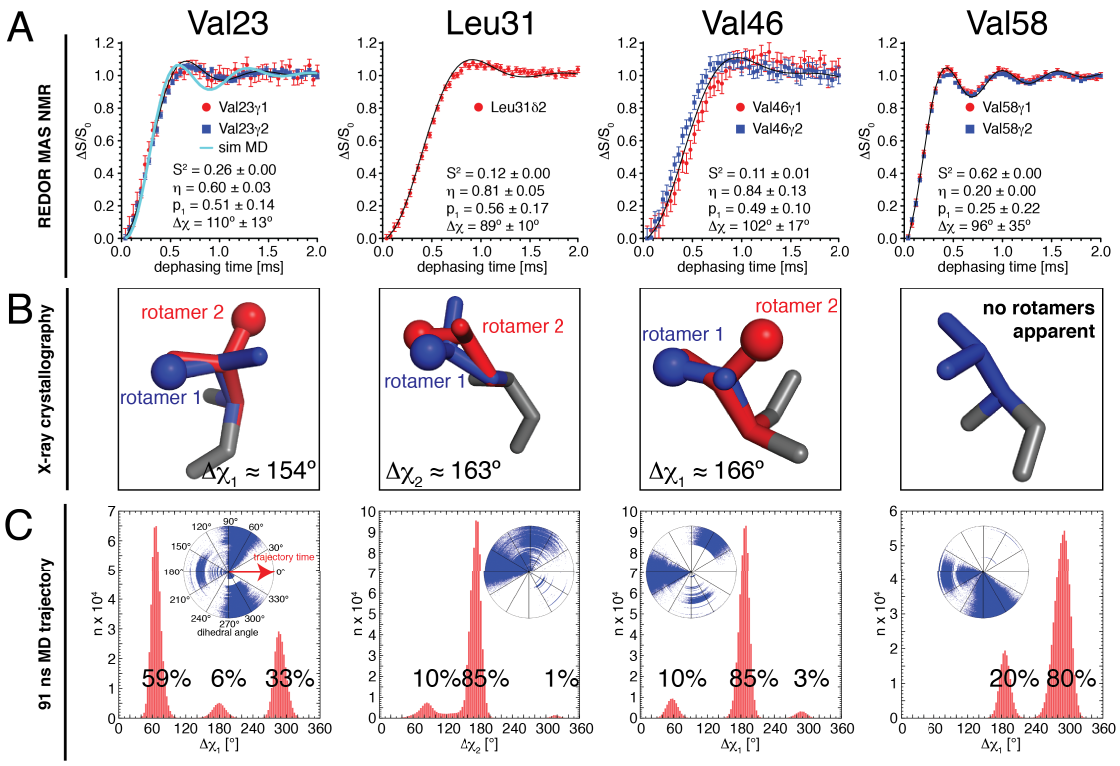

Figure 3.35: (A) ^{1}H-detected REDOR dephasing curves for a selectively Val/Leu methyl-labeled α-spectrin SH3 sample (for sample details see Table 2.1, page 21) were recorded at an external magnetic field of 14.1 T (600 MHz), using the pulse sequence in Figure 3.31A (page 78). The MAS frequency was set to 50 kHz, while the effective temperature was adjusted to 20-25 °C. The ζ-delay was set to 4 µs. The signal-to-noise ratio for a 2D experiment with a total experimental time of ≈1.4 h was 14:1 (obtained for Leu8δ2). Here, the order parameter, S^2, is the slow motion order parameter, S^2_{axis}, in equation 3.29 (page 86). The data was analyzed as described in section 3.4.2 (page 80). For valine residues, a simultaneous fit of both methyls, γ1 and γ2, was employed. Besides the dipolar coupling anisotropy and the asymmetry, the rotameric populations, p_1 and $p_2 = 1 \quad p_1$, and the jump angle, $\Delta\chi$, were determined, assuming a two-site jump model. The cyan curve for Val23 was determined using the distribution of the $\Delta\chi_1$ dihedral angles from the MD simulation in (C). An effective dipole tensor was calculated by setting the populations and the dihedral angles of the MD histograms equal to p_i and γ_i in equation 3.30, respectively. (B) The occurence of rotamers is illustrated using X-ray structures of α-spectrin SH3. The structures with the PDB ID 1U06 [Chevelkov et al., 2005c] and 2NUZ [Chevelkov et al., 2007b], respectively, were employed, which were determined at 100 K (1.49 Å resolution) and 293 K (1.85 Å resolution). For all plots, the 1U06 structure was used, except for Val23. Val23 showed rotamers in both structures with the same $\Delta\chi_1$ angle (≈ 154°), however, for the plot, the 2NUZ structure was employed. (C) Rotameric states were determined by a 91 ns MD simulation. The trajectory was kindly provided by Yi Xue and Nikolai Skrynnikov (Purdue University, Purdue, West Lafayette) [Chevelkov et al., 2007c, Xue et al., 2007]. Dihedral angles ($\Delta\chi_1$ for Val, $\Delta\chi_2$ for Leu) were determined over the total trajectory of all four α-spectrin SH3 molecules in the crystallographic unit. The histograms (bin = 100) were fitted by a normal distribution, $a\frac{1}{\sigma\sqrt{2\pi}}\exp\left[\ 0.5\left(\frac{x\ \mu}{\sigma}\right)^2\right]$. The population of the different rotamers were quantified by the area under the respective curve, which is determined by the fitting factor a. In addition, the angular distribution was plotted in a circle plot, in which the trajectory time runs from the origin outwards.

this model, REDOR dephasing curves can be simulated, using an asymmetric dipole tensor. For a n-site jump model, the asymmetric dipole tensor $\widehat{d}_{\text{jump}}$ is determined by the weighted sum of n dipole tensors (equation 3.10, page 74), which are rotated along a threefold symmetry axis by the jump angle γ_i

$$\widehat{d}_{\text{jump}} = \sum_{i=1}^{n} p_i \widehat{d}[\alpha, \beta, \gamma_i] \tag{3.30}$$

with the Euler angles of the rotation $[\alpha, \beta, \gamma_i] = \left[0, \cos^{-1}\frac{1}{3}, \gamma_i\right]$ and the population of the rotameric state, p_i. The sum of the populations is equal to 1 ($\sum p_i = 1$). Figure 3.36 shows REDOR dephasing curves assuming a two- or three-site rotameric jump model. The curves were determined by numerical simulations, using the tensor in equation 3.30. In the two-site jump model, the oscillation frequency decreases, while increasing the population of the second rotamer, which is twisted by 120°. Furthermore, the oscillation becomes damped, hence, the asymmetry η increases ($\eta > 0$). A similar trend was observed for a three-site jump model. For this model, the angles were set to 60°, -60° and 180°. Changing the relative difference angle between the rotameric states from 120° to 90° yields an asymmetric behaviour, too.

In principle, analytical expressions can be obtained to explicitly calculate the tensor asymmetry η in dependency of the populations and the jump angle, especially for the simple case of a two-site jump model [Schanda et al., 2011a]. However, for a larger number of rotamers, analytical expressions become exceedingly complicated, particularly, if a normal angular distribution is applied, which is a realistic presumption (*vide infra*). In this manner, we determined the populations and jump angles for the methyl groups, depicted in Figure 3.35A, by numerical simulations with GAMMA [Smith et al., 1994], assuming a two-site jump model. The experimental dephasing curves were fitted employing the same procedure as before (section 3.4.2, page 80).

The fitting to the two-site jump model revealed, that the rotameric population p_1 for Val23, Leu31 and Val46 was on average 52% (±12%). Only Val58 displayed a significantly smaller population of 25% (±22%). The jump angle was very similar among the illustrated residues (including Val58). The average angle was 99° (±19°), which indicates a similar conformation

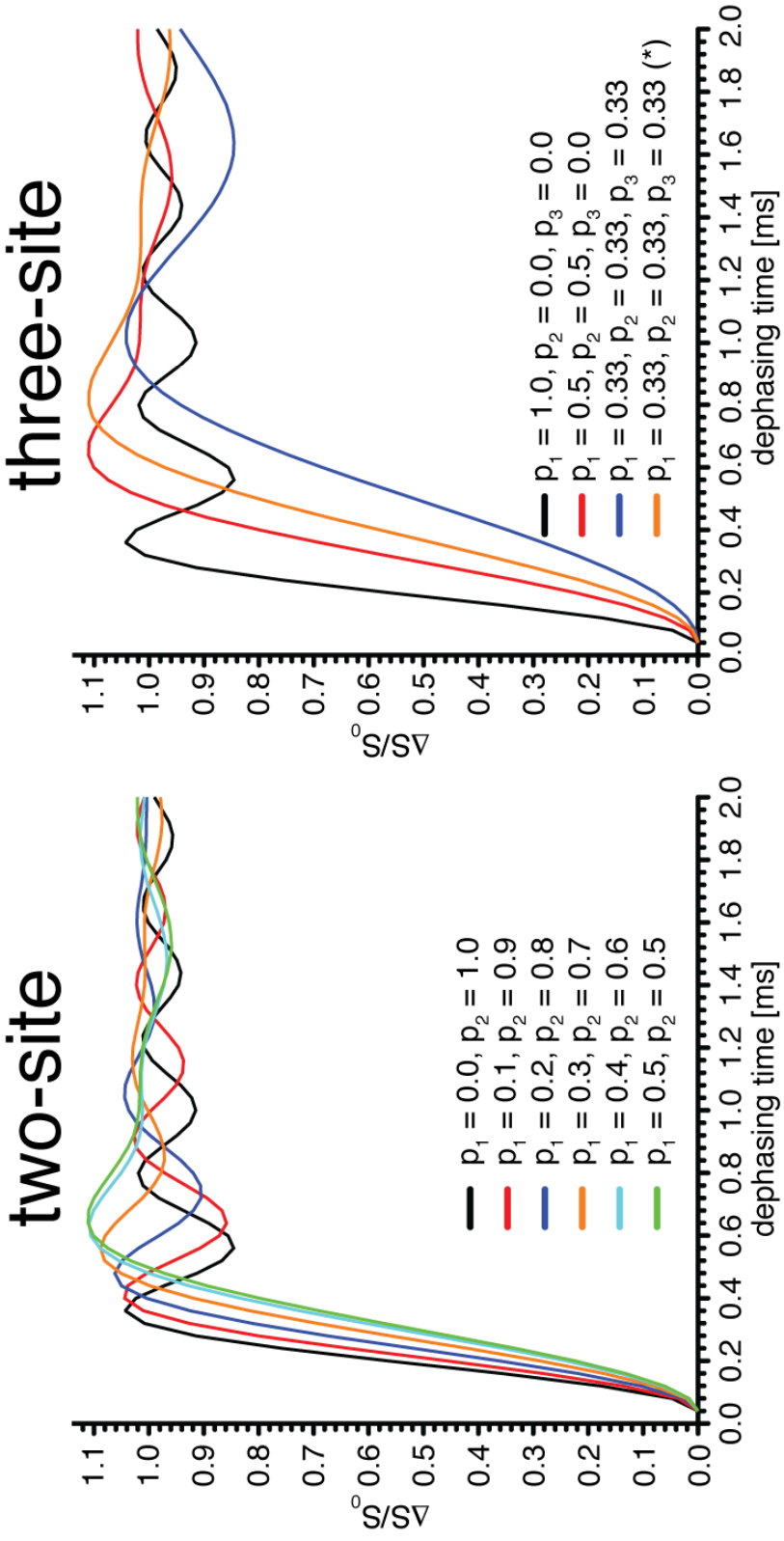

Figure 3.36: Simulated REDOR dephasing curves, assuming a two- (left) or three-site (right) rotameric jump model. The dipole (and CSA) tensor was calculated as described by equation 3.30. So far, the SIMPSON simulation software [Bak et al., 2000] does not allow user-specified tensors, therefore the GAMMA simulation software was employed [Smith et al., 1994]. The inital simulation script for GAMMA was kindly provided by Dr. Paul Schanda (IBS, Grenoble). For the two-site jump model, a jump angle of 120° was assumed, for the three-site jump model, the γ angles were set to 60°, -60° and 180°, respectively. For the orange curve (labeled with an asterisk), the angles were set to 0°, 90° and 180°. For all curves, the dipolar coupling anisotropy was set to 7500 Hz, the MAS frequency to 50 kHz and the ζ-delay to 4 μs.

for the rotamers, however, with different populations.

The rotameric states were also visible in the X-ray structures of α-spectrin SH3. Here, two X-ray structures were employed, which have been determined at different temperatures. In particular, the structures with the PDB IDs 1U06 (100 K, 1.49 Å resolution) [Chevelkov et al., 2005c] and 2NUZ (293 K, 1.85 Å) [Chevelkov et al., 2007b] were used, respectively. The three-dimensional structure of Val23, Leu31, Val46 and Val58 are illustrated in Figure 3.35B. The first rotameric state was highlighted in blue and, if available, the second rotameric state in red. Obviously, only Val23, Leu31 and Val46 display two rotameric states, while for Val58 only one state was apparent by X-ray. The dihedral angles ($\Delta\chi_1$ for Val and $\Delta\chi_2$ for Leu), to transform one rotamer into the other, were between 154° and 166°. Comparing the X-ray dihedral angles to the jump-angles, which were determined by REDOR experiments (Figure 3.35A), indicates, that the jump angles are 40°-70° smaller than the X-ray dihedral angles. The employed jump-model only assumes rotameric jumps along the threefold axis, however, librational motions of the same are not considered. This way, some part of the motional amplitude of S_{axis} detected via REDOR experiments is attributed to librational motions. This presumption is supported by the X-ray structures (Figure 3.35B). In all three cases, the threefold axis for both rotamers were slightly out of alignment, in particular for Leu31, which hints the existence of librational motions.

In principle, rotameric jumps are observable as well in Molecular Dynamics (MD) trajectories. MD simulation has been used as a complementary tool to solution- and solid-state NMR to study motional parameters [Chatfield et al., 1998, Best et al., 2005, Chevelkov et al., 2007c, Xue et al., 2007, Xu et al., 2009, Chevelkov et al., 2010, Shaw et al., 2010]. Here, we employed a 91 ns MD trajectory, provided by the Skrynnikov lab [Xue et al., 2007]. The goal of the MD simulation was to determine dynamical information for crystalline, rather than soluble α-spectrin SH3. Details on the setup of MD are given in the reference of Chevelkov et al. [2007c]. In brief, the crystallographic unit cell was constructed with four α-spectrin SH3 molecules, using the 1U06 structure (determined at 100 K) [Chevelkov et al., 2007b] and the 2NUZ dimensions of the unit cell (determined at 293 K) [Chevelkov et al., 2007b]. The periodic boundary condition was modeled to recreate the crystal lattice and the respective crystal contacts. The trajectory was calculated using the CHARMM software package [Brooks et al., 1983] and analyzed by trjtool,

developed and kindly provided by Yi Xue and Nikolai Skrynnikov (Chevelkov et al. [2007c], Xue et al. [2007]).

Figure 3.35C shows the analyzed trajectories for Val23, Leu31, Val46 and Val58. To determine rotameric states, the $\Delta\chi_1$ (for Val) and $\Delta\chi_2$ (for Leu) dihedral angles were determined and plotted as histrograms. To improve the statistics, the data from all four α-spectrin SH3 molecules in the simulated crystallographic unit were combined. Obviously, rotamers were determined for all illustrated residues, interestingly also for Val58, which did not display a second rotamer in the X-ray structure (Figure 3.35B). Fitting the distributions allows to quantify the population of the rotameric states. Except for Val58, three different rotameric states were detected, however, only two states were significantly populated ($\geq 10\%$). The relative angular difference between the rotameric states is 120°, which corresponds to the minimum energy conformation to avoid steric clashes.

If the rotation around the χ_1 angle is the only acting motion for the Val methyl groups, then, in principle, the experimental REDOR dephasing curves can be simulated considering only the populations and the angles of the rotameric states, detected via the MD simulation. In this manner, an effective dipole tensor was calculated, as described by equation 3.30 (page 88). The values for γ_i and p_i in equation 3.30 correspond to the rotameric angle and the relative frequency in the histograms of Figure 3.35C, respectively. A REDOR dephasing curve was calculated for Val23 and plotted in Figure 3.35A (in cyan). However, the simulated dephasing curve, based on MD parameters, did not sufficiently fit the experimental data, even allowing a scaling of the methyl ^{1}H,^{13}C rigid-limit value (-21794.4 Hz) and fitting towards a minimum RMSD. This hints, that, besides rotameric jumps, other motions affect the ^{1}H,^{13}C dipole tensor and hence the here determined order parameter, S^2_{axis}.

3.4.5 Val/Leu vs. RAP labeling

Methyl groups are valuable probes for structure and dynamics investigations of proteins and possess favorable relaxation properties, such as short T_1 and long T_2 times in deuterated microcrystalline protein samples. An efficient labeling scheme for selective Ile-δ1 and Leu-δ1,2/Val-γ1,2 methyl labeling was introduced for solution-state NMR [Gardner and Kay, 1997, Goto

et al., 1999, Tugarinov and Kay, 2003, 2004a, Tugarinov et al., 2006]. Later on, the approach was applied to microcrystalline proteins in the solid-state [Agarwal et al., 2008, Schanda et al., 2011a, Huber et al., 2012], next to other methyl-selective labeling schemes [Agarwal et al., 2006, Agarwal and Reif, 2008].

Here, we compared ^{1}H,^{13}C dipolar coupling anisotropies and asymmetries determined by a selectively Val/Leu methyl-labeled α-spectrin SH3 versus a 5% RAP sample, respectively. As described in the Materials and Methods (section 2.1.3, page 20), to yield a selectively Val/Leu methyl-labeled α-spectrin SH3 sample, the protein expression was carried out in the presence of α-ketoisovalerate. The sample, which is referred to as the $^{13}CD_2H$ sample, was uniformly deuterated, except for one proton, attached to one of the Val (Leu) methyl carbons, which was ^{13}C-labeled, while all other carbons remained at natural abundance. The 5% RAP sample was expressed as described previously (section 2.1.3, page 20).

Shown in Figure 3.37A are 2D ^{1}H,^{13}C HMQC spectra of both α-spectrin SH3 samples. Since the 5% RAP sample was uniformly ^{13}C labeled, the evolution of ^{13}C,^{13}C scalar couplings compromises the resolution in the methyl region, except for methionine residues. In the $^{13}CD_2H$ sample only one carbon was isotopically enriched, which improved the methyl resolution (red spectrum).

However, the aliphatic scalar couplings can be decoupled using a constant-time HSQC experiment (Figure 3.17A, page 55). As can be seen in Figure 3.37B, the application of a constant-time sequence yielded the same resolution for a 5% RAP sample, as compared to a $^{13}CD_2H$ sample. The ^{1}H (^{13}C) line widths were about 30 Hz (25 Hz) for both samples. In a constant-time experiment, the t_1 evolution period is not a function of T_2 relaxation, which is beneficial for mirror-image linear prediction [Zhu and Bax, 1990, Vandeven and Philippens, 1992]. Doubling the indirect t_1 evolution period by linear prediction yielded a further improvement of the ^{13}C resolution. The ^{13}C line width amounted to 16 Hz, employing the 5% RAP sample.

REDOR dephasing curves were obtained, using the pulse sequence in Figure 3.31A (page 78). As can be seen in Figure 3.38, the dephasing curves for both samples, $^{13}CD_2H$ and 5% RAP, progressed very similarly. All curves were fitted, following the same procedure as before (section 3.4.2, page 80). The fitted values were summarized as bar plots in Figure 3.39A. The linear

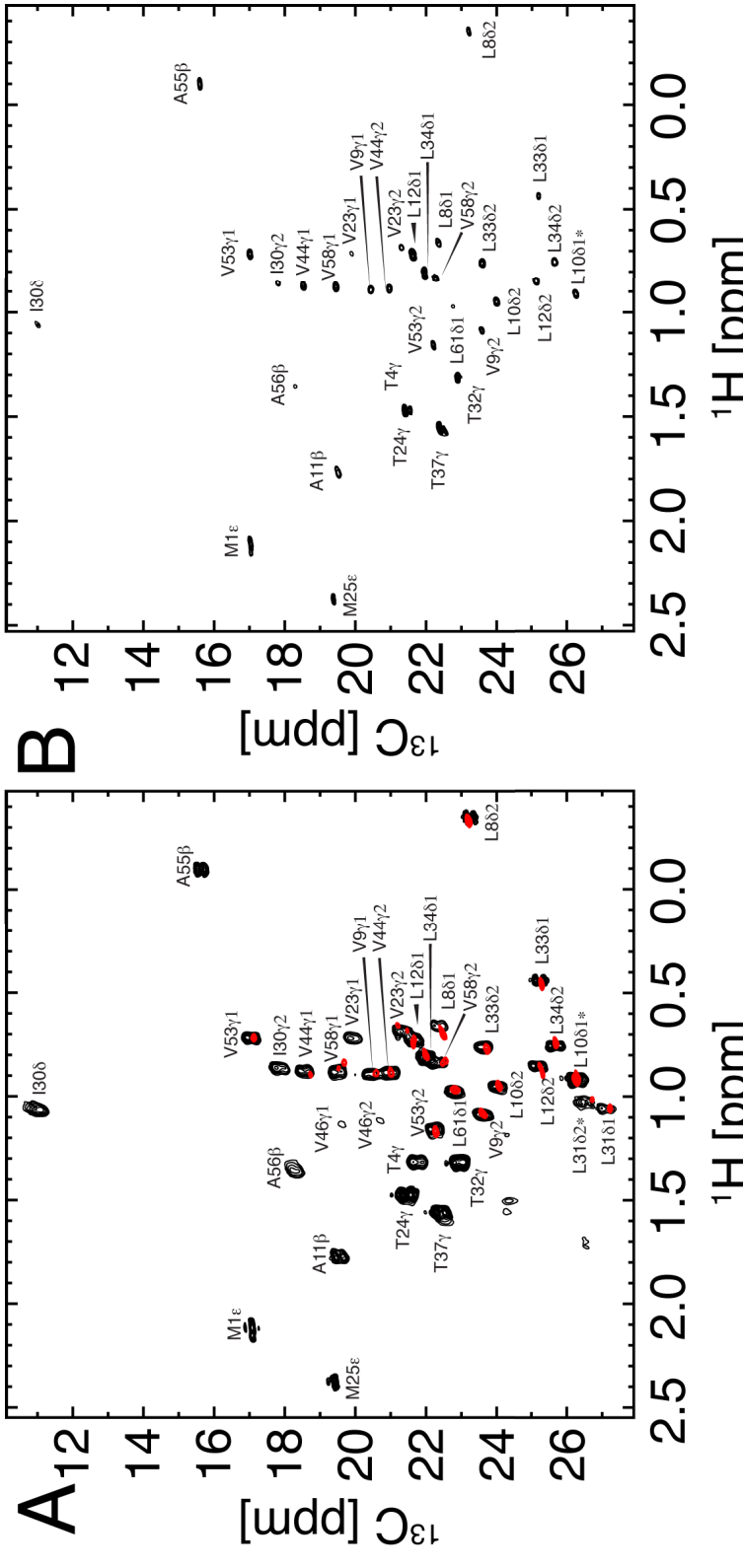

Figure 3.37: 2D ^{1}H,^{13}C methyl correlation spectra of a 5% RAP and a $^{13}CD_2H$ sample of α-spectrin SH3 at an external magnetic field of 14.1 T (600 MHz), adjusting the MAS frequency to 50 kHz and the effective temperature to 20-25 °C. 2-3 kHz low-power WALTZ-16 ^{2}H decoupling was employed during the ^{13}C evolution period [Shaka et al., 1983]. (A) The HMQC spectrum of the 5% RAP sample is shown (black), superimposed by the respective spectrum of the $^{13}CD_2H$ sample (red). The ^{13}C line width of the $^{13}CD_2H$ sample was 25 Hz. The ^{1}H line width of the 5% RAP ($^{13}CD_2H$) sample was 30 Hz (28 Hz). (B) ^{1}H,^{13}C constant-time HSQC spectrum [Vuister and Bax, 1992] of the 5% RAP sample is plotted, using the pulse sequence shown in Figure 3.17 (page 55), setting the constant-time delay $T = 1/J_{C^{\alpha},C^{\beta}} = 28.6$ ms. The ^{13}C line width was 25 Hz (16 Hz by doubling the indirect evolution period via mirror-image linear prediction [Zhu and Bax, 1990]).

correlation coefficients were 0.95 and 0.75 for the anisotropies and asymmetries, respectively, which indicates, that both parameters are highly, correlated (Figure 3.39B).

It should be noted, however, that using RAP samples all methyl groups become accessible. In this manner, REDOR dephasing curves and dipolar coupling tensors were also determined for Alaβ, Ileγ2/δ1, Metϵ and Thrγ2, respectively (Figure 3.38). Ala11β displayed the largest squared order parameter ($S^2 = 0.80$) among all methyls.

For Ile30δ1 a very low order parameter was obtained ($S^2 = 0.27$), while the dipolar coupling asymmetry was significantly high ($\eta = 0.60 \pm 0.02$). Interestingly, the dephasing curve could not be fitted sufficiently by an asymmetric tensor. This hints, the presence of a more complex motion on a slower timescale (μs). In principle, the dephasing curve could be fitted adequately by assuming contributions from one or many additional dipolar coupling tensors, with different anisotropies and asymmetries [Schanda et al., 2011a].

Furthermore, dipole parameters were obtained for the N-terminal residues Met1ϵ and Thr4γ2. These residues were absent in the X-ray structures of α-spectrin SH3 due to dynamical disorder, which is also indicated by very low squared order parameters of 0.00-0.01 (Figure 3.38 and Table 7, page 224).

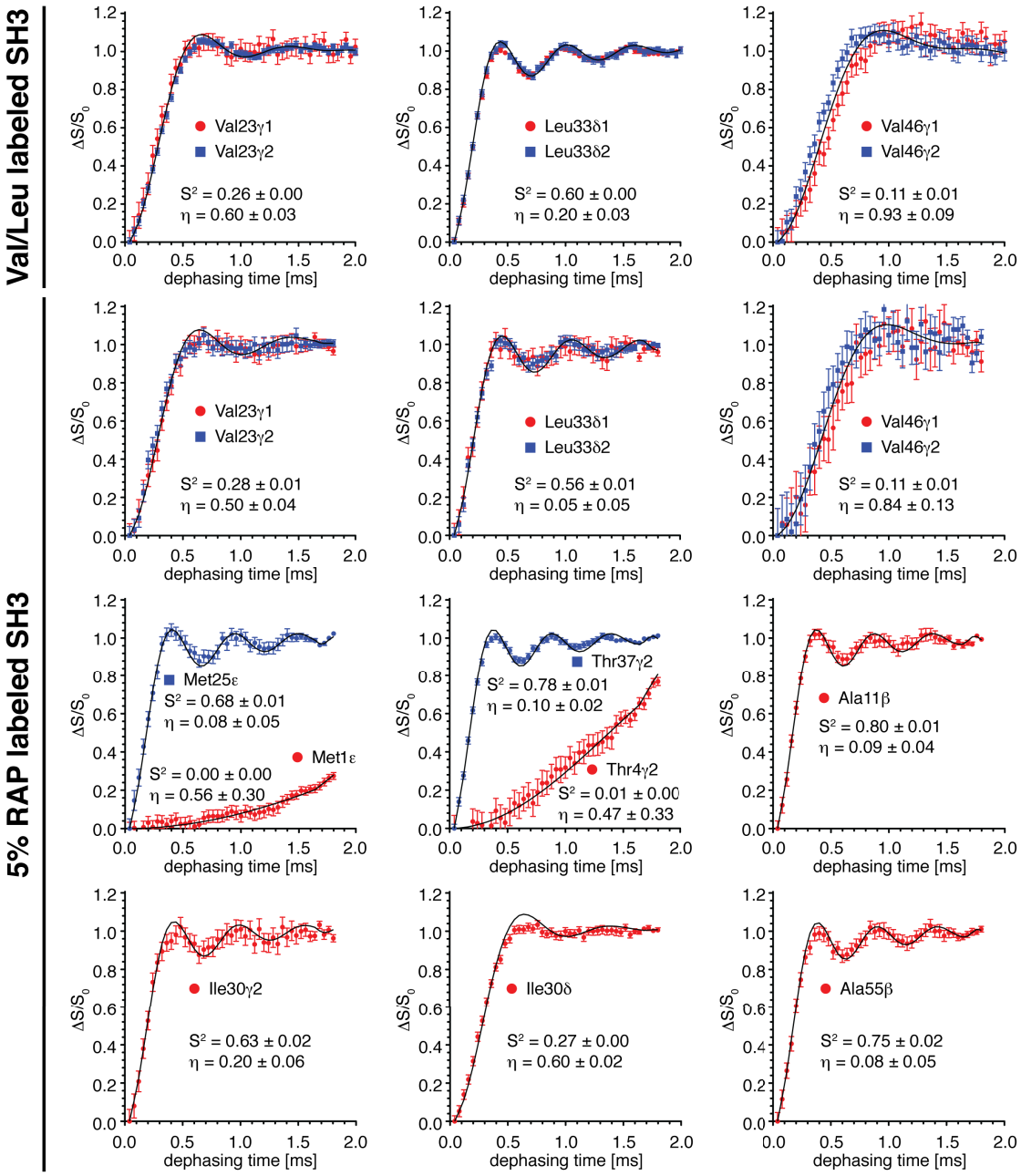

Figure 3.38: ^{1}H-detected REDOR dephasing curves, using a selectively Val/Leu methyl-labeled and a 5% RAP labeled sample of α-spectrin SH3, respectively. The external magnetic field was 14.1 T (600 MHz) at an effective temperature of 20-25 °C. The MAS frequency was set to 50 kHz and the ζ-delay to 4 µs (Figure 3.31A, page 78). The methyl order parameter S^2 (S^2_{axis} in equation 3.29, page 86) was determined as described in the figure caption of Figure 3.33 (page 84). In the first two rows, the dephasing curves were fitted by simultaneously minimizing the RMSD for both methyl sites (γ_1/γ_2 for Val and δ_1/δ_2 for Leu), which improved the fitting convergence.

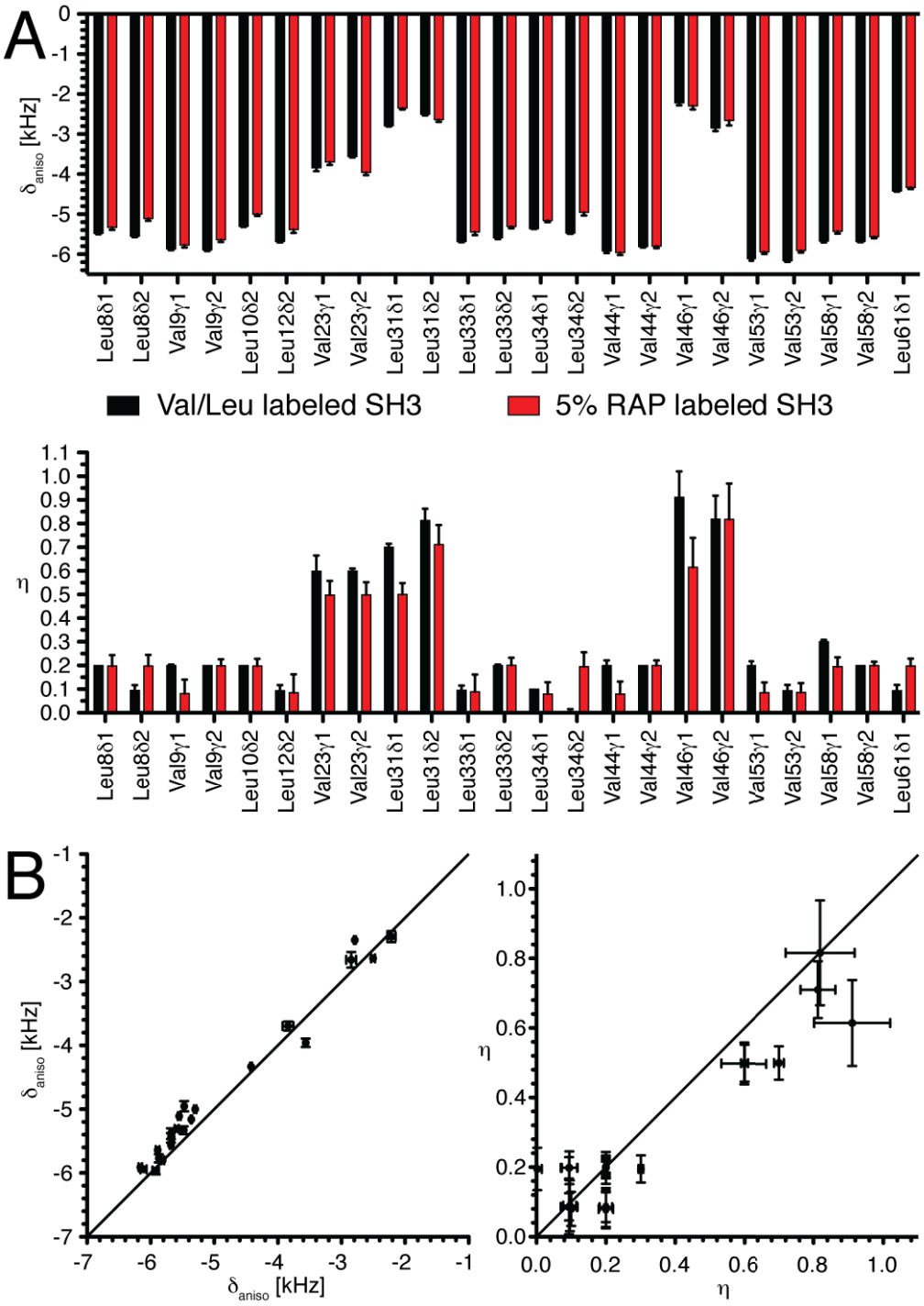

Figure 3.39: (A) Dipolar coupling anisotropies δ_{aniso} (top) and asymmetries η (bottom), using the selectively Val/Leu methyl-labeled $^{13}CD_2H$ (black) and the 5% RAP sample of α-spectrin SH3 (red), respectively. All values were determined by fitting REDOR dephasing curves (Figure 3.38). (B) The anisotropies and asymmetries of both samples were linearly correlated, setting the slope to 1.0 and the y-intercept to 0.0. The correlation coefficient was 0.95 and 0.75 for δ_{aniso} and η, respectively.

3.5 Determination of ^{13}C aliphatic backbone and side chain T_1 relaxation

Despite the close packing in globular proteins, substantial motions on the picosecond time scale occur, which enable their functional activity [Levy et al., 1981a, Karplus and Petsko, 1990, Henzler-Wildman et al., 2007]. NMR spectroscopy is particularly sensitive to ps-ns motions, which can be probed by ^{15}N and ^{13}C T_1 relaxation experiments [Kuhlmann et al., 1970, Allerhand et al., 1971, Kay et al., 1989, Mittermaier and Kay, 2006], respectively.

The relaxation rate $R_1(^{13}C) = 1/T_1(^{13}C)$ (in the following, the same set of equations apply for ^{1}H,^{15}N relaxation) [Kay et al., 1989, Chevelkov et al., 2009b] is related to the ^{1}H,^{13}C dipolar coupling anisotropy d, the chemical shift anisotropy c and the spectral density function $J_m(\omega)$:

$$R_1(^{13}C) = \frac{1}{T_1(^{13}C)} = \frac{d^2}{10}\left[J_0(\omega_H - \omega_C) + 3J_1(\omega_C) + 6J_2(\omega_H + \omega_C)\right] + \frac{2}{15}c^2 J_1(\omega_C) \qquad (3.31)$$

with

$$d = \frac{\gamma_H \gamma_C \hbar}{r_{HC}^3} \qquad (3.32)$$

and

$$c = \gamma_C B_0 \left(\sigma_\parallel - \sigma_\perp\right) = \gamma_C B_0 \Delta\sigma. \qquad (3.33)$$

γ_H and γ_C are the gyromagnetic ratios for ^{1}H and ^{13}C, respectively. $\hbar$ is the reduced Planck constant and r_{HC}^3 describes the ^{1}H,^{13}C distance. The average ^{1}Hα,^{13}Cα backbone distance is 1.11 Å (1.015 Å for backbone $^1H^N$,^{15}N) [Alkaraghouli and Koetzle, 1975, Yao et al., 2001, 2008b].

In this study, chemical shift anisotropies $|\Delta\sigma| = \left|\sigma_\parallel - \sigma_\perp\right|$ of 20 ppm [Tjandra and Bax, 1997b] and 170 ppm [Wu et al., 1995, Chekmenev et al., 2004], respectively, were assumed for ^{13}Cα and ^{15}N. For an axially symmetric tensor, the perpendicular, $\sigma_\perp$, and parallel, $\sigma_\parallel$,

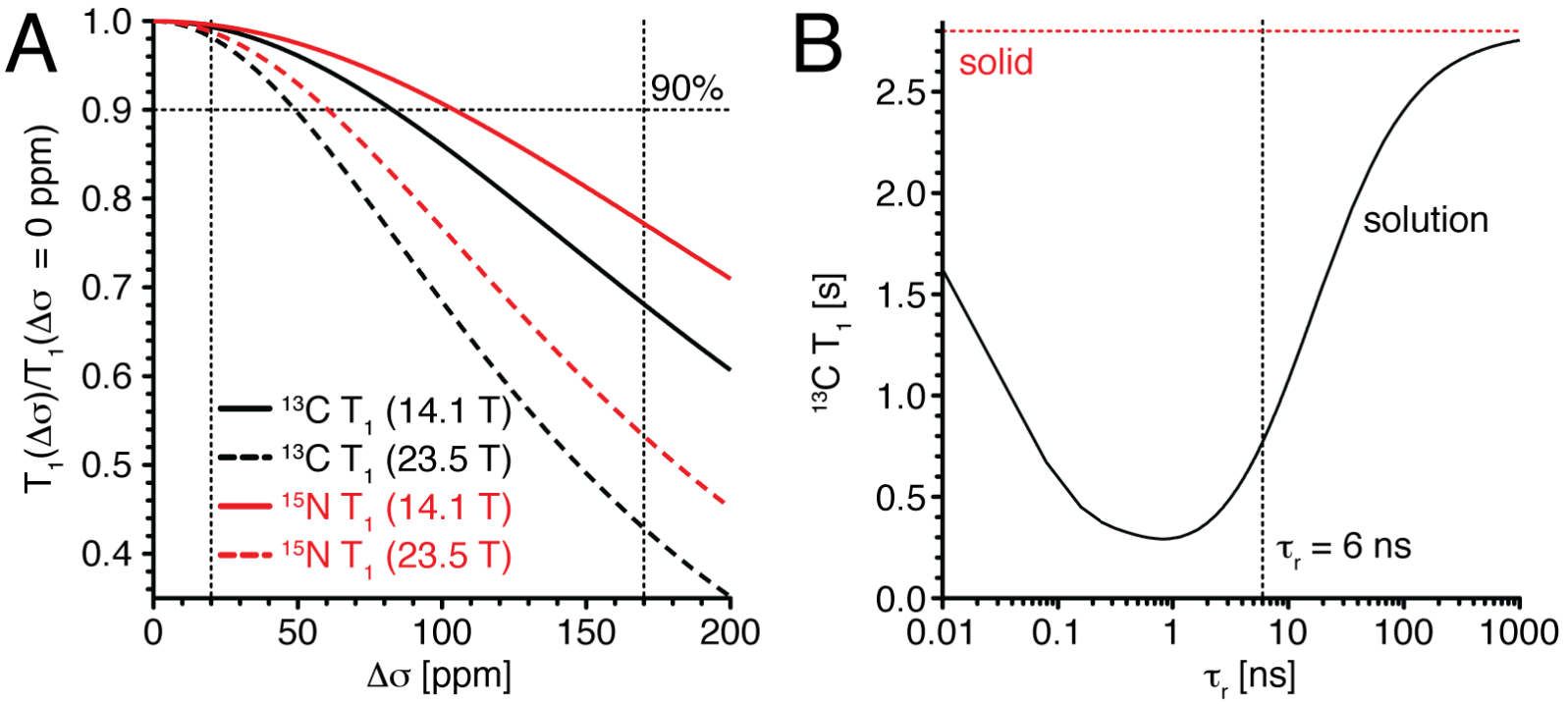

Figure 3.40: (A) The CSA contribution to the T_1 relaxation was plotted as a function of the absolute $\Delta\sigma$ value for ^{13}C (black) and ^{15}N (red) T_1 relaxation. The vertical lines were plotted at 20 ppm and 170 ppm, indicating the average $\Delta\sigma$ value for $^{13}C\alpha$ and ^{15}N nuclei, respectively [Wu et al., 1995, Tjandra and Bax, 1997b, Ishima et al., 2001, Chekmenev et al., 2004, Wylie et al., 2005, 2009]. The CSA contribution to T_1 relaxation of $^{13}C\alpha$ (^{15}N) was <2% (≈30-50%) at magnetic field strengths between 14.1 T (600 MHz) and 23.5 T (1000 MHz). The horizontal line was plotted at 90%, respectively. (B) ^{13}C T_1 time as a function of the rotational correlation time τ_r. The solid limit ($\tau_r \rightarrow \infty$) is depicted by a horizontal red, dashed line. The vertical line was plotted at $\tau_r = 6$ ns, which is the rotational correlation time of α-spectrin SH3 in solution, based on ^{15}N data [Reif et al., 2006]. The simulations in (A) and (B) were performed, using equation 3.31 (page 97) and 3.48 (page 102) with following parameters: $\tau_f = 0.01$ ns, $\tau_s = 1$ ns, $S^2 = 0.8$, $S_s^2 = 0.9$, $|\Delta\sigma| = 20$ ppm (in (B)), $\omega_H = 600.13$ MHz, $\omega_C = 150.91$ MHz, $\omega_N = 60.82$ MHz.

components are defined as [Hall and Fushman, 2006]:

$$\sigma_{\perp} = -\frac{1}{3}\Delta\sigma \tag{3.34}$$

$$\sigma_{\parallel} = \frac{2}{3}\Delta\sigma. \tag{3.35}$$

$\Delta\sigma$ is related to σ_{xx}, σ_{yy}, σ_{zz} by

$$\Delta\sigma = \sigma_{zz} - \frac{1}{2}\left(\sigma_{xx} + \sigma_{yy}\right). \tag{3.36}$$

However, Chemical Shift Anisotropy (CSA) relaxation contributes marginally to the backbone $^{13}C\alpha$ T_1 time, as illustrated in Figure 3.40A. With $|\Delta\sigma| = 20$ ppm, the contribution is <2%. Even assuming an anisotropy up to 40 ppm, which was the largest value for GB1 [Wylie et al., 2011], the contribution rises to 3-7%. Only anisotropies beyond 50-80 ppm significantly influence $^{13}C\alpha$ T_1 times ($\geq$10%). Such large anisotropies are common for ^{15}N backbone residues ($|\Delta\sigma| =$ 170 ppm) with CSA contributions on the order of $\approx$30-50%.

As discussed by Torchia and Szabo [1982] and Giraud et al. [2005], due to the lack of molecular tumbling in the solid-state, the spectral density function $J_m(\omega)$ depends on the orientation of a crystallite in a rotor-fixed coordinate axis frame and requires powder averaging and averaging over the MAS rotation period. However, for high order parameters ($S^2 > 0.7$) and internal correlation times in the ps-ns range, powder and MAS averaging can be neglected ($J_m(\omega) \approx J(\omega)$) [Schanda et al., 2010] and the Model-Free Formalism (MFF) can be applied [Lipari and Szabo, 1982a,b, Clore et al., 1990b].

In general, the spectral density function, which determines the relaxation (equation 3.31), is described by [Lipari and Szabo, 1982a, Frederick et al., 2008]

$$J(\omega) = 2\int_0^{\infty} \cos(\omega t) C(t) dt, \tag{3.37}$$

in which $C(t)$ is the total autocorrelation function. In the MFF the assumption is made, that $C(t)$

can be factored into two correlation functions, $C_O(t)$ and $C_I(t)$,

$$C(t) = C_O(t)C_I(t), \tag{3.38}$$

since their motions are independent and separated by different time scales. Here, $C_O(t)$ describes the isotropic molecular reorientation (only relevant for solvated molecules)

$$C_O(t) = \frac{1}{5}e^{-t/\tau_r}, \tag{3.39}$$

with τ_r as the rotational correlation time, while $C_I(t)$ describes the internal motion within the reference frame of the macromolecule, respectively:

$$C_I(t) = \langle P_2\left(\hat{\mu}(0)\cdot\hat{\mu}(t)\right)\rangle\,. \tag{3.40}$$

$P_2(x) = \frac{1}{2}\left(3x^2-1\right)$ is the second Legendre polynomial and $\hat{\mu}$ the time-dependent unit vector, describing the orientation of the interaction vector in a molecular-fixed reference frame. This description applies to the major relaxation-inducing interactions, dipole-dipole, quadrupole and CSA, respectively. If the motion is of Markovian nature, which is the case for diffusive and jump-like motions, or in general for motions without memory, then the internal correlation function can be expressed by exponentials with the correlation times τ_i, as

$$C_I(t) = \sum_{i=0} a_i e^{-t/\tau_i}. \tag{3.41}$$

Since the exact number of exponential terms and their weightings in equation 3.41 are determined by a specific motional model, Lipari and Szabo [1982a] only deduced universal properties of the internal correlation function $C_I(t)$ from equation 3.40, as its value at the time $t = 0$

$$C_I(0) = \langle P_2\left(\hat{\mu}(0)\cdot\hat{\mu}(0)\right)\rangle = 1, \tag{3.42}$$

which is determined by the scalar of the unit vector $\hat{\mu}$ ($\hat{\mu}(0)\cdot\hat{\mu}(0) = 1$). It was shown, that, however, the limiting value at $t = \infty$ is a model-independent measure of the spatial restriction or

the motional amplitude

$$C_I(\infty) = \mathscr{S}^2, \tag{3.43}$$

with $\mathscr{S}$ as the general order parameter, which varies between 0 (entirely isotropic motion) and 1 (total motional restriction), respectively. To first approximation, the internal correlation function in equation 3.41 can be expressed as a single exponential function

$$C_I^{\text{approx}}(t) = \mathscr{S}^2 + \left(1 - \mathscr{S}^2\right) e^{-t/\tau_e}, \tag{3.44}$$

which simultaneously fulfills conditions 3.42 and 3.43. The effective correlation time τ_e is determined by

$$\tau_e = \frac{1}{1 - \mathscr{S}^2} \int_0^\infty \left(C_I(t) - \mathscr{S}^2\right) dt, \tag{3.45}$$

in which $C_I(t)$ is described by equation 3.41. The limitations of the MFF in terms of describing the spatial symmetry of the motion have been investigated over the past years and new generalizations of the MFF were suggested [Meirovitch et al., 2003, 2010], which, however, suffer from data overfitting [Frederick et al., 2008].

To take account of the time scale and amplitude of slow and fast motions, two correlation times, τ_s and τ_f, and two order parameters, S_s and S_f, were introduced, respectively [Clore et al., 1990b], latter are related to the generalized order parameter S by:

$$S^2 = S_f^2 S_s^2 = \left(\frac{\delta}{\delta_{\text{rigid}}}\right)^2, \tag{3.46}$$

in which δ is the dipolar coupling anisotropy and δ_{rigid} the rigid-limit value determined for a ^{1}Hα,^{13}Cα (^{1}H^N,^{15}N) distance of 1.11 Å (1.015 Å), respectively. In the solid-state, the order parameter can be obtained by recoupling experiments, as discussed in section 3.4 (page 74).

If the time scale of the correlation times τ_s and τ_f differ at least by one order of magnitude,

the internal correlation function can be described by [Clore et al., 1990b]

$$\begin{aligned} C_I^{\text{approx}}(t) &= S^2 + \left(1 - S_f^2\right) e^{-t/\tau_f} + \left(S_f^2 - S^2\right) e^{-t/\tau_s} \\ &= S^2 + \left(1 - S_f^2\right) e^{-t/\tau_f} + S_f^2 \left(1 - S_s^2\right) e^{-t/\tau_s} \end{aligned} \tag{3.47}$$

Since NMR spectroscopy operates in frequency units, the spectral density is calculated by employing equations 3.37, 3.38, 3.39, 3.47:

$$J(\omega) = S^2 \frac{\tau_r}{1+(\omega\tau_r)^2} + (1-S_f^2)\frac{\tau_f'}{1+(\omega\tau_f')^2} + S_f^2(1-S_s^2)\frac{\tau_s'}{1+(\omega\tau_s')^2}, \tag{3.48}$$

with

$$\frac{1}{\tau_f'} = \frac{1}{\tau_f} + \frac{1}{\tau_r} \tag{3.49}$$

$$\frac{1}{\tau_s'} = \frac{1}{\tau_s} + \frac{1}{\tau_r}. \tag{3.50}$$

For a molecule in solution the term, $S^2 \frac{\tau_r}{1+(\omega\tau_r)^2}$, in equation 3.48 significantly shortens T_1 times in the solution-state, as compared to the solid-state (Figure 3.40B, page 98). The solid-state spectral density function, which was employed for the analysis of backbone and side chain motions, reduces to ($\tau_r \to \infty$) [Chevelkov et al., 2009b]

$$J(\omega)_{\text{solid}} = (1-S_f^2)\frac{\tau_f}{1+(\omega\tau_f)^2} + S_f^2(1-S_s^2)\frac{\tau_s}{1+(\omega\tau_s)^2}. \tag{3.51}$$

^{13}C methyl relaxation of a solvated molecule can be described by a simplified spectral density function as [Lipari and Szabo, 1982b, Agarwal et al., 2008]

$$J(\omega)^{\text{methyl}} = \frac{1}{5}\left[\alpha S_f^2 \frac{\tau_r}{1+(\omega\tau_r)^2} + (1-\alpha S_f^2)\frac{\tau}{1+(\omega\tau)^2}\right], \tag{3.52}$$

with

$$\alpha = \left(\frac{3\cos^2 \theta_{HCC} - 1}{2} \right)^2 \tag{3.53}$$

$$\frac{1}{\tau} = \frac{1}{\tau_f} + \frac{1}{\tau_r} \tag{3.54}$$

The prefactor α reduces to 0.111 for tetrahedral geometry ($\theta_{HCC} = 109.5°$). In the solid-state ($\tau_r \to \infty$) the spectral density function is determined as

$$J(\omega)^{\text{methyl}}_{\text{solid}} = \frac{1}{5} \left[(1 - \alpha S_f^2) \frac{\tau_f}{1 + (\omega\tau)^2} \right]. \tag{3.55}$$

In the following, an experimental approach for the determination of T_1 relaxation times in the solid-state is presented.

3.5.1 Experimental determination of ^{13}C T_1 times

Experimental ^{13}C T_1 times were determined for a 25% RAP sample at 24 kHz MAS frequency, using the pulse sequence shown in Figure 3.41A. The ^{1}H Larmor frequency was 700 MHz (16.4 T). To reduce cross-correlation effects, ^{1}H and ^{15}N (^{2}H for experiments at an external magnetic field of 11.7 T) π pulses were employed every 20 ms (Δ = 20 ms) throughout the ^{13}C recovery period [Kay et al., 1992, Palmer et al., 1992, Yamazaki et al., 1994b, Agarwal et al., 2008]. However, ^{13}Cα and ^{15}N (^{2}H) cross-correlation effects are marginal. CP was used for magnetization transfer to yield an in-phase S_x operator ($S = {}^{13}$C). A series of 2D experiments was recorded, varying the recovery delay from 0 s to 6 s. Peak volumes were determined by integration, while the measuring uncertainty was set to two times the standard deviation of the noise.

In Figure 3.42 the normalized magnetization decay of four ^{13}Cα backbone resonances was plotted as a function of the recovery time. The decay was fitted to a mono-exponential function

$$\frac{I(t)}{I(0)} = ae^{-t/T_1}. \tag{3.56}$$

However, the decay curves of several residues, as depicted in Figure 3.42 for Ser19, Asn35

and Lys39, respectively, significantly deviated from a mono-exponential behaviour. For these residues, a multi-exponential decay

$$\frac{I(t)}{I(0)} = \sum_{i=1}^{n} a_i e^{-t/T_{1,i}}, \tag{3.57}$$

had to be considered. Here, we employed a bi-exponential function, which could adequately fit all decay curves ($R^2 \geq 0.96$).

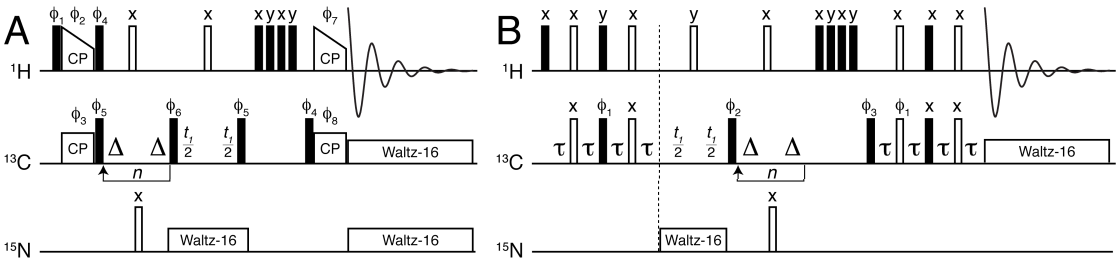

Figure 3.41: ^{1}H-detected pulse sequences for the determination of ^{13}C T_1 times, employing (A) CP or (B) refocussed INEPT for magnetization transfer, respectively. The phase cycle was as follows: (A) ϕ_1 = 4×(y, -y), 4×(x, -x), ϕ_2 = 8×(x), 8×(y), ϕ_3 = 4×(x), 4×(-x), 4×(y), 4×(-y), ϕ_4 = 2×(y, y, -y, -y), 2×(x, x, -x, -x), ϕ_5 = 8×(y), 8×(x), ϕ_6 = 8×(-y), 8×(-x), ϕ_7 = 8×(x), 8×(y), 8×(-x), 8×(-y), ϕ_8 = 8×(x), 8×(y), ϕ_{rec} = (x, -x, -x, x), (-x, x, x, -x), (-y, y, y, -y), (y, -y, -y, y), (-x, x, x, -x), (x, -x, -x, x), (y, -y, -y, y), (-y, y, y, -y). (B) ϕ_1 = 2×(x), 2×(-x), ϕ_2 = 4×(-y), 4×(y), ϕ_3 = (y, -y), ϕ_{rec} = (x, -x, -x, x), (-x, x, x, -x). Quadrature detection in ω_1 was achieved using TPPI [Marion and Wuthrich, 1983]. τ was set to $1/4J_{HC} \approx 1.92$ ms and Δ to 20 ms, respectively. The recovery delay was adjusted by multiples of 2Δ.

In principle, T_1 times in the solid-state are orientation dependent, as pointed out in the seminal study by Torchia and Szabo [1982]. During MAS, the autocorrelation function, which determines relaxation, remains dependent on the Euler angles, θ_{CM} and ϕ_{CM}, which transform the crystal-fixed (C) to the magic-axis (M) coordinate system, respectively. In this manner, the relaxation function is not mono-exponential and a superposition of different T_1 values is obtained by recording a decay curve. However, the multi-exponential behaviour observed in the T_1 decay curves of the 25% RAP sample was rather attributed to ^{13}C,^{13}C spin diffusion, as will be shown in the following. Nevertheless, obtaining T_1 from the initial slope of the relaxation function yields an orientation independent value, just as for solvated molecules [Torchia and Szabo, 1982].

To simulate ^{13}C T_1 relaxation under the influence of ^{13}C,^{13}C spin diffusion, we assumed a

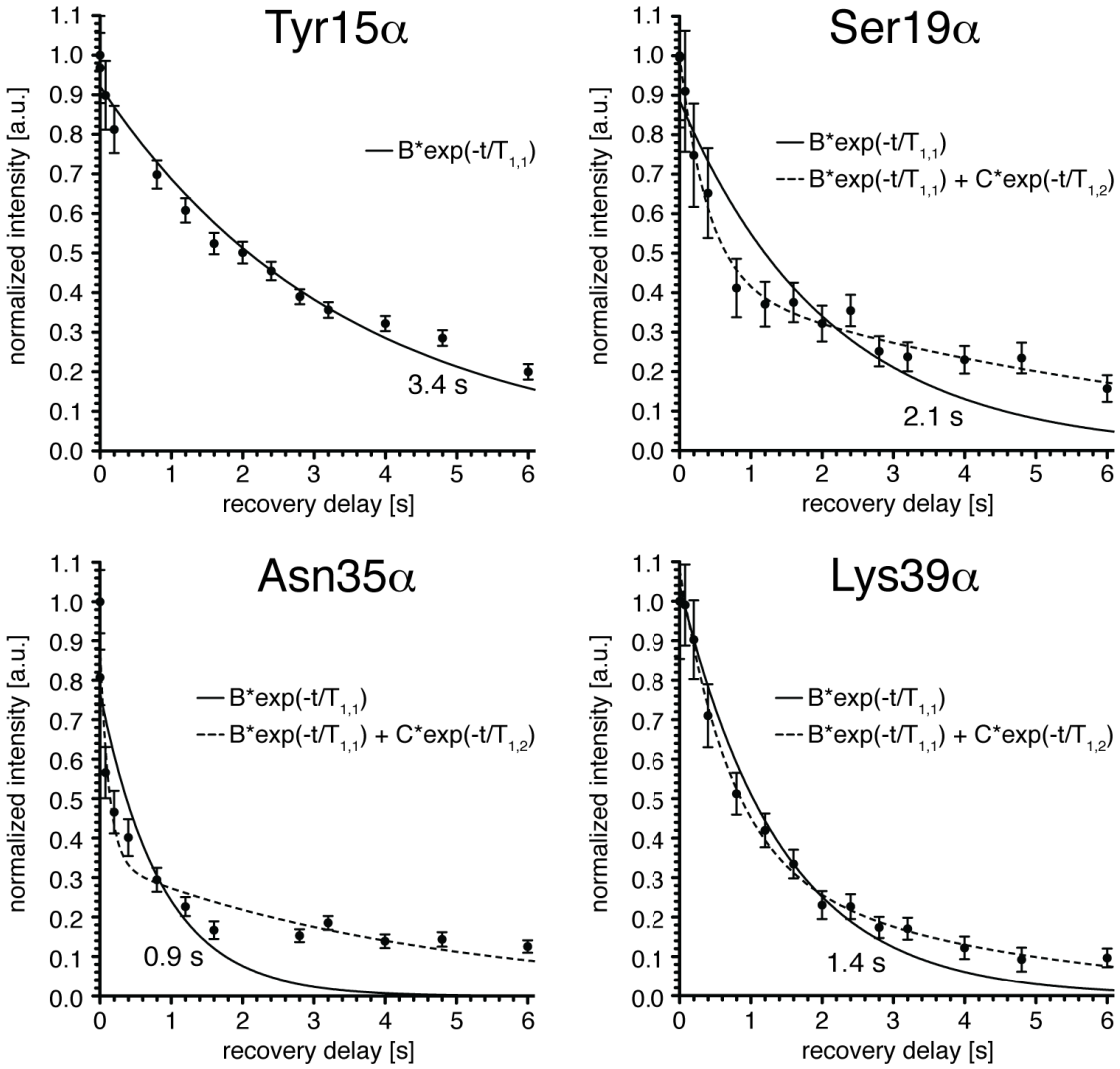

Figure 3.42: $^{13}C\alpha$ backbone T_1 decay curves of a 25% α-spectrin SH3 RAP sample at 16.4 T (700 MHz) and a MAS frequency of 24 kHz using the pulse sequence in Figure 3.41A. The experimental error was set to twice the standard deviation of the noise. All residues were normalized and fitted by a mono-exponential function $Be^{-T_{1,1}/t}$ (solid lines). The T_1 time from the mono-exponential fit is denoted for each plot. Several residues, as depicted for residues Ser19, Asn35, Lys39, respectively, showed a decay with higher numbers of exponentials (dashed lines).

simple model [Yamazaki et al., 1994b, Engelke and Ruterjans, 1995]

$$L_A \xleftarrow{\rho_A} [A] \underset{\sigma}{\overset{\sigma}{\rightleftarrows}} [B] \xrightarrow{\rho_B} L_B, \tag{3.58}$$

in which the carbon magnetization $[A]$ and $[B]$ of the spins A and B, respectively, decay with the autorelaxation rates $\rho_A = 1/T_{1,A}$ and $\rho_B = 1/T_{1,B}$, while L_A and L_B describe the magnetization of the "lattice". To take account of spin diffusion, the spin diffusion rate σ was introduced. We obtained the kinetic matrix

$$\frac{d}{dt}\begin{bmatrix} [A](t) \\ [B](t) \end{bmatrix} = \begin{bmatrix} -(\sigma+\rho_A) & \sigma \\ \sigma & -(\sigma+\rho_B) \end{bmatrix} \begin{bmatrix} [A](t) \\ [B](t) \end{bmatrix}. \tag{3.59}$$

The solution of the differential matrix equation is

$$\begin{bmatrix} [A](t) \\ [B](t) \end{bmatrix} = \begin{bmatrix} \zeta(t)\left\{\left[1-e^{\lambda t}\right](A_0(\rho_A-\rho_B)-2B_0\sigma)+\left[1+e^{\lambda t}\right]A_0\lambda\right\} \\ \zeta(t)\left\{\left[1-e^{\lambda t}\right](-B_0(\rho_A-\rho_B)-2A_0\sigma)+\left[1+e^{\lambda t}\right]B_0\lambda\right\} \end{bmatrix}, \tag{3.60}$$

with

$$\zeta(t) = \frac{1}{2\lambda}\exp\left[-\frac{1}{2}(\lambda+\rho_A+\rho_B+2\sigma)t\right] \tag{3.61}$$

and

$$\lambda = \sqrt{4\sigma^2+(\rho_A-\rho_B)^2}. \tag{3.62}$$

As apparent from equation 3.60, the magnetization decay of spin A is bi-exponential for $\sigma > 0$. For a numerical example, we assumed, that the initial magnetization of $A_0 = 1.0$ and $B_0 = 0.0$, hence, spin A was totally polarized and spin B relaxed to its equilibrium state. The autorelaxation rates were set to $\rho_A = 0.1\ \mathrm{s}^{-1}$ and $\rho_B = 0.2\ \mathrm{s}^{-1}$. As expected from the model, with $\sigma = 0\ \mathrm{s}^{-1}$, we obtained a mono-exponential decay (black circles) for $[A](t)$

$$[A](t) = e^{-0.1t}. \tag{3.63}$$

The mono-exponential fit is indicated by the black solid line in Figure 3.43. However, setting $\sigma = 1$ s $^{-1}$ yielded a bi-exponential decay (red triangles)

$$[A](t) = 0.48e^{-2.15t} + 0.52e^{-0.15t}, \tag{3.64}$$

which could not be fitted by a mono-exponential function, as illustrated in Figure 3.43 (red solid line), only considering higher exponential terms (dashed red line).

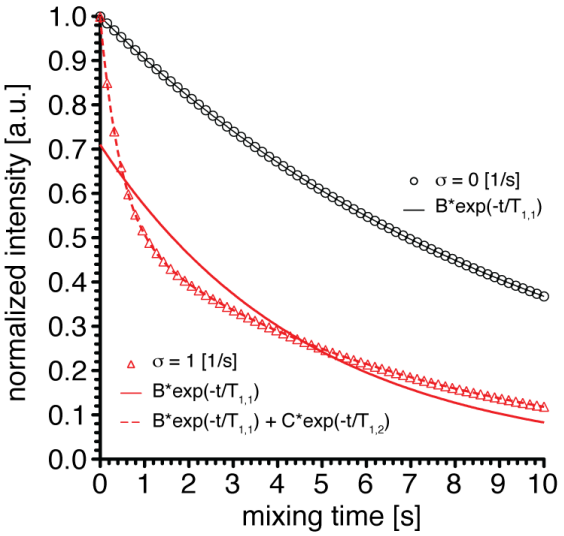

Figure 3.43: Influence of ^{13}C,^{13}C spin diffusion on ^{13}C T_1 relaxation decay curves. As expected, setting the spin diffusion rate constant σ to 0.0 s $^{-1}$ (black circles) yielded a mono-exponential decay (black solid line). However, a spin diffusion rate of > 0 s $^{-1}$ (here $\sigma = 1$ s $^{-1}$) yielded a bi-exponential decay (red triangles), which could be fitted assuming two exponentials (red dashed line), while mono-exponential fitting was not sufficient (red solid line). The curves were calculated using the equation for spin A (equation 3.60, page 106) with $A_0 = 1.0$, $B_0 = 0.0$, $\rho_A = 0.1$ and $\rho_B = 0.2$, respectively.

It should be noted, that fitting the bi-exponential decay by $I(t)/I(0) = \sum_{i=1}^{2} a_i e^{-t/T_{1,i}}$ did not directly give rise to $\rho_A = 1/T_{1,A}$ and $\rho_B = 1/T_{1,B}$, since the exponents of both of the exponentials in the sum above are, in principle, a function of ρ_A, ρ_B and σ, respectively (cf. equations 3.61 and 3.62, page 106). Therefore, the independent determination of autorelaxation and spin diffusion rates requires the assumption of a model, such as described by 3.58 (page 106). For a more realistic treatment, generally, the spin diffusion between more than two spins has to be considered, which introduces more fitting parameters, which may result in overfitting.

However, to minimize ^{13}C,^{13}C spin diffusion and render the T_1 decay mono-exponential (in

the limits of Torchia and Szabo [1982]), a 10% RAP sample was employed, which had been expressed, using [u-^{2}H, 2-^{13}C]-glycerol and Na^{1}H^{13}CO$_3$ as the carbon source [LeMaster and Kushlan, 1996, Castellani et al., 2002], respectively. As determined by the bacterial metabolism, roughly every second carbon was ^{13}C labeled.

Considering the backbone (side chains are discussed in section 3.5.2, page 114), the carbon in the α position was ^{13}C labeled, while the carbonyl and the β carbon were ^{12}C labeled and therefore NMR inactive (Figure 3.44). The only exceptions were Ile and Val, which had been isotopically labeled also in the β position (^{13}Cβ). Furthermore, the backbone α carbon nuclei of Arg, Gln, Glu, Leu and Pro residues have a very low probability of isotopically enrichment.

The probabilities determined by LeMaster and Kushlan [1996] and Castellani et al. [2002] for thioredoxin and α-spectrin SH3, respectively, show small variations in terms of the probability of ^{13}C incorporation, which might be protein-specific. Systematic errors may have also arisen due to different expression times for both proteins and different methods to quantify the level of isotopical enrichment. For the quantification in the case of thioredoxin solution-state NMR and GC-MS [Lemaster and Cronan, 1982, LeMaster and Kushlan, 1996] was employed, while the quantification of α-spectrin SH3 is only based on *J*-coupling patterns from solution-state NMR experiments [Castellani et al., 2002]. However, the estimated labeling patterns are very similar from both studies and could be experimentally validated comparing the ^{1}H,^{13}C HMQC 2D spectra of a 25% RAP (Figure 3.26, page 68) and a 10% RAP-glycerol sample (Figure 3.27, page 69), respectively.

In addition to sparsely labeling, fast MAS was employed, which had several reasons:

(i) As shown in Figure 3.8 (page 44) fast MAS ($\geq$40 kHz) improves the resolution, due to averaging of coherent contributions to the T_2 decay [Lewandowski et al., 2011b], which effectively increases the T_2 time (Figure 3.7B, page 42).

(ii) The sensitivity improves as well at fast spinning, employing scalar coupling based magnetization transfers (Figure 3.7A, page 42). For this purpose, we employed a refocussed INEPT transfer scheme for the determination of ^{13}C T_1 times. The pulse sequence is depicted in Figure 3.41B (page 104).

(iii) According to Kubo and Mcdowell [1988], Lange et al. [2003], the spin diffusion rate is

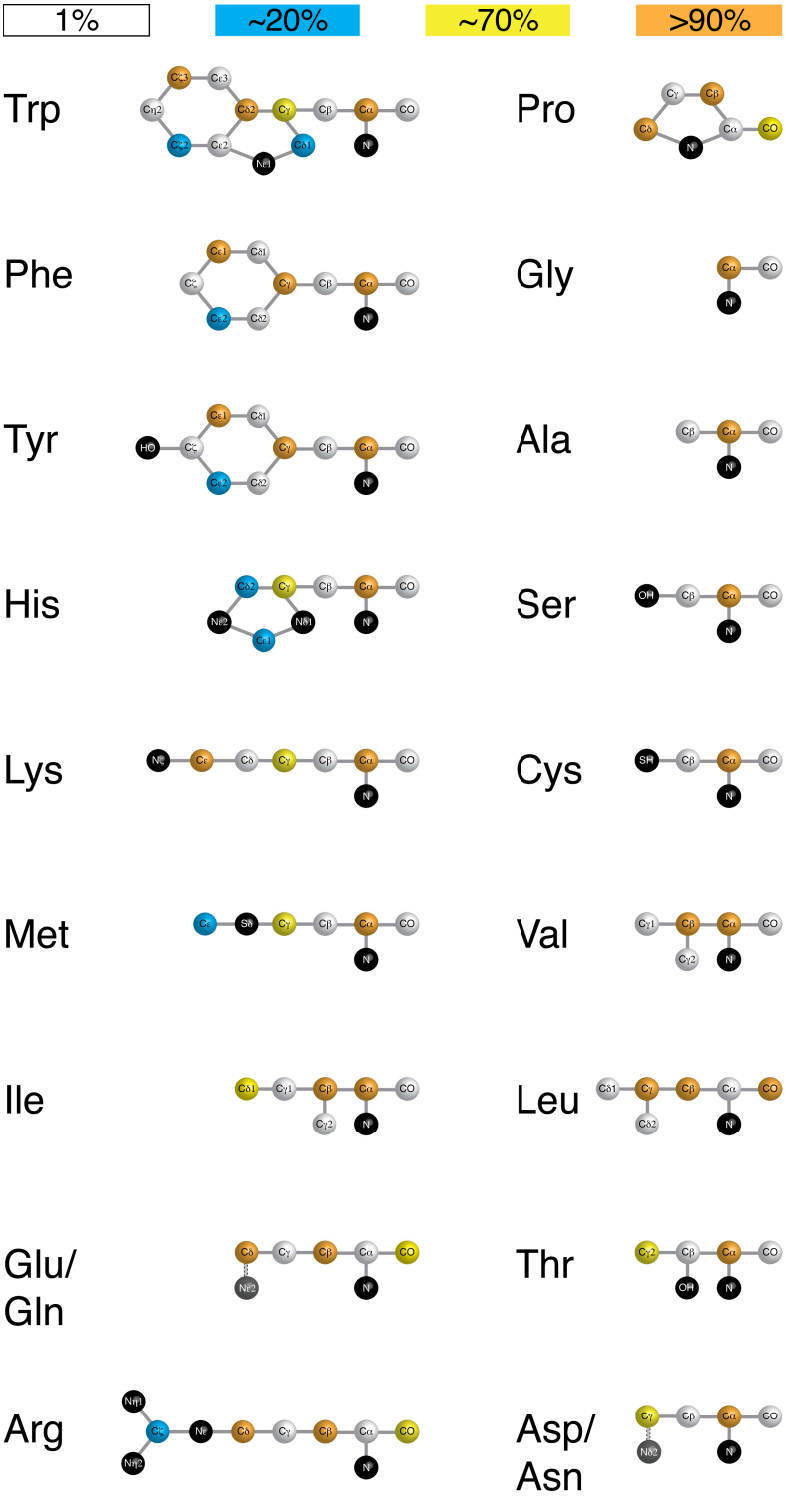

Figure 3.44: The carbon labeling pattern yielded by employing [u-^{2}H, 2-^{13}C]-glycerol and Na^{1}H$^{13}CO_3$ as the carbon source during protein expression. The colors were mapped to the approximate probability of retrieving a ^{13}C nucleus at the specified position in the amino acid. Black spheres represent non-carbon nuclei. The figure was modified after LeMaster and Kushlan [1996].

a function of the inverse distance of the dipolar coupled spins ($r_{i,j}^{-6}$), the isotropic chemical shift difference of spin i and j and scales inversely with the magic-angle rotation frequency. Accordingly, fast spinning decreases the spin diffusion rate and enables obtaining "real", motionally determined, T_1 times, as can be seen for the case of $\sigma = 0\ s^{-1}$ (Figure 3.43, page 107).

(iv) It was recently shown by Fry et al. [2011], that the backbone ^{15}N and ^{13}C' T_1 times are largely dependent on the MAS frequency. This effect is attributed to Chemical Shift Anisotropy Enabled Spin Diffusion (CSD), which is largely unaffected by deuteration. It occurs especially for uniformly labeled residues, in which relaxation sinks are coupled to nuclei with a large CSA. For ^{15}N (^{13}C) it is predominantly the coupling between the backbone amide (^{13}C') and the amine (methyl), acting as relaxation sinks. However, it was shown, that the CSD contribution is strongly dependent on the MAS frequency, ν_r. At slow MAS frequencies, CSD has a large influence on the T_1 time, but exceeding twice the chemical shift separation of the involved spins, $\nu_r > 2|\nu_i^{CS} - \nu_j^{CS}|$, entirely quenches the CSD cross-relaxation effect. In principle, considering a ^{13}C' and a methyl spin pair at a ^{1}H Larmor frequency of 850 MHz (500 MHz), ν_r has to be larger than 60-70 kHz (36-42 kHz), respectively. We determined T_1 times at both fields, 850 MHz and 500 MHz, while setting the MAS frequency to 50 kHz, which might be insufficient at the higher field in terms of CSD suppression. It should be noted, that here, we were only considering aliphatic carbons, which are less affected by CSD, due to a significantly smaller CSA and a smaller chemical shift separation of the involved spins. In any case, as can be seen from the labeling pattern of the here employed RAP-glycerol sample (Figure 3.44), the carbonyl nuclei are unlabeled for almost all amino acids, except for Arg, Glu, Gln, Leu and Pro. On the other hand, most of the methyl groups, which can act as relaxation sinks, were unlabeled, except for Ileδ1, Metϵ and Thrγ2, respectively, which, however, lack isotopical enrichment of the respective carbonyl. As an experimental validation, we determined the bulk T_1 time from 1D experiments as a function of the MAS frequency (Figure 3.45). The T_1 time increases up to a plateau around 45 kHz, which further confirms, that the T_1 decay at a MAS frequency of 50 kHz yields only motionally determined T_1 times, while coherent effects are averaged.

Considering all aforementioned factors (*vide supra*), we recorded T_1 decay curves for a 10% RAP-glycerol sample of α-spectrin SH3 (grown on [u-^{2}H, 2-^{13}C]-glycerol and Na^{1}H^{13}CO$_3$) at

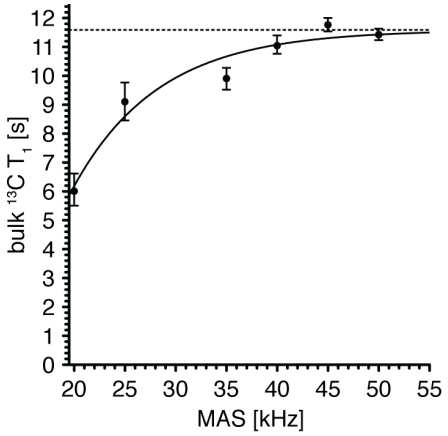

Figure 3.45: Bulk $^{13}C\alpha$ T_1 time as a function of the MAS frequency at an external magnetic field of 11.7 T (500 MHz), using the 10% α-spectrin SH3 RAP-glycerol sample. The T_1 time increases up to a plateau at 45 kHz MAS. The effective sample temperature was kept constant at 20-25 °C. The error of the T_1 times was determined by 1,000 cycles of Monte Carlo simulations, using two times the standard deviation from the noise as the measuring uncertainty. The bulk $^{13}C\alpha$ T_1 times were obtained by ^{1}H-detected inversion recovery experiments, using the first increment of the 2D pulse sequence, illustrated in Figure 3.41B (page 104).

a MAS frequency of 50 kHz, using the pulse sequence shown in Figure 3.41B. We employed two external magnetic fields, 11.7 T (500 MHz) and 20.0 T (850 MHz), respectively. For comparison, the T_1 decay curves of a 25% RAP and a 10% RAP-glycerol sample at 24 kHz spinning and an external magnetic field of 16.4 T (700 MHz) were also determined and plotted in Figure 3.46.

Already at a MAS frequency of 24 kHz, a large difference in the T_1 times between the uniformly ^{13}C (25% RAP, black) and the sparsely ^{13}C labeled (10% RAP-glycerol, blue) sample was observed at 16.4 T (700 MHz). The T_1 times were about a factor of three longer, employing the RAP-glycerol sample, while all experimental settings (temperature, external magnetic field, MAS frequency, pulse sequence) were equal for both experimental series. The bi-exponential decay was most pronounced for Trp41 using the 25% RAP sample (cf. Figure 3.42, page 105). However, using the 10% RAP-glycerol sample, yielded a mono-exponentially decaying curve for the same residue (Trp41, Figure 3.46), indicating, that ^{13}C,^{13}C spin diffusion contributes significantly to the T_1 decay of the uniformly ^{13}C labeled 25% RAP sample.

Increasing the MAS frequency to 50 kHz clearly increased the T_1 times furthermore (red curves in Figure 3.46). The experiment at 50 kHz spinning was carried out at 20.0 T (850 MHz).

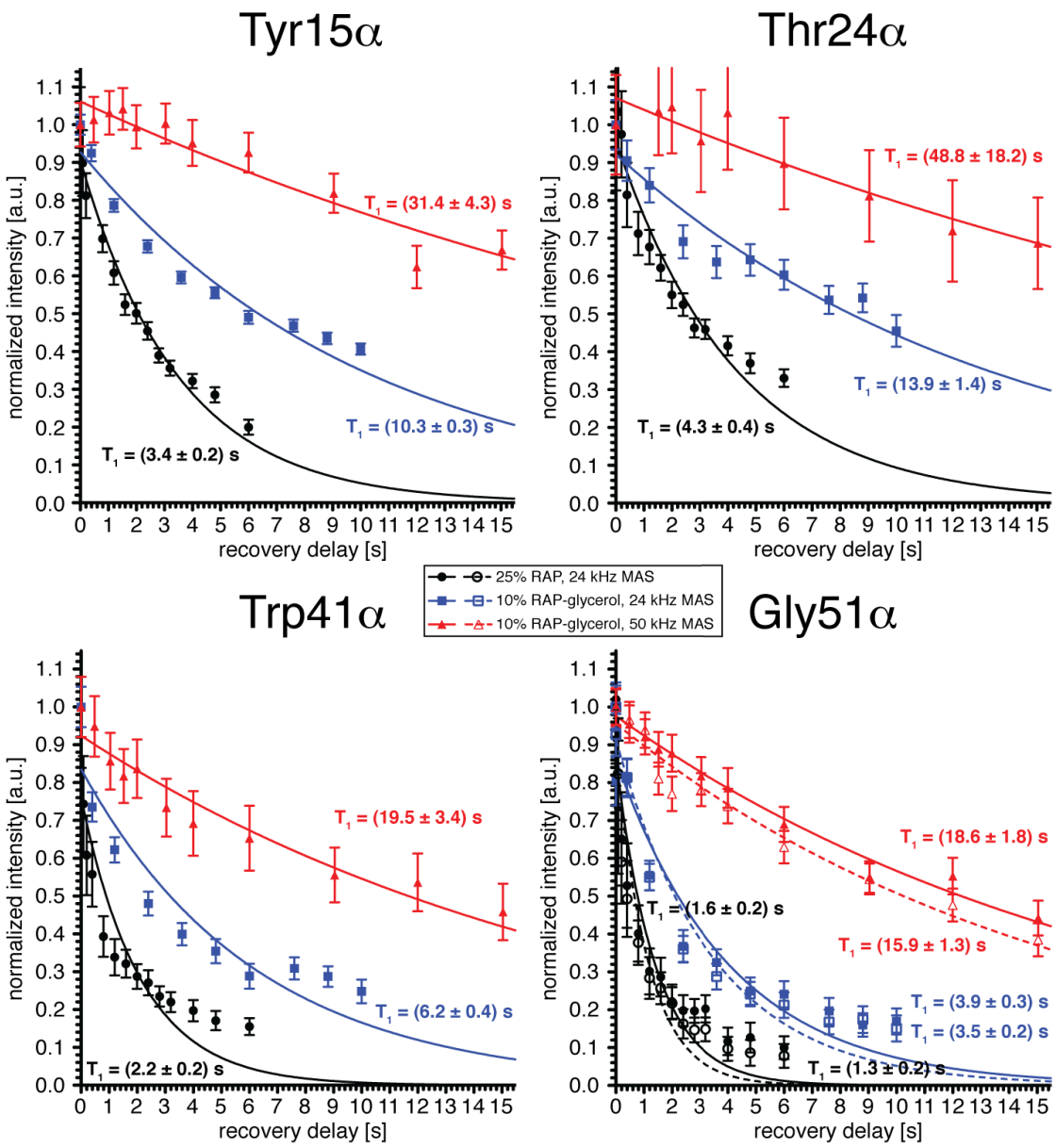

Figure 3.46: Comparison of $^{13}C\alpha$ backbone T_1 decay curves for a 25% RAP-glucose and a 10% RAP-glycerol sample of α-spectrin SH3 (sample details are given in Table 2.1, page 21), determined at a MAS frequency of 24 kHz and 50 kHz, respectively. The experiments at 24 kHz and 50 kHz were carried out at a ^1H Larmor frequency of 700 MHz (16.4 T) and 850 MHz (20.0 T), using the pulse sequences in Figure 3.41A (700 MHz) and 3.41B (850 MHz), respectively. The effective temperature in all experiments was adjusted to 20-25 °C. Clearly, significantly longer T_1 times were determined for the RAP-glycerol sample and at the higher MAS frequency.

The difference to the 25% RAP sample at 24 kHz spinning was about an order of magnitude. As supported by the T_1 plateau, which was determined to be at 45 kHz spinning (Figure 3.45), it is assumed, that the ^{13}C T_1 will not significantly change at spinning frequencies exceeding 50 kHz.

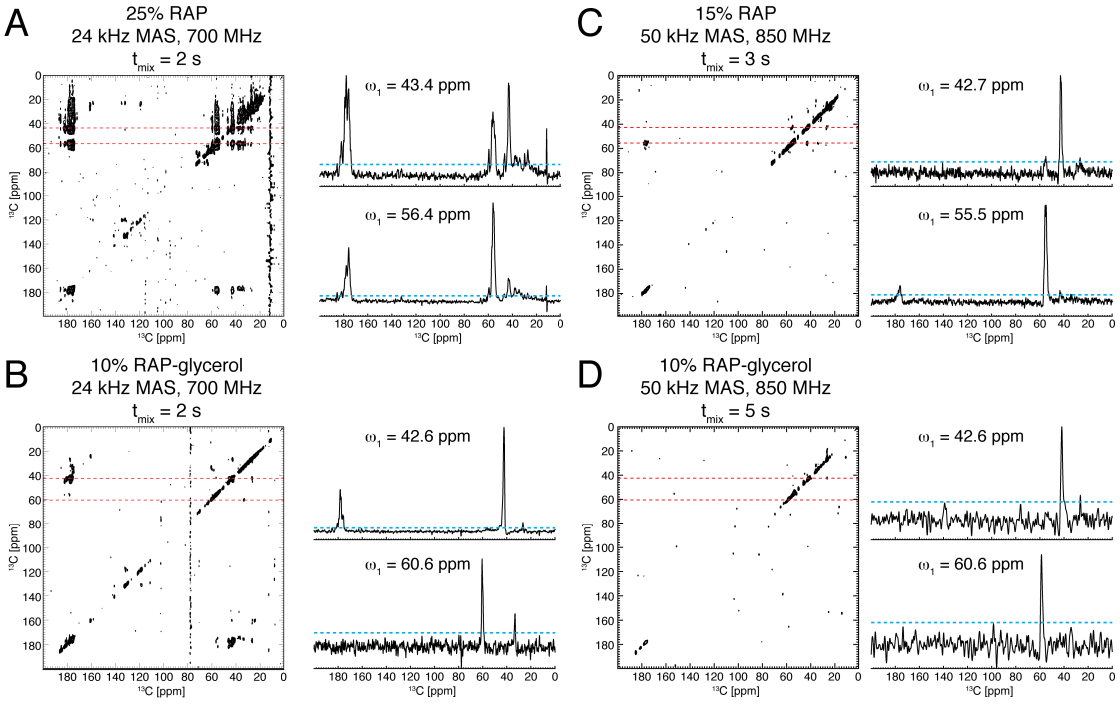

Figure 3.47: ^{13}C,^{13}C PDSD spectra of α-spectrin SH3 RAP-glucose and -glycerol samples as a function of the MAS frequency. The effective temperature in all experiments was kept constant at ≈20-25 °C. The employed MAS frequency, ^{1}H Larmor frequency and the PDSD mixing time are given in the figure titles, respectively. The location of the 1D slices along the indirect ω_1 dimension is indicated by red horizontal lines in the 2D spectra. The cyan horizontal line in the 1D slices depicts the lowest contour level employed for plotting the respective 2D spectra.

Experimentally, spin diffusion can be detected via Proton-Driven Spin Diffusion (PDSD) spectra. To quantitatively determine the experimental level of spin diffusion, we recorded 2D ^{13}C,^{13}C PDSD experiments. Two PDSD spectra were acquired at an external magnetic field of 16.4 T (700 MHz) and a MAS frequency of 24 kHz, using a 25% RAP and 10% RAP-glycerol sample of α-spectrin SH3, respectively. Apparently, at 24 kHz spinning, using the 25% RAP sample (Figure 3.47A), proton-driven spin diffusion still enables magnetization transfers within the spin systems, as can be seen by the buildup of numerous cross-peaks.

In principle, spin diffusion also acts during the inversion recovery delay $2n\Delta$, employed in the

^{13}C T_1 relaxation experiment (Figure 3.41, page 104). The recovery time was varied from 0 s to 6 s. Here, significant spin diffusion was observed already at 2 s (Figure 3.47A), which supports the presumption of a secondary pathway for magnetization decay, besides autorelaxation, observed in the T_1 experiment of the 25% RAP sample (Figure 3.42, page 105).

The 2D PDSD spectrum of a sparsely ^{13}C labeled 10% RAP-glycerol sample displayed a largely reduced number of cross-peaks and, therefore, strongly suppressed spin diffusion (Figure 3.47B). The experimental parameters were the same as for the 25% RAP sample (Figure 3.47A). In this manner, already at a moderate spinning frequency of 24 kHz, ^{13}C,^{13}C spin diffusion was severely reduced and thereby, a mono-exponential T_1 decay was observed for the 10% RAP-glycerol sample (Figure 3.46, blue curves), due to the lack of magnetization leakage by spin diffusion.

It should be noted, that ^{13}Cβ,^{13}C' cross-peaks in Figure 3.47A-B were due to the matching of the rotational resonance condition [Raleigh et al., 1988]. For this reason, ^{13}Cβ T_1 times, obtained at 16.4 T (700 MHz) and 24 kHz MAS, were excluded from the analysis of side chain relaxation (section 3.5.2, page 114).

At a MAS frequency of 50 kHz, spin diffusion was almost completely suppressed for a 15% RAP sample (Figure 3.47C) and barely detectable for a 10% RAP-glycerol (Figure 3.47D) sample, respectively, even though the spin diffusion time was raised to 5 s. For the 15% RAP sample (Figure 3.47C) still a few ^{13}Cα,^{13}C' cross-peaks were detected, as well as cross-peaks within the aliphatic region. This indicated, that ^{13}C T_1 times obtained by uniformly ^{13}C labeled RAP-glucose samples, might still be partially determined by spin diffusion. Accordingly, we picked only the data of the 10% RAP-glycerol sample at 500 MHz and 850 MHz and 50 kHz spinning, respectively, to determine backbone and side chain dynamics parameters. Side chain T_1 values are discussed in the next section (3.5.2).

3.5.2 Side chain ^{13}C T_1 times

The Reduced Adjoining Protonation (RAP) labeling scheme enables the detection of backbone, as well as side chain resonances. Therefore, dynamics parameters, such as ^{13}C T_1 times, can be obtained also for side chain moieties, using the same sample and spectra as employed for the

determination of $^{13}C\alpha$ backbone T_1 times.

Side chain T_1 decay curves are shown in Figure 3.48 for a 10% RAP-glycerol and a 15% and 25% RAP-glucose sample of α-spectrin SH3, respectively. Methine, methylene and methyl residues were divided into three rows. Thereby, methine and methylene residues displayed a similarly strong MAS dependency as backbone residues (cf. Figure 3.46, page 112).

However, methyl ^{13}C T_1 times were largely independent of the MAS frequency and whether uniformly or sparsely ^{13}C labeling was employed. The small MAS dependency of methyls was attributed to the reduced methyl dipolar coupling anisotropy (cf. equation 3.27, page 83), which decreases the spin diffusion rate.

To proceed with the quantitative dynamics analysis of backbone and side chain T_1 times, the dataset of the 10% RAP-glycerol sample at 500 MHz and 850 MHz and at a rotation frequency of 50 kHz was selected.

3.5.3 Determination of motional parameters using ^{13}C and ^{15}N relaxation data

Dynamics parameters can be obtained from T_1 relaxation data due to the relation between the T_1 time and motional correlation times and amplitudes, respectively. In the following, details about the data analysis for the determination of ^{13}C backbone and side chain motional parameters are presented, as well as a combinatorial study of ^{15}N and ^{13}C backbone dynamics. Experimental order parameters, as determined by recoupling experiments (section 3.4, page 74), were employed as motional amplitudes.

3.5.3.1 Data analysis

The theoretical framework of T_1 relaxation is given in the introduction (section 3.5, page 97). The most essential equations will be given briefly in the following. The experimentally determined ^{13}C T_1 times are related to the spectral density function as [Kay et al., 1989, Chevelkov

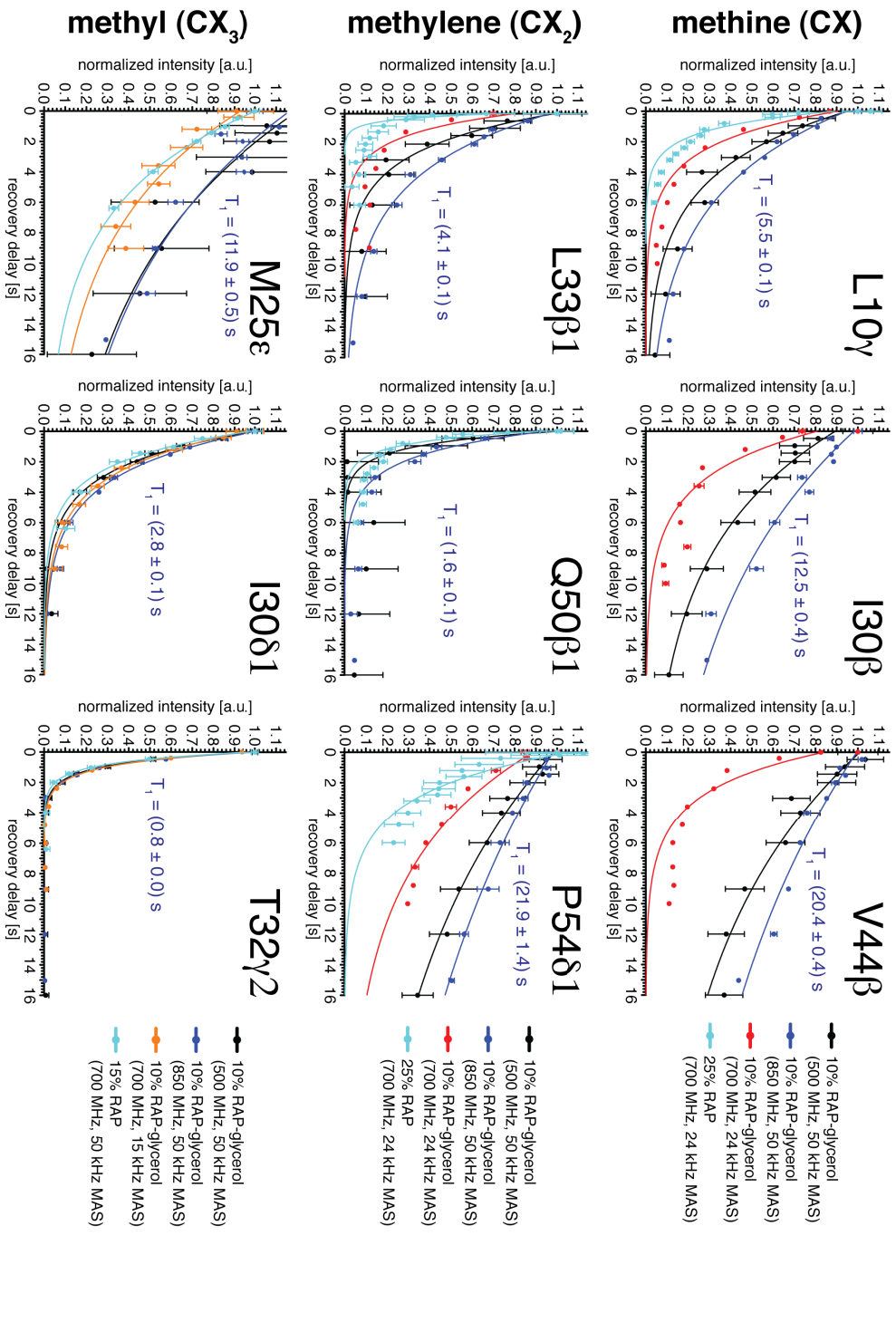

Figure 3.48: ^{13}C side chain T_1 decay curves using a 10% RAP-glycerol sample of α-spectrin SH3, recorded at a MAS frequency of 15 kHz and 24 kHz (^{1}H Larmor frequency was 700 MHz) and 50 kHz (500 MHz, 850 MHz), as well as using a 15% and 25% RAP sample, recorded at 15 kHz and 24 kHz spinning and 700 MHz ^{1}H Larmor frequency, respectively. The fitted T_1 times for the 10% RAP-glycerol sample at 50 kHz spinning and 20.0 T (850 MHz) are given in the figure text.

et al., 2009b]

$$\frac{1}{T_1(^{13}C)} = \frac{d^2}{10}\left[J_0(\omega_H - \omega_C) + 3J_1(\omega_C) + 6J_2(\omega_H + \omega_C)\right] + \frac{2}{15}c^2 J_1(\omega_C),$$
$$d = \frac{\gamma_H \gamma_C \hbar}{r_{HC}^3}, \qquad c = \gamma_C B_0 \left(\sigma_\parallel - \sigma_\perp\right) = \gamma_C B_0 \Delta\sigma \tag{3.65}$$

In principle, the dipolar part has to be scaled by the number of bound protons. Employing the extended Model-Free Formalism (MFF), which accounts of internal motions on a fast and slow time scale, respectively, the spectral density function for backbone and side chain nuclei in the solid-state can be described by

$$J(\omega) = (1 - S_f^2)\frac{\tau_f}{1 + (\omega\tau_f)^2} + S_f^2(1 - S_s^2)\frac{\tau_s}{1 + (\omega\tau_s)^2},$$
$$S^2 = S_f^2 S_s^2 = \left(\frac{\delta}{\delta_{\text{rigid}}}\right)^2. \tag{3.66}$$

Here, the fitting parameters were S_s, τ_s and τ_f, respectively, since S_f was determined by the experimentally obtained generalized order parameter S (section 3.4, page 74) as $S_f = S/S_s$.

For the analysis of methyl resonances, a simplified spectral density function was employed [Lipari and Szabo, 1982b, Agarwal et al., 2008]

$$J(\omega)^{\text{methyl}} = \frac{1}{5}\left[\left(1 - \frac{1}{9}S_f^2\right)\frac{\tau_f}{1 + (\omega\tau_f)^2}\right]. \tag{3.67}$$

Here, only τ_f was fitted, since S_f was determined experimentally (section 3.4.5, page 91).

The fitting of the dynamics parameters S_s, τ_s and τ_f for backbone and side chain resonances was performed by a χ^2 minimization [Dellwo and Wand, 1989]

$$\chi^2_{^{13}\text{C}} = \sum_i \left[\frac{1}{T_{1,i}^{\text{exp}}}\left(T_{1,i}^{\text{sim}} - T_{1,i}^{\text{exp}}\right)\right]^2. \tag{3.68}$$

Here, the index i runs over both ^{13}C T_1 parameter sets, obtained at the external magnetic fields of 11.7 T (500 MHz) and 20.0 T (850 MHz), respectively. A matrix of $\chi^2_{^{13}\text{C}}$ values was calculated,

using the parameter space: $S_s^2 \in [S^2, 0.995]$ (step: 0.005), $\tau_s \in [0.001, 599.751]$ (step: 0.25) [ns], $\tau_f \in [0.001, 19.999]$ (step: 0.002) [ns]. The optimal parameter set of S_s, τ_s and τ_f (only τ_f for methyls) was obtained at the global minimum of the $\chi^2_{^{13}\mathrm{C}}$ matrix. To estimate the parameter errors, Monte Carlo simulations were performed (cf. section 3.4.2, page 80), employing the squared uncertainty of the experimental values, $(\delta T_1)^2$ and $(\delta S^2)^2$, as the variance for generating a normal distribution around the best fit values, $T_{1,\mathrm{best}}$ and S^2_{best}, respectively.

The ^{1}H,^{15}N backbone dynamics of α-spectrin SH3 was studied earlier by Chevelkov et al. [Chevelkov, 2007, Chevelkov et al., 2009b]. The same set of equations, 3.65 and 3.66, apply to T_1 relaxation of ^{15}N backbone nuclei. For obtaining ^{15}N backbone dynamics parameters, ^{1}H,^{15}N dipole-dipole / ^{15}N CSA cross-correlated relaxation rates, $\eta^{\mathrm{DD/CSA}}$, were employed [Chevelkov et al., 2007a], in addition to ^{15}N T_1 times. They are related to spectral densities, as [Tjandra et al., 1996]

$$\eta^{\mathrm{DD/CSA}} = \frac{dc}{15}\left[4J(0) + 3J(\omega_N)\right] P_2(\cos\theta), \tag{3.69}$$

in which $P_2(x) = \frac{1}{2}\left(3x^2 - 1\right)$ is the second Legendre polynomial and θ the angle between the ^{1}H,^{15}N bond vector and the principal axis of the nearly axially symmetric ^{15}N CSA shielding tensor. θ was set to 20°. Experimental T_1 and $\eta^{\mathrm{DD/CSA}}$ values, adapted from Chevelkov et al. [Chevelkov, 2007, Chevelkov et al., 2009b], were available from an external magnetic field of 14.09 T (600 MHz) and 21.14 T (900 MHz) for T_1 and 14.09 T (600 MHz) for $\eta^{\mathrm{DD/CSA}}$, respectively. Here, we calculated the dynamics parameters (S_s^2, τ_s, τ_f), and, additionally, estimated error margins (via Monte Carlo simulations), which have not been obtained, so far. To take account of the cross-correlated relaxation rate, the χ^2 function was expanded to

$$\chi^2_{^{15}\mathrm{N}} = \sum_i \left[\frac{1}{T^{\mathrm{exp}}_{1,i}}\left(T^{\mathrm{sim}}_{1,i} - T^{\mathrm{exp}}_{1,i}\right)\right]^2 + \left[\frac{1}{\eta^{\mathrm{exp}}}\left(\eta^{\mathrm{sim}} - \eta^{\mathrm{exp}}\right)\right]^2 \tag{3.70}$$

The generalized ^{1}H,^{15}N backbone order parameter, S, was available from cross polarization phase-inverted (CPPI) experiments [Chevelkov et al., 2009a].

3.5.3.2 ^{13}C and ^{15}N dynamics parameters

^{13}C and ^{15}N motional parameters were quantified within the extended Model-Free Formalism (MFF), using relaxation data. Experimental backbone $^{13}C\alpha$ T_1 times, determined at two external magnetic fields, 11.7 T (500 MHz) and 20.0 T (850 MHz), respectively, were fitted by optimization of S_s, τ_s and τ_f, as described in the previous section (section 3.5.3.1, page 115).

Prior to the analysis of the fitted dynamics parameters, experimental and back-calculated $^{13}C\alpha$ T_1 times were linearly correlated, to determine, how well the relaxation data can be reproduced by the MFF. The linear correlation of $^{13}C\alpha$ T_1 at both fields is shown in Figure 3.49A-B. Blue crosses indicate the best fit value at the global minimum of the $\chi^2_{^{13}C}$ minimization grid, while empty black circles depict the average value over an ensemble of 500 Monte Carlo simulations. As hinted by the high correlation coefficient of experimental and back-calculated $^{13}C\alpha$ T_1 times ($R^2 \geq 0.85$, Figure 3.49A-B), the MFF sufficiently describes the present data. Here, Glu22, Thr24 and Pro54 were excluded from the analysis, because the exceptionally high experimental uncertainty of their T_1 times in either one of the employed datasets, accumulated to a large error bar for the back-calculated T_1 time.

Similarly, ^{15}N backbone T_1 times and $\eta^{\mathrm{DD/CSA}}$ rates were fitted to dynamics parameters within the framework of the MFF (Figure 3.50A-C). T_1 times obtained at an external magnetic field of 14.09 T (600 MHz) and 21.14 T (900 MHz) were employed, as well as $\eta^{\mathrm{DD/CSA}}$ measured at 14.09 T (600 MHz). The ^{15}N backbone data was adapted from Chevelkov et al. [Chevelkov et al., 2007a, Chevelkov, 2007, Chevelkov et al., 2009a,b]. The linear correlation coefficient of experimental and back-calculated values was just as high, $R^2 \geq 0.98$.

In the following, for all ^{13}C χ^2 plots, ^{1}H,^{13}C order parameter were employed, which had been obtained, using the 10% RAP-glycerol sample (Figure 3.34, page 85). Due to the improved resolution, as compared to uniformly ^{13}C labeled RAP samples (cf. Figure 3.26, page 68, Figure 3.27, page 69), additional, non-overlapping backbone resonances were available, which improved the total statistics. However, due to the limited sampling of the REDOR dephasing curves of about 1 ms and the availability of only one dataset (only one ζ-delay) for the RAP-glycerol sample, order parameters obtained for the 15% RAP-glucose sample were used for the ultimate quantification of dynamics parameters (Figure 3.55, page 128). Dipolar order parameters deter-

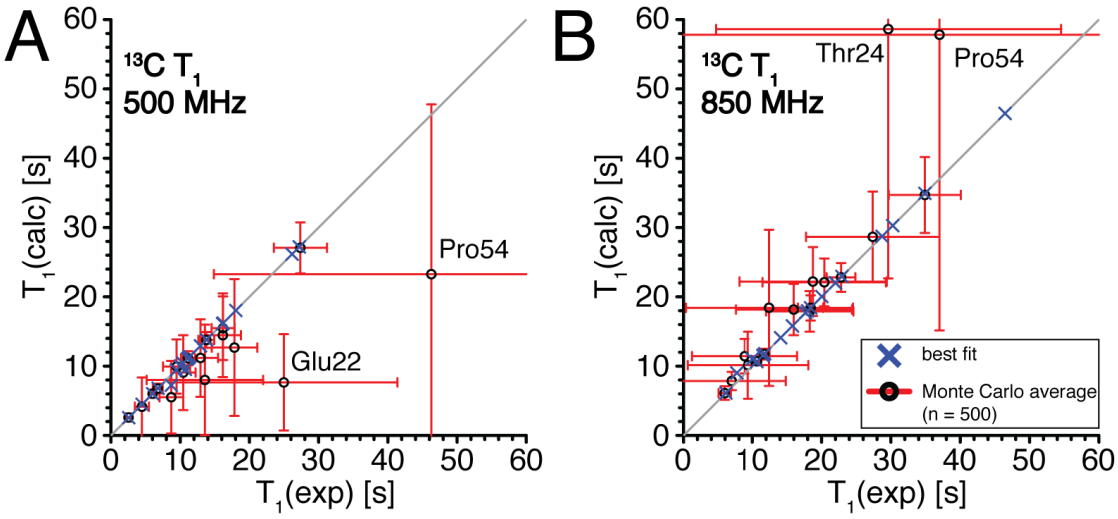

Figure 3.49: Model validation of ^{13}Cα T_1 relaxation data by linearly correlating experimental and back-calculated ^{13}Cα backbone T_1 times of α-spectrin SH3, employing the framework of the Model-Free Formalism (MFF). The ^{13}Cα T_1 values were fitted by a χ^2 minimization (equation 3.68, page 117) using ^{13}C T_1 times from two external magnetic fields, 11.7 T (500 MHz, A) and 20.0 T (850 MHz, B), respectively, and experimentally obtained ^{1}Hα,^{13}Cα backbone order parameter (section 3.4.3, page 83). The best fit value at the global minimum of the $\chi^2_{^{13}C}$ minimization grid is indicated by a blue cross for each residue. The uncertainties of the back-calculated parameters were estimated by an ensemble of 500 Monte Carlo simulations, using the squared uncertainty of the experimental values as the variance for generating a normal distribution around the best fit values. The averages of the back-calculated Monte Carlo values are depicted as empty circles (black) and the standard deviation is given by error bars (red). As expected, the error bars for the experimental and back-calculated values were about equal. The correlation coefficient for the best fit value and the Monte Carlo average was ≥ 0.995 and ≥ 0.848 (excluding Glu22, Thr24 and Pro54), respectively.

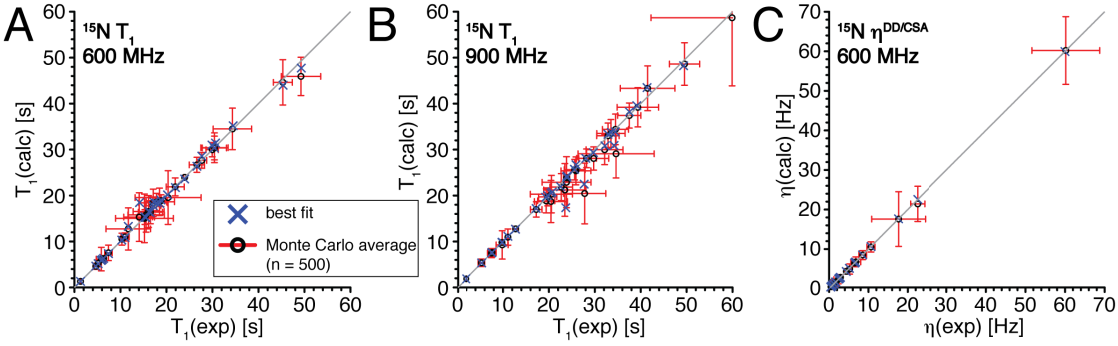

Figure 3.50: Model validation of ^{15}N relaxation data by linearly correlating experimental and back-calculated ^{15}N backbone T_1 times and $\eta^{DD/CSA}$ rates of α-spectrin SH3, employing the framework of the MFF. ^{15}N T_1 (A-B) and $\eta^{DD/CSA}$ rates (C), adapted from Chevelkov et al. [Chevelkov et al., 2007a, Chevelkov, 2007, Chevelkov et al., 2009a,b], were fitted using equation 3.70. Here, the linear correlation coefficient for the best fit value and the Monte Carlo average was ≥ 0.983 and ≥ 0.979, respectively.

mined for the 15% RAP sample displayed a higher accuracy and precision as a result of higher spectral sensitivity and an improved fitting convergence, using two complementary datasets (two ζ-delays, details are given in section 3.4.2, page 80).

Representative plots of χ^2 as a function of S_s, τ_s and τ_f for $^{13}C\alpha$ nuclei are shown in Figure 3.51. The fast and slow correlation times, τ_f and τ_s, ranged from picoseconds to a few nanoseconds and from tens to hundreds of nanoseconds, respectively. As required by the MFF, the time scales were separated by at least one order of magnitude. The squared order parameter for slow motions, S_s^2, was greater or equal to 0.87. However, the fit did not converge in all cases, as can be seen for Lys39 and Asp40, respectively. Particularly for these residues, the τ_f values were exceptionally long and ranged into the low-nanosecond regime. In total, the fitting only converged for 10 out of 25 residues (40%).

On the other hand, the ^{15}N backbone resonances displayed an improved fitting profile (Figure 3.52). Here, 22 out of 32 residues converged (69%). This improvement was attributed to the addition of orthogonal data by the cross-correlated relaxation rates. Leaving out this additional relaxation data, gives rise to a similar convergence profile as for the ^{13}C data [Chevelkov et al., 2009b].

However, while fitting the ^{15}N data and exploiting the benefit of adding cross-correlated relaxation rates, still ≈30% of the resonances could not be fitted reliably. We investigated the possibility of performing a simultaneous fit of $^{13}C\alpha$ and ^{15}N relaxation data, to improve the overall fitting convergence of backbone relaxation data. As demonstrated by others, using solution-state NMR and MD simulations as complementary techniques to study protein dynamics [Chatfield et al., 1998, Zhu et al., 1998, Guenneugues et al., 1999, Idiyatullin et al., 2003], the motional time scale and amplitudes of $^{1}H\alpha$,$^{13}C\alpha$ and $^{1}H^{N}$,^{15}N bond vectors were determined to be very similar, which is also supported by the present data, comparing $^{13}C\alpha$ and ^{15}N backbone order parameters (cf. Figure 4.4A-B, page 175).

In this regard, we back-calculated backbone $^{13}C\alpha$ T_1 times, using S_s, τ_s and τ_f, respectively, derived only from ^{15}N relaxation data. As can be seen in Figure 3.53, experimental and back-calculated T_1 times were approximately linearly correlated, hinting the similarity of $^{13}C\alpha$ and ^{15}N parameters in terms of motion. However, for statistically substantiated conclusions, more

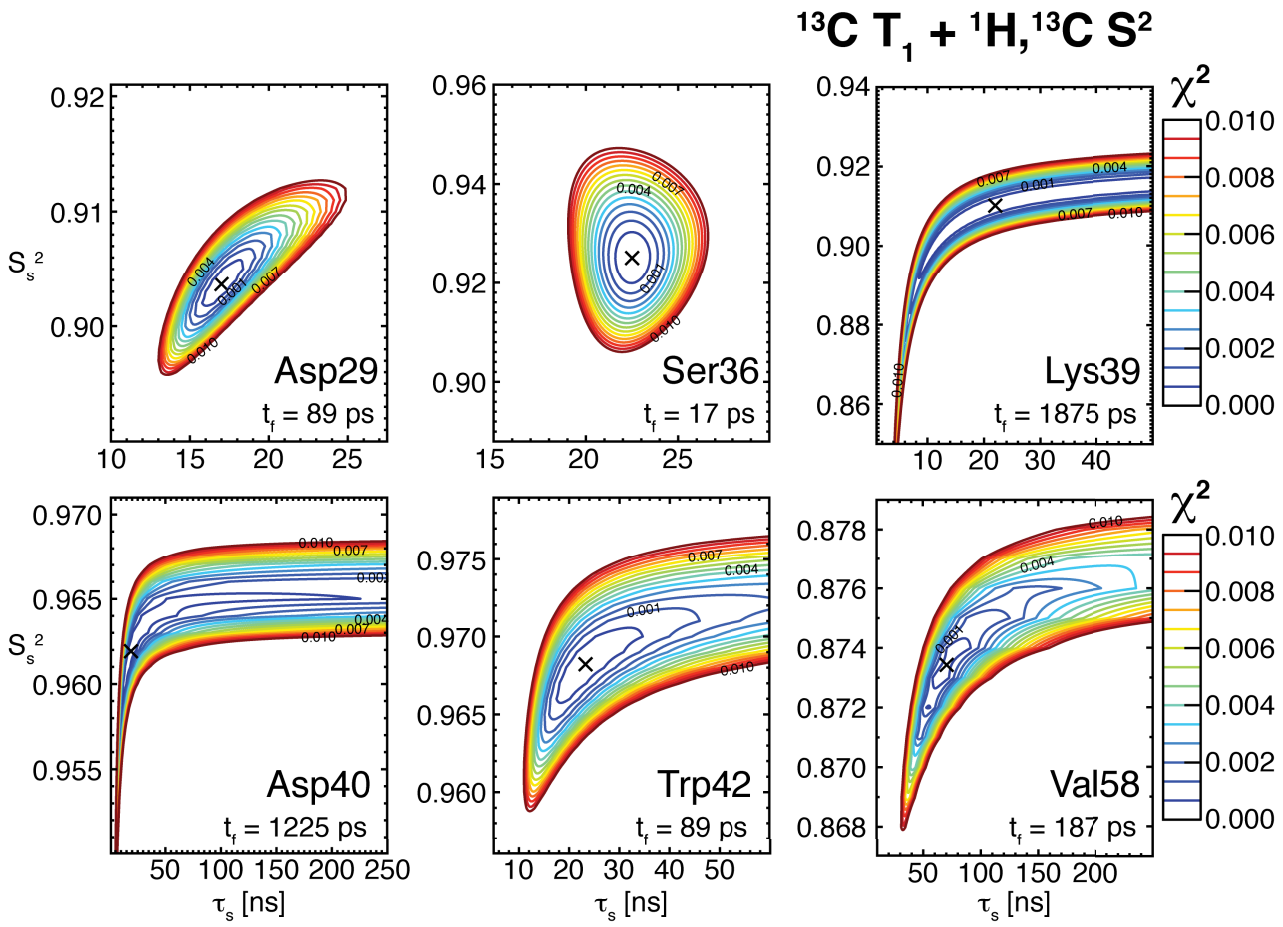

Figure 3.51: ^{13}Cα backbone dynamics parameters determined by a χ^2 minimization (described in section 3.5.3.1, page 115), using ^{13}C T_1 values obtained from two external magnetic fields, 11.7 T (500 MHz) and 20.0 T (850 MHz), respectively, and ^{1}Hα,^{13}Cα backbone order parameters (section 3.4.3, page 83). The cross depicts the global minimum. Here, the employed order parameters were determined using the 10% RAP-glycerol sample (cf. Figure 3.34, page 85) due to the access to more resolved resonances as compared to the datasets of the 15% RAP-glucose sample. However, for the ultimate calculation of dynamics parameters (Figure 3.55, page 128), the order parameters using the 15% RAP-glucose datasets were employed, due to the improved accuracy and precision.

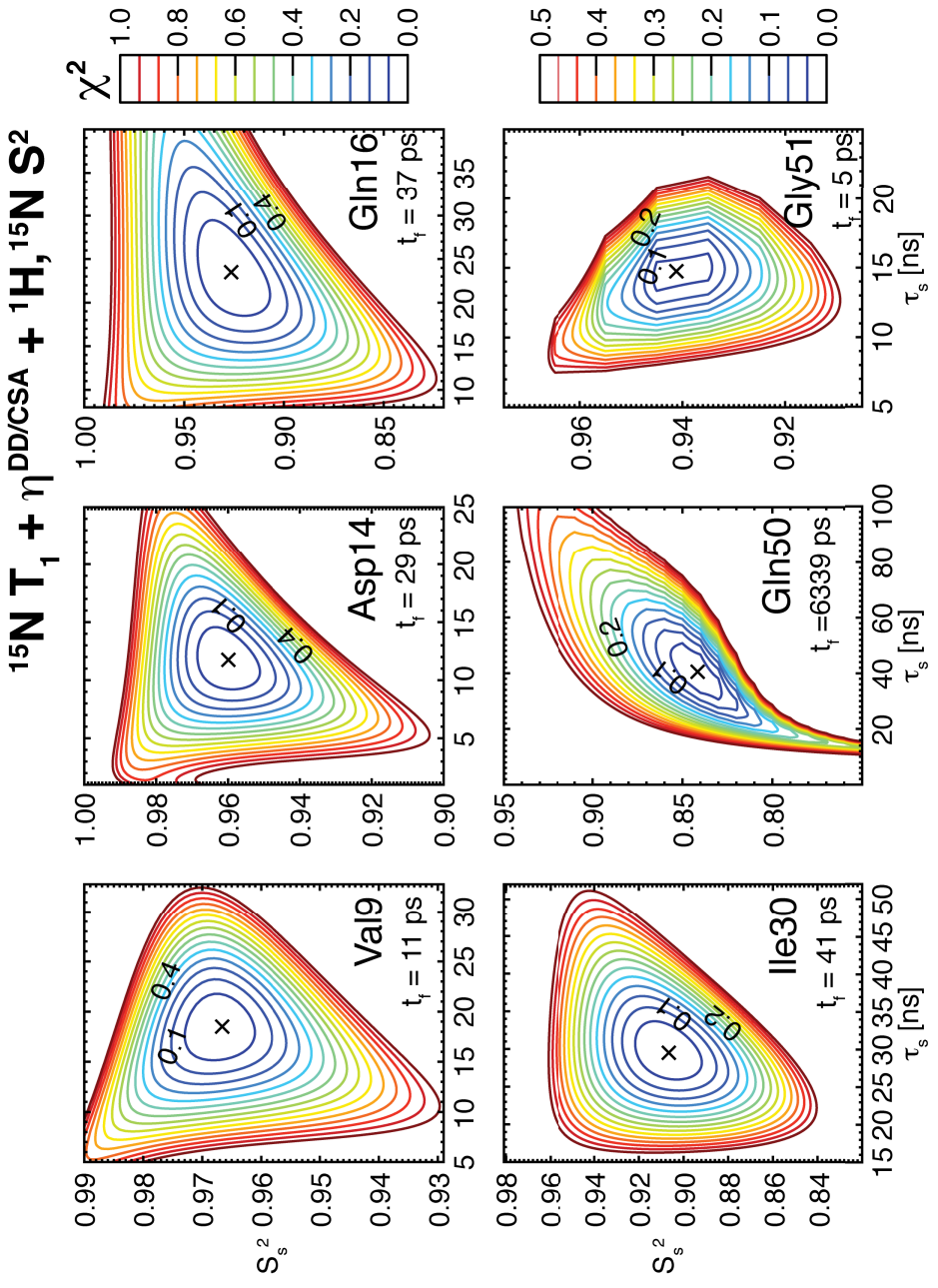

Figure 3.52: ^{15}N backbone dynamics parameters determined by a χ^2 minimization (described in section 3.5.3.1, page 115), using ^{15}N T_1 times (14.09 T and 21.14 T), ^1H,^{15}N order parameters and cross-correlated relaxation rates (14.09 T), respectively.

data points are required. Here, only eight resonances were employed, of which three were non-converging, since the intersection of simultaneously available ^{13}Cα and ^{15}N backbone data for the same residue was rather limited.

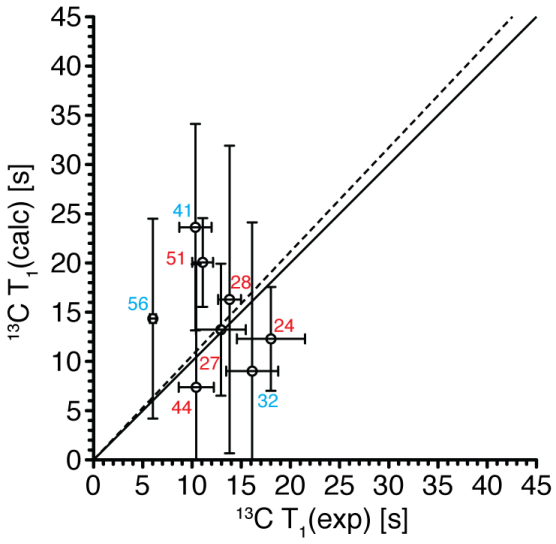

Figure 3.53: Linear correlation of experimental and back-calculated ^{13}C T_1 times, employing the dynamics parameters, obtained from ^{15}N relaxation data. Here, the best fit values of all employed parameters were used, while the error for the ^{15}N dynamics parameters S_s, τ_s, τ_f was adapted from Figure 3.55 (page 128). Constraining the y-intercept of the linear function to zero, yielded a slope of 1.057. The dashed line depicts the ideal correlation with a slope equal to one. The red and cyan colored labels depict the converging and non-converging residues, based on their χ^2 profile using only ^{15}N relaxation data.

To probe the influence of ^{13}Cα data on the convergence profile of ^{15}N backbone residues, which displayed a non-converging χ^2 minimization profile, we fitted ^{15}N backbone data simultaneously with the respective ^{13}Cα relaxation data, employing the following χ^2 function:

$$\chi^2 = \sum_i \left[\frac{1}{T_{1,i}^{^{15}\mathrm{N,exp}}} \left(T_{1,i}^{^{15}\mathrm{N,sim}} \quad T_{1,i}^{^{15}\mathrm{N,exp}} \right) \right]^2 + \left[\frac{1}{\eta^{^{15}\mathrm{N,exp}}} \left(\eta^{^{15}\mathrm{N,sim}} \quad \eta^{^{15}\mathrm{N,exp}} \right) \right]^2 + \sum_i \left[\frac{1}{T_{1,i}^{^{13}\mathrm{C,exp}}} \left(T_{1,i}^{^{13}\mathrm{C,sim}} \quad T_{1,i}^{^{13}\mathrm{C,exp}} \right) \right]^2 . \tag{3.71}$$

χ^2 minimization profiles, combining ^{15}N and ^{13}Cα relaxation data, are shown in Figure 3.54. The left, middle and right column represent minimization profiles, employing only ^{15}N backbone relaxation data (^{15}N T_1 and $\eta^{\mathrm{DD/CSA}}$), ^{15}N and ^{13}Cα T_1 or ^{15}N, ^{13}Cα T_1 and ^{1}Hα,^{13}Cα S^2 order

parameters, respectively.

For validation of this combinatorial approach, a "negative control" was established. In this manner, a resonance, which already converges, using only ^{15}N relaxation data, was fitted simultaneously to the joint data from ^{15}N and $^{13}C\alpha$, respectively. Therefore, for a validation of this approach, within the formerly mentioned statistical limitations of the data (*vide supra*), no significant changes of the dynamics parameters were acceptable, while adding $^{13}C\alpha$ to ^{15}N relaxation data, respectively. The only approvable impact on the fitting was an equal or, ideally, steeper convergence around the χ^2 minimum.

Here, Tyr15 was employed as a "negative control" in Figure 3.54. As can be seen, following the plots for Tyr15 in the first row of Figure 3.54, S_s, τ_s and τ_f were about the same in all plots, however, the convergence profile was improved. The approach was also validated for further "negative controls", as for Lys27 and Gly51, which also displayed similar or enhanced convergence profiles, while the extracted dynamics parameters were the same with or without addition of $^{13}C\alpha$ relaxation data, respectively.

Therefore, we proceeded with non-converging ^{15}N backbone resonances, as illustrated in Figure 3.54 for Ser19, Trp41 and Ala56. For all residues, a significantly improved convergence profile was gained by addition of $^{13}C\alpha$ relaxation data, comparing the left and right column, respectively. Even though $^{1}H^{N}$,^{15}N and $^{1}H\alpha$,$^{13}C\alpha$ backbone order parameters were similar (cf. Figure 4.4A-B, page 175), a higher fitting performance was obtained by employing the experimentally determined $^{1}H\alpha$,$^{13}C\alpha$ (right column), instead of the $^{1}H^{N}$,^{15}N (middle column) backbone order parameter. It should be noted, that only the accuracy for the fitted dynamics parameters was improved by addition of $^{13}C\alpha$ relaxation data, however, the precision was reduced by introduction of additional measuring uncertainties.

The quantification of motional parameters using $^{13}C\alpha$ and ^{15}N relaxation data is given in Figure 3.55. Here, the amplitudes (A) and correlation times of slow (B) and fast motions (C) were determined within the Model-Free Formalism (MFF). To estimate the uncertainties of the parameters, 500 Monte Carlo simulations were carried out. The average values are depicted as empty circles (black) and the standard deviation of the ensemble is shown by error bars (red). The best fit values are illustrated as crosses (blue).

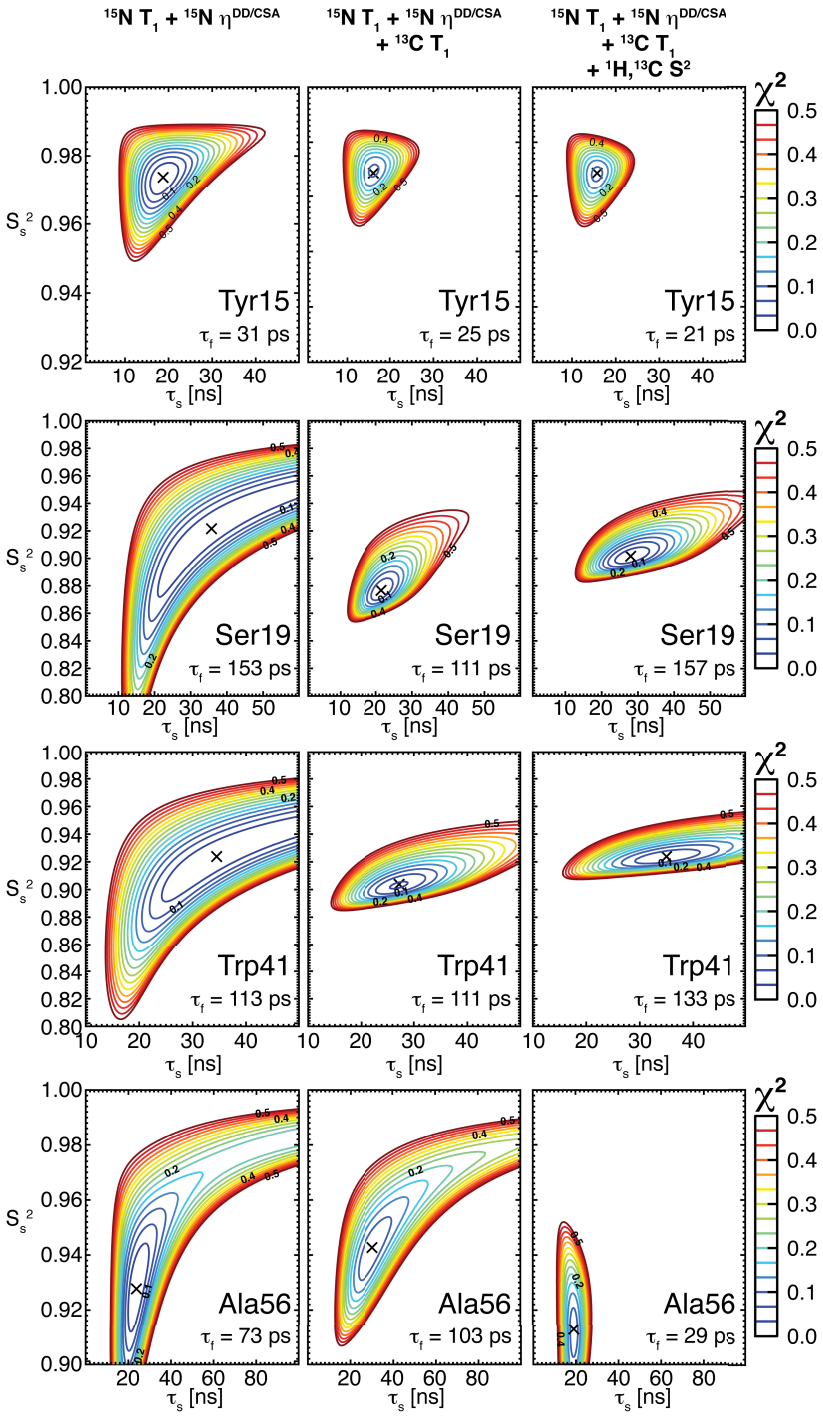

Figure 3.54: Determination of motional parameters via simultaneous χ^2 minimization of backbone ^{15}N and ^{13}Cα relaxation data, respectively. For the minimization profiles represented in the left column only ^{15}N T_1 (at two external magnetic fields) and $\eta^{DD/CSA}$ data was employed (details given in the caption of Figure 3.52). For obtaining the plots in the middle column, ^{15}N T_1 and $\eta^{DD/CSA}$ were supplemented with ^{13}Cα T_1 data (at two magnetic fields, details given in the caption of Figure 3.51), but using the ^{1}H^N,^{15}N S^2 value, in place of the ^{1}Hα,^{13}Cα order parameter. In the right column, all experimentally available data was employed, in particular, ^{15}N T_1 and $\eta^{DD/CSA}$ values, as well as ^{13}Cα T_1 times with ^{1}Hα,^{13}Cα order parameters (using the 10% RAP-glycerol dataset, cf. Figure 3.34, page 85). The fitting was performed by minimization of equation 3.71 (page 124).

Analog trends were determined for $^{13}C\alpha$- and ^{15}N-derived backbone order parameters (Figure 3.55A). One prominent difference was observed for Thr32 in the β_2 strand. The ^{13}C data indicated a high order parameter ($S^2 = 0.87 \pm 0.06$, cf. Figure 4.4, page 175), while the ^{15}N data displayed a lower parameter ($S^2 = 0.78 \pm 0.09$), however, with a larger error bar. In the same way, similar slow and fast motional correlation times were observed, but on average ^{15}N backbone resonances displayed shorter correlation times on both time scales. This is also observed in MD simulations [Guenneugues et al., 1999, Idiyatullin et al., 2003]. In total, the protein dynamics determined by $^{13}C\alpha$ or ^{15}N backbone resonances, respectively, reflected very similar amplitudes and time scales of motions.

Besides backbone, the RAP labeling enables the access to side chain resonances as well. Therefore, a χ^2 minimization was carried out using ^{13}C side chain T_1 times from two external magnetic fields (11.7 T and 20.0 T). For methine and methylene residues the same spectral density function was employed, as for the backbone (equation 3.66, page 117), while for methyl resonances a simplified function was used (equation 3.67, page 117).

Representative χ^2 minimization profiles are shown in Figure 3.56. Just as for backbone resonances, the side chain relaxation data did not converge for all resonances and only allowed for an approximate estimation of the motional parameters S_s, τ_s and τ_f, respectively. Here, 14 out of 30 residues converged (47%). Since only one parameter (τ_f) was employed for fitting the methyl resonances, a one-dimensional minimization was performed, yielding ideal convergence due to the lack of degeneracy, as in the case of three-dimensional fitting of backbone, methine and methylene data, respectively.

Methine, methylene and methyl contour plots are illustrated in the first, second and third row of Figure 3.56, respectively. In general, the motional correlation times and order parameters decrease, moving from methine to methyl resonances. This trend was expected, as longer side chains typically posses smaller rotational energy barriers [Lipari and Szabo, 1982b, Keniry et al., 1984, Best et al., 2004].

To improve the fitting convergence of the side chain residues, complementary relaxation data from ^{2}H can be added [Batchelder et al., 1982, 1983, Muhandiram et al., 1995, Millet et al., 2002, Skrynnikov et al., 2002, Hologne et al., 2005, Reif et al., 2006, Xue et al., 2007, Sheppard

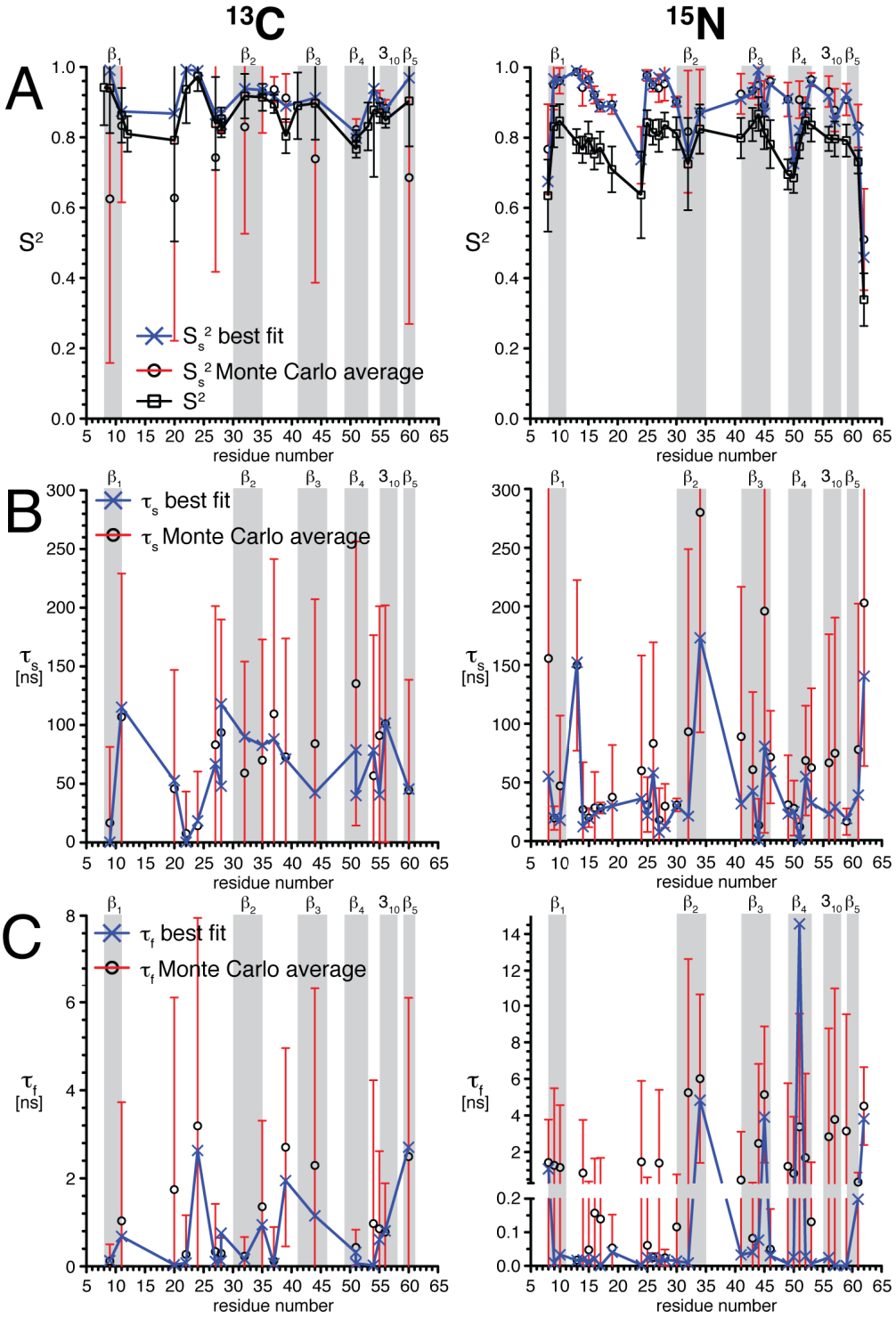

Figure 3.55: Motional parameters for the backbone of α-spectrin SH3, determined within the framework of the Model-Free Formalism (MFF), using $^{13}C\alpha$ (left column) and ^{15}N (right column) relaxation data. (A-C) The squared generalized (S^2) and slow motion order parameters (S_s^2), as well as fast (τ_f) and slow (τ_s) motional correlation times were plotted as a function of the residue number. The best fit and the Monte Carlo average ($n = 500$) are depicted by blue crosses and black, empty circles, respectively. The secondary structure elements are indicated by gray bars.

et al., 2009, Vugmeyster et al., 2009, 2010]. However, in the solid-state, so far, only ^{2}H lineshape analysis and T_1 experiments have been carried out for deuterated methyl groups of α-spectrin SH3 [Hologne et al., 2005, Reif et al., 2006]. The same set of experiments could be employed for side chains, as well as for $^{2}H\alpha$,$^{13}C\alpha$ backbone residues of α-spectrin SH3. In principle, the experiments can be carried out using the 10% RAP-glycerol or 15% RAP-glucose sample, as aliphatic sites are estimated to be 90-95% and 84-90% deuterated, respectively, based on previous isotopic quantifications (Table 3.2, page 38).

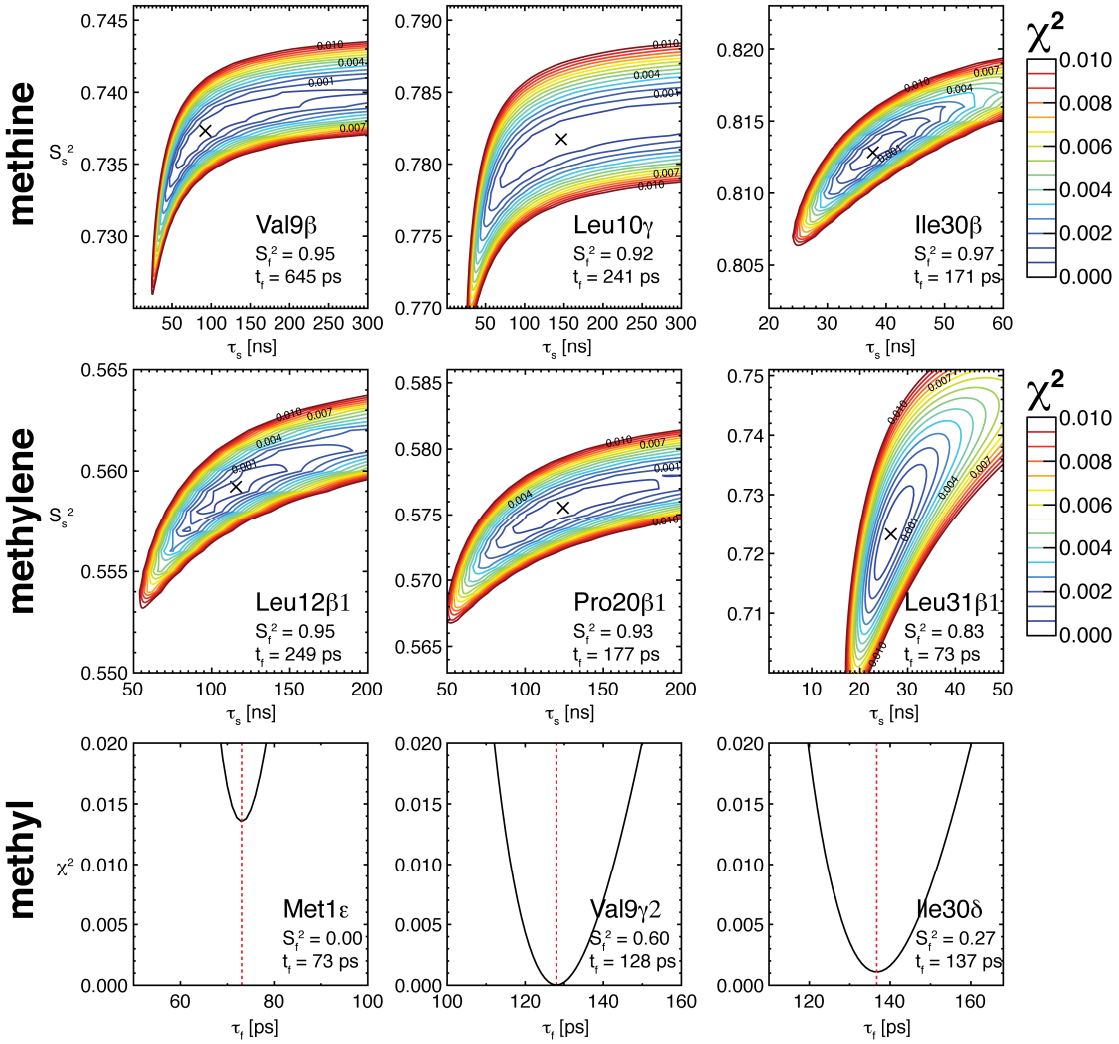

Figure 3.56: ^{13}C side chain dynamics parameters determined by a χ^2 minimization, using ^{1}H,^{13}C order parameters and ^{13}C T_1 times, obtained at two external magnetic fields, 11.7 T (500 MHz) and 20.0 T (850 MHz), respectively, using equation 3.68 (page 117). For fitting of methine and methylene resonances, the same spectral density function was employed, as for the ^{13}Cα backbone (equation 3.66, page 117). For methyl residues the spectral density function described by equation 3.67 (page 117) was used. However, for methylene and methyl residues one and two additional dipolar relaxation terms were employed (cf. equation 3.65, page 117), respectively, to account for relaxation mediated by the dipolar coupling between ^{13}C and ^{2}H. The ^{2}H,^{13}C bond length was set to 1.0948 Å [Mirkin and Krimm, 2009] and 1.115 Å [Ishima et al., 2001] for methylene and methyl resonances, respectively.

3.6 Investigation of amyloid fibrils using the RAP labeling scheme

In the previous sections, we employed α-spectrin SH3 as a model system to establish the Reduced Adjoining Protonation (RAP) labeling scheme. So far, as described in the previous sections, experimental approaches were developed for structural and dynamical investigations, as well as for resonance assignment. Here, we applied the RAP labeling to amyloid fibrils, formed by the Alzheimer's disease $A\beta_{1\text{-}40}$ peptide. Amyloid fibrils are found in the brains of Alzheimer's and Parkinson's disease patients, as well as in the pancreas of type 2 diabetes patients [Sipe, 1992, Sacchettini and Kelly, 2002, Tycko, 2006]. Here, we show initial results obtained for RAP labeled $A\beta_{1\text{-}40}$ fibrils.

To achieve maximal resolution, highly proton diluted RAP samples of $A\beta_{1\text{-}40}$ were prepared, in combination with seeding of the fibrillization process, according to the protocol given in the Materials and Methods section 2.2 (page 24). We expressed $A\beta_{1\text{-}40}$ on a M9 medium containing 5% H_2O and 95% D_2O, respectively. Using the purified $A\beta_{1\text{-}40}$ monomers, fibrils were grown, as recently proposed by Dasari [2011] and del Amo et al. [2012]. In total, two fibril samples were prepared, in the following, referred to as sample S1 and S2, respectively. Both were prepared under the same conditions, however S2 was prepared using 75 mM Cu(II)EDTA in the fibrillization buffer during fibril growth. The obtained S2 fibrils were afterwards washed two times with a PBS buffer containing 40% deuterated glycerol.

In Figure 3.57A, ^{13}C 1D spectra of an uniformly protonated $A\beta_{1\text{-}40}$ sample (top), and the S1 (middle) and S2 (bottom) 5% RAP samples are represented, respectively. The 1D spectra of all preparations, fully and partially protonated, superimposed well, indicating similar fibrillar structures.

We obtained ^{13}C, as well as ^{1}H bulk T_1 times, for both 5% $A\beta_{1\text{-}40}$ RAP samples (Figure 3.57B-C). The average ^{1}H (^{13}C) T_1 time was 1.6 s (11.7 s) and 0.5 s (2.4 s), employing the S1 and S2 samples, respectively. In total, the T_1 time was reduced by a factor of 3-5, using the S2 sample, which was due to the presence of Cu(II)EDTA inducing T_1 Paramagnetic Relaxation Enhancement (PRE).

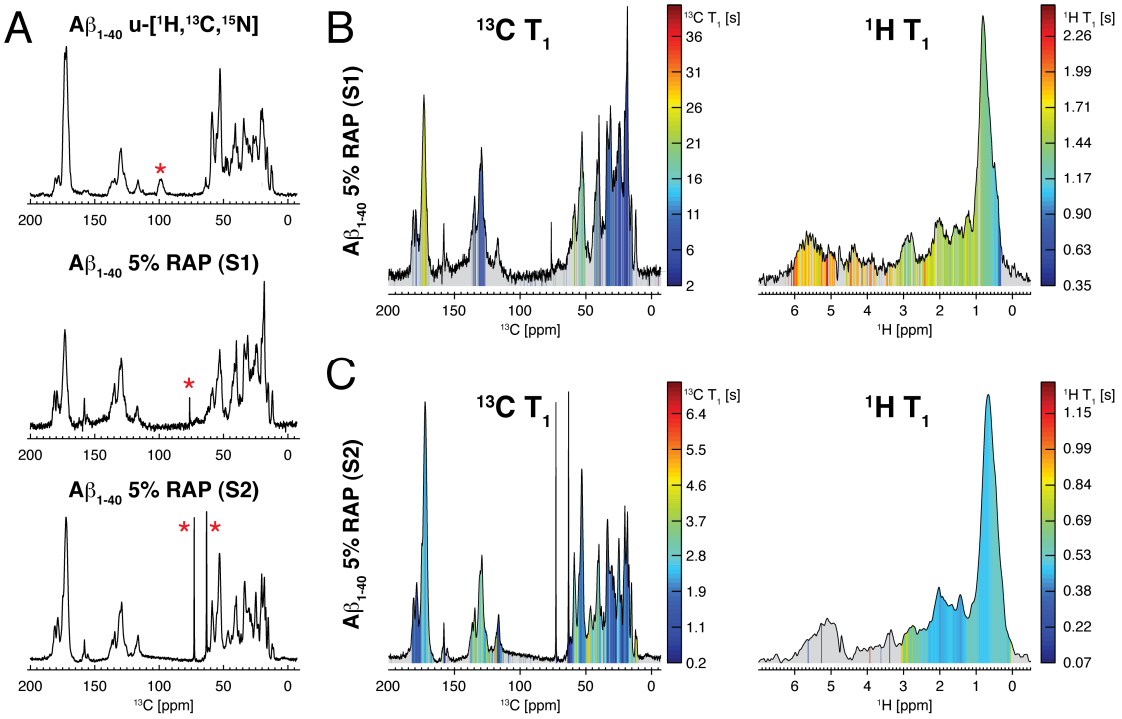

Figure 3.57: (A) ^{13}C 1D spectra of A$\beta_{1\text{-}40}$ fibrils. Here, an uniformly protonated (top spectrum, recorded at a MAS frequency of 13 kHz and 700 MHz, kindly provided by Dr. Juan Miguel Lopéz del Amo, TU München) and two 5% RAP labeled samples, S1 (middle, 20 kHz MAS, 700 MHz) and S2 (bottom, 19 kHz MAS, 600 MHz), respectively, were employed. The top spectrum was extracted from a 2D PDSD experiment, using 50 ms ^{13}C,^{13}C mixing. The S1 and S2 spectra were obtained by ^{13}C-excitation and direct ^{13}C-acquisition. The fibril samples were prepared from the 12th generation of seeds (details given in Materials and Methods, page 24). The fibrils in the S2 sample were grown in a buffer containing 75 mM Cu(II)EDTA and washed two times with a PBS buffer containing 40% (v/v) uniformly deuterated glycerol. The red asterisk depicts spinning sidebands (top), spectrometer artifacts (middle) and glycerol peaks (bottom spectrum). (B-C) The bulk ^{13}C and ^{1}H T_1 times were obtained for both A$\beta_{1\text{-}40}$ samples. The 1D plots were color-coded by the respective T_1 times.

Due to the limited resolution in 1D spectroscopy, ^{13}C,^{13}C 2D spectra were recorded, employing the S1 (Figure 3.58A) and S2 (B) A$\beta_{1\text{-}40}$ samples, respectively. Adiabatic RFDR was used for homonuclear mixing, setting the mixing time to 9.4-9.9 ms. Both spectra (in red) were ^{13}C-excited and compared to a ^{1}H-excited PDSD spectrum of a protonated u-[^{13}C,^{15}N] labeled A$\beta_{1\text{-}40}$ sample at 50 ms mixing (in black). The spectra were superimposed, while maximizing the overlap of the ^{13}Cβ,^{13}Cα dimensions. In (A-B) the side chain region of the S1 and S2 sample displayed a ^{2}H-induced isotope chemical shift offset with respect to the PDSD spectrum of the uniformly protonated sample. The ^{2}H isotope shift amounts to -0.3 ppm per bound deuteron [Gardner et al., 1997]. Accordingly, the largest chemical shift offsets were obtained for methyl resonances, as $^{13}CD_3$ is the predominant isotopomer in a 5% RAP sample (cf. Figure 3.21A,

page 61).

The spectrum of the S1 5% $A\beta_{1\text{-}40}$ RAP sample showed a high degree of similarity in comparison to the uniformly protonated fibrils (Figure 3.58A). For example, in the Ala $^{13}C\beta$,$^{13}C\alpha$ region, we found a similar pattern as observed previously [del Amo et al., 2012], indicating an asymmetric dimer structure (discussed in section 4.1.3, page 168).

The S2 $A\beta_{1\text{-}40}$ sample, which was grown in the presence of 75 mM Cu(II)EDTA and washed with a 40% glycerol buffer, however, showed slight differences in comparison to the uniformly protonated fibril sample (Figure 3.58B). These differences were particularly pronounced for the alanine residues. Here, Ala21 and Ala30 displayed a rather different chemical shift pattern, even though the same seeds were employed as for the S1 sample.

We recorded ^{1}H,^{13}C HMQC 2D spectra of the S1 and S2 5% $A\beta_{1\text{-}40}$ RAP samples, as shown in Figure 3.59. The full spectra of the fibrils in (A) display the typical aliphatic pattern, as determined for microcrystalline α-spectrin SH3 (cf. Figure 3.6, page 41), however, with lower resolution. The ^{1}H line width was about 130 Hz. The lower resolution might be a result of residual heterogeneity and conformational exchange.

The enlarged side chain region in (B) shows that $^{1}H\beta$,$^{13}C\beta$ resonances are well dispersed, which is a prerequisite for a complete assignment, however, significant differences were observerd, comparing the S1 and S2 sample, respectively. The differences were most pronounced in the methyl region in (C).

For further characterization of the 5% RAP labeled $A\beta_{1\text{-}40}$ fibrils in terms of dynamics, ^{1}H,^{13}C correlation spectra were compared, using either INEPT or CP magnetization transfers (Figure 3.60A). The results are discussed in section 4.1.3 (page 168). Furthermore, the ^{1}H,^{13}C HMQC spectrum of the fibrils was compared to a ^{1}H,^{13}C HSQC solution-state NMR spectrum of monomeric, dissolved $A\beta_{1\text{-}40}$ (Figure 3.60B).

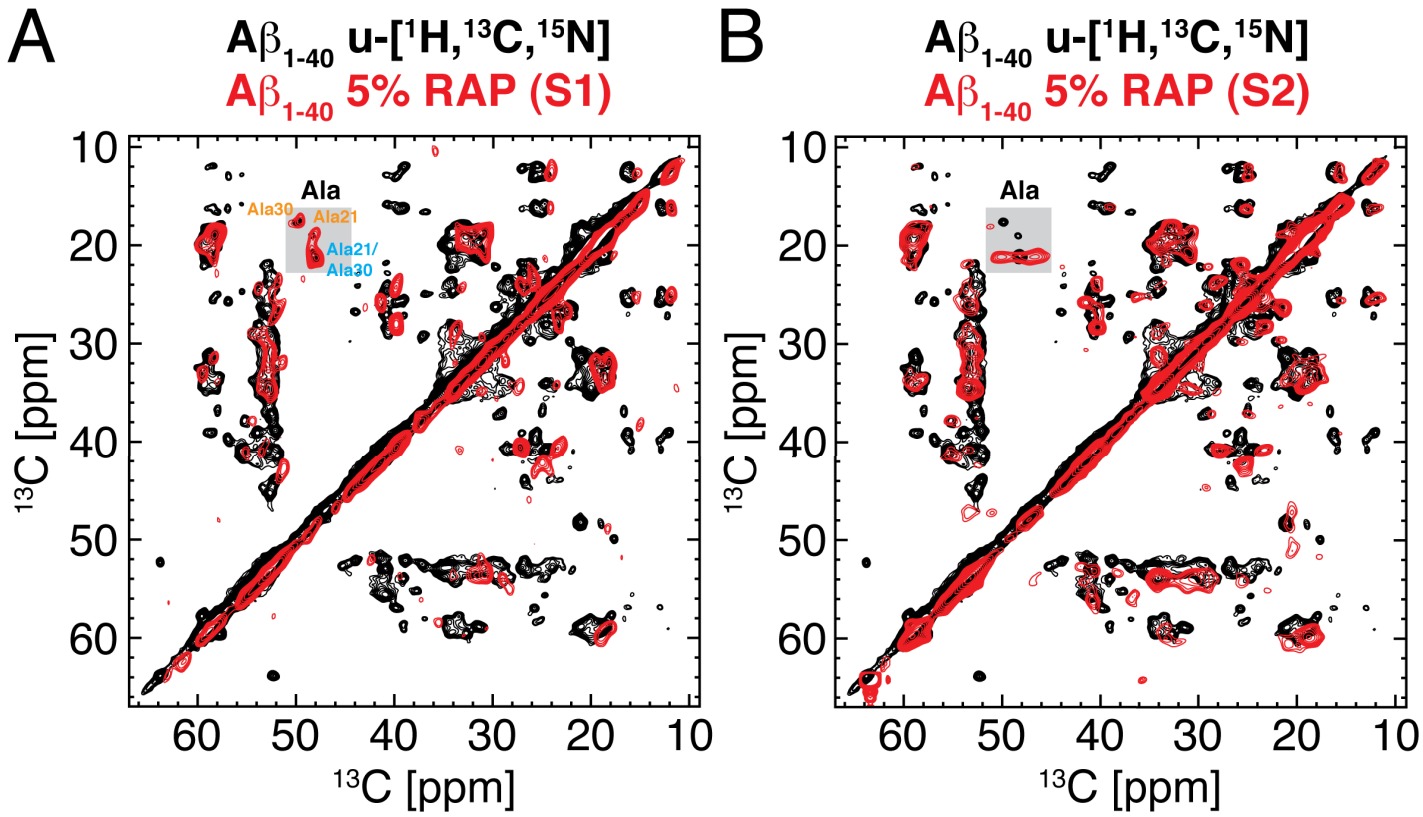

Figure 3.58: $^{13}C,^{13}C$ correlation spectra of $A\beta_{1\text{-}40}$ fibrils. The PDSD spectrum of an uniformly protonated sample at 50 ms homonuclear mixing is shown in black in (A-B). The spectrum was kindly provided by Dr. Juan Miguel Lopéz del Amo (TU München). ^{13}C-excited adiabatic RFDR spectra [Leppert et al., 2003] are plotted in red, employing the (A) S1 and (B) S2 5% $A\beta_{1\text{-}40}$ RAP sample, respectively, using the pulse sequence in Figure 3.19A (page 59). The mixing time for the S1 (S2) spectrum was 9.9 ms (9.4 ms). The magnetic field strength and MAS settings were as in Figure 3.57. The $^{13}C\beta,^{13}C\alpha$ alanine region was gray shaded and Ala21 and Ala30 labeled, employing previously reported assignments [del Amo et al., 2012]. Orange and cyan labels depict peaks, originating from conformer I and II within the asymmetric subunit, respectively.

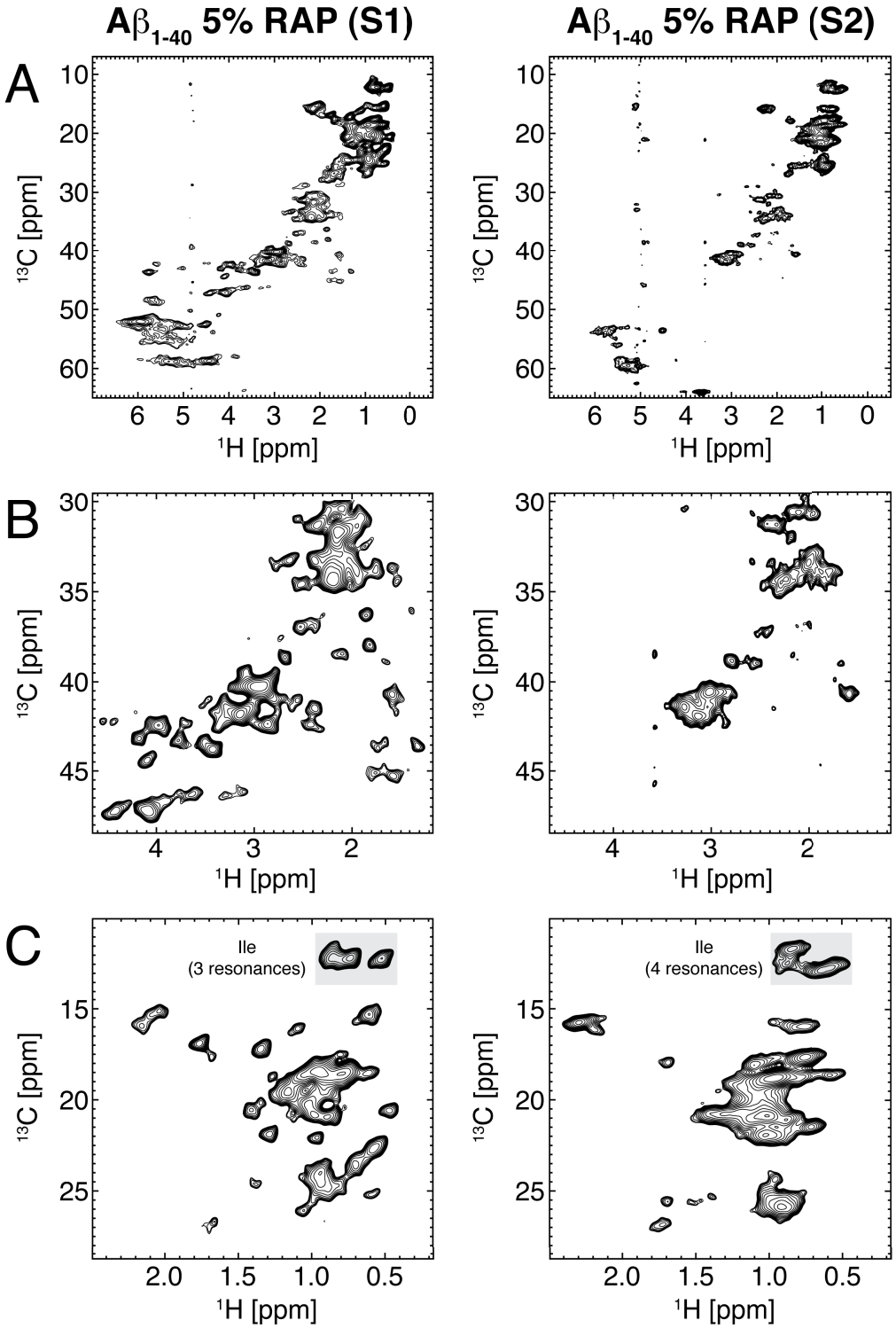

Figure 3.59: ^{1}H,^{13}C HMQC 2D spectra of A$\beta_{1\text{-}40}$ fibrils, using the S1 (left) and S2 (right) sample, respectively. The full spectrum (A) is represented enlarged in (B) and (C), displaying the side chain and methyl region. The S1 (S2) spectrum was recorded at an external magnetic field of 700 MHz (600 MHz) and a MAS frequency of 20 kHz (19 kHz). Isoleucine δ1 resonances are gray shaded.

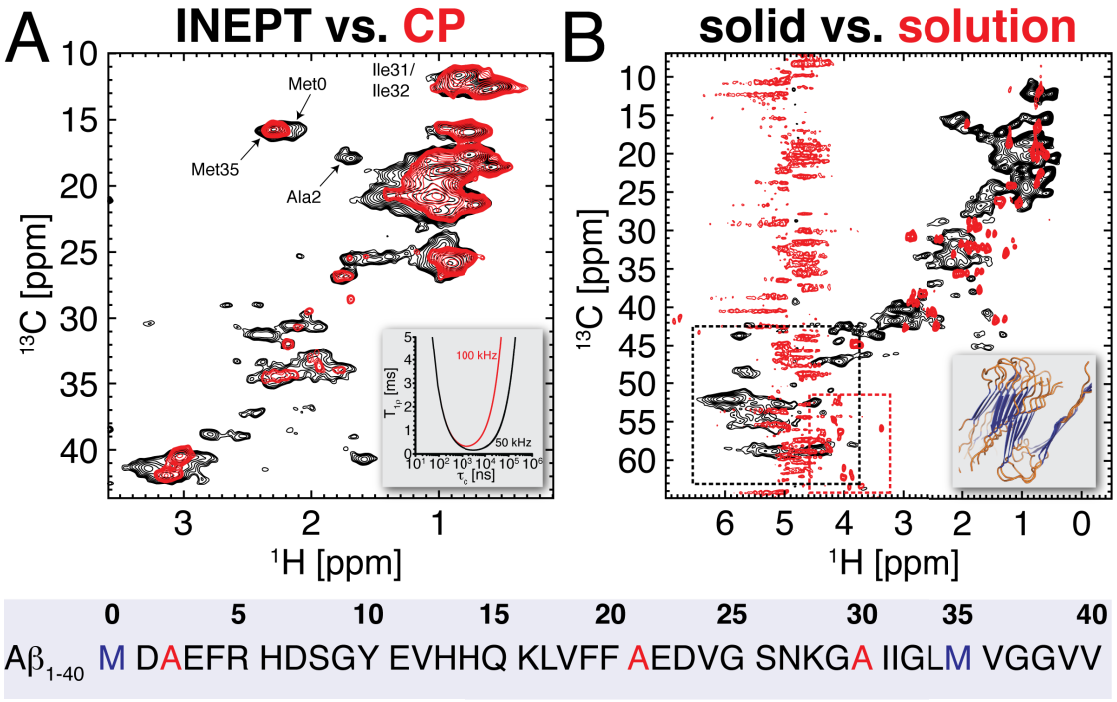

Figure 3.60: (A) INEPT ^{1}H,^{13}C HMQC (black) and CP (red) transfer was compared, using the S2 5% Aβ$_{1\text{-}40}$ RAP sample. Both spectra were recorded under the same conditions at an external magnetic field of 14.1 T (600 MHz) and a MAS frequency of 19 kHz. Missing peaks indicate differential dynamics or heterogeneity. In combination with the average chemical shift, Met0 and Ala2 were tentatively assigned. The primary Aβ$_{1\text{-}40}$ sequence is given at the bottom of the figure. Methionine (blue) and alanine (red) residues were highlighted in the sequence. The inset figure illustrates ^{13}C $T_{1\rho}$ as a function of the correlation time τ_c at an virtual magnetic field strength of 14.1 T. $T_{1\rho}$ is given by $1/T_{1\rho} = 0.5d^2\,[4J(\omega_1) + J(\omega_H \quad \omega_C) + 3J(\omega_C) + 6J(\omega_H + \omega_C) + 6J(\omega_H)]$, in which ω_1 is the rf power of the applied spin-lock field [Abragam, 1961, Jones, 1966, Wang, 1992, Lim et al., 1999]. A simplified spectral density function was assumed, $J(\omega) = \tau_c / \left[1 + (\omega\tau_c)^2\right]$, as well as two spin-lock fields, 50 kHz and 100 kHz, represented in black and red, respectively. (B) The solution-state HSQC spectrum of monomeric Aβ$_{1\text{-}40}$ was compared to the solid-state HMQC spectrum of fibrillar Aβ$_{1\text{-}40}$. For the solution-state experiment, 90 µM of a 15% Aβ$_{1\text{-}40}$ RAP sample in a 20 mM sodium hydroxide buffer (75% H_2O / 25% D_2O) was employed. The spectrum was recorded at an external magnetic field of 17.6 T (750 MHz). Solvent suppression for the ^{1}Hα region was insufficient due to the high amount of residual water (75%). The solid-state spectrum was recorded at a magnetic field strength of 16.4 T (700 MHz) and a MAS frequency of 20 kHz, using fibrils grown with 5% Aβ$_{1\text{-}40}$ RAP labeled peptide. The black and red dashed boxes depict the ^{1}Hα,^{13}Cα region of the fibrils and the solubilized monomers, respectively. The inset figure illustrates the Aβ$_{1\text{-}40}$ structure, as determined by solid-state NMR (PDB: 2LMN) [Petkova et al., 2006] (cf. Figure 1.6, page 17).

3.7 Protein-RNA interfaces probed by ^{1}H-detected MAS solid-state NMR spectroscopy

Herein we suggest an approach to characterize protein-RNA interfaces, which is based on ^{1}H-detected Magic Angle Spinning (MAS) solid-state NMR experiments, using protonated and deuterated samples. We applied this approach to study the protein-RNA interaction of the archaeal L7Ae protein (≈13.4 kDa) from *Pyrococcus furiosus* (PF) with a 26-mer box C/D RNA (≈8.6 kDa), represented in Figure 3.61. With regard to the relatively small size of the complex of about 22 kDa, investigation by solution-state NMR is particularly advantageous in terms of sensitivity and resolution, respectively, as compared to solid-state NMR. However, the fully assembled sRNP complex exceeds the molecular weight limit, imposed by molecular tumbling, which is currently the limitation in solution-state NMR applications. Solid-state NMR is not subject to size limitations. Therefore, as a test case, we chose this small model system from PF to establish solid-state NMR methods, which later on can be applied to the fully assembled complex.

So far, the crystal structure only of a homolog complex from *Archaeoglobus fulgidus* (AF) was solved by X-ray diffraction (PDB: 1RLG) [Moore et al., 2004]. The here studied L7Ae-box C/D RNA complex from PF could not be crystallized [Jehle et al., 2010a]. The only available X-ray structure from PF consists of the three RNP core proteins, L7Ae, Nop56/58 and fibrillarin, co-crystallized with a half-mer box C/D RNA and a substrate RNA (PDB: 3NMU) [Xue et al., 2010]. In Figure 3.62A we virtually truncated the box C/D RNA sequences from both species to the same size to allow for direct structural comparison of the L7Ae-box C/D RNA complex in both organisms, AF and PF, respectively. We observed a high structural homology for both complexes. Minimizing the RMSD over all nitrogen nuclei yielded an overall RMSD of 0.70 Å (Figure 3.62A). Therefore, in the following, we used the available X-ray structure from AF as a model for the here studied L7Ae-box C/D complex of PF.

For the solid-state NMR studies, two differently labeled L7Ae-box C/D RNA complexes were prepared. In both cases, the protein was uniformly deuterated and isotopically ^{15}N enriched. The RNA was either synthesized from uniformly ^{1}H,^{13}C,^{15}N or ^{2}H,^{13}C,^{15}N labeled nucleotides. The

respective samples are referred to as the ^{1}H- and ^{2}H-RNA sample, respectively. In both samples, labile protons were back-exchanged to a level of about 10%.

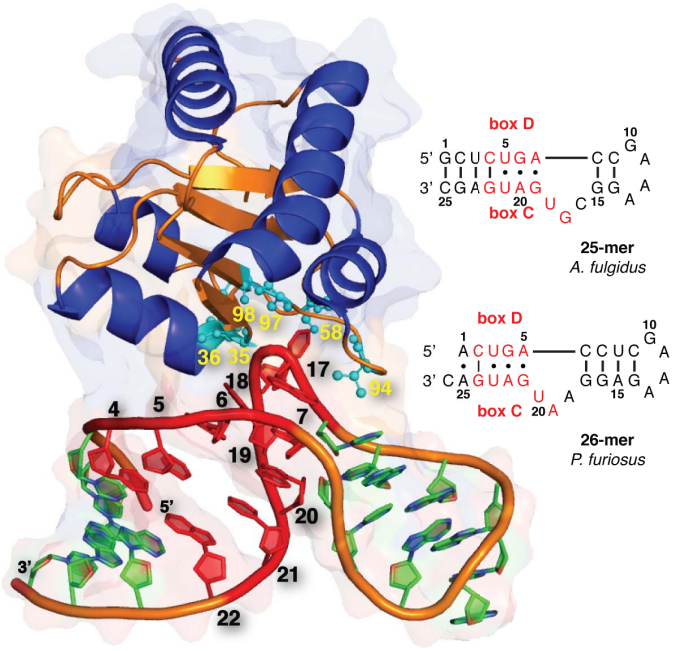

Figure 3.61: Crystal structure of the L7Ae-box C/D RNA complex from *Archaeoglobus fulgidus* (AF) (PDB: 1RLG). In this study, the homologous L7Ae from *Pyrococcus furiosus* (PF) in complex with the illustrated 26-mer box C/D RNA from the same organism was investigated. The box C/D elements are highlighted in red, the protein residues at the interaction sites are shown in cyan (Gly35, Thr36, Asp58, Val94, Ala97, Ser98). β-sheets and loops of L7Ae are in gold, helices in marine blue. *Reproduced with kind permission from Asami, S., et al., Angew. Chem. Int. Ed. 2013, 52 (8), pp 2345-2349. Copyright 2013 Wiley-VCH Verlag GmbH Co. KGaA. DOI: 10.1002/anie.201208024.*

3.7.1 ^{13}C- and ^{15}N-detected spectra of the L7Ae-box C/D RNA complex

For a characterization of the ^{1}H- and ^{2}H-RNA sample of the L7Ae-box C/D complex from PF, we initially recorded ^{13}C- and ^{15}N-detected 1D spectra. These experiments allowed to rapidly verify the isotopic labeling of both biomolecules, to estimate the sample amount in the rotor, as well as the homogeneity. The L7Ae protein was uniformly ^{15}N-labeled, while the 26-mer box C/D RNA was uniformly ^{15}N- and ^{13}C-labeled, respectively. By this means, only RNA signals were expected in ^{13}C-detected 1D spectra, whereas we expected RNA, as well as protein signals, in ^{15}N-detected spectra.

In Figure 3.63 the average chemical shift distribution from the BMRB RNA database was plot-

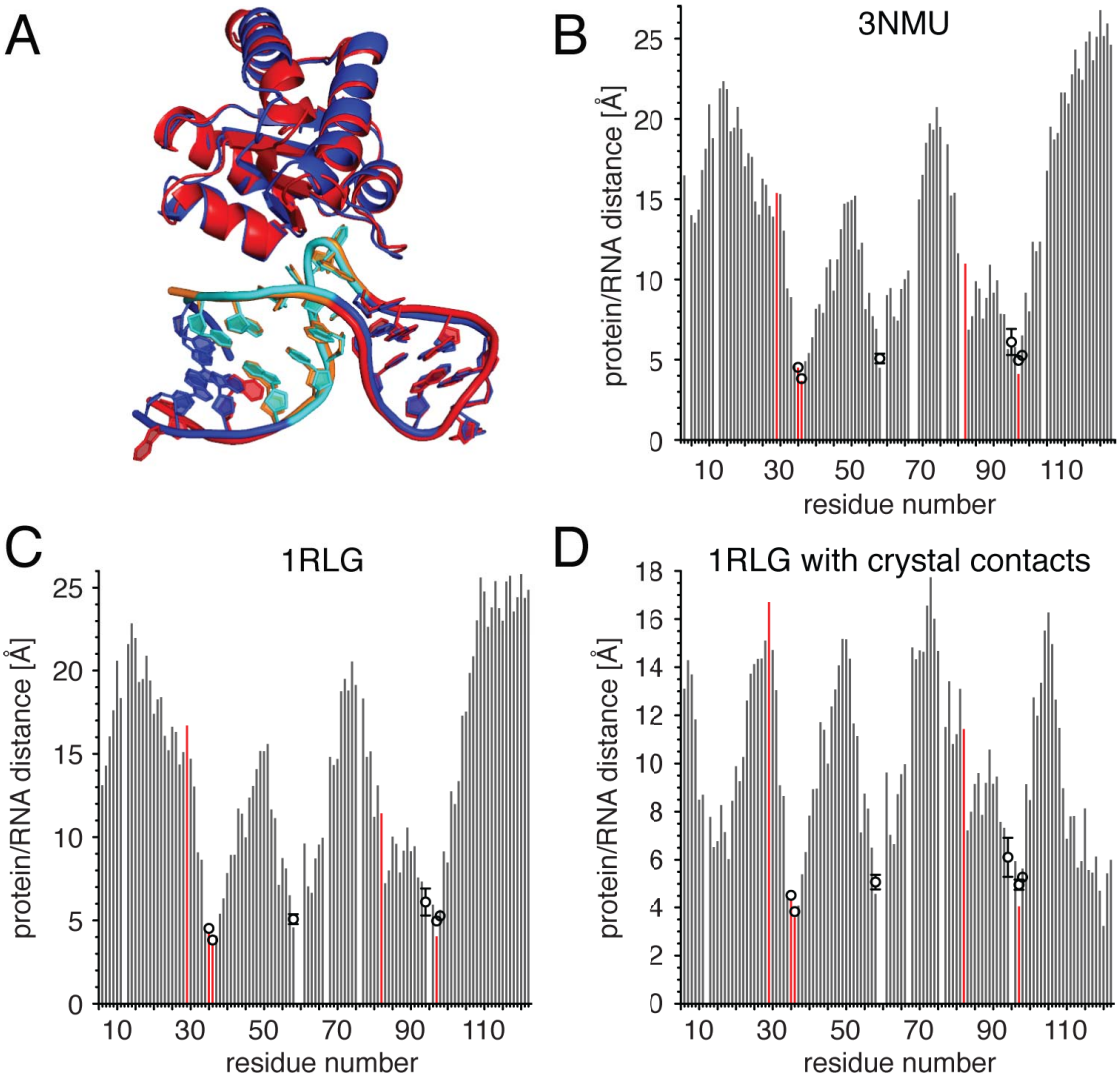

Figure 3.62: Comparison of L7Ae-box C/D RNA complex from *Archaeoglobus fulgidus* (AF) (PDB: 1RLG) and *Pyrococcus furiosus* (PF) (PDB: 3NMU) and the respective distances from every protein backbone $^{1}H^{N}$ to the closest RNA $^{1}H^{C}$ nucleus. (A) The crystal structures of the two species were aligned by minimizing the RMSD over all nitrogen nuclei. The complex from AF (PF) is colored in blue (red) and the respective box C/D RNA elements are colored in cyan (orange). The alignment revealed a high structural similarity, yielding an overall RMSD of 0.70 Å. In (B-D) the closest $^{1}H^{N}$,$^{1}H^{C}$ distance from the protein backbone to the RNA is shown as a function of the protein primary sequence. The experimentally determined values and the color-coding of the bars are as in Figure 3.69A. As expected from the high structural similarity, similar distances were obtained for (B) PF and (C) AF, respectively. Throughout this study, the crystal structure of AF was employed as the model structure. (D) To take crystal contacts into account, molecules in the symmetry-related unit cell (within 5 Å) of the AF-complex (PDB: 1RLG) were constructed and included for distance calculations. The protein-RNA interface remained unperturbed, the major differences clustered at the N- and C-terminus. Ala48 was chosen as the reference peak for normalizing the intensities prior to the calculation of the $I[^{1}H]/I[^{2}H]$ ratio. Protein/RNA interactions could be excluded for this residue. *Reproduced with kind permission from Asami, S., et al., Angew. Chem. Int. Ed. 2013, 52 (8), pp 2345-2349. Copyright 2013 Wiley-VCH Verlag GmbH Co. KGaA. DOI: 10.1002/anie.201208024.*

ted on top of the experimental ^{13}C- (left column) and ^{15}N-detected (right column) 1D spectra, employing the ^{1}H- and ^{2}H-RNA sample, respectively. The 1D spectra revealed a high structural homogeneity for both precipitated complexes. However, the sensitivity was significantly higher for the ^{1}H-RNA sample, since the sample amount was ≈5 times higher and furthermore, protons were employed for CP magnetization transfer, which were less abundant in the ^{2}H-RNA sample. The protons in the ^{2}H-RNA sample were essentially located at the exchangeable sites and originated from the back-exchange with the proton reservoir in the buffer (10%/90% H_2O/D_2O composition). Generally, with regard to the applied isotopic labeling, all expected spectral windows were detected.

3.7.2 Homonuclear ^{13}C,^{13}C 2D spectra and T_1 relaxation of the ^{1}H-RNA sample

For further characterization, 2D ^{13}C,^{13}C correlation experiments were performed, employing the ^{1}H-RNA sample, which was assembled, using the uniformly protonated box C/D RNA. An adiabatic RFDR sequence was used for homonuclear ^{13}C,^{13}C mixing [Leppert et al., 2003]. The mixing time was set to 19.8 ms. As shown in Figure 3.64A, the ^{1}H-RNA sample displayed a very high resolution for the entire spectrum. We detected numerous correlations within the bases and the sugars (Figure 3.64A-B), as well as many long-range contacts between the ribose and base resonances (Figure 3.64C), which enable the identification of spin systems as an initial step for RNA assignment.

However, the 2D ^{13}C,^{13}C RFDR spectrum (Figure 3.64) showed an asymmetric distribution of peak volumes, comparing both sides of the diagonal, in particular for the RNA bases. This was attributed to (1) different initial magnetizations, M_i^0, directly after the cross polarization (CP) step, as well as to (2) considerably different T_1 relaxation times for dipolar coupled nuclei S_i and S_j, respectively.

The first aspect becomes apparent by considering the proton distribution in RNA molecules (Figure 3.63, structures on the right). For example, the C5 nucleus in a purine bases (adenine, guanine) has no directly bonded proton, unlike C8. Therefore, during the ^{1}H,^{13}C CP magnetization transfer step, the magnetization buildup for C5 is reduced, hence M_{C5}^0 is small, as compared to the magnetization M_{C8}^0 of C8. Here, the same ^{13}C,^{13}C RFDR mixing scheme was employed

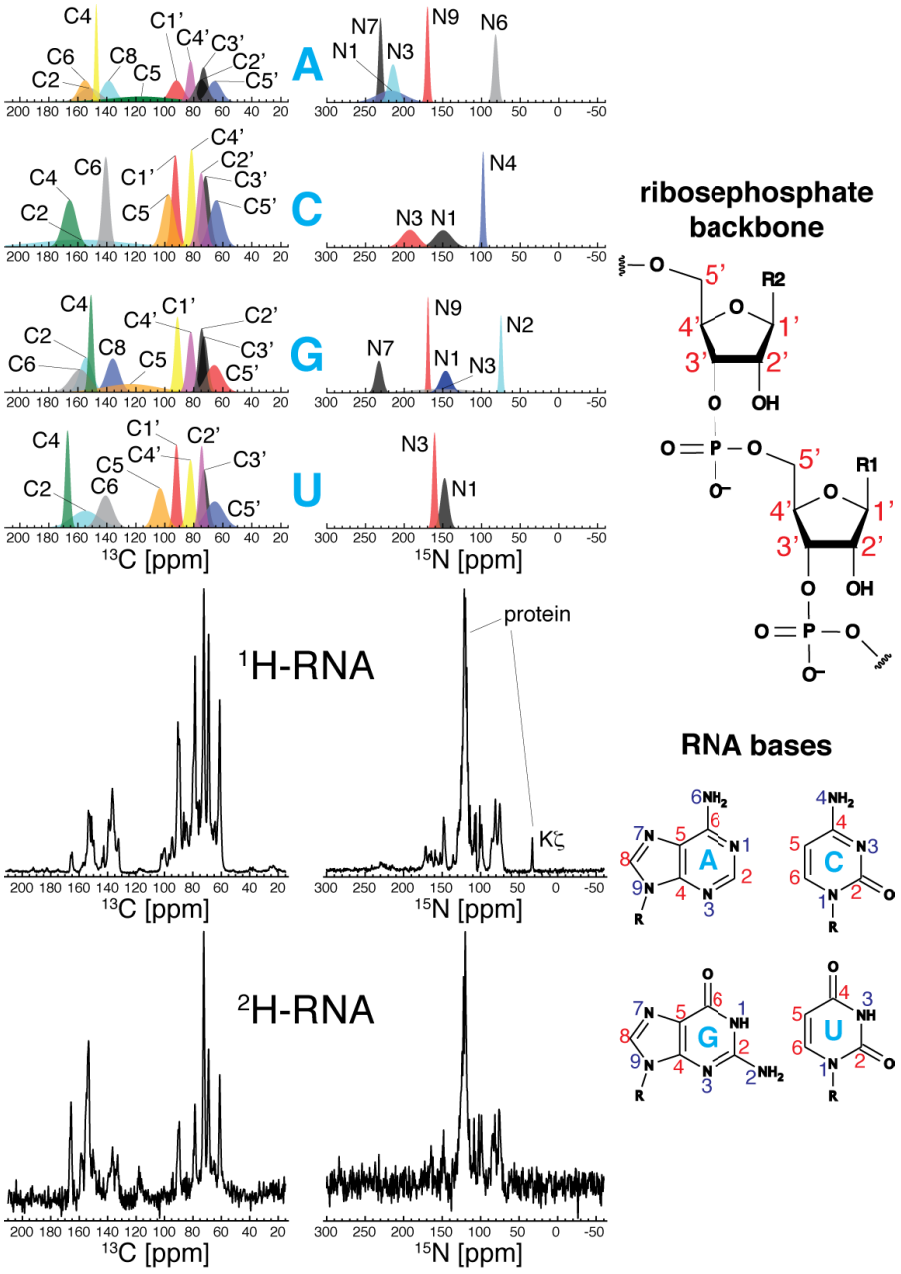

Figure 3.63: ^{13}C- and ^{15}N-detected 1D plots of the L7Ae-box C/D complex, employing the ^{1}H- and ^{2}H-RNA sample, respectively. The average chemical shift distribution for the RNA bases were plotted on top (values obtained from the BMRB database). For the ^{1}H-RNA (^{2}H-RNA) sample the CP contact times were 600 µs (3000 µs) and 1200 µs (800 µs) for the ^{13}C- and ^{15}N-detected spectrum, respectively. During acquisition, ≈86 kHz SPINAL64 [Fung et al., 2000] (2-3 kHz WALTZ-16 [Shaka et al., 1983]) decoupling was employed. The spectra were recorded at an external magnetic field of 16.4 T (700 MHz ^{1}H Larmor frequency), except the ^{13}C-spectrum of the ^{2}H-RNA sample, which was recorded at 14.1 T (600 MHz). The expected chemical shift range with regard to the utilized isotopic labeling schemes, was experimentally observed for both biomolecules. To guide the eye, the nomenclature of the ribosephosphate backbone and the RNA bases, adenine, cytosine, guanine and uracil, are mapped on the respective structures.

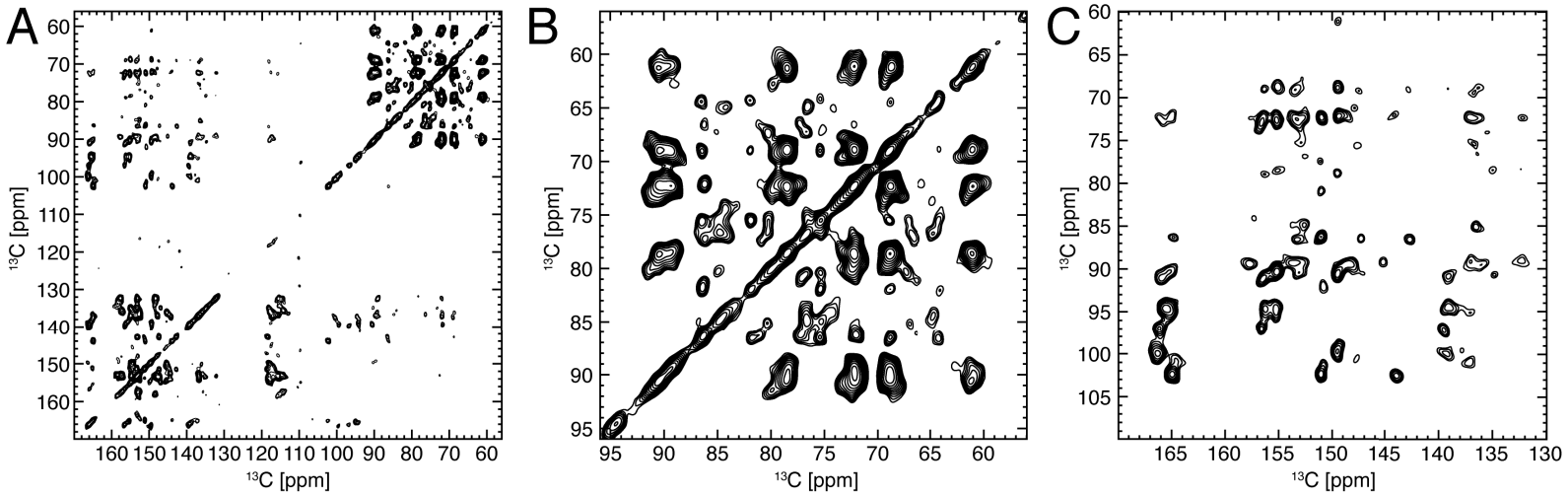

Figure 3.64: ^{13}C,^{13}C RFDR spectra of the L7Ae-box C/D RNA complex, employing the ^{1}H-RNA sample. The MAS frequency was adjusted to 20 kHz at an external magnetic field of 14.1 T (600 MHz ^{1}H Larmor frequency) and an effective temperature of ≈7-10 °C. For homonuclear mixing an adiabatic RFDR sequence was used [Leppert et al., 2003] with a mixing time t_{mix} of 19.8 ms. The length of the rotor-synchronized π pulse was equal to one rotor period (50 µs) and applied with a rf field strength of ≈76 kHz. (A) The full spectral width is shown, we obtained high resolution for all spectral regions of the RNA. Correlations (B) within the RNA sugars were detected, as well as (C) a number of long-range ^{13}C,^{13}C contacts between the ribose and the base moieties, respectively.

as for α-spectrin SH3, as shown in Figure 3.19 (page 59), but in a SH3 RAP sample, the proton concentration was almost isotropic for the different aliphatic sites (Table 3.2, page 38).

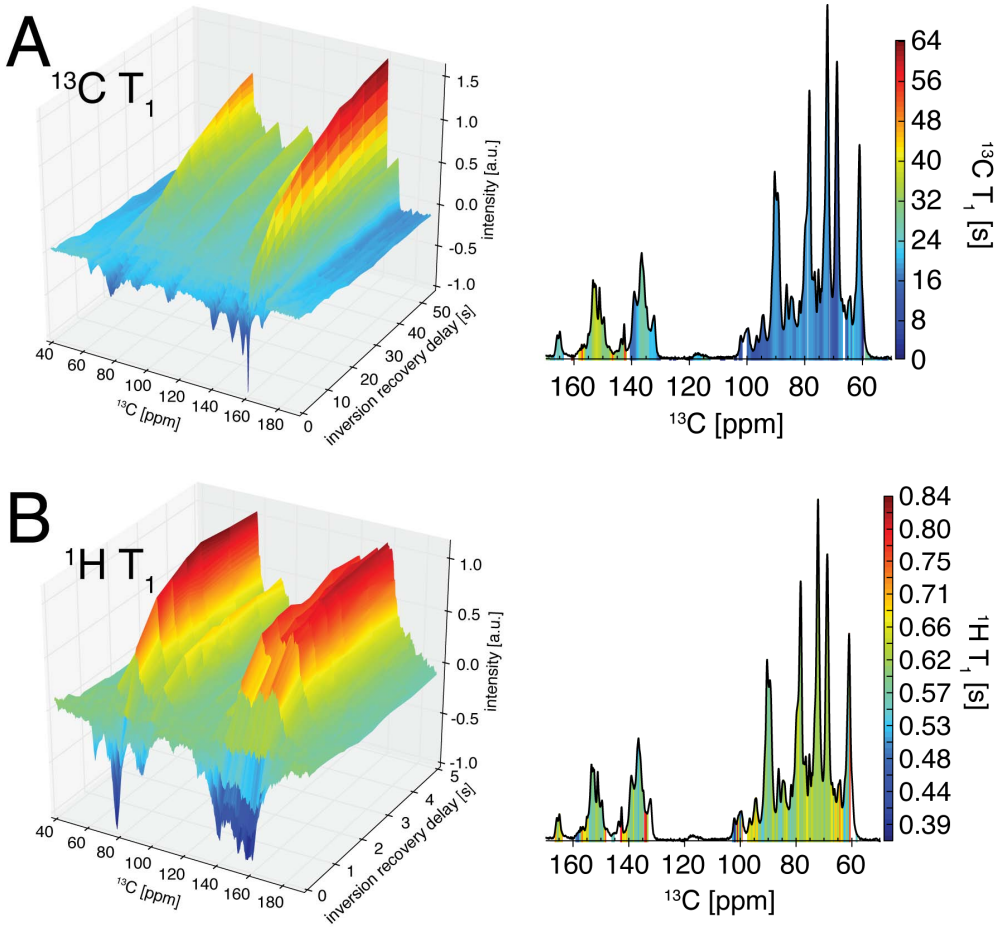

Figure 3.65: (A) ^{13}C and (B) ^{1}H inversion recovery experiments of the ^{1}H-RNA sample. The ^{13}C (^{1}H) experiment was acquired at an external field of 14.1 T (9.4 T). The MAS frequency was adjusted to 20 kHz and the effective temperature to ≈0–3 °C. For the ^{13}C inversion recovery experiment, direct excitation was employed, in this manner, a π pulse was applied on ^{13}C, right after the recycle delay. For the ^{1}H experiment, ^{1}H,^{13}C CP was employed, applying also a ^{1}H π pulse after the recycle delay, prior to the CP transfer block. The 1D plots on the right are color-coded by the respective T_1 times for the bulk ^{13}C and ^{1}H resonances, respectively. The ^{13}C bulk T_1 times were two orders of magnitudes larger, than the ^{1}H T_1 times.

To examine the second aspect concerning different T_1 relaxation times, we recorded an inversion recovery experiment to determine bulk ^{13}C T_1 times. In Figure 3.65A, the progression of the bulk ^{13}C magnetization is shown, as a function of the inversion recovery time, which was varied from 0 s to 55 s. The ^{13}C T_1 times for the sugar moieties were almost 2-3× shorter than the base T_1 times, respectively, but they were all on the timescale of several seconds, while

the ^{13}C,^{13}C RFDR mixing was on the order of milliseconds. Therefore, T_1 relaxation was not playing a major role during the ^{13}C,^{13}C RFDR mixing period. In total, the asymmetry of the ^{13}C,^{13}C 2D (Figure 3.64) is essentially attributed to the anisotropic occurence of protons in the RNA (*vide supra*). We expect a more symmetric spectrum employing longer CP contact times or ^{13}C excitation.

We also determined the bulk ^{1}H T_1 times, as shown in Figure 3.65B. Apparently, ^{1}H T_1 times were more isotropically distributed due to the strong ^{1}H,^{1}H dipolar coupling network. The T_1 times are on the order of several hundreds of milliseconds and almost two orders of magnitude shorter than ^{13}C T_1 times (Figure 3.65A). From an experimental point of view, ^{1}H-excited experiments are more efficient in terms of sensitivity, since a higher signal-to-noise ratio per unit time can be achieved.

3.7.3 Optimization of homonuclear ^{13}C,^{13}C mixing

To obtain the optimal homonuclear mixing scheme for RNA molecules, we compared PDSD [Szeverenyi et al., 1982] and adiabatic RFDR spectra [Leppert et al., 2003]. Due to the beneficial relaxation properties (Figure 3.65), we employed ^{1}H-excitation for all following experiments. The PDSD experiment relies on ^{13}C,^{13}C magnetization transfer, which is promoted by ^{1}H,^{1}H spin diffusion. RFDR mixing relies on the direct dipolar recoupling of ^{13}C,^{13}C nuclei by application of rotor-synchronized π pulses during MAS. Unlike PDSD, which requires a dipolar coupled proton bath, RFDR mixing can also be applied to deuterated samples [Huang et al., 2011b], as demonstrated for α-spectrin SH3 (cf. Figure 3.19, page 59).

We recorded PDSD spectra for the ^{1}H-RNA sample, using homonuclear mixing times of 400 ms, 1000 ms and 2000 ms (Figure 3.66A-C), respectively, and detected several long-range contacts between RNA ribose and bases. Long-range contacts are most relevant for the assignment of spin systems and for the determination of tertiary structure informations.

The RFDR spectra are shown in Figure 3.66D-E, using 19.8 ms and 22.5 ms mixing, respectively. A high number of long-range contacts was detected, many more as compared to the superimposed PDSD spectrum with 2000 ms mixing time (Figure 3.66E).

We also recorded a rotor-asynchronized adiabatic RFDR spectrum, which shows exclusively

chemical shift correlations via scalar couplings and allowed to differentiate between through space and bond correlations (Figure 3.66F, red) [Baldus and Meier, 1996, Leppert et al., 2004]. These types of spectra can support the RNA assignment procedure, since every cross peak originates from bonded carbons. A RNA assignment approach is presented in section 3.7.8 (page 157).

3.7.4 ^{1}H-detected ^{1}H,^{15}N correlation spectra of the protein-RNA complex in the solid-state

In ^{1}H-detected ^{1}H,^{15}N correlation experiments at moderate MAS frequencies in the range of 15-20 kHz all expected resonances from the protein and the RNA were detected (Figure 3.67A), using CP transfers. In protein-RNA complexes, the spectral windows for protein and RNA resonances do not significantly overlap [Furtig et al., 2003]. The imino and amino spectral regions can in principle contain resonances of histidine and arginine sidechains, respectively (one histidine and four arginine residues were found in the primary sequence of L7Ae).

The average ^{1}H (^{15}N) line width for the protein was on the order of ≈100 Hz (≈60 Hz), whereas the line widths for the amino and imino resonances amounted to ≈150 Hz (≈140 Hz) and ≈300 Hz (≈160 Hz), respectively. In addition, we also recorded a scalar transfer based ^{1}H,^{15}N HSQC spectrum, to probe the flexible regions of the complex (Figure 3.67A, spectrum in orange). However, only protein resonances were detected in this experiment. RNA resonances were beyond detection. The differential line widths for the protein and the RNA resonances might be a result of chemical exchange, local dynamics, or structural heterogeneity resulting from crystal imperfections.

Superposition of the solid-state with a solution-state spectrum revealed a high structural similarity, with a comparable resolution in both states (Figure 3.67B). For the solution-state experiment, a protein-RNA complex was employed with u-[^{1}H,^{15}N] labeled L7Ae protein and unlabeled box C/D RNA, respectively.

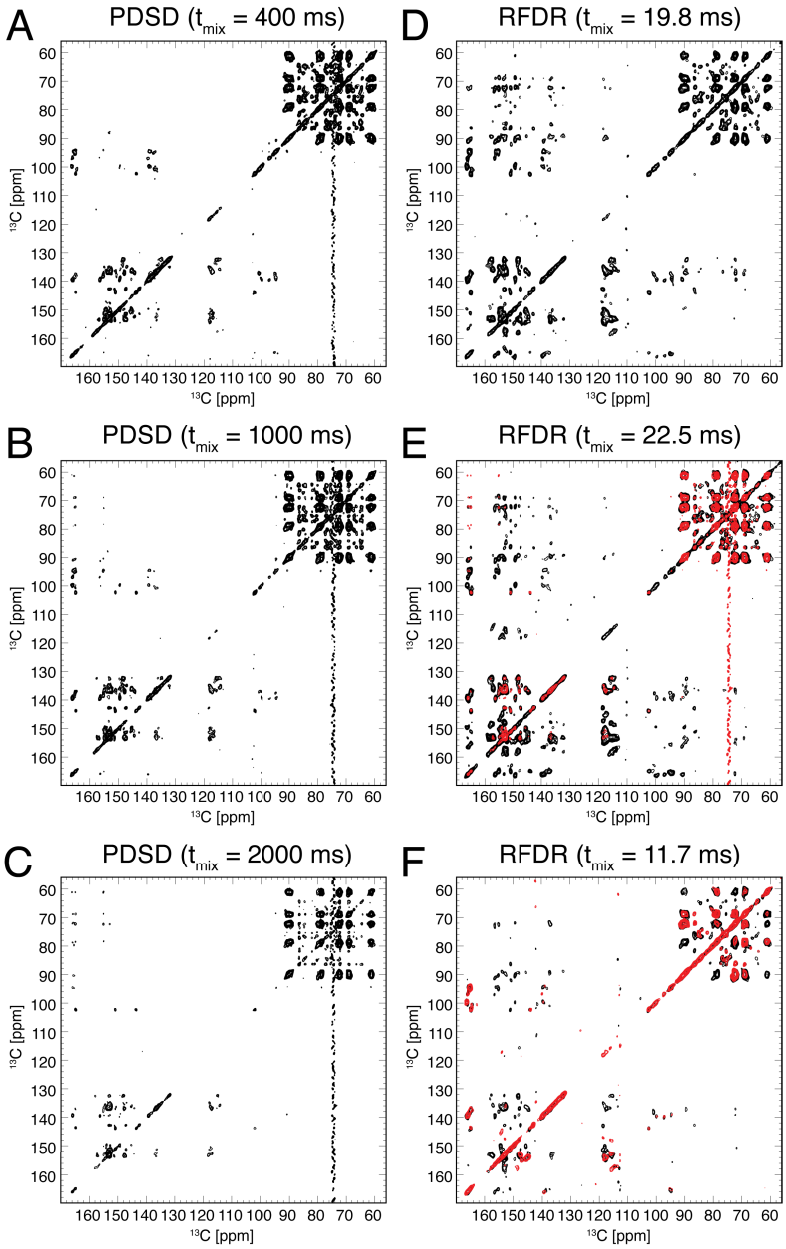

Figure 3.66: ^{13}C,^{13}C correlation spectra of the L7Ae-box C/D RNA complex, using the ^{1}H-RNA sample and setting the MAS frequency to 20 kHz. We employed ≈80 kHz ^{1}H SPINAL64 [Fung et al., 2000] decoupling during the indirect and direct ^{13}C evolution periods. In (A-C) PDSD spectra were plotted with a homonuclear mixing time of 400 ms, 1000 ms and 2000 ms, respectively. The external magnetic field was 16.4 T (700 MHz ^{1}H Larmor frequency) and the effective temperature ≈17 °C. The ^{1}H,^{13}C CP contact time was 600 µs. (D-E) shows rotor-synchronized adiabatic ^{13}C,^{13}C RFDR spectra, using 19.8 ms and 22.5 ms mixing times, respectively. The spectra were measured at an external field of 14.1 T (600 MHz) and an effective sample temperature of ≈7 °C. The CP contact time was 1000 µs. In (E) the RFDR spectrum (black) was superimposed by the PDSD spectrum (red) with 2000 ms mixing time, shown in (C). For (E) the CP contact time was prolonged to 3000 µs. In (F) two ^{13}C,^{13}C adiabatic RFDR spectra were superimposed. For the spectrum in black and red a dipolar (t_{mix} =11.7 ms) [Leppert et al., 2003] and scalar (t_{mix} =11.52 ms) [Leppert et al., 2004] adiabatic mixing scheme was employed, respectively. The spectra were recorded at an external magnetic field of 14.1 T (600 MHz) and the CP contact time was set to 1000 µs.

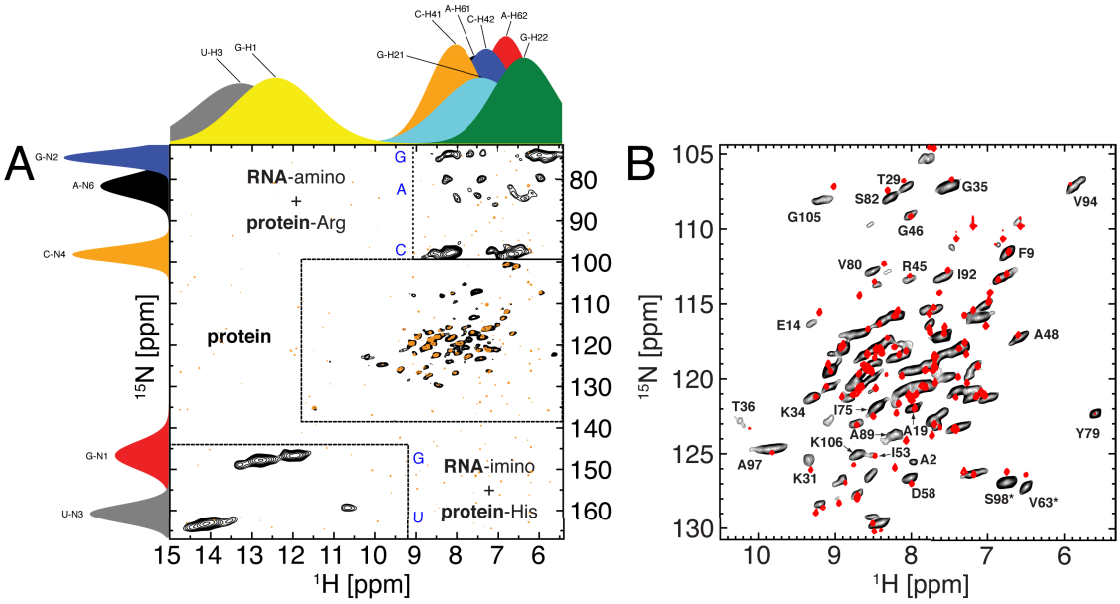

Figure 3.67: (A) ^{1}H-detected ^{1}H,^{15}N correlation spectrum of the precipitated L7Ae-box C/D RNA complex from PF, employing a ^{2}H-RNA sample. Here, the chemical shift distribution (from the diamagnetic BMRB data set) was plotted along the chemical shift axes, showing the different, non-overlapping spectral windows of RNA and protein. Clearly, the characteristic protein and RNA spectral patterns were observed. The processing was optimized for each region, to account for different natural line widths of the biomolecules. The spectrum was recorded at an external magnetic field of 16.4 T (700 MHz), 20 kHz MAS frequency, and an effective temperature of ≈27 °C. The imino region showed enhanced sensitivity and resolution at lower temperatures. Therefore, this region was extracted from a spectrum at ≈0 °C, 15 kHz rotation frequency, and an external field of 14.1 T (600 MHz). The spectral regions for the nucleobases, as expected from the average chemical shift in the BMRB database, are indicated (blue labels). Additionally, a ^{1}H,^{15}N HSQC spectrum was recorded ($1/2J_{NH}$ = 4.34 ms) and superimposed (orange spectrum). (B) Protein region of the ^{1}H-RNA sample with tentative assignments transferred from solution-state NMR (solution-state spectrum shown in red). Ser98 and Val63 (indicated by asterisks) were folded. *Reproduced with kind permission from Asami, S., et al., Angew. Chem. Int. Ed. 2013, 52 (8), pp 2345-2349. Copyright 2013 Wiley-VCH Verlag GmbH Co. KGaA. DOI: 10.1002/anie.201208024.*

3.7.5 Probing the protein-RNA interface

Herein we suggest an experimental strategy for the identification of the protein-RNA interface. The method is based on the fact, that in the ^{1}H-RNA sample, protein regions in close proximity to RNA protons show reduced signal intensities due to dipole-mediated line broadening. As illustrated in Figure 3.68, amide protein moieties, which are distant from RNA protons (>6 Å), show similar signal intensities for both, the ^{1}H- and ^{2}H-RNA samples ($I[^{1}H]/I[^{2}H] \approx 1$), respectively. On the other hand, protein amide resonances at the interface yield a smaller intensity in the ^{1}H-RNA sample, therefore, $I[^{1}H]/I[^{2}H] < 1$. Since the absolute intensities are also dependent on the amount of the sample, we normalized the intensities for both samples, prior

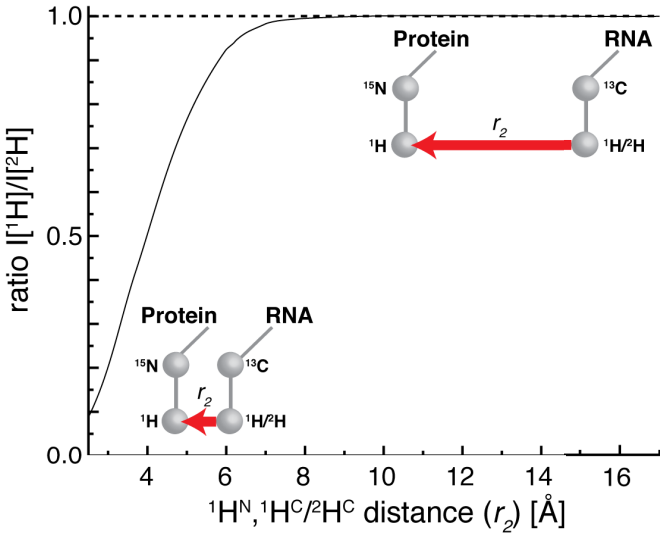

Figure 3.68: Approach for the identification of protein-RNA interfaces, employing protonated and deuterated RNA, respectively. At the protein-RNA interface, the intensity ratio, $I[^1H]/I[^2H]$, of the ^{1}H- and ^{2}H-RNA sample, is less than one, since protein amides in the ^{1}H-RNA sample are broadened by the dipolar coupling to non-exchangeable RNA protons, therefore $I[^1H] < I[^2H]$ and $I[^1H]/I[^2H] < 1$ (left side of the curve). For protein amides, which are distant from RNA protons, both intensities are similar, hence, $I[^1H]/I[^2H] \approx 1$ (curve plateau).

to calculating the $I[^1H]/I[^2H]$ ratio. For that purpose, we employed Ala48, which was highly resolved (Figure 3.67B) and quite distant from the nearest RNA $^1H^C$ proton (14.7 Å). Crystal contacts were taken into account (Figure 3.62D, page 139). Only protein $^1H^N$ backbone to RNA $^1H^C$ contacts were considered, since exchangeable protons were back-exchanged to 10% and, to first approximation, $^1H^N$,$^1H^N$ dipole interactions can be neglected.

In Figure 3.69A the smallest distance between a protein backbone $^1H^N$ proton and a RNA $^1H^C$ proton was plotted as a function of the protein residue number. The distances were extracted from the AF crystal structure (PDB: 1RLG), which can be used as a model owing to its high homology (Figure 3.62A, page 139). The minima in the distance plot (Figure 3.69A) indicate protein residues at the protein-RNA interface, in particular Gly35, Thr36, Asp58, Val94, Ala97 and Ser98.

The proximity of protein residues to the RNA can be obtained experimentally by the comparison of the normalized intensities of the ^{1}H- and the ^{2}H-RNA samples. The same contour levels were employed for each set of cross peaks to allow for comparison (Figure 3.69B). For example, the intensities of Gly35, Thr36 and Ala97 were significantly attenuated in the ^{1}H-RNA sample,

since these residues were close to non-exchangeable $^{1}H^{C}$ RNA protons (within 3.6-4.3 Å), unlike Thr29 and Ser82, which were far apart (>11 Å).

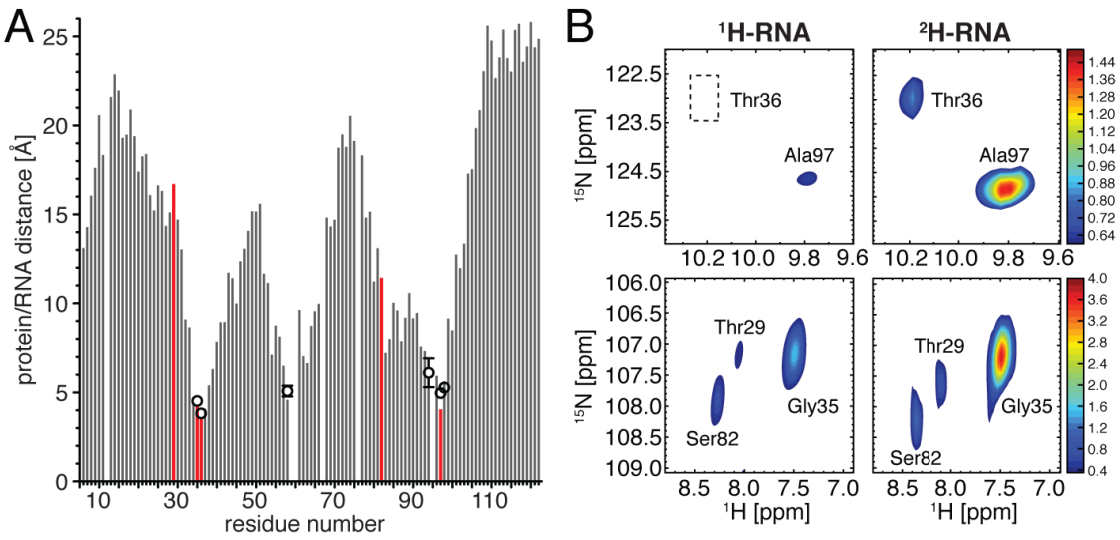

Figure 3.69: (A) Distance between protein backbone $^{1}H^{N}$ proton and the closest RNA $^{1}H^{C}$ proton as a function of the protein primary sequence. Calculated distances were based on the crystal structure of the L7Ae-box C/D RNA complex from AF (PDB: 1RLG; protons were added using WHAT IF [Vriend, 1990]). Missing bars were due to proline residues. Experimentally determined distances were plotted as empty circles. (B) ^{1}H,^{15}N correlation plots, employing the ^{1}H- (left) and ^{2}H-RNA (right) samples, respectively. Absolute intensities were normalized using Ala48. The illustrated residues (Thr29, Gly35, Thr36, Ser82, Ala97) were highlighted by red bars in (A). As expected, the protein residues, which were in close proximity to the RNA (Gly35, Thr36, Ala97), showed a reduced intensity in the ^{1}H-RNA sample. *Reproduced with kind permission from Asami, S., et al., Angew. Chem. Int. Ed. 2013, 52 (8), pp 2345-2349. Copyright 2013 Wiley-VCH Verlag GmbH Co. KGaA. DOI: 10.1002/anie.201208024.*

3.7.6 Determination of quantitative distance and angle restraints for protein-RNA interfaces

To quantitatively describe the experimental $I[^{1}H]/I[^{2}H]$ intensity ratios, we carried out spin simulations, employing the SIMPSON software package [Bak et al., 2000]. To construct an adequate spin system, we considered a spin geometry consisting of four nuclei, resembling the protein $^{1}H^{N}$,^{15}N nuclei and the RNA $^{1}H^{C}$,^{13}C nuclei (Figure 3.70), respectively. Since the signal attenuation in the ^{1}H,^{15}N correlation of the protein in close proximity to the RNA is induced by dipole-mediated line broadening, the simulated $I[^{1}H]/I[^{2}H]$ ratio was expected to be dependent on the distance, as well as on the orientation of all considered dipoles. Therefore, we introduced two angles, β_1 and β_2, to allow sampling of all orientations of the $^{1}H^{N}$,^{15}N and $^{1}H^{C}$,^{13}C dipole

tensors with respect to each other. Besides the β_1 and β_2 angles, the only other variable was the $^1H^N$,$^1H^C$ distance. All other dipolar couplings and orientations were calculated accordingly.

As expected, we found that the simulated $I[^1H]/I[^2H]$ ratios depend on the relative orientation of the two dipole-dipole vectors. This dependency decreases with increasing distance. Furthermore, the simulation revealed an up to fourfold degeneracy in the angular space (Figure 3.70). To reduce the degeneracy, we determined the β_1 and β_2 angle distribution for the L7Ae-box C/D RNA complex as well as for two additional protein-RNA complexes and used their common angle interval for constraining the angular space during the fitting procedure (Figure 3.71). The simulated data matrix, $I[^1H]/I[^2H]$, as a function of the $^1H^N$,$^1H^C$ distance, β_1 and β_2 is represented in Figure 3.72A.

The fit of the experimental data did not assume a prior knowledge of the structure of the system. For the fitting of the experimentally determined $I[^1H]/I[^2H]$ intensity ratios, first the peak volumes were determined by integration, employing in-house Python scripts using the I/O routines of nmrglue v0.2 [Helmus and Jaroniec, 2013]. The error of the peak volume was set to two times the noise RMSD. The noise level was determined individually for every peak by averaging over 1,000 equally sized random boxes in the noise region of the spectrum. A grid of simulated data was created, using the interval $[0°, 180°]$ (5° steps) for β_1, $[0°, 355°]$ (5° steps) for β_2, and [2.5 Å, 102.9 Å] for the $^1H^N$,$^1H^C$ distance r_2 (nomenclature given in Figure 3.70, page 151). The peak height for the $^1H^N$ resonance was determined and stored into the matrix $I_H(\beta_1, \beta_2, r_2)$ and $I_D(\beta_1, \beta_2, r_2)$, employing the ^{1}H- or ^{2}H-RNA spin system, respectively. The ratio matrix $R(\beta_1, \beta_2, r_2)$ was calculated by $I_H(\beta_1, \beta_2, r_2)/I_D(\beta_1, \beta_2, r_2)$. As can be seen in Figure 3.70, the contour plots show an up to four fold degeneracy for the β_1 / β_2 angle space.

We quantified the occurrence of β_1 and β_2 for different protein-RNA complexes (Figure 3.71). In the analysis, protein $^1H^N$ and RNA $^1H^C$ pairs only within 6 Å were considered. We found, that the β_2 angle adopts values in the range $[70°, 100°]$, whereas the full range of values was found for β_1. To reduce the degeneracy and improve the fitting, we thus constrained the angular space to two times the standard deviation from each expectation value.

As a first attempt, we assumed a linear arrangement of the $^1H^N$,^{15}N and $^1H^C$,^{13}C dipole tensors, which yielded a poor correlation (Figure 3.72B, cyan). However, introducing the angles β_1

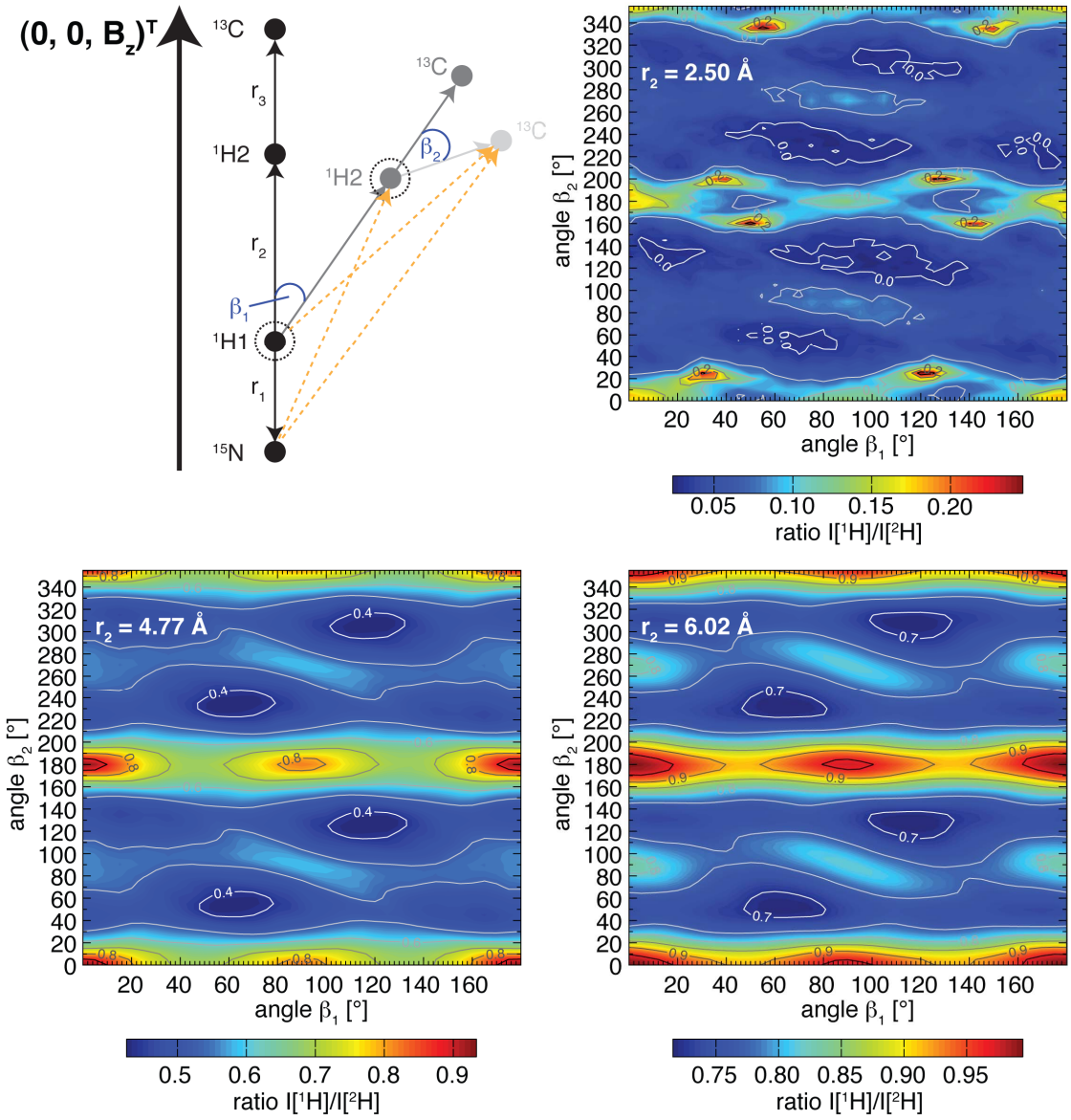

Figure 3.70: Numerical simulation of the illustrated four-spin system using SIMPSON [Bak et al., 2000]. The respective tensor magnitudes and orientations were calculated as a function of the ^{1}H1,^{1}H2 distance r_2 and the angles β_1 and β_2. All possible dipolar couplings were taken into account, as well as the spatial orientation of the planar spin system, which was defined only by the β Euler angle ($\Omega = (0, \beta, 0)$). The isotropic chemical shift values were set according to the average shift found in the BMRB. The chemical shift anisotropies (asymmetries) in [ppm] for ^{1}H2, ^{13}C, ^{1}H1, ^{15}N were as follows: -4.55 (0.9) [Aravamudhan et al., 1979], -118.5 (0.9) [Stueber and Grant, 2002], 7.67 (0.65) [Wu et al., 1995], 170 (0.2) [Bak et al., 2002, Schanda et al., 2010]. The ^{1}H Larmor frequency was set to 700 MHz and the MAS frequency to 20 kHz. Here, only the ^{1}H1 resonance was detected and the FID apodized with a line broadening of 5 Hz. After Fourier transformation, the peak height for ^{1}H1 was extracted. For simulating the spin system of the ^{2}H-RNA sample, the ^{1}H2 proton was replaced by a deuteron ($C_Q/2\pi$ = 150 kHz). In the contour plots, the intensity ratio $I[^1H]/I[^2H]$ was plotted as a function of the angles β_1 and β_2 for three different ^{1}H1,^{1}H2 distances (2.50 Å, 4.77 Å and 6.02 Å). The ratios were normalized with respect to the maximal value obtained at $r_2 \rightarrow \infty$. *Reproduced with kind permission from Asami, S., et al., Angew. Chem. Int. Ed. 2013, 52 (8), pp 2345-2349. Copyright 2013 Wiley-VCH Verlag GmbH Co. KGaA. DOI: 10.1002/anie.201208024.*

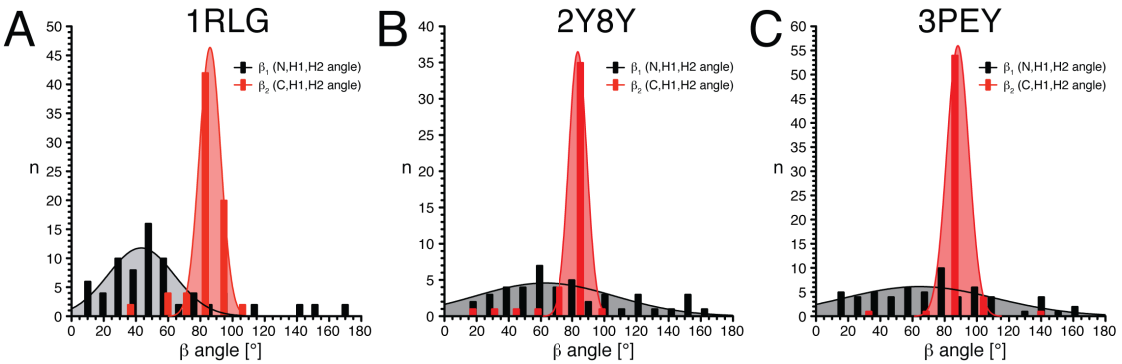

Figure 3.71: Distribution of angles β_1 and β_2 for different protein-RNA complexes. Here, $(180^\circ \quad \beta_1)$ corresponds to $\angle$(N,H1,H2) and $(180^\circ \quad \beta_2)$ to $\angle$(C,H2,H1), respectively, as illustrated in Figure 3.70. The coordinate of the carbon nucleus C was replaced by its projection onto the N,H1,H2 plane. The employed protein-RNA complexes were the L7Ae-box C/D RNA complex from *A. fulgidus* (PDB: 1RLG) [Moore et al., 2004], the Cse3-RNA complex from *T. thermophilus* (PDB: 2Y8Y) [Sashital et al., 2011] and the Dbp5-RNA complex from *S. cerevisiae* (PDB: 3PEY) [Montpetit et al., 2011], respectively. Assuming a normal distribution for 1RLG, 2Y8Y and 3PEY, the following expectation values/standard deviations for β_1 (β_2) were extracted: 43/21 (86/7), 63/44 (84/6) and 64/47 (88/7) [°]. *Reproduced with kind permission from Asami, S., et al., Angew. Chem. Int. Ed. 2013, 52 (8), pp 2345-2349. Copyright 2013 Wiley-VCH Verlag GmbH Co. KGaA. DOI: 10.1002/anie.201208024.*

and β_2, improved the correlation significantly (Figure 3.72B, black). As expected, restricting the β_2 angular space resulted in smaller errors; however, it did not significantly change the absolute determined distances (Figure 3.72B, red). The determined parameters are summarized in Table 3.4 and the obtained distances were plotted in Figure 3.69A, together with the distances from the crystal structure. The estimated distances and angles were within the error margins. For the experiments, we used only about 2 mg of the ^{2}H-RNA sample. Obviously, a higher fitting accuracy can be achieved by increasing the experimental sensitivity for the two samples.

It should be noted, that the proton density of RNA is naturally much lower than that of a protein. Here, the low proton density simplified the determination of structural parameters, since, to first approximation, every protein $^1H^N$ was in proximity to only very few RNA $^1H^C$ protons.

3.7.7 Detection of site-resolved protein-RNA contacts by long-range transfers

Since protein and RNA offer non-overlapping spectral regions, we were able to obtain protein-RNA contacts via long-range ^{1}H,^{13}C CP transfers in ^{13}C-detected 2D ^{1}H,^{13}C HETCOR experiments, employing the ^{2}H-RNA sample. Here, we used the ^{2}H-RNA sample, since in a

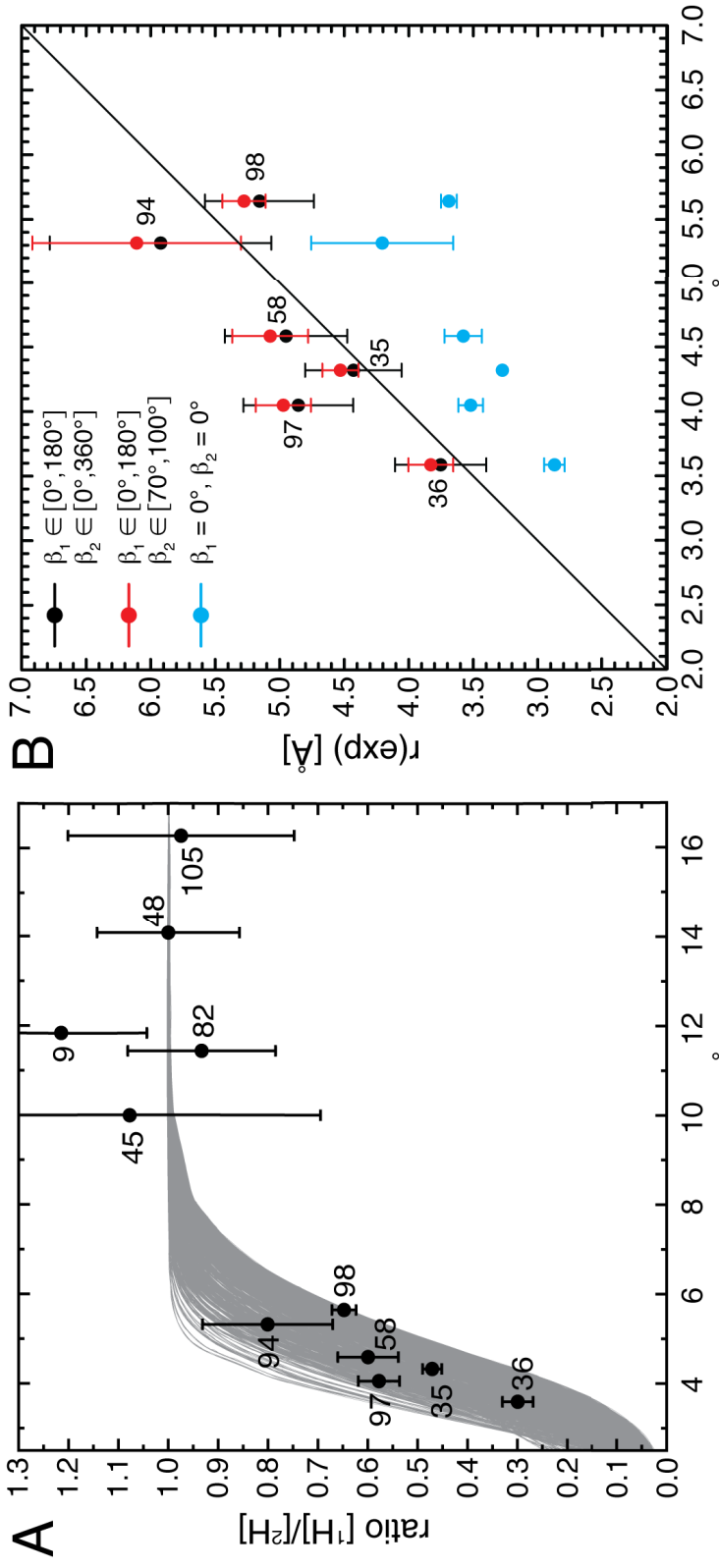

Figure 3.72: (A) Fit of the experimentally determined $I[^1H]/I[^2H]$ intensity ratios. The experimental $I[^1H]/I[^2H]$ ratios were plotted in black as a function of $r(cryst)$, the $^1H^N$(protein),$^1H^C$(RNA) distance, which was extracted from the crystal structure of the L7Ae-box C/D RNA complex (PDB: 1RLG). The full array of simulated curves employed for the fitting procedure was plotted in gray. The fitted distances are shown in Figure 3.69A and given in Table 3.4. The error of the experimental intensities was set to two times the noise RMSD. The uncertainty of the intensity ratios were then determined by error propagation. (B) Correlation plot of $^1H^N$(protein),$^1H^C$(RNA) distances extracted from the crystal structure, $r(cryst)$, and from the experimental $I[^1H]/I[^2H]$ ratios by simulation, $r(exp)$. For the fitting procedure, three different cases were assumed: 1) $\beta_1 \in [0°, 180°]$, $\beta_2 \in [0°, 360°]$ (black), 2) $\beta_1 \in [0°, 180°]$, $\beta_2 \in [70°, 100°]$ (red) and 3) $\beta_1 = \beta_2 = 0°$ (cyan). For case 2), the angular space of β_2 was constrained, as depicted in Figure 3.71. Obviously, introducing the angles β_1 and β_2 significantly improved the fit and yielded a linear correlation between the experiment and the distance extracted from the X-ray structure. When the intercept of a linear function was set to zero, the obtained slopes were roughly 1.05, 1.08 and 0.76 for the nonlinear/unrestricted, the nonlinear/restricted, and the linear arrangements, respectively. In this manner, for protein-RNA complexes a robust structural restraint could be obtained, that did not rely on prior structural knowledge. The error of the experimental distances $r(exp)$ was estimated by 1,000 Monte Carlo simulations using a normal distribution for the intensity ratios $I[^1H]/I[^2H]$. *Reproduced with kind permission from Asami, S., et al., Angew. Chem. Int. Ed. 2013, 52 (8), pp 2345-2349. Copyright 2013 Wiley-VCH Verlag GmbH Co. KGaA. DOI: 10.1002/anie.201208024.*

Table 3.4: Summary of determined distances and angles for residues at the protein-RNA interface of the L7Ae-box C/D complex, based on the combined application of the ^{1}H- and ^{2}H-RNA sample, respectively. Here, the β_2 angle was constrained to the interval $[70°, 100°]$ (Figure 3.71, page 152). *Reproduced with kind permission from Asami, S., et al., Angew. Chem. Int. Ed. 2013, 52 (8), pp 2345-2349. Copyright 2013 Wiley-VCH Verlag GmbH Co. KGaA. DOI: 10.1002/anie.201208024.*

Protein residue	Exp. ratio[a]	d^{cryst} (d^{exp}) [Å][b]	$\beta_1{}^{cryst}$($\beta_1{}^{exp}$) [°][c]	$\beta_2{}^{cryst}$($\beta_2{}^{exp}$) [°][d]
Gly35	0.47 ± 0.02	4.32 (4.53 ± 0.14)	138 (93 ± 16)	89 (86 ± 7)
Thr36	0.30 ± 0.03	3.59 (3.83 ± 0.17)	56 (94 ± 23)	90 (85 ± 6)
Asp58	0.60 ± 0.06	4.59 (5.08 ± 0.30)	48 (90 ± 21)	95 (87 ± 4)
Val94	0.80 ± 0.13	5.32 (6.11 ± 0.81)	65 (24 ± 43)	32 (88 ± 7)
Ala97	0.58 ± 0.04	4.05 (4.97 ± 0.21)	91 (95 ± 2)	88 (85 ± 1)
Ser98	0.65 ± 0.02	5.64 (5.28 ± 0.17)	60 (62 ± 14)	85 (72 ± 6)

[a] Experimental intensity ratios $I[^1H]/I[^2H]$. Intensities from the ^{1}H- and ^{2}H-RNA sample were normalized using the peak volume of Ala48. [b] Protein $^{1}H^{N}$ to RNA $^{1}H^{C}$ distances determined from the X-ray structure and experimentally. [c] β_1 and [d] β_2 angles, obtained from the crystal structure and the fitting.

deuterated sample dipolar truncation is significantly reduced, which enables the determination of long-range contacts, as shown in the following.

For the HETCOR experiment, a ^{1}H evolution period was introduced, prior to the ^{1}H,^{13}C CP transfer block. During the ^{1}H evolution period, 2-3 kHz WALTZ-16 [Shaka et al., 1983] decoupling was employed on the ^{13}C and ^{15}N channels, respectively. During the ^{13}C acquisition, ^{1}H was decoupled, using the same settings. The pulse sequence was similiar to the sequence shown in Figure 3.23B (page 65), omitting the RFDR mixing period.

To optimize the ^{1}H,^{13}C CP transfer, we determined the magnetization buildup for the RNA ribose and the bases as a function of the CP contact time. We recorded a series of 1D spectra, varying the CP contact time from 1 ms to 10 ms (Figure 3.73A). From the extracted intensities, we could determine the contact times for the maximal CP transfer (Figure 3.73B). The maximum was achieved at 6.3 ms and 8.1 ms for the ribose and the bases, respectively.

Finally, the combination of a ^{1}H,^{15}N and a ^{1}H,^{13}C spectrum enabled the determination of protein-RNA contacts, as illustrated for Ala97 (Figure 3.74). We detected a contact between Ala97 and C5' from the RNA ribose. The $^{1}H^{N}$,^{13}C5' distance in the crystal structure (PDB: 1RLG) was ≈4.9 Å, therefore the ^{1}H,^{13}C dipolar coupling anisotropy was about 250 Hz (cf.

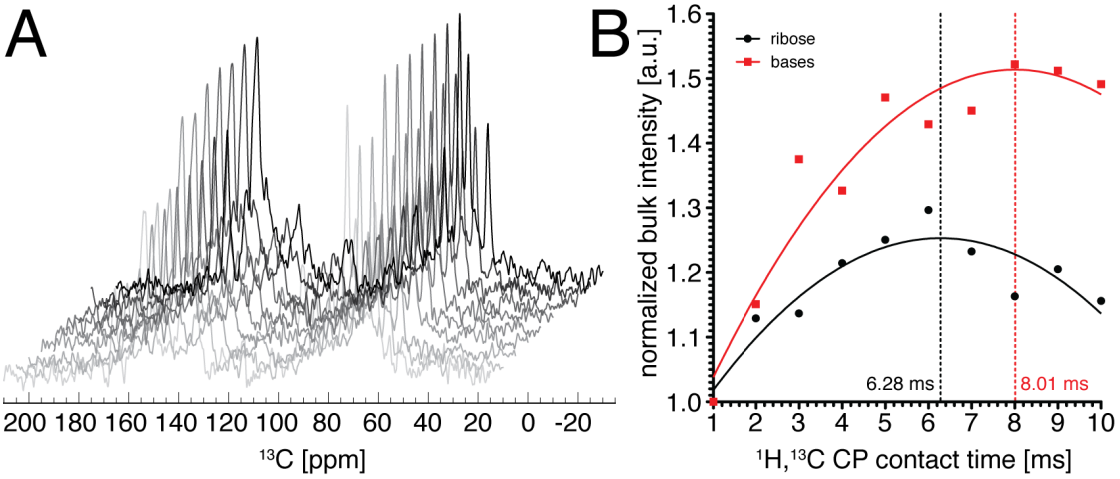

Figure 3.73: Optimization of the ^{1}H,^{13}C cross polarization (CP) contact time for the L7Ae-box C/D complex, using the ^{2}H-RNA sample. The CP buildup was recorded as a function of the contact time at an external magnetic field of 14.1 T (600 MHz), adjusting the MAS frequency to 15 kHz. The effective sample temperature was ≈0 °C. The ^{13}C rf field strength during CP was set to 50 kHz, while the ^{1}H rf field strength was ramped linearly (100-75%) around the $n = 1$ Hartmann-Hahn matching condition. The ^{1}H rf field strength at the center of the linear ramp (87.5%) was experimentally optimized to 67 kHz. With a recycle delay of 3 s, 512 FIDs were accumulated. (A) 1D spectra were acquired with contact times varying from 1 ms to 10 ms (1 ms steps). (B) The bulk intensity for the ribose and the base region was normalized by the intensity of the first experimental point at a contact time of 1 ms, respectively. The intensity maximum for the ribose (bases) was 6.3 ms (8.1 ms).

equation 3.9, page 74). For an efficient long-range transfer, long ^{1}H,^{13}C CP contact times were necessary, as also indicated in Figure 3.73.

In Figure 3.74 the red ^{1}H,^{13}C HETCOR spectrum was recorded with a CP time of 4 ms, the black with 10 ms, respectively. The Ala97-C5' contact was only visible with the longer contact time, which was expected, due to the small dipolar coupling anisotropy between both nuclei. Additionally, long-range contacts between the imino protons and ^{13}C nuclei of the RNA bases were detected. Since the sample amount of the ^{2}H-RNA sample employed here was limited to only 2 mg, we expect more non-trivial, long-range correlations, using a higher sample amount.

This approach is an alternative to the method presented in section 3.7.5 (page 147) and assists, to identify the protein-RNA interface. The advantage here is, that, at the same time, interacting protein, as well as RNA resonances can be identified. However, ^{1}H,^{13}C HETCOR experiments suffer from low sensitivity, due to ^{13}C detection.

With a higher sample amount and the employment of ^{1}H-detection, the experiment could be

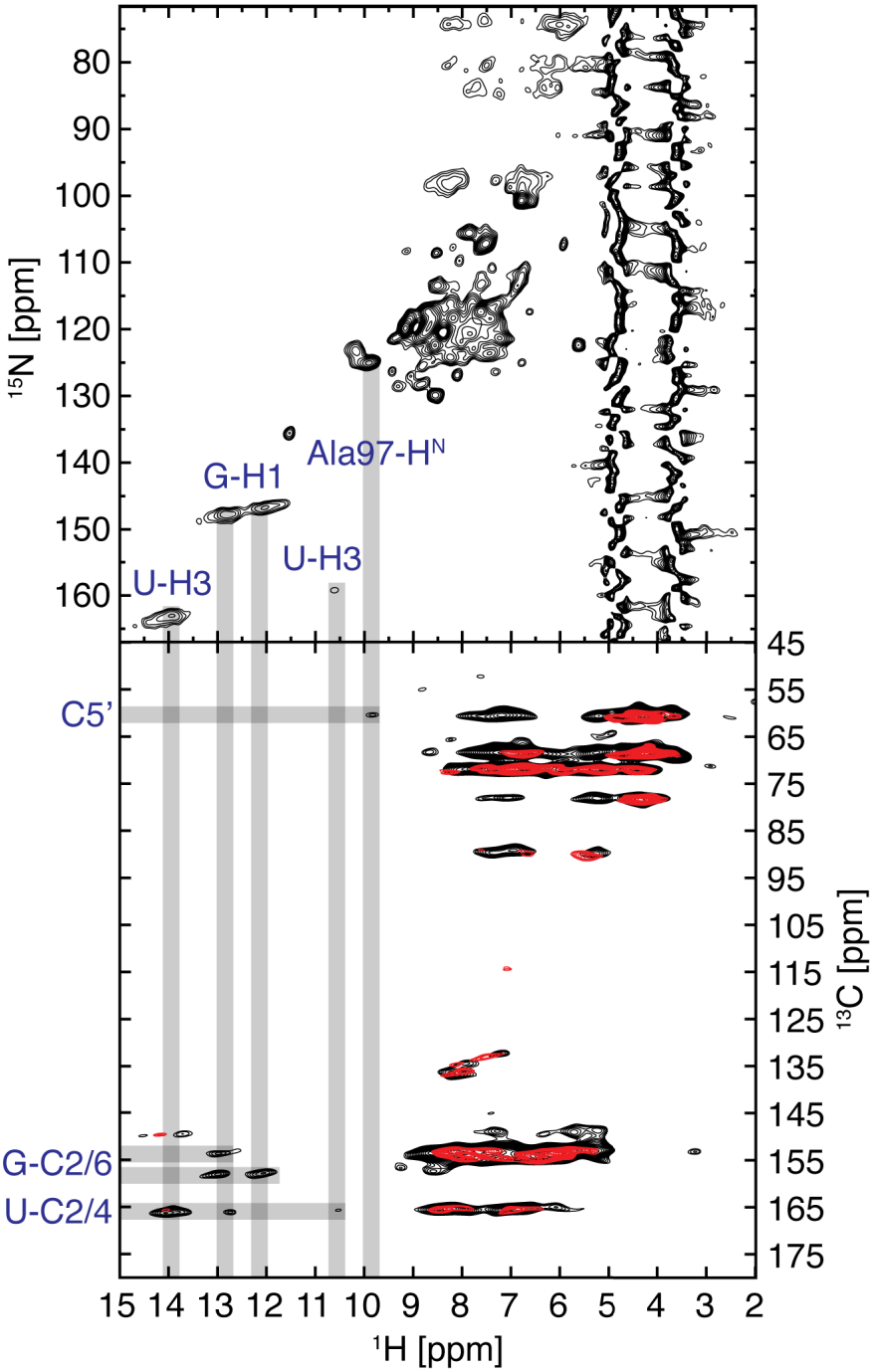

Figure 3.74: Determination of site-resolved protein-RNA contacts by comparison of 2D ^{1}H-detected ^{1}H,^{15}N (top) and ^{13}C-detected ^{1}H,^{13}C HETCOR (bottom) spectra, using the ^{2}H-RNA sample. The acquisition parameters for the ^{1}H,^{15}N spectrum were as in Figure 3.67A. The ^{1}H,^{13}C HETCOR spectrum was recorded at an external magnetic field of 14.1 T (600 MHz). For the black (red) spectrum the MAS frequency was adjusted to 15 kHz (20 kHz), the effective temperature was set to ≈0 °C (12 °C) and the ^{1}H,^{13}C CP contact time to 10 ms (4 ms). Gray stripes indicate tentative assignments, based on the combination of both spectra and average chemical shift values (BMRB database).

extended to a 3D or even 4D experiment by addition of a ^{15}N evolution period and a ^{13}C,^{13}C mixing and ^{13}C evolution period, to allow an unambiguous correlation of interacting protein and RNA nuclei, respectively.

3.7.8 RNA assignment approach

For the assignment of protein resonances in the solid-state, routinely NCOCX/NCACX experiments are employed. However, for RNA molecules, these experiments are insufficient to perform sequential resonance assignment, due to the structural arrangement of the RNA [Riedel et al., 2005]. The nucleosides are connected by NMR-inactive oxygen nuclei, which hamper through-bond correlation experiments (cf. Figure 3.63, page 141). Isotopic enrichment with NMR-active ^{17}O nuclei is unfeasible considering the expenses. That way, only long-range, through-space magnetization transfers can be employed, to establish a sequential RNA assignment.

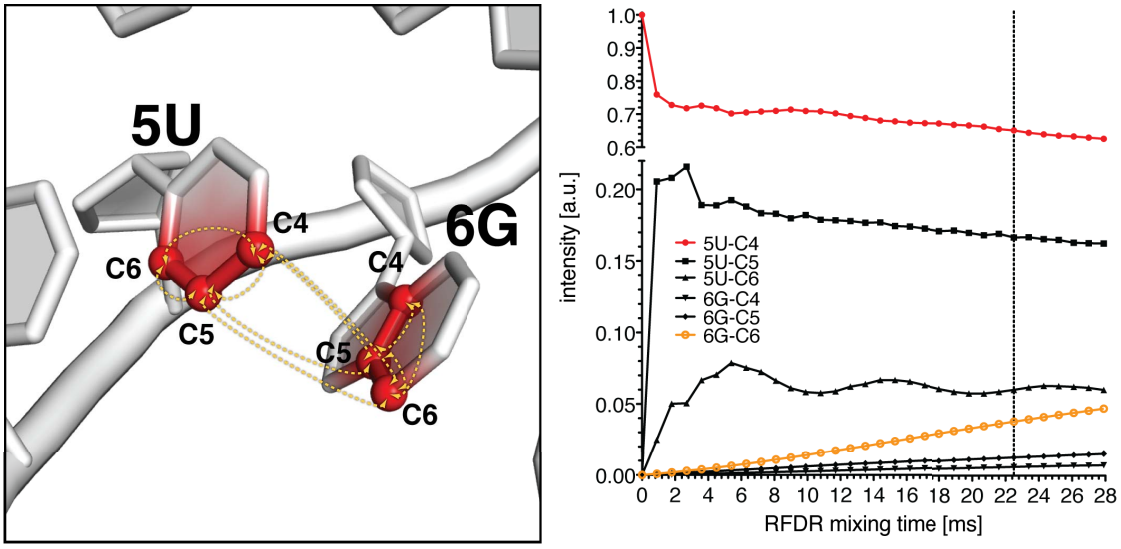

Figure 3.75: Numerical simulation of an adiabatic RFDR mixing sequence [Leppert et al., 2003], employing the spin system (six spins) displayed on the left. The simulations were performed with SIMPSON [Bak et al., 2000]. The external magnetic field was 14.1 T (600 MHz ^{1}H Larmor frequency) and the MAS frequency was set to 20 kHz. The experimentally used tanh/tan pulse shape was read in as the rf Hamiltonian during RFDR mixing. The maximal rf field strength was 96 kHz, applying a (p5)(m4) phase cycle for the RFDR inversion pulses [Tycko et al., 1985]. The R value, representing the product of the pulse bandwidth and the pulse length, was 63. The inversion pulse length was adjusted to one rotor period (50 µs). (Left) Dashed arrows in the structure indicate the considered dipolar couplings. For orientation, the distance between 5U-C4 and 6G-C6 is 3.7 Å. The spin system was created with SIMMOL [Bak et al., 2002], using average chemical shift values from the BMRB database and the coordinates from the 1RLG PDB structure of AF. (Right) The red and the orange curve show the magnetization trend of 5U-C4 and 6G-C6 throughout the homonuclear mixing period, respectively. The vertical line is at 22.5 ms mixing.

To evaluate the efficiency for obtaining long-range correlations with an adiabatic RFDR mixing scheme [Leppert et al., 2003], we carried out numerical simulations with the six spin system illustrated in Figure 3.75 (left) using the SIMPSON software package [Bak et al., 2000]. The coordinates for the RNA residues 5U and 6G were extracted from the 1RLG PDB structure by SIMMOL [Bak et al., 2002]. To simulate the adiabatic RFDR sequence, the experimental tanh/tan pulse shape was directly read into the simulation as the rf Hamiltonian during RFDR mixing. In Figure 3.75 (left), the dashed arrows indicate the considered dipolar couplings. Since the simulation was intended as an optimization of the mixing parameters for the ^{2}H-RNA sample, to first approximation, no protons had been included into the spin system. The influence of ^{2}H for the simulation was expected to be negligible.

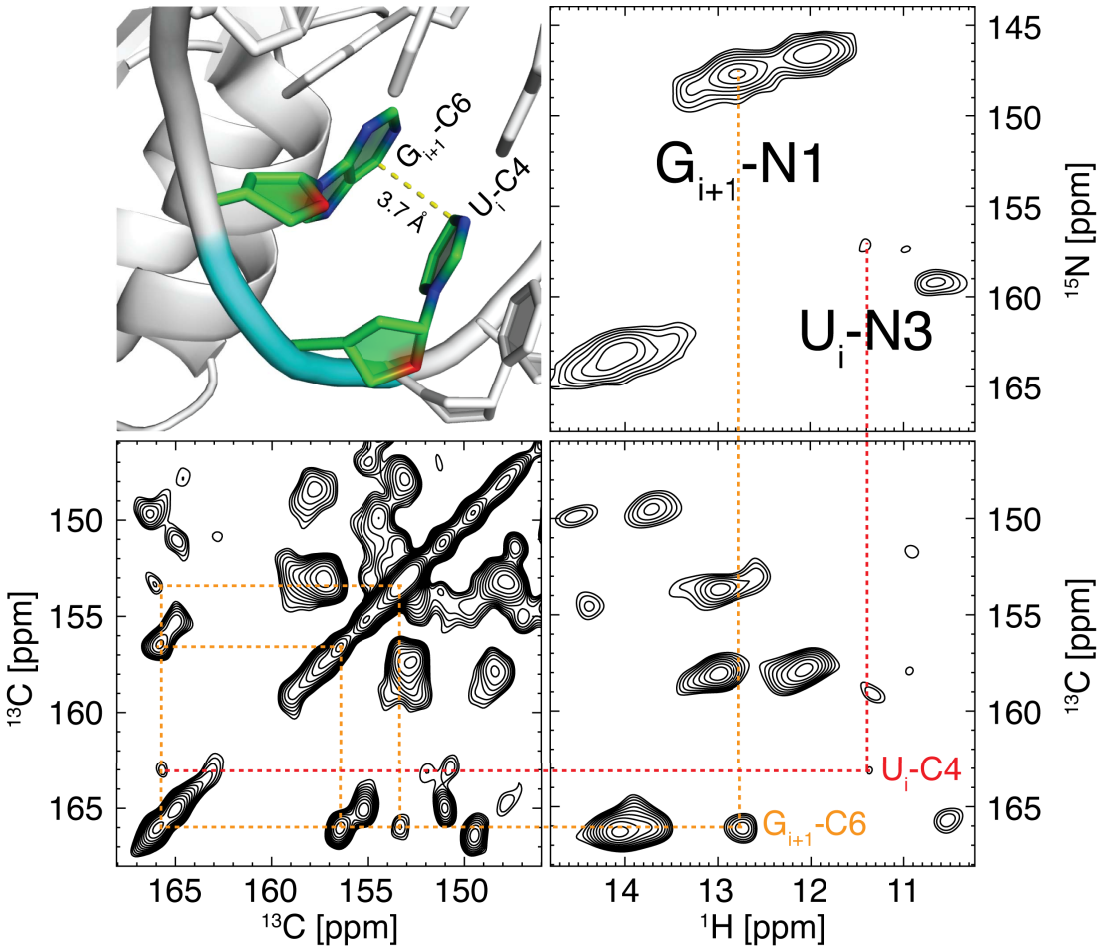

Figure 3.76: Sequential assignment strategy for RNA residues. Detection of inter-residual, sequential RNA long-range contacts by a combination of ^{1}H,^{15}N, ^{1}H,^{13}C and ^{13}C,^{13}C spectra, respectively. The mixing time for the ^{13}C,^{13}C RFDR experiment was 22.5 ms. The long mixing time allowed to determine long-range, inter-residual contacts, here, between U$_i$-C4 and G$_{i+1}$-C6, which had a ^{13}C,^{13}C distance of 3.7 Å, according to the 1RLG PDB structure. Due to the higher sample amount, the ^{1}H-RNA sample was employed for the ^{13}C,^{13}C correlation spectrum, otherwise the ^{2}H-RNA sample was used.

In the initial density operator $\rho(0)$ only the [5U-C4] nucleus was longitudinally polarized ($\rho(0) = [\text{5U-C4}]_z$). The magnetization progression for all nuclei was determined as a function of the mixing time (Figure 3.75, right). At 22.5 ms mixing, we determined an intensity ratio of 17:1 between 5U-C4 and 6G-C6, which are 3.7 Å apart. Therefore, in a 2D ^{13}C,^{13}C RFDR experiment, the peak intensity of the $\Omega_1(\text{5U-C4}), \Omega_2(\text{6G-C6})$ cross peak was expected to be $\approx$6%, compared to the diagonal magnetization of $\Omega_1(\text{5U-C4}), \Omega_2(\text{5U-C4})$. Here, Ω_1 and Ω_2 were the chemical shift values for the indirect and direct acquisition dimension, respectively.

To experimentally obtain sequential RNA assignments, we recorded three different 2D spectra, in particular a ^{1}H,^{15}N, ^{1}H,^{13}C and a ^{13}C,^{13}C spectrum, respectively, as shown in Figure 3.76. The ^{13}C,^{13}C spectrum (bottom, left) was acquired with the same parameters used for the simulation in Figure 3.75. As expected from the simulation, we detected long-range contacts, for example, shown here between U$_i$-C4 and G$_{i+1}$-C6.

Tracing the ^{13}C chemical shift horizontally to the ^{1}H,^{13}C spectrum (Figure 3.76, bottom, right), allowed to determine the respective ^{1}H chemical shift values of the proximal U$_i$-H^{N3} and G$_{i+1}$-H^{N1} protons, bound to U$_i$-N3 and G$_{i+1}$-N1, respectively. By tracing the ^{1}H^{N} chemical shifts vertically to the ^{1}H,^{15}N spectrum (top, right), we could also identify the corresponding ^{15}N chemical shifts, U$_i$-N3 and G$_{i+1}$-N1. In total, we could sequentially assign a U$_i$,G$_{i+1}$ pair, via long RFDR mixing, and determine the respective ^{13}C, ^{15}N and ^{1}H chemical shifts. Nevertheless, more sequential assignments are necessary to locate the U$_i$,G$_{i+1}$ pair unambiguously within the primary sequence of the RNA. However, the long-range cross peaks were too weak, employing a higher sample amount would promote the assignment procedure significantly. Furthermore, higher sensitivity enables the extension to 3D and 4D experiments, to reduce spectral ambiguity.

4 Discussion and Conclusions

4.1 Reduced Adjoining Protonation (RAP) labeling scheme

The herein introduced Reduced Adjoining Protonation (RAP) labeling scheme was shown to be suited for various applications in biomolecular solid-state NMR spectroscopy, such as correlation spectroscopy, resonance assignments, determination of structural restraints and dynamics. We demonstrated its versatile use in the crystalline SH3 domain of chicken α-spectrin and the non-crystalline $A\beta_{1\text{-}40}$ amyloid fibrils. All results are discussed in the following.

4.1.1 Optimal RAP sample

The RAP labeling scheme yields randomly protonated samples in a deuterated matrix. The degree of protonation can be adjusted by the relative amount of H_2O in the M9 growth medium. To determine the spectroscopic optimal protonation level, we presented a systematic analysis of sensitivity and resolution of different randomly protonated microcrystalline α-spectrin SH3 samples as a function of the MAS frequency. Not surprisingly, fast MAS spinning is most beneficial for sensitivity and resolution in ^{1}H-detected INEPT based ^{1}H,^{13}C correlation experiments, due to the elongation of the effective T_2 times for ^{1}H and ^{13}C, respectively.

We found, that a α-spectrin SH3 RAP sample expressed from a M9 minimal medium with a H_2O content of 15% to 25%, rotated at 60 kHz MAS, yielded the best compromise in terms of spectroscopic performance. For the 25% RAP sample, the relative sensitivity gain at 60 kHz MAS is on average $\approx$4.5 and $\approx$4 fold for backbone and methyl resonances, respectively (cf. Figure 3.7A, page 42). The ratio of absolute peak intensities for a fully-packed 3.2 mm rotor at 20 kHz MAS (700 MHz) to a 1.3 mm rotor at 60 kHz (850 MHz) amounts to $\approx$1.1-1.3, whereas

the ratio of the active sample volumes is on the order of ≈20, indicating a significant saving of isotopically enriched protein material, using 1.3 mm rotors. The 3.2 mm rotor was packed by a benchtop centrifuge ($\approx 40 \times 10^3$ *g*), while the 1.3 mm rotor was packed by ultracentrifugation ($\approx 135 \times 10^3$ *g*). This might account for a factor of 1-2 in the amount of material in the 1.3 mm rotor. In addition to reduced ^{1}H dipolar dephasing at high MAS frequencies, this enhancement is also attributed to a higher efficiency of the 1.3 mm probe [Hoult and Richards, 1976].

We performed 2D ^{1}H,^{13}C HMQC experiments at a MAS rotation frequency of 40 kHz, and determined residue-specific ^{1}H line widths for a 5% and a 25% RAP sample (cf. Figure 3.12B, page 50). For the 25% RAP sample, the average ^{1}H line width amounts to 44-49 Hz. The line width for the 5% RAP sample is on the same order, which is supported by the ^{1}H T_2 echo experiments, carried out at 60 kHz MAS (cf. Figure 3.7B, page 42).

The highest sensitivity was obtained for the 25% RAP sample rotated at 60 kHz (cf. Figure 3.7A, page 42). Under these conditions, dipole mediated line broadening was not yet outperforming sensitivity and resolution. However, the use of a higher relative concentration of H_2O in the bacterial growth medium seems unfavorable due to an increase of the $^{13}CDH_2$ isotopomer, which results in additional resonances and, thus, in a decrease of resolution (cf. Figure 3.21, page 61).

In the course of the experimental series with increasing MAS frequencies, the samples became dehydrated. However, a sealing method was suggested, which enabled long-term measurements at spinning frequencies ≥50 kHz. In total, we expect that, enhanced coherence lifetimes at fast rotation will facilitate solution-state like multi-bond experiments in the future, and allow scalar transfers even for weakly coupled spin systems [Linser et al., 2008, Schanda et al., 2009].

Recently, high-resolution DQ-^{2}Hα,^{13}Cα correlation spectra using perdeuterated α-spectrin SH3 were reported [Agarwal et al., 2009]. The observed resonances in the here presented ^{1}Hα,^{13}Cα correlation experiment using α-spectrin SH3 RAP samples (cf. Figure 3.6B, page 41) match rather well the ^{2}Hα,^{13}Cα correlation spectra. The experimental ^{2}H line width for the ^{2}Hα resonances was (30 ± 9) Hz. The ^{1}Hα line width in the presented ^{1}H,^{13}C HMQC spectra of a 5% RAP sample amounted to (50 ± 9) Hz at a MAS frequency of 20 kHz and an external magnetic field of 14.1 T (600 MHz). Taking the 6.5 times smaller gyromagnetic ratio of deuterium

$\gamma(^2\mathrm{H})$ to protons $\gamma(^1\mathrm{H})$ into account, the resolution in the ^{1}H-detected spectrum is improved by a factor of about two. At the same time, the signal-to-noise is increased by a factor of

$$0.05 \times \frac{\gamma(^1\mathrm{H})^{5/2}}{\gamma(^2\mathrm{H})\gamma(^{13}\mathrm{C})^{3/2}} \approx 0.05 \times 52 \approx 3$$

(to first approximation, the prefactor of 0.05 takes account of the proton concentration of the 5% RAP sample).

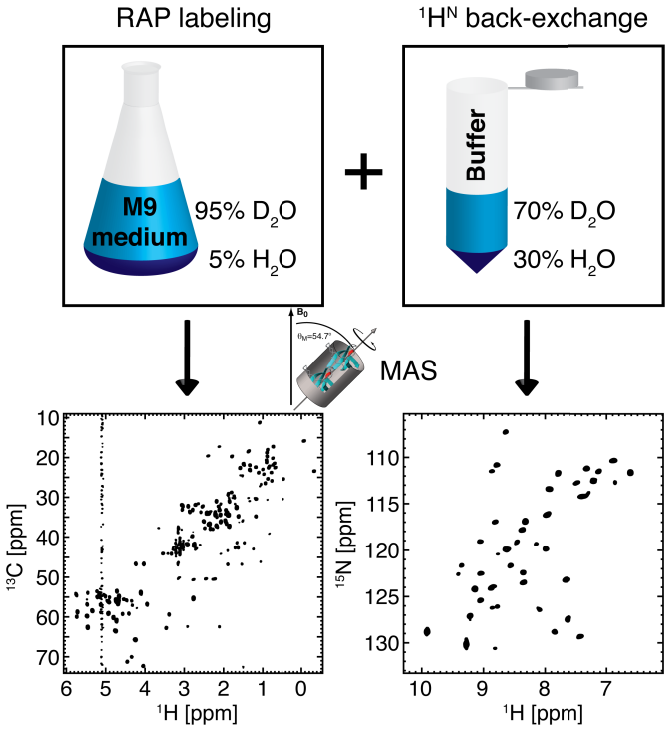

Figure 4.1: Combination of the RAP approach with back-exchanging of labile protons to determine ^{1}H-detected high-resolution ^{1}H,^{13}C and ^{1}H,^{15}N correlation spectra, using the same sample. Here, for the ^{1}H,^{13}C spectrum (left, 14.1 T), however, a 5% RAP labeled α-spectrin SH3 sample was employed, while the ^{1}H,^{15}N spectrum (right, 16.4 T) was obtained, using a 25% RAP labeled sample, which was back-exchanged in a 30%/70% H_2O/D_2O buffer, respectively. For both samples the MAS frequency was adjusted to 20 kHz.

Sensitivity and resolution of resonances in the aliphatic region of ^{1}H,^{13}C HMQC spectra using RAP samples were not compromised, even though the amount of protons had been increased in comparison to the previously presented approaches [Agarwal et al., 2006, Agarwal and Reif, 2008, Agarwal et al., 2008]. In contrast to an approach designed for the determination of high-resolution ^{1}H,^{15}N correlations, in which the exchangeable protons have to be partially replaced

with deuterons [Chevelkov et al., 2006, Akbey et al., 2010], the presented RAP labeling scheme does not require an $^{1}H/^{2}H$ exchange step. This will be of particular importance for the investigation of membrane proteins, which have very stable amide protons, that might not exchange within months.

However, the RAP labeling can be combined with back-exchanging of labile protons, as stochastical incorporation of protons in both approaches reduces the probability of high proton concentrations for a single protein molecule. In Figure 4.1 the $^{1}H,^{13}C$ HMQC spectrum of a 5% RAP sample was plotted (left) next to the $^{1}H,^{15}N$ correlation spectrum of a 25% RAP sample, back-exchanged in a 30%/70% H_2O/D_2O buffer (right). Even though both labeling schemes were employed at the same time, using relatively high proton concentrations, high-resolution spectra were obtained already at moderate MAS frequencies. In principle, the here presented analysis of sensitivity and resolution as a function of the RAP proton concentration and MAS frequency has to be extended by an additional dimension, accounting for the degree of back-exchanged protons. However, a 15% RAP labeled sample, back-exchanged in a 20%/80% H_2O/D_2O buffer seems to be a reasonable compromise.

In conclusion, we could demonstrate that the presented RAP labeling scheme facilitates ^{1}H detection of aliphatic resonances and opens a new avenue for biomolecular MAS solid-state NMR spectroscopy. The presented RAP approach is easy to implement and allows to bypass more complicated labeling schemes, which rely on selectively labeled precursors, such as [1,3]-^{13}C or [2]-^{13}C glycerol [LeMaster and Kushlan, 1996, Hong and Jakes, 1999, Castellani et al., 2002], or which rely on dilution of exchangeable protons [Chevelkov et al., 2006].

However, we also investigated the possibility of RAP labeling, combined with sparse isotopical ^{13}C enrichment using [u-^{2}H, 2-^{13}C]-glycerol as the carbon source, instead of u-[$^{2}H,^{13}C$]-glucose. That way, a 10% RAP-glycerol sample of α-spectrin SH3 was prepared, employing 10% H_2O and 90% D_2O in the M9 expression buffer. The recorded $^{1}H,^{13}C$ correlation spectra yielded excellent signal dispersions (Figure 4.2) due to the elimination of homonuclear J-couplings and the reduction of spectral crowding, as only every second carbon was isotopically ^{13}C-labeled. In principle, for a full characterization of RAP-glycerol samples, the site-specific ^{1}H concentrations remain to be determined, since glycerol enters the amino acid metabolism at

a different level than glucose [Lemaster and Cronan, 1982]. These can be obtained by solution-state NMR experiments, which were already carried out here for the RAP-glucose samples.

To first order approximation, half of the ^{13}C resonances are attenuated, using [u-^{2}H, 2-^{13}C]-glycerol as the carbon source. However, to detect the missing resonances, a complementary RAP sample could be prepared, employing [u-^{2}H, 1,3-^{13}C]-glycerol in the M9 expression medium. An 1:1 mixed sample could be employed to obtain the full spectrum, but with improved resolution, as ^{13}C,^{13}C scalar couplings are eliminated, which could be used for the determination of intermolecular contacts [Castellani et al., 2002, Loquet et al., 2010, 2012].

To spectroscopically improve the ^{13}C resolution by removing ^{13}C,^{13}C scalar couplings in uniformly ^{13}C-labeled RAP-glucose samples, two approaches were probed. As known from solution-state NMR, constant-time experiments can be employed, in which ^{13}C,^{13}C J-couplings are refocussed during a constant evolution period [Vuister and Bax, 1992]. We showed, that high MAS frequencies enable ^{1}H,^{13}C constant-time HSQC experiments in the solid-state using RAP-glucose samples, while employing 2-3 kHz low-power decoupling (cf. Figure 3.17B, page 55). The experiment requires long ^{13}C T_2 times, which are, however, limited for ^{13}Cα backbone resonances. For this case, we implemented a homonuclear ^{13}C'+^{13}Cβ-selective scalar decoupling sequence, which can be employed in "real"-time during the ^{13}Cα evolution period. That way, ^{1}Hα,^{13}Cα correlations were obtained by a cross polarization (CP) based sequence at a moderate spinning frequency of 24 kHz. Spectra with a significantly improved backbone resolution were yielded (cf. Figure 3.16B, page 54).

4.1.2 Access to secondary and tertiary structure information

NMR spectroscopy is a powerful tool for structural investigations of biomolecules at atomic resolution. Since chemical shifts provide a direct access to secondary structure informations [Spera and Bax, 1991, Wishart et al., 1991], the assignment of resonances is crucial for proceeding with structural studies, as well as for investigating protein dynamics.

In RAP samples, assignments are more difficult to obtain in comparison to homogeneously labeled samples, due to the stochastic incorporation of protons. For that reason, HCCH type experiments cannot easily be implemented. For RAP samples, complementary assignment strategies

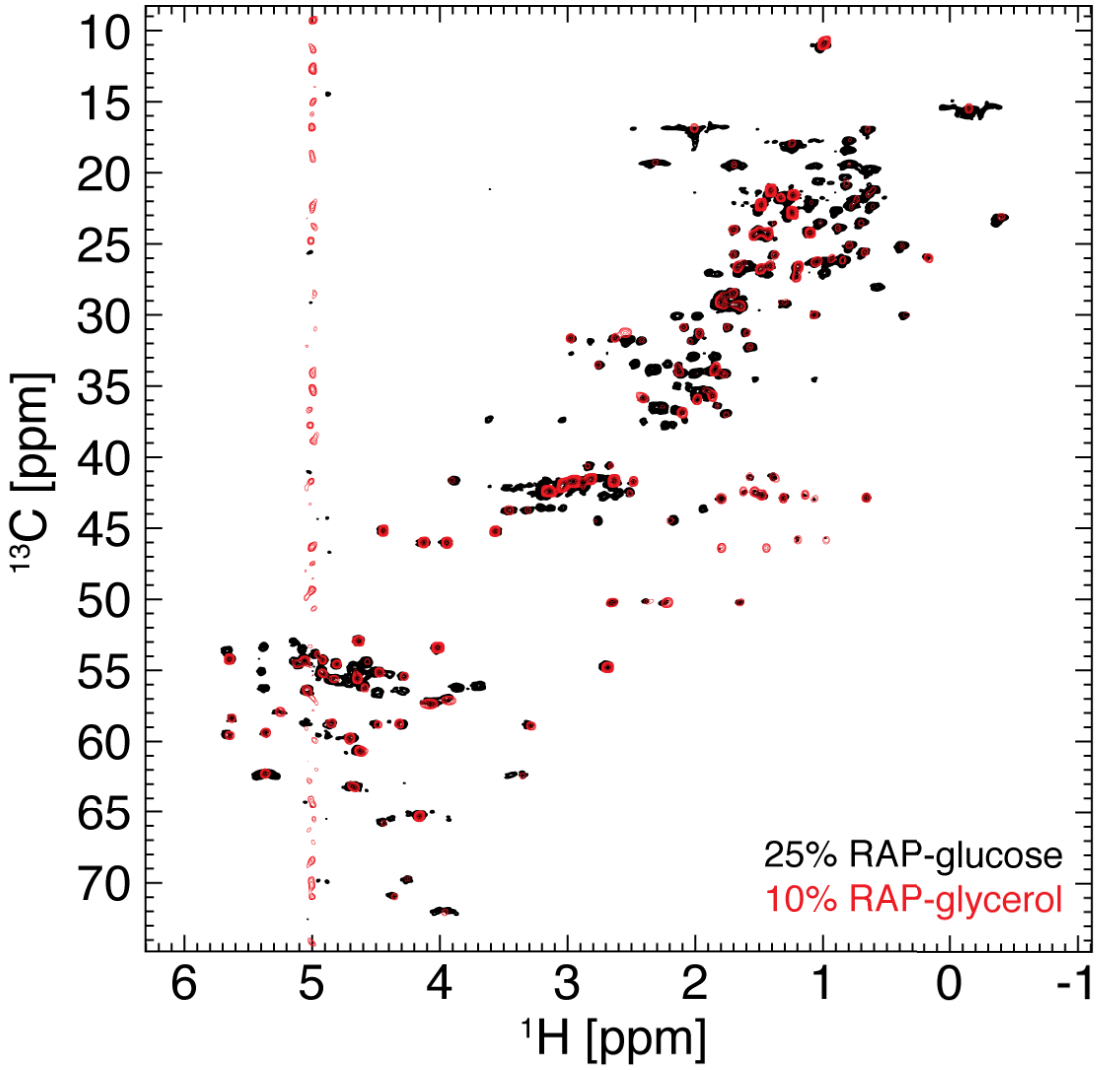

Figure 4.2: Comparison of ^{1}H,^{13}C HMQC spectra of a 25% RAP-glucose (black) to a 10% RAP-glycerol sample (red) of α-spectrin SH3, employing u-[^{2}H,^{13}C]-glucose and [u-^{2}H, 2-^{13}C]-glycerol as the carbon source in the M9 minimal medium, respectively. Both spectra were recorded at the same effective temperature of ≈15-20 °C and external magnetic field of 20 T (850 MHz). The MAS frequency was adjusted to 40 kHz and 50 kHz, employing the RAP-glucose and RAP-glycerol sample, respectively.

need to be established. We showed, that all resonances can be unambiguously assigned using 3D HCC and CCH type correlation experiments, yielding assignment of ≈90% of the ^{1}Hα,^{13}Cα backbone, and side chain resonances of a 15% RAP sample of α-spectrin SH3. In both experiments, ^{13}C,^{13}C mixing is achieved, using an adiabatic RFDR sequence [Leppert et al., 2003]. Compared to PDSD and RAD/DARR, the RFDR sequence displayed the best mixing performance (cf. Figure 3.18, page 57).

The 3D CCH experiment exploits ^{13}C paramagnetic relaxation enhancement to accelerate data acquisition and proton detection for high sensitivity [Linser et al., 2007, Wickramasinghe et al., 2009]. In order to improve the resolution, the spectral width was reduced to the aliphatic region. Therefore, the CP condition was optimized to suppress ^{13}C' excitation and prevent folding artifacts (cf. Figure 3.28, page 70). Originally, the 3D CCH experiment was recorded with carbon direct excitation. Alternatively, the experiment can be performed by transferring magnetization simultaneously from the deuteron and the proton to the carbon spin.

The 3D HCC experiment allows easy assignment of ^{1}Hα resonances in cases where the ^{1}Hα resonance is perturbed by the solvent signal. As shown here, homonuclear scalar decoupling in the indirect and, as demonstrated by Chevelkov et al. [2005a], in the direct carbon dimension allows to significantly increase the spectral resolution.

For comparison, representative strip plots of the 3D HCC and the 3D CCH experiment are shown in Figure 4.3. In particular for sequential assignment experiments, a four-channel probe with high-power capabilities for ^{1}H, ^{2}H, ^{13}C and ^{15}N in combination with optimum control strategies to overcome bandwidth limitations will yield a further increase in experimental sensitivity [Wei et al., 2011].

The assigned chemical shifts only yield limited structural information. However, to be able to determine *de novo* structures, internuclear long-range restraints are essential. In uniformly labeled samples, long-range interactions are difficult to obtain due to the truncation of the dipolar coupling. Therefore, labeling schemes are exploited, that rely on spin dilution. In RAP samples, the proton spin system is diluted, which enabled high-resolution proton detection. Therefore, we established a ^{13}C-resolved 3D H(H)CH correlation experiment, which allowed the identification of ^{1}H,^{1}H interactions among side chains, which are close in space. The experiment was derived

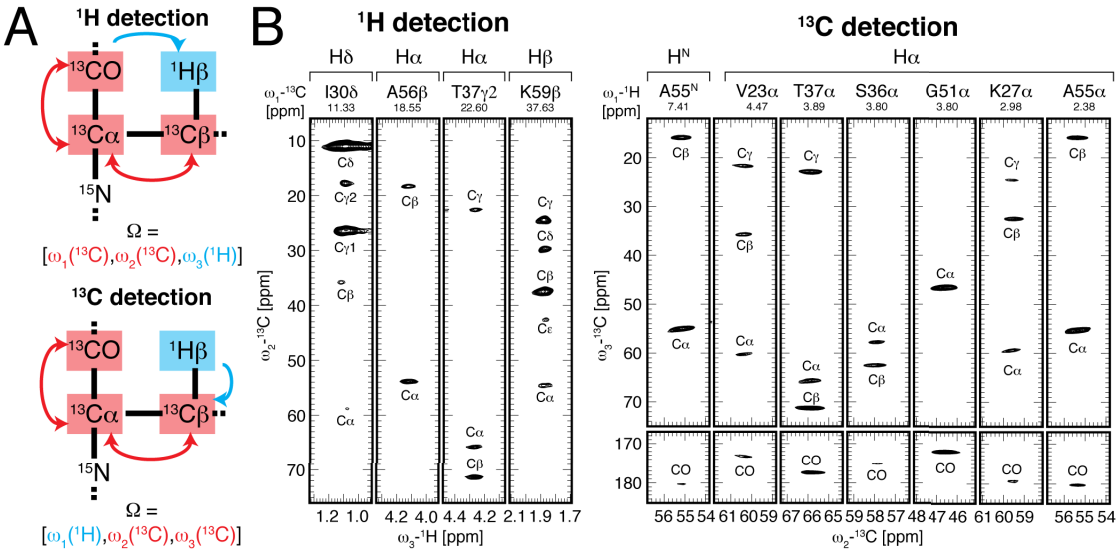

Figure 4.3: (A) Schematic illustration of the magnetization transfer pathway in the ^{1}H-detected CCH (left) and the ^{13}C-detected HCC experiment (right), respectively. (B) 2D strips extracted from the 3D ^{1}H-detected CCH (left, cf. Figure 3.24, page 66) and the ^{13}C-detected HCC correlation experiment (right, cf. Figure 3.25, page 67) recorded for a 15% RAP sample of α-spectrin SH3. *Reproduced with permission from Asami, S., et al., Acc. Chem. Res., 2013, 46 (9), pp 2089–2097. Copyright 2013 American Chemical Society. DOI: 10.1021/ar400063y.*

from the solution-state ^{1}H,^{13}C NOESY-HMQC experiment [Ikura et al., 1990b, Zuiderweg et al., 1990], while the NOESY mixing was replaced by ^{1}H,^{1}H RFDR recoupling. Similar approaches for determination of proton-proton contacts were proposed, employing perdeuterated and selectively methyl labeled samples [Zhou et al., 2007, Huber et al., 2011, Knight et al., 2011, Linser et al., 2011a]. However, in combination with fast MAS, it is expected, that the RAP labeling yields significantly more information, as the entire side chain is labeled and detectable.

4.1.3 Investigation of A$\beta_{1\text{-}40}$ amyloid fibrils

The structural investigation of insoluble, biomolecular systems, such as membrane proteins and, especially, protein aggregates, are highly limited with the traditional biophysical methods, X-ray crystallography and solution-state NMR spectroscopy, as solubility is a prerequisite for both techniques. On the other hand, solid-state NMR spectroscopy is particularly useful to investigate these systems, as it does not require dissolved molecules and is not subject to a size limitation. However, solid-state NMR spectroscopy of uniformly protonated samples suffers from low sensitivity and resolution due to the detection of nuclei with small gyromagnetic ratios, as ^{13}C and

^{15}N, and the presence of ^{1}H,^{1}H dipolar couplings, which induce severe line broadening. Therefore, for the investigation of the Alzheimer's disease A$\beta_{1\text{-}40}$ amyloid fibrils, deuteration was employed (cf. section 1.2, page 7). Very few fibril studies have been reported, which rely on ^{1}H-detected experiments, making use of deuteration. So far, exclusively perdeuterated and $^{1}H^{N}$ back-exchanged fibrils were employed [Linser et al., 2011b, Morris et al., 2012].

Here, A$\beta_{1\text{-}40}$ fibrils were prepared, using the herein introduced RAP labeling scheme, which enables proton detection, while maintaining high resolution in the aliphatic region. Two 5% RAP samples were prepared, sample S1 and S2, respectively. Unlike for S1, the fibril formation of the S2 sample was conducted in the presence of 75 mM Cu(II)EDTA. After the fibril growth, the S2 fibrils were additionally washed two times with a PBS buffer containing 40% deuterated glycerol.

For the initial characterization of both samples, ^{13}C spectra were recorded, since the majority of previously reported solid-state NMR data is based on ^{13}C-detection [Petkova et al., 2005, 2006, Bertini et al., 2011a, Dasari et al., 2011, Bieschke et al., 2012, Lopez Del Amo et al., 2012, Lopez del Amo et al., 2012]. The comparison of ^{13}C 1D and 2D spectra of S1 and S2 with uniformly protonated fibrils showed a good resonance overlap and indicated similar folds, as well as homogeneous sample preparations of both RAP labeled samples (Figure 3.57A, page 132 and Figure 3.58, page 134). However, slight differences were obtained for the S2 sample, which were most obvious for the alanine residues.

A$\beta_{1\text{-}40}$ contains three alanine residues, however, only two were visible, as one (Ala2) is located in the structurally disordered N-terminus [Petkova et al., 2006]. Due to the proposed asymmetry of the dimer, two sets of chemical shifts were expected for every residue and, therefore, in total, four resonances for both detectable alanines. In this manner, as shown in Figure 3.58A (page 134), Ala21 and Ala30 were identified for conformer I (orange label) and II (cyan), respectively, based on previous assignments [del Amo et al., 2012].

For the preparation of the S2 fibrils, Cu(II)EDTA was employed to make use of PRE to increase the spectral sensitivity by shortening the experimental recycle delay time (Figure 3.57, page 132). Additionally, the fibrils were washed with glycerol to improve the sample homogeneity. Glycerol is a protecting osmolyte, which pushes the protein folding equilibrium towards the

native state [Bolen, 2004, Street et al., 2006]. Therefore, it was hypothesized, that washing fibrils with glycerol might reduce structural heterogeneities and improve the resolution. However, experimentally no improvement in resolution was obtained. In total, it could not be unambiguously identified, whether Cu(II)EDTA and/or the glycerol washing induced changes in the fibrillar structure with respect to the S1 sample, since two parameters changed from the S1 to the S2 preparation.

In general, isoleucine $\delta 1$ methyl groups show very distinct chemical shifts in the ^{1}H and ^{13}C dimension of ^{1}H,^{13}C correlation spectra. The respective region in a ^{1}H,^{13}C HMQC spectrum was gray shaded in Figure 3.59C (page 135). Isoleucine was, therefore, employed to identify the number of asymmetric subunits in ^{1}H,^{13}C HMQC spectra, as the A$\beta_{1\text{-}40}$ sequence contained two isoleucines, Ile31 and Ile32. The appearance of four isoleucine $\delta 1$ resonances would hint the presence of an asymmetric dimeric subunit. As expected from previous results (Figure 3.58, page 134) [del Amo et al., 2012], we detected four isoleucine resonances for the S2 sample, while the S1 sample showed clearly three resonances, however, the fourth resonance was most probably overlapped.

The estimated number of all experimentally detected methyl resonances for the S1 sample was approximately 35. A maximum of 25 methyl resonances would be expected for a symmetric A$\beta_{1\text{-}40}$ molecule, whereas an asymmetric dimer would yield twice as many resonances. Clearly, the number of experimentally observed methyl resonances exceeds the theoretical upper limit of a symmetric molecule. However, the experimental number falls below the limit for an asymmetric dimer, which is attributed to the large overlap in the methyl region (Figure 3.59C, page 135). The addition of another ^{13}C dimension, as in the here suggested CCH/HCC 3D experiments (cf. Figure 4.3, page 168), would enable an unambiguous determination of the number of methyl resonances. In total, we could show, that an asymmetric dimer was obtained for both labeling schemes, either employing protonated or deuterated fibrils.

For further characterization of the 5% RAP labeled A$\beta_{1\text{-}40}$ fibrils, the residual dynamics was probed by comparing scalar- (black) and dipolar-based (red) ^{1}H,^{13}C correlation spectra (Figure 3.60A, page 136). So far, no ^{1}H chemical shift assignments were available for A$\beta_{1\text{-}40}$, therefore, only qualitative conclusions could be drawn. However, in the future, ^{1}H,^{13}C assignments will

be obtained by the here proposed assignment experiments (cf. section 4.1.2, page 165).

Several methylene and methine peaks were not detected in the CP experiment (Figure 3.60A, page 136), indicating large amplitude sub-µs motions for these residues, which average the ^{1}H,^{13}C dipolar coupling anisotropy, or slow µs-ms motions, which interfere with the CP magnetization buildup. In the inset of Figure 3.60A (page 136), the theoretical $T_{1\rho}$ time (spin-lattice relaxation time in the rotating frame [Jones, 1966]) was plotted as a function of the motional correlation time, τ_c, for two rf spin-lock fields, with $\omega_1/2\pi$ equal to 50 kHz (black) and 100 kHz (red), respectively. Clearly, motion on the µs-ms timescale yields reduced $T_{1\rho}$ times, which hamper the CP magnetization buildup. The sensitivity in the INEPT experiment, on the other hand, is, to first order approximation, only limited by ^{13}C T_2 times, which are susceptible to motions on the slower ms-s timescale [Wang, 1992].

Based only on the average chemical shift and the differential dynamics determined by comparing INEPT and CP transfers, the Met0 and Ala2 methyl groups could be tentatively assigned (Figure 3.60A, page 136). Here, the A$\beta_{1\text{-}40}$ peptide was obtained by recombinant overexpression in *E. coli* (Materials and Methods, page 24), therefore, a methionine at position 1 (termed here position 0) was leading the A$\beta_{1\text{-}40}$ peptide sequence (the primary sequence of A$\beta_{1\text{-}40}$ is given at the bottom of Figure 3.60, page 136). Two particular methyl resonances in the methionine and alanine region were only observable in the INEPT spectrum, while they were beyond detection in the CP experiment. This observation indicates the presence of fast (sub-µs) or intermediate dynamics (µs-ms) for these residues. To distinguish between both timescales, ^{1}H,^{13}C dipolar dephasing (section 4.1.4, page 172) and relaxation dispersion curves [Tollinger et al., 2012] can be obtained, to probe fast and intermediate dynamics, respectively.

So far, residues 0-11 were undetectable in CP-based experiments [Petkova et al., 2006, del Amo et al., 2012], which was attributed to the flexibility and structural disorder of the N-terminus. The flexible N-terminus contains a methionine (Met0) and an alanine residue (Ala2). In combination with the average chemical shift, the missing methyl resonances in the CP spectrum were, therefore, tentatively assigned to Met0 and Ala2 (Figure 3.60A, page 136).

In Figure 3.60B (page 136), ^{1}H,^{13}C correlation spectra of fibrils and solubilized, monomeric A$\beta_{1\text{-}40}$ were compared. As concluded from the chemical shifts found for the amide resonances

of monomeric A$\beta_{1\text{-}40}$ [Lopez del Amo et al., 2012], A$\beta_{1\text{-}40}$ displays a random coil structure in a 10-20 mM sodium hydroxide solution. Therefore, we also expected random coil shifts for the ^{1}Hα,^{13}Cα backbone region. As presumed, rather narrowly dispersed ^{1}Hα,^{13}Cα resonances were experimentally observed for a monomeric sodium hydroxide solution of a 15% A$\beta_{1\text{-}40}$ RAP sample (red spectrum, Figure 3.60B). Comparing this spectrum to the spectrum of a monomeric solution of uniformly protonated A$\beta_{1\text{-}40}$ (50 µM u-[^{1}H,^{13}C,^{15}N] A$\beta_{1\text{-}40}$, dissolved in a buffer with 10 mM NaCl and 100 mM Na_2HPO_4 at pH 7.5, kindly provided by Maria Stavropoulou, TU München) showed a very good overlap, in spite of the different sample conditions (data not shown).

However, the fibrils yielded a much higher dispersion of ^{1}Hα,^{13}Cα backbone resonances, indicating folding and, therefore, the presence of secondary structure. It is well-known from solution-state NMR, that the chemical shift difference to the respective random coil value is highly dependent on the secondary structure motif [Spera and Bax, 1991, Wishart et al., 1991]. In Figure 3.60B, the dashed boxes depict the ^{1}Hα,^{13}Cα region of fibrillar (black) and dissolved, monomeric (red) A$\beta_{1\text{-}40}$. Despite the poor solvent suppression in the solution-state spectrum, a clear shift to higher ("downfield") and lower ("upfield") chemical shift values was observed for the fibrils in the ^{1}Hα and ^{13}Cα dimensions with respect to the monomeric form. A downfield and upfield shift for ^{1}Hα and ^{13}Cα resonances is highly correlated to β-sheet formation [Wishart, 2011]. In fact, the structure of A$\beta_{1\text{-}40}$ fibrils, as determined by solid-state NMR [Petkova et al., 2006], is exclusively composed of parallel β-sheets and loops (inset of Figure 3.60B).

In the future, ^{1}H,^{13}C assignments will be obtained, using A$\beta_{1\text{-}40}$ RAP samples, which, in turn, will enable the investigation of the structure (cf. section 4.1.2, page 165) and the dynamics (cf. section 4.1.4, page 172, and section 4.1.5, page 191) of amyloid fibrils to gain insights into their arrangement and stability.

4.1.4 Dipolar coupling order parameters as a direct probe for sub-µs motions

4.1.4.1 ^{13}C vs. ^{15}N backbone order parameter

The application of MAS averages anisotropic interactions, as the dipolar coupling (cf. Figure 1.1, page 5), and mimics the molecular tumbling of molecules in solution. However, the dipolar

coupling anisotropy is a direct dynamical probe for sub-µs motions as its amplitude is averaged by motions on the respective timescale [Gross et al., 1997]. In the solid-state, various schemes were introduced to recouple dipolar interactions during MAS [Roberts et al., 1987, Hohwy et al., 2000, Zhao et al., 2001a,b, Dvinskikh et al., 2003, 2005, Chevelkov et al., 2009a]. It turned out, that a Rotational-Echo Double-Resonance (REDOR) type experiment [Gullion and Schaefer, 1989, Pan et al., 1990, Jaroniec et al., 2000] performs best for deuterated proteins in terms of insensitivity to rf miscalibration, rf inhomogeneity and *I*/*S* spin CSA [Schanda et al., 2011b], respectively. It was shown numerically, that the presence of remote proton spins was the most severe source of error, which, however, can be by-passed by the use of deuterated protein samples. The REDOR sequence was applied, so far, to perdeuterated and selectively ILV methyl-labeled samples [Schanda et al., 2010, 2011a]. The herein introduced RAP labeled samples yield at the same time order parameters for all aliphatic sites and ^{13}C T_1 times, using the same sample.

Focussing on backbone dynamics, all α-spectrin SH3 ^{1}Hα,^{13}Cα S^2 values and asymmetries were plotted as a function of the residue number (Figure 4.4A), next to the ^{1}H$^{\mathrm{N}}$,^{15}N backbone order parameters (^{1}H$^{\mathrm{N}}$,^{15}N S^2 values were taken from Chevelkov et al. [2009a]). A very similar trend was observed for both dynamics probes. The averaged squared order parameter $\langle S^2 \rangle$ for ^{1}Hα,^{13}Cα was 0.87 ± 0.06. A significantly lower average value was observed for ^{1}H$^{\mathrm{N}}$,^{15}N, $\langle S^2 \rangle$ was determined to be 0.78 ± 0.09. This observation was reported in earlier studies and was attributed to the freedom of intact amide groups to rotate around the connecting Cα_i and Cα_{i-1} bond with little disturbance of the rest of the structure [Smith et al., 1995, Idiyatullin et al., 2003]. These motions about the Cα_{i-1}-Cα_i axis, which connects sequential amino acids, was shown to be dominant, as compared to motions about the remaining two orthogonal axes [Bouvignies et al., 2005]. On the contrary, this type of reorientational motion is hindered for Hα,Cα groups, especially for long-chain amino acids, which explains the shift to larger squared order parameters. This motional restriction was also reflected by low ^{1}Hα,^{13}Cα asymmetry parameters η (Figure 4.4A, blue bars) with an average value of 0.21 ± 0.11. To improve the accuracy and precision of both asymmetry and dipolar coupling anisotropy, two complementary REDOR datasets with two ζ-delays were employed, which improved the fitting convergence of

the dipolar dephasing curves.

However, the average error for the asymmetry parameter was still about 50%, therefore, only limited quantitative conclusions can be drawn. Nevertheless, all asymmetries were larger than zero, hinting a small contribution of about 7-13% from an additional rotameric population, in case a two-site rotameric jump model is assumed (described in section 4.1.4.2, page 181). Exceptionally high asymmetries were observed for Leu8α and Val9α, however, with large experimental uncertainties, indicative of a particularly low spectral sensitivity for these residues.

The generalized order parameter S^2 is a model independent measure of the motional amplitude. However, in the past, various analytical interpretations of the order parameter were suggested, to picture the motion of backbone, side chain and methyl moieties [Lipari and Szabo, 1982b, Jarymowycz and Stone, 2006]. The most frequently used motional model to interpret the model independent order parameter is the diffusion-in-the-cone model [Kinosita et al., 1977, Lipari and Szabo, 1980, 1981]. The model assumes free diffusion of the bond vector within a cone of semiangle θ, while $0^\circ \leq \theta \leq 90^\circ$. The order parameter S^2_{cone} is related to θ as

$$S^2_{\text{cone}} = \left[\frac{1}{2}\cos\theta\,(1+\cos\theta)\right]^2, \tag{4.1}$$

or solved for θ

$$\theta = \cos^{-1}\left[\frac{1}{2}\left(\sqrt{1+8S_{\text{cone}}}-1\right)\right]. \tag{4.2}$$

In Figure 4.5A, the order parameter S^2_{cone} was plotted as a function of θ (black curve). The full range of the order parameter ($0 \leq S^2_{\text{cone}} \leq 1$) is defined by θ. The average ^{1}Hα,^{13}Cα squared backbone order parameter of α-spectrin SH3 was obtained to be 0.87 (Figure 4.4A), which corresponds to librational motion of the ^{1}Hα,^{13}Cα bond vector within a cone of about 17°, as determined by equation 4.2.

Another prominent model is the jump model, which assumes, that the bond vector "jumps" between two different, discrete states i and j, separated by the angle ϕ_{ij}. The probability for residency in both states are p_i and p_j with $p_i + p_j = 1$, respectively [Wittebort and Szabo, 1978,

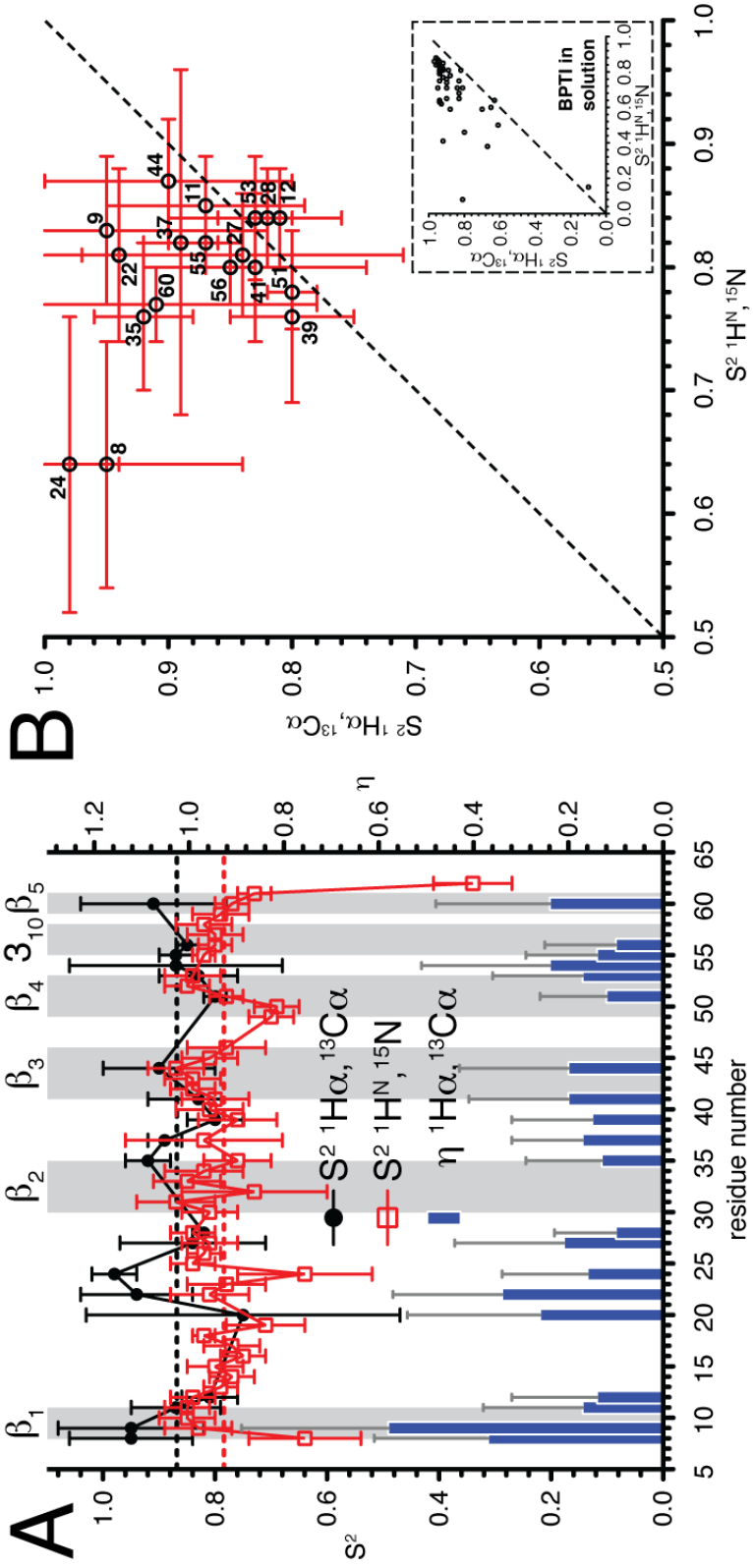

Figure 4.4: In (A) the order parameters S^2 (left y-axis, circles and squares) and the asymmetries η (right y-axis, blue bars) of the ^{1}Hα,^{13}Cα backbone resonances were plotted as a function of the residue number. S^2 was determined, using a 15% α-spectrin SH3 RAP sample (details are given in the caption of Figure 3.33, page 84). For comparison, ^{1}H^N,^{15}N backbone order parameters are shown as empty, red squares. The ^{1}H^N,^{15}N S^2 values were taken from Chevelkov et al. [2009a]. The averaged order parameter is depicted by a dashed black and red line for ^{1}Hα,^{13}Cα and ^{1}H^N,^{15}N S^2, respectively. All employed values are given in the appendix (Table 4, page 220 and Table 10, page 229). The employed rigid-limit bond lengths were 1.11 Å [Alkaraghouli and Koetzle, 1975, Yao et al., 2001] and 1.015 Å [Yao et al., 2008b] for ^{1}Hα,^{13}Cα and ^{1}H^N,^{15}N, respectively. (B) Linear correlation of the ^{1}Hα,^{13}Cα and ^{1}H^N,^{15}N backbone squared order parameters. The linear function with a slope of 1.0 and a y-intercept of 0.0 is plotted as a dashed black line. In the inset figure, the correlation of both order parameters was plotted for the soluble protein Bovine Pancreatic Trypsin Inhibitor (BPTI). The order parameters for BPTI were determined by others, using a 1 ns MD trajectory. The values were taken from Smith et al. [1995]. A very similar pattern was obtained, comparing ^{1}Hα,^{13}Cα and ^{1}H^N,^{15}N order parameters for both samples, microcrystalline α-spectrin SH3 and dissolved BPTI, respectively.

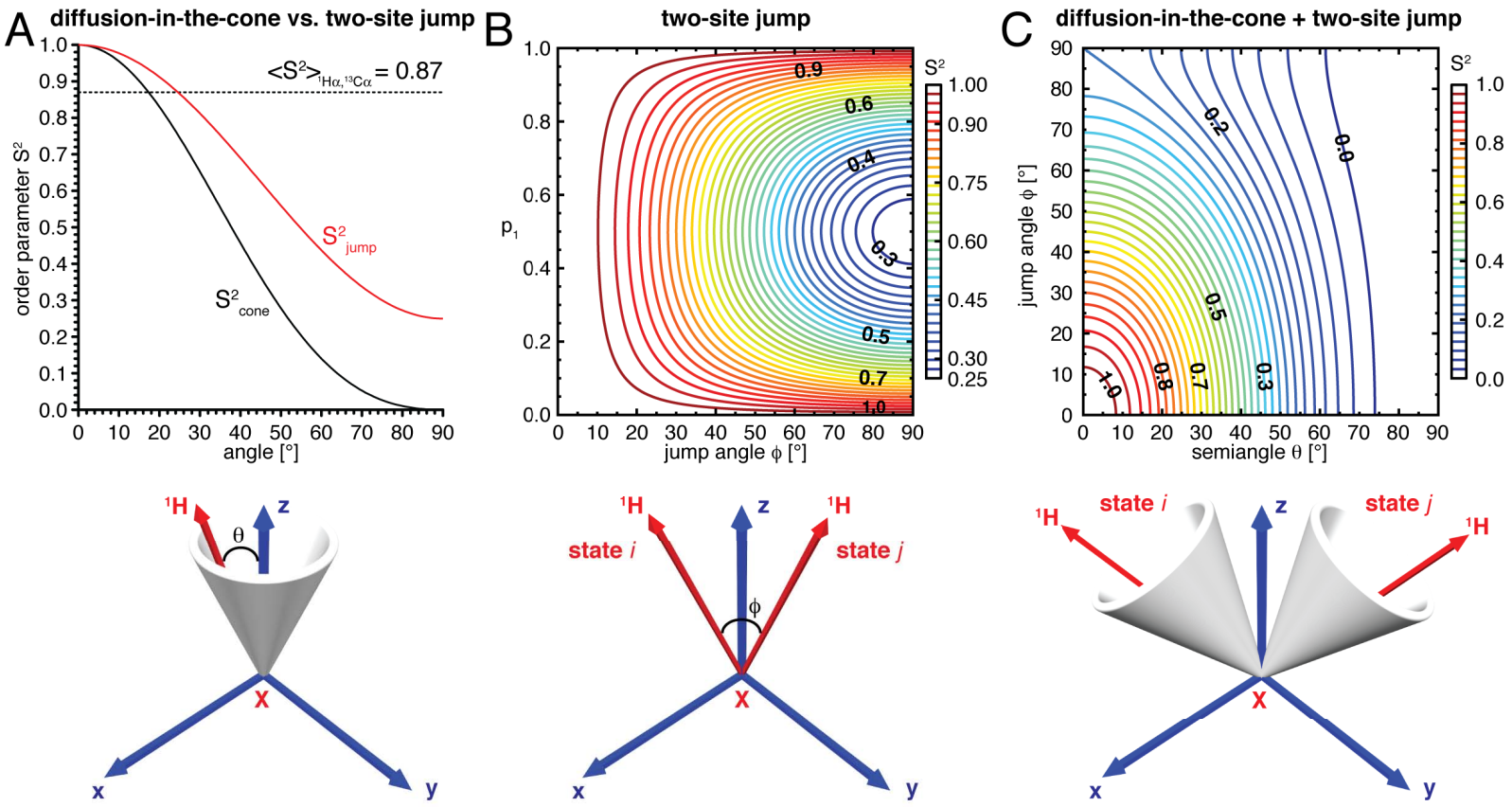

Figure 4.5: (A) The diffusion-in-the-cone order parameter, S^2_{cone}, is plotted as a function of the semiangle, using equation 4.1 (black curve). The red curve depicts the two-site jump model (S^2_{jump}), assuming equal populations, $p_i = p_j = 0.5$ (equation 4.4). The average ^{1}Hα,^{13}Cα squared order parameter of α-spectrin SH3, $\langle S^2 \rangle_{^1\text{H}\alpha,^{13}\text{C}\alpha} = 0.87$ (cf. Figure 4.4A, page 175), is indicated as a dashed, horizontal line. (B) The dependency of the order parameter S^2_{jump} on the jump angle and the population is shown as a contour plot. (C) Assuming equal populations ($p_i = p_j = 0.5$), the general order parameter $S^2 = S^2_{\text{cone}} \times S^2_{\text{jump}}$ is plotted as a function of the semiangle θ and the jump angle ϕ. A pictorial representation of diffusion-in-the-cone, two-site jump and their combination is given as a vector model at the bottom of the figure (A-C).

Clore et al., 1990a,b]. The order parameter S^2_{jump} is defined as

$$S^2_{\text{jump}} = \sum_i \sum_j p_i p_j P_2(\cos\phi_{ij}) \tag{4.3}$$

with the second Legendre polynomial $P_2(\cos\phi_{ij}) = \frac{1}{2}\left(3\cos^2\phi_{ij} - 1\right)$. In Figure 4.5B, S^2_{jump} is plotted as a function of the jump angle ϕ_{ij} and the population p_i, with $p_j = 1 - p_i$. As opposed to the diffusion-in-the-cone model, here, the total range of order parameter values is not defined. The definition range has a lower limit of 0.25 ($0.25 \leq S^2_{\text{jump}} \leq 1$), as the limitation to jumps between discrete states imposes a restriction to the motional freedom. This is also indicated by the red curve in Figure 4.5A, assuming equal populations. For the special case of equal populations ($p_i = p_j = 0.5$), equation 4.3 simplifies to

$$S^2_{\text{jump}} = \frac{1}{4}\left(3\cos^2\phi_{ij} + 1\right). \tag{4.4}$$

To describe backbone dynamics, occuring on the fast ps-ns time scale, usually the diffusion-in-the-cone and the two-state jump model are combined [Clore et al., 1990a]. As proposed by Clore et al. [1990b], the sufficient description of backbone dynamics requires the introduction of two order parameters, S^2_f and S^2_s, for fast and slow motions, respectively. S^2_f takes account of fast random thermal motions on the picosecond timescale ($\omega\tau \ll 1$), which can be well described with the diffusion-in-the-cone model ($S^2_f = S^2_{\text{cone}}$) [Clore et al., 1990a]. On the other hand, S^2_s takes account of the slower, rare, discrete transitions on the time scale of several hundreds of picoseconds to a few nanoseconds ($\omega\tau \approx 1$), which is well represented in the jump model ($S^2_s = S^2_{\text{jump}}$). The occurence of both time scales is supported by protein MD simulations [Karplus and Mccammon, 1979, 1983, Levitt, 1983, Elber and Karplus, 1987, Levitt and Sharon, 1988, Post et al., 1989]. Therefore, to combine the diffusion-in-the-cone and the jump model, the generalized order parameter $S^2 = S^2_f \times S^2_s = S^2_{\text{cone}} \times S^2_{\text{jump}}$ is employed. That way, the bond vector is pictured to jump between the states i and j, while it can diffuse freely within the cone of state i and j, respectively. The generalized order parameter S^2 is plotted in Figure 4.5C as a function of the semiangle θ and the jump angle ϕ_{ij}, assuming equal populations for both states ($p_i = p_j = 0.5$). The total value range of S^2 is represented. To separate S^2_f and S^2_s from the

experimentally determined generalized order parameter S^2, T_1 relaxation data can be employed, as will be discussed in section 4.1.5 (page 191).

As can be seen in Figure 4.4B, the order parameters for both backbone sites, ^{1}Hα,^{13}Cα and ^{1}H^N,^{15}N, were approximately linearly correlated, aside from two significant exceptions, Leu8 and Thr24, which, however, show large error bars. Most values cluster in the region above the diagonal, indicating larger squared order parameters for ^{1}Hα,^{13}Cα, as compared to ^{1}H^N,^{15}N, which was expected due to the different degree of mobility for both dynamics probes (*vide supra*).

For validation with another well established model system, we compared the correlation plot obtained for α-spectrin SH3 (Figure 4.4B) to data obtained for the Bovine Pancreatic Trypsin Inhibitor (BPTI) protein. The BPTI protein has been extensively studied in the past by solution-state NMR [Richarz et al., 1980b, Levy et al., 1982, Wagner, 1983, Nirmala and Wagner, 1988, Berndt et al., 1992, Otting et al., 1993, Szyperski et al., 1993] and MD simulations [Brooks and Karplus, 1983, Levy et al., 1981a, 1982, Lipari et al., 1982]. In Figure 4.4B, H^N,N and Hα,Cα squared order parameters for the water dissolved BPTI protein were correlated, as shown in the inset of Figure 4.4B. These order parameters were calculated from MD simulations [Smith et al., 1995]. A very similar pattern, as observed for α-spectrin SH3 in the solid-state, was yielded, with an offset to higher order parameters for Hα,Cα.

Here, the H^N,N and Hα,Cα order parameters of BPTI were determined by a 1 ns MD trajectory, carried out by Smith et al. [1995]. In general, a good agreement between order parameters derived from MD simulations and NMR is yielded [Chandrasekhar et al., 1992]. The generalized order parameter S^2 is defined as the value of the internal correlation function at infinite time, $\lim_{t\to\infty} C_I(t) = S^2$, which is a model-independent measure of the amplitude of internal motion [Lipari and Szabo, 1982a]. It can be extracted from a MD trajectory as

$$S^2 = \frac{4\pi}{5} \sum_{m=-2}^{2} \langle Y_{2m}^*(\Omega)\rangle \langle Y_{2m}(\Omega)\rangle, \tag{4.5}$$

with $Y_{2m}(\Omega)$ describing the second-order spherical harmonics and $\Omega = (\theta, \phi)$ the direction of the internuclear vector in the molecular frame, while the angular brackets denote the time averaging

[Bruschweiler and Wright, 1994].

The squared order parameter is defined as the ratio of the dipolar coupling anisotropy to the rigid-limit value, therefore, S^2 is strongly influenced by the magnitude of the rigid-limit anisotropy. In the literature, $^1H^N$,^{15}N ($^1H\alpha$,$^{13}C\alpha$) bond lengths of 1.015 Å [Yao et al., 2008b] (1.10 Å [Lipari and Szabo, 1982a, Henry and Szabo, 1985, Tam et al., 1991]) and 1.02 Å [Bernado and Blackledge, 2004] (1.11 Å [Alkaraghouli and Koetzle, 1975, Yao et al., 2001]) were reported, which leads to smaller generalized order parameters in the latter case. Accurate determination of equilibrium bond lengths is difficult, as the bond length is influenced by dynamics. S^2 can be corrected by the factor r_a^6/r_b^6, in which r_a and r_b are the rigid-limit bond lengths. This yields $S^2_{1.02\text{ Å}} = 1.03 \times S^2_{1.015\text{ Å}}$ for $^1H^N$,^{15}N and $S^2_{1.10\text{ Å}} = 0.95 \times S^2_{1.11\text{ Å}}$ for $^1H\alpha$,$^{13}C\alpha$, respectively. The correction by variation of the rigid-limit bond length would, however, only yield an isotropic offset of both order parameters in Figure 4.4B.

An anisotropic, residue-specific offset of the $^1H^N$,^{15}N order parameters to smaller amplitudes may also partially be attributed to hydrogen bonding of $^1H^N$ amide protons, which induces a bond lengthening of the ^{15}N–^1H bond [Steiner, 1995]. As determined by X-ray diffraction and neutron scattering, the lengthening of the X–H (X = N, O) bond length can vary between 0.02 and 0.08 Å for moderate hydrogen bonds ($r_{H\cdots A}$ = 1.5 to 2.2 Å, A is the acceptor), respectively [Taylor et al., 1984, Steiner, 2002]. For example, considering a $^1H^N$,^{15}N dipolar coupling anisotropy of 9151 Hz, which corresponds to a bond length of 1.1 Å, yields an squared order parameter of $S^2 = 0.62$ (equation 3.14, page 76), when assuming a rigid-limit $^1H^N$,^{15}N bond length of 1.015 Å ($\delta_D = 11648$ Hz) [Yao et al., 2008b]. In case of a hydrogen bond, this bond length may extend to 1.1 Å + 0.08 Å ≡ 1.18 Å, which yields a significantly smaller squared order parameter of $S^2 = 0.41$.

The majority of the amide resonances of α-spectrin SH3, which were employed for the correlation plot in Figure 4.4B, are involved in hydrogen bonds. It was shown for α-spectrin SH3, however, that the $^1H^N$,^{15}N dipolar coupling anisotropy and hydrogen bonding are only weakly correlated [Chevelkov et al., 2009a]. In principle, weak hydrogen bonds can also form with the Hα proton of the Hα,Cα backbone, however, inducing a lengthening of Hα,Cα bond of about 0.008 Å, which has a marginal effect on the order parameter. To improve the linear correlation

of $^{1}H\alpha$,$^{13}C\alpha$ and $^{1}H^{N}$,^{15}N order parameters a correction term can be employed to account for hydrogen bonds.

The dipolar coupling anisotropy and, therefore, the order parameter is a field-independent quantity. However, depending on the experimental method employed for its determination, systematic variations can occur. These variations were shown to be significant [Schanda et al., 2011b], comparing dipolar coupling anisotropies, determined by the REDOR [Gullion and Schaefer, 1989] or the CPPI [Dvinskikh et al., 2003] recoupling sequence, respectively. In the present thesis, the REDOR sequence was employed for the determination of the ^{1}H,^{13}C aliphatic order parameters, while $^{1}H^{N}$,^{15}N order parameters were obtained by Chevelkov et al. [2009a] using CPPI. It was shown in a recent study by Schanda et al. [2011b], that the CPPI sequence and the extracted dipolar coupling anisotropies were much more sensitive to rf inhomogeneity and miscalibration, as compared to REDOR. The anisotropies, determined by the REDOR sequence, were only affected by remote protons, which, however, are highly diluted, employing deuterated samples. Therefore, prospectively, the $^{1}H^{N}$,^{15}N order parameters of α-spectrin SH3 should be re-determined, using the REDOR sequence, to reduce the influence of rf inhomogeneity and miscalibration and to minimize systematic errors, when comparing the parameters to the $^{1}H\alpha$,$^{13}C\alpha$ backbone data. In principle, $^{1}H\alpha$,$^{13}C\alpha$ and $^{1}H^{N}$,^{15}N order parameters could be determined using the same sample, since high resolution and sensitivity can be obtained for both spectral regions, combining the here introduced RAP labeling and back-exchanging of amide protons (cf. Figure 4.1, page 163).

As shown by Chevelkov et al. [2010], experimentally determined $^{1}H^{N}$,^{15}N order parameters of α-spectrin SH3 in the solid- and solution-state displayed a remarkable agreement, indicating, that protein motions in the native, hydrated state are retained in the crystal. Only small deviations were obtained upon crystallization. Furthermore, they recorded a 50 ns MD trajectory for α-spectrin SH3, while taking account of the crystal lattice environment. A very good correlation between order parameters derived by experiment and from the MD trajectory, using equation 4.5, was obtained. Similarly, experimental $^{1}H\alpha$,$^{13}C\alpha$ order parameters, obtained here, could be validated, in the future, by comparison with simulated order parameters, estimated from the MD trajectory. Additionally, other complementary dynamics probes, as $^{13}C'$,$^{13}C\alpha$ [Fischer et al.,

1998], can be employed, for obtaining a detailed view of the underlying motional modes in the protein backbone.

In conclusion, the RAP labeling scheme was shown to enable the access to backbone order parameters of α-spectrin SH3. That way, ^{1}Hα,^{13}Cα backbone dipolar coupling anisotropies and asymmetries were obtained with high accuracy, using REDOR dephasing curves. The parameters were obtained using only one sample, a 15% RAP sample, which is a major advantage over current solution-state NMR approaches. For the determination of the Residual Dipolar Coupling (RDC), which is the solution-state NMR counterpart to the solid-state dipolar coupling anisotropy, accurate data from multiple, but orthogonal, alignment media are essential [Meiler et al., 2001, Tolman et al., 2001, Clore and Schwieters, 2004, Lange et al., 2008, Yao et al., 2008a]. Solid-state dipolar coupling anisotropies are sensitive to motions up to several microseconds [Chevelkov et al., 2010], on the other hand, solution-state RDCs can be used to probe motions faster than milliseconds, as the couplings are about three orders of magnitude smaller than in the solid-state. However, as shown recently, millisecond motions can be probed in the solid-state by relaxation dispersion experiments [Tollinger et al., 2012]. To yield a higher spectral resolution for the experimental determination of dipolar couplings, we showed, that the RAP-glycerol labeling can be employed.

4.1.4.2 Side chain and methyl dynamics

Similar to backbone motions (section 4.1.4.1, page 172), analytical functions for the interpretation of the model-independent generalized order parameter S^2 of side chains and methyls were introduced. In the Woessner model [Woessner, 1962a], the H,C bond vector of a methyl group freely diffuses about a fixed axis, which yields an order parameter

$$S^2_{\text{Woessner}} = \left[P_2\left(\cos\beta\right)\right]^2, \tag{4.6}$$

with β being the angle between the bond vector and the rotation axis and $P_2(\cos\beta)$ the second Legendre polynomial $\frac{1}{2}\left(3\cos^2\beta - 1\right)$ [Lipari and Szabo, 1982a,b]. The same equation was derived, assuming rotameric jumps of the methyl group among three equivalent sites.

For an ideal tetrahedral geometry, $\beta = 180^\circ - 109.5^\circ = 70.5^\circ$, yielding $S^2_{\text{Woessner}} = 0.111$. Therefore, the generalized order parameter for a methyl group is given by

$$S^2 = S^2_{\text{axis}} \times S^2_{\text{Woessner}} = 0.111 \times S^2_{\text{axis}}, \tag{4.7}$$

where S^2_{axis} is the order parameter for the motion of the rotation axis of the methyl group. As before, the generalized order parameter S^2 was determined as the ratio of the experimentally obtained dipolar coupling anisotropy to the rigid-limit value. The here employed rigid-limit ^{1}H,^{13}C bond length for methyl groups was 1.115 Å [Henry and Szabo, 1985, Ishima et al., 2001].

Furthermore, S^2_{axis} in equation 4.7 can be linked to a motional model, as the diffusion-in-the-cone model, described in the previous section (cf. Figure 4.5, page 176). Alternatively, the restricted diffusion model for side chain motions can be employed [London and Avitabile, 1978, Wittebort and Szabo, 1978, Lipari and Szabo, 1982b, Nicholson et al., 1992, Engelke and Ruterjans, 1998, Daley and Sykes, 2004], as rotations about the preceeding axis also reorientates the methyl rotation axis. For example, as depicted by the structural model in Figure 4.6D for valine, three different rotameric states are illustrated, which are yielded by χ_1 rotations about the Cα,Cβ bond vector. However, the sterical hindrance in context of a globular protein reduces the possible motional range, which is especially pronounced for longer chain amino acids [Hanssum and Ruterjans, 1983], as isoleucine and methionine. The order parameter for restricted diffusion, S^2_{rest}, was derived to be [Lipari and Szabo, 1982b]

$$S^2_{\text{rest}} = [P_2(\cos\beta_0)]^2 + \frac{3\sin^2\beta_0\sin^2\gamma_0}{\gamma_0^2}\left(\cos^2\beta_0 + \frac{1}{4}\sin^2\beta_0\cos^2\gamma_0\right), \tag{4.8}$$

where β_0 is the angle between the restricted reorientation axis and the methyl rotation axis, in the case of valine, between the Cα,Cβ and the Cβ,Cγ1/Cγ2 bond vector, respectively. $\pm\gamma_0$ defines the angular range of rotation about the restricted reorientation axis (Cα,Cβ for valine) and is the measure for side chain motion. β_0, however, is a fixed angle and equal to 70.5° for all methyl-bearing amino acids, except for methionine, where β_0 is 80°. For both cases, $\beta_0 = 70.5^\circ$ (black) and $\beta_0 = 80^\circ$ (red), S^2_{rest} was plotted as a function of γ_0 (Figure 4.6A).

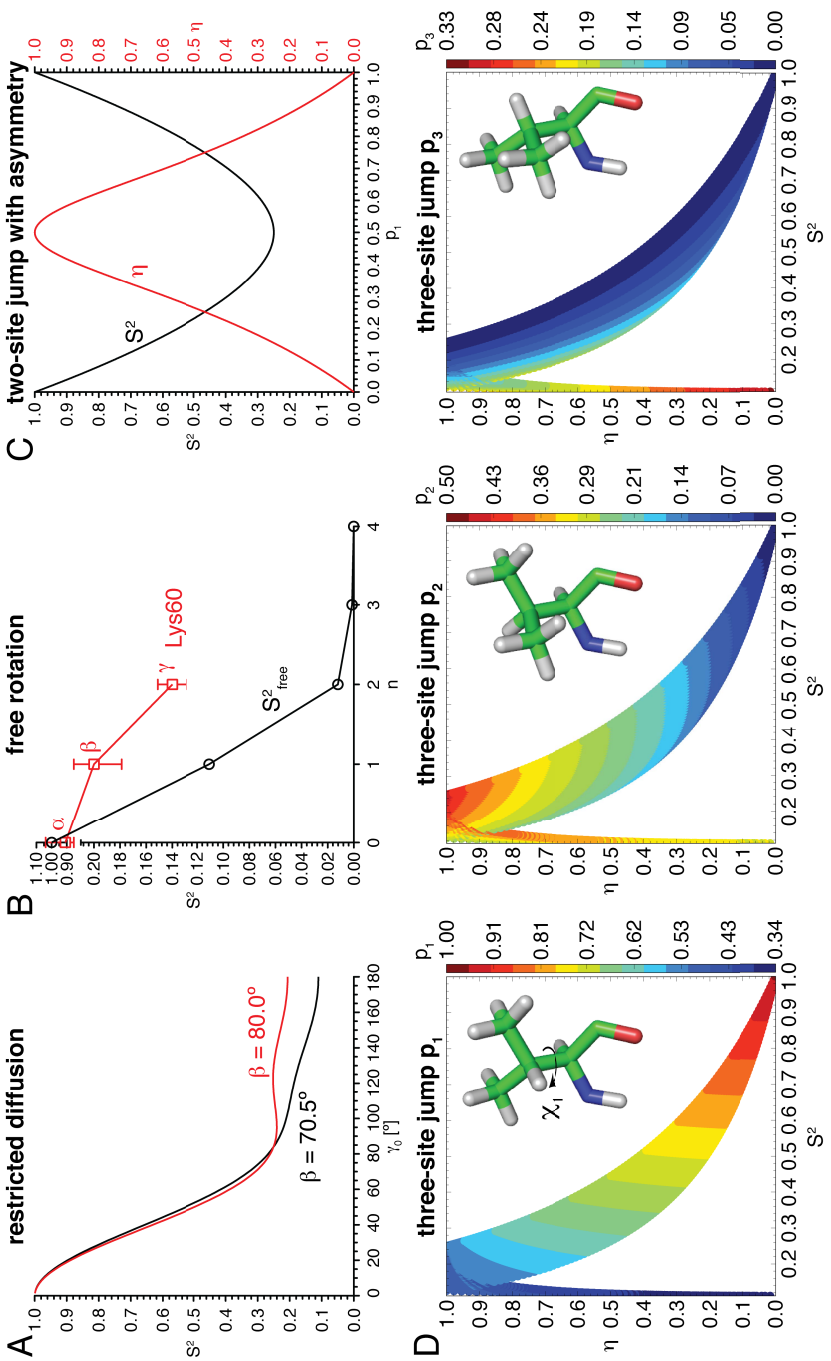

Figure 4.6: Motional models for side chain and methyl dynamics. (A) The squared order parameter, assuming the restricted diffusion model, was plotted as a function of the angular reorientation γ_0, using equation 4.8 (page 182). (B) The order parameter for a free rotation about the side chain $\chi_1, \chi_2, \chi_3, \chi_4$ dihedral angles of a lysine molecule is shown (equation 4.9, page 184). β was set to 70.5°, assuming ideal tetrahedral geometry. The red curve depicts the experimentally determined order parameter for Lys60 of α-spectrin SH3, using a 15% RAP sample. (C) Two- and (D) three-site jump model, which links the order parameter and the asymmetry to rotameric populations [Schanda et al., 2011a]. For structural illustration, three rotameric states of valine are shown. For (D) the conditions $p_1 \geq p_2 \geq p_3$ and $\sum_i p_i = 1$ were assumed. The analytical expressions for both models were kindly provided by Dr. Paul Schanda (IBS, Grenoble). The figures in (D) were adapted from Schanda et al. [2011a], however, here, the squared order parameter was plotted.

Free rotation corresponds to an angular range of $\gamma_0 = \pm 180°$, therefore, yielding the minimum value of the order parameter, $S^2_{\text{rest,min}} = [P_2(\cos\beta_0)]^2$ (0.111 and 0.207 for β_0 equal to 70.5° and 80°). As pointed out by Lipari and Szabo [1982b], this theoretical minimum of S^2_{rest} can be used as the definition of a lower limit of the generalized order parameter for restricted diffusion. That way, if the experimentally determined generalized order parameter S^2 is smaller than $S^2_{\text{rest,min}} \times S^2_{\text{Woessner}} = [P_2(\cos\beta_0)]^2 \times P_2(\cos\beta)$, then the restricted diffusion model is not sufficient to describe the present side chain dynamics.

In principle, if the reorientation about the successive side chain rotation axes are not sterically hindered, then the order parameter S^2_n for the nth carbon can be described by [Woessner, 1962a, Wallach, 1967, Lipari and Szabo, 1982b]

$$S^2_n = [P_2(\cos\beta)]^{2n}. \tag{4.9}$$

Figure 4.6B depicts the order parameter S^2_n as a function of the side chain position n, expected for a lysine residue, where $n = 0,1,2,3,4$ means the α, β, γ, δ and ϵ position, respectively. The order parameter decreases while moving along the side chain from the backbone to the terminal carbon. This trend was also observed in MD simulations [Levy et al., 1981b, Best et al., 2005].

In the present thesis, side chain and methyl motions were investigated by REDOR dephasing experiments, employing the RAP labeling scheme. A representative section of experimentally derived side chain and methyl order parameters and asymmetries is shown in Figure 4.7, next to the backbone values, where available. All employed values are given in the appendix (Table 4, page 220, Table 5, page 221, Table 6, page 223, Table 7, page 224).

The here depicted backbone and side chain dynamics parameters (Figure 4.7) were obtained, using a 15% RAP sample of α-spectrin SH3. For the methyl parameters two different samples were employed. For valine and leucine methyl parameters, a selectively Val/Leu methyl-labeled $^{13}CD_2H$ sample of α-spectrin SH3 was used, due to the high sensitivity, while the alanine and threonine methyl parameters shown in Figure 4.7 were determined, employing a 5% RAP sample. It should be noted, that, as compared to selectively methyl labeled samples, the RAP labeling enables the access to all aliphatic sites, including all types of methyl groups (Alaβ, Ileγ2, Ileδ1, Leuδ1/2, Metϵ, Thrγ2, Valγ1/2, cf. Table 7, page 224).

In principle, the methyl proton concentration for the $^{13}CD_2H$ sample was expected to be higher than for the 5% RAP sample, especially within the hydrophobic protein core, which typically shows the highest methyl density. In the $^{13}CD_2H$ sample either one of the methyl groups of valine and leucine residues is protonated, yielding an average proton concentration of about 17% for any Valγ or Leuδ moiety (according to equation 3.6, page 37), however, in a 5% RAP labeled sample, the methyl concentration was shown to be on the order of 1-2% (cf. Table 3.2, page 38). As reported recently [Schanda et al., 2011a], the REDOR sequence is particularly sensitive to remote protons (*vide supra*). Therefore, we compared order parameters and asymmetries obtained from the $^{13}CD_2H$ sample to the 5% RAP sample of α-spectrin SH3, and yielded the same values within the experimental error. In Figure 4.7, instead of the generalized order parameter, the squared order parameter of the methyl symmetry axis, S^2_{axis}, is plotted, according to equation 4.7 (page 182).

Alanine residues are particularly interesting in terms of dynamics, as the methyl group directly relates to backbone motions, since it is directly bonded to the Cα atom [Henry et al., 1986]. In this manner, the spectroscopic advantages of methyl groups, as high sensitivity and resolution, can be exploited to probe the backbone dynamics with improved experimental accuracy and precision. As shown in Figure 4.7, the order parameter for the backbone Ala-^{13}Cα and the adjacent ^{13}Cβ are, as expected, rather similar, for all alanine residues. The slightly smaller order parameter for the ^{1}Hβ,^{13}Cβ dipole tensor of alanine is indicative of additional librational motion of the ^{13}Cα,^{13}Cβ methyl rotation axis. Except for Val23, Val46 and Leu31, all methyl groups in Figure 4.7 show small motional amplitudes. This is also hinted by small asymmetry parameters.

The asymmetry parameter contains information about the anisotropy of the side chain motion on the sub-microsecond timescale. Analytical equations to link the methyl order and asymmetry parameter to a motional model were given by Schanda et al. [2011a]. To determine an expression for rotameric populations as a function of dipole anisotropy and asymmetry, two (three) dipolar tensors were weighted by p_1 and $p_2 = 1 - p_1$ (p_1, p_2 and $p_3 = 1 - p_1 - p_2$) and rotated by 120° to each other to simulate a two-site (three-site) jump scenario. Prior to rotation, all tensors were tilted by the tetrahedral angle 109.5°. The principal components (eigenvalues) of

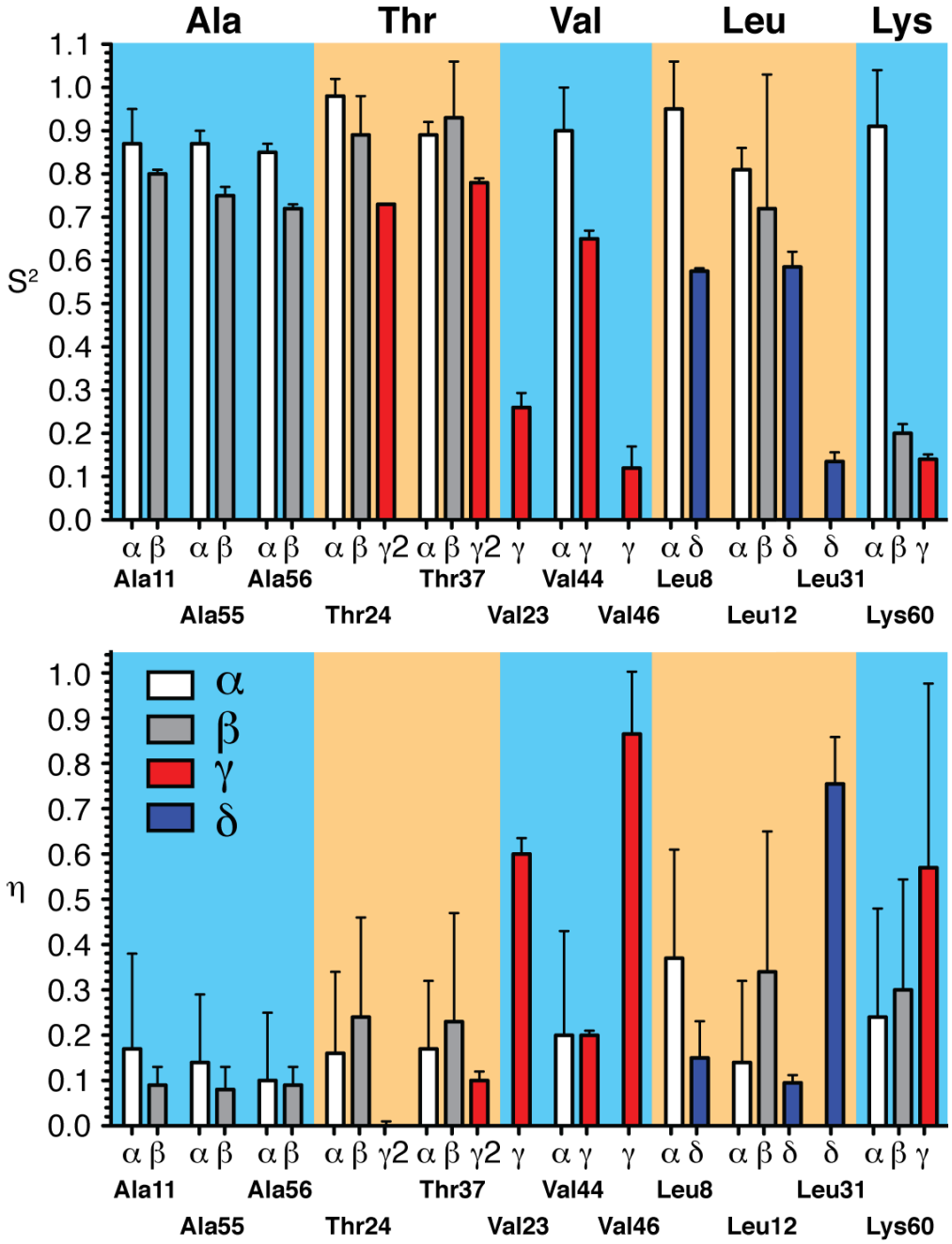

Figure 4.7: Experimentally derived ^{1}H,^{13}C order parameters and asymmetries for backbone, side chain and methyl resonances of α-spectrin SH3. For the backbone and side chain dynamics parameters, a 15% RAP sample was employed. The parameters for valine and leucine methyl groups were obtained from a selectively Val/Leu methyl-labeled $^{13}CD_2H$ sample of α-spectrin SH3, while alanine and threonine parameters were obtained, using a 5% RAP sample, respectively. Valγ1/2, Leuδ1/2, Lysβ1/2, Lysγ1/2 S^2 and η values were averaged. The error bar for the average value $\bar{x}$ was determined as $\Delta\bar{x} = \sigma_x + \frac{1}{2}\sqrt{(\Delta x_1)^2 + (\Delta x_2)^2}$, where σ_x is the standard deviation of the values x_1 and x_2 and Δx_1 and Δx_2 are the experimental uncertainties. For methyl resonances, the squared order parameter of the methyl rotation axis, S^2_{axis}, is plotted, according to equation 4.7 (page 182). A ^{1}H,^{13}C methyl bond length of 1.115 Å [Henry and Szabo, 1985, Ishima et al., 2001] was assumed. All employed values are given in the appendix (page 215).

the resulting tensor were ordered by the convention $|D_{yy}| \leq |D_{xx}| \leq |D_{zz}|$. The order parameter S and asymmetry η were finally determined as

$$S = D_{zz} - \frac{1}{3}\mathrm{Tr}(D) \tag{4.10}$$

$$\eta = \frac{D_{yy} - D_{xx}}{D_{zz}}, \tag{4.11}$$

with the trace $\mathrm{Tr}(D) = D_{xx} + D_{yy} + D_{zz}$.

For the two-site jump model, the squared order parameter and the asymmetry were plotted as a function of the population of one of the rotamers (Figure 4.6C, page 183). For equal populations, the squared order parameter had its minimum at a value of 0.25, which was also yielded in the backbone jump model (cf. Figure 4.5B), while the asymmetry value was maximal ($\eta = 1$). This clearly shows, that changes in the populations have a significant influence on the experimentally determined order parameter and asymmetry, and vice versa.

In the three-site jump model, shown in Figure 4.6D, the maximum of the asymmetry parameter ($\eta = 1$) was yielded at equal populations, $p_1 = p_2 = p_3 = \frac{1}{3}$, while the minimum of the order parameter, $S^2 = 0.111$, was consistent with the result from the Woessner model (cf. equation 4.6, page 181) [Woessner, 1962a].

In general, specific rotameric conformations are more likely than others, which is a result of different rotational energy barriers for particular rotameric states. Typically, for leucine and threonine side chains, rotations about two dihedral angles, χ_1 and χ_2, are possible. Jumps about two or more axes cannot be unambiguously disentangled using only the order parameter and the asymmetry of the methyl groups. However, specifically for leucine and threonine, only two rotameric states are primarily populated [Lovell et al., 2000, Schanda et al., 2011a]. This could be also derived from the MD trajectory for α-spectrin SH3 [Chevelkov et al., 2007c, Xue et al., 2007]. Therefore, to first order approximation, the two-site jump model was expected to be sufficient, to describe the leucine and threonine motion.

Except for Leu61 (cf. Table 7, page 224) and, especially, Leu31 (Figure 4.7), no substantial methyl group mobility for the leucine residues in α-spectrin SH3 were observed. Leu31δ1/2 showed a very low squared order parameter, $S^2 = 0.14$, averaged for both methyls. It should be

noted, that this value falls below the lower limit of 0.25, postulated by the two-site jump model (Figure 4.6C, page 183). This indicates, that additional librational motions of the methyl rotation axes were present. In the crystal structure of α-spectrin SH3, accordingly, two rotamer conformations were apparent for Leu31, clearly showing a displacement of the Cβ,Cγ axis (Figure 3.35B, page 87). Considering only the averaged asymmetry value for Leu31δ1/2 ($\eta = 0.76$), population levels of 64% and 36% were yielded, respectively. In the future, these experimentally derived population levels will be compared to values, extracted from MD simulations, with long trajectory times of ≥ 1 µs to take account of the dynamic timescale, which is affecting the dipolar coupling tensor. In addition, any type of displacement of the methyl axis, relative to a fixed molecular frame, can be detected by the MD trajectory.

Interestingly, the Leu61δ1 methyl group displayed a significantly reduced squared order parameter ($S^2 = 0.37$), but an unexpectedly small asymmetry ($\eta = 0.09$), pointing to population levels of 6% and 94%, respectively. It seems that, librational motions of the methyl axes are dominant, while rotameric jumps have a negligible influence. Again, comparison to MD data might allow for a more detailed analysis of the side chain mobility. The threonine methyls in α-spectrin SH3 are rather rigid on the sub-µs timescale (Figure 4.7, page 186). Only Thr4γ2 was highly dynamic ($S^2 = 0.01$), which is expected, as it is located in the flexible N-terminus.

For valine methyl groups three different rotameric states are expected, gauche(-) ($\chi_1 = -60°$), gauche(+) ($\chi_1 = 60°$) and trans ($\chi_1 = 180°$), which can be interconverted by 120° rotations around χ_1 [Lovell et al., 2000, Schanda et al., 2011a]. We only detected significant dynamics for Val23 and Val46 (Figure 4.7, page 186), as well as for Val58 (Table 7, page 224). The dynamic property of Val23 can also be observed by ^{2}H line shape analysis, as reported earlier [Hologne et al., 2006, 2005]. Even though a slightly faster timescale is probed by ^{2}H, we obtained the same asymmetry parameters, using REDOR dipolar dephasing curves. However, the methyl groups of Val46 could not be analyzed by ^{2}H experiments, as Val46 is too mobile to yield sufficient sensitivity, during the ^{2}H,^{13}C cross polarization (CP) magnetization transfer. On the contrary, scalar INEPT-based transfers were used here for the REDOR experiments, which particularly yields high sensitivity for mobile residues. It should be noted, that scalar magnetization transfer experiments, which require long coherence life times, were enabled by deuteration,

employing the RAP labeling scheme. Alternatively, high-power decoupling could be employed, using uniformly protonated samples [Tian et al., 2009, Tang et al., 2010], which, however, still yields shorter apparent T_2 times, as compared to deuterated samples [Linser et al., 2008, 2010, 2011b], and might damage the probe, as well as the sample, due to heating effects induced by the high-power rf decoupling.

In principle, two rotameric states for Val23 and Val46 are visible in the X-ray strucutre of α-spectrin SH3 (Figure 3.35B, page 87). For Val58, no rotamers were apparent in the X-ray structure, as the population of the second rotameric state was too low. However, the MD trajectory revealed the presence of two populated states for Val58 (80% and 20%, Figure 3.35C, page 87). The REDOR experiments yielded a significant asymmetry parameter of $\eta = 0.20$, which corresponds to similar population levels (87% and 13%).

Val23 and Val46 showed three rotameric states in the MD trajectory (Figure 3.35B, page 87). Applying the three-site jump model (Figure 4.6D, page 183) yielded population levels of 62%, 27% and 11% for Val23 and 47%, 26% and 26% for Val46, respectively, using the experimentally determined order and asymmetry parameters (Figure 4.7, page 186). For Val46 the experimental population levels differ from the MD derived values (85%, 10%, 3%). This might be attributed to insufficient sampling of the MD trajectory, as it was only recorded for 91 ns and, as mentioned before (*vide supra*), Val46 is most probably undergoing slow dynamics on the µs time scale, since it is not detectable by CP experiments. However, the rotameric populations extracted from the MD trajectory of Val23 matched the experimental parameters rather well (62%, 27%, 11%). Therefore, we back-calculated a REDOR dephasing curve, using the dihedral angles and rotameric populations from the MD simulation, which yielded a good agreement to the experimental curve. The agreement between simulation and experiment might be improved by a longer trajectory and incorporation of librational motions of the methyl axes. If all types of motions are considered, then ideally, the simulation can be performed assuming a fixed value for the dipolar coupling anisotropy of $\delta_{\text{rigid}} \times |P_2(\cos\beta)| = \frac{1}{3}\delta_{\text{rigid}}$ (for ideal tetrahedral geometry with $\beta = 70.5°$).

The distribution of Alaβ, Thrγ2, Valγ1/2, Leuδ1/2 and Metϵ methyl order parameters, S^2_{axis} (equation 4.7, page 182), is shown in Figure 4.8. As stated above, the order parameter decreases

for longer side chains, indicating an enhanced mobility. A similar distribution of methyl order parameters was reported by Best et al. [2004], employing order parameters derived from MD simulations for 18 different proteins.

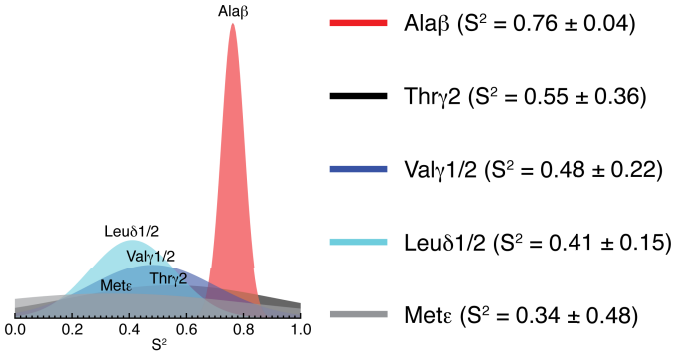

Figure 4.8: Distribution of methyl S^2_{axis} order parameters for α-spectrin SH3. Normal distributions for Alaβ, Thrγ2, Valγ1/2, Leuδ1/2 and Metε were plotted, using S^2_{axis} average values and standard deviations, respectively. Here, the order parameters obtained for the 5% RAP sample were employed (Table 7, page 224).

Order and asymmetry parameters were also determined for non-methyl side chains, as for Lys60, shown in Figure 4.7 (page 186). The order parameter decreases, while the asymmetry increases, as more rotameric states become populated. If the side chain rotations are not sterically hindered, then a decay of the squared order parameter S^2 by a factor of $[P_2(\cos\beta)]^2 = 0.111$ ($\beta = 70.5°$) is expected, moving along the side chain from the backbone to the terminal carbon (equation 4.9, page 184). In principle, experimentally determined order parameters, which are higher than these limiting values, indicate sterical hindrance of the side chain. In Figure 4.6B (page 183), the order parameters for Lys60 were plotted, next to the limiting values. Even though the order parameter significantly decreases along the side chain, the sterical hindrance of free diffusion becomes apparent, which was also reported earlier for this residue [Xue et al., 2007]. Determination of order parameters and asymmetries as a function of temperature will also allow to estimate activation energies for side chain rotations [Lee and Wand, 2001, Lee et al., 2002, Latanowicz, 2005, Igumenova et al., 2006, Song et al., 2007, Xue et al., 2007]. However, to determine a more detailed view of the side chain motional modes, in the future, order parameters and asymmetries along the chain will be combined to reduce the degeneracy of the motional interpretation, accompanied by analysis of single dipolar bond vectors. For that purpose, the here introduced RAP labeling scheme is superior to earlier reported labeling schemes in the

solid-state, as it enables the access to the dynamics parameters for all aliphatic sites, using one sample.

In general, side chain order parameters can also be obtained computationally by MD simulations [Hu et al., 2005, Watanabe et al., 2013] or experimentally by solution-state NMR, using chemical shifts [Hansen and Kay, 2011], scalar couplings [Chou et al., 2003, Kraszni et al., 2004, Tugarinov and Kay, 2004b] or RDCs [Mittermaier and Kay, 2001], respectively. These techniques could be applied as well to α-spectrin SH3. However, generally, these approaches require either high resolution structures or soluble proteins. Both are rather limited for large macromolecular complexes or insoluble, but biologically relevant, aggregates. These types of systems are accessible, however, by solid-state NMR spectroscopy. The here introduced solid-state NMR approaches for determination of protein dynamics were validated with the model system α-spectrin SH3 and will be applied in the future to other biological systems, as amyloid fibrils (cf. section 4.1.3, page 168).

4.1.5 Fast time scale motions probed by T_1 relaxation experiments in the solid-state

Spin relaxation is particularly sensitive to ps-ns motions, which can be probed by T_1 relaxation experiments [Kuhlmann et al., 1970, Allerhand et al., 1971, Kay et al., 1989, Mittermaier and Kay, 2006]. Nuclear relaxation is essentially induced by the motional modulation of the dipolar coupling to the directly bound proton and by Chemical Shift Anisotropy (CSA). The T_1 times are related to the ^{1}H,X (X = ^{13}C, ^{15}N) dipolar coupling anisotropy d, the CSA c, and the spectral density function $J_m(\omega)$ (cf. equation 3.31, page 97) [Torchia and Szabo, 1982, Kay et al., 1989, Abragam, 1961].

The CSA is determined by the difference of the parallel and perpendicular components of the chemical shift tensor and accounts for about 30-50% of ^{15}N backbone T_1 relaxation, whereas insignificant CSA contributions in the range of 2-7% are expected for ^{13}Cα at currently available external magnetic fields (Figure 3.40A, page 98). For the analysis of backbone T_1 relaxation data, in principle, the CSA for all sites must be known, since the CSA varies strongly along the primary sequence [Tjandra and Bax, 1997a, Fushman et al., 1998, Wylie et al., 2009, 2011].

However, due to its small contribution to $^{13}C\alpha$ T_1 relaxation at currently available B_0 fields, CSA can be safely neglected and elaborate experimental approaches can be omitted. This indicates a methodological advantage of studying $^{13}C\alpha$ over ^{15}N backbone T_1 relaxation.

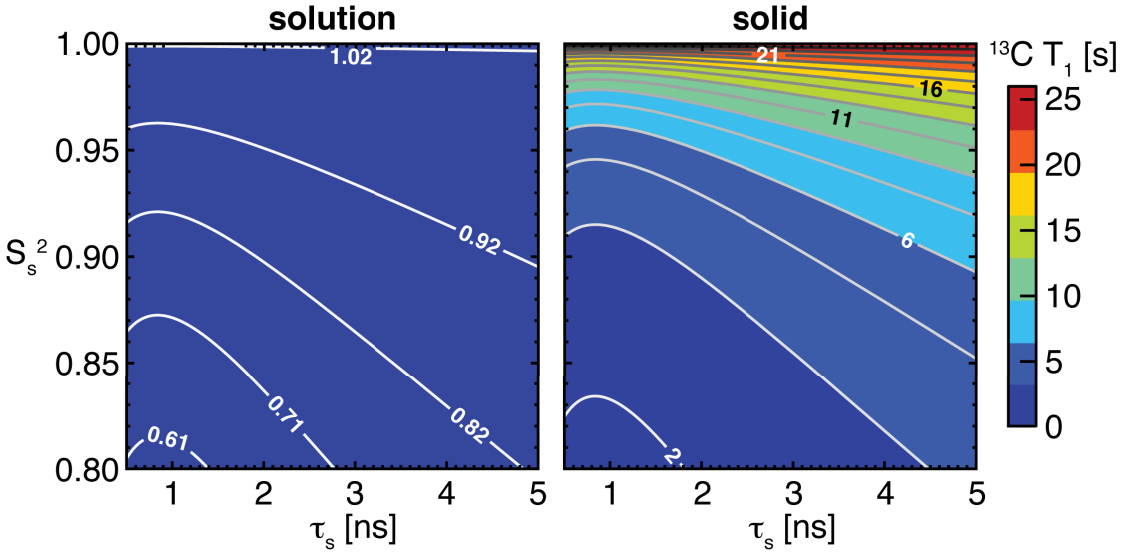

Figure 4.9: Comparison of T_1 relaxation for backbone resonances in solution and in the solid-state, employing equations $\frac{1}{T_{1,X}} = \frac{d^2}{10}[J_0(\omega_H - \omega_X) + 3J_1(\omega_X) + 6J_2(\omega_H + \omega_X)] + \frac{2}{15}c^2 J_1(\omega_X)$ (with $X = ^{13}C$, ^{15}N) and $J(\omega) = S^2 \frac{\tau_r}{1+(\omega\tau_r)^2} + (1 - S_f^2)\frac{\tau'_f}{1+(\omega\tau'_f)^2} + S_f^2(1 - S_s^2)\frac{\tau'_s}{1+(\omega\tau'_s)^2}$ with $\frac{1}{\tau'_f} = \frac{1}{\tau_f} + \frac{1}{\tau_r}$ and $\frac{1}{\tau'_s} = \frac{1}{\tau_s} + \frac{1}{\tau_r}$ [Kay et al., 1989, Clore et al., 1990b]. S^2, τ_r and τ_f were set to 0.8, 6.0 ns and 0.01 ns, respectively, assuming an external magnetic field of 14.1 T (^{1}H Larmor frequency of 600 MHz). Solution- (left) and solid-state (right) $^{13}C\alpha$ T_1 times were plotted as a function of the slow correlation time and order parameter, respectively. Clearly, very small variations were obtained for solution-state T_1 times, whereas solid-state T_1 times can be very different depending on the parameters for fast and slow local motions.

The most established approach to analytically link motional amplitudes and correlation times with spin relaxation was formulated by Lipari and Szabo [Brown, 1982, Lipari and Szabo, 1982a,b, Brown, 1984], which is referred to as the Model-Free Formalism (MFF). It was further extended by Clore et al. [1990b] to account for two time scales of internal motions. The extended model-free approach was employed in the present thesis. Further details are discussed in the respective section (3.5, page 97).

In the solid-state, molecular tumbling is absent and, therefore, relaxation is only determined by internal dynamics, as opposed to proteins in solution, in which significant contributions to relaxation originate from molecular tumbling (Figure 3.40B, page 98). As a consequence and

as illustrated in Figure 4.9, T_1 times vary only marginally in solution, whereas variations of roughly up to two orders of magnitude can be found in the solid-state. This result encouraged us, to determine T_1 relaxation times in the solid-state, as it is much more sensitive to internal dynamics, compared to molecules in solution.

In order to theoretically interpret the $^{13}C\alpha$ T_1 times in the solid-state, two major obstacles have to be overcome. One is the orientational dependency of the spectral density function $J_m(\omega)$ and the other ^{13}C,^{13}C spin diffusion, promoted by a strong ^{1}H,^{1}H dipolar coupled spin bath [Krushelnitsky et al., 2006, Giraud et al., 2007, Lewandowski et al., 2010]. As discussed by Torchia and Szabo [1982], the spectral density function in the solid-state is dependent on the crystallite orientations and, thus, magic angle spinning must be taken into account. That way, T_1 times in the solid-state become orientation dependent and yield, in principal, a multi-exponentially decaying relaxation function. However, it was suggested [Torchia and Szabo, 1982], to fit the initial slope by a mono-exponential function, which directly provides orientation-independent powder and MAS averaged T_1 times, similar to solution-state. More rigorous treatments of relaxation in the solid-state, performing explicit calculations, yield only small deviations from the initial slope approximation [Lipari and Szabo, 1981, Giraud et al., 2005]. Furthermore, it was shown, that for ^{15}N backbone order parameters with S^2 exceeding 0.7, the diffusion-in-a-cone approach, using the "explicit average sum" treatment [Giraud et al., 2005], displays marginal differences to relaxation times derived by a model-free treatment, respectively [Schanda et al., 2010]. Therefore, the model-free treatment remains valid for interpretation of solid-state relaxation parameters [Skrynnikov, 2007, Chevelkov et al., 2009b, Schanda et al., 2010].

In contrast to relaxation, which is based on motional modulations of dipolar, CSA or quadrupolar interactions at the Larmor frequency of the respective spin, spin diffusion is a dipole-mediated coherent mechanism. Both, however, affect the measured T_1 times. To obtain incoherent, solely dynamically determined T_1 times, fast spinning at the magic angle was proposed [Lewandowski et al., 2010], since spin diffusion scales inversely with the MAS frequency [Kubo and Mcdowell, 1988, Lange et al., 2003]. However, spinning only at 60 kHz is still not sufficient to eliminate spin diffusion in uniformly protonated and ^{13}C labeled proteins. This was demonstrated for the uniformly protonated GB1 protein by recording ^{13}C,^{13}C PDSD spectra

[Lewandowski et al., 2010], which showed numerous cross peaks within the aliphatic region, clearly revealing the presence of spin diffusion at 60 kHz spinning. In addition to fast spinning, deuteration can be employed, which chemically suppresses spin diffusion [Krushelnitsky et al., 2006, Giraud et al., 2007, Lewandowski et al., 2010]. The application of deuteration to improve spectral sensitivity and resolution was discussed previously (section 4.1.1, page 161 and section 1.2, page 7).

A further potential mechanism, distorting experimentally observed T_1 relaxation times, is Paramagnetic Relaxation Enhancement (PRE), induced by paramagnetic impurities in the crystal lattice. Hereby, the dipolar interaction between unpaired electrons and the nuclear spin severely reduces the nuclear T_1 relaxation times [Rollin and Hatton, 1948, Bloembergen, 1949, Linser et al., 2007, Clore and Iwahara, 2009, Wickramasinghe et al., 2009, Panich and Furman, 2012]. For example, for a CaF_2 crystal the theoretical and experimental ^{19}F T_1 times deviate by a factor of about 10^6, owing to PRE by paramagnetic impurities in the crystal [Bloembergen, 1949]. However, in the present study, the α-spectrin SH3 protein was crystallized from solvent. Thereby, the potential paramagnetic impurities were dissolved by water molecules. Rapid tumbling of the solubilized paramagnetic atoms reduces their PRE in the microcrystals. That way, the PRE effect in α-spectrin SH3 microcrystals was assumed to be on a similar order as for solvated α-spectrin SH3. This assumption is supported by a recent study, which revealed a high similarity [Agarwal et al., 2008], when comparing α-spectrin SH3 ^{13}C methyl T_1 times in the solid- and the solution-state, respectively. As Molecular Dynamics (MD) simulation is a complementary tool for the determination of protein dynamics, experimental T_1 relaxation times of soluble proteins were compared to relaxation times, derived from MD trajectories [Prompers and Bruschweiler, 2002, Chen et al., 2004, Nederveen and Bonvin, 2005, Showalter and Brüschweiler, 2007]. In general, a good correlation was obtained, which further confirms, that the influence of paramagnetic impurities can be neglected for the present study.

The herein introduced Reduced Adjoining Protonation (RAP) labeling scheme yields uniformly ^{13}C labeled proteins in a deuterated matrix and is, therefore, ideally suited for determination of aliphatic ^{13}C T_1 times of a protein and at the same time facilitates the application of ^1H detection schemes to improve the experimental sensitivity. In contrast to ^{15}N spectroscopy,

which primarily targets the amide backbone, the aliphatic spectrum includes backbone as well as side chain resonances.

The backbone $^{13}C\alpha$ T_1 times of all samples, employed in the thesis, are shown in Figure 4.10A-F. In general, the T_1 times increase with higher levels of deuteration, sparsely ^{13}C labeling and fast magic-angle spinning. Comparing Figure 4.10D with Figure 4.10E reveals, that at 50 kHz spin diffusion was still not entirely suppressed using the 15% RAP sample. This observation is supported by the detection of cross-peaks in the respective PDSD spectrum (Figure 3.47C, page 113). Higher levels of protonation and lower MAS frequencies, as for the 25% RAP sample spun at 24 kHz (Figure 4.10F), almost unified the ^{13}C backbone T_1 values, which hampers their interpretation in terms of dynamics. These results show with a high evidence, that the previously proposed approach of obtaining ^{13}C T_1 times at 60 kHz, using uniformly protonated protein samples [Lewandowski et al., 2010] cannot be employed to quantify protein dynamics, as the relaxation data is severely perturbed by coherent effects. Even the highly proton diluted 15% RAP sample displayed significant spin diffusion at 50 kHz MAS and mixing times in the range of the T_1 relaxation times. This indicated, that, next to protons, spin dilution of carbons was required to reduce ^{13}C,^{13}C spin diffusion and render the T_1 decay mono-exponential (cf. Figure 3.45, page 111, Figure 3.46, page 112, Figure 3.48, page 116). Therefore, the 10% RAP-glycerol sample was used for the quantification of dynamics throughout the thesis.

Comparing the ^{13}C T_1 values for the 10% RAP-glycerol sample at 50 kHz MAS, recorded at an external magnetic field of 500 MHz (11.7 T) and 850 MHz (20.0 T), revealed, that on average the T_1 values at the higher field were significantly longer. The average ^{13}C T_1 time at 500 MHz and 850 MHz were 11.0 s and 17.9 s, respectively. For a more detailed view, theoretical ^{13}C T_1 times were calculated as a function of the fast motional correlation time, τ_f, using equation 3.51 (page 102). Setting the slow motion order parameter S_s^2 to 1.0, showed almost no difference in the calculated T_1 values at both employed fields (500 MHz, black, solid, and 850 MHz, red, dashed), while changing τ_f from 1 ps to 100 ps (Figure 4.10G). This indicated, that the T_1 contribution from the fast time scale of motion within its typical time scale is very small. Fast correlation times are usually shorter than 50 ps (vertical line in Figure 4.10G) and, in this range, negligible [Clore et al., 1990b,a, Stone et al., 1992, Barchi et al., 1994].

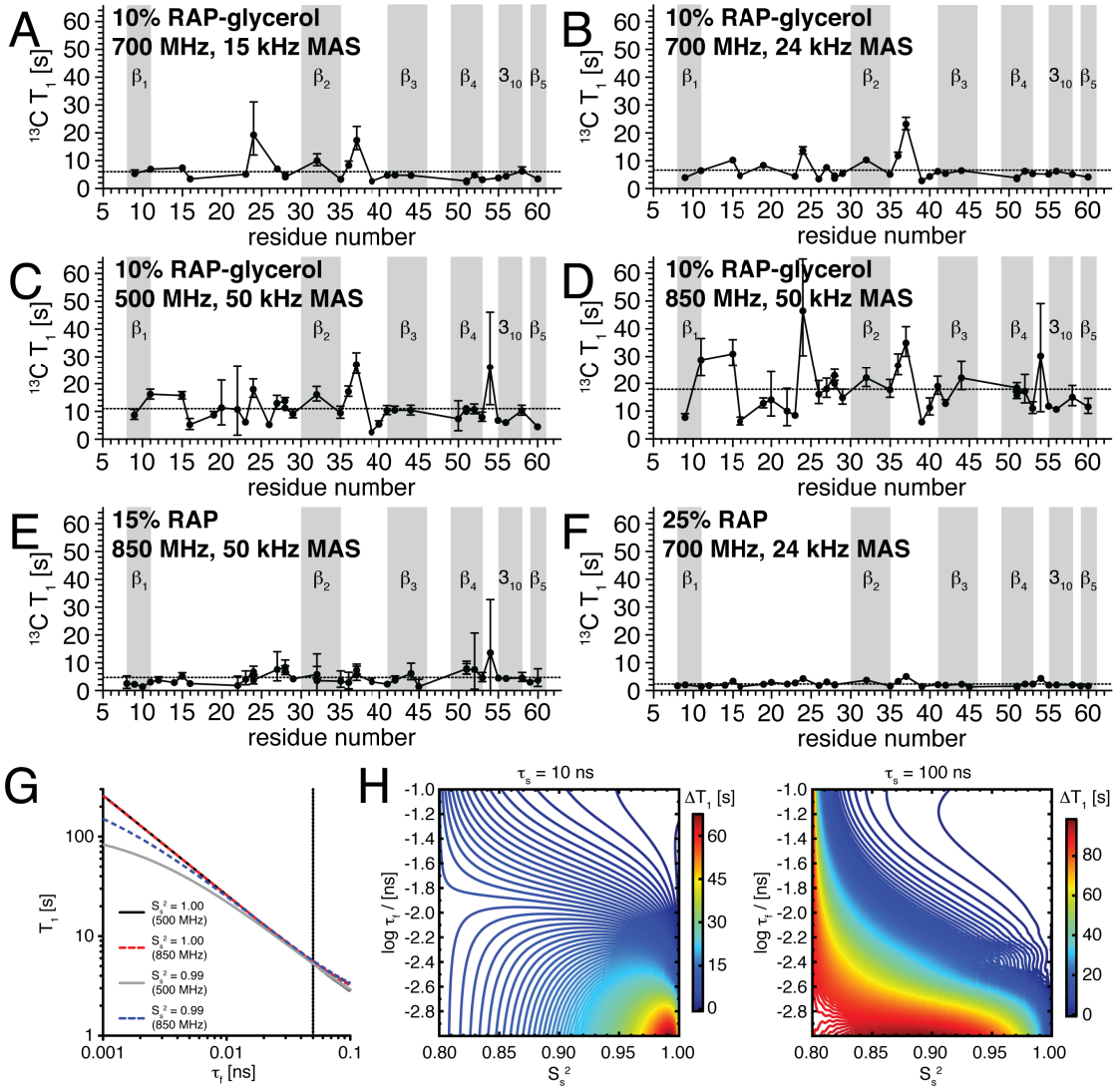

Figure 4.10: Backbone ^{13}Cα T_1 times for a 10% RAP-glycerol, 15% and 25% RAP-glucose sample of α-spectrin SH3 at an external magnetic field of 11.7 T, 16.4 T, 20.0 T (500 MHz, 700 MHz, 850 MHz) and a MAS frequency of 15 kHz, 24 kHz and 50 kHz, respectively. The plots (A-F) were ordered by the employed ^{1}H concentration and the MAS frequency (values given in the respective figure title). The T_1 errors were estimated from Monte Carlo simulations, setting the measuring uncertainty of the intensities to two times the standard deviation of the noise. The dashed horizontal line depicts the average T_1 value over all residues. The secondary structure elements are indicated by gray bars. In (G), the ^{13}C T_1 time was plotted, as a function of the fast motional correlation time τ_f. Two different external magnetic fields were employed, with ^{1}H Larmor frequencies of 500 MHz (11.7 T) and 850 MHz (20.0 T), as well as two different values for the squared slow motion order parameter S_s^2, 1.00 and 0.99, respectively. The vertical line depicts the τ_f value at 50 ps. The slow motional correlation time, τ_s, was set to 10 ns and the generalized order parameter, S^2, to 0.8. In (H) the T_1 difference, $\Delta T_1 = T_1^{20.0\,\mathrm{T}} \quad T_1^{11.7\,\mathrm{T}}$, was plotted as a function of the slow order parameter and the fast correlation time for two values of τ_s, 10 ns (left) and 100 ns (right), respectively. For (G-H) the spectral density function in the solid-state, given by equation 3.51 (page 102), was assumed [Chevelkov et al., 2009b].

The difference of T_1 at both fields, $\Delta T_1 = T_1^{20.0\,\mathrm{T}} - T_1^{11.7\,\mathrm{T}}$, might be employed as an indicator of slow motions, when the fast correlation time τ_f is smaller than 50 ps. In the case of absence of slow motions ($S_s^2 = 1.0$), ΔT_1 is equal to zero. This is the case, for example, for the ^{1}Hα,^{13}Cα backbone dynamics of Val9 in α-spectrin SH3, which showed a difference $\Delta T_1^{^{13}\mathrm{C}}$ of -0.87 s and yielded a high slow motion order parameter ($S_s^2 = 0.991$) (cf. Table 11, page 232). This was also validated by the ^{1}H$^{\mathrm{N}}$,^{15}N backbone dynamics data of Val9, which yielded $S_s^2 = 0.968$, however, $\Delta T_1^{^{15}\mathrm{N}}$ was equal to 15.21 s, which is unexpectedly high (cf. Table 12, page 233). Looking at theoretical curves showed, that slightly increasing the amplitude of the slow motion by setting $S_s^2 = 0.99$ yields significant T_1 differences ($\Delta T_1 > 0$, Figure 4.10G, 500 MHz, gray, solid, and 850 MHz, blue, dashed). Therefore, a quantification of the amount of slow dynamics, only relying on the difference of the T_1 values, is rather limited, as variations of both correlation times induce large changes in ΔT_1 (Figure 4.10H).

Instead, we performed a grid search over the physically meaningful parameter space for S_s^2, τ_s and τ_f within the extended Model-Free Formalism [Clore et al., 1990b] (described in section 3.5.3.1, page 115), employing the here obtained ^{1}H,^{13}C T_1 times and order parameters, using α-spectrin SH3 RAP samples. For comparison, additionally, ^{1}H$^{\mathrm{N}}$,^{15}N backbone dynamics parameters were determined, using published experimental values [Chevelkov et al., 2007a, 2008, 2009a,b]. The uncertainties of the parameters were estimated by Monte Carlo simulations.

The results for both backbone probes are summarized in Figure 3.55 (page 128). Large error bars were yielded for both ^{1}Hα,^{13}Cα and ^{1}H$^{\mathrm{N}}$,^{15}N backbone, especially for the correlation times, which indicates, that they are less affected by T_1 in comparison to order parameters. Furthermore, uncertainties of multiple experimental variables, as T_1, generalized order parameter and η (only for ^{1}H$^{\mathrm{N}}$,^{15}N), accumulate in the fitted dynamics parameters. Therefore, the comparison of ^{1}Hα,^{13}Cα and ^{1}H$^{\mathrm{N}}$,^{15}N dynamics will be based on the best fit, instead of the Monte Carlo average values.

In Figure 4.11A-C (left column), the best fit values for S_s^2, τ_s and τ_f were plotted as a function of the residue number of α-spectrin SH3, while error bars were omitted for the sake of clarity. As the availability of dynamics parameters for the same residue in both datasets (^{1}Hα,^{13}Cα and ^{1}H$^{\mathrm{N}}$,^{15}N) was limited, the trend of the dynamics parameters along the protein primary sequence

Table 4.1: Overview of the generalized order parameter, S^2 (cf. Figure 4.4, page 175), and the fitted dynamics parameters, S_s^2, τ_s and τ_f, for the ^{1}Hα,^{13}Cα and ^{1}H^N,^{15}N backbone probes of α-spectrin SH3. $\bar{x}$ and $\tilde{x}$ are the mean and the median of all employed best fit values (cf. appendix, Table 11, page 232 and Table 12, page 233), respectively.

		^{1}Hα,^{13}Cα	^{1}H^N,^{15}N
S^2	$\bar{x}$	0.87 ± 0.06	0.78 ± 0.09
	$\tilde{x}$	0.87	0.81
S_s^2	$\bar{x}$	0.89 ± 0.05	0.88 ± 0.11
	$\tilde{x}$	0.88	0.91
τ_s [ns]	$\bar{x}$	68 ± 32	41 ± 42
	$\tilde{x}$	69	28
τ_f [ns]	$\bar{x}$	0.665 ± 0.753	0.905 ± 2.778
	$\tilde{x}$	0.466	0.025

was rather compared, which in turn showed common characteristics. Similar trends for both backbone probes were obtained, especially for the slow order parameter (Figure 4.11A) and slow correlation time (B), while the fast correlation time displayed a number of deviations (C). Larger variations of the fast correlation times were, however, expected, as they exhibit a broad convergence profile due to their small contribution to the T_1 time for motions on the respective time scale (Figure 4.10H).

The average S_s^2, τ_s and τ_f values for the ^{1}Hα,^{13}Cα and ^{1}H^N,^{15}N backbone of α-spectrin SH3 are given in Table 4.1. In general, the dynamics parameters for the ^{1}H^N,^{15}N backbone pointed towards faster motions, compared to ^{1}Hα,^{13}Cα, as indicated by the fact, that the order parameters, as well as the motional correlation times on both time scales displayed smaller values. Accordingly, it was shown by MD simulations in combination with NMR data, that, as compared to Cα, amide groups have a higher degree of motional freedom, since the N,C' plane, enclosed by Cα_i and Cα_{i-1}, can rotate around the Φ_i, Ψ_{i-1} dihedral angles, inducing only little disturbance to adjacent residues [Fadel et al., 1995, Smith et al., 1995, Bouvignies et al., 2005].

To further validate the experimentally obtained differences between the motional ^{1}Hα,^{13}Cα and ^{1}H^N,^{15}N backbone parameters of α-spectrin SH3, we compared the experimental results to MD-derived dynamics parameters of the crystalline Bovine Pancreatic Trypsin Inhibitor (BPTI) protein, which were reported by Smith et al. [1995]. In general, the angular correlation function

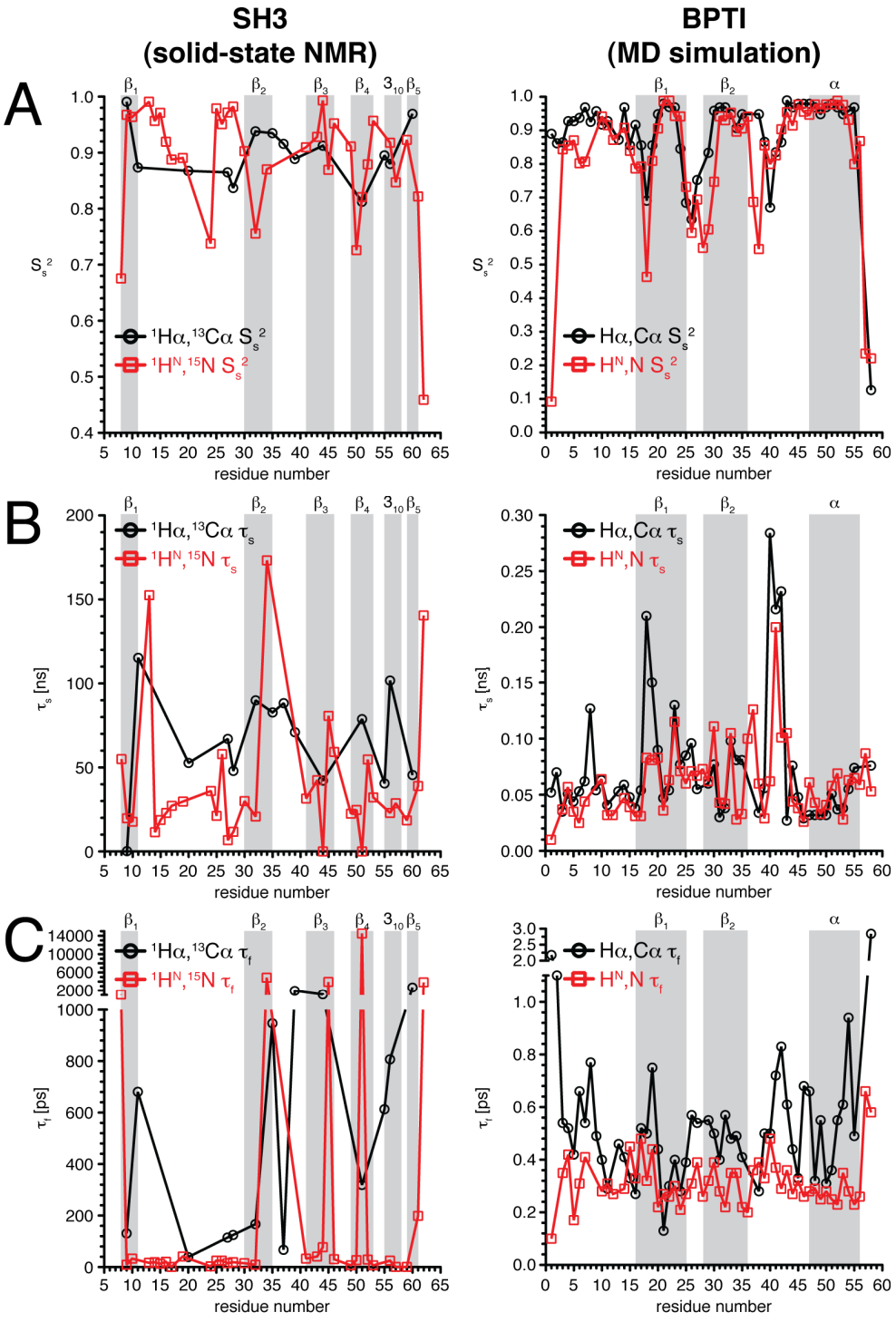

Figure 4.11: In the left column, the best fit values, obtained for (A) S_s^2, (B) τ_s and (C) τ_f, using α-spectrin SH3 ^{1}Hα,^{13}Cα and $^1H^N$,^{15}N backbone relaxation data and order parameters, were plotted as a function of the primary sequence. The values are given in the appendix (Table 11, page 232 and Table 12, page 233). In the right column, MD-derived motional parameters for the Hα,Cα and H^N,N backbone of the Bovine Pancreatic Trypsin Inhibitor (BPTI) protein were plotted as a function of the residue number. The total MD trajectory time was 1 ns. The values were taken from Smith et al. [1995]. The secondary structure elements for α-spectrin SH3 and BPTI are indicated by gray bars.

for the Hα,Cα or H^N,N backbone, is defined as [Chatfield et al., 1998]

$$C_I(t) = \langle P_2 [\hat{\mu}(\tau) \cdot \hat{\mu}(\tau + t)] \rangle, \tag{4.12}$$

with the second Legendre polynomial, $P_2(x) = \frac{1}{2}\left(3x^2 - 1\right)$, and the time-dependent interatomic unit vector along the H,X (X = Cα, N) bond, $\hat{\mu}$, respectively. Using the correlation function in equation 4.12, the generalized order parameter, S^2, can be calculated as

$$S^2 = \lim_{t \to \infty} C_I(t), \tag{4.13}$$

and the correlation time as

$$\tau = \frac{1}{1 - S^2} \int_0^\infty \left[C_I(t) - S^2 \right] dt \tag{4.14}$$

[Lipari and Szabo, 1982a]. To take account of fast and slow motions of the BPTI backbone, the extended MFF was employed for the internal correlation function, which is given by

$$C_I(t) = S^2 + \left(1 - S_f^2\right) e^{-t/\tau_f} + S_f^2 \left(1 - S_s^2\right) e^{-t/\tau_s} \tag{4.15}$$

[Clore et al., 1990b]. Similar to fitting experimental T_1 data, S_s^2, τ_s and τ_f can be obtained by a χ^2 minimization, using the MD trajectory of BPTI and equation 4.15 [Smith et al., 1995].

In Figure 4.11A-C (page 199, right column), all MD-derived S_s^2, τ_s and τ_f values for Hα,Cα and H^N,N of BPTI were plotted. As for the solid-state NMR-derived parameters of α-spectrin SH3, the slow order parameter and the slow correlation time showed very similar trends, with an offset to faster motions for the H^N,N backbone. A smaller correlation of τ_f values was yielded, which is in accordance with α-spectrin SH3. It should be noted, that the MD-derived motional correlation times were limited by the total MD trajectory time of 1 ns. As hinted by the experimental correlation times, which were up to three orders of magnitudes larger for α-spectrin SH3 as compared to the BPTI simulation, a significantly longer MD trajectory is required, to reproduce the experimental T_1 times. Therefore, the existing 91 ns trajectory of α-spectrin SH3 [Chevelkov et al., 2007c, Xue et al., 2007] has to be extended, in the future, to at

least 1 µs to allow for more substantiated conclusions about protein dynamics in the crystal lattice. To minimize systematic errors on the experimental side, the $^{1}H^{N}$,^{15}N backbone T_1, $^{1}H^{N}$,^{15}N dipole-dipole / ^{15}N CSA cross-correlated relaxation rates and order parameters will be re-determined at a MAS frequency $\geq$ 40 kHz to reduce coherent contributions. Furthermore, for the experimental evaluation of the $^{1}H^{N}$,^{15}N backbone order parameters, accordingly, INEPT-based REDOR experiments will be employed.

The χ^2 convergence profile for $^{1}H^{N}$,^{15}N backbone resonances was more beneficial compared to $^{1}H\alpha$,$^{13}C\alpha$, as additional, orthogonal data from $^{1}H^{N}$,^{15}N dipole-dipole / ^{15}N CSA cross-correlated relaxation rates was incorporated into the fitting procedure [Chevelkov et al., 2007a, 2009b]. Similar experiments are more difficult for the $^{1}H\alpha$,$^{13}C\alpha$ backbone, particularly in uniformly ^{13}C labeled samples, as the backbone $^{13}C\alpha$ is directly bonded to ^{13}C' and $^{13}C\beta$ (for non-glycine residues), which complicate the spectra and the determination of cross-correlated relaxation rates. In principle, $^{13}C\alpha$-selective pulses can be employed to simplify the rate determination, however, long pulses relative to the apparent $^{13}C\alpha$ T_2 times [Tang et al., 2010] are necessary, which reduce the achievable spectral sensitivity. As high MAS frequencies elongate the apparent ^{13}C T_2 times (cf. Figure 3.17, page 55), we expect, that experiments for obtaining $^{1}H\alpha$,$^{13}C\alpha$ dipole-dipole / ^{13}C' CSA cross-correlated relaxation rates [Yang et al., 1997a, 1998a, Sprangers et al., 2000] become feasible, combining RAP samples, high external magnetic fields and fast spinning.

Even though the $^{1}H^{N}$,^{15}N backbone data showed a distinct minimum on the χ^2 grid for ≈70% of the residues, still ≈30% of the residues were non-converging and could not be fitted reliably. However, as suggested by the similarity of dynamics parameters at the Hα,Cα and H^{N},N backbone sites (Figure 4.11, page 199), a joint fit of experimental $^{1}H\alpha$,$^{13}C\alpha$ and $^{1}H^{N}$,^{15}N dynamics parameters was assumed to be valid. In this manner, incorporation of experimental $^{1}H\alpha$,$^{13}C\alpha$ dynamics data, improved the fitting convergence of the otherwise non-converging $^{1}H^{N}$,^{15}N residues and allowed to determine unambiguous motional parameters (cf. Figure 3.54, page 126).

As all aliphatic sites are detectable in RAP samples (cf. Figure 4.2, page 166), side chain T_1 times were obtained, in addition to the backbone. For an overview, all experimentally determined

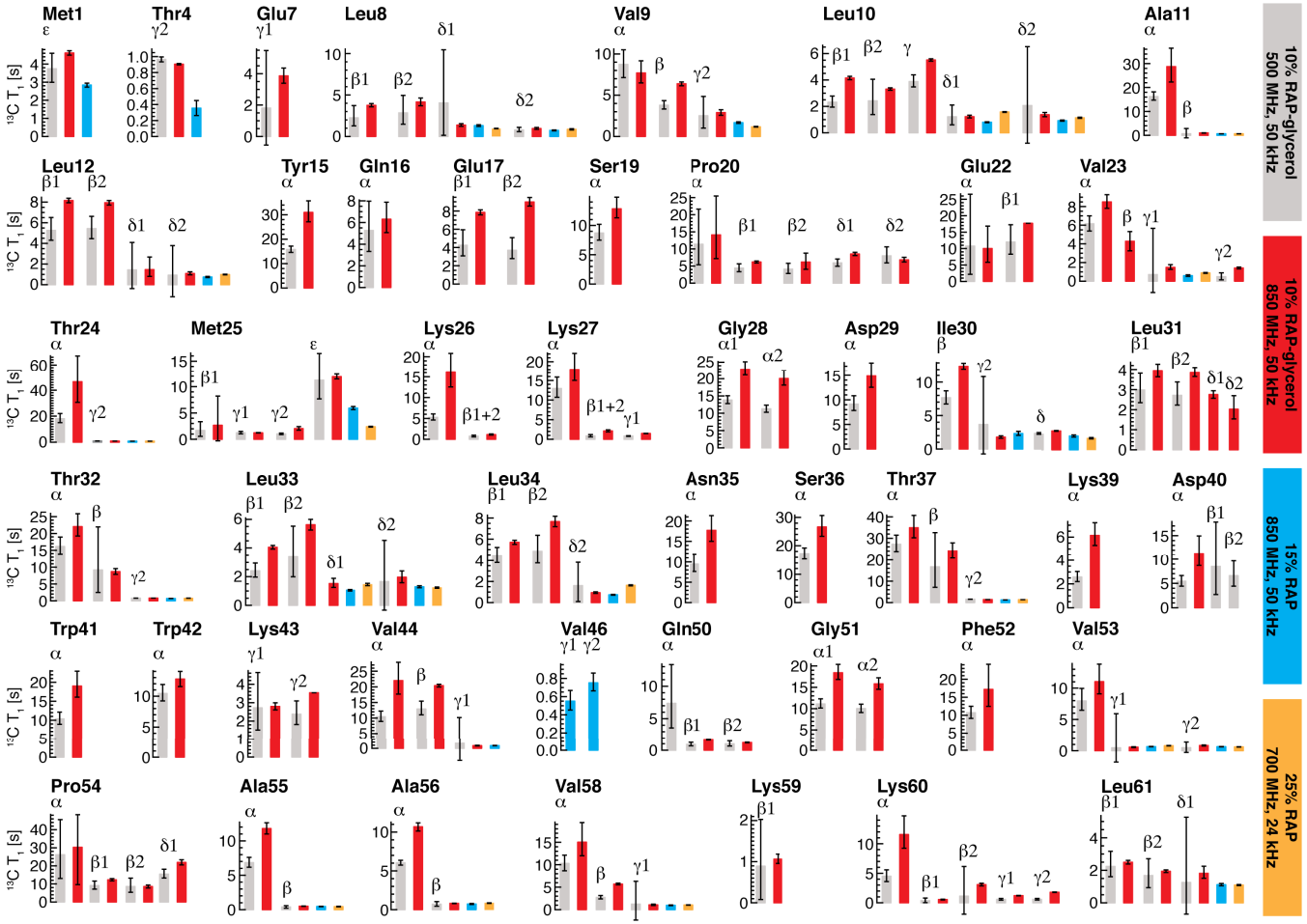

Figure 4.12: Collected ^{13}C T_1 times for the 10% RAP-glycerol sample and the 15% and 25% RAP-glucose samples of α-spectrin SH3, respectively. The error bars were asymmetric in case of inequality between the average T_1 value, described by $\bar{x}$, and the best fitting T_1 value, described by x_{best}. Here, the lower and upper error bar was determined by $\delta_{\text{low}} = x_{\text{best}} \quad (\bar{x} \quad \delta x)$ and $\delta_{\text{up}} = (\bar{x} + \delta x) \quad x_{\text{best}}$, in which δx was the standard deviation of the T_1 Monte Carlo average ($n = 1000$). In case of equality between $\bar{x}$ and x_{best}, δ_{low} and δ_{up} reduce to δx.

^{13}C T_1 times, using the 10% RAP-glycerol and the 15% and 25% RAP samples of α-spectrin SH3 were plotted in Figure 4.12. The T_1 times ranged from ≈0.5 s to ≈30 s. The longest T_1 times were determined for ^{13}Cα backbone, and the shortest for ^{13}C methyl resonances, respectively. For proteins in solution, however, the situation is reversed, ^{13}C methyl resonances yield longer T_1 times than the backbone.

In the solution-state, essentially molecular tumbling induces ^{13}Cα backbone relaxation. Neglecting internal motions, the spectral density function at the frequency ω for a dissolved, isotropically tumbling molecule is described by [Richarz et al., 1980a]

$$J(\omega) = \frac{\tau_r}{1+(\omega\tau_r)^2}, \tag{4.16}$$

with the rotational correlation time τ_r. However, methyls rotate rapidly about their threefold symmetry axis and, therefore, the spectral density is described by [Woessner, 1962b, Agarwal et al., 2008]

$$J(\omega) = \left(1-\alpha S_f^2\right)\frac{\tau}{1+(\omega\tau)^2} + \alpha S_f^2 \frac{\tau_r}{1+(\omega\tau_r)^2} \tag{4.17}$$

with

$$\alpha = \left(\frac{3\cos^2\theta_{HCC}-1}{2}\right)^2 \tag{4.18}$$

and

$$\frac{1}{\tau} = \frac{1}{\tau_f} + \frac{1}{\tau_r}, \tag{4.19}$$

in which $\alpha \approx 0.111$ ($\theta_{HCC} = 109.5°$ for ideal tetrahedral geometry) and τ_f is the motional correlation time of the fast methyl rotation.

The T_1 time of a ^{13}Cα backbone and a ^{13}C methyl resonance was calculated using equation 4.16 and 4.17, respectively, and plotted in Figure 4.13. As can be seen in Figure 4.13A, solution-state ^{13}C T_1 times for methyls were longer as for the backbone, employing typical fast methyl rotational correlation times of a few picoseconds. Here, methyl T_1 curves were generated, set-

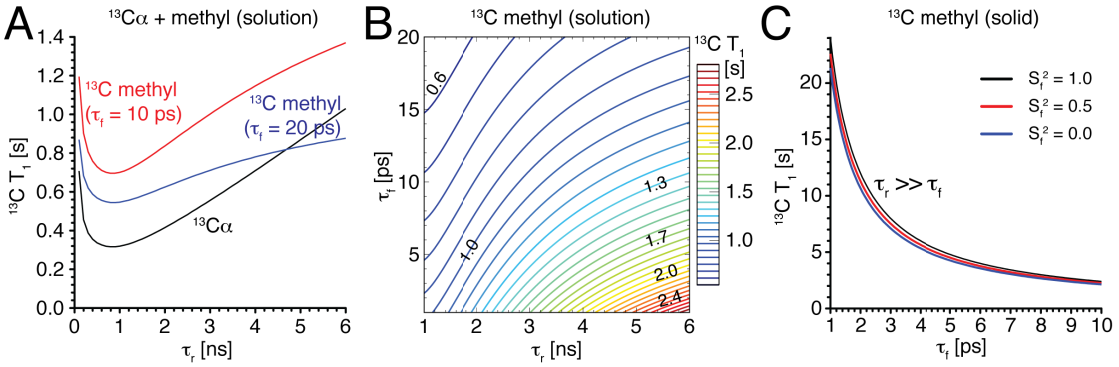

Figure 4.13: Comparison of ^{13}C backbone and methyl T_1 relaxation. For the simulations, the spectral density functions given by equation 4.16 and 4.17 ($S_f^2 = 1$, unless stated otherwise), respectively, were employed. The T_1 times were calculated by equation 3.31 (page 97). To take account of the number of attached protons to a methyl group, equation 3.31 was multiplied by three. In (A) the T_1 time for a backbone and methyl carbon was calculated as a function of the rotational correlation time, τ_r. For the methyl relaxation, two curves were plotted, setting the fast correlation time, τ_f, either to 10 ps (red) or 20 ps (blue), respectively. (B) The methyl ^{13}C T_1 time was simulated as a function of τ_r and τ_f. (C) Methyl T_1 times in a solid molecule ($\tau_r \rightarrow \infty$) as a function of τ_f and S_f^2. For all simulations the external magnetic field was set to 14.1 T (600 MHz).

ting τ_f to 10 ps (red) or 20 ps (blue), respectively. Generally, methyl T_1 times decrease with increasing τ_f (Figure 4.13B).

In the solid-state the situation is different due to the absence of molecular tumbling. Since $\tau_r \rightarrow \infty$, the backbone ^{13}C$\alpha$ T_1 time is, in principle, infinitely long, disregarding internal backbone dynamics. However, inherent fast methyl rotations remain in the solid-state and cause relaxation, as illustrated in Figure 4.13C. Therefore, in the solid-state, ^{13}C T_1 times for methyls are typically shorter, than for the ^{13}Cα backbone, which was also found experimentally (Figure 4.12).

The impact of S_f^2 on the methyl ^{13}C T_1 relaxation times is negligible, as opposed to the fast correlation time τ_f (Figure 4.13C). That way, the methyl T_1 time in the solid-state allows for direct quantification of τ_f (cf. Figure 3.56, page 130), whereas for solubilized proteins, the rotational correlation time τ_r has to be determined as well [Agarwal et al., 2008].

Methyl dynamics parameters were obtained by fitting the experimental T_1 times, using the spectral density function in equation 3.67 (page 117). The correlation time for fast motions, τ_f, was the only fitting parameter, as the order parameter was experimentally determined (cf. Figure 3.39, page 96), which allowed unambiguous fitting of the methyl data. Typical fast

correlation times of tens of picoseconds were obtained (cf. Figure 3.56, page 130) [Richarz et al., 1980a, Ishima et al., 2001, Skrynnikov et al., 2002, Agarwal et al., 2008]. However, the determination of dynamics parameters for methine and methylene residues was hampered, as the χ^2 minimization displayed an insufficient convergence profile for most of the residues (cf. Figure 3.56, page 130). In the future, to obtain dynamics informations from complementary experiments, ^{2}H T_1 [Batchelder et al., 1982, 1983, Muhandiram et al., 1995, Millet et al., 2002, Skrynnikov et al., 2002, Sheppard et al., 2009], as well as ^{1}H,^{13}C-^{1}H,^{13}C dipole-dipole cross-correlated relaxation experiments can be carried out [Yang et al., 1998b, 1999, Carlomagno et al., 2001, Schwalbe et al., 2001]. In principle, both experiments are enabled by the herein introduced RAP labeling scheme, as protonated and deuterated methine and methylene moieties are present in RAP samples (cf. Figure 3.4, page 37).

The presented dynamics parameters of α-spectrin SH3 can, in principle, be obtained from solution-state NMR spectroscopy. However, the here established approach for the determination of ps-ns dynamics will be applied to other biological systems, which exceed the tumbling limit of solution-state NMR, to gain insight into functional activity and assembly of large, insoluble biomolecules, as membrane proteins and fibrils (cf. section 4.1.3, page 168).

4.2 Protein-RNA complexes in the solid-state

Biomolecular solid-state NMR spectroscopy primarily pivots on proteins, while, so far, RNA or DNA samples were merely studied [Riedel et al., 2006, Cherepanov et al., 2010, Huang et al., 2010, Jehle et al., 2010a, Huang et al., 2011b, Sergeyev et al., 2011], which is largely attributed to the lack of protocols for sample preparation [Huang et al., 2012]. Furthermore, as RNA/DNA sequences are encoded by only four nucleobases, a significantly higher degeneracy and spectral overlap is expected as compared to proteins, which are encoded by twenty different amino acids.

Ribonucleic acids play a major role in cellular processes. Here, we investigated the archaeal L7Ae-box C/D protein-RNA complex of *Pyrococcus furiosus* (PF). The complex is part of a small ribonucleoprotein (sRNP) particle, which is involved in 2'-O-methylation of ribosomal RNA to induce correct folding. High-resolution structures are only available for a homolog

structure of *Archaeoglobus fulgidus* (AF) [Moore et al., 2004], however, yielding 62% sequence homology to the L7Ae protein in PF, as determined by SWISS-MODEL [Peitsch, 1995, Arnold et al., 2006, Kiefer et al., 2009].

The soluble complex was precipitated from a polyethylene glycol buffer by vapor diffusion, following the precipitation protocol of Jehle et al. [2010a] (cf. Materials and Methods, page 28). Two different complexes were employed, either with protonated or deuterated uniformly [^{13}C,^{15}N] labeled RNA, while the protein was u-[^{2}H,^{15}N] labeled in both cases. Already initial ^{13}C- and ^{15}N-detected 1D spectra indicated homogeneous sample preparations.

2D ^{13}C,^{13}C RFDR spectra revealed a high resolution for the RNA, as only the ribonucleotides were ^{13}C labeled, unlike the protein (Figure 3.64, page 142). A similar resolution was recently reported for a 14-mer RNA hairpin, studied by MAS solid-state NMR [Cherepanov et al., 2010]. However, the RNA spectra published by Cherepanov et al. [2010] were not recorded for a solid, but a frozen solution. Classical solid-state experiments, as cross polarization (CP), could not be applied and furthermore ^{13}C T_1 times on the order of 200-300 ms were obtained, yielding overall a very low sensitivity.

For the herein investigated protein-RNA complex, however, very efficient CP transfers were achieved, which is supported by CP buildup curves (Figure 3.73, page 155). Additionally, bulk ^{13}C T_1 times were determined to be on the order of a few tens of seconds (Figure 3.65A, page 143), which is expected for a solid molecule.

As both the L7Ae protein and the 26-mer box C/D RNA were uniformly ^{15}N-labeled, ^{1}H-detected ^{1}H,^{15}N correlation spectra were recorded, which showed all expected resonances from protein and RNA (Figure 3.67A, page 147). RNA resonances displayed a lower resolution as compared to the protein, which might be attributed to chemical exchange broadening of RNA amino and imino resonances [Furtig et al., 2003], even though the effective sample temperature was about 0 °C. However, protein resonances were rather narrow, again indicating sample homogeneity. The average ^{1}H line width was about 100 Hz. Comparing the protein region of the precipitated complex to a solution-state spectrum displayed a good overlap, suggesting a similar fold in both states.

Supported by the high sensitivity and resolution, which is obtained for ^{1}H-detected ^{1}H,^{15}N

correlation experiments, a novel approach for the determination of the protein-RNA interface was introduced. The ^{1}H gyromagnetic ratio is about 6.5 times larger than the γ value for ^{2}H nuclei, therefore, the dipolar coupling in ^{2}H,X spin pairs is severely reduced, as compared to the corresponding protonated ^{1}H,X pairs, respectively. To exploit this nuclear magnetic property, ^{1}H,^{15}N spectra were compared, using the ^{1}H- and the ^{2}H-RNA sample, referring to the L7Ae-box C/D complex formed by employing either ^{1}H,^{13}C,^{15}N or ^{2}H,^{13}C,^{15}N labeled nucleotides. That way, non-exchangeable carbon sites were either protonated ($^{1}H^{C}$) or deuterated ($^{2}H^{C}$), respectively.

Since at the interface the protein and the RNA have the smallest distance to each other, intermolecular dipolar couplings between protein $^{1}H^{N}$ and RNA $^{1}H^{C}$ displayed a measurable interaction, as the dipolar coupling is a function of r^{-3}. These intermolecular couplings caused dipole mediated line broadening and attenuated especially the protein resonances, which were in the vicinity of non-exchangeable RNA protons. However, considering the same interaction site, but using the ^{2}H-RNA sample, showed a rather marginal interaction, due to the much smaller γ value for ^{2}H. Therefore, comparing the protein ^{1}H,^{15}N peak volume ratio, obtained for the ^{1}H- and ^{2}H-RNA sample, revealed the interaction site, since ratios smaller than one can only be obtained for resonances, which are broadened by close RNA $^{1}H^{C}$ protons (Figure 3.68, page 148 and Figure 3.69B, page 149).

By employing numerical spin simulations, these peak volume ratios were related to absolute $^{1}H^{N}$(protein),$^{1}H^{C}$(RNA) distances, while yielding a high correlation to the experimental distances determined by X-ray crystallography (Figure 3.69A, page 149 and Figure 3.72, page 153). Furthermore, orientational angles were obtained, which, however, were less correlated due to a high angular degeneracy (Figure 3.70, page 151). To reduce the degeneracy, the angular space was restricted to limits, derived from other known protein-RNA complexes. Here, we considered only two additional protein-RNA complexes (Figure 3.71, page 152), however, the analysis would benefit from including more complexes to identify the most common set of angular limits. In principle, physical boundary conditions, as van der Waals radii, could be utilized to restrict the distance as well as the angular search space *a priori*.

As the approach only requires 2D ^{1}H,^{15}N spectra from both complexes, it enables a very

simple and fast access to the determination of protein-RNA interfaces. However, as the approach is based on dipole mediated line broadening, the peak volume ratio obtained for both samples is highly dependent on the MAS frequency, as shown by simulation in Figure 4.14. Fast spinning yields efficient averaging of anisotropic interactions, as the dipolar coupling. Therefore, at high spinning frequencies the peak volume ratio of the ^{1}H- and ^{2}H-RNA sample tends to one, which simultaneously reduces the detection sphere for internuclear distances. To antagonize this effect, active recoupling could be employed [Roberts et al., 1987, Gullion and Schaefer, 1989, Hohwy et al., 2000, Zhao et al., 2001b, Dvinskikh et al., 2003]. In general, this approach yields only distance and angular informations, it does not identify the interacting nuclei. In this way, solely protein nuclei at the interface are identified, unlike the corresponding interacting RNA nuclei.

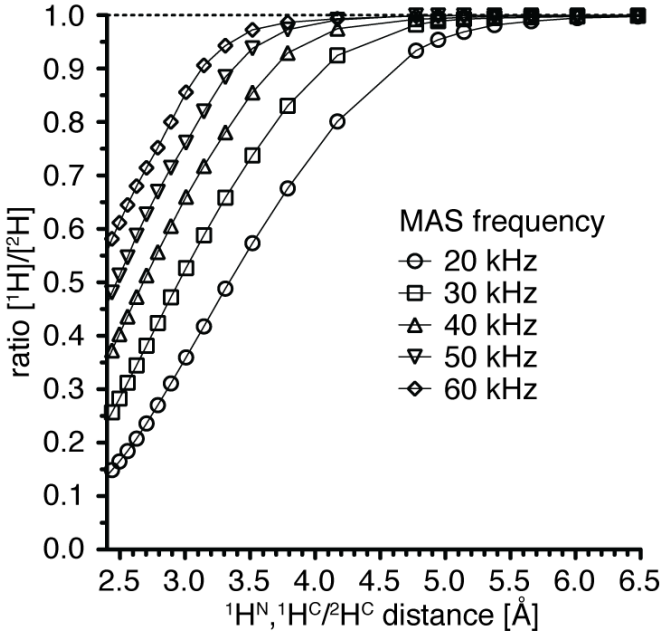

Figure 4.14: Simulated $I[^{1}H]/I[^{2}H]$ ratio as a function of the $^{1}H^{N}$-$^{1}H^{C}/^{2}H^{C}$ distance. In the simulation, the MAS frequency was varied from 20 kHz to 60 kHz, while all dipolar angles were constrained to zero. As expected, with increasing spinning frequencies the ratio tends towards one due to a more efficient averaging of the dipolar coupling Hamiltonian. The external magnetic field strength was set to 16.4 T (^{1}H Larmor frequency of 700 MHz).

Additionally, the protein-RNA interface was probed by ^{1}H,^{13}C HETCOR experiments, in which the dipolar coupling was actively recoupled via cross polarization (CP), employing long contact times of several milliseconds (Figure 3.74, page 156). However, as the sensitivity was limited due to ^{13}C-detection, only one contact was determined between protein amide and RNA

ribose, respectively. Despite the low sensitivity, the advantage of the HETCOR approach is, in principle, the ability to identify protein as well as RNA resonances at the interface, as opposed to the previously discussed method. However, a significantly higher sample amount would be required for unambiguous identification of interacting nuclei at the protein-RNA interface.

Generally, to determine sequential RNA assignments, through-space magnetization transfers have to be employed, as the sequence of NMR-active nuclei (^{13}C, ^{15}N, ^{31}P) is interrupted by NMR-inactive nuclei (^{17}O), unlike for the protein backbone. Therefore, inter-residual RNA through-space contacts have to be obtained, requiring an efficient dipolar recoupling sequence. To obtain the optimal condition for ^{13}C,^{13}C mixing, PDSD and RFDR spectra were compared (Figure 3.66, page 146). The RFDR sequence yielded the best mixing performance as the most long-range contacts between the ribose and the base were detected, which enables the identification of nucleobase spin systems. This is also supported by six spin simulations, which indicate, that RFDR mixing allows to obtain inter-residual contacts within ≈3.7 Å (Figure 3.75, page 157).

For obtaining unambiguous RNA assignments, ^{1}H,^{15}N, ^{1}H,^{13}C and a ^{13}C,^{13}C spectrum were combined, which yielded sequential assignments for a U_i,G_{i+1} pair (Figure 3.76, page 159). Again, the approach was essentially limited by the spectral sensitivity and, therefore, the sample amount. To improve intra-residual assignments within the base, ^{13}C,^{15}N transfer experiments, as TEDOR, could be employed, as suggested recently [Riedel et al., 2005].

In conclusion, we could show, that high-resolution spectra for a protein-RNA complex can be obtained, using deuterated samples. To the best of our knowledge, this is the first time that ^{1}H-detected ^{1}H,^{15}N correlation spectra of a protein-RNA complex are presented in the solid-state. Initial RNA assignment experiments were shown, which can be improved by additional dimensions. Furthermore, by introducing a novel approach for the determination of structural parameters in the solid-state, we could identify the protein-RNA interface and extract distance and orientational informations for the affected protein residues.

The fact, that the extinction of amide proton resonances in the ^{1}H-RNA sample depends on the distance and the relative orientation of the atom pairs, opens new possibilities for structure calculation protocols. In addition to a distance restraint, an angular restraint can now be em-

ployed for systems, for which only sparse data is available. This should make it possible to determine complex structures with improved accuracy. These parameters can be incorporated as restraints into an iterative structure calculation algorithm. We believe, that this approach can be applied to other protein-RNA complexes, as well as to protein-ligand complexes in general. The L7Ae-box C/D RNA complex served here as a model system. In the future, we aim to investigate fully assembled sRNP [Lin et al., 2011] complexes, which exceed the molecular weight limit imposed by molecular tumbling, a current limitation in solution-state NMR applications.

Outlook

Proteins are involved in various biochemical processes, such as signaling, genome regulation and catalysis [Ishima and Torchia, 2000]. Protein structural analysis is an essential step for the understanding of their functional activity. Routinely, high-resolution structures are determined by X-ray crystallography and NMR spectroscopy. However, these atomic resolution structures only provide a static picture, which alone cannot fully explain the protein function [Kay, 1998]. To understand the interplay between protein structure and function, the determination of protein dynamics becomes essential.

In this thesis, we introduced solid-state NMR methodologies to detect protein motions on the sub-μs timescale. In particular, we were able to obtain ^{13}C T_1 relaxation times and ^{1}H,^{13}C order parameters for all aliphatic sites, which was enabled by the here introduced Reduced Adjoining Protonation (RAP) labeling scheme. The application of the Model-Free Formalism (MFF) [Brown, 1982, Lipari and Szabo, 1982a, Brown, 1984, Lipari and Szabo, 1982b, Clore et al., 1990b] allowed us to determine internal correlation times, as well as model-independent order parameters, which are a measure of motional amplitudes.

As discussed in section 4.1.4 (page 172), the model-free order parameter, S^2, can be analytically interpreted within a motional model, as the diffusion-in-the-cone [Kinosita et al., 1977, Lipari and Szabo, 1980, 1981] or the jump model [Wittebort and Szabo, 1978, Clore et al., 1990a,b]. Alternatively, order parameters can be examined from a thermodynamic point of view and related to conformational entropy ($\mathscr{S}_{\text{conf}}$) [Akke et al., 1993, Li et al., 1996, Yang and Kay, 1996a, Yang et al., 1997b]. This can be readily understood, as the order parameter is a measure for the range of structural states, which can be accessed by a specific bond vector [Stone, 2001]. Therefore, changes in the generalized order parameter, S^2, for example, upon ligand binding,

are indicative of changes in the range of accessible states and, thus, the conformational entropy [Peng, 2012]. Assuming a diffusion-in-the-cone model for the motion of the bond vector, yields for the conformational entropy [Yang and Kay, 1996b]

$$\mathscr{S}_{\text{conf}} = k_{\text{B}} \ln \left[\pi \left(3 - \sqrt{1 + 8S} \right) \right], \tag{4.20}$$

where k_{B} is the Boltzmann constant. As the estimation of the entropy requires an assumption of the nature of the bond vector, various physically reasonable models were suggested, which, however, yielded consistent $\mathscr{S}_{\text{conf}}$ values within a factor of about two [Akke et al., 1993, Li et al., 1996, Yang and Kay, 1996b, Stone et al., 2001]. More recently, Li and Bruschweiler [2009] reported a "dictionary" to convert order parameters into side chain entropies, which was derived from MD simulations for three different proteins. Parameters were obtained from 4 ns and 100 ns subtrajectories, respectively. However, averaging over both, displayed no significant differences. This hints, that the sub-µs timescale motions probed by the here suggested solid-state NMR experiments, samples the necessary motional time window, which determines the conformational entropy.

Moreover, in the context of protein binding, Wand and co-workers were able to show [Marlow et al., 2010], that the conformational entropy, involved in forming the complex of the solubilized calmodulin protein with peptide ligands, can be linearly correlated with NMR derived methyl order parameters [Schwalbe and Rinnenthal, 2010]. By this, they introduced an "entropy meter", which can be used as a powerful tool for drug design, as these entropies cannot be determined from static structures [Peng, 2012].

Allosteric folding processes and enzyme catalysis occur on a µs-ms timescale (cf. Figure 1.3, page 11). In this regard, Bruschweiler et al. [2009] were able to show, that allosteric signal transmission is mediated by isoleucine side chains along the protein, using relaxation dispersion experiments [Loria et al., 1999, Hansen et al., 2008, Korzhnev and Kay, 2008]. However, fast nanosecond motions can also regulate dynamics on the slower microsecond timescale [Wand, 2001b,a, Mayer et al., 2003], as the correlation of fast internal motions may allow to overcome activation barriers, which influences the kinetics of catalysis [Bruice and Benkovic, 2000, Osborne et al., 2001, Mayer et al., 2003]. Mayer et al. [2003] detected correlated internal protein

motions, when studying the fast timescale $^{1}H^{N}$,^{15}N backbone dynamics of ten mutants of the immunoglobulin binding domain of protein G. They analyzed the covariation of backbone order parameters and motional correlation times, which revealed short- and long-range dynamical correlations throughout the protein.

As solid-state NMR spectroscopy is not subject to size limitations, we believe, that the aforementioned approaches to study the functional dynamics of proteins can be applied, in the future, to large biomolecular complexes, such as membrane proteins and amyloid fibrils, which are not easily accessible by X-ray crystallography or solution-state NMR. The similarity of internal dynamics, comparing solubilized and microcrystalline proteins, encourages the determination of dynamics in the solid-state [Chevelkov et al., 2007c, Agarwal et al., 2008, Chevelkov et al., 2010]. Additionally, the absence of molecular tumbling in the crystal renders dynamics experiments more sensitive to the nanosecond regime, while motions comparable or slower than the tumbling of the solubilized protein remain undetected. The employment of different dynamics probes, as also shown in the present work, enables the simultaneous detection of dynamics occuring on different molecular axes. Here, we supplemented previously reported $^{1}H^{N}$,^{15}N [Chevelkov et al., 2009b] with $^{1}H\alpha$,$^{13}C\alpha$ backbone, as well as aliphatic side chain dynamics data. This is essential to determine a complete motional picture of the protein of interest, since motions parallel to the $^{1}H^{N}$,^{15}N bond do not contribute to the ^{15}N relaxation, as the motion does not reorientate the bond vector with respect to the magnetic field [Kay, 1998]. To probe motions on a slower µs-ms regime, relaxation dispersion experiments were recently suggested for microcrystalline proteins [Tollinger et al., 2012].

In total, we showed, that the combination of RAP labeling and fast spinning enables the detection of motionally determined relaxation parameters. The addition of further dynamics probes, such as ^{2}H, will support the unambiguous determination of the underlying motional model, which can be complemented by MD derived parameters from long trajectories. In the future, the investigation of dynamics in the solid-state will allow for better insight into the function and stability of large, insoluble biomolecules, which, so far, cannot be investigated by traditional techniques.

Appendix: Tables

Table 2: ^{1}Hα,^{13}Cα backbone chemical shifts obtained for a 15% RAP sample of the SH3 domain of chicken α-spectrin at pH 7.5-8.5, employing a HCC experiment (cf. Figure 3.23, page 65). The experiment was carried out at an external magnetic field of 16.4 T (700 MHz) and a MAS frequency of 18 kHz. *Reproduced with kind permission from Asami, S., et al., J. Biol. NMR, 2012, 52 (1), pp 31-39. Copyright 2012 Springer Science and Business Media. DOI: 10.1007/s10858-011-9591-4.*

i	**residue**	^{1}Hα **[ppm]**	^{13}C' **[ppm]**	^{13}Cα **[ppm]**	^{13}Cβ **[ppm]**	^{13}Cγ **[ppm]**
8	Leu8	4.90	177.2	53.6	-	25.3
9	Val9	4.77	172.8	58.2	35.1	19.6
10	Leu10	4.68	176.8	53.4	45.4	26.3
11	Ala11	4.12	178.1	53.3	18.8	-
12	Leu12	3.29	-	56.7	41.8	25.6
13	Tyr13	4.15	173.9	56.1	42.7	-
14	Asp14	4.10	176.4	55.4	41.1	179.6
15	Tyr15	4.03	172.7	61.0	42.9	-
16	Gln16	4.06	174.1	54.7	28.5	32.9
17	Glu17	3.70	175.9	56.9	29.9	33.9
19	Ser19	3.35	173.1	57.5	62.7	-
20	Pro20	3.91	177.2	66.3	31.2	26.5
22	Glu22	4.85	-	56.7	32.6	36.9
23	Val23	4.17	171.8	60.1	34.5	20.5
24	Thr24	4.88	174.4	62.4	71.1	20.7
25	Met25	4.52	173.6	54.7	35.5	30.7

Continued on next page

Table 2 – *Continued from previous page*

i	**residue**	^{1}**H**α **[ppm]**	^{13}**C' [ppm]**	^{13}**C**α **[ppm]**	^{13}**C**β **[ppm]**	^{13}**C**γ **[ppm]**
26	Lys26	4.46	174.9	54.3	33.3	-
27	Lys27	2.72	177.9	59.2	31.3	23.5
28	Gly28	3.94	173.6	45.6	-	-
28	Gly28	2.99	173.6	45.6	-	-
29	Asp29	4.30	-	55.9	41.7	179.4
31	Leu31	4.53	176.6	53.7	41.5	
32	Thr32	4.15	173.8	63.4	68.8	22.2
33	Leu33	3.91	-	55.4	42.7	-
34	Leu34	4.21	177.3	55.7	-	-
35	Asn35	4.26	174.6	54.8	39.7	175.6
36	Ser36	3.55	173.8	57.7	61.2	-
37	Thr37	3.63	176.2	65.6	70.0	21.7
38	Asn38	4.60	174.8	54.8	40.7	178.4
39	Lys39	3.72	176.3	59.1	32.0	22.8
40	Asp40	4.05	177.2	56.7	43.8	180.0
41	Trp41	4.50	174.6	56.7	-	-
42	Trp42	5.10	174.2	54.3	-	-
44	Val44	4.88	173.3	59.7	36.0	17.7
45	Glu45	4.83	-	55.6	33.2	36.9
50	Gln50	5.14	175.9	54.0	30.7	32.9
51	Gly51	3.48	170.6	46.4	-	-
52	Phe52	5.12	175.4	59.7	41.9	-
53	Val53	4.25	172.7	59.1	32.8	16.2
54	Pro54	2.81	177.9	62.7	29.1	27.1
55	Ala55	2.13	178.9	55.1	14.7	-

Continued on next page

Table 2 – *Continued from previous page*

i	**residue**	^{1}Hα [ppm]	^{13}C' [ppm]	^{13}Cα [ppm]	^{13}Cβ [ppm]	^{13}Cγ [ppm]
56	Ala56	3.46	177.9	53.7	17.3	-
58	Val58	5.14	173.8	58.7	34.8	21.7
59	Lys59	4.38	-	54.8	36.2	-
60	Lys60	3.98	176.4	59.0	32.0	24.8
61	Leu61	3.96	-	54.9	40.8	25.5

Table 3: ^{1}H,^{13}C chemical shifts of α-spectrin SH3, obtained for a 15% RAP sample at pH 7.5-8.5, employing a HCC experiment (cf. Figure 3.23, page 65) at an external magnetic field of 16.4 T (700 MHz) and a MAS frequency of 18 kHz.

i	residue	^{1}H [ppm]	^{13}C [ppm]
7	Glu7-Hα,Cα	5.19	55.20
7	Glu7-Hγ,Cγ	1.65	37.13
8	Leu8-Hα,Cα	4.90	53.61
8	Leu8-Hβ1,Cβ	0.57	45.91
8	Leu8-Hβ2,Cβ	0.32	45.91
8	Leu8-Hγ,Cγ	0.27	26.75
8	Leu8-Hδ1,Cδ1	0.05	22.70
8	Leu8-Hδ2,Cδ2	-1.00	23.51
9	Val9-Hα,Cα	4.77	58.22
9	Val9-Hβ,Cβ	1.41	36.26
9	Val9-Hγ1,Cγ1	0.46	23.89
9	Val9-Hγ2,Cγ2	0.28	20.83
10	Leu10-Hα,Cα	4.68	53.31
10	Leu10-Hβ1,Cβ	1.24	46.81
10	Leu10-Hβ2,Cβ	1.01	46.81
10	Leu10-Hγ,Cγ	0.65	26.47
10	Leu10-Hδ1,Cδ1	0.32	24.27
10	Leu10-Hδ2,Cδ2	0.27	26.75
11	Ala11-Hα,Cα	4.12	53.27
11	Ala11-Hβ,Cβ	1.13	18.92
12	Leu12-Hα,Cα	3.29	56.68
12	Leu12-Hβ1,Cβ	0.77	43.50
12	Leu12-Hβ2,Cβ	0.24	43.50
12	Leu12-Hγ,Cγ	0.90	26.97
12	Leu12-Hδ1,Cδ1	0.15	22.10
12	Leu12-Hδ2,Cδ2	0.22	25.57
13	Tyr13-Hα,Cα	4.15	56.08
13	Tyr13-Hβ1,Cβ	2.87	44.24
13	Tyr13-Hβ2,Cβ	1.35	44.24
14	Asp14-Hα,Cα	4.10	55.37
14	Asp14-Hβ1,Cβ	2.10	42.29
15	Tyr15-Hα,Cα	4.03	60.95
15	Tyr15-Hβ1,Cβ	2.50	43.28
16	Gln16-Hα,Cα	4.06	54.69
16	Gln16-Hβ1,Cβ	1.29	29.60
16	Gln16-Hγ1,Cγ	1.77	34.25
17	Glu17-Hα,Cα	3.70	56.91
17	Glu17-Hβ1,Cβ	1.51	31.38
17	Glu17-Hβ2,Cβ	1.23	31.38
17	Glu17-Hγ,Cγ	1.59	35.15
19	Ser19-Hα,Cα	3.35	57.48
19	Ser19-Hβ1,Cβ	3.02	64.05
19	Ser19-Hβ2,Cβ	2.75	64.05
20	Pro20-Hα,Cα	3.91	66.32
20	Pro20-Hβ1,Cβ	1.80	32.31
20	Pro20-Hβ2,Cβ	1.46	32.31
20	Pro20-Hγ1,Cγ	1.32	27.85
20	Pro20-Hγ2,Cγ	0.93	27.85
20	Pro20-Hδ1,Cδ	2.04	51.20
22	Glu22-Hα,Cα	4.85	56.70
22	Glu22-Hβ1,Cβ	2.18	33.78
22	Glu22-Hβ2,Cβ	1.76	33.78
22	Glu22-Hγ1,Cγ	1.46	37.81
23	Val23-Hα,Cα	4.17	60.09
23	Val23-Hβ,Cβ	1.39	35.61
23	Val23-Hγ1,Cγ1	0.09	20.35
23	Val23-Hγ2,Cγ2	0.05	21.64
24	Thr24-Hα,Cα	4.88	62.41
24	Thr24-Hβ,Cβ	3.36	72.08
24	Thr24-Hγ2,Cγ2	0.85	20.75
25	Met25-Hα,Cα	4.52	54.66
25	Met25-Hβ1,Cβ	1.25	36.77
25	Met25-Hγ1,Cγ	2.39	32.05
25	Met25-Hγ2,Cγ	2.10	32.05
25	Met25-Hϵ,Cϵ	1.80	18.66
26	Lys26-Hα,Cα	4.46	54.30
26	Lys26-Hβ1,Cβ	1.19	34.59
26	Lys26-Hγ1,Cγ	1.19	24.28
26	Lys26-Hδ1,Cδ	1.16	29.07
26	Lys26-Hϵ1,Cϵ	2.51	42.63
27	Lys27-Hα,Cα	2.77	59.23
27	Lys27-Hβ1,Cβ	0.98	32.62
27	Lys27-Hγ1,Cγ	0.54	24.62
27	Lys27-Hδ1,Cδ	1.10	29.83
27	Lys27-Hϵ1,Cϵ	2.38	42.26
28	Gly28-Hα1,Cα	3.94	45.65
28	Gly28-Hα2,Cα	2.99	45.65
29	Asp29-Hα,Cα	4.30	55.91
29	Asp29-Hβ1,Cβ	2.31	42.95
30	Ile30-Hα,Cα	4.47	58.88
30	Ile30-Hβ,Cβ	1.86	36.52
30	Ile30-Hγ11,Cγ1	1.07	26.70
30	Ile30-Hγ2,Cγ2	0.22	18.14
30	Ile30-Hδ,Cδ	0.42	11.19
31	Leu31-Hα,Cα	4.53	53.73
31	Leu31-Hβ1,Cβ	1.02	42.82
31	Leu31-Hδ1,Cδ1	0.39	27.50
31	Leu31-Hδ2,Cδ2	0.29	26.72

i	residue	^{1}H [ppm]	^{13}C [ppm]	*i*	residue	^{1}H [ppm]	^{13}C [ppm]	*i*	residue	^{1}H [ppm]	^{13}C [ppm]
32	Thr32-Hα,Cα	4.15	63.36	40	Asp40-Hβ1,Cβ	2.28	44.93	52	Phe52-Hα,Cα	5.07	59.86
32	Thr32-Hβ,Cβ	3.66	70.20	40	Asp40-Hβ2,Cβ	1.65	44.93	52	Phe52-Hβ1,Cβ	2.69	43.39
32	Thr32-Hγ2,Cγ2	0.69	22.20	41	Trp41-Hα,Cα	4.50	56.75	52	Phe52-Hβ2,Cβ	2.00	43.39
33	Leu33-Hα,Cα	3.93	55.42	41	Trp41-Hβ1,Cβ	2.43	33.22	53	Val53-Hα,Cα	4.25	59.14
33	Leu33-Hβ1,Cβ	1.22	43.25	41	Trp41-Hβ2,Cβ	2.21	33.22	53	Val53-Hβ,Cβ	1.33	34.38
33	Leu33-Hβ2,Cβ	0.40	43.25	42	Trp42-Hα,Cα	5.10	54.32	53	Val53-Hγ1,Cγ1	0.08	17.35
33	Leu33-Hγ,Cγ	0.92	27.35	42	Trp42-Hβ1,Cβ	2.10	32.07	53	Val53-Hγ2,Cγ2	0.55	22.56
33	Leu33-Hδ1,Cδ1	0.11	23.91	43	Lys43-Hβ1,Cβ	0.91	34.77	54	Pro54-Hα,Cα	2.81	62.71
33	Leu33-Hδ2,Cδ2	-0.18	25.54	43	Lys43-Hβ2,Cβ	0.57	34.77	54	Pro54-Hβ1,Cβ	0.52	30.38
34	Leu34-Hα,Cα	4.21	55.71	43	Lys43-Hγ1,Cγ	0.38	26.06	54	Pro54-Hβ2,Cβ	-0.26	30.38
34	Leu34-Hβ1,Cβ	0.63	43.42	43	Lys43-Hγ2,Cγ	-0.44	26.06	54	Pro54-Hγ1,Cγ	-0.05	28.31
34	Leu34-Hγ,Cγ	0.92	27.35	43	Lys43-Hδ1,Cδ	0.81	29.57	54	Pro54-Hδ1,Cδ	1.74	50.70
34	Leu34-Hδ1,Cδ1	0.17	22.30	44	Val44-Hα,Cα	4.88	59.69	55	Ala55-Hα,Cα	2.13	55.11
34	Leu34-Hδ2,Cδ2	0.17	25.57	44	Val44-Hβ,Cβ	1.56	37.31	55	Ala55-Hβ,Cβ	-0.71	14.80
35	Asn35-Hα,Cα	4.26	54.84	44	Val44-Hγ1,Cγ1	0.25	18.91	56	Ala56-Hα,Cα	3.46	53.74
35	Asn35-Hβ1,Cβ	2.36	41.18	44	Val44-Hγ2,Cγ2	0.25	21.28	56	Ala56-Hβ,Cβ	0.53	17.41
35	Asn35-Hβ2,Cβ	2.23	41.18	45	Glu45-Hα,Cα	4.83	55.63	57	Tyr57-Hα,Cα	4.84	55.14
36	Ser36-Hα,Cα	3.55	57.75	45	Glu45-Hβ1,Cβ	1.58	34.29	57	Tyr57-Hβ1,Cβ	2.39	37.88
36	Ser36-Hβ1,Cβ	2.27	62.64	45	Glu45-Hγ1,Cγ	1.67	38.27	58	Val58-Hα,Cα	5.14	58.67
36	Ser36-Hβ2,Cβ	1.39	62.64	46	Val46-Hβ,Cβ	1.97	33.80	58	Val58-Hβ,Cβ	1.29	36.16
37	Thr37-Hα,Cα	3.63	65.58	46	Val46-Hγ1,Cγ1	0.50	20.08	58	Val58-Hγ1,Cγ1	0.23	19.82
37	Thr37-Hβ,Cβ	3.82	71.50	46	Val46-Hγ2,Cγ2	0.47	20.90	58	Val58-Hγ2,Cγ2	0.21	22.79
37	Thr37-Hγ2,Cγ2	0.92	21.72	49	Arg49-Hβ1,Cβ	1.61	34.33	59	Lys59-Hα,Cα	4.63	54.90
38	Asn38-Hα,Cα	4.60	54.75	49	Arg49-Hβ2,Cβ	1.35	34.33	59	Lys59-Hβ1,Cβ	1.16	37.39
38	Asn38-Hβ1,Cβ	3.39	42.04	49	Arg49-Hγ1,Cγ	1.45	27.52	59	Lys59-Hγ1,Cγ	0.95	24.86
38	Asn38-Hβ2,Cβ	2.71	42.04	49	Arg49-Hδ1,Cδ	2.87	44.16	59	Lys59-Hδ1,Cδ	1.20	29.88
39	Lys39-Hα,Cα	3.72	59.16	50	Gln50-Hα,Cα	5.18	53.94	59	Lys59-Hϵ1,Cϵ	2.51	42.66
39	Lys39-Hβ1,Cβ	1.67	32.65	50	Gln50-Hβ1,Cβ	1.41	31.82	60	Lys60-Hα,Cα	3.98	59.05
39	Lys39-Hγ1,Cγ	1.07	24.51	50	Gln50-Hβ2,Cβ	0.99	31.82	60	Lys60-Hβ1,Cβ	1.43	33.42
39	Lys39-Hδ1,Cδ	1.10	28.46	50	Gln50-Hγ1,Cγ	1.69	34.06	60	Lys60-Hβ2,Cβ	1.21	33.42
39	Lys39-Hϵ1,Cϵ	2.38	42.26	50	Gln50-Hγ2,Cγ	1.40	34.06	60	Lys60-Hγ1,Cγ	1.16	26.04
40	Asp40-Hα,Cα	4.05	56.67	51	Gly51-Hα1,Cα	3.48	46.37	60	Lys60-Hγ2,Cγ	0.87	26.04

i	**residue**	^{1}**H**	^{13}**C**
		[ppm]	**[ppm]**
60	Lys60-Hδ1,Cδ	1.12	29.71
60	Lys60-Hϵ1,Cϵ	2.29	42.12
61	Leu61-Hα,Cα	3.96	54.93
61	Leu61-Hβ1,Cβ	1.00	41.55
61	Leu61-Hβ2,Cβ	0.74	41.55
61	Leu61-Hγ,Cγ	1.08	27.15
61	Leu61-Hδ1,Cδ1	0.35	23.12
61	Leu61-Hδ2,Cδ2	0.27	26.58

Table 4: Dipolar coupling order parameters of ^{1}Hα,^{13}Cα backbone resonances of α-spectrin SH3 are listed. The parameters were determined by REDOR dephasing experiments, using a 15% RAP sample (cf. Figure 4.4A, page 175). For every residue the dipolar coupling anisotropy δ_D, the tensor asymmetry η and the resulting squared order parameter S^2 is given. A ^{1}Hα,^{13}Cα bond length of 1.11 Å was assumed [Alkaraghouli and Koetzle, 1975, Yao et al., 2001]. For error estimation, 1,000 Monte Carlo simulations were performed. The experiments were carried out at an external magnetic field of 11.7 T (500 MHz), a MAS frequency of 40 kHz, and for two ζ-delays, 1.1 us and 1.5 us, respectively (details are given in section 3.4.2, page 80).

i	**residue**	δ_D **[Hz]**	$\Delta\delta_D$ **[Hz]**	η	$\Delta\eta$	S^2	ΔS^2
8	Leu8α	-21491	1220	0.37	0.24	0.95	0.11
9	Val9α	-21517	1459	0.58	0.31	0.95	0.13
11	Ala11α	-20594	925	0.17	0.21	0.87	0.08
12	Leu12α	-19920	621	0.14	0.18	0.81	0.05
20	Pro20α	-19111	3575	0.26	0.28	0.75	0.28
22	Glu22α	-21407	1095	0.34	0.23	0.94	0.10
24	Thr24α	-21845	471	0.16	0.18	0.98	0.04
27	Lys27α	-20215	1596	0.21	0.23	0.84	0.13
28	Gly28α1	-20019	256	0.10	0.13	0.82	0.02
28	Gly28α2	-20406	387	0.13	0.16	0.85	0.03
35	Asn35α	-21133	441	0.13	0.16	0.92	0.04
37	Thr37α	-20884	303	0.17	0.15	0.89	0.03
39	Lys39α	-19817	598	0.15	0.17	0.80	0.05
41	Trp41α	-20094	1107	0.20	0.21	0.83	0.09
44	Val44α	-20899	1203	0.20	0.23	0.90	0.10
51	Gly51α1	-19734	301	0.12	0.14	0.80	0.02
51	Gly51α2	-19338	305	0.11	0.14	0.77	0.02
53	Val53α	-20153	824	0.17	0.19	0.83	0.07
54	Pro54α	-20554	2244	0.24	0.27	0.87	0.19
55	Ala55α	-20623	331	0.14	0.15	0.87	0.03
56	Ala56α	-20358	265	0.10	0.15	0.85	0.02

Continued on next page

Table 4 – *Continued from previous page*

i	**residue**	δ_D **[Hz]**	$\Delta\delta_D$ **[Hz]**	η	$\Delta\eta$	S^2	ΔS^2
60	Lys60α	-21028	1502	0.24	0.24	0.91	0.13

Table 5: Dipolar coupling order parameters of ^{1}H,^{13}C side chain resonances of a 15% RAP sample of α-spectrin SH3. Details are given in the caption of Table 4 (page 220).

i	**residue**	δ_D **[Hz]**	$\Delta\delta_D$ **[Hz]**	η	$\Delta\eta$	S^2	ΔS^2
7	Glu7γ1+2	-2439	259	0.52	0.44	0.01	0.00
9	Val9β	-17677	1225	0.18	0.21	0.64	0.09
10	Leu10γ	-16570	2023	0.23	0.25	0.56	0.14
12	Leu12β2	-18805	4050	0.34	0.31	0.72	0.31
12	Leu12δ2	-5873	218	0.40	0.26	0.07	0.01
17	Glu17β1	-14604	479	0.22	0.26	0.44	0.03
17	Glu17β2	-17153	1092	0.17	0.21	0.60	0.08
20	Pro20β1	-17571	1178	0.18	0.21	0.63	0.08
20	Pro20δ1	-18648	1780	0.33	0.24	0.71	0.14
22	Glu22β1	-19627	1161	0.23	0.22	0.79	0.09
24	Thr24β	-20848	1097	0.24	0.22	0.89	0.09
25	Met25γ1	-16473	508	0.24	0.19	0.56	0.03
25	Met25γ2	-1761	197	0.47	0.35	0.01	0.00
26	Lys26β1+2	-12465	92	0.46	0.10	0.32	0.00
27	Lys27β1+2	-15989	268	0.22	0.15	0.52	0.02
27	Lys27γ1	-13473	218	0.14	0.16	0.37	0.01
30	Ile30β	-16482	2300	0.23	0.26	0.56	0.16
31	Leu31β1+2	-18991	2999	0.41	0.27	0.74	0.23

Continued on next page

Table 5 – *Continued from previous page*

i	**residue**	δ_D **[Hz]**	$\Delta\delta_D$ **[Hz]**	η	$\Delta\eta$	S^2	ΔS^2
32	Thr32β	-19442	1403	0.20	0.22	0.77	0.11
33	Leu33β1	-18135	1586	0.24	0.24	0.67	0.12
34	Leu34δ2	-5642	233	0.30	0.30	0.07	0.01
37	Thr37β	-21251	1548	0.23	0.24	0.93	0.13
40	Asp40β1	-19428	1676	0.25	0.25	0.77	0.13
40	Asp40β2	-19079	871	0.15	0.19	0.75	0.07
43	Lys43δ1+2	-11749	472	0.20	0.25	0.28	0.02
43	Lys43γ2	-15465	2926	0.37	0.31	0.49	0.19
44	Val44β	-11115	525	0.26	0.30	0.25	0.02
50	Gln50β1	-15476	948	0.27	0.27	0.49	0.06
50	Gln50β2	-14965	3351	0.31	0.32	0.46	0.21
54	Pro54β1	-16763	1182	0.21	0.23	0.58	0.08
54	Pro54δ1	-18874	1323	0.19	0.22	0.73	0.10
54	Pro54γ1+2	-16422	2029	0.24	0.27	0.55	0.14
58	Val58β	-17156	966	0.19	0.21	0.60	0.07
59	Lys59β1	-14463	306	0.31	0.22	0.43	0.02
60	Lys60β1	-9668	217	0.25	0.23	0.19	0.01
60	Lys60β2	-10180	265	0.35	0.26	0.21	0.01
60	Lys60γ1	-8242	425	0.67	0.36	0.14	0.01
60	Lys60γ2	-8367	489	0.47	0.39	0.14	0.02

Table 6: Dipolar coupling order parameters of ^{1}H,^{13}C methyl resonances, obtained by REDOR dephasing experiments at an external magnetic field of 14.1 T (600 MHz) and a MAS frequency of 50 kHz, using a $^{13}CD_2H$ sample of α-spectrin SH3. The ζ-delay was set to 4 μs.

i	**residue**	δ_D **[Hz]**	$\Delta\delta_D$ **[Hz]**	η	$\Delta\eta$	S^2	ΔS^2
8	Leu8δ1	-5480	20	0.20	0.00	0.57	0.00
8	Leu8δ2	-5550	22	0.10	0.02	0.58	0.00
9	Val9γ1	-5871	25	0.20	0.00	0.65	0.01
9	Val9γ2	-5890	29	0.20	0.00	0.66	0.01
10	Leu10δ1	-5040	10	0.20	0.00	0.48	0.00
10	Leu10δ2	-5300	20	0.20	0.00	0.53	0.00
12	Leu12δ1	-5430	12	0.10	0.00	0.56	0.00
12	Leu12δ2	-5680	21	0.09	0.02	0.61	0.00
23	Val23γ1	-3840	86	0.60	0.07	0.28	0.01
23	Val23γ2	-3561	24	0.60	0.01	0.24	0.00
31	Leu31δ1	-2790	16	0.70	0.01	0.15	0.00
31	Leu31δ2	-2503	31	0.81	0.05	0.12	0.00
33	Leu33δ1	-5680	20	0.10	0.02	0.61	0.00
33	Leu33δ2	-5591	32	0.20	0.00	0.59	0.01
34	Leu34δ1	-5360	10	0.10	0.00	0.54	0.00
34	Leu34δ2	-5471	17	0.00	0.01	0.57	0.00
44	Val44γ1	-5920	49	0.20	0.02	0.66	0.01
44	Val44γ2	-5810	22	0.20	0.00	0.64	0.00
46	Val46γ1	-2214	65	0.91	0.11	0.09	0.01
46	Val46γ2	-2847	77	0.82	0.10	0.15	0.01
53	Val53γ1	-6112	49	0.20	0.02	0.71	0.01
53	Val53γ2	-6161	27	0.09	0.02	0.72	0.01
58	Val58γ1	-5669	35	0.30	0.01	0.61	0.01
58	Val58γ2	-5680	20	0.20	0.00	0.61	0.00

Continued on next page

Table 6 – *Continued from previous page*

i	**residue**	δ_D **[Hz]**	$\Delta\delta_D$ **[Hz]**	η	$\Delta\eta$	S^2	ΔS^2
61	Leu61δ1	-4421	14	0.09	0.02	0.37	0.00

Table 7: Dipolar coupling order parameters of ^{1}H,^{13}C methyl resonances, obtained by REDOR dephasing experiments at an external magnetic field of 14.1 T (600 MHz) and a MAS frequency of 50 kHz, using a 5% RAP sample of α-spectrin SH3. The ζ-delay was set to 4 μs.

i	**residue**	δ_D **[Hz]**	$\Delta\delta_D$ **[Hz]**	η	$\Delta\eta$	S^2	ΔS^2
1	Met1ϵ	-363	16	0.56	0.30	0.00	0.00
4	Thr4γ2	-763	41	0.47	0.33	0.01	0.00
8	Leu8δ1	-5330	61	0.20	0.05	0.54	0.01
8	Leu8δ2	-5108	59	0.20	0.05	0.49	0.01
9	Val9γ1	-5768	64	0.08	0.06	0.63	0.01
9	Val9γ2	-5640	50	0.20	0.03	0.60	0.01
10	Leu10δ1	-4072	39	0.03	0.05	0.31	0.01
10	Leu10δ2	-4999	41	0.20	0.03	0.47	0.01
11	Ala11β	-6502	59	0.09	0.04	0.80	0.01
12	Leu12δ1	-4431	25	0.30	0.00	0.37	0.00
12	Leu12δ2	-5384	84	0.09	0.08	0.55	0.02
23	Val23γ1	-3697	72	0.50	0.06	0.26	0.01
23	Val23γ2	-3958	66	0.50	0.05	0.30	0.01
24	Thr24γ2	-6189	20	0.00	0.01	0.73	0.00
25	Met25ϵ	-6001	59	0.08	0.05	0.68	0.01
30	Ile30δ	-3791	34	0.60	0.02	0.27	0.00
30	Ile30γ2	-5758	93	0.20	0.06	0.63	0.02
31	Leu31δ1	-2348	37	0.50	0.05	0.10	0.00

Continued on next page

Table 7 – *Continued from previous page*

i	**residue**	δ_D **[Hz]**	$\Delta\delta_D$ **[Hz]**	η	$\Delta\eta$	S^2	ΔS^2
31	Leu31δ2	-2633	58	0.71	0.08	0.13	0.01
32	Thr32γ2	-6010	30	0.09	0.03	0.68	0.01
33	Leu33δ1	-5448	75	0.09	0.07	0.56	0.02
33	Leu33δ2	-5307	48	0.20	0.03	0.53	0.01
34	Leu34δ1	-5160	37	0.08	0.05	0.50	0.01
34	Leu34δ2	-4953	80	0.20	0.06	0.46	0.01
37	Thr37γ2	-6429	29	0.10	0.02	0.78	0.01
44	Val44γ1	-5960	60	0.08	0.05	0.67	0.01
44	Val44γ2	-5799	48	0.20	0.02	0.64	0.01
46	Val46γ1	-2295	87	0.62	0.12	0.10	0.01
46	Val46γ2	-2658	122	0.82	0.15	0.13	0.01
53	Val53γ1	-5941	48	0.09	0.04	0.67	0.01
53	Val53γ2	-5909	46	0.09	0.04	0.66	0.01
55	Ala55β	-6304	68	0.08	0.05	0.75	0.02
56	Ala56β	-6153	59	0.09	0.04	0.72	0.01
58	Val58γ1	-5431	54	0.20	0.04	0.56	0.01
58	Val58γ2	-5561	40	0.20	0.02	0.59	0.01
61	Leu61δ1	-4330	41	0.20	0.03	0.36	0.01

Table 8: Dipolar coupling order parameters of ^{1}Hα,^{13}Cα backbone resonances of α-spectrin SH3, determined by REDOR dephasing experiments, using a 10% RAP-glycerol sample (cf. Figure 3.34, page 85). The experiments were carried out at an external magnetic field of 11.7 T (500 MHz), a MAS frequency of 50 kHz, and a ζ-delay of 1.5 us, respectively.

i	**residue**	δ_D **[Hz]**	$\Delta\delta_D$ **[Hz]**	η	$\Delta\eta$	S^2	ΔS^2
9	Val9α	-19345	1015	0.21	0.18	0.77	0.08
11	Ala11α	-20746	682	0.50	0.09	0.88	0.06
15	Tyr15α	-20765	470	0.30	0.07	0.88	0.04
16	Gln16α	-20432	3556	0.52	0.35	0.86	0.30
19	Ser19α	-20571	685	0.10	0.12	0.87	0.06
20	Pro20α	-12152	9045	0.65	0.43	0.30	0.45
22	Glu22α	-12301	10288	0.73	0.41	0.31	0.52
23	Val23α	-17924	602	0.30	0.12	0.66	0.04
24	Thr24α	-21652	1171	0.10	0.17	0.96	0.10
26	Lys26α	-19882	638	0.09	0.11	0.81	0.05
27	Lys27α	-19906	1482	0.42	0.22	0.81	0.12
28	Gly28α1	-19839	513	0.30	0.08	0.81	0.04
28	Gly28α2	-19064	512	0.09	0.09	0.74	0.04
29	Asp29α	-20623	1471	0.41	0.22	0.87	0.12
32	Thr32α	-19748	1061	0.10	0.16	0.80	0.09
35	Asn35α	-20791	1714	0.60	0.24	0.89	0.15
36	Ser36α	-20355	568	0.18	0.10	0.85	0.05
37	Thr37α	-20257	534	0.19	0.10	0.84	0.04
39	Lys39α	-20091	968	0.31	0.16	0.83	0.08
40	Asp40α	-21158	1190	0.10	0.16	0.92	0.10
41	Trp41α	-20892	934	0.31	0.14	0.89	0.08
42	Trp42α	-21157	857	0.41	0.12	0.92	0.07
44	Val44α	-21612	1642	0.50	0.22	0.96	0.15

Continued on next page

Table 8 – *Continued from previous page*

i	**residue**	δ_D **[Hz]**	$\Delta\delta_D$ **[Hz]**	η	$\Delta\eta$	S^2	ΔS^2
50	Gln50α	-19984	3021	0.26	0.36	0.82	0.25
51	Gly51α1	-19500	552	0.09	0.10	0.78	0.04
51	Gly51α2	-20044	699	0.30	0.12	0.82	0.06
52	Phe52α	-20261	826	0.19	0.14	0.84	0.07
53	Val53α	-18193	1243	0.42	0.17	0.68	0.09
54	Pro54α	-17472	3923	0.65	0.38	0.63	0.28
55	Ala55α	-20134	603	0.30	0.09	0.83	0.05
56	Ala56α	-18941	298	0.08	0.07	0.74	0.02
58	Val58α	-20311	1090	0.20	0.18	0.85	0.09
60	Lys60α	-18197	1503	0.41	0.25	0.68	0.11

Table 9: Dipolar coupling order parameters of ^{1}H,^{13}C side chain resonances of α-spectrin SH3, determined by REDOR dephasing experiments, using a 10% RAP-glycerol sample (cf. Figure 3.34, page 85). The experiments were carried out at an external magnetic field of 11.7 T (500 MHz), a MAS frequency of 50 kHz, and a ζ-delay of 1.5 us, respectively.

i	**residue**	δ_D **[Hz]**	$\Delta\delta_D$ **[Hz]**	η	$\Delta\eta$	S^2	ΔS^2
7	Glu7γ1	-7446	6822	0.52	0.47	0.11	0.21
8	Leu8β1	-17013	2963	0.26	0.33	0.59	0.21
8	Leu8β2	-17739	3343	0.63	0.33	0.64	0.24
9	Val9β	-18397	611	0.31	0.11	0.69	0.05
10	Leu10β1	-19234	1199	0.20	0.20	0.76	0.09
10	Leu10β2	-18883	4853	0.27	0.38	0.73	0.38
10	Leu10γ	-18746	574	0.30	0.10	0.72	0.04
12	Leu12β1	-16820	1749	0.82	0.25	0.58	0.12

Continued on next page

Table 9 – *Continued from previous page*

i	**residue**	δ_D **[Hz]**	$\Delta\delta_D$ **[Hz]**	η	$\Delta\eta$	S^2	ΔS^2
12	Leu12β2	-17845	1198	0.14	0.20	0.65	0.09
17	Glu17β1	-18351	2328	0.20	0.30	0.69	0.18
17	Glu17β2	-20375	3254	0.36	0.36	0.85	0.27
20	Pro20β1	-16102	1249	0.23	0.24	0.53	0.08
20	Pro20β2	-18918	2084	0.23	0.27	0.73	0.16
20	Pro20δ1	-19293	1161	0.21	0.21	0.76	0.09
20	Pro20δ2	-18420	1497	0.33	0.27	0.70	0.11
22	Glu22β1	-20758	3232	0.37	0.34	0.88	0.27
24	Thr24β	-9192	11346	0.50	0.49	0.17	0.43
25	Met25β1	-19324	2636	0.35	0.33	0.77	0.21
25	Met25γ1	-16519	761	0.20	0.17	0.56	0.05
25	Met25γ2	-14607	483	0.09	0.11	0.44	0.03
26	Lys26β1+2	-13574	891	0.52	0.20	0.38	0.05
27	Lys27β1+2	-17587	2084	0.44	0.30	0.63	0.15
27	Lys27γ1	-14868	394	0.50	0.08	0.45	0.02
30	Ile30β	-19538	738	0.07	0.11	0.78	0.06
31	Leu31β1	-17123	1411	0.31	0.25	0.60	0.10
31	Leu31β2	-17528	1509	0.42	0.25	0.63	0.11
32	Thr32β	-11285	9937	0.60	0.47	0.26	0.46
33	Leu33β1	-19304	1093	0.20	0.19	0.76	0.09
33	Leu33β2	-18683	3387	0.65	0.37	0.72	0.26
34	Leu34β1	-19094	773	0.19	0.14	0.75	0.06
34	Leu34β2	-18744	1763	0.34	0.25	0.72	0.14
37	Thr37β	-17768	9761	0.69	0.42	0.65	0.71
40	Asp40β1	-14922	11877	0.57	0.48	0.46	0.73

Continued on next page

Table 9 – *Continued from previous page*

i	**residue**	δ_D **[Hz]**	$\Delta\delta_D$ **[Hz]**	η	$\Delta\eta$	S^2	ΔS^2
40	Asp40β2	-19611	2991	0.49	0.35	0.79	0.24
43	Lys43γ1	-15335	1766	0.19	0.27	0.48	0.11
43	Lys43γ2	-15630	1186	0.40	0.23	0.50	0.08
44	Val44β	-19650	1169	0.59	0.18	0.79	0.09
50	Gln50β1	-14731	1488	0.41	0.25	0.44	0.09
50	Gln50β2	-14616	1933	0.24	0.26	0.44	0.12
54	Pro54β1	-18558	1440	0.22	0.24	0.71	0.11
54	Pro54β2	-20047	3203	0.35	0.35	0.82	0.26
54	Pro54δ1	-18034	973	0.61	0.17	0.67	0.07
58	Val58β	-17927	1023	0.72	0.18	0.66	0.08
59	Lys59β1	-14238	3036	0.27	0.36	0.42	0.18
60	Lys60β1	-8453	9309	0.53	0.49	0.15	0.32
60	Lys60β2	-11011	12435	0.54	0.47	0.25	0.56
60	Lys60γ1	-8788	537	0.79	0.22	0.16	0.02
60	Lys60γ2	-8139	535	0.52	0.27	0.14	0.02
61	Leu61β1	-16539	1688	0.17	0.25	0.56	0.11

Table 10: Dipolar coupling order parameters of $^1H^N$,^{15}N backbone resonances of α-spectrin SH3 are listed. The order parameters were determined by CPPI experiments, using a perdeuterated sample, back-exchanged in a 10%/90% H_2O/D_2O buffer. The experiments were carried out at an external magnetic field of 9.4 T (400 MHz), while the MAS frequency was adjusted to 20 kHz. The values were taken from Chevelkov et al. [2009a], while employing a $^1H^N$,^{15}N rigid-limit bond length of 1.015 Å [Yao et al., 2008b].

i	**residue**	δ_D **[Hz]**	$\Delta\delta_D$ **[Hz]**	S^2	ΔS^2
8	Leu8N	9282	750	0.64	0.10

Continued on next page

Table 10 – *Continued from previous page*

i	**residue**	δ_D **[Hz]**	$\Delta\delta_D$ **[Hz]**	S^2	ΔS^2
9	Val9N	10623	375	0.83	0.06
10	Leu10N	10726	300	0.85	0.05
11	Ala11N	10715	225	0.85	0.04
12	Leu12N	10651	225	0.84	0.04
13	Tyr13N	10355	225	0.79	0.03
14	Asp14N	10194	250	0.77	0.04
15	Tyr15N	10421	300	0.80	0.05
16	Gln16N	10114	300	0.75	0.04
17	Glu17N	10235	300	0.77	0.05
18	Lys18N	10521	150	0.82	0.02
19	Ser19N	9815	450	0.71	0.07
22	Glu22N	10508	450	0.81	0.07
23	Val23N	10280	450	0.78	0.07
24	Thr24N	9299	900	0.64	0.12
25	Met25N	10696	225	0.84	0.04
26	Lys26N	10516	225	0.82	0.03
27	Lys27N	10458	300	0.81	0.05
28	Gly28N	10654	225	0.84	0.04
30	Ile30N	10496	300	0.81	0.05
31	Leu31N	10840	450	0.87	0.07
32	Thr32N	9919	900	0.73	0.13
33	Leu33N	10756	375	0.85	0.06
34	Leu34N	10578	450	0.82	0.07
35	Asn35N	10168	375	0.76	0.06
37	Thr37N	10562	900	0.82	0.14

Continued on next page

Table 10 – *Continued from previous page*

i	**residue**	δ_D **[Hz]**	$\Delta\delta_D$ **[Hz]**	S^2	ΔS^2
39	Lys39N	10129	450	0.76	0.07
40	Asp40N	10514	375	0.81	0.06
41	Trp41N	10412	375	0.80	0.06
42	Trp42N	10663	225	0.84	0.04
43	Lys43N	10661	300	0.84	0.05
44	Val44N	10849	300	0.87	0.05
45	Glu45N	10508	300	0.81	0.05
46	Val46N	10298	450	0.78	0.07
49	Arg49N	9715	300	0.70	0.04
50	Gln50N	9644	300	0.69	0.04
51	Gly51N	10255	225	0.78	0.03
52	Phe52N	10729	225	0.85	0.04
53	Val53N	10651	300	0.84	0.05
55	Ala55N	10533	150	0.82	0.02
56	Ala56N	10399	225	0.80	0.03
57	Tyr57N	10396	325	0.80	0.05
58	Val58N	10550	300	0.82	0.05
59	Lys59N	10367	300	0.79	0.05
60	Lys60N	10219	225	0.77	0.03
61	Leu61N	9962	225	0.73	0.03
62	Asp62N	6780	750	0.34	0.07

Table 11: Motional parameters for the ^{1}Hα,^{13}Cα backbone of α-spectrin SH3, assuming the Model-Free Formalism. For S_s^2, τ_s and τ_f, the best fit and the average over the Monte Carlo ensemble ($n = 500$) are given. The fitting was performed by a χ^2 minimization, employing equation 3.68 (page 117) and using ^{13}C T_1 values, obtained at 11.7 T (500 MHz) and 20.0 T (850 MHz) for a 10% RAP-glycerol sample, as well as ^{1}Hα,^{13}Cα order parameters of a 15% RAP-glucose sample (cf. Table 4, page 220).

i	**residue**	$T_{1,\mathbf{11.7\ T}}^{\mathbf{calc}}$ **[s]**	$\Delta T_{1,\mathbf{11.7\ T}}^{\mathbf{calc}}$ **[s]**	$T_{1,\mathbf{11.7\ T}}^{\mathbf{exp}}$ **[s]**	$\Delta T_{1,\mathbf{11.7\ T}}^{\mathbf{exp}}$ **[s]**	$T_{1,\mathbf{20.0\ T}}^{\mathbf{calc}}$ **[s]**	$\Delta T_{1,\mathbf{20.0\ T}}^{\mathbf{calc}}$ **[s]**	$T_{1,\mathbf{20.0\ T}}^{\mathbf{exp}}$ **[s]**	$\Delta T_{1,\mathbf{20.0\ T}}^{\mathbf{exp}}$ **[s]**	$S_{s,\mathbf{best}}^2$	$S_{s,\mathbf{avg}}^2$	$\Delta S_{s,\mathbf{avg}}^2$	$\tau_{s,\mathbf{best}}$ **[ns]**	$\tau_{s,\mathbf{avg}}$ **[ns]**	$\Delta\tau_{s,\mathbf{avg}}$ **[ns]**	$\tau_{f,\mathbf{best}}$ **[ns]**	$\tau_{f,\mathbf{avg}}$ **[ns]**	$\Delta\tau_{f,\mathbf{avg}}$ **[ns]**
9	Val9α	5.53	5.23	8.73	1.71	6.97	7.89	7.86	1.33	0.991	0.625	0.467	0.251	16.715	64.650	0.131	0.120	0.381
11	Ala11α	15.48	4.59	16.20	1.67	27.39	9.62	28.68	6.51	0.874	0.833	0.218	115.251	106.994	122.161	0.681	1.036	2.694
20	Pro20α	8.02	7.96	13.57	8.40	12.44	12.09	18.42	11.27	0.868	0.628	0.406	52.751	45.753	101.206	0.039	1.746	4.364
22	Glu22α	7.66	6.95	24.99	16.39	9.36	8.73	10.14	4.84	0.992	0.699	0.445	0.251	7.708	35.728	0.081	0.272	0.891
24	Thr24α	12.69	9.87	17.85	3.29	29.63	24.92	58.64	35.97	0.990	0.667	0.460	18.501	14.189	46.148	2.633	3.192	4.760
27	Lys27α	11.18	5.61	12.95	2.54	15.99	8.41	18.18	3.71	0.865	0.743	0.325	67.001	83.281	118.083	0.115	0.336	1.086
28	Gly28α1	11.23	1.08	11.23	1.08	20.12	2.22	20.12	2.22	0.868	0.875	0.036	118.001	103.607	96.541	0.757	0.714	0.855
28	Gly28α2	13.78	1.15	13.78	1.15	22.82	2.07	22.82	2.07	0.837	0.844	0.029	48.001	93.612	96.283	0.125	0.295	0.352
32	Thr32α	14.47	6.04	16.17	2.62	20.40	8.91	22.10	3.45	0.938	0.830	0.304	90.001	59.094	95.020	0.167	0.231	0.437
35	Asn35α	9.94	3.90	9.50	1.96	18.31	6.30	17.91	2.94	0.935	0.930	0.117	82.751	70.070	102.845	0.947	1.356	1.956
37	Thr37α	27.08	3.67	27.38	3.85	34.90	5.18	34.70	5.48	0.916	0.936	0.036	88.251	109.552	131.911	0.067	0.128	0.768
39	Lys39α	2.60	0.37	2.55	0.40	5.95	0.89	6.12	0.98	0.889	0.912	0.069	71.001	72.931	100.853	1.949	2.709	2.253
44	Val44α	9.08	5.40	10.46	1.76	18.76	10.67	22.23	4.96	0.913	0.739	0.352	42.251	84.083	123.311	1.151	2.295	4.023
51	Gly51α1	10.01	0.99	10.01	0.99	15.77	1.37	15.77	1.37	0.797	0.798	0.039	40.001	112.443	104.807	0.071	0.299	0.325
51	Gly51α2	11.14	1.01	11.14	1.01	18.42	1.81	18.42	1.81	0.812	0.822	0.030	78.751	135.350	120.968	0.319	0.432	0.404
54	Pro54α	23.29	24.48	46.29	31.40	37.01	39.54	57.83	42.67	0.939	0.642	0.415	78.501	56.835	119.781	0.025	0.975	3.252
55	Ala55α	6.78	0.71	6.78	0.71	11.74	0.78	11.74	0.78	0.895	0.902	0.032	40.501	91.156	110.126	0.613	0.856	1.765
56	Ala56α	6.04	0.33	6.04	0.33	10.71	0.56	10.71	0.56	0.880	0.883	0.024	101.751	101.146	100.846	0.807	0.782	1.107
60	Lys60α	4.15	4.22	4.48	1.02	8.85	7.62	11.45	2.50	0.969	0.686	0.416	45.501	44.566	94.020	2.707	2.493	3.609

Table 12: Motional parameters for the $^{1}H^{N}$,^{15}N backbone of α-spectrin SH3, assuming the Model-Free Formalism. For S_s^2, τ_s and τ_f, the best fit and the average over the Monte Carlo ensemble ($n = 500$) are given. The fitting was performed by a χ^2 minimization, employing equation 3.70 (page 118) and using ^{15}N T_1 values [Chevelkov et al., 2008], obtained at 14.1 T (600 MHz) and 21.1 T (900 MHz) for a α-spectrin SH3 sample, which was uniformly ^{2}H and ^{15}N labeled and back-exchanged in a 10%/90% H_2O/D_2O buffer, prior to crystallization. Furthermore, ^{1}H,^{15}N dipole-dipole / ^{15}N CSA cross-correlated relaxation rates (η) [Chevelkov et al., 2007a], and ^{1}H,^{15}N order parameter [Chevelkov et al., 2009a] were incorporated. The experimental values were taken from the references given.

i	residue	$T_{1,14.1\,T}^{calc}$ [s]	$\Delta T_{1,14.1\,T}^{calc}$ [s]	$T_{1,14.1\,T}^{exp}$ [s]	$\Delta T_{1,14.1\,T}^{exp}$ [s]	$T_{1,21.1\,T}^{calc}$ [s]	$\Delta T_{1,21.1\,T}^{calc}$ [s]	$T_{1,21.1\,T}^{exp}$ [s]	$\Delta T_{1,21.1\,T}^{exp}$ [s]	$\eta_{14.1\,T}^{calc}$ [Hz]	$\Delta\eta_{14.1\,T}^{calc}$ [Hz]	$\eta_{14.1\,T}^{exp}$ [Hz]	$\Delta\eta_{14.1\,T}^{exp}$ [Hz]	$S_{z,best}^2$	$S_{z,avg}^2$	$\Delta S_{z,avg}^2$	$\tau_{e,best}$ [ns]	$\tau_{e,avg}$ [ns]	$\Delta\tau_{e,avg}$ [ns]	$\tau_{f,best}$ [ns]	$\tau_{f,avg}$ [ns]	$\Delta\tau_{f,avg}$ [ns]
8	Leu8	4.61	0.66	4.65	0.55	5.37	0.81	5.32	0.71	17.62	6.90	17.68	6.85	0.676	0.767	0.128	55.001	155.653	175.277	1.081	1.428	2.346
9	Val9	34.50	4.52	34.35	4.17	48.63	4.62	49.56	3.29	0.74	0.43	0.74	0.43	0.968	0.951	0.071	19.751	19.587	10.014	0.009	1.271	4.215
10	Leu10	19.57	5.84	20.36	7.17	22.91	5.54	23.85	5.32	0.74	0.42	0.74	0.41	0.964	0.962	0.037	17.751	47.026	59.994	0.033	1.156	3.412
13	Tyr13	45.94	4.16	49.25	4.27	43.35	4.87	41.52	5.94	1.16	0.21	1.16	0.21	0.991	0.987	0.009	152.501	149.778	72.930	0.017	0.018	0.005
14	Asp14	15.81	3.76	15.59	3.94	18.86	2.62	19.43	1.87	0.68	0.44	0.68	0.44	0.957	0.943	0.052	11.501	26.714	40.260	0.019	0.865	2.909
15	Tyr15	29.99	1.55	29.96	1.33	37.42	2.73	37.52	2.53	0.59	0.36	0.59	0.36	0.971	0.965	0.023	18.751	19.474	8.381	0.013	0.048	0.357
16	Gln16	15.35	1.62	15.34	1.64	19.72	1.96	19.75	1.98	1.64	0.55	1.64	0.55	0.920	0.922	0.025	23.001	28.090	30.688	0.021	0.158	1.505
17	Glu17	18.62	1.88	17.84	2.22	29.98	3.25	32.14	4.02	2.77	0.58	2.77	0.58	0.888	0.891	0.017	27.251	27.994	4.730	0.001	0.140	1.561
19	Ser19	11.00	0.89	11.01	0.89	12.77	0.58	12.77	0.58	2.70	0.37	2.70	0.37	0.891	0.895	0.027	29.751	37.273	44.447	0.041	0.054	0.100
24	Thr24	10.53	1.29	10.34	0.43	16.99	1.66	17.25	1.26	8.51	1.14	8.55	0.97	0.738	0.750	0.081	36.001	59.915	98.214	0.003	1.475	4.435
25	Met25	30.41	3.25	30.46	2.97	33.00	2.78	32.87	2.45	0.54	0.33	0.54	0.33	0.979	0.977	0.015	21.251	30.667	23.668	0.025	0.061	0.567
26	Lys26	30.36	2.58	30.44	2.62	33.52	3.03	33.53	3.09	2.62	0.26	2.62	0.26	0.951	0.950	0.019	58.001	83.181	86.331	0.025	0.026	0.012
27	Lys27	16.54	3.47	16.13	3.37	21.85	2.94	22.70	2.46	0.80	0.60	0.80	0.60	0.972	0.941	0.040	6.751	17.491	27.389	0.015	1.412	4.010
28	Gly28	27.65	1.71	27.69	1.08	34.41	3.32	34.51	2.86	1.35	1.00	1.35	1.00	0.982	0.953	0.047	14.151	29.565	19.003	0.019	0.025	0.025
30	Ile30	18.89	1.29	18.83	1.34	28.10	2.04	28.22	2.16	2.81	0.58	2.81	0.59	0.903	0.903	0.015	30.001	30.607	5.529	0.015	0.116	0.673
32	Thr32	6.18	2.57	5.85	1.09	9.28	3.09	9.83	1.31	4.97	1.27	5.22	0.62	0.756	0.817	0.174	20.751	93.212	155.939	0.009	5.265	7.316
34	Leu34	7.55	1.69	7.40	0.82	10.96	1.77	11.08	0.14	21.43	4.45	22.55	1.80	0.870	0.875	0.120	173.251	280.566	187.939	4.853	6.033	4.613
41	Trp41	16.39	2.51	16.53	2.61	20.32	4.07	20.56	4.59	2.60	0.68	2.61	0.67	0.910	0.925	0.057	31.501	88.978	127.975	0.033	0.486	2.648
43	Lys43	21.90	1.94	21.91	1.95	25.63	2.24	25.62	2.28	2.88	0.54	2.88	0.54	0.928	0.934	0.022	42.501	60.798	66.225	0.041	0.083	0.265
44	Val44	15.32	5.28	14.08	3.34	21.24	5.73	23.48	4.59	0.49	0.35	0.50	0.35	0.993	0.949	0.055	0.001	12.738	23.176	0.077	2.487	4.349
45	Glu45	5.25	0.76	5.16	0.43	7.49	1.01	7.50	0.87	10.56	1.29	10.64	1.02	0.869	0.893	0.069	80.751	196.205	189.888	3.931	5.163	3.733
46	Val46	23.96	0.34	23.96	0.25	23.87	0.72	23.87	0.66	2.32	1.07	2.32	1.07	0.952	0.961	0.014	59.251	71.497	39.535	0.031	0.050	0.120
49	Arg49	18.65	2.99	18.50	3.25	25.38	3.03	25.90	3.25	1.63	0.35	1.63	0.35	0.911	0.909	0.048	22.501	30.832	42.073	0.007	1.232	4.546
50	Gln50	6.09	0.17	6.08	0.18	9.79	0.29	9.80	0.31	6.76	0.57	6.76	0.57	0.726	0.734	0.039	24.751	27.692	23.652	0.027	0.851	3.099
51	Gly51	17.81	1.89	17.04	1.74	28.07	2.53	29.76	3.26	0.90	0.40	0.90	0.40	0.821	0.908	0.053	0.001	11.479	7.522	14.507	3.393	6.196
52	Phe52	26.70	1.63	26.62	1.67	39.22	4.29	39.40	4.52	6.79	1.27	6.79	1.27	0.879	0.891	0.025	54.751	68.533	46.864	0.029	1.705	4.602
53	Val53	44.65	4.93	45.29	2.06	58.70	14.81	59.92	17.65	1.30	0.56	1.30	0.56	0.957	0.966	0.019	32.251	62.441	67.822	0.007	0.131	1.320
56	Ala56	15.05	5.28	15.23	6.27	18.72	4.59	20.45	3.60	1.68	0.57	1.68	0.57	0.918	0.932	0.044	23.001	66.662	109.631	0.025	2.856	5.929
57	Tyr57	12.76	4.58	14.11	4.83	20.46	6.61	27.81	4.59	4.38	0.41	4.39	0.38	0.847	0.879	0.061	28.751	74.757	115.804	0.001	3.796	7.172
59	Lys59	18.43	2.98	17.13	3.12	29.10	5.26	34.64	8.29	1.31	0.60	1.31	0.60	0.923	0.909	0.045	18.501	16.099	11.584	0.001	3.168	6.393
61	Leu61	6.34	0.35	6.36	0.35	7.64	0.87	7.62	0.90	6.48	0.65	6.48	0.65	0.822	0.834	0.061	39.001	77.939	124.550	0.199	0.367	0.523
62	Asp62	1.33	0.10	1.33	0.11	1.90	0.12	1.90	0.12	60.21	8.56	60.21	8.55	0.459	0.510	0.144	140.501	203.218	139.400	3.831	4.530	2.130

Appendix: Scripts

In the following, the most relevant pulse sequences, simulation and evaluation scripts, which were developed throughout the thesis, are given. Lengthy sequences were reduced to the key elements.

Pulse sequences

hXHhmqc

```
;hXH_hmqc
;d1 : recycle delay
;d8 : 1/(2 * J(HX))
;p1 : 1H 90deg pulse
;p3 : X 90deg pulse
;pl1 : 1H power level
;pl2 : X power level
;pl13: Y power level decoupling
;cnst1 : J(HX) scalar coupling [Hz]
;d11 :delay for disk I/O        [30 msec]
;d12 :short switching delay [3 usec]

;AG Reif, Sam Asami, TU Munich

"d8=1/(2*cnst1)"
"d11=30m"
"d12=2u"

"in0=inf1/2"

1 ze
2 d1 do:f2 do:f3
  d12 pl2:f2 pl13:f3
  d12 pl1:f1

  (p1 ph1):f1

  d8
  (p3 ph3):f2
  d12 cpds3:f3
  d0
  (p1*2 ph2):f1
  d0
  (p3 ph4):f2
  d8 pl12:f2

  d12 cpds2:f2

  go=2 ph31
  d12 do:f2  do:f3          ;decoupler off
  d11 mc #0 to 2 F1PH (ip3, id0)
HaltAcqu, d11
exit
```

HhXH_hmqc_rfdr

```
;HhXH_hmqc_rfdr
;d1 : recycle delay
;d8 : 1/(2 * J(HX))
;d11 :delay for disk I/O        [30 msec]
;d12 :short switching delay [3 usec]
;p1 : 1H 90deg pulse
;p3 : X 90deg pulse
;p20 : 1H RFDR pi pulse
;pl1 : 1H power level
;pl2 : X power level
;pl3 : Y power level [0 W, not used]
;pl12 : X power level decoupling
;pl13 : Y power level decoupling
;pl20 : 1H RFDR pi power level
;spnam1 : 1H RFDR pi pulse shape
;cnst1 : J(HX) scalar coupling [Hz]
;l1 : number of RFDR pi pulses
;l31 : MAS frequency [Hz]

;Sam Asami, AG Reif, TU Munich

#include <Avance.incl>
#include <Delay.incl>

"in0=inf1" ; 1H
"in10=inf2/2" ; X

"in2=in10"
"d12=2u"
"d11=30m"

"d0=3u"
"d10=3u"

define delay tper
define delay tmix
"d20=(0.5s/l31)-(p20/2)"

"tper=1/l31"
"tmix=l1*tper"
"cnst10=tmix"
"cnst11=tper"

"cnst20=0"

"d8 = 1/(2*cnst1)"

aqseq 321

1 ze
2 d1 do:f1 do:f2 do:f3 ;decouplers off

  d12 reset:f1 reset:f2 reset:f3
  d12 pl1:f1

  d12 pl12:f2 pl13:f3
  d12 cpds2:f2 cpds3:f3

  d12 fq=cnst22:f1
  (p1 ph2):f1
  d0
  (p1 ph1):f1
  d12 fq=cnst20:f1

  d12 do:f2 do:f3
  d12 pl20:f1

3
  d20
  (p20:spf1 ph27):f1
  d20 ipp27
  lo to 3 times l1
  d12 pl1:f1
  d12 pl2:f2
  (p1 ph0):f1
  d8
  (p3 ph3):f2
  d12 cpds3:f3
  d10
  (p1*2 ph0):f1
  d10
  d12 do:f3
  (p3 ph4):f2
  d8

  d12 pl12:f2 ;pl13:f3
  d12 cpd2:f2 ;cpd3:f3

  go=2 ph31
```

```
  d11 do:f1 do:f2 do:f3 mc #0 to 2
     F1PH(rd10 & ip2, id0)
     F2PH(ip3, id10)
exit
```

HXX_cp_rfdr

```
;HXX_cp_rfdr
;d1 : recycle delay
;d11 :delay for disk I/O        [30 msec]
;d12 :short switching delay [3 usec]
;p1 : X 90deg pulse
;p3 : 1H 90deg pulse
;p15 : 1H,X cp contact time
;p20 : X RFDR pi pulse
;pl1 : X power level
;pl2 : 1H power level
;pl3 : Y power level [0 W, not used]
;pl11 : 1H power level decoupling
;pl12 : X power level decoupling
;pl13 : Y power level decoupling
;pl15 : X cp power level
;pl16 : 1H cp power level
;pl20 : X RFDR pi power level
;spnam1 : 1H cp ramp shape
;spnam10 : X RFDR pi pulse shape
;cnst20 : zero [Hz]
;cnst21 : 13C offset middle of aliphates [Hz]
;l1 : number of RFDR pi pulses
;l31 : MAS frequency [Hz]

;Sam Asami, AG Reif, TU Munich

define delay tper
define delay tmix

"d11=30m"
"d12=3u"

"in0=inf1"

"tper=1/l31"
"tmix=9*p20*l1"
"cnst10=tmix"
"cnst11=tper"

"cnst20=0"
1 ze                    ;accumulate into an empty memory

2 d1 do:f2 do:f3           ;recycle delay, decoupler off in go-loop

  d12 pl2:f2 pl13:f3    ;preselect pl2 drive power for F2, pl1 for F1

  d12 pl11:f1
  d12 cpds1:f1

  d12 fq=cnst21:f2

  (p3 ph1):f2              ;proton 90 pulse

  d0

  d12 do:f1

  d12 fq=cnst20:f2

  (p15:spf1 pl16 ph0):f2 (p15 pl15 ph2):f1

  d12 pl12:f2 pl1:f1
  d12 cpds2:f2 cpds3:f3
  d12

  d10

  (p1 ph5):f1
  d12
  d12 do:f2 do:f3

  d12 pl20:f1

3
    (p20:spf10 ph10):f1
    (p20:spf10 ph11):f1
    (p20:spf10 ph12):f1
    (p20:spf10 ph13):f1
    (p20:spf10 ph14):f1

    (p20:spf10 ph15):f1
    (p20:spf10 ph16):f1
    (p20:spf10 ph17):f1
    (p20:spf10 ph18):f1
lo to 3 times l1
```

```
  d12 pl1:f1
  (p1 ph6):f1

  d12 pl12:f2   pl13:f3
  d12 cpds2:f2 cpds3:f3

  d12
  go=2 ph31
  d12 do:f1 do:f2  do:f3          ;decoupler off

  d11 mc #0 to 2
    F1PH (rd10&ip1, id0)
    F2PH (ip5, id10)
HaltAcqu, 1m
exit
```

HC_cp_homCdec.wsct

```
;HC_cp_homCdec.wsct
;d1 : recycle delay
;d11 :delay for disk I/O        [30 msec]
;d12 :short switching delay [3 usec]
;p1 : 1H 90deg pulse
;p3 : 13C 90deg pulse
;p10 : 1H solvent supp. pulse [~10-20 ms]
;p15 : 1H,13C cp contact time
;p31 : 13C CO+Cb selective pulse length [~4 ms]
;pl1 : 1H power level
;pl2 : 13C power level
;pl3 : Y power level [0 W, not used]
;pl10 : 1H solvent supp. power [~20 kHz]
;pl11 : 1H power level decoupling
;pl12 : 13C power level decoupling
;pl13 : Y power level decoupling
;pl15 : 1H cp power level
;pl16 : 13C cp power level
;pl22 : 13C power level for hom. decoupling
;spnam1 : 1H cp ramp shape
;spnam15 : 13C CO+Cb selective pulse shape
;cpdprg8: 13C hom. decoupling sequence [p5m4sp180.p31]

;Sam Asami, AG Reif, TU Munich

#include <Avance.incl>
#include <Delay.incl>

"in0=inf1"
"in2=in0"

"d11=30m"
"d12=3u"

1 ze
2 d1 do:f1 do:f2 do:f3  ;decouplers off

  d12 reset:f1 reset:f3  reset:f2
  d12  pl1:f1

  p1:f1 ph2
  d12 pl15:f1 pl16:f2

  (p15 ph3):f2 (p15 ph0):f1

  d12 pl11:f1 pl22:f2 pl13:f3
  d12 cpd1:f1 cpd3:f3 cpd8:f2

  d0

  d12 do:f2
  d12 pl2:f2

  p3:f2 ph0
  d12
  d2

  d12 do:f1

  d12 pl10:f1

  (p10 ph0):f1
  (p10 ph1):f1
  (p10 ph0):f1
  (p10 ph1):f1

  p3:f2 ph1

  d12 pl16:f2
  d12 pl15:f1

  (p15 ph6):f2 (p15 ph5):f1

  d12 pl12:f2
  d12  cpd2:f2
```

```
  d12
  go=2 ph31
  d12 do:f1 do:f2 do:f3    ;decouplers off
  d11 mc #0 to 2
    F1PH (ip3, id0 & dd2)
HaltAcqu, lm
exit
```

hXH_hsqc_t1.ws

```
;hXH_hsqc_t1.ws
;d1 : recycle delay
;d4 : 1/(4 * J(HX))
;d11 : delay for disk I/O        [30 msec]
;d12 : short switching delay [3 usec]
;d21 : increment for inv. recovery delay [~20 ms]
;p1 : 1H 90deg pulse
;p3 : X 90deg pulse
;p5 : Y 90deg pulse
;p10 : 1H solvent supp. pulse [~10-20 ms]
;p20 : 1H RFDR pi pulse
;pl1 : 1H power level
;pl2 : X power level
;pl3 : Y power level
;pl10 : 1H solvent supp. power [~20 kHz]
;pl12 : X power level decoupling
;pl13 : Y power level decoupling
;cnst1 : J(HX) scalar coupling [Hz]
;cnst21: 1H offset [Hz]
;l1 : number of cycles of inv. recovery delay

;Sam Asami, AG Reif, TU Munich

#include <Avance.incl>

"in0=inf1/2"

"d4=1.0/(4*cnst1)"

"d11=30ms"
"d12=3u"

;X (= 13C / 15N) T1 inversion recovery period
"d20=d21-p1*2.0"
"d22=d21-p5*2.0"

define delay invrec
"invrec=l1*(2*d21)"
"cnst10=invrec"

1 ze
2 d1 do:f1 do:f2 do:f3
  d12 pl1:f1 pl2:f2

  d12 fq=cnst21:f1

  (p1 ph1):f1
  d4
  (center (p1*2.0 ph0):f1 (p3*2.0 ph0):f2)
  d4
  (center (p1 ph3):f1 (p3 ph7):f2)
  d4
  (center (p1*2.0 ph0):f1 (p3*2.0 ph0):f2)
  d4

  d12 pl13:f3
  d12 cpds3:f3
  d0
  (p1*2.0 pl1 ph3):f1
  d0

  d12 do:f3

; flip back
  (p3 ph5):f2
  d12 do:f1
  d12 pl3:f3

; 13C T1 inversion recovery
3
  d20
  (p1*2.0 ph0):f1
  (p5*2.0 ph0):f3
  d22
lo to 3 times l1

;z filter and 1H saturation for solvent suppression
  d12 fq=0:f1
  d12 pl10:f1
  (p10 ph11):f1
  (p10 ph12):f1
```

```
  (p10 ph11):f1
  (p10 ph12):f1

  d12 pl1:f1

  (p3 ph6):f2

  d4
  (center (p1*2.0 ph0):f1 (p3*2.0 ph0):f2)
  d4
  (center (p1 ph4):f1 (p3 ph9):f2)
  d4
  (center (p1*2.0 ph0):f1 (p3*2.0 ph0):f2)
  d4

  d12 pl12:f2
  d12 cpds2:f2

  go=2 ph31
  d12 do:f2
  d11 mc #0 to 2 F1PH(ip7, id0)
HaltAcqu, 1m
exit
```

hXH_hsqc_redor.ws

```
;hXH_hsqc_redor.ws
;d1 : recycle delay
;d4 : 1/(4 * J(HX))
;d7 : REDOR shift
;d8 : z filter [~5 ms]
;d11 : delay for disk I/O        [30 msec]
;d12 : short switching delay [3 usec]
;d20 : rotor period
;p1 : 1H 90deg pulse
;p3 : X 90deg pulse
;p5 : Y 90deg pulse
;p10 : 1H solvent supp. pulse [~10-20 ms]
;p18 : 1H REDOR pi pulse
;p19 : X REDOR pi pulse
;p20 : 1H RFDR pi pulse
;pl1 : 1H power level
;pl2 : X power level
;pl3 : Y power level [0 W, not used]
;pl10 : 1H solvent supp. power [~20 kHz]
;pl12 : X power level decoupling
;pl13 : Y power level decoupling
;pl18 : 1H REDOR power
;pl19 : X REDOR power
;cnst1 : J(HX) scalar coupling [Hz]
;cnst21: 1H offset [Hz]
;l0 : number REDOR blocks

;Sam Asami, AG Reif, TU Munich
;adapted from: Schanda et al., Angew. Chem. Int. Ed. 2011, 50, 11005-11009

#include <Avance.incl>

define delay tredor
"tredor=2*l0/cnst31"

"d4=1.0/(4.0*cnst1)"

"d11=30ms"
"d12=3u"

"in0=inf1/2"

"cnst19=tredor"

"d20=1/cnst31"  ;rotor period
"d25=larger(0,d7-p18/2)"
"d26=d20-p18-d7-p19*0.5"
"d27=d20-p18*1.5-d7"

1 ze
2 d1 do:f2
  d12 rpp8
  d12 fq=cnst21:f1
  d12 pl1:f1 pl2:f2

; 1H -> 13C INEPT
  (p1 ph1):f1
  d4
  (center (p1*2.0 ph0):f1 (p3*2.0 ph0):f2)
  d4
  (center (p1 ph3):f1 (p3 ph7):f2)
  d4
  (center (p1*2.0 ph0):f1 (p3*2.0 ph0):f2)
  d4

  d12 pl13:f3
  d12 cpds3:f3
```

```
  d0
  (p1*2.0 ph3):f1
  d0
  d12 do:f3

; z-filter
  (p3 ph5):f2
  d8 do:f1
  (p3 ph3):f2

; REDOR period

  d7 pl19:f2 pl18:f1
  (p18  ph8 ipp8):f1
  if(10 > 0)
  {
3 d27
  (p18  ph8 ipp8):f1
  d25
  (p18  ph8 ipp8):f1
  lo to 3 times l0
  }
  d26 dpp8
  (p19  ph15):f2
  d26
  if(10 > 0)
  {
4 (p18  ph8 dpp8):f1
  d25
  (p18  ph8 dpp8):f1
  d27
  lo to 4 times l0
  }
  (p18  ph8 dpp8):f1
  d7
pl2:f2

;z filter and 1H saturation for solvent suppression
  (p3 ph10):f2
  d12 fq=0:f1
  d12 pl10:f1
  (p10 ph11):f1
  (p10 ph12):f1
  (p10 ph11):f1
  (p10 ph12):f1

  d12 pl1:f1
  (p3 ph6):f2

  d4
  (center (p1*2.0 ph0):f1 (p3*2.0 ph0):f2)
  d4
  (center (p1 ph4):f1 (p3 ph9):f2)
  d4
  (center (p1*2.0 ph0):f1 (p3*2.0 ph0):f2)
  d4

  d12 pl12:f2
  d12 cpds2:f2
  go=2 ph31
  d12 do:f2
  d11 mc #0 to 2 F1PH(ip7, id0)
HaltAcqu, lm
exit
```

Numerical spin simulation scripts

SIMPSON: redor_1h_13c.in

```
proc pulseq {} {
  # d7 = REDOR shift [us]
  global par rf_p18 rf_p19 d7

  maxdt 0.5

  set N_REDOR [expr $par(np)]

  set p18 [expr <P18>]
  set p19 [expr <P19>]

  set d20 [expr 1.0e6/$par(spin_rate)]
  set d7 [expr <REDOR_SHIFT>]
  set d25 [expr $d7-0.5*$p18]
  set d26 [expr $d20-$p18-$d7-0.5*$p19]
  set d27 [expr $d20-1.5*$p18-$d7]
```

```
  set dw [expr 0.5e6/$par(spin_rate)]

  #*************************************#
  # propagators ************************#
  #*************************************#
  for { set i_REDOR 0 } { $i_REDOR < $N_REDOR } { incr i_REDOR } {
    reset

    if [expr $i_REDOR == 0] {
      prop 1
      acq
    } elseif [expr $i_REDOR == 1] {
      prop 2
      acq
    } else {

      set count [expr $i_REDOR - 1]

      ####################################################
      # block 2 --> 1st REDOR loop block
      reset
      set i_phase [expr 1 + ($count - 1)*2]
      set i_phase_net [getphase_i $i_phase]
      set i_prop [expr 200 + $i_phase_net]

      prop 20
      prop $i_prop
      store 20

      ####################################################
      # block 5 --> main 2nd REDOR loop block
      reset
      set i_phase [expr 1 + ($count)*2]
      set i_phase_net [getphase_i $i_phase]
      set i_prop [expr 500 + $i_phase_net]

      prop $i_prop
      prop 50
      store 50

      ####################################################
      # set pulse sequence
      reset

      ####################################################
      # block 1
      prop 100

      ####################################################
      # block 2 --> 1st REDOR loop block
      prop 20

      ####################################################
      # block 3 --> REDOR 13C refocussing
      set i_phase [expr 1 + ($count)*2]
      set i_phase_net [getphase_i $i_phase]
      set i_prop [expr 300 + $i_phase_net]
      prop $i_prop

      ####################################################
      # block 5 --> main 2nd REDOR loop block
      prop 50

      ####################################################
      # block 6
      prop 600

      acq
    }
  }
}
```

SIMPSON: protein_rna.in

```
proc main {} {
  global par

  # nuclei:
  # 1 = RNA: G17-H8 (475H8)
  # 2 = RNA: G17-C8 (457C8)
  # 3 = protein: G31-HN (710H)
  # 4 = protein: G31-N (706N)

  set pi [expr asin(1)*2.0]

  # Dipole: H2-->C (1-2)
  set r3  [dip2dist 1H 13C -23268]

  # Dipole: H1-->N (3-4)
  set r1  [dip2dist 1H 15N 12180]

  puts "\n1H RNA (4spin_2x1h_0x2h_1x13c_1x15n, 2 angles)\n"
```

```
foreach {angle_beta2} { 0.0001 54.7356 90 10 20 30 40 50 60 70 80 } {
  foreach {angle_beta1} { 0.0001 54.7356 90 } {

    set angle_beta1_rad [expr $angle_beta1*$pi/180.0]
    set angle_beta2_rad [expr $angle_beta2*$pi/180.0]

    foreach {dipole_scale} { 1 0.00001 0.0001 0.001 0.01 0.1 0.2 0.3
                             0.4 0.5 0.6 0.7 0.8 0.9 1.5 2 2.5 3 3.5
                             4 4.5 5 5.5 6 6.5 7 7.5 8 } {
      set var {};

      ############################
      # CALCULATE PARAMETERS
      ############################

      # H1-->H2 (3-1)
      set dipole_H1_H2 [expr -1103.5*$dipole_scale]
      set dist_H1_H2  [dip2dist 1H 1H $dipole_H1_H2]
      set r2 [expr $dist_H1_H2]

      # H2-->C (1-2)
      set dist_H2_C  [expr $r3]
      set dipole_H2_C  [dist2dip 13C 1H $dist_H2_C]

      # N-->H2 (4-1)
      set dist_N_H2  [expr ( (-$r2*sin($angle_beta1_rad))**2 +
                             ($r2*cos($angle_beta1_rad)+$r1)**2 )**0.5]
      set dipole_N_H2 [dist2dip 15N 1H $dist_N_H2]

      # H1-->C (3-2)
      set dist_H1_C  [expr ( (-$r3*sin($angle_beta1_rad+$angle_beta2_rad)-
                             $r2*sin($angle_beta1_rad))**2 + ($r3*
                             cos($angle_beta1_rad+$angle_beta2_rad)+$r2*cos($angle_beta1_rad))**2 )**0.5]
      set dipole_H1_C  [dist2dip 13C 1H $dist_H1_C]

      # N-->C (4-2)
      set dist_N_C  [expr ( (-$r3*sin($angle_beta1_rad+$angle_beta2_rad)-
                               $r2*sin($angle_beta1_rad))**2 + ($r3*
                               cos($angle_beta1_rad+$angle_beta2_rad)+$r2*cos($angle_beta1_rad)+$r1)**2 )**0.5 ]
      set dipole_N_C  [dist2dip 13C 15N $dist_N_C]

      # angle: N_H1_N_H2 = alpha1
      set angle_N_H1_N_H2_rad [expr acos( ($r1*$r2*cos($angle_beta1_rad)+$r1**2) /
                ($r1*(($r2*sin($angle_beta1_rad))**2 + ($r2*cos($angle_beta1_rad)+$r1)**2)**0.5) ) ]
      set angle_N_H1_N_H2 [expr 180.0*($angle_N_H1_N_H2_rad)/$pi]
      set angle_alpha1 [expr $angle_N_H1_N_H2]

      # angle: H1_H2_H1_C = alpha2
      set angle_H1_H2_H1_C_rad [expr acos( ($r2*$r3*cos($angle_beta1_rad+$angle_beta2_rad)+
          $r2**2*cos($angle_beta1_rad)) / ($r2*((-$r3*sin($angle_beta1_rad+$angle_beta2_rad)-
          $r2*sin($angle_beta1_rad))**2 + ($r3*cos($angle_beta1_rad+$angle_beta2_rad)
          +$r2*cos($angle_beta1_rad))**2)**0.5) ) ]
      set angle_H1_H2_H1_C [expr 180.0*($angle_H1_H2_H1_C_rad)/$pi]
      set angle_alpha2 [expr $angle_H1_H2_H1_C]

      # angle: N_H1_N_C = alpha3
      set angle_N_H1_N_C_rad [expr acos( ($r1*$r3*cos($angle_beta1_rad+$angle_beta2_rad)+
            $r1*$r2*cos($angle_beta1_rad)+$r1**2) / ($r1*((-$r3*sin($angle_beta1_rad+$angle_beta2_rad)-
            $r2*sin($angle_beta1_rad))**2+($r3*cos($angle_beta1_rad+$angle_beta2_rad)+
            $r2*cos($angle_beta1_rad)+$r1)**2)**0.5) ) ]
      set angle_N_H1_N_C [expr 180.0*($angle_N_H1_N_C_rad)/$pi]
      set angle_alpha3 [expr $angle_N_H1_N_C]

      ############################
      # SET DIPOLAR COUPLINGS
      ############################

      # H1-->H2 (3-1)
      lappend var [list dipole_1_3_aniso $dipole_H1_H2]

      # H2-->C (1-2)
      lappend var [list dipole_1_2_aniso $dipole_H2_C]

      # N-->H2 (4-1)
      lappend var [list dipole_1_4_aniso $dipole_N_H2]

      # H1-->C (3-2)
      lappend var [list dipole_2_3_aniso $dipole_H1_C]

      # N-->C (4-2)
      lappend var [list dipole_2_4_aniso $dipole_N_C]

      ############################
      # SET DIPOLAR EULER ANGLES
      ############################

      # H1-->H2 (3-1)
      lappend var [list dipole_1_3_beta $angle_beta1]

      # H2-->C (1-2)
      lappend var [list dipole_1_2_beta [expr $angle_beta1+$angle_beta2]]

      # N-->H2 (4-1)
      lappend var [list dipole_1_4_beta $angle_alpha1]

      # H1-->C (3-2)
      lappend var [list dipole_2_3_beta $angle_alpha2]
```

```
            # N-->C (4-2)
            lappend var [list dipole_2_4_beta $angle_alpha3]

            puts "H1,N distance = $r1"
            puts "H1,H2 distance = $r2"
            puts "H2,C distance = $r3"

            puts "angle(beta1) = $angle_beta1"
            puts "angle(beta2) = $angle_beta2"
            puts "angle(alpha1) = $angle_alpha1"
            puts "angle(alpha2) = $angle_alpha2"
            puts "angle(alpha3) = $angle_alpha3"
            puts "dipole_scale = $dipole_scale"
            puts ""

            set f [fsimpson $var]

            fphase $f -scale [ expr 0.2*96/100]
            faddlb $f 5 0
            fzerofill $f 131072
            fft $f
            fextract $f  5500  6240

            set spename [fsave $f 4spin_2x1h_0x2h_1x13c_1x15n_1beta$angle_beta1
                \_2beta$angle_beta2\_scale$dipole_scale.spe]
            funload $f
        }
    }
  }
}
```

Bibliography

A. Abragam. *The Principles of Nuclear Magnetism*. Clarendon Press, Oxford, 1961.

V. Agarwal and B. Reif. Residual methyl protonation in perdeuterated proteins for multi-dimensional correlation experiments in mas solid-state nmr spectroscopy. *J. Magn. Reson.*, 194(1):16–24, 2008.

V. Agarwal, A. Diehl, N. Skrynnikov, and B. Reif. High resolution h-1 detected h-1,c-13 correlation spectra in mas solid-state nmr using deuterated proteins with selective h-1,h-2 isotopic labeling of methyl groups. *J. Am. Chem. Soc.*, 128 (39):12620–12621, 2006.

V. Agarwal, Y. Xue, B. Reif, and N. R. Skrynnikov. Protein side-chain dynamics as observed by solution- and solid-state nmr spectroscopy: A similarity revealed. *J. Am. Chem. Soc.*, 130 (49):16611–16621, 2008.

V. Agarwal, K. Faelber, P. Schmieder, and B. Reif. High-resolution double-quantum deuterium magic angle spinning solid-state nmr spectroscopy of perdeuterated proteins. *J. Am. Chem. Soc.*, 131(1):2–+, 2009.

V. Agarwal, R. Linser, U. Fink, K. Faelber, and B. Reif. Identification of hydroxyl protons, determination of their exchange dynamics, and characterization of hydrogen bonding in a microcrystallin protein. *J. Am. Chem. Soc.*, 132(9):3187–3195, 2010.

U. Akbey, H. Oschkinat, and B. J. van Rossum. Double-nucleus enhanced recoupling for efficient c-13 mas nmr correlation spectroscopy of perdeuterated proteins. *J. Am. Chem. Soc.*, 131(47):17054–+, 2009.

U. Akbey, S. Lange, W. T. Franks, R. Linser, K. Rehbein, A. Diehl, B. J. van Rossum, B. Reif, and H. Oschkinat. Optimum levels of exchangeable protons in perdeuterated proteins for proton detection in mas solid-state nmr spectroscopy. *J. Biomol. NMR*, 46(1):67–73, 2010.

U. Akbey, F. Camponeschi, B. J. van Rossum, and H. Oschkinat. Triple resonance cross-polarization for more sensitive (13)c mas nmr spectroscopy of deuterated proteins. *ChemPhysChem*, 12(11):2092–2096, 2011.

M. Akke, R. Brueschweiler, and A. G. Palmer. Nmr order parameters and free energy: an analytical approach and its application to cooperative calcium(2+) binding by calbindin d9k. *J. Am. Chem. Soc.*, 115(21):9832–9833, 1993.

H. M. Al-Hashimi, H. Valafar, M. Terrell, E. R. Zartler, M. K. Eidsness, and J. H. Prestegard. Variation of molecular alignment as a means of resolving orientational ambiguities in protein structures from dipolar couplings. *J. Magn. Reson.*, 143(2):402–406, 2000.

A. R. Alkaraghouli and T. F. Koetzle. Neutron-diffraction study of l-phenylalanine hydrochloride. *Acta Crystallogr., Sect. B: Struct. Sci.*, 31(Oct15):2461–2465, 1975.

A. Allerhand, D. Doddrell, U. Glushko, D. W. Cochran, E. Wenkert, P. J. Lawson, and F. R. N. Gurd. Carbon-13 fourier tranform nuclear magnetic resonance .3. conformation and segmental motion of native and denatured ribonuclease-a in solution - application of natural-abundance carbon-13 partially relaxed fourier transform nuclear magnetic resonance. *J. Am. Chem. Soc.*, 93(2):544–&, 1971.

W. A. Anderson and R. Freeman. Influence of a second radiofrequency field on high-resolution nuclear magnetic resonance spectra. *J. Chem. Phys.*, 37(1):85–&, 1962.

E. R. Andrew, A. Bradbury, and R. G. Eades. Nuclear magnetic resonance spectra from a crystal rotated at high speed. *Nature*, 182(4650):1659–1659, 1958.

A. Ansari, J. Berendzen, S. F. Bowne, H. Frauenfelder, I. E. Iben, T. B. Sauke, E. Shyamsunder, and R. D. Young. Protein states and proteinquakes. *Proc. Natl. Acad. Sci. U. S. A.*, 82 (15):5000–4, 1985.

S. Aravamudhan, U. Haeberlen, H. Irngartinger, and C. Krieger. Pyromellitic acid dianhydride - crystal-structure and anisotropic proton magnetic shielding. *Mol. Phys.*, 38(1): 241–255, 1979.

K. Arnold, L. Bordoli, J. Kopp, and T. Schwede. The swiss-model workspace: a web-based environment for protein structure homology modelling. *Bioinformatics*, 22(2):195–201, 2006.

A. S. Arseniev, V. I. Kondakov, V. N. Maiorov, and V. F. Bystrov. Nmr solution spatial structure of short scorpion insectotoxin-i5a. *Febs. Lett.*, 165(1):57–62, 1984.

R. H. Austin, K. W. Beeson, L. Eisenstein, H. Frauenfelder, and I. C. Gunsalus. Dynamics of ligand-binding to myoglobin. *Biochemistry-Us*, 14(24):5355–5373, 1975.

M. Bak, J. T. Rasmussen, and N. C. Nielsen. Simpson: A general simulation program for solid-state nmr spectroscopy. *J. Magn. Reson.*, 147(2):296–330, 2000.

M. Bak, R. Schultz, T. Vosegaard, and N. C. Nielsen. Specification and visualization of anisotropic interaction tensors in polypeptides and numerical simulations in biological solid-state nmr. *J. Magn. Reson.*, 154(1):28–45, 2002.

M. Baldus and B. H. Meier. Total correlation spectroscopy in the solid state. the use of scalar couplings to determine the through-bond connectivity. *J. Magn. Reson. Ser. A*, 121(1): 65–69, 1996.

M. Baldus, A. T. Petkova, J. Herzfeld, and R. G. Griffin. Cross polarization in the tilted frame: assignment and spectral simplification in heteronuclear spin systems. *Mol. Phys.*, 95(6): 1197–1207, 1998.

J. J. Barchi, B. Grasberger, A. M. Gronenborn, and G. M. Clore. Investigation of the backbone dynamics of the igg-binding domain of streptococcal protein-g by heteronuclear 2-dimensional h-1-n-15 nuclear-magnetic-resonance spectroscopy. *Protein Sci.*, 3(1):15–21, 1994.

E. W. Bastiaan, C. Maclean, P. C. M. Van Zijl, and A. A. Bothner. High-resolution nmr of liquids and gases: Effects of magnetic-field-induced molecular alignment. In G. A. Webb, editor, *Annual Reports on NMR Spectroscopy*, volume 19, pages 35–77. Academic Press, 1987. ISBN 0066-4103.

L. S. Batchelder, C. E. Sullivan, L. W. Jelinski, and D. A. Torchia. Characterization of leucine side-chain reorientation in collagen fibrils by solid-state h-2 nmr. *Proc. Natl. Acad. Sci. U. S. A.*, 79(2):386–389, 1982.

L. S. Batchelder, C. H. Niu, and D. A. Torchia. Methyl reorientation in polycrystalline amino-acids and peptides - a h-2 nmr spin-lattice relaxation study. *J. Am. Chem. Soc.*, 105(8): 2228–2231, 1983.

A. Bax, G. W. Vuister, S. Grzesiek, F. Delaglio, A. C. Wang, R. Tschudin, and G. Zhu. Measurement of homo- and heteronuclear j couplings from quantitative j correlation. *Methods Enzymol*, 239:79–105, 1994.

A. Bax, G. Kontaxis, and N. Tjandra. Dipolar couplings in macromolecular structure determination. *Methods Enzymol.*, 339:127–74, 2001.

E. D. Becker, J. A. Ferretti, and T. C. Farrar. Driven equilibrium fourier transform spectroscopy . a new method for nuclear magnetic resonance signal enhancement. *J. Am. Chem. Soc.*, 91(27):7784–&, 1969.

A. E. Bennett, J. H. Ok, R. G. Griffin, and S. Vega. Chemical-shift correlation spectroscopy in rotating solids - radio frequency-driven dipolar recoupling and longitudinal exchange. *J. Chem. Phys.*, 96(11):8624–8627, 1992.

A. E. Bennett, C. M. Rienstra, J. M. Griffiths, W. G. Zhen, P. T. Lansbury, and R. G. Griffin. Homonuclear radio frequency-driven recoupling in rotating solids. *J. Chem. Phys.*, 108(22): 9463–9479, 1998.

P. Bernado and M. Blackledge. Anisotropic small amplitude peptide plane dynamics in proteins from residual dipolar couplings. *J. Am. Chem. Soc.*, 126(15):4907–4920, 2004.

K. D. Berndt, P. Guntert, L. P. M. Orbons, and K. Wuthrich. Determination of a high-quality nuclear-magnetic-resonance solution structure of the bovine pancreatic trypsin-inhibitor and comparison with 3 crystal-structures. *J. Mol. Biol.*, 227 (3):757–775, 1992.

I. Bertini, L. Gonnelli, C. Luchinat, J. F. Mao, and A. Nesi. A new structural model of a beta(40) fibrils. *J. Am. Chem. Soc.*, 133(40):16013–16022, 2011a.

I. Bertini, C. Luchinat, G. Parigi, E. Ravera, B. Reif, and P. Turano. Solid-state nmr of proteins sedimented by ultracentrifugation. *Proc. Natl. Acad. Sci. U. S. A.*, 108(26):10396–10399, 2011b.

R. B. Best, J. Clarke, and M. Karplus. The origin of protein sidechain order parameter distributions. *J. Am. Chem. Soc.*, 126(25):7734–7735, 2004.

R. B. Best, J. Clarke, and M. Karplus. What contributions to protein side-chain dynamics are probed by nmr experiments? a molecular dynamics simulation analysis. *J. Mol. Biol.*, 349 (1):185–203, 2005.

A. Bielecki, A. C. Kolbert, and M. H. Levitt. Frequency-switched pulse sequences: Homonuclear decoupling and dilute spin nmr in solids. *Chem. Phys. Lett.*, 155(4-5):341–346, 1989.

J. Bieschke, M. Herbst, T. Wiglenda, R. P. Friedrich, A. Boeddrich, F. Schiele, D. Kleckers, J. M. Lopez del Amo, B. A. Gruning, Q. Wang, M. R. Schmidt, R. Lurz, R. Anwyl, S. Schnoegl, M. Fandrich, R. F. Frank, B. Reif, S. Gunther, D. M. Walsh, and E. E. Wanker. Small-molecule conversion of toxic oligomers to nontoxic beta-sheet-rich amyloid fibrils. *Nat. Chem. Biol.*, 8(1):93–101, 2012.

C. C. F. Blake, D. F. Koenig, G. A. Mair, A. C. T. North, D. C. Phillips, and V. R. Sarma. Structure of hen egg-white lysozyme - a 3-dimensional fourier synthesis at 2a resolution. *Nature*, 206(4986):757–&, 1965.

N. Bloembergen. On the interaction of nuclear spins in a crystalline lattice. *Physica*, 15(3–4):386–426, 1949.

A. Bockmann, C. Gardiennet, R. Verel, A. Hunkeler, A. Loquet, G. Pintacuda, L. Emsley, B. H. Meier, and A. Lesage. Characterization of different water pools in solid-state nmr protein samples. *J. Biomol. NMR*, 45(3):319–27, 2009.

G. Bodenhausen and R. Freeman. Correlation of proton and c-13 nmr-spectra by heteronuclear 2-dimensional spectroscopy. *J. Magn. Reson.*, 28(3):471–476, 1977.

D. W. Bolen. Effects of naturally occurring osmolytes on protein stability and solubility: issues important in protein crystallization. *Methods*, 34(3):312–322, 2004.

L. Bosman, P. K. Madhu, S. Vega, and E. Vinogradov. Improvement of homonuclear dipolar decoupling sequences in solid-state nuclear magnetic resonance utilising radiofrequency imperfections. *J. Magn. Reson.*, 169(1):39–48, 2004.

G. Bouvignies, P. Bernado, S. Meier, K. Cho, S. Grzesiek, R. Bruschweiler, and M. Blackledge. Identification of slow correlated motions in proteins using residual dipolar and hydrogen-bond scalar couplings. *Proc. Natl. Acad. Sci. U. S. A.*, 102(39):13885–13890, 2005.

G. E. P. Box and M. E. Muller. A note on the generation of random normal deviates. *Ann. Math. Stat.*, 29(2):610–611, 1958.

W. Braun, G. Wider, K. H. Lee, and K. Wuthrich. Conformation of glucagon in a lipid water interphase by h-1 nuclear magnetic-resonance. *J. Mol. Biol.*, 169(4):921–948, 1983.

B. Brooks and M. Karplus. Harmonic dynamics of proteins - normal-modes and fluctuations in bovine pancreatic trypsin-inhibitor. *Proc. Natl. Acad. Sci. U. S. A.*, 80(21):6571–6575, 1983.

B. R. Brooks, R. E. Bruccoleri, B. D. Olafson, D. J. States, S. Swaminathan, and M. Karplus. Charmm - a program for macromolecular energy, minimization, and dynamics calculations. *J. Comput. Chem.*, 4(2):187–217, 1983.

M. F. Brown. Theory of spin-lattice relaxation in lipid bilayers and biological-membranes - h-2 and n-14 quadrupolar relaxation. *J. Chem. Phys.*, 77(3):1576–1599, 1982.

M. F. Brown. Theory of spin-lattice relaxation in lipid bilayers and biological-membranes - dipolar relaxation. *J. Chem. Phys.*, 80(6):2808–2831, 1984.

T. C. Bruice and S. J. Benkovic. Chemical basis for enzyme catalysis. *Biochemistry-Us*, 39(21):6267–74, 2000.

R. Bruschweiler and P. E. Wright. Nmr order parameters of biomolecules - a new analytical representation and application to the gaussian axial fluctuation model. *J. Am. Chem. Soc.*, 116(18):8426–8427, 1994.

S. Bruschweiler, P. Schanda, K. Kloiber, B. Brutscher, G. Kontaxis, R. Konrat, and M. Tollinger. Direct observation of the dynamic process underlying allosteric signal transmission. *J. Am. Chem. Soc.*, 131(8):3063–8, 2009.

D. P. Burum and R. R. Ernst. Net polarization transfer via a j-ordered state for signal enhancement of low-sensitivity nuclei. *J. Magn. Reson.*, 39(1):163–168, 1980.

A. Camara-Artigas, M. Andujar-Sanchez, E. Ortiz-Salmeron, C. Cuadri, E. S. Cobos, and J. M. Martin-Garcia. High-resolution structure of an alpha-spectrin sh3-domain mutant with a redesigned hydrophobic core. *Acta Crystallogr. F*, 66: 1023–1027, 2010.

T. Carlomagno, M. J. Blommers, J. Meiler, B. Cuenoud, and C. Griesinger. Determination of aliphatic side-chain conformation using cross-correlated relaxation: application to an extraordinarily stable 2'-aminoethoxy-modified oligonucleotide triplex. *J. Am. Chem. Soc.*, 123(30):7364–70, 2001.

M. M. Carrio, R. Cubarsi, and A. Villaverde. Fine architecture of bacterial inclusion bodies. *Febs. Lett.*, 471(1):7–11, 2000.

F. Castellani, B. van Rossum, A. Diehl, M. Schubert, K. Rehbein, and H. Oschkinat. Structure of a protein determined by solid-state magic-angle-spinning nmr spectroscopy. *Nature*, 420(6911):98–102, 2002.

J. Cavanagh, W. J. Fairbrother, A. G. Palmer, and N. J. Skelton. *Protein NMR Spectroscopy*. Academic Press, 1996.

I. Chandrasekhar, G. M. Clore, A. Szabo, A. M. Gronenborn, and B. R. Brooks. A 500-ps molecular-dynamics simulation study of interleukin-1-beta in water - correlation with nuclear-magnetic-resonance spectroscopy and crystallography. *J. Mol. Biol.*, 226(1):239–250, 1992.

D. C. Chatfield, A. Szabo, and B. R. Brooks. Molecular dynamics of staphylococcal nuclease: Comparison of simulation with n-15 and c-13 nmr relaxation data. *J. Am. Chem. Soc.*, 120(21):5301–5311, 1998.

N. E. Chayen and E. Saridakis. Protein crystallization: from purified protein to diffraction-quality crystal. *Nat. Methods*, 5(2):147–153, 2008.

E. Y. Chekmenev, Q. W. Zhang, K. W. Waddell, M. S. Mashuta, and R. J. Wittebort. N-15 chemical shielding in glycyl tripeptides: Measurement by solid-state nmr and correlation with x-ray structure. *J. Am. Chem. Soc.*, 126(1):379–384, 2004.

J. Chen, r. Brooks, C. L., and P. E. Wright. Model-free analysis of protein dynamics: assessment of accuracy and model selection protocols based on molecular dynamics simulation. *J. Biomol. NMR*, 29(3):243–57, 2004.

A. V. Cherepanov, C. Glaubitz, and H. Schwalbe. High-resolution studies of uniformly c-13,n-15-labeled rna by solid-state nmr spectroscopy. *Angew. Chem., Int. Ed.*, 49(28): 4747–4750, 2010.

V. Chevelkov. *Development of MAS solid state NMR methods for structural and dynamical characterization of biomolecules*. PhD thesis, Humboldt-Universität zu Berlin, 2007.

V. Chevelkov and B. Reif. Trosy effects in mas solid-state nmr. *Concepts Magn. Reson. A*, 32A(2):143–156, 2008.

V. Chevelkov, B. J. van Rossum, F. Castellani, K. Rehbein, A. Diehl, M. Hohwy, S. Steuernagel, F. Engelke, H. Oschkinat, and B. Reif. H-1 detection in mas solid-state nmr spectroscopy of biomacromolecules employing pulsed field gradients for residual solvent suppression. *J. Am. Chem. Soc.*, 125(26):7788–7789, 2003.

V. Chevelkov, Z. Chen, W. Bermel, and B. Reif. Resolution enhancement in mas solid-state nmr by application of 13c homonuclear scalar decoupling during acquisition. *J. Magn. Reson.*, 172(1):56–62, 2005a.

V. Chevelkov, Z. J. Chen, W. Bermel, and B. Reif. Resolution enhancement in mas solid-state nmr by application of c-13 homonuclear scalar decoupling during acquisition. *J. Magn. Reson.*, 172(1):56–62, 2005b.

V. Chevelkov, K. Faelber, A. Diehl, U. Heinemann, H. Oschkinat, and B. Reif. Detection of dynamic water molecules in a microcrystalline sample of the sh3 domain of a-spectrin by mas solid-state nmr. *J. Biomol. NMR*, 31(4):295–310, 2005c.

V. Chevelkov, K. Faelber, A. Diehl, U. Heinemann, H. Oschkinat, and B. Reif. Detection of dynamic water molecules in a microcrystalline sample of the sh3 domain of alpha-spectrin by mas solid-state nmr. *J. Biomol. NMR*, 31(4):295–310, 2005d.

V. Chevelkov, K. Rehbein, A. Diehl, and B. Reif. Ultrahigh resolution in proton solid-state nmr spectroscopy at high levels of deuteration. *Angew. Chem., Int. Ed.*, 45(23):3878–3881, 2006.

V. Chevelkov, A. Diehl, and B. Reif. Quantitative measurement of differential n-15-h-alpha/beta t-2 relaxation rates in a perdeuterated protein by mas solid-state nmr spectroscopy. *Magn. Reson. Chem.*, 45:S156–S160, 2007a.

V. Chevelkov, K. Faelber, A. Schrey, K. Rehbein, A. Diehl, and B. Reif. Differential line broadening in mas solid-state nmr due to dynamic interference. *J. Am. Chem. Soc.*, 129(33): 10195–10200, 2007b.

V. Chevelkov, A. V. Zhuravleva, Y. Xue, B. Reif, and N. R. Skrynnikov. Combined analysis of n-15 relaxation data from solid- and solution-state nmr spectroscopy. *J. Am. Chem. Soc.*, 129(42):12594–+, 2007c.

V. Chevelkov, A. Diehl, and B. Reif. Measurement of n-15-t-1 relaxation rates in a perdeuterated protein by magic angle spinning solid-state nuclear magnetic resonance spectroscopy. *J. Chem. Phys.*, 128(5):–, 2008.

V. Chevelkov, U. Fink, and B. Reif. Accurate determination of order parameters from h-1,n-15 dipolar couplings in mas solid-state nmr experiments. *J. Am. Chem. Soc.*, 131(39): 14018–14022, 2009a.

V. Chevelkov, U. Fink, and B. Reif. Quantitative analysis of backbone motion in proteins using mas solid-state nmr spectroscopy. *J. Biomol. NMR*, 45(1-2):197–206, 2009b.

V. Chevelkov, Y. Xue, R. Linser, N. R. Skrynnikov, and B. Reif. Comparison of solid-state dipolar couplings and solution relaxation data provides insight into protein backbone dynamics. *J. Am. Chem. Soc.*, 132(14):5015–+, 2010.

J. J. Chou, D. A. Case, and A. Bax. Insights into the mobility of methyl-bearing side chains in proteins from (3)j(cc) and (3)j(cn) couplings. *J. Am. Chem. Soc.*, 125(29):8959–8966, 2003.

P. Cicchetti, B. J. Mayer, G. Thiel, and D. Baltimore. Identification of a protein that binds to the sh3 region of abi and is similar to bcr and gap-rho. *Science*, 257(5071):803–806, 1992.

G. M. Clore and A. M. Gronenborn. Determination of 3-dimensional structures of proteins in solution by nuclear-magnetic-resonance spectroscopy. *Protein Eng.*, 1(4):275–288, 1987.

G. M. Clore and A. M. Gronenborn. Structures of larger proteins in solution - 3-dimensional and 4-dimensional heteronuclear nmr-spectroscopy. *Science*, 252(5011):1390–1399, 1991.

G. M. Clore and A. M. Gronenborn. Nmr structure determination of proteins and protein complexes larger than 20 kda. *Curr. Opin. Chem. Biol.*, 2(5):564–570, 1998a.

G. M. Clore and A. M. Gronenborn. New methods of structure refinement for macromolecular structure determination by nmr. *Proc. Natl. Acad. Sci. U. S. A.*, 95(11):5891–5898, 1998b.

G. M. Clore and J. Iwahara. Theory, practice, and applications of paramagnetic relaxation enhancement for the characterization of transient low-population states of biological macromolecules and their complexes. *Chem. Rev.*, 109(9):4108–39, 2009.

G. M. Clore and C. D. Schwieters. Amplitudes of protein backbone dynamics and correlated motions in a small alpha/beta protein: Correspondence of dipolar coupling and heteronuclear relaxation measurements. *Biochemistry-Us*, 43(33): 10678–10691, 2004.

G. M. Clore, A. M. Gronenborn, A. T. Brunger, and M. Karplus. Solution conformation of a heptadecapeptide comprising the dna-binding helix-f of the cyclic-amp receptor protein of escherichia-coli - combined use of h-1 nuclear magnetic-resonance and restrained molecular-dynamics. *J. Mol. Biol.*, 186(2):435–455, 1985.

G. M. Clore, P. C. Driscoll, P. T. Wingfield, and A. M. Gronenborn. Analysis of the backbone dynamics of interleukin-1-beta using 2-dimensional inverse detected heteronuclear n-15-h-1 nmr-spectroscopy. *Biochemistry-Us*, 29(32):7387–7401, 1990a.

G. M. Clore, A. Szabo, A. Bax, L. E. Kay, P. C. Driscoll, and A. M. Gronenborn. Deviations from the simple 2-parameter model-free approach to the interpretation of n-15 nuclear magnetic-relaxation of proteins. *J. Am. Chem. Soc.*, 112(12): 4989–4991, 1990b.

G. M. Clore, E. C. Murphy, A. M. Gronenborn, and A. Bax. Determination of three-bond (1)h3 '-p-31 couplings in nucleic acids and protein nucleic acid complexes by quantitative j correlation spectroscopy. *J. Magn. Reson.*, 134(1):164–167, 1998.

G. M. Clore, M. R. Starich, C. A. Bewley, M. L. Cai, and J. Kuszewski. Impact of residual dipolar couplings on the accuracy of nmr structures determined from a minimal number of noe restraints. *J. Am. Chem. Soc.*, 121(27):6513–6514, 1999.

A. Cooper. Thermodynamic fluctuations in protein molecules. *Proc. Natl. Acad. Sci. U. S. A.*, 73(8):2740–2741, 1976.

G. Cornilescu, F. Delaglio, and A. Bax. Protein backbone angle restraints from searching a database for chemical shift and sequence homology. *J. Biomol. NMR*, 13(3):289–302, 1999.

H. L. Crespi and J. J. Katz. High resolution proton magnetic resonance studies of fully deuterated and isotope hybrid proteins. *Nature*, 224(5219):560–&, 1969.

H. L. Crespi, Rosenber.Rm, and J. J. Katz. Proton magnetic resonance of proteins fully deuterated except for 1h-leucine side chains. *Science*, 161(3843):796–&, 1968.

M. E. Daley and B. D. Sykes. Characterization of threonine side chain dynamics in an antifreeze protein using natural abundance c-13 nmr spectroscopy. *J. Biomol. NMR*, 29(2): 139–150, 2004.

M. Dasari. *Expression purification and structural studies of Alzheimer's disease amyloid β peptides*. PhD thesis, 2011.

M. Dasari, A. Espargaro, R. Sabate, J. M. Lopez del Amo, U. Fink, G. Grelle, J. Bieschke, S. Ventura, and B. Reif. Bacterial inclusion bodies of alzheimer's disease beta-amyloid peptides can be employed to study native-like aggregation intermediate states. *ChemBioChem*, 12(3):407–23, 2011.

G. De Paepe, J. R. Lewandowski, A. Loquet, A. Bockmann, and R. G. Griffin. Proton assisted recoupling and protein structure determination. *J. Chem. Phys.*, 129(24), 2008.

W. A. Decatur and M. J. Fournier. rrna modifications and ribosome function. *Trends Biochem. Sci.*, 27(7):344–351, 2002.

J. M. L. del Amo, M. Schmidt, U. Fink, M. Dasari, M. Fandrich, and B. Reif. An asymmetric dimer as the basic subunit in alzheimer's disease amyloid beta fibrils. *Angew. Chem., Int. Ed.*, 51(25):6136–6139, 2012.

F. Delaglio, S. Grzesiek, G. W. Vuister, G. Zhu, J. Pfeifer, and A. Bax. Nmrpipe - a multidimensional spectral processing system based on unix pipes. *J. Biomol. NMR*, 6(3):277–293, 1995.

M. J. Dellwo and A. J. Wand. Model-independent and model-dependent analysis of the global and internal dynamics of cyclosporine-a. *J. Am. Chem. Soc.*, 111(13):4571–4578, 1989.

M. Duer. *Solid-State NMR Spectroscopy - Principles and Applications*. Blackwell Science, 2002.

S. D. Durbin and G. Feher. Protein crystallization. *Annu. Rev. Phys. Chem.*, 47:171–204, 1996.

S. V. Dvinskikh, H. Zimmermann, A. Maliniak, and D. Sandstrom. Separated local field spectroscopy of columnar and nematic liquid crystals. *J. Magn. Reson.*, 163(1):46–55, 2003.

S. V. Dvinskikh, H. Zimmermann, A. Maliniak, and D. Sandstrom. Heteronuclear dipolar recoupling in solid-state nuclear magnetic resonance by amplitude-, phase-, and frequency-modulated lee-goldburg cross-polarization. *J. Chem. Phys.*, 122(4), 2005.

R. Elber and M. Karplus. Multiple conformational states of proteins - a molecular-dynamics analysis of myoglobin. *Science*, 235(4786):318–321, 1987.

J. Engelke and H. Ruterjans. Determination of c-13-alpha relaxation-times in uniformly c-13/n-15-enriched proteins. *J. Biomol. NMR*, 5(2):173–182, 1995.

J. Engelke and H. Ruterjans. Dynamics of beta-ch and beta-ch2 groups of amino acid side chains in proteins. *J. Biomol. NMR*, 11(2):165–183, 1998.

M. Ernst, A. Samoson, and B. H. Meier. Low-power decoupling in fast magic-angle spinning nmr. *Chem. Phys. Lett.*, 348 (3-4):293–302, 2001.

A. R. Fadel, D. Q. Jin, G. T. Montelione, and R. M. Levy. Crankshaft motions of the polypeptide backbone in molecular-dynamics simulations of human type-alpha transforming growth-factor. *J. Biomol. NMR*, 6(2):221–226, 1995.

M. Falb, I. Amata, F. Gabel, B. Simon, and T. Carlomagno. Structure of the k-turn u4 rna: a combined nmr and sans study. *Nucleic Acids Res.*, 38(18):6274–6285, 2010.

B. T. Farmer and R. A. Venters. Assignment of side-chain c-13 resonances in perdeuterated proteins. *J. Am. Chem. Soc.*, 117 (14):4187–4188, 1995.

S. B. Feng, C. Kasahara, R. J. Rickles, and S. L. Schreiber. Specific interactions outside the proline-rich core of two classes of src homology 3 ligands. *Proc. Natl. Acad. Sci. U. S. A.*, 92 (26):12408–12415, 1995.

X. Feng, M. Eden, A. Brinkmann, H. Luthman, L. Eriksson, A. Graslund, O. N. Antzutkin, and M. H. Levitt. Direct determination of a peptide torsional angle psi by double-quantum solid-state nmr. *J. Am. Chem. Soc.*, 119(49):12006–12007, 1997.

N. Ferguson, J. Becker, H. Tidow, S. Tremmel, T. D. Sharpe, G. Krause, J. Flinders, M. Petrovich, J. Berriman, H. Oschkinat, and A. R. Fersht. General structural motifs of amyloid protofilaments. *Proc. Natl. Acad. Sci. U. S. A.*, 103(44): 16248–16253, 2006.

C. Fernandez and G. Wider. Trosy in nmr studies of the structure and function of large biological macromolecules. *Curr. Opin. Struct. Biol.*, 13(5):570–580, 2003.

J. Fiaux, E. B. Bertelsen, A. L. Horwich, and K. Wuthrich. Nmr analysis of a 900k groel-groes complex. *Nature*, 418(6894): 207–211, 2002.

M. W. F. Fischer, L. Zeng, A. Majumdar, and E. R. P. Zuiderweg. Characterizing semilocal motions in proteins by nmr relaxation studies. *Proc. Natl. Acad. Sci. U. S. A.*, 95(14): 8016–8019, 1998.

W. T. Franks, D. H. Zhou, B. J. Wylie, B. G. Money, D. T. Graesser, H. L. Frericks, G. Sahota, and C. M. Rienstra. Magic-angle spinning solid-state nmr spectroscopy of the beta 1 immunoglobulin binding domain of protein g (gb1): N-15 and c-13 chemical shift assignments and conformational analysis. *J. Am. Chem. Soc.*, 127(35):12291–12305, 2005.

W. T. Franks, B. J. Wylie, H. L. F. Schmidt, A. J. Nieuwkoop, R. M. Mayrhofer, G. J. Shah, D. T. Graesser, and C. M. Rienstra. Dipole tensor-based atomic-resolution structure determination of a nanocrystalline protein by solid-state nmr. *Proc. Natl. Acad. Sci. U. S. A.*, 105(12):4621–4626, 2008.

H. Frauenfelder, G. A. Petsko, and D. Tsernoglou. Temperature-dependent x-ray-diffraction as a probe of protein structural dynamics. *Nature*, 280(5723):558–563, 1979.

H. Frauenfelder, S. G. Sligar, and P. G. Wolynes. The energy landscapes and motions of proteins. *Science*, 254(5038): 1598–1603, 1991.

K. K. Frederick, K. A. Sharp, N. Warischalk, and A. J. Wand. Re-evaluation of the model-free analysis of fast internal motion in proteins using nmr relaxation. *J. Phys. Chem. B*, 112 (38):12095–12103, 2008.

E. A. Fry, S. Sengupta, V. C. Phan, S. Kuang, and K. W. Zilm. Csa-enabled spin diffusion leads to mas rate-dependent t-1's at high field. *J. Am. Chem. Soc.*, 133(5):1156–1158, 2011.

T. Fujiwara, T. Shimomura, Y. Ohigashi, and H. Akutsu. Multidimensional solid-state nuclear magnetic resonance for determining the dihedral angle from the correlation of c-13-h-1 and c-13-c-13 dipolar interactions under magic-angle spinning conditions. *J. Chem. Phys.*, 109(6):2380–2393, 1998.

B. M. Fung, A. K. Khitrin, and K. Ermolaev. An improved broadband decoupling sequence for liquid crystals and solids. *J. Magn. Reson.*, 142(1):97–101, 2000.

B. Furtig, C. Richter, J. Wohnert, and H. Schwalbe. Nmr spectroscopy of rna. *ChemBioChem*, 4(10):936–962, 2003.

D. Fushman, N. Tjandra, and D. Cowburn. Direct measurement of n-15 chemical shift anisotropy in solution. *J. Am. Chem. Soc.*, 120(42):10947–10952, 1998.

K. H. Gardner and L. E. Kay. Production and incorporation of n-15, c-13, h-2 (h-1-delta 1 methyl) isoleucine into proteins for multidimensional nmr studies. *J. Am. Chem. Soc.*, 119 (32):7599–7600, 1997.

K. H. Gardner and L. E. Kay. The use of h-2, c-13, n-15 multidimensional nmr to study the structure and dynamics of proteins. *Annu. Rev. Biophys. Biomol. Struct.*, 27:357–406, 1998.

K. H. Gardner, M. K. Rosen, and L. E. Kay. Global folds of highly deuterated, methyl-protonated proteins by multidimensional nmr. *Biochemistry*, 36(6):1389–1401, 1997.

D. S. Garrett, Y. J. Seok, D. I. Liao, A. Peterkofsky, A. M. Gronenborn, and G. M. Clore. Solution structure of the 30 kda n-terminal domain of enzyme i of the escherichia coli phosphoenolpyruvate:sugar phosphotransferase system by multidimensional nmr. *Biochemistry*, 36(9):2517–2530, 1997.

E. Gasteiger, A. Gattiker, C. Hoogland, I. Ivanyi, R. D. Appel, and A. Bairoch. Expasy: the proteomics server for in-depth protein knowledge and analysis. *Nucleic Acids Res.*, 31(13): 3784–3788, 2003.

M. I. Geli, R. Lombardi, B. Schmelzl, and H. Riezman. An intact sh3 domain is required for myosin i-induced actin polymerization. *EMBO J.*, 19(16):4281–4291, 2000.

N. Giraud, M. Blackledge, M. Goldman, A. Bockmann, A. Lesage, F. Penin, and L. Emsley. Quantitative analysis of backbone dynamics in a crystalline protein from nitrogen-15 spin-lattice relaxation. *J. Am. Chem. Soc.*, 127(51):18190–18201, 2005.

N. Giraud, M. Blackledge, A. Bockmann, and L. Emsley. The influence of nitrogen-15 proton-driven spin diffusion on the measurement of nitrogen-15 longitudinal relaxation times. *J. Magn. Reson.*, 184(1):51–61, 2007.

N. K. Goto, K. H. Gardner, G. A. Mueller, R. C. Willis, and L. E. Kay. A robust and cost-effective method for the production of val, leu, ile (delta 1) methyl-protonated n-15-, c-13-, h-2-labeled proteins. *J. Biomol. NMR*, 13(4):369–374, 1999.

A. Grommek, B. H. Meier, and M. Ernst. Distance information from proton-driven spin diffusion under mas. *Chem. Phys. Lett.*, 427(4-6):404–409, 2006.

J. D. Gross, D. E. Warschawski, and R. G. Griffin. Dipolar recoupling in mas nmr: A probe for segmental order in lipid bilayers. *J. Am. Chem. Soc.*, 119(4):796–802, 1997.

S. Grzesiek and A. Bax. Correlating backbone amide and side-chain resonances in larger proteins by multiple relayed triple resonance nmr. *J. Am. Chem. Soc.*, 114(16):6291–6293, 1992.

S. Grzesiek, J. Anglister, and A. Bax. Correlation of backbone amide and aliphatic side-chain resonances in c-13/n-15-enriched proteins by isotropic mixing of c-13 magnetization. *J. Magn. Reson. Ser. B*, 101(1):114–119, 1993.

S. Grzesiek, P. Wingfield, S. Stahl, J. D. Kaufman, and A. Bax. 4-dimensional n-15-separated noesy of slowly tumbling perdeuterated n-15-enriched proteins - application to hiv-1 nef. *J. Am. Chem. Soc.*, 117(37):9594–9595, 1995.

M. Guenneugues, B. Gilquin, N. Wolff, A. Menez, and S. Zinn-Justin. Internal motion time scales of a small, highly stable and disulfide-rich protein: A n-15, c-13 nmr and molecular dynamics study. *J. Biomol. NMR*, 14(1):47–66, 1999.

T. Gullion. Introduction to rotational-echo, double-resonance nmr. *Concepts Magn. Reson.*, 10(5):277–289, 1998.

T. Gullion and J. Schaefer. Rotational-echo double-resonance nmr. *J. Magn. Reson.*, 81(1):196–200, 1989.

T. Gullion and J. Schaefer. Elimination of resonance offset effects in rotational-echo, double-resonance nmr. *J. Magn. Reson.*, 92(2):439–442, 1991.

C. Haass and D. J. Selkoe. Soluble protein oligomers in neurodegeneration: lessons from the alzheimer's amyloid beta-peptide. *Nature Rev. Mol. Cell Biol.*, 8(2):101–112, 2007.

U. Haeberlen. *High Resolution NMR in Solids - Selective Averaging*. Academic Press, 1976.

U. Haeberlen and J. S. Waugh. Coherent averaging effects in magnetic resonance. *Phys. Rev.*, 175(2):453–&, 1968.

J. B. Hall and D. Fushman. Variability of the n-15 chemical shielding tensors in the b3 domain of protein g from n-15 relaxation measurements at several fields. implications for backbone order parameters. *J. Am. Chem. Soc.*, 128(24): 7855–7870, 2006.

D. F. Hansen and L. E. Kay. Determining valine side-chain rotamer conformations in proteins from methyl c-13 chemical shifts: Application to the 360 kda half-proteasome. *J. Am. Chem. Soc.*, 133(21):8272–8281, 2011.

D. F. Hansen, P. Vallurupalli, and L. E. Kay. Using relaxation dispersion nmr spectroscopy to determine structures of excited, invisible protein states. *J. Biomol. NMR*, 41(3):113–20, 2008.

H. Hanssum and H. Ruterjans. Anisotropic rotational diffusion of an alpha-helix and analysis of the internal motion of side-chains. *J. Chem. Phys.*, 78(7):4687–4697, 1983.

S. R. Hartmann and E. L. Hahn. Nuclear double resonance in rotating frame. *Phys. Rev.*, 128(5):2042–&, 1962.

H. Heise, W. Hoyer, S. Becker, O. C. Andronesi, D. Riedel, and M. Baldus. Molecular-level secondary structure, polymorphism, and dynamics of full-length alpha-synuclein fibrils studied by solid-state nmr. *Proc. Natl. Acad. Sci. U. S. A.*, 102(44):15871–15876, 2005.

M. Helm. Post-transcriptional nucleotide modification and alternative folding of rna. *Nucleic Acids Res.*, 34(2):721–733, 2006.

J. J. Helmus and C. P. Jaroniec. Nmrglue: an open source python package for the analysis of multidimensional nmr data. *J. Biomol. NMR*, 55(4):355–67, 2013.

J. J. Helmus, K. Surewicz, W. K. Surewicz, and C. P. Jaroniec. Conformational flexibility of y145stop human prion protein amyloid fibrils probed by solid-state nuclear magnetic resonance spectroscopy. *J. Am. Chem. Soc.*, 132(7):2393–2403, 2010.

E. R. Henry and A. Szabo. Influence of vibrational motion on solid-state line-shapes and nmr relaxation. *J. Chem. Phys.*, 82(11):4753–4761, 1985.

G. D. Henry, J. H. Weiner, and B. D. Sykes. Backbone dynamics of a model membrane-protein - c-13 nmr-spectroscopy of alanine methyl-groups in detergent-solubilized m13 coat protein. *Biochemistry-Us*, 25(3):590–598, 1986.

K. Henzler-Wildman and D. Kern. Dynamic personalities of proteins. *Nature*, 450(7172):964–972, 2007.

K. A. Henzler-Wildman, M. Lei, V. Thai, S. J. Kerns, M. Karplus, and D. Kern. A hierarchy of timescales in protein dynamics is linked to enzyme catalysis. *Nature*, 450 (7171):913–U27, 2007.

J. Herzfeld and A. E. Berger. Sideband intensities in nmr-spectra of samples spinning at the magic angle. *J. Chem. Phys.*, 73 (12):6021–6030, 1980.

M. Hochuli, T. Szyperski, and K. Wuthrich. Deuterium isotope effects on the central carbon metabolism of escherichia coli cells grown on a d2o-containing minimal medium. *J. Biomol. NMR*, 17(1):33–42, 2000.

M. Hohwy, C. P. Jaroniec, B. Reif, C. M. Rienstra, and R. G. Griffin. Local structure and relaxation in solid-state nmr: Accurate measurement of amide n-h bond lengths and h-n-h bond angles. *J. Am. Chem. Soc.*, 122(13):3218–3219, 2000.

M. Hologne, K. Faelber, A. Diehl, and B. Reif. Characterization of dynamics of perdeuterated proteins by mas solid-state nmr. *J. Am. Chem. Soc.*, 127(32):11208–11209, 2005.

M. Hologne, V. Chevelkov, and B. Reif. Deuterated peptides and proteins in mas solid-state nmr. *Prog. Nucl. Magn. Reson. Spectrosc.*, 48(4):211–232, 2006.

M. Hong and K. Jakes. Selective and extensive c-13 labeling of a membrane protein for solid-state nmr investigations. *J. Biomol. NMR*, 14(1):71–74, 1999.

M. Hong, J. D. Gross, and R. G. Griffin. Site-resolved determination of peptide torsion angle phi from the relative orientations of backbone n-h and c-h bonds by solid-state nmr. *J. Phys. Chem. B*, 101(30):5869–5874, 1997.

D. I. Hoult and R. E. Richards. Signal-to-noise ratio of nuclear magnetic-resonance experiment. *J. Magn. Reson.*, 24(1):71–85, 1976.

H. Hu, J. Hermans, and A. L. Lee. Relating side-chain mobility in proteins to rotameric transitions: Insights from molecular dynamics simulations and nmr. *J. Biomol. NMR*, 32(2):151–162, 2005.

J. S. Hu and A. Bax. Measurement of three-bond c-13-c-13 j couplings between carbonyl and carbonyl/carboxyl carbons in isotopically enriched proteins. *J. Am. Chem. Soc.*, 118 (34):8170–8171, 1996.

K. Y. Huang, A. B. Siemer, and A. E. McDermott. Homonuclear mixing sequences for perdeuterated proteins. *J. Magn. Reson.*, 208(1):122–127, 2011a.

W. Huang, G. Varani, and G. P. Drobny. C-13/n-15-f-19 intermolecular redor nmr study of the interaction of tar rna with tat peptides. *J. Am. Chem. Soc.*, 132(50):17643–17645, 2010.

W. Huang, G. Varani, and G. P. Drobny. Interactions of protein side chains with rna defined with redor solid state nmr. *J. Biomol. NMR*, 51(3):347–356, 2011b.

W. Huang, M. F. Bardaro, G. Varani, and G. P. Drobny. Preparation of rna samples with narrow line widths for solid state nmr investigations. *J. Magn. Reson.*, 223:51–54, 2012.

M. Huber, S. Hiller, P. Schanda, M. Ernst, A. Bockmann, R. Verel, and B. H. Meier. A proton-detected 4d solid-state nmr experiment for protein structure determination. *ChemPhysChem*, 12:915–918, 2011.

M. Huber, O. With, P. Schanda, R. Verel, M. Ernst, and B. H. Meier. A supplementary coil for (2)h decoupling with commercial hcn mas probes. *J. Magn. Reson.*, 214(1):76–80, 2012.

D. Idiyatullin, I. Nesmelova, V. A. Daragan, and K. H. Mayo. Comparison of (c alpha h)-c-13 and (nh)-n-15 backbone dynamics in protein gb1. *Protein Sci.*, 12(5):914–922, 2003.

T. I. Igumenova and A. E. McDermott. Homo-nuclear 13c j-decoupling in uniformly 13c-enriched solid proteins. *J. Magn. Reson.*, 175(1):11–20, 2005.

T. I. Igumenova, K. K. Frederick, and A. J. Wand. Characterization of the fast dynamics of protein amino acid side chains using nmr relaxation in solution. *Chem. Rev.*, 106(5):1672–1699, 2006.

M. Ikura, L. E. Kay, and A. Bax. A novel approach for sequential assignment of 1h, 13c, and 15n spectra of proteins: heteronuclear triple-resonance three-dimensional nmr spectroscopy. application to calmodulin. *Biochemistry-Us*, 29(19):4659–67, 1990a.

M. Ikura, L. E. Kay, R. Tschudin, and A. Bax. 3-dimensional noesy-hmqc spectroscopy of a c-13-labeled protein. *J. Magn. Reson.*, 86(1):204–209, 1990b.

Y. Ishii, J. P. Yesinowski, and R. Tycko. Sensitivity enhancement in solid-state c-13 nmr of synthetic polymers and biopolymers by h-1 nmr detection with high-speed magic angle spinning. *J. Am. Chem. Soc.*, 123(12):2921–2922, 2001.

R. Ishima and D. A. Torchia. Protein dynamics from nmr. *Nat. Struct. Biol.*, 7(9):740–3, 2000.

R. Ishima, A. P. Petkova, J. M. Louis, and D. A. Torchia. Comparison of methyl rotation axis order parameters derived from model-free analyses of h-2 and c-13 longitudinal and transverse relaxation rates measured in the same protein sample. *J. Am. Chem. Soc.*, 123(25):6164–6171, 2001.

T. Iwatsubo, A. Odaka, N. Suzuki, H. Mizusawa, N. Nukina, and Y. Ihara. Visualization of a-beta-42(43) and a-beta-40 in senile plaques with end-specific a-beta monoclonals - evidence that an initially deposited species is a-beta-42(43). *Neuron*, 13(1):45–53, 1994.

C. P. Jaroniec, B. A. Tounge, C. M. Rienstra, J. Herzfeld, and R. G. Griffin. Recoupling of heteronuclear dipolar interactions with rotational-echo double-resonance at high magic-angle spinning frequencies. *J. Magn. Reson.*, 146(1):132–139, 2000.

C. P. Jaroniec, C. E. MacPhee, N. S. Astrof, C. M. Dobson, and R. G. Griffin. Molecular conformation of a peptide fragment of transthyretin in an amyloid fibril. *Proc. Natl. Acad. Sci. U. S. A.*, 99(26):16748–16753, 2002.

V. A. Jarymowycz and M. J. Stone. Fast time scale dynamics of protein backbones: Nmr relaxation methods, applications, and functional consequences. *Chem. Rev.*, 106(5): 1624–1671, 2006.

J. Jeener, B. H. Meier, P. Bachmann, and R. R. Ernst. Investigation of exchange processes by 2-dimensional nmr-spectroscopy. *J. Chem. Phys.*, 71(11):4546–4553, 1979.

S. Jehle, M. Falb, J. P. Kirkpatrick, H. Oschkinat, B. J. van Rossum, G. Althoff, and T. Carlomagno. Intermolecular protein-rna interactions revealed by 2d p-31-n-15 magic angle spinning solid-state nmr spectroscopy. *J. Am. Chem. Soc.*, 132(11):3842–3846, 2010a.

S. Jehle, P. Rajagopal, B. Bardiaux, S. Markovic, R. Kuhne, J. R. Stout, V. A. Higman, R. E. Klevit, B. J. van Rossum, and H. Oschkinat. Solid-state nmr and saxs studies provide a structural basis for the activation of alpha b-crystallin oligomers. *Nat. Struct. Mol. Biol.*, 17(9):1037–U1, 2010b.

S. Jehle, B. S. Vollmar, B. Bardiaux, K. K. Dove, P. Rajagopal, T. Gonen, H. Oschkinat, and R. E. Klevit. N-terminal domain of alpha b-crystallin provides a conformational switch for multimerization and structural heterogeneity. *Proc. Natl. Acad. Sci. U. S. A.*, 108(16):6409–6414, 2011.

G. P. Jones. Spin-lattice relaxation in rotating frame - weak-collision case. *Phys. Rev.*, 148(1):332–&, 1966.

H. R. Kalbitzer, R. Leberman, and A. Wittinghofer. H-1-nmr spectroscopy on elongation-factor tu from escherichia-coli - resolution enhancement by perdeuteration. *Febs. Lett.*, 180 (1):40–42, 1985.

V. Kanelis, J. D. Forman-Kay, and L. E. Kay. Multidimensional nmr methods for protein structure determination. *IUBMB Life*, 52(6):291–302, 2001.

R. Kaptein, E. R. P. Zuiderweg, R. M. Scheek, R. Boelens, and W. F. Vangunsteren. A protein-structure from nuclear magnetic-resonance data - lac repressor headpiece. *J. Mol. Biol.*, 182(1):179–182, 1985.

M. Karplus. Vicinal proton coupling in nuclear magnetic resonance. *J. Am. Chem. Soc.*, 85(18):2870–+, 1963.

M. Karplus and J. A. Mccammon. Protein structural fluctuations during a period of 100-ps. *Nature*, 277(5697):578–578, 1979.

M. Karplus and J. A. Mccammon. Dynamics of proteins - elements and function. *Annu. Rev. Biochem.*, 52:263–300, 1983.

M. Karplus and G. A. Petsko. Molecular-dynamics simulations in biology. *Nature*, 347(6294):631–639, 1990.

B. K. Kay. Sh3 domains come of age. *Febs. Lett.*, 586(17): 2606–2608, 2012.

B. K. Kay, M. P. Williamson, and P. Sudol. The importance of being proline: the interaction of proline-rich motifs in signaling proteins with their cognate domains. *Faseb J.*, 14(2): 231–241, 2000.

L. E. Kay. Protein dynamics from nmr. *Nat. Struct. Biol.*, 5 Suppl:513–7, 1998.

L. E. Kay. Solution nmr spectroscopy of supra-molecular systems, why bother? a methyl-trosy view. *J. Magn. Reson.*, 210(2):159–170, 2011.

L. E. Kay, D. A. Torchia, and A. Bax. Backbone dynamics of proteins as studied by n-15 inverse detected heteronuclear nmr-spectroscopy - application to staphylococcal nuclease. *Biochemistry-Us*, 28(23):8972–8979, 1989.

L. E. Kay, M. Ikura, R. Tschudin, and A. Bax. 3-dimensional triple-resonance nmr-spectroscopy of isotopically enriched proteins. *J. Magn. Reson.*, 89(3):496–514, 1990.

L. E. Kay, L. K. Nicholson, F. Delaglio, A. Bax, and D. A. Torchia. Pulse sequences for removal of the effects of cross-correlation between dipolar and chemical-shift anisotropy relaxation mechanism on the measurement of heteronuclear t1 and t2 values in proteins. *J. Magn. Reson.*, 97(2):359–375, 1992.

C. Kehlet, J. T. Nielsen, Z. Tosner, and N. C. Nielsen. Resolution-enhanced solid-state nmr (13)c-(13)c correlation spectroscopy by optimal control dipolar-driven spin-state-selective coherence transfer. *J. Phys. Chem. Lett.*, 2(6):543–547, 2011.

J. C. Kendrew, G. Bodo, H. M. Dintzis, R. G. Parrish, H. Wyckoff, and D. C. Phillips. 3-dimensional model of the myoglobin molecule obtained by x-ray analysis. *Nature*, 181 (4610):662–666, 1958.

M. A. Keniry, A. Kintanar, R. L. Smith, H. S. Gutowsky, and E. Oldfield. Nuclear magnetic-resonance studies of amino-acids and proteins - deuterium nuclear magnetic-resonance relaxation of deuteriomethyl-labeled amino-acids in crystals and in halobacterium-halobium and escherichia-coli cell-membranes. *Biochemistry-Us*, 23(2):288–298, 1984.

F. Kiefer, K. Arnold, M. Kunzli, L. Bordoli, and T. Schwede. The swiss-model repository and associated resources. *Nucleic Acids Res.*, 37:D387–D392, 2009.

K. Kinosita, S. Kawato, and A. Ikegami. Theory of fluorescence polarization decay in membranes. *Biophys. J.*, 20(3):289–305, 1977.

T. Kiss. Small nucleolar rna-guided post-transcriptional modification of cellular rnas. *EMBO J.*, 20(14):3617–3622, 2001.

Z. Kiss-Laszlo, Y. Henry, and T. Kiss. Sequence and structural elements of methylation guide snornas essential for site-specific ribose methylation of pre-rrna. *EMBO J.*, 17(3):797–807, 1998.

I. R. Kleckner and M. P. Foster. An introduction to nmr-based approaches for measuring protein dynamics. *BBA-Proteins Proteom.*, 1814(8):942–968, 2011.

M. J. Knight, A. L. Webber, A. J. Pell, P. Guerry, E. Barbet-Massin, I. Bertini, I. C. Felli, L. Gonnelli, R. Pierattelli, L. Emsley, A. Lesage, T. Herrmann, and G. Pintacuda. Fast resonance assignment and fold determination of human superoxide dismutase by high-resolution proton-detected solid-state mas nmr spectroscopy. *Angew. Chem. Int. Ed. Engl.*, 50 (49):11697–701, 2011.

D. M. Korzhnev and L. E. Kay. Probing invisible, low-populated states of protein molecules by relaxation dispersion nmr spectroscopy: an application to protein folding. *Acc. Chem. Res.*, 41(3):442–51, 2008.

F. A. Kovacs, D. J. Fowler, G. J. Gallagher, and L. K. Thompson. A practical guide for solid-state nmr distance measurements in proteins. *Concepts Magn. Reson. A*, 30A(1):21–39, 2007.

M. Kraszni, Z. Szakacs, and B. Noszal. Determination of rotamer populations and related parameters from nmr coupling constants: a critical review. *Anal. Bioanal. Chem.*, 378(6): 1449–1463, 2004.

A. Krushelnitsky, T. Brauniger, and D. Reichert. N-15 spin diffusion rate in solid-state nmr of totally enriched proteins: The magic angle spinning frequency effect. *J. Magn. Reson.*, 182(2):339–342, 2006.

A. Kubo and C. A. Mcdowell. Spectral spin diffusion in polycrystalline solids under magic-angle spinning. *J. Chem. Soc., Faraday Trans. I*, 84:3713–3730, 1988.

K. F. Kuhlmann, D. M. Grant, and R. K. Harris. Nuclear overhauser effects and c-13 relaxation times in c-13- h! double resonance spectra. *J. Chem. Phys.*, 52(7):3439–&, 1970.

A. Kumar, R. R. Ernst, and K. Wuthrich. A two-dimensional nuclear overhauser enhancement (2d noe) experiment for the elucidation of complete proton-proton cross-relaxation networks in biological macromolecules. *Biochem. Bioph. Res. Co.*, 95(1):1–6, 1980.

D. M. Kushlan and D. M. Lemaster. Resolution and sensitivity enhancement of heteronuclear correlation for methylene resonances via h-2-enrichment and decoupling. *J. Biomol. NMR*, 3(6):701–708, 1993.

S. Laage, A. Marchetti, J. Sein, R. Pierattelli, H. J. Sass, S. Grzesiek, A. Lesage, G. Pintacuda, and L. Emsley. Band-selective 1h-13c cross-polarization in fast magic angle spinning solid-state nmr spectroscopy. *J. Am. Chem. Soc.*, 130(51):17216–7, 2008.

S. Laage, A. Lesage, L. Emsley, I. Bertini, I. C. Felli, R. Pierattelli, and G. Pintacuda. Transverse-dephasing optimized homonuclear j-decoupling in solid-state nmr spectroscopy of uniformly 13c-labeled proteins. *J. Am. Chem. Soc.*, 131(31): 10816–7, 2009.

A. Lange, K. Seidel, L. Verdier, S. Luca, and M. Baldus. Analysis of proton-proton transfer dynamics in rotating solids and their use for 3d structure determination. *J. Am. Chem. Soc.*, 125(41):12640–12648, 2003.

O. F. Lange, N. A. Lakomek, C. Fares, G. F. Schroder, K. F. A. Walter, S. Becker, J. Meiler, H. Grubmuller, C. Griesinger, and B. L. de Groot. Recognition dynamics up to microseconds revealed from an rdc-derived ubiquitin ensemble in solution. *Science*, 320(5882):1471–1475, 2008.

L. Latanowicz. Nmr relaxation study of methyl groups in solids from low to high temperatures. *Concepts Magn. Reson. A*, 27A(1):38–53, 2005.

A. L. Lee and A. J. Wand. Microscopic origins of entropy, heat capacity and the glass transition in proteins. *Nature*, 411 (6836):501–504, 2001.

A. L. Lee, K. A. Sharp, J. K. Kranz, X. J. Song, and A. J. Wand. Temperature dependence of the internal dynamics of a calmodulin-peptide complex. *Biochemistry-Us*, 41(46): 13814–13825, 2002.

D. M. Lemaster. Isotope labeling in solution protein assignment and structural-analysis. *Prog. Nucl. Magn. Reson. Spectrosc.*, 26:371–419, 1994.

D. M. Lemaster and J. E. Cronan. Biosynthetic production of c-13-labeled amino-acids with site-specific enrichment. *J. Biol. Chem.*, 257(3):1224–1230, 1982.

D. M. LeMaster and D. M. Kushlan. Dynamical mapping of e-coli thioredoxin via c-13 nmr relaxation analysis. *J. Am. Chem. Soc.*, 118(39):9255–9264, 1996.

D. M. Lemaster and F. M. Richards. Nmr sequential assignment of escherichia-coli thioredoxin utilizing random fractional deuteriation. *Biochemistry*, 27(1):142–150, 1988.

J. Leppert, B. Heise, O. Ohlenschlager, M. Gorlach, and R. Ramachandran. Broadband rfdr with adiabatic inversion pulses. *J. Biomol. NMR*, 26(1):13–24, 2003.

J. Leppert, O. Ohlenschlager, M. Gorlach, and R. Ramachandran. Adiabatic tobsy in rotating solids. *J. Biomol. NMR*, 29 (2):167–173, 2004.

A. Lesage, D. Sakellariou, S. Hediger, B. Elena, P. Charmont, S. Steuernagel, and L. Emsley. Experimental aspects of proton nmr spectroscopy in solids using phase-modulated homonuclear dipolar decoupling. *J. Magn. Reson.*, 163(1): 105–113, 2003.

M. Levitt. Molecular-dynamics of native protein .2. analysis and nature of motion. *J. Mol. Biol.*, 168(3):621–657, 1983.

M. Levitt and R. Sharon. Accurate simulation of protein dynamics in solution. *Proc. Natl. Acad. Sci. U. S. A.*, 85(20): 7557–7561, 1988.

M. H. Levitt. *Spin Dynamics*. John Wiley & Sons, Ltd, 2008.

M. H. Levitt, A. C. Kolbert, A. Bielecki, and D. J. Ruben. High-resolution h-1-nmr in solids with frequency-switched multiple-pulse sequences. *Solid State Nucl. Magn. Reson.*, 2 (4):151–163, 1993.

R. M. Levy, M. Karplus, and J. A. Mccammon. Increase of c-13 nmr relaxation-times in proteins due to picosecond motional averaging. *J. Am. Chem. Soc.*, 103(4):994–996, 1981a.

R. M. Levy, M. Karplus, and P. G. Wolynes. Nmr relaxation parameters in molecules with internal motion - exact langevin trajectory results compared with simplified relaxation models. *J. Am. Chem. Soc.*, 103(20):5998–6011, 1981b.

R. M. Levy, C. M. Dobson, and M. Karplus. Dipolar nmr relaxation of non-protonated aromatic carbons in proteins - structural and dynamical effects. *Biophys. J.*, 39(1):107–113, 1982.

J. R. Lewandowski, J. Sein, H. J. Sass, S. Grzesiek, M. Blackledge, and L. Emsley. Measurement of site-specific 13c spin-lattice relaxation in a crystalline protein. *J. Am. Chem. Soc.*, 132(24):8252–4, 2010.

J. R. Lewandowski, J. N. Dumez, U. Akbey, S. Lange, L. Emsley, and H. Oschkinat. Enhanced resolution and coherence lifetimes in the solid-state nmr spectroscopy of perdeuterated proteins under ultrafast magic-angle spinning. *J. Phys. Chem. Lett.*, 2(17):2205–2211, 2011a.

J. R. Lewandowski, H. J. Sass, S. Grzesiek, M. Blackledge, and L. Emsley. Site-specific measurement of slow motions in proteins. *J. Am. Chem. Soc.*, 133(42):16762–16765, 2011b.

D. W. Li and R. Bruschweiler. A dictionary for protein side-chain entropies from nmr order parameters. *J. Am. Chem. Soc.*, 131(21):7226–7, 2009.

Z. Li, S. Raychaudhuri, and A. J. Wand. Insights into the local residual entropy of proteins provided by nmr relaxation. *Protein Sci.*, 5(12):2647–2650, 1996.

A. R. Lim, G. T. Schueneman, and B. M. Novak. The t-l rho c-13 spin-lattice relaxation time of interpenetrating networks by solid state nmr. *Solid State Commun.*, 109(7):465–470, 1999.

J. Z. Lin, S. M. Lai, R. Jia, A. B. Xu, L. M. Zhang, J. Lu, and K. Q. Ye. Structural basis for site-specific ribose methylation by box c/d rna protein complexes. *Nature*, 469(7331):559–U140, 2011.

J. P. Linge, S. I. O'Donoghue, and M. Nilges. Automated assignment of ambiguous nuclear overhauser effects with aria. *Methods Enzymol.*, 339:71–90, 2001.

R. Linser. Backbone assignment of perdeuterated proteins using long-range h/c-dipolar transfers. *J. Biomol. NMR*, 52(2): 151–158, 2012.

R. Linser, V. Chevelkov, A. Diehl, and B. Reif. Sensitivity enhancement using paramagnetic relaxation in mas solid-state nmr of perdeuterated proteins. *J. Magn. Reson.*, 189(2):209–216, 2007.

R. Linser, U. Fink, and B. Reif. Proton-detected scalar coupling based assignment strategies in mas solid-state nmr spectroscopy applied to perdeuterated proteins. *J. Magn. Reson.*, 193(1):89–93, 2008.

R. Linser, U. Fink, and B. Reif. Narrow carbonyl resonances in proton-diluted proteins facilitate nmr assignments in the solid-state. *J. Biomol. NMR*, 47(1):1–6, 2010.

R. Linser, B. Bardiaux, V. Higman, U. Fink, and B. Reif. Structure calculation from unambiguous long-range amide and methyl (1)h-(1)h distance restraints for a microcrystalline protein with mas solid-state nmr spectroscopy. *J. Am. Chem. Soc.*, 133(15):5905–12, 2011a.

R. Linser, M. Dasari, M. Hiller, V. Higman, U. Fink, J. M. L. del Amo, S. Markovic, L. Handel, B. Kessler, P. Schmieder, D. Oesterhelt, H. Oschkinat, and B. Reif. Proton-detected solid-state nmr spectroscopy of fibrillar and membrane proteins. *Angew. Chem., Int. Ed.*, 50(19):4508–4512, 2011b.

G. Lipari and A. Szabo. Effect of librational motion on fluorescence depolarization and nuclear magnetic-resonance relaxation in macromolecules and membranes. *Biophys. J.*, 30(3): 489–506, 1980.

G. Lipari and A. Szabo. Pade approximants to correlation-functions for restricted rotational diffusion. *J. Chem. Phys.*, 75(6):2971–2976, 1981.

G. Lipari and A. Szabo. Model-free approach to the interpretation of nuclear magnetic-resonance relaxation in macromolecules .1. theory and range of validity. *J. Am. Chem. Soc.*, 104(17):4546–4559, 1982a.

G. Lipari and A. Szabo. Model-free approach to the interpretation of nuclear magnetic-resonance relaxation in macromolecules .2. analysis of experimental results. *J. Am. Chem. Soc.*, 104(17):4559–4570, 1982b.

G. Lipari, A. Szabo, and R. M. Levy. Protein dynamics and nmr relaxation - comparison of simulations with experiment. *Nature*, 300(5888):197–198, 1982.

Y. J. Liu, D. Q. Zhao, R. Altman, and O. Jardetzky. A systematic comparison of 3 structure determination methods from nmr data - dependence upon quality and quantity of data. *J. Biomol. NMR*, 2(4):373–388, 1992.

J. A. B. Lohman and C. Maclean. Alignment effects on high-resolution nmr-spectra, induced by the magnetic-field. *Chem. Phys.*, 35(3):269–274, 1978.

J. A. B. Lohman and C. Maclean. Magnetic-susceptibility anisotropies from quadrupolar magnetic-field effects in high-field h-2 nmr. *Mol. Phys.*, 38(4):1255–1261, 1979.

R. E. London and J. Avitabile. Calculated c-13 nmr relaxation parameters for a restricted internal diffusion-model - application to methionine relaxation in dihydrofolate-reductase. *J. Am. Chem. Soc.*, 100(23):7159–7165, 1978.

J. M. Lopez del Amo, U. Fink, M. Dasari, G. Grelle, E. E. Wanker, J. Bieschke, and B. Reif. Structural properties of egcg-induced, nontoxic alzheimer's disease abeta oligomers. *J. Mol. Biol.*, 421(4-5):517–24, 2012.

J. M. Lopez Del Amo, M. Schmidt, U. Fink, M. Dasari, M. Fandrich, and B. Reif. An asymmetric dimer as the basic subunit in alzheimer's disease amyloid beta fibrils. *Angew. Chem. Int. Ed. Engl.*, 51(25):6136–9, 2012.

A. Loquet, B. Bardiaux, C. Gardiennet, C. Blanchet, M. Baldus, M. Nilges, T. Malliavin, and A. Bockmann. 3d structure determination of the crh protein from highly ambiguous solid-state nmr restraints. *J. Am. Chem. Soc.*, 130(11):3579–3589, 2008.

A. Loquet, K. Giller, S. Becker, and A. Lange. Supramolecular interactions probed by c-13-c-13 solid-state nmr spectroscopy. *J. Am. Chem. Soc.*, 132(43):15164–15166, 2010.

A. Loquet, G. Lv, K. Giller, S. Becker, and A. Lange. C-13 spin dilution for simplified and complete solid-state nmr resonance assignment of insoluble biological assemblies. *J. Am. Chem. Soc.*, 133(13):4722–4725, 2011.

A. Loquet, N. G. Sgourakis, R. Gupta, K. Giller, D. Riedel, C. Goosmann, C. Griesinger, M. Kolbe, D. Baker, S. Becker, and A. Lange. Atomic model of the type iii secretion system needle. *Nature*, 486(7402):276–+, 2012.

J. P. Loria, M. Rance, and A. G. Palmer. A relaxation-compensated carr-purcell-meiboom-gill sequence for characterizing chemical exchange by nmr spectroscopy. *J. Am. Chem. Soc.*, 121(10):2331–2332, 1999.

S. C. Lovell, J. M. Word, J. S. Richardson, and D. C. Richardson. The penultimate rotamer library. *Proteins*, 40(3):389–408, 2000.

I. J. Lowe. Free induction decays of rotating solids. *Phys. Rev. Lett.*, 2(7):285–287, 1959.

S. Luca, H. Heise, and M. Baldus. High-resolution solid-state nmr applied to polypeptides and membrane proteins. *Accounts Chem. Res.*, 36(11):858–865, 2003.

P. Lundstrom, K. Teilum, T. Carstensen, I. Bezsonova, S. Wiesner, D. F. Hansen, T. L. Religa, M. Akke, and L. E. Kay. Fractional c-13 enrichment of isolated carbons using [1-c-13]- or [2-c-13]-glucose facilitates the accurate measurement of dynamics at backbone c-alpha and side-chain methyl positions in proteins. *J. Biomol. NMR*, 38(3):199–212, 2007.

B. A. Lyons, M. Tashiro, L. Cedergren, B. Nilsson, and G. T. Montelione. An improved strategy for determining resonance assignments for isotopically enriched proteins and its application to an engineered domain of staphylococcal protein-a. *Biochemistry-Us*, 32(31):7839–7845, 1993.

B. E. Maden. The numerous modified nucleotides in eukaryotic ribosomal rna. *Prog. Nucleic Acid. Res. Mol. Biol.*, 39:241–303, 1990.

A. Mainz, S. Jehle, B. J. van Rossum, H. Oschkinat, and B. Reif. Large protein complexes with extreme rotational correlation times investigated in solution by magic-angle-spinning nmr spectroscopy. *J. Am. Chem. Soc.*, 131(44):15968–+, 2009.

T. Manolikas, T. Herrmann, and B. H. Meier. Protein structure determination from c-13 spin-diffusion solid-state nmr spectroscopy. *J. Am. Chem. Soc.*, 130(12):3959–3966, 2008.

A. Marchetti, S. Jehle, M. Felletti, M. J. Knight, Y. Wang, Z. Q. Xu, A. Y. Park, G. Otting, A. Lesage, L. Emsley, N. E. Dixon, and G. Pintacuda. Backbone assignment of fully protonated solid proteins by 1h detection and ultrafast magic-angle-spinning nmr spectroscopy. *Angew. Chem., Int. Ed.*, 51(43):10756–10759, 2012.

D. Marion and K. Wuthrich. Application of phase sensitive two-dimensional correlated spectroscopy (cosy) for measurements of h-1-h-1 spin-spin coupling-constants in proteins. *Biochem. Biophys. Res. Commun.*, 113(3):967–974, 1983.

J. L. Markley, I. Putter, and Jardetzk.O. High-resolution nuclear magnetic resonance spectra of selectively deuterated staphylococcal nuclease. *Science*, 161(3847):1249–&, 1968.

D. Marks and S. Vega. A theory for cross-polarization nmr of nonspinning and spinning samples. *J. Magn. Reson. Ser. A*, 118(2):157–172, 1996.

P. R. L. Markwick, T. Malliavin, and M. Nilges. Structural biology by nmr: Structure, dynamics, and interactions. *PLoS Comput. Biol.*, 4(9), 2008.

M. S. Marlow, J. Dogan, K. K. Frederick, K. G. Valentine, and A. J. Wand. The role of conformational entropy in molecular recognition by calmodulin. *Nat. Chem. Biol.*, 6(5):352–8, 2010.

B. J. Mayer. Sh3 domains: complexity in moderation. *J. Cell Sci.*, 114(7):1253–1263, 2001.

K. L. Mayer, M. R. Earley, S. Gupta, K. Pichumani, L. Regan, and M. J. Stone. Covariation of backbone motion throughout a small protein domain. *Nat. Struct. Biol.*, 10(11):962–5, 2003.

B. H. Meier. Cross polarization under fast magic angle spinning - thermodynamical considerations. *Chem. Phys. Lett.*, 188 (3-4):201–207, 1992.

B. H. Meier and R. R. Ernst. Elucidation of chemical-exchange networks by 2-dimensional nmr-spectroscopy - heptamethylbenzenonium ion. *J. Am. Chem. Soc.*, 101(21):6441–6442, 1979.

B. H. Meier, F. Graf, and R. R. Ernst. Structure and dynamics of intramolecular hydrogen-bonds in carboxylic-acid dimers - a solid-state nmr-study. *J. Chem. Phys.*, 76(2):767–774, 1982.

J. Meiler, J. J. Prompers, W. Peti, C. Griesinger, and R. Bruschweiler. Model-free approach to the dynamic interpretation of residual dipolar couplings in globular proteins. *J. Am. Chem. Soc.*, 123(25):6098–6107, 2001.

E. Meirovitch, Y. E. Shapiro, Z. C. Liang, and J. H. Freed. Mode-coupling srls versus mode-decoupled model-free n-h bond dynamics: Mode-mixing and renormalization. *J. Phys. Chem. B*, 107(36):9898–9904, 2003.

E. Meirovitch, Y. E. Shapiro, A. Pohmeno, and J. H. Freed. Structural dynamics of bio-macromolecules by nmr: The slowly relaxing local structure approach. *Prog. Nucl. Magn. Reson. Spectrosc.*, 56(4):360–405, 2010.

G. Metz, X. L. Wu, and S. O. Smith. Ramped-amplitude cross-polarization in magic-angle-spinning nmr. *J. Magn. Reson. Ser. A*, 110(2):219–227, 1994.

O. Millet, D. R. Muhandiram, N. R. Skrynnikov, and L. E. Kay. Deuterium spin probes of side-chain dynamics in proteins. 1. measurement of five relaxation rates per deuteron in c-13-labeled and fractionally h-2-enriched proteins in solution. *J. Am. Chem. Soc.*, 124(22):6439–6448, 2002.

N. G. Mirkin and S. Krimm. Conformation dependence of the (cd alpha)-d-alpha stretch mode in peptides. ii. explicitly hydrated alanine peptide structures. *Biopolymers*, 91(9):791–800, 2009.

A. Mittermaier and L. E. Kay. chi(1) torsion angle dynamics in proteins from dipolar couplings. *J. Am. Chem. Soc.*, 123(28): 6892–6903, 2001.

A. Mittermaier and L. E. Kay. Review - new tools provide new insights in nmr studies of protein dynamics. *Science*, 312 (5771):224–228, 2006.

G. T. Montelione, B. A. Lyons, S. D. Emerson, and M. Tashiro. An efficient triple resonance experiment using c-13 isotropic mixing for determining sequence-specific resonance assignments of isotopically-enriched proteins. *J. Am. Chem. Soc.*, 114(27):10974–10975, 1992.

B. Montpetit, N. D. Thomsen, K. J. Helmke, M. A. Seeliger, J. M. Berger, and K. Weis. A conserved mechanism of dead-box atpase activation by nucleoporins and insp(6) in mrna export. *Nature*, 472(7342):238–242, 2011.

T. Moore, Y. M. Zhang, M. O. Fenley, and H. Li. Molecular basis of box c/d rna-protein interactions: Cocrystal structure of archaeal l7ae and a box c/d rna. *Structure*, 12(5):807–818, 2004.

C. R. Morcombe, V. Gaponenko, R. A. Byrd, and K. W. Zilm. Diluting abundant spins by isotope edited radio frequency field assisted diffusion. *J. Am. Chem. Soc.*, 126(23):7196–7197, 2004.

C. R. Morcombe, E. K. Paulson, V. Gaponenko, R. A. Byrd, and K. W. Zilm. H-1-n-15 correlation spectroscopy of nanocrystalline proteins. *J. Biomol. NMR*, 31(3):217–230, 2005.

J. P. Morken, T. M. Kapoor, S. B. Feng, F. Shirai, and S. L. Schreiber. Exploring the leucine-proline binding pocket of the src sh3 domain using structure-based, split-pool synthesis and affinity-based selection. *J. Am. Chem. Soc.*, 120(1):30–36, 1998.

G. A. Morris. Sensitivity enhancement in n-15-nmr - polarization transfer using the inept pulse sequence. *J. Am. Chem. Soc.*, 102(1):428–429, 1980.

G. A. Morris and R. Freeman. Enhancement of nuclear magnetic-resonance signals by polarization transfer. *J. Am. Chem. Soc.*, 101(3):760–762, 1979.

V. K. Morris, R. Linser, K. L. Wilde, A. P. Duff, M. Sunde, and A. H. Kwan. Solid-state nmr spectroscopy of functional amyloid from a fungal hydrophobin: a well-ordered beta-sheet core amidst structural heterogeneity. *Angew. Chem. Int. Ed. Engl.*, 51(50):12621–5, 2012.

K. T. Mueller. Analytic solutions for the time evolution of dipolar-dephasing nmr signals. *J. Magn. Reson. Ser. A*, 113 (1):81–93, 1995.

D. R. Muhandiram, T. Yamazaki, B. D. Sykes, and L. E. Kay. Measurement of h-2 t-1 and t-1p relaxation-times in uniformly c-13-labeled and fractionally h-2-labeled proteins in solution. *J. Am. Chem. Soc.*, 117(46):11536–11544, 1995.

H. Muirhead and M. F. Perutz. Structure of haemoglobin - a 3-dimensional fourier synthesis of reduced human haemoglobin at 5.5 a resolution. *Nature*, 199(489):633–&, 1963.

A. Musacchio, M. Noble, R. Pauptit, R. Wierenga, and M. Saraste. Crystal-structure of a src-homology-3 (sh3) domain. *Nature*, 359(6398):851–855, 1992.

A. Musacchio, M. Wilmanns, and M. Saraste. Structure and function of the sh3 domain. *Prog. Biophys. Mol. Bio.*, 61(3): 283–297, 1994.

A. J. Nederveen and A. M. J. J. Bonvin. Nmr relaxation and internal dynamics of ubiquitin from a 0.2 s md simulation. *J. Chem. Theory Comput.*, 1(3):363–374, 2005.

L. K. Nicholson, L. E. Kay, D. M. Baldisseri, J. Arango, P. E. Young, A. Bax, and D. A. Torchia. Dynamics of methyl-groups in proteins as studied by proton-detected c-13 nmr-spectroscopy - application to the leucine residues of staphylococcal nuclease. *Biochemistry-Us*, 31(23):5253–5263, 1992.

D. Nietlispach, R. T. Clowes, R. W. Broadhurst, Y. Ito, J. Keeler, M. Kelly, J. Ashurst, H. Oschkinat, P. J. Domaille, and E. D. Laue. An approach to the structure determination of larger proteins using triple resonance nmr experiments in conjunction with random fractional deuteration. *J. Am. Chem. Soc.*, 118(2):407–415, 1996.

N. R. Nirmala and G. Wagner. Measurement of c-13 relaxation-times in proteins by two-dimensional heteronuclear h1-c-13 correlation spectroscopy. *J. Am. Chem. Soc.*, 110(22):7557–7558, 1988.

A. D. Omer, S. Ziesche, H. Ebhardt, and P. P. Dennis. In vitro reconstitution and activity of a c/d box methylation guide ribonucleoprotein complex. *Proc. Natl. Acad. Sci. U. S. A.*, 99 (8):5289–5294, 2002.

S. Oruganti, Y. M. Zhang, H. Z. Li, H. Robinson, M. P. Terns, R. M. Terns, W. Yang, and H. Li. Alternative conformations of the archaeal nop56/58-fibrillarin complex imply flexibility in box c/d rnps. *J. Mol. Biol.*, 371(5):1141–1150, 2007.

M. J. Osborne, J. Schnell, S. J. Benkovic, H. J. Dyson, and P. E. Wright. Backbone dynamics in dihydrofolate reductase complexes: role of loop flexibility in the catalytic mechanism. *Biochemistry-Us*, 40(33):9846–59, 2001.

H. Oschkinat, C. Griesinger, P. J. Kraulis, O. W. Sorensen, R. R. Ernst, A. M. Gronenborn, and G. M. Clore. 3-dimensional nmr-spectroscopy of a protein in solution. *Nature*, 332 (6162):374–376, 1988.

G. Otting, E. Liepinsh, and K. Wuthrich. Disulfide bond isomerization in bpti and bpti(g36s) - an nmr-study of correlated mobility in proteins. *Biochemistry-Us*, 32(14):3571–3582, 1993.

A. W. Overhauser. Paramagnetic relaxation in metals. *Phys. Rev.*, 89(4):689–700, 1953a.

A. W. Overhauser. Polarization of nuclei in metals. *Phys. Rev.*, 92(2):411–415, 1953b.

G. E. Pake. Nuclear resonance absorption in hydrated crystals - fine structure of the proton line. *J. Chem. Phys.*, 16(4): 327–336, 1948.

A. G. Palmer. Nmr characterization of the dynamics of biomacromolecules. *Chem. Rev.*, 104(8):3623–3640, 2004.

A. G. Palmer, N. J. Skelton, W. J. Chazin, P. E. Wright, and M. Rance. Suppression of the effects of cross-correlation between dipolar and anisotropic chemical-shift relaxation mechanisms in the measurement of spin spin relaxation rates. *Mol. Phys.*, 75(3):699–711, 1992.

Y. Pan, T. Gullion, and J. Schaefer. Determination of c-n internuclear distances by rotational-echo double-resonance nmr of solids. *J. Magn. Reson.*, 90(2):330–340, 1990.

A. M. Panich and G. B. Furman. Nuclear spin–lattice relaxation and paramagnetic defects in carbon nanomaterials. *Diam. Relat. Mater.*, 23(0):157–161, 2012.

A. K. Paravastu, I. Qahwash, R. D. Leapman, S. C. Meredith, and R. Tycko. Seeded growth of beta-amyloid fibrils from alzheimer's brain-derived fibrils produces a distinct fibril structure. *Proc. Natl. Acad. Sci. U. S. A.*, 106(18):7443–7448, 2009.

S. H. Park, B. B. Das, F. Casagrande, Y. Tian, H. J. Nothnagel, M. N. Chu, H. Kiefer, K. Maier, A. A. De Angelis, F. M. Marassi, and S. J. Opella. Structure of the chemokine receptor cxcr1 in phospholipid bilayers. *Nature*, 491(7426): 779–+, 2012.

J. Pauli, B. van Rossum, H. Forster, H. J. M. de Groot, and H. Oschkinat. Sample optimization and identification of signal patterns of amino acid side chains in 2d rfdr spectra of the alpha-spectrin sh3 domain. *J. Magn. Reson.*, 143(2):411–416, 2000.

J. Pauli, M. Baldus, B. van Rossum, H. de Groot, and H. Oschkinat. Backbone and side-chain c-13 and n-15 signal assignments of the alpha-spectrin sh3 domain by magic angle spinning solid-state nmr at 17.6 tesla. *ChemBioChem*, 2(4): 272–281, 2001.

E. K. Paulson, C. R. Morcombe, V. Gaponenko, B. Dancheck, R. A. Byrd, and K. W. Zilm. Sensitive high resolution inverse detection nmr spectroscopy of proteins in the solid state. *J. Am. Chem. Soc.*, 125(51):15831–15836, 2003.

M. C. Peitsch. Protein modeling by e-mail. *Bio-Technology*, 13 (7):658–660, 1995.

J. W. Peng. Exposing the moving parts of proteins with nmr spectroscopy. *J. Phys. Chem. Lett.*, 3(8):1039–1051, 2012.

K. Pervushin. Impact of transverse relaxation optimized spectroscopy (trosy) on nmr as a technique in structural biology. *Q. Rev. Biophys.*, 33(2):161–197, 2000.

K. Pervushin, R. Riek, G. Wider, and K. Wuthrich. Attenuated t-2 relaxation by mutual cancellation of dipole-dipole coupling and chemical shift anisotropy indicates an avenue to nmr structures of very large biological macromolecules in solution. *Proc. Natl. Acad. Sci. U. S. A.*, 94(23):12366–12371, 1997.

A. T. Petkova, R. D. Leapman, Z. H. Guo, W. M. Yau, M. P. Mattson, and R. Tycko. Self-propagating, molecular-level polymorphism in alzheimer's beta-amyloid fibrils. *Science*, 307(5707):262–265, 2005.

A. T. Petkova, W. M. Yau, and R. Tycko. Experimental constraints on quaternary structure in alzheimer's beta-amyloid fibrils. *Biochemistry-Us*, 45(2):498–512, 2006.

A. Pines, M. G. Gibby, and J. S. Waugh. Proton-enhanced nmr of dilute spins in solids. *J. Chem. Phys.*, 59(2):569–590, 1973.

C. B. Post, C. M. Dobson, and M. Karplus. A molecular-dynamics analysis of protein structural elements. *Proteins*, 5(4):337–354, 1989.

J. H. Prestegard. New techniques in structural nmr - anisotropic interactions. *Nat. Struct. Biol.*, 5:517–522, 1998.

J. H. Prestegard and A. I. Kishore. Partial alignment of biomolecules: an aid to nmr characterization. *Curr. Opin. Chem. Biol.*, 5(5):584–590, 2001.

J. H. Prestegard, H. M. Al-Hashimi, and J. R. Tolman. Nmr structures of biomolecules using field oriented media and residual dipolar couplings. *Q. Rev. Biophys.*, 33(04):371–424, 2000.

J. J. Prompers and R. Bruschweiler. General framework for studying the dynamics of folded and nonfolded proteins by nmr relaxation spectroscopy and md simulation. *J. Am. Chem. Soc.*, 124(16):4522–34, 2002.

D. P. Raleigh, M. H. Levitt, and R. G. Griffin. Rotational resonance in solid-state nmr. *Chem. Phys. Lett.*, 146(1-2):71–76, 1988.

B. E. Ramirez and A. Bax. Modulation of the alignment tensor of macromolecules dissolved in a dilute liquid crystalline medium. *J. Am. Chem. Soc.*, 120(35):9106–9107, 1998.

B. Reif. Ultra-high resolution in mas solid-state nmr of perdeuterated proteins: Implications for structure and dynamics. *J. Magn. Reson.*, 216:1–12, 2012.

B. Reif and R. G. Griffin. H-1 detected h-1, n-15 correlation spectroscopy in rotating solids. *J. Magn. Reson.*, 160(1):78–83, 2003.

B. Reif, M. Hennig, and C. Griesinger. Direct measurement of angles between bond vectors in high-resolution nmr. *Science*, 276(5316):1230–1233, 1997.

B. Reif, M. Hohwy, C. P. Jaroniec, C. M. Rienstra, and R. G. Griffin. Nh-nh vector correlation in peptides by solid-state nmr. *J. Magn. Reson.*, 145(1):132–141, 2000.

B. Reif, C. P. Jaroniec, C. M. Rienstra, M. Hohwy, and R. G. Griffin. H-1-h-1 mas correlation spectroscopy and distance measurements in a deuterated peptide. *J. Magn. Reson.*, 151 (2):320–327, 2001.

B. Reif, B. J. van Rossum, F. Castellani, K. Rehbein, A. Diehl, and H. Oschkinat. Characterization of h-1-h-1 distances in a uniformly h-2,n-15-labeled sh3 domain by mas solid-state nmr spectroscopy. *J. Am. Chem. Soc.*, 125(6):1488–1489, 2003.

B. Reif, Y. Xue, V. Agarwal, M. S. Pavlova, M. Hologne, A. Diehl, Y. E. Ryabov, and N. R. Skrynnikov. Protein side-chain dynamics observed by solution- and solid-state nmr: Comparative analysis of methyl h-2 relaxation data. *J. Am. Chem. Soc.*, 128(38):12354–12355, 2006.

R. B. Ren, B. J. Mayer, P. Cicchetti, and D. Baltimore. Identification of a 10-amino acid proline-rich sh3 binding-site. *Science*, 259(5098):1157–1161, 1993.

R. Richarz, K. Nagayama, and K. Wuthrich. C-13 nuclear magnetic-resonance relaxation studies of internal mobility of the polypeptide-chain in basic pancreatic trypsin-inhibitor and a selectively reduced analog. *Biochemistry-Us*, 19(23): 5189–5196, 1980a.

R. Richarz, H. Tschesche, and K. Wuthrich. C-13 nuclear magnetic-resonance studies of the selectively isotope-labeled reactive site peptide-bond of the basic pancreatic trypsin-inhibitor in the complexes with trypsin, trypsinogen, and anhydrotrypsin. *Biochemistry-Us*, 19(25):5711–5715, 1980b.

K. Riedel, J. Leppert, O. Ohlenschlager, M. Gorlach, and R. Ramachandran. Tedor with adiabatic inversion pulses: Resonance assignments of c-13/n-15 labelled rnas. *J. Biomol. NMR*, 31(1):49–57, 2005.

K. Riedel, C. Herbst, S. Hafner, J. Leppert, O. Ohlenschlaeger, M. S. Swanson, M. Gorlach, and R. Ramachandran. Constraints on the structure of (cug)(97) rna from magic-angle-spinning solid-state nmr spectroscopy. *Angew. Chem., Int. Ed.*, 45(34):5620–5623, 2006.

C. M. Rienstra, M. Hohwy, L. J. Mueller, C. P. Jaroniec, B. Reif, and R. G. Griffin. Determination of multiple torsion-angle constraints in u-c-13,n-15-labeled peptides: 3d h-1-n-15-c-13-h-1 dipolar chemical shift nmr spectroscopy in rotating solids. *J. Am. Chem. Soc.*, 124(40):11908–11922, 2002a.

C. M. Rienstra, L. Tucker-Kellogg, C. P. Jaroniec, M. Hohwy, B. Reif, M. T. McMahon, B. Tidor, T. Lozano-Perez, and R. G. Griffin. De novo determination of peptide structure with solid-state magic-angle spinning nmr spectroscopy. *Proc. Natl. Acad. Sci. U. S. A.*, 99(16):10260–10265, 2002b.

J. E. Roberts, G. S. Harbison, M. G. Munowitz, J. Herzfeld, and R. G. Griffin. Measurement of heteronuclear bond distances in polycrystalline solids by solid-state nmr techniques. *J. Am. Chem. Soc.*, 109(14):4163–4169, 1987.

B. V. Rollin and J. Hatton. Nuclear paramagnetism at low temperatures. *Phys. Rev.*, 74(3):346–346, 1948.

D. Rovnyak. Tutorial on analytic theory for cross-polarization in solid state nmr. *Concepts Magn. Reson. A*, 32A(4):254–276, 2008.

J. C. Sacchettini and J. W. Kelly. Therapeutic strategies for human amyloid diseases. *Nat. Rev. Drug Discov.*, 1(4):267–275, 2002.

D. Sakellariou, A. Lesage, P. Hodgkinson, and L. Emsley. Homonuclear dipolar decoupling in solid-state nmr using continuous phase modulation. *Chem. Phys. Lett.*, 319(3-4): 253–260, 2000.

M. Salzmann, K. Pervushin, G. Wider, H. Senn, and K. Wuthrich. Trosy in triple-resonance experiments: New perspectives for sequential nmr assignment of large proteins. *Proc. Natl. Acad. Sci. U. S. A.*, 95(23):13585–13590, 1998.

M. Salzmann, G. Wider, K. Pervushin, H. Senn, and K. Wuthrich. Trosy-type triple-resonance experiments for sequential nmr assignments of large proteins. *J. Am. Chem. Soc.*, 121(4):844–848, 1999.

A. Samoson, T. Tuherm, and Z. Gan. High-field high-speed mas resolution enhancement in h-1 nmr spectroscopy of solids. *Solid. State. Nucl. Mag.*, 20(3-4):130–136, 2001.

D. G. Sashital, M. Jinek, and J. A. Doudna. An rna-induced conformational change required for crispr rna cleavage by the endoribonuclease cse3. *Nat. Struct. Mol. Biol.*, 18(6): 680–U77, 2011.

J. Schaefer and E. O. Stejskal. C-13 nuclear magnetic-resonance of polymers spinning at magic angle. *J. Am. Chem. Soc.*, 98 (4):1031–1032, 1976.

H. Schagger and G. von Jagow. Tricine-sodium dodecyl sulfate-polyacrylamide gel electrophoresis for the separation of proteins in the range from 1 to 100 kda. *Anal. Biochem.*, 166(2): 368–79, 1987.

P. Schanda, M. Huber, R. Verel, M. Ernst, and B. H. Meier. Direct detection of (3h)j(nc ') hydrogen-bond scalar couplings in proteins by solid-state nmr spectroscopy. *Angew. Chem., Int. Ed.*, 48(49):9322–9325, 2009.

P. Schanda, B. H. Meier, and M. Ernst. Quantitative analysis of protein backbone dynamics in microcrystalline ubiquitin by solid-state nmr spectroscopy. *J. Am. Chem. Soc.*, 132(45): 15957–15967, 2010.

P. Schanda, M. Huber, J. Boisbouvier, B. H. Meier, and M. Ernst. Solid-state nmr measurements of asymmetric dipolar couplings provide insight into protein side-chain motion. *Angew. Chem., Int. Ed.*, 50(46):11005–11009, 2011a.

P. Schanda, B. H. Meier, and M. Ernst. Accurate measurement of one-bond h-x heteronuclear dipolar couplings in mas solid-state nmr. *J. Magn. Reson.*, 210(2):246–259, 2011b.

H. Schwalbe and J. Rinnenthal. Thermodynamics: the world is flat. *Nat. Chem. Biol.*, 6(5):312–3, 2010.

H. Schwalbe, T. Carlomagno, M. Hennig, J. Junker, B. Reif, C. Richter, and C. Griesinger. Cross-correlated relaxation for measurement of angles between tensorial interactions. *Methods Enzymol.*, 338:35–81, 2001.

D. J. Selkoe. Alzheimer's disease: Genes, proteins, and therapy. *Physiol. Rev.*, 81(2):741–766, 2001.

I. V. Sergeyev, L. A. Day, A. Goldbourt, and A. E. McDermott. Chemical shifts for the unusual dna structure in pf1 bacteriophage from dynamic-nuclear-polarization-enhanced solid-state nmr spectroscopy. *J. Am. Chem. Soc.*, 133(50): 20208–20217, 2011.

S. A. Shahid, B. Bardiaux, W. T. Franks, L. Krabben, M. Habeck, B. J. van Rossum, and D. Linke. Membrane-protein structure determination by solid-state nmr spectroscopy of microcrystals. *Nat. Methods*, 9(12):1212–U119, 2012.

A. J. Shaka, J. Keeler, T. Frenkiel, and R. Freeman. An improved sequence for broad-band decoupling - waltz-16. *J. Magn. Reson.*, 52(2):335–338, 1983.

X. Shan, K. H. Gardner, D. R. Muhandiram, N. S. Rao, C. H. Arrowsmith, and L. E. Kay. Assignment of n-15, c-13(alpha), c-13(beta), and hn resonances in an n-15, c-13, h-2 labeled 64 kda trp repressor-operator complex using triple-resonance nmr spectroscopy and h-2-decoupling. *J. Am. Chem. Soc.*, 118(28):6570–6579, 1996.

D. E. Shaw, P. Maragakis, K. Lindorff-Larsen, S. Piana, R. O. Dror, M. P. Eastwood, J. A. Bank, J. M. Jumper, J. K. Salmon, Y. B. Shan, and W. Wriggers. Atomic-level characterization of the structural dynamics of proteins. *Science*, 330(6002):341–346, 2010.

A. Shekhtman, R. Ghose, M. Goger, and D. Cowburn. Nmr structure determination and investigation using a reduced proton (redpro) labeling strategy for proteins. *FEBS Lett.*, 524(1-3):177–82, 2002.

Y. Shen, O. Lange, F. Delaglio, P. Rossi, J. M. Aramini, G. H. Liu, A. Eletsky, Y. B. Wu, K. K. Singarapu, A. Lemak, A. Ignatchenko, C. H. Arrowsmith, T. Szyperski, G. T. Montelione, D. Baker, and A. Bax. Consistent blind protein structure generation from nmr chemical shift data. *Proc. Natl. Acad. Sci. U. S. A.*, 105(12):4685–4690, 2008.

Y. Shen, F. Delaglio, G. Cornilescu, and A. Bax. Talos plus : a hybrid method for predicting protein backbone torsion angles from nmr chemical shifts. *J. Biomol. NMR*, 44(4):213–223, 2009.

D. Sheppard, D. W. Li, R. Bruschweiler, and V. Tugarinov. Deuterium spin probes of backbone order in proteins: H-2 nmr relaxation study of deuterated carbon alpha sites. *J. Am. Chem. Soc.*, 131(43):15853–15865, 2009.

F. Shewmaker, R. B. Wickner, and R. Tycko. Amyloid of the prion domain of sup35p has an in-register parallel beta-sheet structure. *Proc. Natl. Acad. Sci. U. S. A.*, 103(52):19754–19759, 2006.

L. Shi, X. Peng, M. A. Ahmed, D. Edwards, L. S. Brown, and V. Ladizhansky. Resolution enhancement by homonuclear j-decoupling: application to three-dimensional solid-state magic angle spinning nmr spectroscopy. *J. Biomol. NMR*, 41(1):9–15, 2008.

S. A. Showalter and R. Brüschweiler. Validation of molecular dynamics simulations of biomolecules using nmr spin relaxation as benchmarks: application to the amber99sb force field. *J. Chem. Theory Comput.*, 3(3):961–975, 2007.

J. D. Sipe. Amyloidosis. *Annu. Rev. Biochem.*, 61:947–975, 1992.

N. R. Skrynnikov. Asymmetric doublets in mas nmr: coherent and incoherent mechanisms. *Magn. Reson. Chem.*, 45:S161–S173, 2007.

N. R. Skrynnikov, N. K. Goto, D. W. Yang, W. Y. Choy, J. R. Tolman, G. A. Mueller, and L. E. Kay. Orienting domains in proteins using dipolar couplings measured by liquid-state nmr: Differences in solution and crystal forms of maltodextrin binding protein loaded with beta-cyclodextrin. *J. Mol. Biol.*, 295(5):1265–1273, 2000.

N. R. Skrynnikov, O. Millet, and L. E. Kay. Deuterium spin probes of side-chain dynamics in proteins. 2. spectral density mapping and identification of nanosecond time-scale side-chain motions. *J. Am. Chem. Soc.*, 124(22):6449–6460, 2002.

P. E. Smith, R. C. Vanschaik, T. Szyperski, K. Wuthrich, and W. F. Vangunsteren. Internal mobility of the basic pancreatic trypsin-inhibitor in solution - a comparison of nmr spin relaxation measurements and molecular-dynamics simulations. *J. Mol. Biol.*, 246(2):356–365, 1995.

S. A. Smith. *GAMMA Manual - Rank 2 Interactions*. 1999.

S. A. Smith, T. O. Levante, B. H. Meier, and R. R. Ernst. Computer-simulations in magnetic-resonance - an object-oriented programming approach. *J. Magn. Reson. Ser. A*, 106 (1):75–105, 1994.

I. Solomon. Relaxation processes in a system of 2 spins. *Phys. Rev.*, 99(2):559–565, 1955.

X. J. Song, P. F. Flynn, K. A. Sharp, and A. J. Wand. Temperature dependence of fast dynamics in proteins. *Biophys. J.*, 92 (6):L43–L45, 2007.

O. W. Sorensen, G. W. Eich, M. H. Levitt, G. Bodenhausen, and R. R. Ernst. Product operator-formalism for the description of nmr pulse experiments. *Prog. Nucl. Magn. Reson. Spectrosc.*, 16:163–192, 1983.

S. Spera and A. Bax. Empirical correlation between protein backbone conformation and c-alpha and c-beta c-13 nuclear-magnetic-resonance chemical-shifts. *J. Am. Chem. Soc.*, 113 (14):5490–5492, 1991.

R. Sprangers and L. E. Kay. Quantitative dynamics and binding studies of the 20s proteasome by nmr. *Nature*, 445(7128): 618–622, 2007.

R. Sprangers, M. J. Bottomley, J. P. Linge, J. Schultz, M. Nilges, and M. Sattler. Refinement of the protein backbone angle psi in nmr structure calculations. *J. Biomol. NMR*, 16(1):47–58, 2000.

T. Steiner. Lengthening of the n-h bond in n-h-center-dot-center-dot-center-dot-n hydrogen-bonds - preliminary structural data and implications of the bond valence concept. *J. Chem. Soc. Chem. Commun.*, (13):1331–1332, 1995.

T. Steiner. The hydrogen bond in the solid state. *Angew. Chem., Int. Ed.*, 41(1):48–76, 2002.

E. O. Stejskal, J. Schaefer, and J. S. Waugh. Magic-angle spinning and polarization transfer in proton-enhanced nmr. *J. Magn. Reson.*, 28(1):105–112, 1977.

M. J. Stone. Nmr relaxation studies of the role of conformational entropy in protein stability and ligand binding. *Acc. Chem. Res.*, 34(5):379–88, 2001.

M. J. Stone, W. J. Fairbrother, A. G. Palmer, J. Reizer, M. H. Saier, and P. E. Wright. Backbone dynamics of the bacillus-subtilis glucose permease-iia domain determined from n-15 nmr relaxation measurements. *Biochemistry-Us*, 31(18): 4394–4406, 1992.

M. J. Stone, S. Gupta, N. Snyder, and L. Regan. Comparison of protein backbone entropy and beta-sheet stability: Nmr-derived dynamics of protein g b1 domain mutants. *J. Am. Chem. Soc.*, 123(1):185–6, 2001.

S. K. Straus, T. Bremi, and R. R. Ernst. Resolution enhancement by homonuclear j decoupling in solid-state mas nmr. *Chem. Phys. Lett.*, 262(6):709–715, 1996.

T. O. Street, D. W. Bolen, and G. D. Rose. A molecular mechanism for osmolyte-induced protein stability. *Proc. Natl. Acad. Sci. U. S. A.*, 103(38):13997–14002, 2006.

D. Stueber and D. M. Grant. C-13 and n-15 chemical shift tensors in adenosine, guanosine dihydrate, 2 '-deoxythymidine, and cytidine. *J. Am. Chem. Soc.*, 124(35):10539–10551, 2002.

N. M. Szeverenyi, M. J. Sullivan, and G. E. Maciel. Observation of spin exchange by two-dimensional fourier-transform c-13 cross polarization-magic-angle spinning. *J. Magn. Reson.*, 47(3):462–475, 1982.

T. Szyperski, P. Luginbuhl, G. Otting, P. Guntert, and K. Wuthrich. Protein dynamics studied by rotating frame n-15 spin relaxation-times. *J. Biomol. NMR*, 3(2):151–164, 1993.

K. Takegoshi, S. Nakamura, and T. Terao. C-13-h-1 dipolar-assisted rotational resonance in magic-angle spinning nmr. *Chem. Phys. Lett.*, 344(5-6):631–637, 2001.

K. Takegoshi, S. Nakamura, and T. Terao. C-13-h-1 dipolar-driven c-13-c-13 recoupling without c-13 rf irradiation in nuclear magnetic resonance of rotating solids. *J. Chem. Phys.*, 118(5):2325–2341, 2003.

H. S. Tam, J. I. Choe, and M. D. Harmony. Molecular-structure of polyatomic-molecules using scaled moments of inertia. *J. Phys. Chem.*, 95(23):9267–9272, 1991.

M. Tang, G. Comellas, L. J. Mueller, and C. M. Rienstra. High resolution 13c-detected solid-state nmr spectroscopy of a deuterated protein. *J. Biomol. NMR*, 48(2):103–11, 2010.

R. Taylor, O. Kennard, and W. Versichel. The geometry of the n-h ... o=c hydrogen-bond .3. hydrogen-bond distances and angles. *Acta Crystallogr., Sect. B: Struct. Sci.*, 40(Jun):280–288, 1984.

Y. Tian, L. Chen, D. Niks, J. M. Kaiser, J. Lai, C. M. Rienstra, M. F. Dunn, and L. J. Mueller. J-based 3d sidechain correlation in solid-state proteins. *Phys. Chem. Chem. Phys.*, 11 (32):7078–86, 2009.

N. Tjandra and A. Bax. Large variations in c-13(alpha) chemical shift anisotropy in proteins correlate with secondary structure. *J. Am. Chem. Soc.*, 119(40):9576–9577, 1997a.

N. Tjandra and A. Bax. Solution nmr measurement of amide proton chemical shift anisotropy in n-15-enriched proteins. correlation with hydrogen bond length. *J. Am. Chem. Soc.*, 119(34):8076–8082, 1997b.

N. Tjandra and A. Bax. Direct measurement of distances and angles in biomolecules by nmr in a dilute liquid crystalline medium. *Science*, 278(5340):1111–1114, 1997c.

N. Tjandra, A. Szabo, and A. Bax. Protein backbone dynamics and n-15 chemical shift anisotropy from quantitative measurement of relaxation interference effects. *J. Am. Chem. Soc.*, 118(29):6986–6991, 1996.

M. Tollinger, A. C. Sivertsen, B. H. Meier, M. Ernst, and P. Schanda. Site-resolved measurement of microsecond-to-millisecond conformational-exchange processes in proteins by solid-state nmr spectroscopy. *J. Am. Chem. Soc.*, 134(36): 14800–14807, 2012.

J. R. Tolman, J. M. Flanagan, M. A. Kennedy, and J. H. Prestegard. Nuclear magnetic dipole interactions in field-oriented proteins - information for structure determination in solution. *Proc. Natl. Acad. Sci. U. S. A.*, 92(20):9279–9283, 1995.

J. R. Tolman, H. M. Al-Hashimi, L. E. Kay, and J. H. Prestegard. Structural and dynamic analysis of residual dipolar coupling data for proteins. *J. Am. Chem. Soc.*, 123(7):1416–1424, 2001.

D. A. Torchia and A. Szabo. Spin-lattice relaxation in solids. *J. Magn. Reson.*, 49(1):107–121, 1982.

J. Tritt-Goc. Proton dipolar coupling tensors in barium nitroprusside trihydrate. *J. Phys. Chem. Solids*, 56(7):935–942, 1995.

J. Tritt-Goc, N. Piõlewski, and U. Haeberlen. Nmr chemical shift and asymmetric dipolar tensors of water protons in sodium nitroprusside (snp). *Chem. Phys.*, 102(1,Âì2):133–140, 1986.

V. Tugarinov and L. E. Kay. Ile, leu, and val methyl assignments of the 723-residue malate synthase g using a new labeling strategy and novel nmr methods. *J. Am. Chem. Soc.*, 125 (45):13868–13878, 2003.

V. Tugarinov and L. E. Kay. An isotope labeling strategy for methyl trosy spectroscopy. *J. Biomol. NMR*, 28(2):165–172, 2004a.

V. Tugarinov and L. E. Kay. Stereospecific nmr assignments of prochiral methyls, rotameric states and dynamics of valine residues in malate synthase g. *J. Am. Chem. Soc.*, 126(31): 9827–9836, 2004b.

V. Tugarinov, R. Muhandiram, A. Ayed, and L. E. Kay. Four-dimensional nmr spectroscopy of a 723-residue protein: Chemical shift assignments and secondary structure of malate synthase g. *J. Am. Chem. Soc.*, 124(34):10025–10035, 2002.

V. Tugarinov, P. M. Hwang, J. E. Ollerenshaw, and L. E. Kay. Cross-correlated relaxation enhanced h-1-c-13 nmr spectroscopy of methyl groups in very high molecular weight proteins and protein complexes. *J. Am. Chem. Soc.*, 125(34): 10420–10428, 2003.

V. Tugarinov, W. Y. Choy, V. Y. Orekhov, and L. E. Kay. Solution nmr-derived global fold of a monomeric 82-kda enzyme. *Proc. Natl. Acad. Sci. U. S. A.*, 102(3):622–627, 2005.

V. Tugarinov, V. Kanelis, and L. E. Kay. Isotope labeling strategies for the study of high-molecular-weight proteins by solution nmr spectroscopy. *Nat. Protoc.*, 1(2):749–754, 2006.

K. Tyc and J. A. Steitz. U3, u8 and u13 comprise a new class of mammalian snrnps localized in the cell nucleolus. *EMBO J.*, 8(10):3113–3119, 1989.

R. Tycko. Molecular structure of amyloid fibrils: insights from solid-state nmr. *Q. Rev. Biophys.*, 39(1):1–55, 2006.

R. Tycko, A. Pines, and J. Guckenheimer. Fixed-point theory of iterative excitation schemes in nmr. *J. Chem. Phys.*, 83(6): 2775–2802, 1985.

B. J. van Rossum, F. Castellani, K. Rehbein, J. Pauli, and H. Oschkinat. Assignment of the nonexchanging protons of the alpha-spectrin sh3 domain by two- and three-dimensional h-1-c-13 solid-state magic-angle spinning nmr and comparison of solution and solid-state proton chemical shifts. *ChemBioChem*, 2(12):906–914, 2001.

F. J. M. Vandeven and M. E. P. Philippens. Optimization of constant-time evolution in multidimensional nmr experiments. *J. Magn. Reson.*, 97(3):637–644, 1992.

S. Ventura, J. Zurdo, S. Narayanan, M. Parreno, R. Mangues, B. Reif, F. Chiti, E. Giannoni, C. M. Dobson, F. X. Aviles, and L. Serrano. Short amino acid stretches can mediate amyloid formation in globular proteins: The src homology 3 (sh3) case. *Proc. Natl. Acad. Sci. U. S. A.*, 101(19):7258–7263, 2004.

A. R. Viguera, L. Serrano, and M. Wilmanns. Different folding transition states may result in the same native structure. *Nat. Struct. Biol.*, 3(10):874–880, 1996.

E. Vinogradov, P. K. Madhu, and S. Vega. High-resolution proton solid-state nmr spectroscopy by phase-modulated lee-goldburg experiment. *Chem. Phys. Lett.*, 314(5-6):443–450, 1999.

W. F. Vranken, W. Boucher, T. J. Stevens, R. H. Fogh, A. Pajon, M. Llinas, E. L. Ulrich, J. L. Markley, J. Ionides, and E. D. Laue. The ccpn data model for nmr spectroscopy: development of a software pipeline. *Proteins*, 59(4):687–96, 2005.

G. Vriend. What if - a molecular modeling and drug design program. *J. Mol. Graphics*, 8(1):52–&, 1990.

L. Vugmeyster, D. Ostrovsky, J. J. Ford, S. D. Burton, A. S. Lipton, G. L. Hoatson, and R. L. Vold. Probing the dynamics of a protein hydrophobic core by deuteron solid-state nuclear magnetic resonance spectroscopy. *J. Am. Chem. Soc.*, 131 (38):13651–13658, 2009.

L. Vugmeyster, D. Ostrovsky, M. Moses, J. J. Ford, A. S. Lipton, G. L. Hoatson, and R. L. Vold. Comparative dynamics of leucine methyl groups in fmoc-leucine and in a protein hydrophobic core probed by solid-state deuteron nuclear magnetic resonance over 7-324 k temperature range. *J. Phys. Chem. B*, 114(48):15799–15807, 2010.

G. W. Vuister and A. Bax. Resolution enhancement and spectral editing of uniformly c-13-enriched proteins by homonuclear broad-band c-13 decoupling. *J. Magn. Reson.*, 98(2):428–435, 1992.

G. Wagner. Characterization of the distribution of internal motions in the basic pancreatic trypsin-inhibitor using a large number of internal nmr probes. *Q. Rev. Biophys.*, 16(1):1–57, 1983.

G. Wagner, W. Braun, T. F. Havel, T. Schaumann, N. Go, and K. Wuthrich. Protein structures in solution by nuclear-magnetic-resonance and distance geometry - the polypeptide fold of the basic pancreatic trypsin-inhibitor determined using 2 different algorithms, disgeo and disman. *J. Mol. Biol.*, 196(3):611–639, 1987.

G. Wagner, S. G. Hyberts, and T. F. Havel. Nmr structure determination in solution - a critique and comparison with x-ray crystallography. *Annu. Rev. Biophys. Biomol. Struct.*, 21: 167–198, 1992.

D. Wallach. Effect of internal rotation on angular correlation functions. *J. Chem. Phys.*, 47(12):5258–&, 1967.

A. J. Wand. On the dynamic origins of allosteric activation. *Science*, 293(5534):1395, 2001a.

A. J. Wand. Dynamic activation of protein function: a view emerging from nmr spectroscopy. *Nat. Struct. Biol.*, 8(11): 926–31, 2001b.

L. Wang, S. K. Maji, M. R. Sawaya, D. Eisenberg, and R. Riek. Bacterial inclusion bodies contain amyloid-like structure. *PLoS Biol.*, 6(8):1791–1801, 2008.

Y.-S. Wang. Nmr rotating-frame relaxation measurements of conformational exchanges on the microsecond time scale. part i: Theory. *Concepts Magn. Reson.*, 4(4):327–337, 1992.

C. Wasmer, A. Lange, H. Van Melckebeke, A. B. Siemer, R. Riek, and B. H. Meier. Amyloid fibrils of the het-s(218-289) prion form a beta solenoid with a triangular hydrophobic core. *Science*, 319(5869):1523–1526, 2008.

H. Watanabe, M. Elstner, and T. Steinbrecher. Rotamer decomposition and protein dynamics: Efficiently analyzing dihedral populations from molecular dynamics. *J. Comput. Chem.*, 34(3):198–205, 2013.

D. X. Wei, U. Akbey, B. Paaske, H. Oschkinat, B. Reif, M. Bjerring, and N. C. Nielsen. Optimal h-2 rf pulses and h-2-c-13 cross-polarization methods for solid-state h-2 mas nmr of perdeuterated proteins. *J. Phys. Chem. Lett.*, 2(11):1289–1294, 2011.

N. P. Wickramasinghe, S. Parthasarathy, C. R. Jones, C. Bhardwaj, F. Long, M. Kotecha, S. Mehboob, L. W. Fung, J. Past, A. Samoson, and Y. Ishii. Nanomole-scale protein solid-state nmr by breaking intrinsic 1ht1 boundaries. *Nat. Methods*, 6 (3):215–8, 2009.

M. P. Williamson, T. F. Havel, and K. Wuthrich. Solution conformation of proteinase inhibitor-iia from bull seminal plasma by h-1 nuclear magnetic-resonance and distance geometry. *J. Mol. Biol.*, 182(2):295–315, 1985.

D. S. Wishart. Interpreting protein chemical shift data. *Prog. Nucl. Magn. Reson. Spectrosc.*, 58(1-2):62–87, 2011.

D. S. Wishart, B. D. Sykes, and F. M. Richards. Relationship between nuclear-magnetic-resonance chemical-shift and protein secondary structure. *J. Mol. Biol.*, 222(2):311–333, 1991.

R. J. Wittebort and A. Szabo. Theory of nmr relaxation in macromolecules - restricted diffusion and jump models for multiple internal rotations in amino-acid side-chains. *J. Chem. Phys.*, 69(4):1722–1736, 1978.

D. E. Woessner. Spin relaxation processes in a 2-prton system undergoing anisotropic reorientation. *J. Chem. Phys.*, 36(1): 1–&, 1962a.

D. E. Woessner. Nuclear spin relaxation in ellipsoids undergoing rotational brownian motion. *J. Chem. Phys.*, 37(3):647–&, 1962b.

C. H. Wu, A. Ramamoorthy, L. M. Gierasch, and S. J. Opella. Simultaneous characterization of the amide h-1 chemical shift,h-1-n-15 dipolar, and n-15 chemical-shift interaction tensors in a peptide-bond by 3-dimensional solid-state nmr-spectroscopy. *J. Am. Chem. Soc.*, 117(22):6148–6149, 1995.

K. Wuthrich. Nmr studies of structure and function of biological macromolecules (nobel lecture). *Angew. Chem., Int. Ed.*, 42 (29):3340–3363, 2003.

B. J. Wylie, T. Franks, D. T. Graesser, and C. M. Rienstra. Site-specific c-13 chemical shift anisotropy measurements in a uniformly n-15,c-13-labeled microcrystalline protein by 3d magic-angle spinning nmr spectroscopy. *J. Am. Chem. Soc.*, 127(34):11946–11947, 2005.

B. J. Wylie, C. D. Schwieters, E. Oldfield, and C. M. Rienstra. Protein structure refinement using c-13 alpha chemical shift tensors. *J. Am. Chem. Soc.*, 131(3):985–992, 2009.

B. J. Wylie, L. J. Sperling, A. J. Nieuwkoop, W. T. Franks, E. Oldfield, and C. M. Rienstra. Ultrahigh resolution protein structures using nmr chemical shift tensors. *Proc. Natl. Acad. Sci. U. S. A.*, 108(41):16974–16979, 2011.

J. Xu, Y. Xue, and N. R. Skrynnikov. Detection of nanosecond time scale side-chain jumps in a protein dissolved in water/glycerol solvent. *J. Biomol. NMR*, 45(1-2):57–72, 2009.

S. Xue, R. Y. Wang, F. P. Yang, R. M. Terns, M. P. Terns, X. X. Zhang, E. S. Maxwel, and H. Li. Structural basis for substrate placement by an archaeal box c/d ribonucleoprotein particle. *Mol. Cell*, 39(6):939–949, 2010.

Y. Xue, M. S. Pavlova, Y. E. Ryabov, B. Reif, and N. R. Skrynnikov. Methyl rotation barriers in proteins from h-2 relaxation data. implications for protein structure. *J. Am. Chem. Soc.*, 129(21):6827–6838, 2007.

T. Yamazaki, W. Lee, C. H. Arrowsmith, D. R. Muhandiram, and L. E. Kay. A suite of triple-resonance nmr experiments for the backbone assignment of n-15, c-13, h-2 labeled proteins with high-sensitivity. *J. Am. Chem. Soc.*, 116(26):11655–11666, 1994a.

T. Yamazaki, R. Muhandiram, and L. E. Kay. Nmr experiments for the measurement of carbon relaxation properties in highly enriched, uniformly c-13,n-15-labeled proteins - application to c-13(alpha) carbons. *J. Am. Chem. Soc.*, 116(18):8266–8278, 1994b.

D. Yang and L. E. Kay. Contributions to conformational entropy arising from bond vector fluctuations measured from nmr-derived order parameters: Application to protein folding. *J. Mol. Biol.*, 263(2):369–382, 1996a.

D. Yang and L. E. Kay. Contributions to conformational entropy arising from bond vector fluctuations measured from nmr-derived order parameters: application to protein folding. *J. Mol. Biol.*, 263(2):369–82, 1996b.

D. Yang, R. Konrat, and L. E. Kay. A multidimensional nmr experiment for measurement of the protein dihedral angle based on cross-correlated relaxation between 1h13c dipolar and 13c‘ (carbonyl) chemical shift anisotropy mechanisms. *J. Am. Chem. Soc.*, 119(49):11938–11940, 1997a.

D. Yang, Y.-K. Mok, J. D. Forman-Kay, N. A. Farrow, and L. E. Kay. Contributions to protein entropy and heat capacity from bond vector motions measured by nmr spin relaxation. *J. Mol. Biol.*, 272(5):790–804, 1997b.

D. Yang, K. H. Gardner, and L. E. Kay. A sensitive pulse scheme for measuring the backbone dihedral angle psi based on cross-correlation between (13)c (alpha)- (1)halpha dipolar and carbonyl chemical shift anisotropy relaxation interactions. *J. Biomol. NMR.*, 11(2):213–20, 1998a.

D. Yang, A. Mittermaier, Y. K. Mok, and L. E. Kay. A study of protein side-chain dynamics from new 2h auto-correlation and 13c cross-correlation nmr experiments: application to the n-terminal sh3 domain from drk. *J. Mol. Biol.*, 276(5):939–54, 1998b.

D. Yang, Y.-K. Mok, D. R. Muhandiram, J. D. Forman-Kay, and L. E. Kay. 1h13c dipoledipole cross-correlated spin relaxation as a probe of dynamics in unfolded proteins: application to the drkn sh3 domain. *J. Am. Chem. Soc.*, 121(14):3555–3556, 1999.

D. W. Yang, R. Konrat, and L. E. Kay. A multidimensional nmr experiment for measurement of the protein dihedral angle psi based on cross-correlated relaxation between (h alpha-13c alpha)-h-1 dipolar and c-13’ (carbonyl) chemical shift anisotropy mechanisms. *J. Am. Chem. Soc.*, 119(49):11938–11940, 1997c.

J. Yang, M. L. Tasayco, and T. Polenova. Dynamics of reassembled thioredoxin studied by magic angle spinning nmr: Snapshots from different time scales. *J. Am. Chem. Soc.*, 131(38):13690–13702, 2009.

L. Yao, B. Vogeli, D. A. Torchia, and A. Bax. Simultaneous nmr study of protein structure and dynamics using conservative mutagenesis. *J. Phys. Chem. B*, 112(19):6045–6056, 2008a.

L. S. Yao, B. Vogeli, J. F. Ying, and A. Bax. Nmr determination of amide n-h equilibrium bond length from concerted dipolar coupling measurements. *J. Am. Chem. Soc.*, 130(49):16518–+, 2008b.

X. L. Yao, K. Schmidt-Rohr, and M. Hong. Medium- and long-distance h-1-c-13 heteronuclear correlation nmr in solids. *J. Magn. Reson.*, 149(1):139–143, 2001.

K. Q. Ye, R. Jia, J. Z. Lin, M. H. Ju, J. Peng, A. B. Xu, and L. M. Zhang. Structural organization of box c/d rna-guided rna methyltransferase. *Proc. Natl. Acad. Sci. U. S. A.*, 106(33):13808–13813, 2009.

S. G. Zech, A. J. Wand, and A. E. McDermott. Protein structure determination by high-resolution solid-state nmr spectroscopy: application to microcrystalline ubiquitin. *J. Am. Chem. Soc.*, 127(24):8618–26, 2005.

X. Zhao, M. Eden, and M. H. Levitt. Recoupling of heteronuclear dipolar interactions in solid-state nmr using symmetry-based pulse sequences. *Chem. Phys. Lett.*, 342(3-4):353–361, 2001a.

X. Zhao, J. L. Sudmeier, W. W. Bachovchin, and M. H. Levitt. Measurement of nh bond lengths by fast magic-angle spinning solid-state nmr spectroscopy: A new method for the quantification of hydrogen bonds. *J. Am. Chem. Soc.*, 123(44):11097–11098, 2001b.

D. H. Zhou and C. M. Rienstra. High-performance solvent suppression for proton detected solid-state nmr. *J. Magn. Reson.*, 192(1):167–172, 2008.

D. H. Zhou, J. J. Shea, A. J. Nieuwkoop, W. T. Franks, B. J. Wylie, C. Mullen, D. Sandoz, and C. M. Rienstra. Solid-rate protein-structure determination with proton-detected triple-resonance 3d magic-angle-spinning nmr spectroscopy. *Angew. Chem., Int. Ed.*, 46(44):8380–8383, 2007.

G. Zhu and A. Bax. Improved linear prediction for truncated signals of known phase. *J. Magn. Reson.*, 90(2):405–410, 1990.

L. Y. Zhu, F. G. Prendergast, and M. D. Kemple. Comparison of n-15- and c-13-determined parameters of mobility in melittin. *J. Biomol. NMR*, 12(1):135–144, 1998.

E. R. P. Zuiderweg, L. P. Mcintosh, F. W. Dahlquist, and S. W. Fesik. 3-dimensional c-13-resolved proton noe spectroscopy of uniformly c-13-labeled proteins for the nmr assignment and structure determination of larger molecules. *J. Magn. Reson.*, 86(1):210–216, 1990.

C. Zwahlen, K. H. Gardner, S. P. Sarma, D. A. Horita, R. A. Byrd, and L. E. Kay. An nmr experiment for measuring methyl-methyl noes in c-13-labeled proteins with high resolution. *J. Am. Chem. Soc.*, 120(30):7617–7625, 1998.

Acknowledgements

First of all, I would like to express my deepest gratitude to my supervisor, **Prof. Dr. Bernd Reif**. Bernd, joining your group was one of the best decisions I ever made. Being around you makes it inevitable to learn from your extensive scientific competence and logical thinking, which are maybe only surmounted by your fair-mindedness, your kindness and your contagious optimism. Your continuous support and interest in my projects were absolutely decisive for my success.

Every scientist realizes at some point, that no scientific fact is really certain, however, except for the fact, that the office, I shared with **Andi**, **Tomas** and **Juan Miguel** had the most collegial and cheerful spirit on the campus. My most sincerest and heartfelt thanks goes to you guys. I will miss the old days with all of you, especially the hip hop fridays, our legendary barbecue and even though, we went through hell in Dietersheim, with you guys, any time again. And Andi, thanks a lot for reading my thesis, in spite of all the stress you had, and naming your son after me, still leaves me speechless. Also many thanks to my former colleagues **Vipin**, **Veniamin**, **Rasmus** and **Murali**.

Regarding the lab work, I thank **Kerstin Steinhagen** and, especially, **Uwe Fink**. Uwe, it took me some time to really get you, but the more I know you, the more amazed I am by your character. The expression, rough shell around a soft core, was made for you. In the lab, I benefited a lot from the wealth of your experience and I always enjoyed our discussions about music.

I thank **Dr. Barth-Jan van Rossum** for organization of the solid-state facility and his technical support at the spectrometer. Of course, I am also very grateful to **Dr. Peter Schmieder** and **Monika Beerbaum** for running the most exceptional solution-

state facility. Peter, thank you for your permanent readiness to help and your notable efficiency for solving problems at the spectrometer. I am also deeply grateful to **Dr. Frank Eisenmenger** for the maintenance of the computer cluster. Frank, thank you very much for all your effort, to keep the systems running and for always doing your best, to take care of all my special requests.

From the administrative staff, I particularly want to thank **Gabriele Schumacher**, **Alexandra Chylla**, **Andrea Steuer**, **Silvia Mauks** and **Marina Spors** for making sure, that all matters of bureaucracy proceeded smoothly and had a happy ending.

Part of the results in the present thesis emerged from several collaborations. To start chronologically, I am very thankful to **Prof. Dr. Beat H. Meier** for sharing his experience and knowledge and his remarkable facility at the ETH Zürich. I am deeply indebted to **Dr. Paul Schanda** for a very fruitful collaboration. Paul, thanks for your continuous support and your willingness to share your scientific competence, I cannot think of a better collaborator. Later on, **Kathrin Székely** joined and completed this collaboration. I am also grateful to **Gabriele Roder**, who perfectly organized my stays in Zürich. The still ongoing collaboration with **Bruker BioSpin GmbH** was of great benefit to my thesis. I want to thank **Dr. Gerhard Althoff** and, especially, **Dr. Sebastian Wegner** for their very kind and excellent technical assistance.

A fundamental factor for the success of the presented work was also the great facility provided by the Leibniz-Institut für Molekulare Pharmakologie (**FMP**) in Berlin. The herein presented research was supported by the Leibniz-Gemeinschaft, the Helmholtz-Gesellschaft, the DFG (Re 1435, SFB 449, SFB 740, SFB 1035), the Center for Integrated Protein Science Munich (CIPS-M) and the Bio-NMR project (European Commission's Framework Program 7, project number: 261863 / BIO-NMR-00010, BIO-NMR-00070).

At the end, Berlin is just one city among many, for me, its special nature, comes from special people. I am very grateful for walking out of it with friends, who made this city temporarily my home. Thank you **CiMa**, **Christine**, **Viktoria** and **Julia**. And

Maria...thanks for the motivation during these last weeks, and even though, I have hardly seen anything of Munich yet, no sight can be more sweet, more sunny and more kind.

Frankfurt will always be a unique place for me, as it combines great memories, the greatest friends and my family in one spot. **Benny**, **Sijo**, thanks guys for a gazillion laughs, for all the old stories, for taking time, whenever I visited on short notice and for always being yourselves.

Finally, I thank my **brother**, whose intriguing phantasy, creativity and intelligence brought me into science. Somehow, it is difficult to express the gratitude to your **parents**, as you owe your life to them. I will always be grateful for everything my parents did for my brother and me. I hope all their efforts and all their losses by leaving their home for us to be safe, will be somewhat compensated by this.

...thanks to all of you!

Publications

Parts of the thesis were published in the following articles:

Asami, S., Reif, B., "Proton-Detected Solid-State NMR Spectroscopy at Aliphatic Sites: Application to Crystalline Systems", *Acc. Chem. Res.*, accepted.

Asami, S., Rakwalska-Bange, M., Carlomagno, T., Reif, B., "Protein-RNA Interfaces Probed by ^{1}H-Detected MAS Solid-State NMR Spectroscopy", *Angew. Chem. Int. Ed.* **52**, 2345-2349 (2013).

Asami, S., Szekely, K., Schanda, P., Meier, B. H., Reif, B., "Optimal degree of protonation for ^{1}H detection of aliphatic sites in randomly deuterated proteins as a function of the MAS frequency", *J. Biol. NMR* **54**, 155-168 (2012).

Asami, S., Reif, B., "Assignment strategies for aliphatic protons in the solid-state in randomly protonated proteins", *J. Biol. NMR* **52**, 31-39 (2012).

Asami, S., Schmieder, P., Reif, B., "High Resolution ^{1}H-Detected Solid-State NMR Spectroscopy of Protein Aliphatic Resonances: Acces to Tertiary Structure Information", *J. Am. Chem. Soc.* **132**, 15133-15135 (2010).

Articles in preparation:

Asami, S., Reif, B., "Quantitative analysis of $^{13}C\alpha$ and ^{15}N backbone dynamics by solid-state NMR spectroscopy", *in preparation*.

Asami, S., Schanda, P., Reif, B., "Sub-μs dynamics probed by ^{1}H,^{13}C order parameters in the solid-state", *in preparation*.

Other published articles:

Lopez, J.J., Kaiser, C., **Asami, S.**, Glaubitz, C., "Higher sensitivity through selective ^{13}C excitation in solid-state NMR spectroscopy", *J. Am. Chem. Soc.* **131**, 15970-15971 (2009).

München, den 26.07.2013 Sam Asami

Eidesstattliche Erklärung

Hiermit versichere ich an Eides Statt, dass ich die hier vorliegende Dissertation eigenständig angefertigt und keine anderen, als die gemäß §6, Absatz 3 der Promotionsordnung vom 01.09.2005 angegebenen Hilfen und Hilfsmittel, verwendet habe.

Ich versichere außerdem, dass ich mich weder um einen Doktorgrad anderwärts beworben habe noch einen entsprechenden Doktorgrad besitze.

Des Weiteren bestätige ich hiermit meine Kenntnis über die dem angestrebten Promotionsverfahren zugrunde liegende Promotionsordnung vom 01.09.2005.

München, den 26.07.2013 Sam Asami